



**HAL**  
open science

# Signal injection and sensorless control of electrical motors

Pascal Combes

► **To cite this version:**

Pascal Combes. Signal injection and sensorless control of electrical motors. Automatic Control Engineering. Ecole Nationale Supérieure des Mines de Paris, 2015. English. NNT : 2015ENMP0053 . tel-01306275

**HAL Id: tel-01306275**

**<https://pastel.hal.science/tel-01306275>**

Submitted on 22 Apr 2016

**HAL** is a multi-disciplinary open access archive for the deposit and dissemination of scientific research documents, whether they are published or not. The documents may come from teaching and research institutions in France or abroad, or from public or private research centers.

L'archive ouverte pluridisciplinaire **HAL**, est destinée au dépôt et à la diffusion de documents scientifiques de niveau recherche, publiés ou non, émanant des établissements d'enseignement et de recherche français ou étrangers, des laboratoires publics ou privés.

École doctorale n°432 : Sciences et Métiers de l'Ingénieur

**Doctorat ParisTech**

**T H È S E**

pour obtenir le grade de docteur délivré par

**l'École Nationale Supérieure des Mines de Paris**

**Spécialité « Mathématique et Automatique »**

*présentée et soutenue publiquement par*

**Pascal COMBES**

le 3 décembre 2015

**Injection de signal et  
contrôle « sans capteurs » des moteurs électriques**

Directeurs de thèse : **Pierre ROUCHON** et **Philippe MARTIN**

**Jury**

**M. Carlos CANUDAS DE WIT**, Directeur de recherche, Gipsa-lab, CNRS  
**M. John CHIASSON**, Professeur, Boise State University  
**M. Alain GLUMINEAU**, Professeur, IRCCyN, École Centrale de Nantes  
**M. Mickaël HILAIRET**, Professeur, FEMTO-ST, Université de Franche-Comté  
**M. François MALRAIT**, Docteur, Schneider Electric Toshiba Inverter Europe  
**M. Philippe MARTIN**, Maître de Recherche, CAS, MINES ParisTech  
**M. Pierre ROUCHON**, Professeur, CAS, MINES ParisTech

Président  
Rapporteur  
Rapporteur  
Examineur  
Examineur  
Examineur  
Examineur

**MINES ParisTech**  
**Centre Automatique et Systèmes, Unité Mathématiques et Systèmes**  
60, boulevard Saint Michel 75272 Paris cedex 06 France

**T  
H  
È  
S  
E**



**ParisTech PhD**

**P h D T H E S I S**

to obtain the Doctor's degree from

**École Nationale Supérieure des Mines de Paris**

**Spécialité "Mathematics and Control"**

*defended in public by*

**Pascal COMBES**

on December 3rd, 2015

**Signal injection and  
"sensorless" control of electric motors**

Advisors: **Pierre ROUCHON** and **Philippe MARTIN**

**Jury**

**M. Carlos CANUDAS DE WIT**, Directeur de recherche, Gipsa-lab, CNRS

**M. John CHIASSON**, Professor, Boise State University

**M. Alain GLUMINEAU**, Professor, IRCCyN, École Centrale de Nantes

**M. Mickaël HILAIRET**, Professor, FEMTO-ST, Université de Franche-Comté

**M. François MALRAIT**, Doctor, Schneider Electric Toshiba Inverter Europe

**M. Philippe MARTIN**, Maître de Recherche, CAS, MINES ParisTech

**M. Pierre ROUCHON**, Professor, CAS, MINES ParisTech

Chair  
Referee  
Referee  
Examiner  
Examiner  
Examiner  
Examiner

**T  
H  
È  
S  
E**

**MINES ParisTech**

**Centre Automatique et Systèmes, Unité Mathématiques et Systèmes**

60, boulevard Saint Michel 75272 Paris cedex 06 France



# Remerciements

Cette thèse CIFRE a été effectuée en collaboration avec MINES ParisTech and STIE (Schneider Toshiba Inverter Europe) et a été financée par l'ANRT (Association Nationale pour la Recherche et la Technologie). Elle n'aurait pu être réalisée sans l'aide et le soutien de nombreuses personnes auxquelles j'aimerais exprimer ma profonde reconnaissance.

Je remercie mes encadrants, Pierre ROUCHON et Philippe MARTIN de MINES ParisTech, et François MALRAIT de STIE, pour le temps qu'ils ont passé à m'aider dans la réalisation de cette thèse. Par leur conseils pertinents, ils m'ont ouvert l'esprit sur de nouveaux horizons de l'automatique ou de l'électrotechnique et par leurs questions pointilleuses, ils m'ont fait voir les points flous de mon raisonnement. Sans eux, ce travail n'aurait pas été aussi innovant et cohérent.

Je souhaite exprimer ma gratitude envers Carlos CANUDAS DE WIT pour avoir accepté de présider mon jury, John CHIASSON and Alain GLUMINEAU pour avoir écrit les rapports et Mickaël HILAIRET pour avoir été membre de mon jury. Je vous remercie beaucoup de l'intérêt que vous avez montré pour mon travail.

Merci beaucoup aussi à Al Kassem JEBAI, qui a initié certaines des idées que j'ai reprises et qui m'a aidé à les comprendre. Plus généralement, je souhaiterais remercier tous les employés de STIE qui ont participé de près ou de loin au bon déroulement de cette thèse, particulièrement mes collègues de l'(ancienne) équipe DCS (Drive Control Systems) pour les discussions intéressantes ou amusantes que nous avons pu avoir. Je remercie aussi mes collègues du CAS MINES ParisTech, où j'ai beaucoup apprécié de travailler. Merci beaucoup pour les discussions enrichissantes. Je souhaite exprimer ma gratitude toute particulière au directeur du CAS, Nicolas PETIT, qui m'a aidé à trouver mon sujet de thèse, mais aussi, mon nouveau travail.

Enfin, je souhaite remercier mes parents de m'avoir donné le goût pour la science et la technologie, et plus généralement toutes les personnes qui m'ont encouragé pendant mes études. Je voudrais tout particulièrement remercier mon frère qui a relu ce long manuscrit. Merci beaucoup à mes amis d'avoir saturé, au sens propre comme au sens figuré, mon pauvre téléphone portable avec des messages d'encouragement la veille de ma soutenance de thèse.

Au cours de ma thèse, j'ai utilisé les logiciels open-source suivants

- FreeFileSync pour sauvegarder régulièrement mon travail
- $\text{T}_{\text{E}}\text{X}$  et  $\text{L}_{\text{A}}\text{T}_{\text{E}}\text{X}$ , distribués par  $\text{M}_{\text{I}}\text{K}_{\text{T}}\text{E}_{\text{X}}$ , pour écrire ce manuscrit et plusieurs autres documents et présentations
- $\text{T}_{\text{E}}\text{X}$ studio, un éditeur  $\text{L}_{\text{A}}\text{T}_{\text{E}}\text{X}$  très prometteur, utilisable et utile malgré l'absence de quelques fonctionnalités et d'une parfaite stabilité
- Un script inspiré de `bibulous.py` pour générer la bibliographie avec des modèles simples, au contraire de ceux utilisés par `bibTEX`

- JabRef pour gérer ma bibliographie
- MSYS2 parce que les merveilleux utilitaires GNU me manquent quand je travaille sous Windows
- Notepad++, un très bon éditeur pour des fichiers texte.

Je suis très reconnaissant envers les équipes de bénévoles qui ont développé ces logiciels et je les encourage à continuer leur travail fantastique.

# Acknowledgments

This thesis was part of a collaboration between MINES ParisTech and STIE (Schneider Toshiba Inverter Europe) and was supported by ANRT (Association Nationale pour la Recherche et la Technologie), the French governmental organization promoting scientific research. It could not have been carried out without the help of many people I would like to thank now.

I would like to express my gratitude to my advisors Pierre ROUCHON et Philippe MARTIN from MINES ParisTech, and François MALRAIT from STIE for the time they spent helping me realize this thesis. Their valuable advice widened my knowledge of the control and electro-technical fields and their punctilious questions highlighted the unclear points in my reasoning. Without them this work would not have been so innovative and consistent.

I am grateful to Carlos CANUDAS DE WIT for having accepted to be the chairman of the jury, to John CHIASSON and Alain GLUMINEAU for being the referees and to Mickaël HILAIRET for taking part in the jury. I thank you for your interest in my ideas.

I am thankful to Al Kassem JEBAI, who initiated some ideas I developed in this work, for helping me understand them. More generally I thank all the people from STIE, who took part directly or indirectly in the realization of this work, especially my colleagues of the (ex) DCS (Drive Control Systems) team for the interesting or funny discussions. I also want to thank my colleagues from the CAS MINES ParisTech, where I also enjoyed working. Thank you so much for the enriching discussions we had. I'm particularly grateful to the head of CAS, Nicolas PETIT, for helping me find not only my thesis subject, but also the job after.

Last but not least I would like to express my gratitude to my parents, who gave me the taste for science and technology, and more generally to all people, who encouraged me. In particular I would like to thank my brother who proofread this quite long manuscript. Many thanks to my friends for overflowing my poor cellular phone with messages of encouragement on the day before my PhD defence.

To realize this thesis I used a lot of open-source software, namely

- FreeFileSync to efficiently manage my backups
- $\text{\TeX}$  and  $\text{\LaTeX}$  from  $\text{\MiKTeX}$  to write this manuscript and many other documents and presentations
- $\text{\TeX}$ studio, a very promising editor for  $\text{\LaTeX}$  documents, still lacking some features and not totally stable, none the less usable and handy
- A hack of `bibulous.py` to generate the bibliography using simpler templates than those of `bibTeX`
- JabRef to manage the bibliography

- MSYS2 because I miss the very useful GNU utilities when I'm working on Windows
- Notepad++ as a wonderful editor for text files.

I'm very liable to the teams which developed these programs and I encourage them to continue doing such a great work.

# Contents

<b>Remerciements</b>	<b>v</b>
<b>Acknowledgments</b>	<b>vii</b>
<b>Contents</b>	<b>ix</b>
<b>Notations</b>	<b>xiii</b>
<b>Introduction (version française)</b>	<b>xix</b>
<b>Introduction</b>	<b>xxi</b>
<b>1 Scientific and industrial context</b>	<b>1</b>
1.1 Electric motors . . . . .	1
1.1.1 The synchronous reluctance motor (SynRM) . . . . .	2
1.1.2 The permanent magnet synchronous motor (PMSM) . . . . .	3
1.1.3 The induction motor (IM) . . . . .	4
1.1.4 Comparison of electric motors . . . . .	5
1.1.5 Applications of electric motors . . . . .	6
1.2 Electric motor control . . . . .	6
1.2.1 Need for control . . . . .	6
1.2.2 Variable Speed Drives (VSDs) . . . . .	7
1.2.3 “U/f” control laws . . . . .	7
1.2.4 “Sensored” control laws . . . . .	8
1.2.5 “Sensorless” control laws . . . . .	8
1.3 Signal injection . . . . .	9
<b>2 Experimental facilities and related problems</b>	<b>11</b>
2.1 Motors . . . . .	11
2.1.1 Synchronous reluctance motor . . . . .	11
2.1.2 Induction motor . . . . .	12
2.2 The dSpace test bench . . . . .	12
2.2.1 The inverter . . . . .	13
2.2.2 dSpace solution . . . . .	15
2.2.3 The current sensors . . . . .	17
2.2.4 The torque-meter . . . . .	17
2.2.5 The encoder . . . . .	17
2.2.6 The load machine . . . . .	18
2.3 Experimental problems . . . . .	19

2.3.1	Inverter voltage drops . . . . .	19
2.3.2	Dead times . . . . .	24
2.3.3	Load machine harmonics . . . . .	25
<b>3</b>	<b>Energy-based modeling of electric machines</b>	<b>29</b>
3.1	Preliminaries: Electric motor modeling . . . . .	29
3.1.1	Traditional microscopic approach . . . . .	29
3.1.2	Macroscopic approach . . . . .	30
3.2	Energy-based modeling for 3 phase electric motors . . . . .	30
3.2.1	Lagrangian modeling . . . . .	31
3.2.2	Hamiltonian modeling . . . . .	31
3.2.3	Using complex state variables . . . . .	32
3.2.4	Application of energy-based modeling to electric machines . . . . .	33
3.3	Frame changes . . . . .	36
3.3.1	Transformations . . . . .	36
3.3.2	Frame orthonormalization . . . . .	37
3.3.3	Synchronous frame . . . . .	38
3.3.4	Rotor-oriented frame . . . . .	40
3.4	Symmetries . . . . .	42
3.4.1	Symmetries due to stator layout . . . . .	44
3.4.2	Symmetries due to rotor layout . . . . .	46
3.5	Connection to the grid . . . . .	50
3.5.1	Connection scheme for the rotor windings . . . . .	52
3.5.2	Rotor without windings . . . . .	53
3.5.3	Star-connected electric machines . . . . .	54
3.5.4	Delta-connected electric machines . . . . .	55
3.6	Unsaturated sinusoidal case . . . . .	56
3.6.1	For the universal electric motor . . . . .	56
3.6.2	For the IM . . . . .	58
3.6.3	For the PMSM . . . . .	59
3.6.4	For the SynRM . . . . .	61
3.7	Non-sinusoidal motor model . . . . .	61
3.7.1	In the general case . . . . .	64
3.7.2	For the IM . . . . .	65
3.7.3	For the PMSM . . . . .	66
3.7.4	For the SynRM . . . . .	67
3.7.5	Experimental results . . . . .	68
3.8	Saturated sinusoidal motor model . . . . .	68
3.8.1	About saliency . . . . .	71
3.8.2	Chord and tangent inductances . . . . .	75
3.9	Partial conclusion . . . . .	77
<b>4</b>	<b>Low-speed observability issues</b>	<b>79</b>
4.1	Low speed observability issues . . . . .	79
4.1.1	Bibliography . . . . .	80
4.1.2	Steady-state trajectory . . . . .	80
4.1.3	Model . . . . .	80
4.1.4	Linear observability . . . . .	82
4.1.5	Nonlinear observability . . . . .	88

4.2	High frequency injection effects . . . . .	93
4.2.1	Bibliography on signal injection . . . . .	94
4.2.2	High-frequency injection . . . . .	94
4.2.3	Second order averaging . . . . .	95
4.2.4	Using lower frequencies . . . . .	97
4.3	Obtaining virtual measurements by HF injection . . . . .	100
4.3.1	Second-order averaging for exponentially stable systems . . . . .	100
4.3.2	Signal injection for nonlinear systems . . . . .	102
4.3.3	Extracting the measurements . . . . .	105
4.4	State estimator using high frequency injection . . . . .	108
4.4.1	Flux estimator . . . . .	108
4.4.2	Full state estimator . . . . .	110
4.5	Partial conclusion . . . . .	112
<b>5</b>	<b>Identification of the magnetic models</b>	<b>115</b>
5.1	Preliminaries: Existing models for electric motors . . . . .	115
5.1.1	Saturation models for SynRMs . . . . .	115
5.1.2	Saturation models for IMs . . . . .	116
5.1.3	Saturated energy-based models for electric motors . . . . .	117
5.2	A saturated SynRM model . . . . .	118
5.2.1	Using HF injection . . . . .	118
5.2.2	Using the Inform method . . . . .	126
5.2.3	A saturated model for the SRM . . . . .	127
5.2.4	Conclusion . . . . .	129
5.3	A saturated IM model . . . . .	130
5.3.1	Zero load tests . . . . .	131
5.3.2	Hysteresis . . . . .	134
5.3.3	A model for zero load test results . . . . .	138
5.3.4	Tests with load . . . . .	140
5.3.5	Modeling tentatives . . . . .	142
5.3.6	Conclusion . . . . .	157
<b>6</b>	<b>“Sensorless” motor control at medium and high speed</b>	<b>159</b>
6.1	A control law for the SynRM . . . . .	159
6.1.1	Preliminary: Existing control laws . . . . .	160
6.1.2	SynRM model . . . . .	160
6.1.3	Control law description . . . . .	161
6.1.4	Stability of the control law . . . . .	165
6.1.5	Torque limitation . . . . .	170
6.1.6	Optimal flux working point . . . . .	173
6.1.7	Simulation results . . . . .	174
6.2	Generalisation to the PMSM . . . . .	178
6.2.1	Estimation of the saliency frame . . . . .	178
6.2.2	Torque limitation . . . . .	179
6.2.3	Optimal flux working point . . . . .	182
6.2.4	Simulation results . . . . .	185
6.3	Partial conclusion . . . . .	185

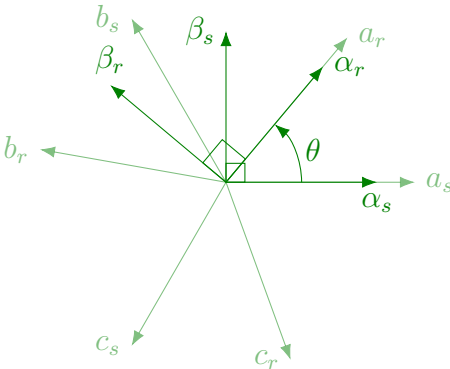
<b>7</b>	<b>“Sensorless” low speed motor control</b>	<b>187</b>
7.1	Using high frequency injection for control . . . . .	187
7.1.1	High frequency injection in closed loop . . . . .	188
7.1.2	A flux ripple observer . . . . .	189
7.1.3	Extracting the information from the current ripple . . . . .	192
7.2	IM low speed “sensorless” control . . . . .	195
7.2.1	Bibliography . . . . .	195
7.2.2	Observing the rotor flux angle . . . . .	196
7.2.3	A control law using the rotor flux angle . . . . .	197
7.2.4	Using HF injection for low speed “sensorless” control . . . . .	199
7.3	Partial conclusion . . . . .	200
	<b>Conclusion</b>	<b>201</b>
	<b>Bibliography</b>	<b>203</b>

# Notations

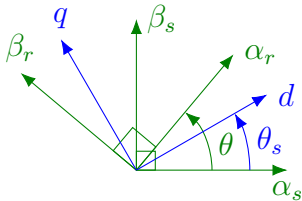
In this section we give a sorted list of the notations employed throughout this document. We do not intend here to give an exhaustive list of all the notations used at some point in this document but only of notations which are employed throughout the document so that the reader can refer to this list to retrieve a notation he forgot.

## Frames

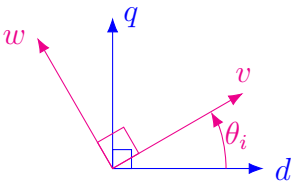
Below are defined frames where vector variables are expressed in this document.



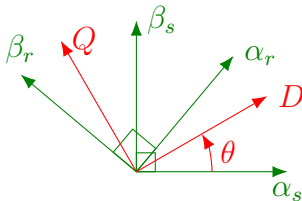
(a) Physical frames  $abc$  linked to stator and rotor and corresponding  $\alpha\beta$  frames.



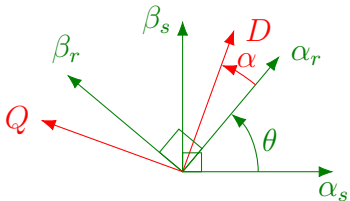
(b) Definition of  $dq$  frame with respect to stator  $\alpha\beta$  frame.



(c) Definition of injection  $vw$  frame with respect to  $dq$  frame.



(d) Definition of  $DQ$  frame with respect to rotor  $\alpha\beta$  frame for geometrically salient motors.



(e) Definition of  $DQ$  frame with respect to rotor  $\alpha\beta$  frame for geometrically non salient motors.  $\alpha$  is the angle of the rotor flux in rotor  $\alpha\beta$  frame.

## Scalar variables

Hereafter are listed the scalar variable notations employed throughout this document.

### Angles

Hereafter are defined the angles used throughout this document. They relate the positions of the frames with respect to one another.

$\theta_m$	Mechanical angle of the rotor
$\theta$	Electrical angle of the rotor
$\theta_s$	Angle of $dq$ frame with respect to stator $\alpha\beta$ frame
$\theta_i$	Angle of injection frame $vw$ with respect to $DQ$ frame

### Angular speeds

The aforementioned angles are linked to the corresponding speeds defined below.

$\omega_m := \dot{\theta}_m$	Mechanical angular speed of the rotor
$\omega := \dot{\theta}$	Electrical angular speed of the rotor
$\omega_s := \dot{\theta}_s$	Angular speed of electrical variables
$\omega_g := \omega_s - \omega$	Slip speed.
$\omega_i := \dot{\theta}_i$	Angular speed of injection with respect to $DQ$ frame

### Mechanical variables

$\rho$	Electrical kinetic momentum
$T_e$	Electromagnetic torque
$T_L$	Load torque

### Motor parameters

$R_s$	Stator resistance
$R_r$	Rotor resistance
$n$	Number of stator pole pairs
$J_L$	Inertia of the load

## Vector variables

Hereafter are listed the vector variable notations employed throughout this document and the related conventions.

### Convention

Throughout this document, space vector representation of electrical values will be extensively used. The vector  $x$  expressed in the frame  $uvw$  will be denoted  $x^{uvw} = (x^u, x^v, x^w)^T$ . The same convention  $f^{uvw}$  will be used for scalar functions of vectors to underline the fact that they are expressed using variables in a given frame. The gradient of  $f^{uvw}$  with respect to  $x^{uvw}$  will be noted  $\frac{\partial f^{uvw}}{\partial x^{uvw}} = \left( \frac{\partial f^{uvw}}{\partial x^u}, \frac{\partial f^{uvw}}{\partial x^v}, \frac{\partial f^{uvw}}{\partial x^w} \right)^T$ ; to be consistent when  $f^{uvw}$  is

a vector function  $\frac{\partial f^{uvw}}{\partial x^{uvw}}$  is the transpose of its Jacobian matrix and for scalar functions

$$\frac{\partial^2 f^{uvw}}{\partial x^{uvw} \partial y^{uvw}} = \begin{pmatrix} \frac{\partial^2 f^{uvw}}{\partial x^u \partial y^u} & \frac{\partial^2 f^{uvw}}{\partial x^u \partial y^v} & \frac{\partial^2 f^{uvw}}{\partial x^u \partial y^w} \\ \frac{\partial^2 f^{uvw}}{\partial x^v \partial y^u} & \frac{\partial^2 f^{uvw}}{\partial x^v \partial y^v} & \frac{\partial^2 f^{uvw}}{\partial x^v \partial y^w} \\ \frac{\partial^2 f^{uvw}}{\partial x^w \partial y^u} & \frac{\partial^2 f^{uvw}}{\partial x^w \partial y^v} & \frac{\partial^2 f^{uvw}}{\partial x^w \partial y^w} \end{pmatrix} = \left( \frac{\partial^2 f^{uvw}}{\partial y^{uvw} \partial x^{uvw}} \right)^T.$$

## Variables

These vector variables will be expressed in one of the frames following the above conventions.

$u_s$	Vector of voltage drops at the bounds of stator windings
$i_s$	Vector of currents in stator windings
$i_r$	Vector of currents in rotor windings
$\phi_s$	Vector of stator flux (linkages)
$\phi_r$	Vector of rotor flux (linkages)
$\varphi_r := \frac{L_m}{L_r} \phi_r$	Vector of equivalent rotor flux on stator

## Equivalence with complex numbers

The two dimensional vector  $x^{uv} = (x^u, x^v)^T$  can be equivalently represented by the scalar complex number  $\underline{x}^{uv} = x^u + jx^v$ . The real values can be recovered by

$$x^u = \Re(\underline{x}^{uv}) = \frac{\underline{x}^{uv} + \underline{x}^{uv*}}{2}$$

$$x^v = \Im(\underline{x}^{uv}) = \frac{\underline{x}^{uv} - \underline{x}^{uv*}}{2j}.$$

Using this convention, the two-dimensional real-valued system

$$\frac{dx^{uv}}{dt} = Ax^{uv} \quad \text{with } A = \begin{pmatrix} a & b \\ c & d \end{pmatrix}$$

can be conveyed using complex variables under the scalar form

$$\frac{d\underline{x}^{uv}}{dt} = \left( \frac{a+d}{2} + j\frac{c-b}{2} \right) \underline{x}^{uv} + \left( \frac{a-d}{2} + j\frac{c+b}{2} \right) \underline{x}^{uv*}.$$

This is equivalent to decompose the matrix  $A \in \mathcal{M}_2(\mathbb{R})$  on the orthogonal basis

$$I_2 = \begin{pmatrix} 1 & 0 \\ 0 & 1 \end{pmatrix} \quad \mathcal{J}_2 = \begin{pmatrix} 0 & -1 \\ 1 & 0 \end{pmatrix} \quad Z = \begin{pmatrix} 1 & 0 \\ 0 & -1 \end{pmatrix} \quad Y = \begin{pmatrix} 0 & 1 \\ 1 & 0 \end{pmatrix}.$$

which is orthogonal with respect to the Frobenius scalar product on the 2x2 real matrix vector space  $\mathcal{M}_n(\mathbb{R})$

$$\langle A|B \rangle = \text{tr}(A^T B) = \text{tr}(B^T A) = \sum_{j=1}^n \sum_{i=1}^n A_{i,j} B_{i,j}.$$

Moreover, as  $I_2$ ,  $Z$  and  $Y$  are symmetric, they define an orthogonal basis of  $\mathcal{S}_2(\mathbb{R})$ , the vector space of 2x2 real symmetric matrices.

## Energy functions

Here are the energy function which are used throughout this manuscript. They will be associated to a superscript to denote the frame in which the electrical vector state variables are expressed. When a subscript is used, it demotes a constraint due to the connection scheme.

$\mathcal{L}$	Lagrangian function
$\mathcal{H}$	Hamiltonian function

## Inductances matrices

These matrices link the fluxes to the currents. Depending on the frame in which these variables are expressed, the expression of the inductances matrix will change, as they do not always commute with the transformation matrices from one frame to another. So the frame is demoted in superscript. Additional subscripts  $m$ ,  $s$  and  $r$  denotes mutual, stator self, rotor self inductances respectively.

$L$	Inductance matrix (link currents to fluxes)
$L^c$	Chord inductance matrix
$L^t$	Tangent inductance matrix
$\Gamma$	Inverse inductance matrix (link fluxes to currents)
$\Gamma_c$	Chord inverse inductance matrix
$\Gamma_t$	Tangent inverse inductance matrix

## Types of variables

Additional superscripts and accents are used to denote the type of the variables

$\underline{x}$	Complex representation of $x$ , vector of $\mathbb{R}^2$ (space vector)
$\bar{x}$	Low frequency value of $x$
$\tilde{x}$	High frequency amplitude of $x$
$x^{nom}$	Nominal value of $x$
$x_e$	Value of the variable $x$ at the considered equilibrium
$\delta x := x - x_e$	Variable $x$ linearized near an equilibrium
$x^r$	Reference value of $x$
$x^f$	Filtered reference value of $x$
$x^m$	Measured value of $x$
$\hat{x}$	Observed/estimated value of $x$
$\Delta x$	Error on variable $x$
$x^l$	Maximum value of variable $x$
$x^s$	Saturated reference for variable $x$
$x^i$	Integral state on variable $x$

## Operators on variables

$x^T$	Transpose of vector or matrix $x$
$x^{-T} := (x^T)^{-1} = (x^{-1})^T$	Inverse transpose of square matrix $x$
$\Re(x)$	Real part of complex number $x$
$\Im(x)$	Imaginary part of complex number $x$
$x^*$	Conjugate of complex scalar, vector or matrix $x$
$x^\dagger := (x^*)^T = (x^T)^*$	Conjugate of transpose of complex vector or matrix $x$
$ x $	Absolute value of real or modulus of complex
$\ x\ $	Norm of vector $x$
$\langle x y \rangle$	Scalar product of vectors $x$ and $y$



# Introduction (version française)

Depuis le XIX<sup>e</sup> siècle, les moteurs électriques ont été largement utilisés dans l'industrie et les transports. Cependant, on les connectait autrefois directement au réseau électrique, alors qu'actuellement on passe de plus en plus par des variateurs de vitesse. Ils permettent de mieux contrôler le point de fonctionnement et, par conséquent, de choisir ceux pour lesquels le rendement est le meilleur, ce qui devient aujourd'hui de plus en plus important à cause de la forte hausse du prix de l'énergie. D'un autre côté, grâce aux progrès faits en électronique, la puissance de calcul devient de moins en moins chère, ce qui permet aux fabricants de variateurs de vitesse d'embarquer des algorithmes de contrôle de plus en plus puissants avec un nombre accru de fonctionnalités. Ainsi, en plus de la simple loi de contrôle  $U/f$ , qui permet seulement de lisser le courant pendant les transitoires, on propose aujourd'hui les lois de contrôle « sans capteur », qui peuvent contrôler avec un bon rendement la vitesse et le couple des moteurs électriques, même si seuls les courants stator sont mesurés.

D'un point de vue industriel, les lois de contrôle « sans capteur » sont intéressantes car elles diminuent les coûts et simplifient la mise en œuvre des moteurs électriques. Cependant, elles ont pour le moment l'inconvénient majeur de ne pas être utilisables à basse vitesse, car l'observabilité des machines électriques dégénère. L'injection de signal haute-fréquence est la solution la plus prometteuse pour palier ce problème, mais ces effets ne sont pas très bien compris jusqu'à maintenant.

L'étude du contrôle « sans capteur » des moteurs électriques et l'injection de signal seront par conséquent l'objet de cette thèse de doctorat, qui a été financée par l'ANRT (Association Nationale pour la Recherche et la Technologie) et s'est déroulée au sein d'une collaboration entre le CAS MINES ParisTech et STIE (Schneider Toshiba Inverter Europe). STIE est l'un des principaux fabricants de variateurs de vitesse. Le travail fait pendant la préparation de cette thèse est résumé dans ce document dont l'organisation est détaillée ci-dessous.

**Dans le chapitre 1** La présentation du contexte industriel et scientifique, esquissée ici, est détaillée.

**Dans le chapitre 2** Les dispositifs expérimentaux fournis par SITE sont décrits ainsi que les problèmes rencontrés en les utilisant.

**Dans le chapitre 3** Une nouvelle approche pour la modélisation des machines électriques est présentée, parce que les effets de l'injection de signal ne peuvent pas être expliqués de façon satisfaisante par le traditionnel modèle sinusoïdal non-saturé. Cette approche permet de modéliser un moteur électrique par une seule fonction scalaire et justifie la modélisation de la saturation dans les repères fictifs, ce qui a toujours été admis mais jamais prouvé à notre connaissance.

**Dans le chapitre 4** L’observabilité des moteurs sinusoïdaux saturés est étudiée en utilisant la nouvelle approche pour la modélisation. On montre ainsi que l’injection de signal haute-fréquence est une solution à la perte d’observabilité à basse vitesse. En effet, l’injection de signal peut être vue comme un moyen d’obtenir des mesures supplémentaires, qui pourront être utilisées pour retrouver les flux ou la vitesse de rotation avec un observateur.

**Dans le chapitre 5** La fonction d’énergie modélisant un moteur synchrone à reluctance réel et un moteur à induction réel est recherché. Il est simple de trouver un modèle pour le moteur synchrone à reluctance et un modèle satisfaisant est proposé. Au contraire, il est beaucoup plus compliqué de trouver le modèle d’un moteur à induction, car les courants et flux rotor ne peuvent pas être mesurés, et malheureusement aucun modèle satisfaisant n’a pu être trouvé.

**Dans le chapitre 6** Une loi de contrôle « sans capteur » pour le moteur synchrone à reluctance est décrite et sa stabilité, prouvée. Grâce aux similarités entre les moteurs synchrones à reluctance et à aimants permanents, qui sont soulignées par la méthode de modélisation proposée, la loi contrôle peut être étendue avec des changements mineurs à ces derniers.

**Dans le chapitre 7** Le contrôle « sans capteur » des moteurs à induction est abordé et les limitations de l’approche traditionnelle sont soulignées. En effet, dans certains cas, l’approche traditionnelle de l’injection de signal peut ne donner aucune information.

Les contributions majeures de cette thèse de doctorat sont

**Modélisation des machines électriques** Grâce à l’approche proposée dans ce manuscrit, la modélisation magnétique dans des repères fictifs est justifiée. De plus, les modèles basés sur l’énergie peuvent être conçus sans connaître les détails de construction du moteur électrique considéré.

**Analyse de l’injection de signal** L’injection de signal, replacée dans un contexte général, s’avère être un moyen d’assurer l’observabilité non-linéaire et peut être vue comme une méthode pour ajouter de nouvelles mesures virtuelles à un système. Ce résultat amène des explications plus simples et plus claires du contrôle sans capteur pour les moteurs électriques.

Quelques uns des résultats présentés ici ont été publiés dans

- [1] A. Jebai, P. Combes, F. Malrait, P. Martin, and P. Rouchon, « Energy-based modeling of electric motors », *IEEE 53rd Annual Conference on Decision and Control (CDC)*, pp. 6009–6016 (2014).
- [12] P. Combes, A. Jebai, F. Malrait, P. Martin, and P. Rouchon, « Adding virtual measurements by HF signal injection », soumis à *American Control Conference (ACC)*, (2016).

# Introduction

Electric motors have widely been used in the industry and transportation since the XIX<sup>th</sup> century. However, they used to be connected directly to the grid, whereas they are now more and more driven by Variable Speed Drives (VSDs). It allows more control on the working point of the electric motor; consequently the most efficient ones can be selected, which is more and more considered nowadays, due to the substantial increase in energy price. Besides, thanks to the progress done in electronics, computational power is less and less expensive, which enables drive manufacturers to embed control algorithms with more and more capabilities and functionalities. Thus, we went from the basic U/f control law, which allows only to smoothen current transients, to so-called “sensorless” control laws, which can efficiently control the speed or torque of electric motors, even though only the currents are measured.

“Sensorless” control is very interesting from an industrial point of view, as it decreases the costs and facilitates implementation of electric motors. However, they currently have a major drawback: they are not usable at low speed, as observability of electric motors degenerates. High frequency injection is the most promising solution to this problem, but its effects are not very well understood until now.

This PhD thesis is thus devoted to the study of “sensorless” control for electric motors and high frequency signal injection. It is funded by French ANRT (Association Nationale pour la Recherche et la Technologie) and supported by a collaboration between CAS MINES ParisTech and STIE (Schneider Toshiba Inverter Europe). STIE is one of the world leaders in electric motor drives manufacturing. A comprehensive summary of the work done is given in this document, which is organized as follows.

**In chapter 1** The presentation of the industrial and scientific context, sketched here, is detailed.

**In chapter 2** The experimental facilities, provided by STIE, are described. The related problems we encountered when acquiring experimental data, are also mentioned.

**In chapter 3** A new framework for electric machine modeling is presented, because the effects of signal injection cannot be satisfactorily explained with the traditional unsaturated sinusoidal model. Thanks to this modeling framework, any electric motor can be described by one scalar energy function. This approach additionally justifies the design of saturation models for electric machines in non physical frames, which has always been taken at granted but was never proven to our knowledge.

**In chapter 4** Using the new modeling approach, the observability of saturated sinusoidal motors is studied, which shows that high frequency signal injection is a solution to avoid loss of observability at low speed. Indeed, signal injection can be seen as a way to get additional virtual measurements, which can then be used to estimate the fluxes or the rotor speed with an observer.

**In chapter 5** The right energy function to model a real Synchronous Reluctance Motor and a real Induction Machine, is searched. For Synchronous Reluctance Motor finding the saturated model is simple and a satisfactory model is proposed. On the opposite, the IM case is much more difficult, as the rotor currents and fluxes cannot be measured, and no satisfactory model was found.

**In chapter 6** A “sensorless” control law for the Synchronous Reluctance Motor at rated and high speed is described and its stability is proven. Thanks to the similarities between Permanent Magnet Synchronous Motors and Synchronous Reluctance Motors, underlined by energy-based modeling, the control law can easily be extended to those motors.

**In chapter 7** Low speed “sensorless” induction motor control using signal injection is considered and the limitations of the traditional approach are highlighted. Indeed, the usual processing of motor response to signal injection may not lead to any information in some cases.

The major contributions of this thesis are

**Electric machine modeling** Thanks to the proposed framework for electric motor modeling, the design of magnetic models in non-physical frames is justified. Moreover, energy-based models can be designed without knowing the details of the motor internal layout;

**Analysis of signal injection** Signal injection is replaced in a general context. It shows that signal injection is a mean of ensuring a nonlinear observability criterion and can be seen as a way to add virtual measurements to a system. This result leads to simpler and clearer explanations for the low speed “sensorless” control of electric motors.

Some of the results presented here were published in

- [1] A. Jebai, P. Combes, F. Malrait, P. Martin, and P. Rouchon, “Energy-based modeling of electric motors”, *IEEE 53rd Annual Conference on Decision and Control (CDC)*, pp. 6009–6016 (2014).
- [12] P. Combes, A. Jebai, F. Malrait, P. Martin, and P. Rouchon, “Adding virtual measurements by HF signal injection”, submitted to *American Control Conference (ACC)*, (2016).

# Chapter 1

## Scientific and industrial context

### Chapitre 1 — Contexte scientifique et industriel

*Ce chapitre détaille la présentation du contexte industriel, technique et scientifique esquissée en introduction. Il présente les défis liés à l'utilisation des moteurs électriques dans l'industrie et les transports. En ce qui concerne leur contrôle, plusieurs possibilités existent : Le contrôle  $U/f$ , le contrôle vectoriel avec capteur de vitesse et le contrôle vectoriel « sans capteur » (de vitesse). C'est cette dernière possibilité qui pose un problème théorique. En effet, à cause de la perte d'observabilité des machines électriques à basse vitesse, le comportement des lois de contrôle dans ce domaine n'est pas satisfaisant. L'injection de signal, évoquée à la fin de ce chapitre, est une méthode prometteuse pour contourner ce problème.*

As was said in the introduction we will study in this document electric motor control. From an industrial point of view this is a very challenging and profitable field where there still exist open scientific questions as will be shown in this chapter.

We first present in section 1.1 the electric motors which will be studied in this document. Then we show in section 1.2 how these machines are controlled and what are the limitations of modern control laws. Signal injection, the method presented in section 1.3, is the most widespread technique to solve the key challenge of the so-called “sensorless” control of electric motors at low speed.

### 1.1 Electric motors

Electric machines are devices which convert energy between mechanical and electrical forms. Electric generators transform mechanical energy into electrical energy. On the opposite, electric motors are devices which convert electrical energy into mechanical energy. As these devices are similarly built, some of the results we obtain can be applied to both types of machines. We thus use the word “machine”, even though we focus on electric motors. As most of them are rotational electric motors, that is to say devices which convert electrical energy into rotational mechanical energy, we consider only them in this manuscript and they will be called simply electric motors. Nevertheless the reader should know that there exist linear electric motors (see [23, sec. 2.7] or [34, sec. 2.2] for instance), transforming electrical energy into translative mechanical energy, which are seldom used even when translative mechanical energy is needed. Rotational electric machines have 2 main mechanical parts: the rotor which rotates and transmits mechanical energy to the load and the stator which is fixed and receives the electrical power from the grid.



(a) Photograph of the SynRM (b) Photograph of a PMSM. (c) Photograph of the IM used in tests.

Figure 1.1 – Photographs of the three main kinds of AC rotating electric motors.

Electric motors can be powered by AC or DC electric networks. AC networks can have any number of phases, the most widespread being the mono-phase and the three-phase networks which can power mono-phase and three-phase electric motors. In this manuscript we will focus only on three-phase AC electric motors and thus often omit the qualification of three-phase AC. We will particularly be interested by

- The Synchronous Reluctance Motor (SynRM) described in section 1.1.1
- The Permanent Magnet Synchronous Motor (PMSM) described in section 1.1.2
- The Induction machine (IM) also known as the asynchronous motor described in section 1.1.3

which are the three most widespread kind of AC electric motors.

But before describing how these electric motors are built we shall make the following remark. The descriptions proposed hereafter are the descriptions of one pole pitch of an electric machine. For a one-pole-pair electric motor this will be the design of the whole machine, however for a two-pole-pair motor this will be the design of one half of the machine, the other half having exactly the same design and so on for higher number  $n$  of pole pairs. This artifact allows to build electric motors yielding a torque multiplied by  $n$  and rotating at a speed divided by  $n$  under the same currents and voltages, which often allows to use smaller mechanical speed reducers.

### 1.1.1 The synchronous reluctance motor (SynRM)

Here is briefly described the construction and operating principles of SynRMs. More details can be found in Sul [23, pp. 55;144–145].

#### 1.1.1.1 Construction

Like most of three-phase AC electric motors the stator of the SynRM supports three electrical windings. These windings are connected to the phases of the grid and are designed by the letters  $a$ ,  $b$  and  $c$ . When powered, an electrical winding creates a magnetic dipole whose magnetic poles are denoted as  $a$  and  $a'$  for the winding  $a$  and so on. The electrical windings are arranged so that the magnetic poles are equally spread around the periphery of the stator in the order:  $a$ ,  $c'$ ,  $b$ ,  $a'$ ,  $c$ ,  $b'$ .

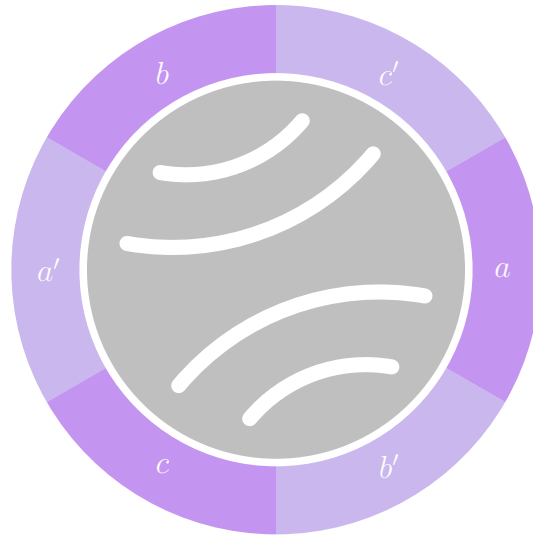


Figure 1.2 – Schematic transverse representation of a three-phase one-pole-pair SynRM

The rotor of the SynRM is built of a laminated ferro-magnetic material in which magnetic barriers are set. This special design creates paths which are favored by the magnetic flux and consequently tend to align with it.

Fig. 1.1a is the photograph of the SynRM which was used for the tests and fig. 1.2 presents a schematic two-dimensional representation of the internal layout of a one-pole-pair SynRM.

### 1.1.1.2 Principle of operation

When the stator is connected to a three-phase balanced electrical power source the currents circulating in the three stator windings create a rotating magnetic field. When this magnetic field crosses the rotor it will follow the aforementioned magnetic paths and the rotor will tend to align with the magnetic flux, thus creating a torque. If it is strong enough, this torque rotates the rotor at the speed of the stator flux. This is the reason why this motor is qualified as synchronous.

## 1.1.2 The permanent magnet synchronous motor (PMSM)

We recall the internal layout of PMSM which can also be found in Chiasson [45, sec. 6.10] or Sul [23, sec. 3.3.3].

### 1.1.2.1 Construction

PMSM stators are built exactly as SyRM stators. However the rotor contains a permanent magnet which can be buried inside the rotor core in the case of the Internal Permanent Magnet (IPM) PMSM or fixed on its surface in the case of the Surface Permanent Magnet (SPM) PMSM. We will show in chapter 3 that both kinds of PMSMs can be modeled in the same way.

Fig. 1.1b is the picture of a PMSM and fig. 1.3 presents a schematic two-dimensional representation of the internal layout a one-pole-pair PMSM.

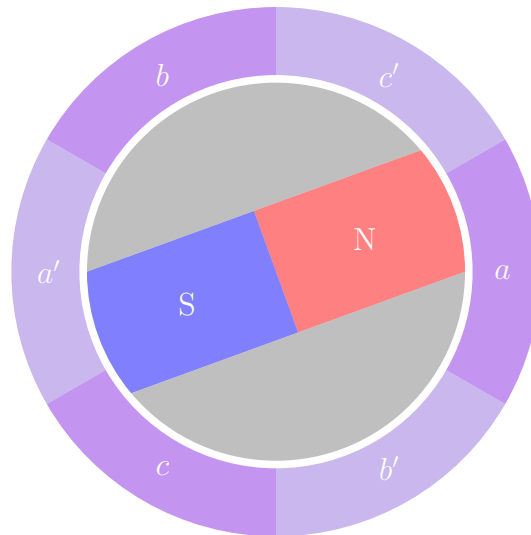


Figure 1.3 – Schematic transverse representation of a three-phase one-pole-pair PMSM.

### 1.1.2.2 Principle of operation

As in the SynRM case a rotating magnetic field is produced by the stator when it is connected to a three-phase electrical network. Similarly to the needle of the compass the permanent magnet in the rotor will tend to align with the rotating magnetic field thus creating a torque and rotating the machine at the speed of the stator magnetic field divided by the number of pole pairs  $n$ . Hence it is qualified as synchronous like the SynRM.

### 1.1.3 The induction motor (IM)

We describe here the construction and operating principles of IMs, which is detailed in Boldea and Nassar [34].

#### 1.1.3.1 Construction

As SynRM and PMSM stators IM stators support electrical windings which are spread in exactly the same way.

However the rotor is built differently: it also supports electrical windings. These windings can be made similarly as stator windings in which case the IM is qualified as rotor-wound. However this design is seldom used and squirrel-cage rotors are preferred because they are cheaper. In squirrel-cage rotors the windings are made of bars linked by 2 rings at the extremities. It is shown in Chiasson [45, sec. 6.7] that squirrel cages can be considered equivalent to short-circuited windings.

Fig. 1.1c is the photograph of a IM and fig. 1.4 presents schematic two-dimensional representations the two kinds of IM.

#### 1.1.3.2 Principle of operation

As for PMSMs and SynRMs the stator windings create a rotating magnetic field when they are connected to a three-phase balanced AC power source. When the rotor does not rotate at the same speed as the magnetic field, its windings are submitted to a varying magnetic flux. As stated by Faraday law an Electro-Motive Force (EMF) is created in

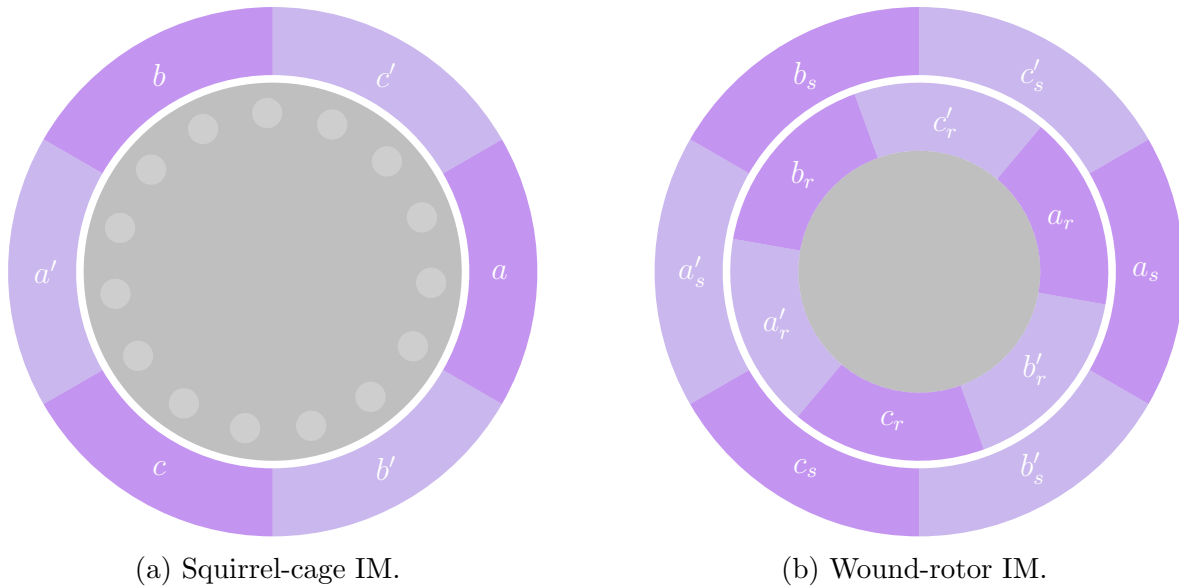


Figure 1.4 – Schematic transverse representations of a three-phase one-pole-pair IMs.

Criterion	SynRM	PMSM	IM
Synchronous	yes	yes	no
Efficiency	++	+++	+
Motor price	++	+++	+
Setup easyness	+	++	+++

Table 1.1 – Comparison of the three kind of AC rotating electric motors.

the rotor windings. The current circulating in the rotor windings creates a magnetic flux which opposes the stator magnetic flux according to Lenz law and thus creates a torque.

Unlike the SynRM and the PMSM presented herein before the IM cannot rotate at the same speed as the stator magnetic fields, since there would be no rotor current and consequently neither rotor flux nor torque. It is shown in Boldea and Nassar [34, ch. 7] or Chiasson [45, ch. 7] that it rotates a little slower depending on the torque needed. This kind of motor is thence qualified as asynchronous.

### 1.1.4 Comparison of electric motors

Table 1.1 compares some essential characteristics of electric motors. As they are the most efficient but also the most expensive PMSMs are mostly used for applications where efficiency is critical. They are also often used in high precision applications because precise operation is easier to achieve on this kind of machines. In contrast IMs are preferred when the price is critical or when the motor is directly connected to electrical grid which is now seldom done. SynRMs, which appeared recently on the market, are now replacing IMs in some applications where the price difference is paid off by the efficiency gain and replacing PMSMs in applications where efficiency is not critical enough.

### 1.1.5 Applications of electric motors

AC electric motors and in particular AC rotational electric motors produce most of the mechanical energy used by industry and households. Their major applications are listed below by categories.

**Hoisting** Electric motors power lifts, conveyor belts and cranes. As it does not really require high efficiency or high precision the IM is most widespread.

**Pumps and fans** For these applications the price matters, thus the IM is preferred. However, as these machines are running a lot, efficiency is taken into consideration and nowadays the SynRM replaces the IM.

**Industry** AC electric motors are used to power industrial appliances such as machine-tools. In machine-tools high precision is needed, thus the PMSMs are widespread.

**Transportation** Electric motors to power some means of transportation such as trains and now cars. In cars the efficiency really matters, thus PMSMs are used. In trains, as high power is needed, IMs are usually used but they begin to be replaced by PMSMs for the efficiency.

## 1.2 Electric motor control

From the explanations given in section 1.1 on how electric motors work, it may seem that they will rotate as soon as they are connected to an AC power source. Even though this is possible this mode of operation has some drawbacks presented in section 1.2.1 and the usage of Variable Speed Drives (VSD or shortly drives) presented in section 1.2.2 is often preferred.

These power electronic devices embed control laws which allow to regulate the speed of the motor to a reference. We chose to separate these control laws in three categories:

**“U/f” control laws** They are the most simple control laws and are presented in section 1.2.3.

**“sensored” control laws** They are more complex but of course more efficient than “U/f” and require a mechanical speed sensor (encoder, resolver or tachometer) and are presented in section 1.2.4

**“sensorless” control laws** These laws require neither position nor speed sensor even though they do control the speed of the motor. They are presented in section 1.2.5

### 1.2.1 Need for control

First of all, as described in section 1.1, when they are directly connected to the grid, electric motors rotate at a fixed speed under a given load. Besides the current needed to start the motor can be very important. This is not satisfactory for most applications. Indeed, the user generally wants the speed to follow a trajectory which ensures the acceleration and sometimes its derivative, the jerk, is bounded. To achieve this, the frequency of the power source must be adjustable.

Secondly, even when the frequency of the power source is suitably adjusted, the speed may depend on the torque for IM or the targeted working point may be an unstable

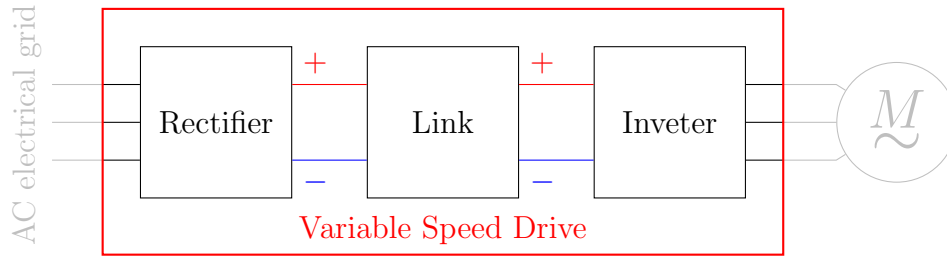


Figure 1.5 – Synoptic scheme of power conversion in a drive.

critical point of the motor. We thus have to control the power source so that the targeted working point is a stable equilibrium for the controlled motor.

Finally there are different ways, more or less efficient, of reaching a working point specified in terms of torque and speed. When electric motors are not controlled properly, the most efficient way is not always selected and their operation may be inefficient.

### 1.2.2 Variable Speed Drives (VSDs)

Due to the problems mentioned in the previous section a VSD is often used to drive a motor. A VSD is a power electronic device which can transform a constant frequency constant amplitude electrical network into an adjustable frequency adjustable amplitude electrical network. Most drives first transform the input AC power into DC power with a rectifier. The variation of the rectified power is then smoothed and finally transformed back to AC power at the desired frequency and amplitude using an inverter. A synoptic scheme of this process is given in fig. 1.5. More information on VSDs can be found in section 2.2.1 of this document Krause, Wasynczuk, *et al.* [56, ch. 13] or Sul [23, sec. 2.18].

Many companies such as Schneider Electric, which supported this work, Siemens, ABB, Toshiba, General Electric design and manufacture VSDs such as the Altivar 71 (see fig. 1.6) by Schneider Electric which is the commercial drive used for experiments (see section 2.2.1 for more details on the test bench). Among other activities these companies must design and implement the control laws which will be able to regulate the speed and stabilize the chosen working point. Over time many such algorithms, categorized hereafter, have been designed to regulate the speed of electric motors. State of the art for motor control can be found in Sul [23], Chiasson [45], Krause, Wasynczuk, *et al.* [56].

### 1.2.3 “U/f” control laws

These control laws, described more extensively in Krause, Wasynczuk, *et al.* [56, ch. 14.2], rely on the model of electric motors on permanent trajectories which shows that when operating at constant flux the needed voltage amplitude is proportional to the frequency of the AC network and thus to the frequency of rotation. The frequency and amplitude of the voltage output by the drive are then adjusted in open-loop to these references. At low speeds a voltage boost is required to compensate for the voltage drop due to the resistance of the stator windings, which become non-negligible with respect to back electromotive forces. There exist many compensation strategies which will not be detailed here (see [56, ch. 14.2]).

However, these laws do not ensure the stability of the chosen working point and worse, they do not ensure that the speed of an IM is equal to the reference. Furthermore,



Figure 1.6 – Photograph of an Altivar 71 built by Schneider Electric, the commercial drive used for experiments.

maximum efficiency cannot be achieved for all working points.

Consequently this control law is only used for applications which are not very dynamic and where the working point does not change much, such as pumps and fans.

#### 1.2.4 “Sensored” control laws

These control laws use current sensors and a mechanical position or speed sensor to measure a part of the state of the motor. Hence, they are qualified as “sensored”. The rest of the state can be estimated thanks to the model of the motor. Extensive study of existing closed-loop control laws can be found in Chiasson [45, ch. 8–9] or Sul [23, ch. 5].

These control laws are used when high performance is needed. Indeed thanks to the speed sensor the desired speed is ensured. Besides, they are stable and maximum efficiency can be reached whatever reachable working point is chosen.

However, these control laws have one drawback: they require a mechanical speed sensor. These sensors are expensive, cumbersome and the measurement signals can be altered by the neighboring high currents. Besides, these sensors can be submitted to dusty or hot environments which can reduce their lifetime. That is why it is interesting to design control laws which do not need such sensors but still ensure the desired working point is reached.

#### 1.2.5 “Sensorless” control laws

These control laws are called “sensorless” because they do not require a mechanical sensor, which is very advantageous as explained at the end of the previous section. Even though the speed is not measured, it can be estimated from the current measurements and these control laws ensure that the required speed is reached with maximum efficiency. For extensive study of “sensorless” control law refer to Glumineau and de Leon Morales [67].

However, these control laws are more sensitive to the accuracy of the model, particularly in the low speed domain. Moreover, the speed of the AC electric motors cannot be estimated when the frequency of the network is zero as is shown in section 4.1.4 of this

document or Glumineau and de Leon Morales [67, ch. 2]. This is a major drawback of these control laws which can thus not be used when low speeds are required. Overcoming this drawback is currently one of the hottest challenge for VSD manufacturers such as Schneider Electric. That is why it will be studied in depth in this manuscript.

### 1.3 Signal injection

Signal injection is the most promising solution to the aforementioned problem of “sensor-less” control laws. Superimposing a signal on the control signals of electric motors was proposed by Jansen and Lorenz [78] for IMs and Corley and Lorenz [85] for PMSMs. The current response of the motor to this supplementary excitation is then extracted from the current measurement and some signal processing allows to retrieve the speed or the position of the rotor at low or even zero speed.

Following the activity in the literature ([2–4] and many others) the most interesting signal injection method is HF signal injection where the frequency of the injected signal is high with respect to the frequency of excitation of the motor and the bandpass of the controllers. That is why it is extensively studied in section 4.2 of this document.

HF signal injection is even proposed in some commercial drives, but these control laws are difficult to tune because the motor response to signal injection is not explained well by the traditional unsaturated motor model. To explain it, magnetic saturation of the motor must be taken into account. This is the reason why we propose a new modeling approach to easily design (magnetically) saturated models for electric motors in chapter 3 and devote chapter 5 to the identification of the parameters of such models.



# Chapter 2

## Experimental facilities and related problems

### Chapitre 2 — Moyens de test et problèmes associés

*Ce chapitre décrit les moyens expérimentaux qui ont été utilisés pour les parties expérimentales de cette thèse. Les caractéristiques des moteurs testés (moteur synchrone à reluctance et moteur à induction) sont données, ainsi que des précisions sur le banc de test. Le cœur de ce banc de test est un système de prototypage rapide dSpace (ACMC solution) pour la commande, associé à un variateur de vitesse industriel pour la puissance. La fin de ce chapitre est consacrée à une étude théorique et expérimentale des limitations du banc de test, telles que la présence de chutes de pont, de temps morts additionnels ou d'harmoniques dues à la non-sinusoidalité de la machine de charge.*

In chapters 5 to 7 we consider electric motor modeling and control. To verify the models or the control laws we design, we had to test them on real machines. The two machines which were used for tests are described in section 2.1. Those machines were set on a test bench which is described in section 2.2.

Of course we had to make some approximations due to the chosen experimental setup. In section 2.3 we describe all the effects which are neglected in later experiments.

## 2.1 Motors

In the experiments which are presented further in this document we used electric motors of two kinds

- A SynRM which is described in section 2.1.1
- An IM which is described in section 2.1.2

### 2.1.1 Synchronous reluctance motor

In the experimental tests, a 0.75kW SynRM built by KSB [5] was used. Its name plate and parameters are given in the table 2.1 below and fig. 1.1a is a photograph of this motor. By convention we set the  $Q$  axis to be aligned with the largest inductance and the  $D$  axis to be aligned with the smallest. This convention was preferred because it is what is obtained when the magnetic field of a PMSM is set to 0.

Rated power	$0.75kW$
Rated mechanical speed	$1500rpm$
Rated torque	$5N.m$
Rated voltage	$400V$ peak
Rated current	$2A$ RMS
Maximum current	$5A$ peak
Number of pole pairs $n$	$2$
Inertia momentum $J_L$	$5 \cdot 10^{-3}kg.m^2$
Stator resistance $R_s$	$6.5\Omega$
Larger inductance $L_s^Q$	$0.3H$
Smaller inductance $L_s^D$	$0.1H$

Table 2.1 – Parameters of the 0.75kW SynRM used in tests.

### 2.1.2 Induction motor

We used in experimental tests a 0.75kW IM built by Leroy Somer [6]. This motor was chosen because it is one of the cheapest on the market and thus is widely used. Its name plate and parameters are given in the table 2.2 below and fig. 1.1c is a photograph of this motor.

Rated power	$0.75kW$
Rated mechanical speed	$1500rpm$
Rated torque	$5N.m$
Rated voltage	$400V$ peak
Rated current	$2A$ RMS
Maximum current	$5A$ peak
Number of pole pairs $n$	$2$
Inertia momentum $J_L$	$5 \cdot 10^{-3}kg.m^2$
Stator resistance $R_s$	$13\Omega$
Rotor resistance $R_r$	$10\Omega$
Mutual inductance $L_m$	$0.42H$
Stator leakage inductance $L_{ls}$	$0.05H$
Rotor leakage inductance $L_{lr}$	$0.05H$

Table 2.2 – Parameters of the 0.75kW IM used in tests.

## 2.2 The dSpace test bench

The test bench used for experiments is described here. Almost all data presented here was measured using this test bench. Only the oscilloscope records were not obtained on this test bench. Fig. 2.1 is a photograph of the test bench is schematically represented in fig. 2.2.

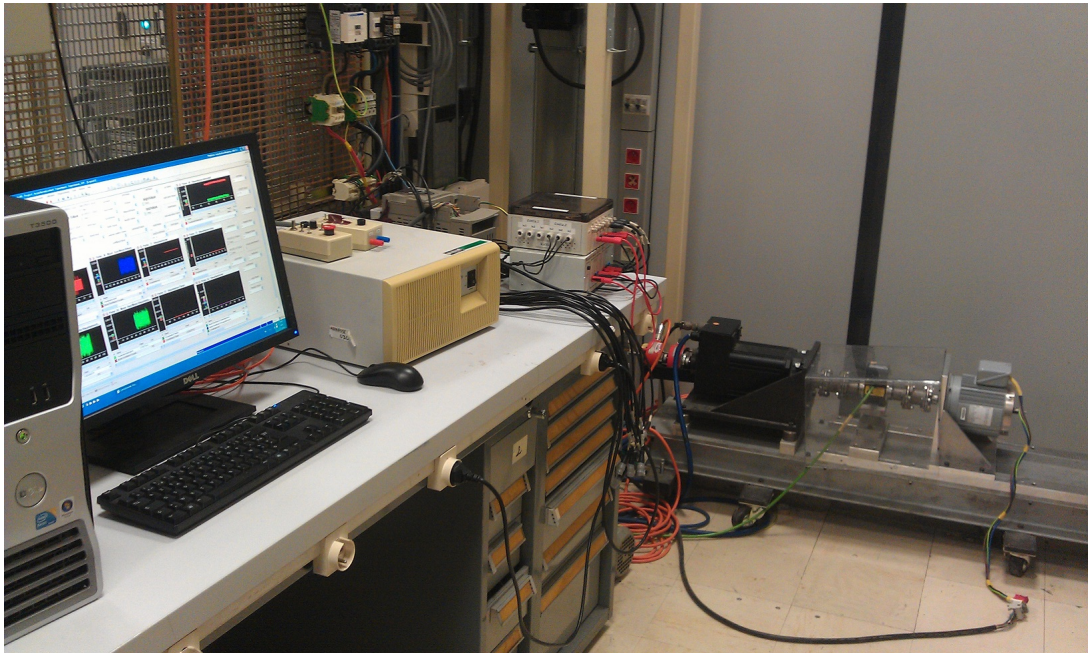


Figure 2.1 – Photograph of the test bench.

On this test bench we can mount any type of rotational electric motor provided some mechanical adaptations and it is under  $1.5kW$  (which is the rated power of the inverter). The shaft of the motor is connected via elastic couplings, a torque-meter (see section 2.2.4) and an incremental encoder (see section 2.2.5) to a load machine (see section 2.2.6).

The motor is powered by the inverter stage of a  $1.5kW$  commercial drive described in section 2.2.1 and the output currents of the drive are measured thanks to external current sensors (see section 2.2.3).

A dSpace<sup>®</sup> box generates the control signal for the inverter and records the measurements. It is controlled thanks to a computer running dSpace<sup>®</sup> software. See section 2.2.2 and [7] for more information on dSpace<sup>®</sup> software and hardware capabilities.

### 2.2.1 The inverter

When high power is involved, it becomes almost impossible and certainly inefficient to build a linear amplifier because this results in dissipating a lot of power in the circuit. The preferred solution is to use PWM (Pulse Width Modulation) where the voltage signal is a square wave with an adjustable duty cycle  $\alpha$ . The potential reference is generally chosen such that the two potential levels are  $\frac{V_{bus}}{2}$  and  $-\frac{V_{bus}}{2}$ . In fig. 2.3 some periods of such a signal are represented. As a phase of an electric motor is equivalent to an RL circuit up to the back EMF (Electro-Motive Force), the voltage seen by the motor is averaged over one period of the PWM signal ( $T_{PWM}$ )

$$v = \frac{1}{T_{PWM}} \int_0^{T_{PWM}} v(s) ds = \alpha \frac{V_{bus}}{2} - (1 - \alpha) \frac{V_{bus}}{2} = \left( \alpha - \frac{1}{2} \right) V_{bus}.$$

Thus any voltage  $v$  between  $-\frac{V_{bus}}{2}$  and  $\frac{V_{bus}}{2}$  can be obtained using two switches as shown in fig. 2.4a.

However, some limitations must be mentioned. Firstly, the two switches must not be closed simultaneously, otherwise the constant voltage is short-circuited. To enforce

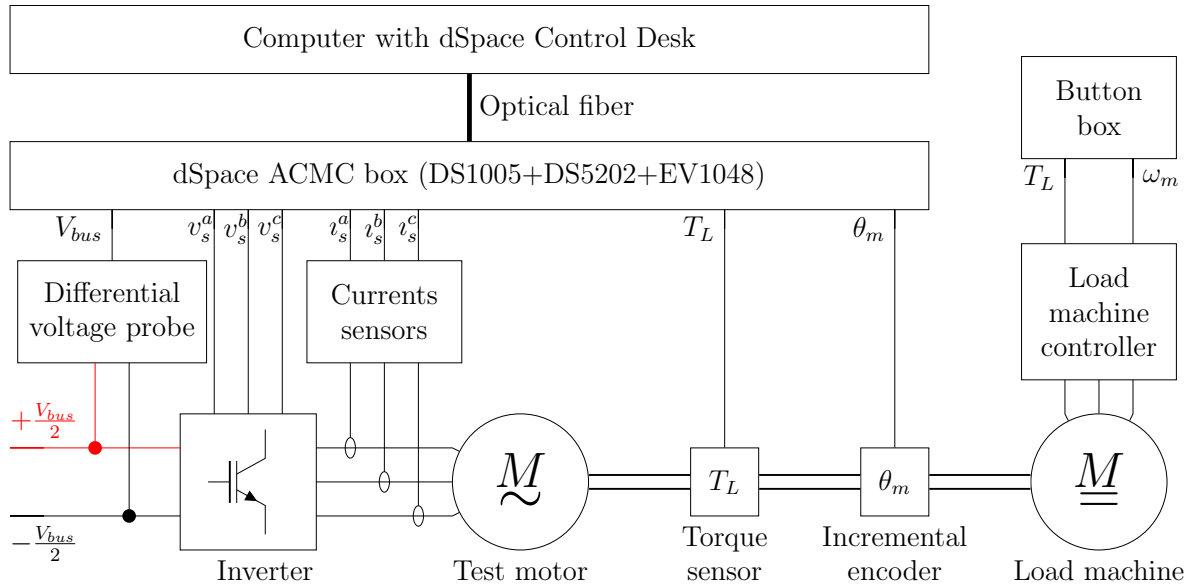


Figure 2.2 – Synoptic scheme of the test bench used for experiments.

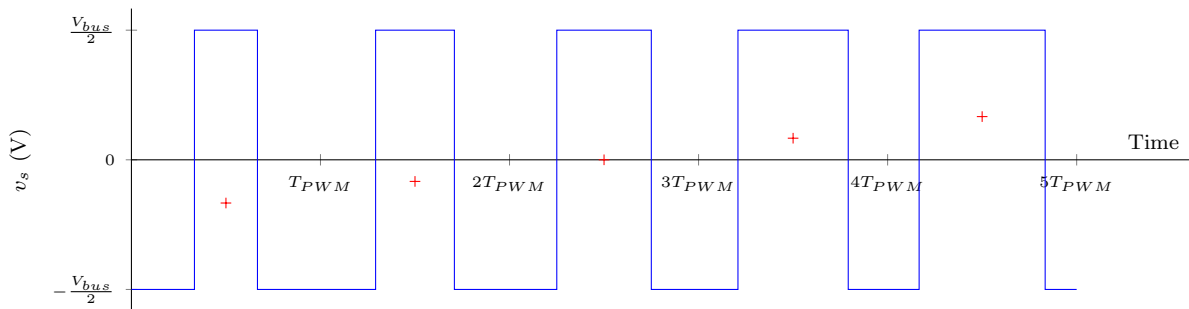


Figure 2.3 – Five periods of a PWM signal in blue solid lines. The red crosses represent the potential seen by a low-pass filter such as a motor

this condition a dead time is added between the commutations of the two switches. This causes some problems described in section 2.3.2. Secondly the switches are built using transistors, specifically IGBTs (Insulated Gate Bipolar Transistors), which are not reversible in current. A so-called freewheeling diode is added to allow the current to flow in the reverse direction. Finally the association of the IGBT and the diode creates a voltage drop, called inverter voltage drop, as the voltage at their bounds is not zero but equal to the PN junction voltage drop. This effect is detailed in section 2.3.1.

To obtain three adjustable potentials the previously described setup is repeated thrice as shown in fig. 2.4b. The 3 PWM waves are synchronized so that the middle of the active range coincide as shown on the upper part of fig. 2.5. When we compute instantaneous values of the star-point potential and the voltages across the windings of a star-connected electric machine, we obtain the curves shown in the lower part of fig. 2.5. There we can see that the voltages change values 6 times in a PWM period. Moreover the potential of the star-point is not zero but instead oscillates between  $-\frac{V_{bus}}{2}$  and  $\frac{V_{bus}}{2}$ . Nevertheless the PWM frequency is chosen high enough so that the effect are averaged by the motor which behaves as a low-pass filter.

In the case of the test bench we use the inverter stage of an ATV71 built by Schneider Electric [8]. We also use the ATV71 ASIC (Application Specific Integrated Circuit) to

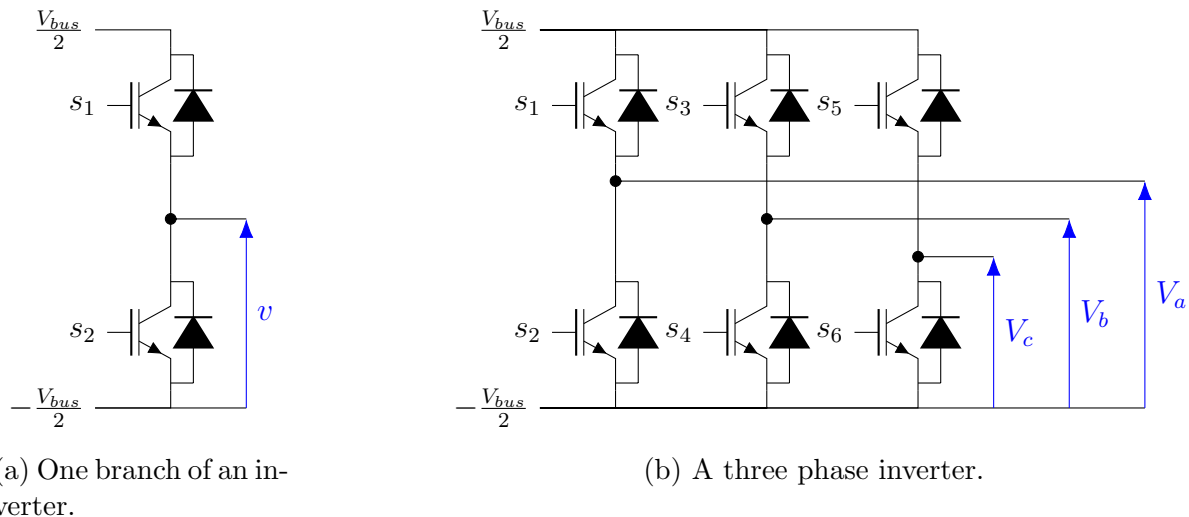


Figure 2.4 – The circuits used to generate adjustable potentials.

symmetrize the three PWM signals coming from dSpace<sup>®</sup> hardware. In the ATV71, the DC voltage  $V_{bus}$  is obtained from the three phase AC network using a diode rectifier and stabilized using a capacitor.

## 2.2.2 dSpace solution

dSpace<sup>®</sup> APMC solution [7] was chosen because it is tailored for fast prototyping of control laws for three-phase electric machines. On the one side, it allows to rapidly generate the code needed to run the control law on dSpace<sup>®</sup> hardware. On the other side, measurements and internal variables of the control law can be recorded for later use using dSpace<sup>®</sup> software. Most experimental data presented here was obtained in this way.

dSpace<sup>®</sup> hardware for fast prototyping of motor control laws consists of three boards which are usually racked in a box (in the center of the photograph fig. 2.1)

**DS1005 board** This is a powerful DSP (Digital Signal Processor) board. The control algorithm runs on this board. It also handles the communication with the computer in real-time through an optical fiber and with the other boards through a proprietary bus called PHS bus.

**DS5202 board** It is a FPGA-based board. With the help of EV1048 board it can handle the generation of the 6 PWM signals needed to control the 6 transistors of an inverter. However we use only three of them and generate the three other using the ASIC built in the drive (see section 2.2.1). It converts encoder signals measured by EV1048 board into a position signal. It also embeds 8 ADCs (Analog to Digital Converters) whose measurements can be averaged and synchronized with PWM.

**EV1048 board** It is a signal conditioning board which outputs the PWM signals generated by the DS5202 board and receives the encoder signals.

The control algorithm running on DS1005 board is easily generated from Simulink<sup>®</sup> thanks to dSpace<sup>®</sup> additions. Only minimal adaptations are needed: the control law must of course be discretized and I/O blocks must be added in the place of the simulated motor.

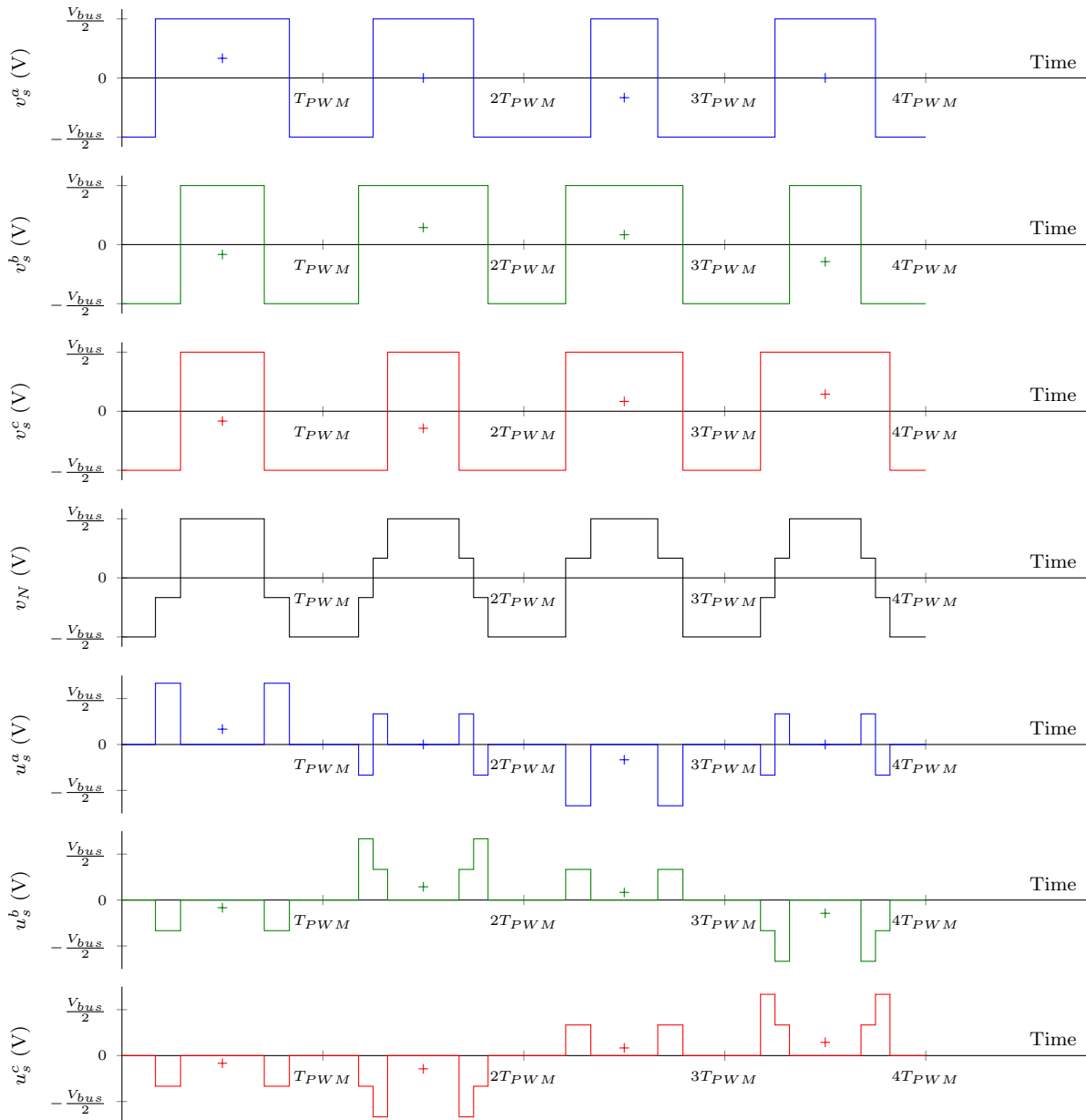


Figure 2.5 – Four periods of a three phase PWM signal, the star-point voltage  $v_N$  and the voltages across the windings in solid lines. The crosses represent the potentials and voltages seen by a low-pass filter such as a motor.

dSpace<sup>®</sup> Control Desk software allows to display in real-time and record the measurements coming from the hardware. It also allows the user to change parameters even while the control law is running.

### 2.2.3 The current sensors

To get accurate current measurements, we used external current sensors. The three currents coming out the drive are measured thanks to three T60404-N4644-X400 currents sensors manufactured by Vacuumschmelze [9]. These are small transformers which reduce the current to an acceptable level for measurement electronics. The signal is then electronically processed to obtain a linear gain.

To filter out disturbances due to switch commutations, the measure is further processed by an active low-pass filter with bandwidth  $1kHz$ .

We calibrated all the currents sensors by connecting them to a voltage source with adjustable current limit, which allowed us to have a variable current pass through the sensors. The currents were measured by the dSpace<sup>®</sup> and a calibrated ampere-meter. We thus found that the current sensors are perfectly linear in the range  $\pm 10A$  and obtained the scaling factor. The measured standard deviation was found to be smaller than  $5 \cdot 10^{-3}A$  for all measurements.

### 2.2.4 The torque-meter

The torque sensor we chose for the test bench is the torquemaster TM207 manufactured by Vibro-meter [10]. It is built of a torsion shaft whose ends are bound to two concentric cylinders which separate a pair of coils. When the torque applied to the torsion shaft varies, induction between the two coils changes. Electronic processing gives the torque up to a scaling factor.

As we do not have any simple way of calibrating the torque sensor we used the information given in the manual [10] which tells us that it outputs a voltage in the range  $\pm 10V$  for a torque in the range  $\pm 20N.m$  and that its accuracy is 0.1% of its nominal torque, which is  $0.01N.m$  in our case.

### 2.2.5 The encoder

The test bench is also equipped with an incremental encoder mounted on the rotating shaft. We used two different encoders: the old NHT912596I from Ideacod and the more recent XCC1912PS11RN from Schneider Electric [11]. Their operating principle is the same: a slotted disk periodically blocks a light beam which is received by a phototransistor. Thus when the shaft rotates a square wave is output from the encoder. In the encoders we use, there are two such tracks in quadrature and a special track with only one slot, which gives a zero. These encoders allow us to obtain the angular position up to a constant.

The problem with dSpace<sup>®</sup> hardware interface for incremental encoders is that when it sees the zero it resets the position to zero and sets a boolean value to one which is not useful for us, as we are not interested in absolute position but only in the angle (modulo  $2\pi$ ). To tackle this problem we used the following procedure:

- First the position provided by dSpace<sup>®</sup> (which starts at 0 at the beginning of the test run) is used to compute the mechanical position  $\theta_m = \text{mod}(\theta_{dS} + \pi, 2\pi) - \pi$ ;

- When the zero is first seen, the value  $\theta_{dS}^0$  is saved;
- Then the saved value is added to the position given by dSpace<sup>®</sup> and the mechanical position is computed as  $\theta_m = \text{mod}(\theta_{dS} + \theta_{dS}^0 + \pi, 2\pi) - \pi$

which can be summarized in the  $z$  space by

$$\theta_{dS}^0(z) = \begin{cases} \theta_{dS}(z) & \text{if the boolean value is false} \\ \theta_{dS}^0(z-1) & \text{if the boolean value is true} \end{cases} \quad (2.1a)$$

$$\theta_m(z) = \begin{cases} \text{mod}(\theta_{dS}(z) + \pi, 2\pi) - \pi & \text{if the boolean value is false} \\ \text{mod}(\theta_{dS}(z) + \theta_{dS}^0(z) + \pi, 2\pi) - \pi & \text{if the boolean value is true} \end{cases} \quad (2.1b)$$

To get the angular speed I use a Luemberger observer for the system

$$\frac{d\theta_m}{dt} = \omega_m \quad (2.2a)$$

$$y = \text{mod}(\theta_m + \pi, 2\pi) - \pi \quad (2.2b)$$

which reads

$$\frac{d\hat{\theta}_m}{dt} = \hat{\omega}_m + K_p^\theta \text{mod}(y - \hat{\theta}_m + \pi, 2\pi) - \pi \quad (2.3a)$$

$$\frac{d\hat{\omega}_m}{dt} = K_i^\theta \text{mod}(y - \hat{\theta}_m + \pi, 2\pi) - \pi. \quad (2.3b)$$

Assuming the speed is constant, the errors  $\Delta\omega_m = \omega_m - \hat{\omega}_m$  and  $\Delta\theta_m = \theta_m - \hat{\theta}_m$  follow the dynamic

$$\frac{d\Delta\theta_m}{dt} = \Delta\omega_m - K_p^\theta \text{mod}(\text{mod}(\theta_m + \pi, 2\pi) - \hat{\theta}_m, 2\pi) + \pi \quad (2.4a)$$

$$\frac{d\Delta\omega_m}{dt} = -K_i^\theta \text{mod}(\text{mod}(\theta_m + \pi, 2\pi) - \hat{\theta}_m, 2\pi) + \pi. \quad (2.4b)$$

This system reaches equilibrium when  $\hat{\theta}_m \equiv \theta_m[2\pi]$  and  $\Delta\omega_m = 0$ . Around such equilibria the system can be linearized under the form

$$\frac{d\Delta\theta_m}{dt} = \Delta\omega_m - K_p^\theta \Delta\theta_m \quad (2.5a)$$

$$\frac{d\Delta\omega_m}{dt} = -K_i^\theta \Delta\theta_m \quad (2.5b)$$

which proves that all equilibria where  $\hat{\theta}_m \equiv \theta_m[2\pi]$  and  $\Delta\omega_m = 0$  are stable. We thus get an estimate of the mechanical speed  $\hat{\omega}_m$ .

## 2.2.6 The load machine

The load machine is a 4kW brush-less DC servomotor BMH22422R1TF2I built by NUM which is controlled using the adapted commercial controller. The fact that the back-EMF of such machines is trapezoidal causes some harmonic problems described in section 2.3.3 even with a suitable controller.

The machine can be controlled in two ways:

- Either a speed reference is given and the torque is limited;

- Or it provides a constant torque whatever the speed.

Controlling the speed and torque reference with dSpace<sup>®</sup> was one of the improvement axes of the test bench we envisaged. However we did not implement it as the test bench could then only be used with dSpace<sup>®</sup>. The speed and torque reference are then adjusted manually thanks to two potentiometers, thus allowing us to get any desired trajectory.

## 2.3 Experimental problems

We here analyze the problems which can arise due to practical imperfections of the test bench described in section 2.2. We show that those imperfections are negligible or we present compensation methods.

### 2.3.1 Inverter voltage drops

Due to the PN junction voltage drop in semi-conductors, the potential we get at the output of the inverter is not exactly the desired one. Besides, the voltage drop in the diodes and the IGBTs are not the same as the IGBTs contain two PN junctions whereas the diodes have only one.

As stated by Weber and Steiner [13], the inverter voltage drops can affect the behavior of the controlled electric machine. We thus have to model them so that we can compensate them (see section 2.3.1.3). In addition to affecting the control signals of the drive, Gabriel, De Belie, *et al.* [14], Guerrero, Leetmaa, *et al.* [15], Wolbank and Machl [16] states that inverter voltage drops can have disturbing effects on the HF injection. We studied this phenomenon to determine how much the HF signal is altered by inverter voltage drops.

First of all, we consider the causes of inverter voltage drops. As said, the inverter voltage drops depend on which element is conducting. The four possible cases are shown in fig. 2.6 and are listed here:

- The upper IGBT is conducting (see fig. 2.6a);
- The upper diode is conducting (see fig. 2.6b);
- The lower IGBT is conducting (see fig. 2.6c);
- The lower diode is conducting (see fig. 2.6d).

Thus, in a three-phase inverter, the voltage drops will depend on the sign of the current (see section 2.3.1.1) but also on the direction of the voltage space vector (see section 2.3.1.2) as there are three output bridges.

#### 2.3.1.1 Influence of the current

To determine the influence of the current on voltage drops, we set different positive voltage references along the axis  $a$  (from  $0V$  to  $30V$ ). We then recorded both the voltage reference  $v_s^r$  and the measured current  $i_s^m$  using dSpace<sup>®</sup>. The voltages between all the phases and the point at  $-\frac{V_{bus}}{2}$  were also measured using a digital oscilloscope. As these voltage measurements are of course PWM signals, we filter them using a sliding average on one period of PWM to obtain  $v_s^m$ .

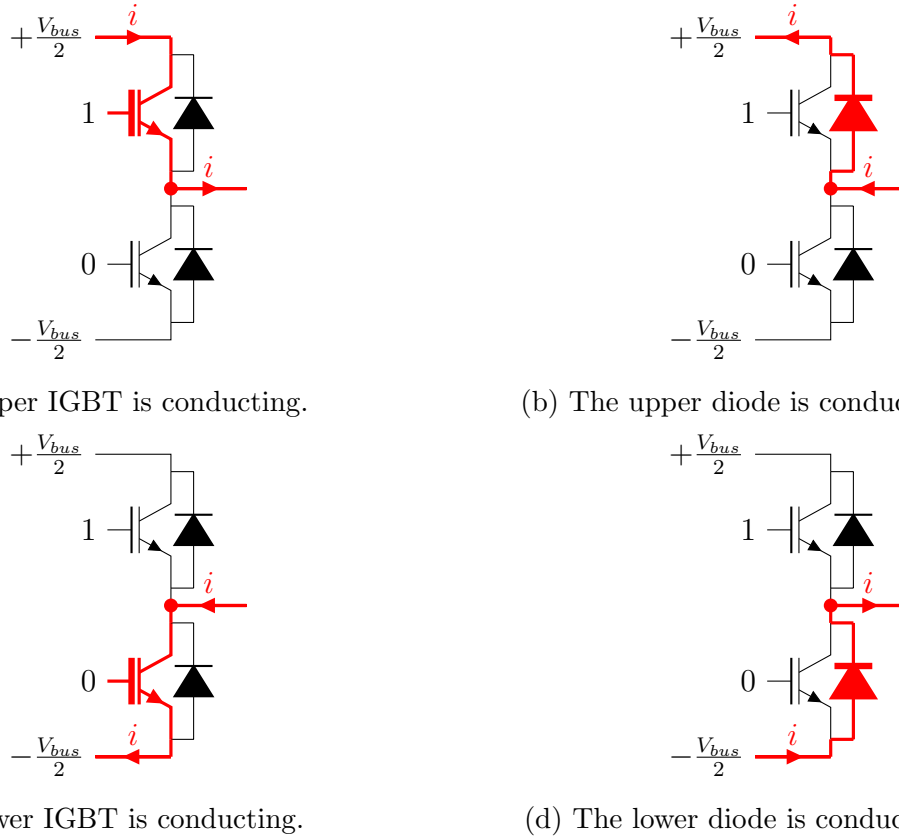


Figure 2.6 – The four different ways the current can cross the output bridge of an inverter.

We can thus compute the voltage drops using either one of the formulae

$$V_{drop} = v_s^r - v_s^m \quad (2.6a)$$

$$V_{drop} = v_s^r - R_s i_s^m \quad (2.6b)$$

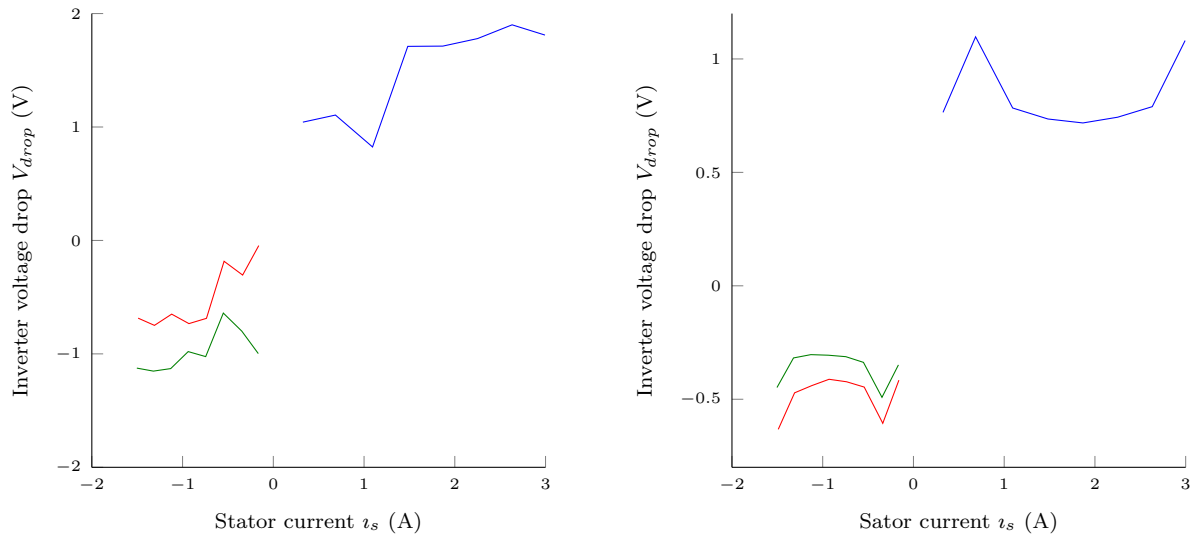
where  $R_s$  is the stator resistance of the motor and was measured using an ohmmeter. Tests are short enough so that we can suppose that the temperature of the motor does not change much. The results are depicted in fig. 2.7 where we can see that, up to the precision of the measurement, the inverter voltage drops do not depend on the current level, but only on its sign.

### 2.3.1.2 Influence of the direction of the voltage space vector

To highlight the influence of the direction of the voltage reference, we used a constant norm voltage reference with a variable direction (one point every  $15^\circ$ ). The voltage drops can now be obtained only using eq. (2.6a) as the resistance may change depending on the orientation. In fig. 2.8 we notice that the voltage drops greatly depend on the voltage reference direction.

As expected, the curves are similar with a phase difference of  $\frac{2\pi}{3}$ . Moreover they look like the theoretical inverter voltage drop curves (see for instance [17]) which is dashed in fig. 2.8. This model for inverter voltage drops reads

$$V_{drop}^{abc} = \frac{1}{3} \begin{pmatrix} 2 & -1 & -1 \\ -1 & 2 & -1 \\ -1 & -1 & 2 \end{pmatrix} V_{drop}^0 \operatorname{sgn}(i_s^{abc}). \quad (2.7)$$



(a) Voltage drops on phases  $a$ ,  $b$  and  $c$  as a function of the stator current computed using the oscilloscope measurement and eq. (2.6a).

(b) Voltage drops on phases  $a$ ,  $b$  and  $c$  as a function of the stator current computed using the current measurement and eq. (2.6b).

Figure 2.7 – The voltage drops computed using both methods proposed in eq. (2.6).

where  $V_{drop}^0 \approx 1V$  in our case.

Such voltage drops may cause torque ripple at integer multiples of  $6\omega_s$  because the three signals combine their effects. Such harmonics were indeed observed on the test bench on both the SynRM and the IM. However, these can also be caused by the motor being not perfectly sinusoidally wound, as shown in section 3.7.5. For the SynRM these harmonics are at the same frequencies as those caused by the load machine (see section 2.3.3 below).

### 2.3.1.3 Inverter voltage drop compensation

The idea is to add the inverter voltage drops forecast by the model eq. (2.7) to the voltage reference. As the function  $\text{sgn}$  is difficult to implement and can cause numerical problems we used the approximation

$$\text{sgn}(x) = \max(\min(ax, 1), -1) \quad (2.8)$$

with a large  $a$  for the implementation of voltage drop compensation (see fig. 2.9).

In fig. 2.10 we compare the potentials we obtain at the output of the drive measured with an oscilloscope at  $25MHz$  with and without inverter voltage drop compensation. From fig. 2.10b we see that inverter voltage drops have a great influence when the voltage is low, however their influence decreases when the voltage is increased as can be noticed in fig. 2.10d. Numeric data in table 2.3 show that at low voltages, the precision of the potential is increased by 2, however at high voltages the effect is less visible.

### 2.3.1.4 Influence of inverter voltage drops on HF injection

As inverter voltage drops only vary when the current orientation changes, their effect on HF injection will be limited because HF injection do not change the sign of the current when the mean current is high enough. Thus inverter voltage drops only affect zero current

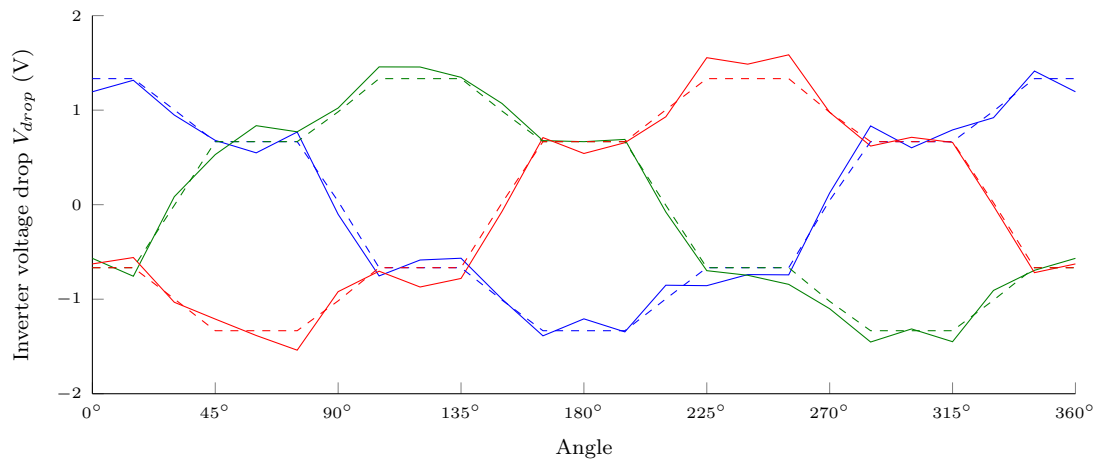


Figure 2.8 – Influence of the orientation of the voltage reference on inverter voltage drops on phases  $a$ ,  $b$  and  $c$ . The model (dashed lines) is compared with the measured data (solid lines).

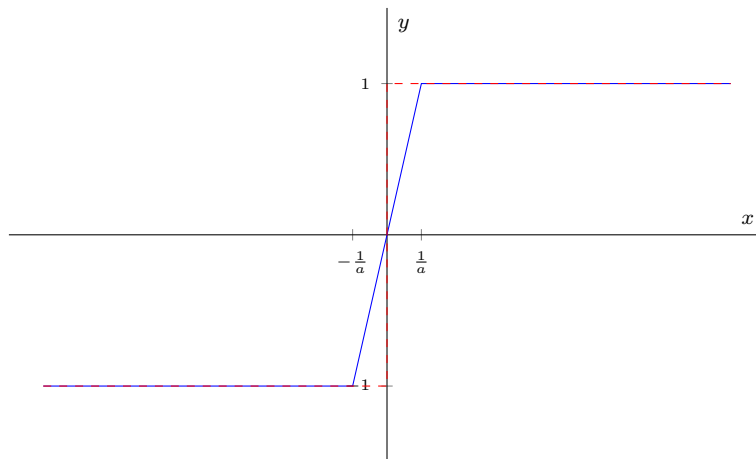
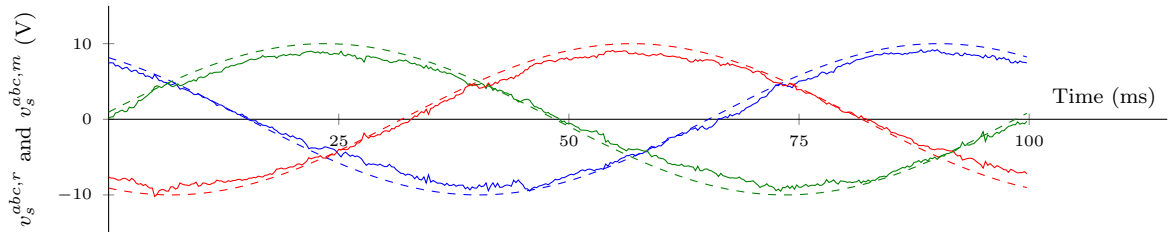
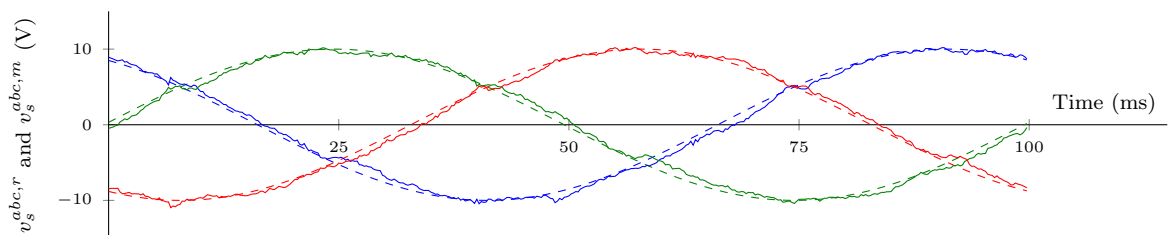


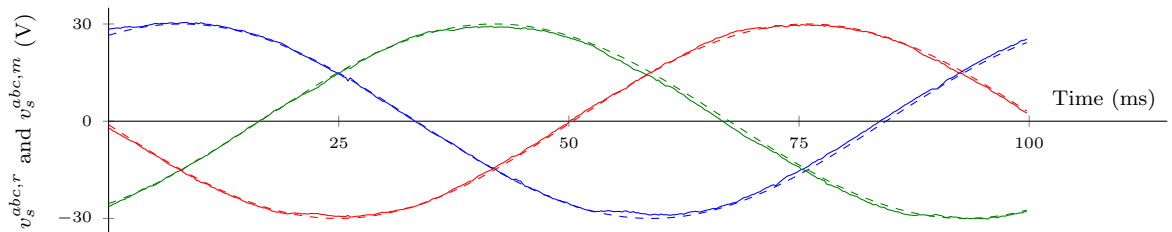
Figure 2.9 – The sign function (dashed red lines) and its approximation eq. (2.8) (solid blue line).



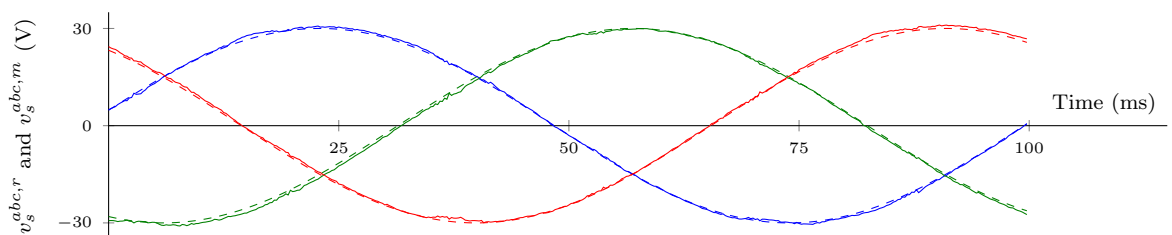
(a) Reference (dashed lines) and measured (solid lines) potentials on phases *a*, *b* and *c* without compensation of inverter voltage drops on a 10V signal at 10Hz.



(b) Reference (dashed lines) and measured (solid lines) potentials on phases *a*, *b* and *c* with compensation of inverter voltage drops on a 10V signal at 10Hz.



(c) Reference (dashed lines) and measured (solid lines) potentials on phases *a*, *b* and *c* without compensation of inverter voltage drops on a 30V signal at 10Hz.



(d) Reference (dashed lines) and measured (solid lines) potentials on phases *a*, *b* and *c* with compensation of inverter voltage drops on a 30V signal at 10Hz.

Figure 2.10 – Experimental results on voltage drop compensation and influence of the voltage reference. The voltage measurements were done using an oscilloscope with a sampling frequency of  $25\text{MHz}$ . The data thus obtained was averaged off-line on each PWM period (6250 points)

Axis	Voltage reference: 10V		Voltage reference: 30V	
	Without	With	Without	With
<i>a</i>	0.79V	0.46V	0.62V	0.38V
<i>b</i>	0.86V	0.50V	0.62V	0.59V
<i>c</i>	0.83V	0.44V	0.47V	0.52V
Average	0.83	0.47	0.56	0.50

Table 2.3 – Mean value of absolute value of inverter voltage drop with and without compensation.

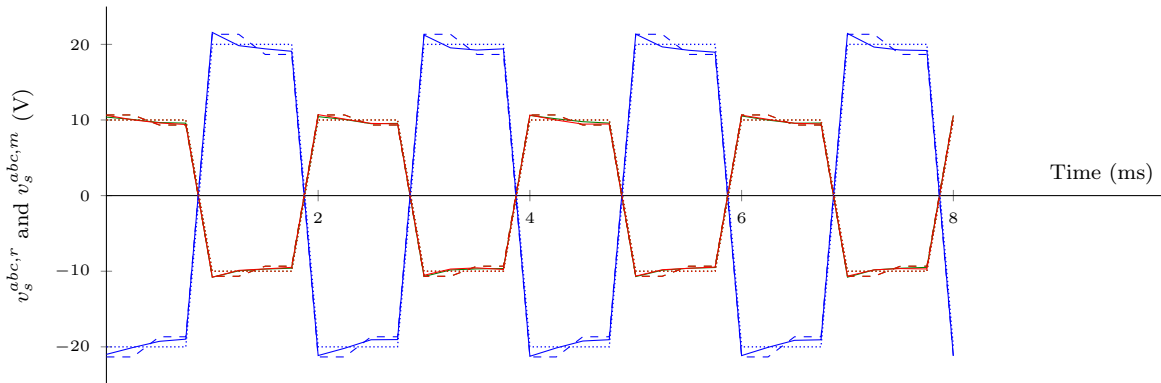


Figure 2.11 – Effect of inverter voltage drop on the 20V 500Hz injected HF voltage signal on phases *a*, *b* and *c*. Comparison between the references (dotted lines), the simulated HF voltage with voltage drop (dashed lines) and the experimental measurement (solid lines).

operation as shown in fig. 2.11. In this case, the HF currents, which are the primitives of the HF voltages, change signs in the middle of the voltage levels. This will create a small step in the middle of the voltage levels as can be seen in fig. 2.11.

In fig. 2.11 we see that the perturbation of the HF voltage signal is minimal even in the worst case where the current changes sign. This is due to the fact that the injection has a large amplitude with respect to voltage drops. In this case, the relative error caused by inverter voltage drops on the HF signal is less than 5% which is negligible. Moreover, the deformation of the current signal is also minimal. With larger injection amplitudes, the inverter voltage drops will affect even less the HF signal. Thus we did not always use voltage drop compensation in our tests.

### 2.3.2 Dead times

As was mentioned in section 2.2.1, the two switches on the same branch of the bridge (see fig. 2.4a) cannot be closed simultaneously, otherwise the DC bus is short-circuited. Moreover, the switches do not commute instantaneously and not necessarily at the same speed. Thus we cannot send the commutation order at the same time for the upper and the lower switches. We must introduce a small interval  $T_0$ , called dead-time, between the open and the close order. The control signals of the upper and lower switches for the bridges look like what is presented in fig. 2.12 where the dead-times have been highlighted. When  $\alpha \in \left[ \frac{T_0}{T_{PWM}}, 1 - \frac{T_0}{T_{PWM}} \right]$  we can set

$$T_h = \alpha T_{PWM} - T_0 \quad (2.9a)$$

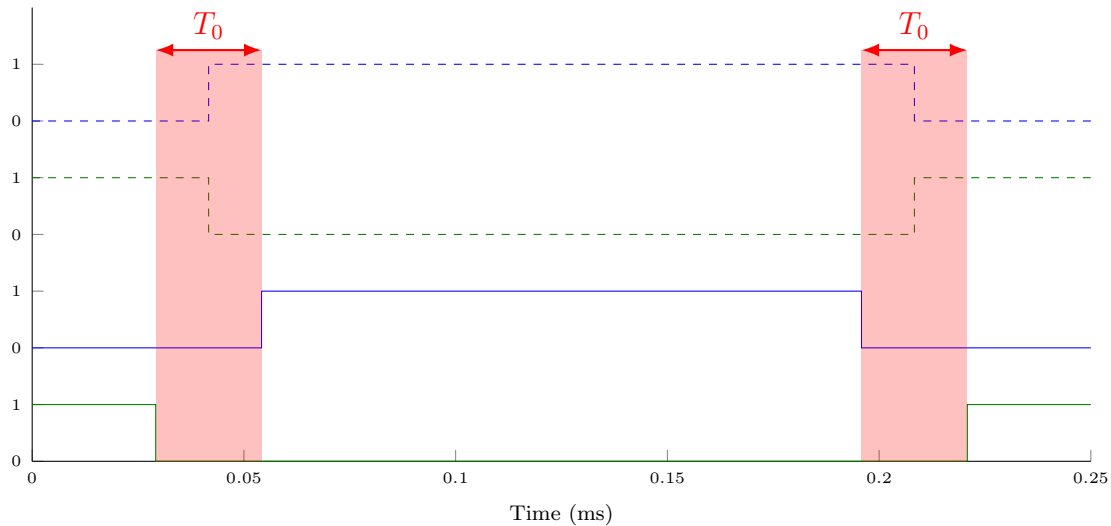


Figure 2.12 – Theoretical (dashed lines) and real (solid lines) control of the upper (blue) and lower (green) switches of an inverter bridge with dead-times highlighted (in red).

$$T_l = (1 - \alpha)T_{PWM} - T_0 \quad (2.9b)$$

where  $T_h$  and  $T_l$  are the times when the upper and lower switch are closed respectively. This does not change the voltage seen by the motor in average as the terms containing  $T_0$  cancel each other out. Otherwise if  $\alpha \in \left[0, \frac{T_0}{T_{PWM}}\right]$

$$T_h = 0 \quad (2.10a)$$

$$T_l = (1 - 2\alpha)T_{PWM} \quad (2.10b)$$

and if  $\alpha \in \left[1 - \frac{T_0}{T_{PWM}}, 1\right]$

$$T_h = (2\alpha - 1)T_{PWM} \quad (2.11a)$$

$$T_l = 0 \quad (2.11b)$$

In this way all potentials in the range  $\left[-\frac{V_{bus}}{2}, \frac{V_{bus}}{2}\right]$  can still be achieved.

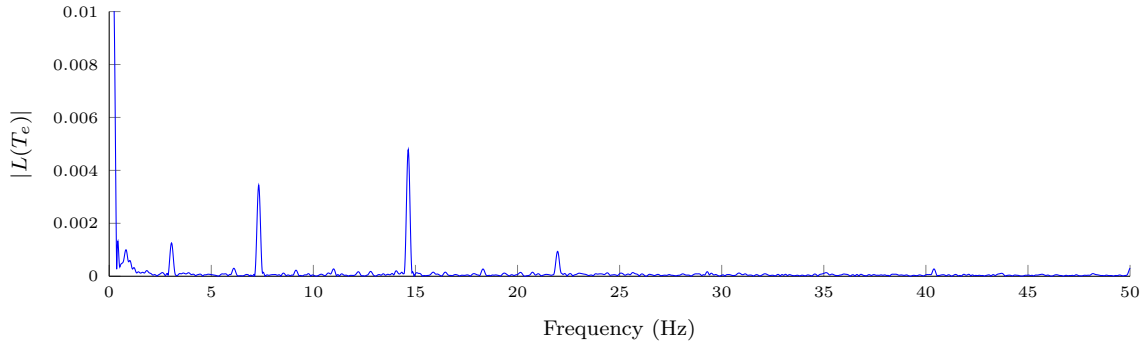
Besides, the switches we use, namely IGBTs, do not commute instantaneously from closed to open state: a small amount of time, called switching time, is needed to commute from closed to open state and vice versa. This additional dead-time must also be taken into account if we want to have the desired voltages at the bounds of the motor.

As was said in section 2.2.1 above, the drive of the test bench contains a specialized ASIC which symmetrizes the PWM orders coming from dSpace<sup>®</sup>, introduces the dead-times and compensates the transistors switching times.

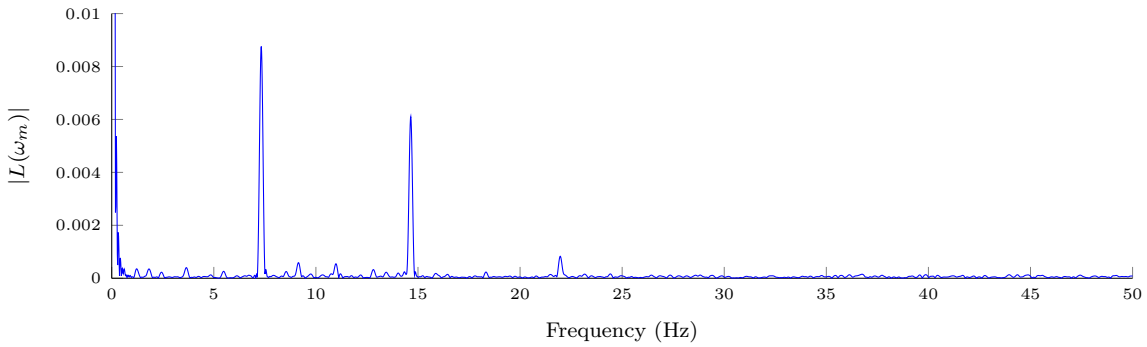
### 2.3.3 Load machine harmonics

As was said in section 2.2.6, the load machine is a brush-less DC motor. These motors are known to generate undesirable load harmonics even with a suitable controller. This was verified on our test bench where important harmonics were observed in the spectrum of the load torque signal at integer multiples of the frequency of rotation.

First, we rotated the motor by hand. Since it is not sinusoidally wound and the magnet is very strong, the saliencies are easily sensed. We thus found 36 saliencies per turn. This



(a) Amplitude spectrum of the electromagnetic torque.



(b) Amplitude spectrum of the mechanical speed.

Figure 2.13 – Spectra of the signals recorded during the experiments to get harmonics caused by the load machine.

means that the motor has 36 slots as the saliencies are caused by the slot boundaries attracting the magnet. This gives us some insight on how the motor is internally built however this does not tell us what harmonics are generated when it is driven by its controller.

To measure the harmonics caused by the load machine, we used the test bench in the opposite direction as usual, that is to say we rotated it at  $\omega_m \approx 0.20Hz$  connected to an IM or an SynRM not fed. In this situation, only the load machine can generate harmonics as the other machine only creates some additional friction torque which is mostly constant. During the experiments we recorded the speed (see fig. 2.13b for its FFT) and the load (see fig. 2.13a for its FFT).

As can be seen in table 2.4, the main harmonics are at frequencies which are at an integer multiple of  $36\omega_m$  (notice that the harmonics at  $15\omega_m$  are very low with respect to the others). These harmonics will be seen on later experiments, mainly on those of section 3.7.5 where we study the harmonics caused by the non-sinusoidality of the motors.

Frequency	$ L(T_e) $	$ L(\omega_m) $	Meaning
$3.067Hz$	$0.001N.m$	—	$15\omega_m$
$7.324Hz$	$0.003N.m$	$0.009Hz$	$36\omega_m$
$14.65Hz$	$0.005N.m$	$0.006Hz$	$72\omega_m$
$21.96Hz$	$0.001N.m$	$0.001Hz$	$108\omega_m$

Table 2.4 – Main harmonics measured when the load machine is driven at  $\omega_m \approx 0.2Hz$  and the motor is not fed.



# Chapter 3

## Energy-based modeling of electric machines

### Chapitre 3 — Modélisation énergétique des machines électriques

*Ce chapitre présente une nouvelle approche pour la modélisation des machines électriques. Elle repose sur des résultats classiques de mécanique analytique qui sont appliqués aux machines électriques. Elle permet de justifier la modélisation de la saturation dans des repères fictifs, alors qu'elle se produit dans le repère physique, ainsi que la conservation de l'expression du couple électromagnétique pour les machines électriques saturées. Les conditions de réciprocité sont automatiquement vérifiées par les modèles construits selon cette approche. En considérant le cas le plus simple, cette approche permet de retrouver facilement les modèles sinusoïdaux non saturés des moteurs électriques, mais elle peut aisément être étendue à la modélisation de moteurs saturés ou/et non sinusoïdaux.*

After a small review of electric motor modeling approaches, we propose here a complete energy-based framework to design electric motor models. This approach requires only a basic understanding on how electric motor are built and the model can be expressed as a single scalar function instead of a set of differential equations and current-flux relations.

Thanks to this approach we are also able to show that electric motors are very similar. This finding is used in chapter 4 where a generic observability study is done and chapter 6 where a generic “sensorless” control law for SynRMs and PMSMs is designed.

### 3.1 Preliminaries: Electric motor modeling

#### 3.1.1 Traditional microscopic approach

Electric machines are traditionally modeled by a microscopic approach relying on the application of Maxwell equations under integral form. Such approaches are developed in Mukerji, Khan, *et al.* [18], Chiasson [45] for instance. The most well known models for electric motors, the unsaturated sinusoidal models, can be obtained with this method by assuming a linear relation between currents and fluxes and sinusoidally distributed windings.

The unsaturated sinusoidal model allows to control electric motors reasonably well and has been intensively used to design control algorithms (see for instance [23, 45, 56]). With a suitable adjustment of parameters all working points for electric motors can be explained. This lead to the design of adaptive control laws for electric machines.

Alternatively, the dependence of the parameters on the working point can be predicted by using nonlinear current-flux relations. Saturated models were proposed since the 1990s (see [19–21] for example) to avoid parameter adaptation which leads to complicated proofs. However nonlinear modeling became really interesting with signal injection (see section 1.3 and [78, 85]). Indeed magnetic saturation is paramount to explain the effects of signal injection (see for instance [22, 78]).

Furthermore electric machines are not precisely sinusoidally wound. Some effort has been invested on extending the basic unsaturated sinusoidal models to account for the effects of non-sinusoidal windings. This reduces torque harmonics (see [24–26]), but can also be used to estimate the position of non-sinusoidally wound electric machines (see [27, 28]).

However these extensions must be done with care. Indeed the current-flux relations must respect the so-called reciprocity condition as stated by Melkebeek and Willems [29], Sauer [30]. Besides this method is also quite tedious and requires the knowledge of the internal layout of electric machines.

### 3.1.2 Macroscopic approach

An alternative modeling approach is based on analytical mechanics (see Landau and Lifshitz [31], Raimond [32]) which allows one to derive dynamic models from the specification of a single scalar function related to energy. The premises of this technique can be found in White and Woodson [33] where the energy function associated with the unsaturated sinusoidal model is given.

When saturated models are designed, the reciprocity conditions are automatically enforced by this approach (see [1]), which is very advantageous. Furthermore it requires only the specification of a single scalar function instead of many vector functions and only requires a basic understanding of the internal layout of electric machines. Hence this approach was proposed to model saturation in electric motors (see [35, 36]). And it was eventually successfully applied by Jebai [37] to model a saturated PMSM. In addition to that Jebai, Combes, *et al.* [1] shows that the unsaturated sinusoidal models are the most basic models which can be obtained when the symmetries of electric machines are considered.

Due to these numerous advantages, this approach was favored in this work to model saturated and non-sinusoidally wound electric motors. It was generalized to show that it can be applied to any kind of electric motor, not only PMSMs.

## 3.2 Energy-based modeling for 3 phase electric motors

As explained in section 3.1 we favor in this work a macroscopic approach based on energy considerations and analytical mechanics. The underlying idea is that the trajectories followed by a system over time are those which are extremal for some function analogous to an energy.

Here is given a small introduction to analytical mechanics which is much more detailed in [31, 32]. Its application to electric machines is also proposed (see [33] for more details).

### 3.2.1 Lagrangian modeling

The physical state of a system can be described by a set of variables called the generalized coordinates of the system and denoted  $q \in \mathbb{R}^n$ . Thus, assigning values to all coordinates of a system uniquely determines its state. The generalized coordinates must be independent from one another.

The time derivatives  $\dot{q} \in \mathbb{R}^n$  of these generalized coordinates are called generalized speeds. Analytical mechanics (see [31, 32]) postulates the existence of a function of generalized coordinates, generalized speeds and optionally of the time,  $\mathcal{L}(q, \dot{q}, t)$ , such that the action  $S$  defined by

$$S := \int_{t_0}^{t_f} \mathcal{L}(q(\tau), \dot{q}(\tau), \tau) d\tau \quad (3.1)$$

is extremal along the trajectories which are followed by the system when it evolves over time without any external force. This stems from a fundamental principle in physics, called the least action principle. Eq. (3.1) is a variational principle under integral form. The corresponding differential form is called the Euler-Lagrange equation and reads

$$\frac{d}{dt} \frac{\partial \mathcal{L}}{\partial \dot{q}} = \frac{\partial \mathcal{L}}{\partial q}. \quad (3.2)$$

Eq. (3.2) is valid only for a system on which no external forces apply. But it can be easily extended to the case where generalized external forces  $Q$  are applied (see Raimond [32, sec. 1.4]). In this case the system follows the dynamic

$$\frac{d}{dt} \frac{\partial \mathcal{L}}{\partial \dot{q}} = \frac{\partial \mathcal{L}}{\partial q} + Q. \quad (3.3)$$

There is one problem with this formulation: eq. (3.3) is not under state form which will not be very practical for simulations and control law design. We are going to solve this problem in the next section.

Moreover, the evolution of  $\mathcal{L}$  over time is

$$\begin{aligned} \frac{d\mathcal{L}}{dt} &= \left( \frac{\partial \mathcal{L}}{\partial q} \right)^T \frac{dq}{dt} + \left( \frac{\partial \mathcal{L}}{\partial \dot{q}} \right)^T \frac{d\dot{q}}{dt} + \frac{\partial \mathcal{L}}{\partial t} \\ &= \dot{q}^T \frac{\partial \mathcal{L}}{\partial q} + \frac{d}{dt} \left( \dot{q}^T \frac{\partial \mathcal{L}}{\partial \dot{q}} \right) - \dot{q}^T \frac{d}{dt} \frac{\partial \mathcal{L}}{\partial \dot{q}} + \frac{\partial \mathcal{L}}{\partial t} \\ &= \frac{d}{dt} \left( \dot{q}^T \frac{\partial \mathcal{L}}{\partial \dot{q}} \right) - \dot{q}^T Q + \frac{\partial \mathcal{L}}{\partial t} \end{aligned} \quad (3.4)$$

which shows that, even in the absence of external forces ( $Q = 0$ ) and when there is no intrinsic variation ( $\frac{\partial \mathcal{L}}{\partial t} = 0$ ), the Lagrangian is not conserved over time. Thus, even though it is homogeneous and analogous to an energy, the Lagrangian is not the energy of the system, which should be conserved over time in this case.

### 3.2.2 Hamiltonian modeling

To get a state form instead of eq. (3.3), we use a Legendre transformation and define  $\mathcal{H}$ , the Hamiltonian of the system. The state variables will be the generalized coordinates  $q \in \mathbb{R}^n$  and the generalized momenta  $p := \frac{\partial \mathcal{L}}{\partial \dot{q}} \in \mathbb{R}^n$ . In this case the Legendre transformation reads

$$\mathcal{H} := \dot{q}^T p - \mathcal{L}. \quad (3.5)$$

Computing the differential of  $\mathcal{H}$  using eq. (3.5) we get

$$d\mathcal{H} = p^T dq + \dot{q}^T dp - \left(\frac{\partial \mathcal{L}}{\partial q}\right)^T dq - \left(\frac{\partial \mathcal{L}}{\partial \dot{q}}\right)^T d\dot{q} - \frac{\partial \mathcal{L}}{\partial t} dt = \dot{q}^T dp - \left(\frac{\partial \mathcal{L}}{\partial q}\right)^T dq - \frac{\partial \mathcal{L}}{\partial t} dt.$$

Hence  $\mathcal{H}$  can be seen as a function of the generalized coordinates  $q$  and of the generalized momenta  $p$  and possibly of the time  $t$ . Identifying the previous formula with the usual formula

$$d\mathcal{H} = \left(\frac{\partial \mathcal{H}}{\partial q}\right)^T dq + \left(\frac{\partial \mathcal{H}}{\partial p}\right)^T dp + \frac{\partial \mathcal{H}}{\partial t} dt,$$

we get the equations of evolution for the generalized coordinates and the generalized momenta, i.e. the state equations of the system

$$\frac{dp}{dt} = -\frac{\partial \mathcal{H}}{\partial q} + Q \quad (3.6a)$$

$$\frac{dq}{dt} = \frac{\partial \mathcal{H}}{\partial p}. \quad (3.6b)$$

The state form eq. (3.6) is usually referred to as Hamilton's equations and is much more convenient for the purposes of simulating the motor and designing control laws.

Moreover, if we take a look back at the considerations of eq. (3.4), we realize that  $\mathcal{H}$  is the conserved quantity when the system evolves in the absence of external forces ( $Q = 0$ ) and intrinsic variation ( $\frac{\partial \mathcal{L}}{\partial t} = -\frac{\partial \mathcal{H}}{\partial t} = 0$ ). This conserved quantity is called the energy of the system. Furthermore, in the presence of external forces, but still in the absence of intrinsic variation ( $\frac{\partial \mathcal{L}}{\partial t} = -\frac{\partial \mathcal{H}}{\partial t} = 0$ ), we have

$$\frac{d\mathcal{H}}{dt} = \dot{q}^T Q. \quad (3.7)$$

Thus,  $\dot{q}^T Q$  is the work of the generalized forces along the trajectory of the system.

### 3.2.3 Using complex state variables

The equations of electric machines are often written using complex state variables (called space vectors) as this allows more compact formulae. Even though this approach is not often used in this document, the result is recalled here. As shown in [35, 36] it is possible to extend analytical mechanics to use complex variables. We have two sets of generalized coordinates:

- The vector of the  $c$  complex valued coordinates  $\underline{q}_c \in \mathbb{C}^c$  and
- The vector of the  $r$  real valued coordinates  $q_r \in \mathbb{R}^r$

The equivalent vector of real-valued coordinates is obtained by taking the real part  $\Re \underline{q}_c$  and imaginary part  $\Im \underline{q}_c$  of the complex coordinates  $\underline{q}_c$  and taking the real coordinates as they are, i.e. define

$$q := \left( \frac{\underline{q}_c + \underline{q}_c^*}{2}, \frac{\underline{q}_c - \underline{q}_c^*}{2j}, q_r \right)^T \in \mathbb{R}^{2c+r}$$

A similar definition can be used to define  $\dot{q}$ , the equivalent set or real-valued speeds associated with  $\dot{q}_r$  and  $\dot{\underline{q}}_c$  as well as  $p$  the equivalent set of real-valued momenta associated with  $p_r$  and  $\underline{p}_c$ .

We can now define

$$\underline{\mathcal{L}}(\underline{q}_c, \underline{q}_c^*, q_r, \dot{\underline{q}}_c, \dot{\underline{q}}_c^*, \dot{q}_r) := \mathcal{L}(q, \dot{q}).$$

where  $\underline{\mathcal{L}}$  is still a real-valued scalar function. Computing partial derivatives of  $\underline{\mathcal{L}}$  with respect to the generalized coordinates, we find

$$\begin{aligned} \frac{\partial \underline{\mathcal{L}}}{\partial \underline{q}_c} &= \frac{\partial q}{\partial \underline{q}_c} \frac{\partial \mathcal{L}}{\partial q} = \frac{1}{2} \frac{\partial \mathcal{L}}{\partial \Re \underline{q}_c} - \frac{j}{2} \frac{\partial \mathcal{L}}{\partial \Im \underline{q}_c} \\ \frac{\partial \underline{\mathcal{L}}}{\partial \underline{q}_c^*} &= \frac{\partial q}{\partial \underline{q}_c^*} \frac{\partial \mathcal{L}}{\partial q} = \frac{1}{2} \frac{\partial \mathcal{L}}{\partial \Re \underline{q}_c} + \frac{j}{2} \frac{\partial \mathcal{L}}{\partial \Im \underline{q}_c} \\ \frac{\partial \underline{\mathcal{L}}}{\partial q_r} &= \frac{\partial q}{\partial q_r} \frac{\partial \mathcal{L}}{\partial q} = \frac{\partial \mathcal{L}}{\partial q_r}. \end{aligned}$$

Similar results are obtained for the partial derivatives with respect to generalized speeds. Thus the Euler-Lagrange equations using complex-valued variables read

$$2 \frac{d}{dt} \frac{\partial \underline{\mathcal{L}}}{\partial \dot{\underline{q}}_c^*} = 2 \frac{\partial \underline{\mathcal{L}}}{\partial \underline{q}_c^*} + \underline{Q}_c \quad (3.8a)$$

$$\frac{d}{dt} \frac{\partial \underline{\mathcal{L}}}{\partial \dot{q}_r} = \frac{\partial \underline{\mathcal{L}}}{\partial q_r} + Q_r \quad (3.8b)$$

where  $Q_r$  are the generalized forces associated with  $q_r$  and  $\underline{Q}_c := \Re \underline{Q}_c + j \Im \underline{Q}_c$ ,  $\Re \underline{Q}_c$  being the generalized forces associated with  $\Re \underline{q}_c$  and  $\Im \underline{Q}_c$  being associated with  $\Im \underline{q}_c$ . The factor 2 in eq. (3.8) comes from the fact that the transformation from complex-valued variable to the associated real-valued variables is not normalized, but it was preferred for historical reasons.

Similarly we can derive Hamilton's equations associated with the complex Hamiltonian defined by

$$\underline{\mathcal{H}}(\underline{q}_c, \underline{q}_c^*, q_r, \underline{p}_c, \underline{p}_c^*, p_r) := \mathcal{H}(q, p)$$

which gives

$$\frac{d\underline{p}_c}{dt} = -2 \frac{\partial \underline{\mathcal{H}}}{\partial \underline{q}_c^*} + \underline{Q}_c \quad (3.9a)$$

$$\frac{dp_r}{dt} = -\frac{\partial \underline{\mathcal{H}}}{\partial q_r} + Q_r \quad (3.9b)$$

$$\frac{d\underline{q}_c}{dt} = 2 \frac{\partial \underline{\mathcal{H}}}{\partial \underline{p}_c^*} \quad (3.9c)$$

$$\frac{dq_r}{dt} = \frac{\partial \underline{\mathcal{H}}}{\partial p_r} \quad (3.9d)$$

### 3.2.4 Application of energy-based modeling to electric machines

We are now going to specify the energy-based formulations developed in sections 3.2.1 and 3.2.2 for electric motors as done in White and Woodson [33].

We are now considering the most general three-phase electric motor possible. It has  $n$  pole pairs and, thus,  $3n$  windings in the stator. It is assumed that the rotor can be modeled by  $3n$  windings as well. They are now considered unconnected so that there are no constraints (see section 3.5 for details on how to handle connection constraints).

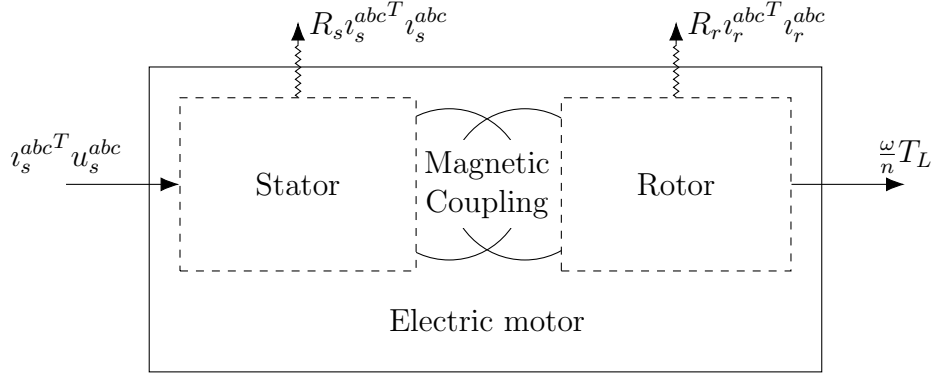


Figure 3.1 – Power exchanges in an electric motor.

As all the poles are built identically, the motor can be reduced to a single pole pair motor by considering electrical equivalent of mechanical variables. The three windings of the equivalent simplified motor will be noted  $a$ ,  $b$  and  $c$ . For such an electromechanical system, the generalized coordinates are

$$q = (\theta, q_s^a, q_s^b, q_s^c, q_r^a, q_r^b, q_r^c)$$

where  $\theta = n\theta_m$  is the electrical rotor angle,  $q_s^{abc}$ , the vector of charges in the stator windings and  $q_r^{abc}$ , the vector of charges in the rotor windings. The associated generalized speeds will be given by

$$\dot{q} = (\omega, i_s^a, i_s^b, i_s^c, i_r^a, i_r^b, i_r^c)$$

where  $\omega = n\omega_m$  is the electrical speed of rotation of the motor,  $i_s^{abc}$ , the vector of currents in the stator windings and  $i_r^{abc}$ , the vector of currents in the rotor windings.

As shown in fig. 3.1, a three-phase electrical motor

- Receives from the grid the electrical power  $i_s^{abcT} u_s^{abc}$ , thus  $u_s^{abc}$ , the vector of the voltage drops across the stator windings, is a generalized force associated with the stator currents  $i_s^{abc}$ ;
- Loses the electrical power  $-R_s i_s^{abcT} i_s^{abc}$  in its stator resistance  $R_s$ , thus  $R_s i_s^{abc}$  is a generalized force associated with the stator currents  $i_s^{abc}$ ;
- Loses the electrical power  $-R_r i_r^{abcT} i_r^{abc}$  in the rotor resistance  $R_r$ , thus  $R_r i_r^{abc}$  is a generalized force associated with the rotor currents  $i_r^{abc}$ ;
- Yields to the load the mechanical power  $-\frac{\omega}{n} T_L$ , where  $T_L$  is the load torque and thus the generalized force associated with the electrical speed  $\omega$  is  $\frac{T_L}{n}$ .

As there is no capacitive element, and consequently, no storage of electrical charges, the energy functions will not depend on the charges. The behavior of a motor does not change over time, so the energy functions will not depend on time either. Thus in the most general case, the Lagrangian of an electric motor expressed using the above defined generalized coordinates and speeds will be of the form

$$\mathcal{L}^{abc}(\theta, \omega, i_s^{abc}, i_r^{abc}). \quad (3.10)$$

We denoted the Lagrangian of the electric motor by  $\mathcal{L}^{abc}$  to underline the fact that it is expressed using variables in the  $abc$  frame. Taking into account the aforementioned generalized forces and applying eq. (3.3) gives

$$\frac{d}{dt} \frac{\partial \mathcal{L}^{abc}}{\partial i_s^{abc}} = u_s^{abc} - R_s i_s^{abc} \quad (3.11a)$$

$$\frac{d}{dt} \frac{\partial \mathcal{L}^{abc}}{\partial i_r^{abc}} = -R_r i_r^{abc} \quad (3.11b)$$

$$\frac{d}{dt} \frac{\partial \mathcal{L}^{abc}}{\partial \omega} = \frac{\partial \mathcal{L}^{abc}}{\partial \theta} - \frac{T_L}{n}. \quad (3.11c)$$

By defining the electromagnetic torque,

$$T_e(\theta, \omega, i_s^{abc}, i_r^{abc}) := n \frac{\partial \mathcal{L}^{abc}}{\partial \theta}(\theta, \omega, i_s^{abc}, i_r^{abc}) \quad (3.12)$$

and the generalized momenta associated with the currents and the speed

$$\phi_s^{abc}(\theta, \omega, i_s^{abc}, i_r^{abc}) := \frac{\partial \mathcal{L}^{abc}}{\partial i_s^{abc}}(\theta, \omega, i_s^{abc}, i_r^{abc}) \quad (3.13a)$$

$$\phi_r^{abc}(\theta, \omega, i_s^{abc}, i_r^{abc}) := \frac{\partial \mathcal{L}^{abc}}{\partial i_r^{abc}}(\theta, \omega, i_s^{abc}, i_r^{abc}), \quad (3.13b)$$

$$\rho(\theta, \omega, i_s^{abc}, i_r^{abc}) := n^2 \frac{\partial \mathcal{L}^{abc}}{\partial \omega}(\theta, \omega, i_s^{abc}, i_r^{abc}), \quad (3.13c)$$

which turn out to be the fluxes through the windings and the electrical kinetic momentum, we recover the motor equations under the usual form (see [23, 45, 56]). Notice the  $n^2$  factor in eq. (3.13c), which stems from the fact that the transformation from the mechanical variables into electrical ones is not normalized. Indeed defining  $\rho := n\rho_m$  and  $\omega := n\omega_m$ , we obtain with variables omitted for the sake of compactness

$$\rho = n \frac{\partial \mathcal{L}^{abc}}{\partial \omega_m} = n \frac{\partial \omega}{\partial \omega_m} \frac{\partial \mathcal{L}^{abc}}{\partial \omega} = n^2 \frac{\partial \mathcal{L}^{abc}}{\partial \omega}$$

However eq. (3.11) is not in state form which is not very practical.

A state form can be obtained by a Legendre transformation, thus defining the Hamiltonian of an electric motor as in section 3.2.2

$$\mathcal{H}^{abc}(\theta, \rho, \phi_s^{abc}, \phi_r^{abc}). \quad (3.14)$$

Applying eq. (3.6a) to this energy function gives the desired state form

$$\frac{d\phi_s^{abc}}{dt} = u_s^{abc} - R_s i_s^{abc}(\theta, \rho, \phi_s^{abc}, \phi_r^{abc}) \quad (3.15a)$$

$$\frac{d\phi_r^{abc}}{dt} = -R_r i_r^{abc}(\theta, \rho, \phi_s^{abc}, \phi_r^{abc}) \quad (3.15b)$$

$$\frac{1}{n} \frac{d\rho}{dt} = T_e(\theta, \rho, \phi_s^{abc}, \phi_r^{abc}) - T_L \quad (3.15c)$$

$$\frac{d\theta}{dt} = \omega \quad (3.15d)$$

with

$$i_s^{abc}(\theta, \rho, \phi_s^{abc}, \phi_r^{abc}) = \frac{\partial \mathcal{H}^{abc}}{\partial \phi_s^{abc}}(\theta, \rho, \phi_s^{abc}, \phi_r^{abc}) \quad (3.16a)$$

$$i_r^{abc}(\theta, \rho, \phi_s^{abc}, \phi_r^{abc}) = \frac{\partial \mathcal{H}^{abc}}{\partial \phi_r^{abc}}(\theta, \rho, \phi_s^{abc}, \phi_r^{abc}) \quad (3.16b)$$

$$T_e(\theta, \rho, \phi_s^{abc}, \phi_r^{abc}) = -n \frac{\partial \mathcal{H}^{abc}}{\partial \theta}(\theta, \rho, \phi_s^{abc}, \phi_r^{abc}) \quad (3.16c)$$

$$\omega(\theta, \rho, \phi_s^{abc}, \phi_r^{abc}) = n^2 \frac{\partial \mathcal{H}^{abc}}{\partial \rho}(\theta, \rho, \phi_s^{abc}, \phi_r^{abc}). \quad (3.16d)$$

The  $n^2$  factor in eq. (3.16d) stems from the same reason as in the Lagrangian case.

### 3.3 Frame changes

For three-phase electric machines the electrical variables are 3 dimensional vectors, which were expressed in the physical frame  $abc$  in the previous section 3.2. However the frame  $abc$  as given lacks an interesting feature: none of its axes are aligned with the rotation axis. We will see later in section 3.4 that this axis plays an important role due to the construction symmetries of electric motors.

Moreover the stator variables are expressed in a frame linked with the stator whereas the rotor variables are expressed in a frame linked with the rotor. This will not be convenient to model the electromagnetic coupling between stator and rotor.

In this section, we define the frames we are going to use. These are similar to those used in the literature (see Krause, Wasynczuk, *et al.* [56, ch. 3] and Sul [23, ch. 3]), but we must explain how to change frames using the Hamiltonian formalism.

#### 3.3.1 Transformations

We are now interested in doing a change of variables in the energy functions. The particular transformations we will use later will be applicable to the Lagrangian or the Hamiltonian. However in the general case presented here, the changes of coordinates can be applied only to the Hamiltonian variables.

A change of variable is a bijective transformation from the initial variables  $(q, p)$  to other variables  $(q', p')$

$$\begin{aligned} \mathcal{T} : \mathbb{R}^n \times \mathbb{R}^n &\rightarrow \mathbb{R}^n \times \mathbb{R}^n \\ (q, p) &\mapsto (q', p'). \end{aligned}$$

We define an energy function in the new state space by  $\widetilde{\mathcal{H}}(q', p') := \mathcal{H}(q(q', p'), p(q', p'))$ . This energy function  $\widetilde{\mathcal{H}}$  is similar to a Hamiltonian, but the state equations using variables  $(q', p')$  may not be given by Hamilton's equations.

A canonical transformation is a transformation which does not change Hamilton's equations. The theory of canonical transformations is very developed and will not be fully detailed (see [32, sec. 2.4]). Yet we present a criterion to check if a transformation is canonical. The chain rule gives us on the one hand

$$\begin{pmatrix} \frac{\partial \mathcal{H}}{\partial q} \\ \frac{\partial \mathcal{H}}{\partial p} \end{pmatrix} = \begin{pmatrix} \frac{\partial q'}{\partial q} & \frac{\partial p'}{\partial q} \\ \frac{\partial q'}{\partial p} & \frac{\partial p'}{\partial p} \end{pmatrix} \begin{pmatrix} \frac{\partial \widetilde{\mathcal{H}}}{\partial q'} \\ \frac{\partial \widetilde{\mathcal{H}}}{\partial p'} \end{pmatrix} = \frac{\partial(q', p')}{\partial(q, p)} \begin{pmatrix} \frac{\partial \widetilde{\mathcal{H}}}{\partial q'} \\ \frac{\partial \widetilde{\mathcal{H}}}{\partial p'} \end{pmatrix}$$

and on the other hand

$$\begin{pmatrix} \frac{dq'}{dt} \\ \frac{dp'}{dt} \end{pmatrix} = \begin{pmatrix} \frac{\partial q'}{\partial q} & \frac{\partial q'}{\partial p} \\ \frac{\partial p'}{\partial q} & \frac{\partial p'}{\partial p} \end{pmatrix}^T \begin{pmatrix} \frac{dq}{dt} \\ \frac{dp}{dt} \end{pmatrix} = \left( \frac{\partial(q', p')}{\partial(q, p)} \right)^T \begin{pmatrix} \frac{dq}{dt} \\ \frac{dp}{dt} \end{pmatrix}$$

where  $\frac{\partial(q', p')}{\partial(p, q)}$  represents the transpose of the Jacobian matrix of the transformation  $\mathcal{T}$ . So the state equations using  $(q', p')$  variables are

$$\begin{pmatrix} \frac{dq'}{dt} \\ \frac{dp'}{dt} \end{pmatrix} = \left( \frac{\partial(q', p')}{\partial(q, p)} \right)^T \begin{pmatrix} 0_n & I_n \\ -I_n & 0_n \end{pmatrix} \frac{\partial(q', p')}{\partial(q, p)} \begin{pmatrix} \frac{\partial \tilde{\mathcal{H}}}{\partial q'} \\ \frac{\partial \tilde{\mathcal{H}}}{\partial p'} \end{pmatrix} = \left( \frac{\partial(q', p')}{\partial(q, p)} \right)^T \mathcal{J}_n \frac{\partial(q', p')}{\partial(q, p)} \begin{pmatrix} \frac{\partial \tilde{\mathcal{H}}}{\partial q'} \\ \frac{\partial \tilde{\mathcal{H}}}{\partial p'} \end{pmatrix}.$$

Thus Hamilton's equations are conserved if and only if

$$\left( \frac{\partial(q', p')}{\partial(q, p)} \right)^T \mathcal{J}_n \frac{\partial(q', p')}{\partial(q, p)} = \mathcal{J}_n \quad (3.17)$$

i.e. the Jacobian matrix of the transformation  $\mathcal{T}$  is symplectic. By extension, the transformation  $\mathcal{T}$  is called a symplectic transformation.

When  $q'$  depends only on  $q$ ,  $p'$  depends only on  $p$  and the transformation between  $q$  and  $q'$  on the one hand and  $p$  and  $p'$  on the other are the same, i.e. the generalized coordinates and momenta are transformed separately but similarly, the Jacobian matrix is diagonal by blocks and the blocks are identical. In this particular case, the condition eq. (3.17) boils down to the block being an orthogonal matrix.

### 3.3.2 Frame orthonormalization

As was said in introduction of section 3.3, the rotation axis of the motor, which will be called the 0-axis and is collinear to the  $abc$  frame vector  $(1, 1, 1)^T$ , plays a major role when construction symmetries are considered (see section 3.4). We will thus select it among the basis vectors of our new frame. Then we choose the  $\alpha$ -axis to be in the plane defined by  $a$ -axis and 0-axis and finally  $\beta$  orthogonal to this plane. After some algebra, we find the transformation matrix from the  $abc$  frame to the  $\alpha\beta 0$  frame (which is the so-called Concordia transformation)

$$P_{abc \rightarrow \alpha\beta 0} := \sqrt{\frac{2}{3}} \begin{pmatrix} 1 & -\frac{1}{2} & -\frac{1}{2} \\ 0 & \frac{\sqrt{3}}{2} & -\frac{\sqrt{3}}{2} \\ \frac{\sqrt{2}}{2} & \frac{\sqrt{2}}{2} & \frac{\sqrt{2}}{2} \end{pmatrix} \quad (3.18)$$

The matrix  $P_{abc \rightarrow \alpha\beta 0}$  is orthogonal, so Hamilton's equations will be left unchanged when the energy is expressed using  $\alpha\beta 0$  state variables,  $\phi_s^{\alpha\beta 0} = P_{abc \rightarrow \alpha\beta 0} \phi_s^{abc}$  and  $\phi_r^{\alpha\beta 0} = P_{abc \rightarrow \alpha\beta 0} \phi_r^{abc}$ . It should be noted that stator variables are still expressed in a stator-linked frame whereas rotor variables are in a rotor-linked frame. We define the Hamiltonian function using these new variables as

$$\mathcal{H}^{\alpha\beta 0}(\theta, \rho, \phi_s^{\alpha\beta 0}, \phi_r^{\alpha\beta 0}) := \mathcal{H}^{abc}(\theta, \rho, P_{abc \rightarrow \alpha\beta 0}^{-1} \phi_s^{\alpha\beta 0}, P_{abc \rightarrow \alpha\beta 0}^{-1} \phi_r^{\alpha\beta 0}). \quad (3.19)$$

Hamilton's equations are not changed, so eq. (3.15) gives

$$\frac{d\phi_s^{\alpha\beta 0}}{dt} = u_s^{\alpha\beta 0} - R_s i_s^{\alpha\beta 0}(\theta, \rho, \phi_s^{\alpha\beta 0}, \phi_r^{\alpha\beta 0}) \quad (3.20a)$$

$$\frac{d\phi_r^{\alpha\beta 0}}{dt} = -R_r i_r^{\alpha\beta 0}(\theta, \rho, \phi_s^{\alpha\beta 0}, \phi_r^{\alpha\beta 0}) \quad (3.20b)$$

$$\frac{1}{n} \frac{d\rho}{dt} = T_e(\theta, \rho, \phi_s^{\alpha\beta 0}, \phi_r^{\alpha\beta 0}) - T_L \quad (3.20c)$$

$$\frac{d\theta}{dt} = \omega \quad (3.20d)$$

with

$$i_s^{\alpha\beta 0}(\theta, \rho, \phi_s^{\alpha\beta 0}, \phi_r^{\alpha\beta 0}) = \frac{\partial \mathcal{H}^{\alpha\beta 0}}{\partial \phi_s^{\alpha\beta 0}}(\theta, \rho, \phi_s^{\alpha\beta 0}, \phi_r^{\alpha\beta 0}) \quad (3.21a)$$

$$i_r^{\alpha\beta 0}(\theta, \rho, \phi_s^{\alpha\beta 0}, \phi_r^{\alpha\beta 0}) = \frac{\partial \mathcal{H}^{\alpha\beta 0}}{\partial \phi_r^{\alpha\beta 0}}(\theta, \rho, \phi_s^{\alpha\beta 0}, \phi_r^{\alpha\beta 0}) \quad (3.21b)$$

$$T_e(\theta, \rho, \phi_s^{\alpha\beta 0}, \phi_r^{\alpha\beta 0}) = -n \frac{\partial \mathcal{H}^{\alpha\beta 0}}{\partial \theta}(\theta, \rho, \phi_s^{\alpha\beta 0}, \phi_r^{\alpha\beta 0}) \quad (3.21c)$$

$$\omega(\theta, \rho, \phi_s^{\alpha\beta 0}, \phi_r^{\alpha\beta 0}) = n^2 \frac{\partial \mathcal{H}^{\alpha\beta 0}}{\partial \rho}(\theta, \rho, \phi_s^{\alpha\beta 0}, \phi_r^{\alpha\beta 0}). \quad (3.21d)$$

### 3.3.3 Synchronous frame

The principle of operation of an electric motor is that the magnetic field rotates at the stator frequency  $\omega_s$ . Thus neither  $abc$  nor  $\alpha\beta 0$  variables will be constant on permanent trajectories, in which the motor turns at constant speed. So we define a new family of frames, called  $dq0$  frames, which are obtained from the  $\alpha\beta 0$  frame by a rotation of angle  $\theta_s$ , with  $\frac{d\theta_s}{dt} = \omega_s$ , around the 0-axis. We are going to express all the variables in this frame, so the transformation matrix for stator variables will be  $P_{\alpha\beta 0 \rightarrow dq0}(\theta_s)$  whereas the transformation matrix for rotor variables will be  $P_{\alpha\beta 0 \rightarrow dq0}(\theta_s - \theta)$ , where

$$P_{\alpha\beta 0 \rightarrow dq0}(\eta) = \begin{pmatrix} \cos \eta & \sin \eta & 0 \\ -\sin \eta & \cos \eta & 0 \\ 0 & 0 & 1 \end{pmatrix} \quad (3.22)$$

The transformation matrices for stator and rotor variables are both orthogonal matrices, but do not define a canonical transformation as they depend on  $\theta$  and  $t$  through  $\theta_s$ . Nevertheless we can define functions analogous to the Lagrangian and the Hamiltonian with altered state equations.

We define an energy function in any  $dq0$  frame by

$$\mathcal{H}^{dq0}(\theta, \rho, \phi_s^{dq0}, \phi_r^{dq0}) := \mathcal{H}^{\alpha\beta 0}(\theta, \rho, P_{\alpha\beta 0 \rightarrow dq0}^{-1}(\theta_s) \phi_s^{dq0}, P_{\alpha\beta 0 \rightarrow dq0}^{-1}(\theta_s - \theta) \phi_r^{dq0}). \quad (3.23)$$

Some calculations are now needed to get the state equations

$$\begin{aligned} \frac{d\phi_s^{dq0}}{dt} &= \frac{d}{dt} \left( P_{\alpha\beta 0 \rightarrow dq0}(\theta_s) \phi_s^{\alpha\beta 0} \right) \\ &= P_{\alpha\beta 0 \rightarrow dq0}(\theta_s) \frac{d\phi_s^{\alpha\beta 0}}{dt} + \frac{d}{dt} (P_{\alpha\beta 0 \rightarrow dq0}(\theta_s)) \phi_s^{\alpha\beta 0} \\ &= P_{\alpha\beta 0 \rightarrow dq0}(\theta_s) (u_s^{\alpha\beta 0} - R_s i_s^{\alpha\beta 0}) + \omega_s P'_{\alpha\beta 0 \rightarrow dq0}(\theta_s) P_{\alpha\beta 0 \rightarrow dq0}^{-1}(\theta_s) \phi_s^{dq0} \end{aligned}$$

$$\frac{d\phi_s^{dq0}}{dt} = u_s^{dq0} - R_s i_s^{dq0}(\theta, \rho, \phi_s^{dq0}, \phi_r^{dq0}) - \mathcal{J}_3 \omega_s \phi_s^{dq0} \quad (3.24a)$$

$$\begin{aligned} \frac{d\phi_r^{dq0}}{dt} &= \frac{d}{dt} \left( P_{\alpha\beta 0 \rightarrow dq0}(\theta_s - \theta) \phi_r^{\alpha\beta 0} \right) \\ &= P_{\alpha\beta 0 \rightarrow dq0}(\theta_s - \theta) \frac{d\phi_r^{\alpha\beta 0}}{dt} + \frac{d}{dt} (P_{\alpha\beta 0 \rightarrow dq0}(\theta_s - \theta)) \phi_r^{\alpha\beta 0} \\ &= -P_{\alpha\beta 0 \rightarrow dq0}(\theta_s - \theta) R_r i_r^{\alpha\beta 0} + (\omega_s - \omega) P'_{\alpha\beta 0 \rightarrow dq0}(\theta_s - \theta) P_{\alpha\beta 0 \rightarrow dq0}^{-1}(\theta_s - \theta) \phi_r^{dq0} \end{aligned} \quad (3.24b)$$

$$\frac{d\phi_r^{dq0}}{dt} = -R_r i_r^{dq0}(\theta, \rho, \phi_s^{dq0}, \phi_r^{dq0}) - \mathcal{J}_3 (\omega_s - \omega(\theta, \rho, \phi_s^{dq0}, \phi_r^{dq0})) \phi_r^{dq0} \quad (3.24c)$$

$$\frac{1}{n} \frac{d\rho}{dt} = T_e(\theta, \rho, \phi_s^{dq0}, \phi_r^{dq0}) - T_L \quad (3.24d)$$

$$\frac{d\theta}{dt} = \omega \quad (3.24d)$$

where we used

$$P'_{\alpha\beta 0 \rightarrow dq0} P_{\alpha\beta 0 \rightarrow dq0}^{-1} = \begin{pmatrix} -\sin \eta & \cos \eta & 0 \\ -\cos \eta & -\sin \eta & 0 \\ 0 & 0 & 0 \end{pmatrix} \begin{pmatrix} \cos \eta & -\sin \eta & 0 \\ \sin \eta & \cos \eta & 0 \\ 0 & 0 & 1 \end{pmatrix} = \begin{pmatrix} 0 & 1 & 0 \\ -1 & 0 & 0 \\ 0 & 0 & 0 \end{pmatrix} =: -\mathcal{J}_3$$

As expected by comparison with the literature (see for instance Chiasson [45, chs. 8–9]), the  $\alpha\beta 0$  to a  $dq0$  frame change leads to the appearance of back electromotive forces in the flux equations. The derivative of  $\mathcal{H}^{dq0}$  with respect to  $\theta$  is also modified, indeed

$$\begin{aligned} \frac{\partial \mathcal{H}^{dq0}}{\partial \theta} &= \frac{\partial \mathcal{H}^{\alpha\beta 0}}{\partial \theta} + \frac{\partial}{\partial \theta} \left( P_{\alpha\beta 0 \rightarrow dq0}^{-1}(\theta_s - \theta) \phi_r^{dq0} \right)^T \frac{\partial \mathcal{H}^{\alpha\beta 0}}{\partial \phi_r^{\alpha\beta 0}} \\ &= \frac{\partial \mathcal{H}^{\alpha\beta 0}}{\partial \theta} - \phi_r^{dq0 T} P_{\alpha\beta 0 \rightarrow dq0}^{-T} (\theta_s - \theta) P_{\alpha\beta 0 \rightarrow dq0}^{-1}(\theta_s - \theta) \frac{\partial \mathcal{H}^{dq0}}{\partial \phi_r^{dq0}} \\ &= \frac{\partial \mathcal{H}^{\alpha\beta 0}}{\partial \theta} + \phi_r^{dq0 T} \mathcal{J}_3 \frac{\partial \mathcal{H}^{dq0}}{\partial \phi_r^{dq0}}, \end{aligned}$$

but derivatives with respect to  $\phi_s^{dq0}$ ,  $\phi_r^{dq0}$  and  $\rho$  do not change. Thus the currents, the speed and the electromagnetic torque are given by

$$i_s^{dq0}(\theta, \rho, \phi_s^{dq0}, \phi_r^{dq0}) = \frac{\partial \mathcal{H}^{dq0}}{\partial \phi_s^{dq0}}(\theta, \rho, \phi_s^{dq0}, \phi_r^{dq0}) \quad (3.25a)$$

$$i_r^{dq0}(\theta, \rho, \phi_s^{dq0}, \phi_r^{dq0}) = \frac{\partial \mathcal{H}^{dq0}}{\partial \phi_r^{dq0}}(\theta, \rho, \phi_s^{dq0}, \phi_r^{dq0}) \quad (3.25b)$$

$$\omega(\theta, \rho, \phi_s^{dq0}, \phi_r^{dq0}) = n^2 \frac{\partial \mathcal{H}^{dq0}}{\partial \rho}(\theta, \rho, \phi_s^{dq0}, \phi_r^{dq0}) \quad (3.25c)$$

$$T_e(\theta, \rho, \phi_s^{dq0}, \phi_r^{dq0}) = -n \frac{\partial \mathcal{H}^{dq0}}{\partial \theta}(\theta, \rho, \phi_s^{dq0}, \phi_r^{dq0}) + n \phi_r^{dq0 T} \mathcal{J}_3 i_r^{dq0}(\theta, \rho, \phi_s^{dq0}, \phi_r^{dq0}) \quad (3.25d)$$

The eqs. (3.25a) and (3.25b) show that energy-based modeling automatically enforces the reciprocity conditions mentioned in Sauer [30] since

$$\frac{\partial i_s^d}{\partial \phi_s^q} = \frac{\partial^2 \mathcal{H}^{dq0}}{\partial \phi_s^d \partial \phi_s^q} = \frac{\partial^2 \mathcal{H}^{dq0}}{\partial \phi_s^q \partial \phi_s^d} = \frac{\partial i_s^q}{\partial \phi_s^d} \quad (3.26a)$$

$$\frac{\partial i_r^d}{\partial \phi_r^q} = \frac{\partial^2 \mathcal{H}^{dq0}}{\partial \phi_r^d \partial \phi_r^q} = \frac{\partial^2 \mathcal{H}^{dq0}}{\partial \phi_r^q \partial \phi_r^d} = \frac{\partial i_r^q}{\partial \phi_r^d}. \quad (3.26b)$$

In fact the reciprocity conditions come from energy conservation considerations.

### 3.3.4 Rotor-oriented frame

#### 3.3.4.1 Salient rotor case

Rotor saliency induces a new privileged direction that we would like to have in our frame. As we will see in sections 3.6 and 3.7, this simplifies energy-based models. The new frame we are looking for is the rotor  $\alpha\beta 0$  frame up to a rotation of a constant angle (as shown in section 3.3.1, constant angle rotations do not affect Hamilton's equations, so we will consider that we chose appropriately the  $a$  axis for this angle to be zero). We define the transformation matrix from the stator  $\alpha\beta 0$  frame to the rotor-linked  $DQ0$  frame by

$$P_{\alpha\beta 0 \rightarrow DQ0}(\theta) = \begin{pmatrix} \cos \theta & \sin \theta & 0 \\ -\sin \theta & \cos \theta & 0 \\ 0 & 0 & 1 \end{pmatrix}. \quad (3.27)$$

Again, this transformation is not canonical due to the dependency on  $\theta$  of the matrix  $P_{\alpha\beta 0 \rightarrow DQ0}$ . But just as in section 3.3.3, we can find equations not very far from Hamilton's equations.

We define an energy function in this frame by

$$\mathcal{H}^{DQ0}(\theta, \rho, \phi_s^{DQ0}, \phi_r^{DQ0}) = \mathcal{H}^{\alpha\beta 0}(\theta, \rho, P_{\alpha\beta 0 \rightarrow DQ0}^{-1}(\theta) \phi_s^{DQ0}, \phi_r^{\alpha\beta 0}). \quad (3.28)$$

Similar calculations as those of eq. (3.24) will give us the state form

$$\frac{d\phi_s^{DQ0}}{dt} = u_s^{DQ0} - R_s i_s^{DQ0}(\theta, \rho, \phi_s^{DQ0}, \phi_r^{DQ0}) - \mathcal{J}_3 \omega \phi_s^{DQ0} \quad (3.29a)$$

$$\frac{d\phi_r^{DQ0}}{dt} = -R_r i_r^{DQ0}(\theta, \rho, \phi_s^{DQ0}, \phi_r^{DQ0}) \quad (3.29b)$$

$$\frac{1}{n} \frac{d\rho}{dt} = T_e(\theta, \rho, \phi_s^{DQ0}, \phi_r^{DQ0}) - T_L \quad (3.29c)$$

$$\frac{d\theta}{dt} = \omega. \quad (3.29d)$$

As previously, the derivative of the energy function with respect to  $\theta$  is modified

$$\begin{aligned} \frac{\partial \mathcal{H}^{DQ0}}{\partial \theta} &= \frac{\partial \mathcal{H}^{\alpha\beta 0}}{\partial \theta} + \frac{\partial}{\partial \theta} \left( P_{\alpha\beta 0 \rightarrow DQ0}^{-1}(\theta) \phi_s^{DQ0} \right)^T \frac{\partial \mathcal{H}^{\alpha\beta 0}}{\partial \phi_s^{\alpha\beta 0}} \\ &= \frac{\partial \mathcal{H}^{\alpha\beta 0}}{\partial \theta} + \phi_s^{DQ0T} P_{\alpha\beta 0 \rightarrow DQ0}^{-T}(\theta) P_{\alpha\beta 0 \rightarrow DQ0}^{-1}(\theta) \frac{\partial \mathcal{H}^{DQ0}}{\partial \phi_s^{DQ0}} \\ &= \frac{\partial \mathcal{H}^{\alpha\beta 0}}{\partial \theta} - \phi_s^{DQ0T} \mathcal{J}_3 \frac{\partial \mathcal{H}^{DQ0}}{\partial \phi_s^{DQ0}} \end{aligned}$$

while the other derivatives of  $\mathcal{H}^{DQ0}$  are not affected. Thus, the current-flux relations, the electromagnetic torque expression and the electrical speed will be given by

$$i_s^{DQ0}(\theta, \rho, \phi_s^{DQ0}, \phi_r^{DQ0}) = \frac{\partial \mathcal{H}^{DQ0}}{\partial \phi_s^{DQ0}}(\theta, \rho, \phi_s^{DQ0}, \phi_r^{DQ0}) \quad (3.30a)$$

$$i_r^{DQ0}(\theta, \rho, \phi_s^{DQ0}, \phi_r^{DQ0}) = \frac{\partial \mathcal{H}^{DQ0}}{\partial \phi_r^{DQ0}}(\theta, \rho, \phi_s^{DQ0}, \phi_r^{DQ0}) \quad (3.30b)$$

$$\omega(\theta, \rho, \phi_s^{DQ0}, \phi_r^{DQ0}) = n^2 \frac{\partial \mathcal{H}^{DQ0}}{\partial \rho}(\theta, \rho, \phi_s^{DQ0}, \phi_r^{DQ0}) \quad (3.30c)$$

$$\begin{aligned} T_e(\theta, \rho, \phi_s^{DQ0}, \phi_r^{DQ0}) &= -n \frac{\partial \mathcal{H}^{DQ0}}{\partial \theta}(\theta, \rho, \phi_s^{DQ0}, \phi_r^{DQ0}) \\ &\quad - n \phi_s^{DQ0T} \mathcal{J}_3 i_s^{DQ0}(\theta, \rho, \phi_s^{DQ0}, \phi_r^{DQ0}). \end{aligned} \quad (3.30d)$$

### 3.3.4.2 Non-salient rotor case

In the case of a non salient motor, we will define the  $DQ0$  frame using the direction of the rotor flux when it is not zero: the  $D$ -axis will be taken collinear with the rotor flux. This is a particular case of the transformations defined in section 3.3.3 since the rotor flux rotates at synchronous speed. The transformation matrix for rotor variables will thus be  $P_{\alpha\beta0 \rightarrow DQ0}(\alpha)$  and for stator variables it will be  $P_{\alpha\beta0 \rightarrow DQ0}(\alpha + \theta)$  where  $\alpha$  is an argument of  $\frac{\phi_r^{\alpha\beta}}{\phi_r^\alpha} = \phi_r^\alpha + j\phi_r^\beta$  and  $P_{\alpha\beta0 \rightarrow DQ0}$  is defined by eq. (3.27). The transformation in the salient case done in section 3.3.4.1 can also be seen as a particular case of this transformation obtained by setting  $\alpha = 0$ . It should be noted that we will always have  $\phi_r^Q = 0$  due to the way the frame was defined. Again this transformation is not canonical.

The energy function in the  $DQ0$  frame is defined as

$$\mathcal{H}^{DQ0}(\theta, \rho, \phi_s^{DQ0}, \phi_r^{DQ0}) := \mathcal{H}^{\alpha\beta0}(\theta, \rho, P_{\alpha\beta0 \rightarrow DQ0}^{-1}(\alpha + \theta)\phi_s^{DQ0}, P_{\alpha\beta0 \rightarrow DQ0}^{-1}(\alpha)\phi_r^{DQ0}). \quad (3.31)$$

We are now looking for the state equations associated with this energy function. The first step is to compute the time derivative of  $\alpha$ , which gives

$$\frac{d\alpha}{dt} = \frac{d}{dt} \arctan\left(\frac{\phi_r^\beta}{\phi_r^\alpha}\right) = \frac{\left(\frac{d\phi_r^{\alpha\beta0}}{dt}\right)^T \mathcal{J}_3 \phi_r^{\alpha\beta0}}{\|\phi_r^{\alpha\beta}\|^2} = \frac{\left(\frac{d\phi_r^{DQ0}}{dt}\right)^T \mathcal{J}_3 \phi_r^{DQ0}}{\|\phi_r^{DQ}\|^2} = -R_r \frac{i_r^Q}{\phi_r^D}. \quad (3.32)$$

Then, we find the time derivatives of the state variables in the  $DQ0$  frame

$$\begin{aligned} \frac{d\phi_s^{DQ0}}{dt} &= \frac{d}{dt} \left( P_{\alpha\beta0 \rightarrow DQ0}(\alpha + \theta) \phi_s^{\alpha\beta0} \right) \\ &= P_{\alpha\beta0 \rightarrow DQ0}(\alpha + \theta) (u_s^{\alpha\beta0} - R_s i_s^{\alpha\beta0}) \\ &\quad + \left( \frac{d\alpha}{dt} + \omega \right) P'_{\alpha\beta0 \rightarrow DQ0}(\alpha + \theta) P_{\alpha\beta0 \rightarrow DQ0}^{-1}(\alpha + \theta) \phi_s^{DQ0} \\ \frac{d\phi_s^{DQ0}}{dt} &= u_s^{DQ0} - R_s i_s^{DQ0} - \mathcal{J}_3 \omega \phi_s^{DQ0} + \mathcal{J}_3 R_r \frac{i_r^Q}{\phi_r^D} \phi_s^{DQ0} \end{aligned} \quad (3.33a)$$

$$\begin{aligned} \frac{d\phi_r^{DQ0}}{dt} &= \frac{d}{dt} \left( P_{\alpha\beta0 \rightarrow DQ0}(\alpha) \phi_r^{\alpha\beta0} \right) \\ &= -P_{\alpha\beta0 \rightarrow DQ0}(\alpha) R_r i_r^{\alpha\beta0} + \frac{d\alpha}{dt} P'_{\alpha\beta0 \rightarrow DQ0}(\alpha) P_{\alpha\beta0 \rightarrow DQ0}^{-1}(\alpha) \phi_r^{DQ0} \\ \frac{d\phi_r^{DQ0}}{dt} &= -R_r i_r^{DQ0} + \mathcal{J}_3 R_r \frac{i_r^Q}{\phi_r^D} \phi_r^{DQ0} \end{aligned} \quad (3.33b)$$

$$\frac{1}{n} \frac{d\rho}{dt} = T_e(\theta, \rho, \phi_s^{DQ0}, \phi_r^{DQ0}) - T_L \quad (3.33c)$$

$$\frac{d\theta}{dt} = \omega. \quad (3.33d)$$

To obtain the current-flux relations, we need the partial derivative of  $\alpha$  with respect to  $\phi_r^{\alpha\beta0}$

$$\frac{\partial \alpha}{\partial \phi_r^{\alpha\beta0}} = \begin{pmatrix} \frac{\partial \alpha}{\partial \phi_r^\alpha} \\ \frac{\partial \alpha}{\partial \phi_r^\beta} \\ \frac{\partial \alpha}{\partial \phi_r^0} \end{pmatrix} = \begin{pmatrix} \frac{\partial}{\partial \phi_r^\alpha} \arctan\left(\frac{\phi_r^\beta}{\phi_r^\alpha}\right) \\ \frac{\partial}{\partial \phi_r^\beta} \arctan\left(\frac{\phi_r^\beta}{\phi_r^\alpha}\right) \\ \frac{\partial}{\partial \phi_r^0} \arctan\left(\frac{\phi_r^\beta}{\phi_r^\alpha}\right) \end{pmatrix} = \begin{pmatrix} -\frac{\phi_r^\beta}{|\phi_r^{\alpha\beta}|^2} \\ \frac{\phi_r^\alpha}{|\phi_r^{\alpha\beta}|^2} \\ 0 \end{pmatrix} = \frac{1}{\|\phi_r^{\alpha\beta}\|^2} \mathcal{J}_3 \phi_r^{\alpha\beta0}.$$

We then find the current-flux relations

$$\begin{aligned} i_s^{DQ0}(\theta, \rho, \phi_s^{DQ0}, \phi_r^{DQ0}) &= P_{\alpha\beta0 \rightarrow DQ0}(\theta + \alpha) \frac{\partial \mathcal{H}^{\alpha\beta 0}}{\partial \phi_s^{\alpha\beta 0}} \\ &= \frac{\partial \mathcal{H}^{DQ0}}{\partial \phi_s^{DQ0}}(\theta, \rho, \phi_s^{DQ0}, \phi_r^{DQ0}) \end{aligned} \quad (3.35a)$$

$$\begin{aligned} i_r^{DQ0}(\theta, \rho, \phi_s^{DQ0}, \phi_r^{DQ0}) &= P_{\alpha\beta0 \rightarrow DQ0}(\alpha) \frac{\partial \mathcal{H}^{\alpha\beta 0}}{\partial \phi_r^{\alpha\beta 0}} \\ &= P_{\alpha\beta0 \rightarrow DQ0}(\alpha) \left( \frac{\partial \phi_s^{DQ0}}{\partial \phi_r^{\alpha\beta 0}} \frac{\partial \mathcal{H}^{DQ0}}{\partial \phi_s^{DQ0}} + \frac{\partial \phi_r^{DQ0}}{\partial \phi_r^{\alpha\beta 0}} \frac{\partial \mathcal{H}^{DQ0}}{\partial \phi_r^{DQ0}} \right) \\ &= P_{\alpha\beta0 \rightarrow DQ0}(\alpha) \left( P'_{\alpha\beta0 \rightarrow DQ0}(\theta + \alpha) \phi_s^{\alpha\beta 0} \left( \frac{\partial \alpha}{\partial \phi_r^{\alpha\beta 0}} \right)^T \right)^T \frac{\partial \mathcal{H}^{DQ0}}{\partial \phi_s^{DQ0}} \\ &\quad + P_{\alpha\beta0 \rightarrow DQ0}(\alpha) P_{\alpha\beta0 \rightarrow DQ0}(\alpha)^T \frac{\partial \mathcal{H}^{DQ0}}{\partial \phi_r^{DQ0}} \\ &\quad + P_{\alpha\beta0 \rightarrow DQ0}(\alpha) \left( P'_{\alpha\beta0 \rightarrow DQ0}(\alpha) \phi_r^{\alpha\beta 0} \left( \frac{\partial \alpha}{\partial \phi_r^{\alpha\beta 0}} \right)^T \right)^T \frac{\partial \mathcal{H}^{DQ0}}{\partial \phi_r^{DQ0}} \\ &= P_{\alpha\beta0 \rightarrow DQ0}(\alpha) \frac{1}{\|\phi_r^{\alpha\beta}\|^2} \mathcal{J}_3 \phi_r^{\alpha\beta 0} \phi_s^{DQ0 T} \mathcal{J}_3 i_s^{DQ0} \\ &\quad + \frac{\partial \mathcal{H}^{DQ0}}{\partial \phi_r^{DQ0}} + P_{\alpha\beta0 \rightarrow DQ0}(\alpha) \frac{1}{\|\phi_r^{\alpha\beta}\|^2} \mathcal{J}_3 \phi_r^{\alpha\beta 0} \phi_r^{DQ0 T} \mathcal{J}_3 \frac{\partial \mathcal{H}^{DQ0}}{\partial \phi_r^{DQ0}} \\ &= \frac{\partial \mathcal{H}^{DQ0}}{\partial \phi_r^{DQ0}} + \frac{1}{\|\phi_r^{\alpha\beta}\|} \left( \phi_s^{DQ0 T} \mathcal{J}_3 i_s^{DQ0} + \phi_r^{DQ0 T} \mathcal{J}_3 \frac{\partial \mathcal{H}^{DQ0}}{\partial \phi_r^{DQ0}} \right) \begin{pmatrix} 0 \\ 1 \\ 0 \end{pmatrix} \\ &= \begin{pmatrix} \frac{\partial \mathcal{H}^{DQ0}}{\partial \phi_r^D}(\theta, \rho, \phi_s^{DQ0}, \phi_r^{DQ0}) \\ \frac{1}{\phi_r^D} \phi_s^{DQ0 T} \mathcal{J}_3 i_s^{DQ0}(\theta, \rho, \phi_s^{DQ0}, \phi_r^{DQ0}) \\ \frac{\partial \mathcal{H}^{DQ0}}{\partial \phi_r^0}(\theta, \rho, \phi_s^{DQ0}, \phi_r^{DQ0}) \end{pmatrix} \end{aligned} \quad (3.35a)$$

as well as the derivative of the energy function with respect to  $\theta$

$$\begin{aligned} \frac{\partial \mathcal{H}^{DQ0}}{\partial \theta} &= \frac{\partial \mathcal{H}^{\alpha\beta 0}}{\partial \theta} + \frac{\partial}{\partial \theta} \left( P_{\alpha\beta0 \rightarrow DQ0}^{-1}(\theta + \alpha) \phi_s^{DQ0} \right)^T \frac{\partial \mathcal{H}^{\alpha\beta 0}}{\partial \phi_s^{\alpha\beta 0}} \\ &= \frac{\partial \mathcal{H}^{\alpha\beta 0}}{\partial \theta} + \phi_s^{DQ0 T} P_{\alpha\beta0 \rightarrow DQ0}^{-T}(\theta + \alpha) P_{\alpha\beta0 \rightarrow DQ0}^{-1}(\theta + \alpha) i_s^{DQ0} \\ &= \frac{\partial \mathcal{H}^{\alpha\beta 0}}{\partial \theta} - \phi_s^{DQ0 T} \mathcal{J}_3 i_s^{DQ0}. \end{aligned}$$

The electromagnetic torque expressed with variables in the  $DQ0$  frame thus reads

$$T_e(\theta, \rho, \phi_s^{DQ0}, \phi_r^{DQ0}) = -n \frac{\partial \mathcal{H}^{DQ0}}{\partial \theta} - n \phi_s^{DQ0 T} \mathcal{J}_3 i_s^{DQ0}(\theta, \rho, \phi_s^{DQ0}, \phi_r^{DQ0}). \quad (3.36)$$

### 3.4 Symmetries

The state equations we found in the previous sections are valid for any electric motor. However, the energy functions, and thus the current-flux relations and electromagnetic

	State equations	Algebraic relations
$abc$	$\frac{d\phi_s^{abc}}{dt} = u_s^{abc} - R_s \iota_s^{abc}$ $\frac{d\phi_r^{abc}}{dt} = -R_r \iota_r^{abc}$ $\frac{1}{n} \frac{d\rho}{dt} = T_e - T_L$ $\frac{d\theta}{dt} = \omega$	$\iota_s^{abc} = \frac{\partial \mathcal{H}^{abc}}{\partial \phi_s^{abc}}$ $\iota_r^{abc} = \frac{\partial \mathcal{H}^{abc}}{\partial \phi_r^{abc}}$ $\omega = n^2 \frac{\partial \mathcal{H}^{abc}}{\partial \rho}$ $T_e = -n \frac{\partial \mathcal{H}^{abc}}{\partial \theta}$
$\alpha\beta 0$	$\frac{d\phi_s^{\alpha\beta 0}}{dt} = u_s^{\alpha\beta 0} - R_s \iota_s^{\alpha\beta 0}$ $\frac{d\phi_r^{\alpha\beta 0}}{dt} = -R_r \iota_r^{\alpha\beta 0}$ $\frac{1}{n} \frac{d\rho}{dt} = T_e - T_L$ $\frac{d\theta}{dt} = \omega$	$\iota_s^{\alpha\beta 0} = \frac{\partial \mathcal{H}^{\alpha\beta 0}}{\partial \phi_s^{\alpha\beta 0}}$ $\iota_r^{\alpha\beta 0} = \frac{\partial \mathcal{H}^{\alpha\beta 0}}{\partial \phi_r^{\alpha\beta 0}}$ $\omega = n^2 \frac{\partial \mathcal{H}^{\alpha\beta 0}}{\partial \rho}$ $T_e = -n \frac{\partial \mathcal{H}^{\alpha\beta 0}}{\partial \theta}$
$dq 0$	$\frac{d\phi_s^{dq 0}}{dt} = u_s^{dq 0} - R_s \iota_s^{dq 0} - \mathcal{J}_3 \omega_s \phi_s^{dq 0}$ $\frac{d\phi_r^{dq 0}}{dt} = -R_r \iota_r^{dq 0} - \mathcal{J}_3 (\omega_s - \omega) \phi_r^{dq 0}$ $\frac{1}{n} \frac{d\rho}{dt} = T_e - T_L$ $\frac{d\theta}{dt} = \omega$	$\iota_s^{dq 0} = \frac{\partial \mathcal{H}^{dq 0}}{\partial \phi_s^{dq 0}}$ $\iota_r^{dq 0} = \frac{\partial \mathcal{H}^{dq 0}}{\partial \phi_r^{dq 0}}$ $\omega = n^2 \frac{\partial \mathcal{H}^{dq 0}}{\partial \rho}$ $T_e = -n \frac{\partial \mathcal{H}^{dq 0}}{\partial \theta} + n \phi_r^{dq 0 T} \mathcal{J}_3 \iota_r^{dq 0}$
Salient $DQ 0$	$\frac{d\phi_s^{DQ 0}}{dt} = u_s^{DQ 0} - R_s \iota_s^{DQ 0} - \mathcal{J}_3 \omega \phi_s^{DQ 0}$ $\frac{d\phi_r^{DQ 0}}{dt} = -R_r \iota_r^{DQ 0}$ $\frac{1}{n} \frac{d\rho}{dt} = T_e - T_L$ $\frac{d\theta}{dt} = \omega$	$\iota_s^{DQ 0} = \frac{\partial \mathcal{H}^{DQ 0}}{\partial \phi_s^{DQ 0}}$ $\iota_r^{DQ 0} = \frac{\partial \mathcal{H}^{DQ 0}}{\partial \phi_r^{DQ 0}}$ $\omega = n^2 \frac{\partial \mathcal{H}^{DQ 0}}{\partial \rho}$ $T_e = -n \frac{\partial \mathcal{H}^{DQ 0}}{\partial \theta} - n \phi_s^{DQ 0 T} \mathcal{J}_3 \iota_s^{DQ 0}$
Non salient $DQ 0$	$\frac{d\phi_s^{DQ 0}}{dt} = u_s^{DQ 0} - R_s \iota_s^{DQ 0} - \mathcal{J}_3 \left( \omega - R_r \frac{\iota_r^Q}{\phi_r^D} \right) \phi_s^{DQ 0}$ $\frac{d\phi_r^{DQ 0}}{dt} = -R_r \iota_r^{DQ 0} + \mathcal{J}_3 R_r \frac{\iota_r^Q}{\phi_r^D} \phi_r^{DQ 0}$ $\frac{1}{n} \frac{d\rho}{dt} = T_e - T_L$ $\frac{d\theta}{dt} = \omega$	$\iota_s^{DQ 0} = \frac{\partial \mathcal{H}^{DQ 0}}{\partial \phi_s^{DQ 0}}$ $\iota_r^{DQ 0} = \left( \begin{array}{c} \frac{\partial \mathcal{H}^{DQ 0}}{\partial \phi_r^D} \\ \frac{1}{\phi_r^D} \left( \phi_s^{DQ 0 T} \mathcal{J}_3 \iota_s^{DQ 0} \right) \\ \frac{\partial \mathcal{H}^{DQ 0}}{\partial \phi_r^0} \end{array} \right)$ $\omega = n^2 \frac{\partial \mathcal{H}^{DQ 0}}{\partial \rho}$ $T_e = -n \frac{\partial \mathcal{H}^{DQ 0}}{\partial \theta} - n \phi_s^{DQ 0 T} \mathcal{J}_3 \iota_s^{DQ 0}$

Table 3.1 – Summary of the equations obtained in the different frames where dependencies have been omitted for the sake of compactness.

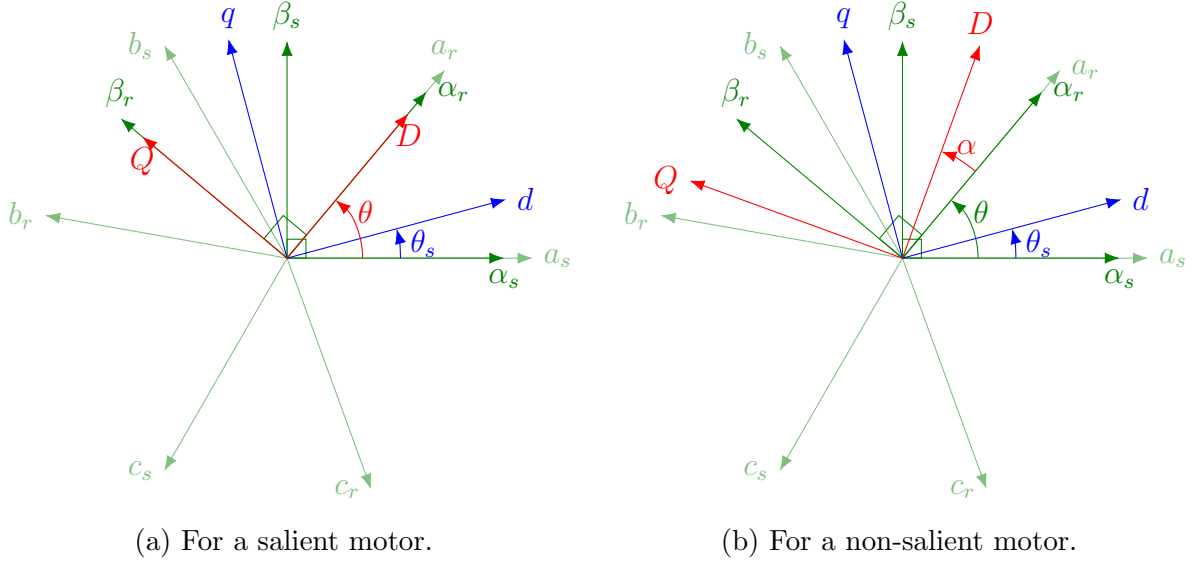


Figure 3.2 – The frames introduced in this section.

torque formula, are not specified. Considering some basic construction symmetries, which are necessarily enforced in any well-built electric machine, will help us to constrain the form of the energy function.

The basic physical principle on which will rely all of the developments done in this section is: Applying a transformation to the motor as a whole does not change its energy. Indeed an electric motor operates similarly whatever its spatial orientation.

### 3.4.1 Symmetries due to stator layout

In three phase electric motors, all the phases are wound identically for the positive and the negative poles. This basic construction symmetry of the stator will allow us to get some constraints on the energy function.

#### 3.4.1.1 Stator phase permutation

If the stator phases are circularly permuted and the rotor is rotated by  $\frac{2\pi}{3}$ , the energy of the motor is not changed, since a rotation of the whole motor by  $-\frac{2\pi}{3}$  around the rotor axis allows us to go back to initial state as shown in fig. 3.3. Thus

$$\mathcal{H}^{abc}(\theta, \rho, \phi_s^{abc}, \phi_r^{abc}) = \mathcal{H}^{abc}(\theta + \frac{2\pi}{3}, \rho, \mathcal{P}^{abc} \phi_s^{abc}, \phi_r^{abc}) \quad (3.37)$$

where the phase permutation matrix is defined as

$$\mathcal{P}^{abc} := \begin{pmatrix} 0 & 0 & 1 \\ 1 & 0 & 0 \\ 0 & 1 & 0 \end{pmatrix}. \quad (3.38)$$

When we rewrite this invariance using  $\alpha\beta 0$  variables, we get

$$\begin{aligned} \mathcal{H}^{\alpha\beta 0}(\theta, \rho, \phi_s^{\alpha\beta 0}, \phi_r^{\alpha\beta 0}) &= \mathcal{H}^{abc}(\theta, \rho, P_{abc \rightarrow \alpha\beta 0}^{-1} \phi_s^{\alpha\beta 0}, P_{abc \rightarrow \alpha\beta 0}^{-1} \phi_r^{\alpha\beta 0}) \\ &= \mathcal{H}^{abc}(\theta + \frac{2\pi}{3}, \rho, \mathcal{P}^{abc} P_{abc \rightarrow \alpha\beta 0}^{-1} \phi_s^{\alpha\beta 0}, P_{abc \rightarrow \alpha\beta 0}^{-1} \phi_r^{\alpha\beta 0}) \\ &= \mathcal{H}^{\alpha\beta 0}(\theta + \frac{2\pi}{3}, \rho, P_{abc \rightarrow \alpha\beta 0} \mathcal{P}^{abc} P_{abc \rightarrow \alpha\beta 0}^{-1} \phi_s^{\alpha\beta 0}, P_{abc \rightarrow \alpha\beta 0} P_{abc \rightarrow \alpha\beta 0}^{-1} \phi_r^{\alpha\beta 0}) \\ \mathcal{H}^{\alpha\beta 0}(\theta, \rho, \phi_s^{\alpha\beta 0}, \phi_r^{\alpha\beta 0}) &= \mathcal{H}^{\alpha\beta 0}(\theta + \frac{2\pi}{3}, \rho, \mathcal{P}^{\alpha\beta 0} \phi_s^{\alpha\beta 0}, \phi_r^{\alpha\beta 0}) \end{aligned} \quad (3.39)$$

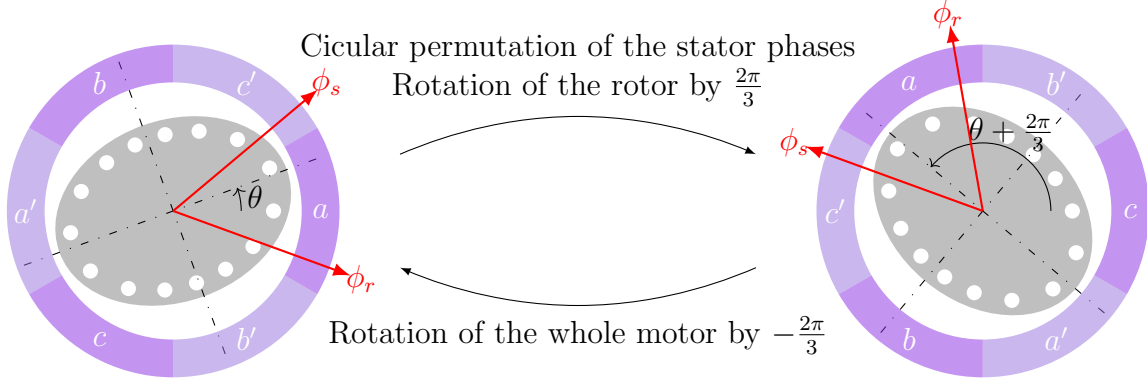


Figure 3.3 – Illustration of the stator phase permutation invariance.

where

$$\mathcal{P}^{\alpha\beta 0} := P_{abc \rightarrow \alpha\beta 0} \mathcal{P}^{abc} P_{abc \rightarrow \alpha\beta 0}^{-1} = \begin{pmatrix} -\frac{1}{2} & -\frac{\sqrt{3}}{2} & 0 \\ \frac{\sqrt{3}}{2} & -\frac{1}{2} & 0 \\ 0 & 0 & 1 \end{pmatrix} = \mathcal{R}^{\alpha\beta 0} \left( \frac{2\pi}{3} \right)$$

with  $\mathcal{R}^{\alpha\beta 0}$  is the matrix of the rotation around the 0-axis expressed in the  $\alpha\beta 0$  frame. This is still not a very simple invariance. However, if we rewrite it in the  $DQ0$  frame, we get

$$\begin{aligned} \mathcal{H}^{DQ0}(\theta, \rho, \phi_s^{DQ0}, \phi_r^{DQ0}) &= \mathcal{H}^{\alpha\beta 0}(\theta, \rho, P_{\alpha\beta 0 \rightarrow DQ0}^{-1}(\alpha + \theta)\phi_s^{DQ0}, P_{\alpha\beta 0 \rightarrow DQ0}^{-1}(\alpha)\phi_r^{DQ0}) \\ &= \mathcal{H}^{\alpha\beta 0}\left(\theta + \frac{2\pi}{3}, \rho, \mathcal{P}^{\alpha\beta 0} P_{\alpha\beta 0 \rightarrow DQ0}^{-1}(\alpha + \theta)\phi_s^{DQ0}, P_{\alpha\beta 0 \rightarrow DQ0}^{-1}(\alpha)\phi_r^{DQ0}\right) \\ &= \mathcal{H}^{DQ0}\left(\theta + \frac{2\pi}{3}, \rho, \right. \\ &\quad \left. P_{\alpha\beta 0 \rightarrow DQ0}(\alpha + \theta + \frac{2\pi}{3}) \mathcal{P}^{\alpha\beta 0} P_{\alpha\beta 0 \rightarrow DQ0}^{-1}(\alpha + \theta)\phi_s^{DQ0}, \right. \\ &\quad \left. P_{\alpha\beta 0 \rightarrow DQ0}(\alpha) P_{\alpha\beta 0 \rightarrow DQ0}^{-1}(\alpha)\phi_r^{DQ0}\right) \\ \mathcal{H}^{DQ0}(\theta, \rho, \phi_s^{DQ0}, \phi_r^{DQ0}) &= \mathcal{H}^{DQ0}\left(\theta + \frac{2\pi}{3}, \rho, \phi_s^{DQ0}, \phi_r^{DQ0}\right). \end{aligned}$$

Notice that the current value of the angles  $\alpha$  and  $\theta$  must be used in the transformation matrices  $P_{\alpha\beta 0 \rightarrow DQ0}$ . That is why between the first and third equalities the angles in the transformation matrices are not the same. This gives after simplification

$$\mathcal{H}^{DQ0}(\theta, \rho, \phi_s^D, \phi_s^Q, \phi_s^0, \phi_r^D, \phi_r^Q, \phi_r^0) = \mathcal{H}^{DQ0}\left(\theta + \frac{2\pi}{3}, \rho, \phi_s^D, \phi_s^Q, \phi_s^0, \phi_r^D, \phi_r^Q, \phi_r^0\right). \quad (3.40)$$

Thus the energy function of any well-built electric motor expressed in the  $DQ0$  frame is  $\frac{2\pi}{3}$ -periodic with respect to  $\theta$ .

### 3.4.1.2 Stator current reversal

If the currents in the stator phases are reversed and the rotor is rotated by an angle of  $\pi$ , the energy is left unaltered, as a rotation of the whole motor by  $-\pi$  puts the motor back in the initial state as is shown in fig. 3.4. Thus we have in the  $abc$  frame

$$\mathcal{H}^{abc}(\theta, \rho, \phi_s^{abc}, \phi_r^{abc}) = \mathcal{H}^{abc}\left(\theta + \pi, \rho, -\phi_s^{abc}, \phi_r^{abc}\right) \quad (3.41)$$

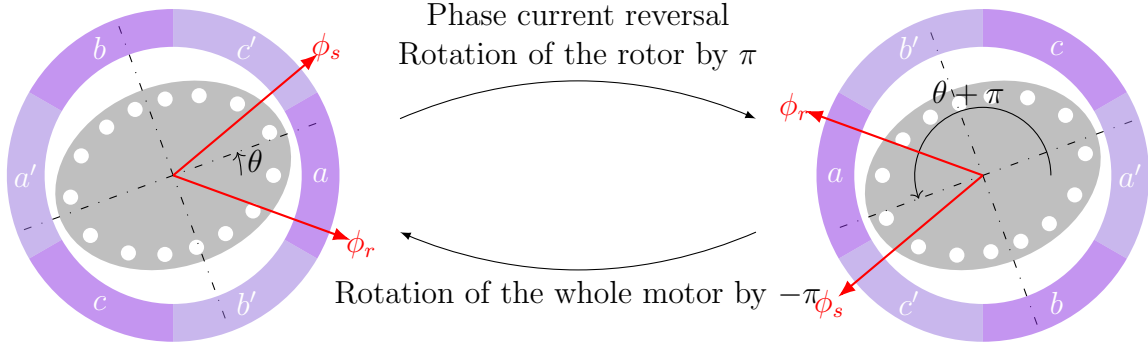


Figure 3.4 – Illustration of the stator phase current reversal invariance.

which gives in the  $\alpha\beta 0$  frame

$$\begin{aligned}
 \mathcal{H}^{\alpha\beta 0}(\theta, \rho, \phi_s^{\alpha\beta 0}, \phi_r^{\alpha\beta 0}) &= \mathcal{H}^{abc}(\theta, \rho, P_{abc \rightarrow \alpha\beta 0}^{-1} \phi_s^{\alpha\beta 0}, P_{abc \rightarrow \alpha\beta 0}^{-1} \phi_r^{\alpha\beta 0}) \\
 &= \mathcal{H}^{abc}(\theta + \pi, \rho, -P_{abc \rightarrow \alpha\beta 0}^{-1} \phi_s^{\alpha\beta 0}, P_{abc \rightarrow \alpha\beta 0}^{-1} \phi_r^{\alpha\beta 0}) \\
 &= \mathcal{H}^{\alpha\beta 0}(\theta + \pi, \rho, -P_{abc \rightarrow \alpha\beta 0} P_{abc \rightarrow \alpha\beta 0}^{-1} \phi_s^{\alpha\beta 0}, P_{abc \rightarrow \alpha\beta 0} P_{abc \rightarrow \alpha\beta 0}^{-1} \phi_r^{\alpha\beta 0}) \\
 \mathcal{H}^{\alpha\beta 0}(\theta, \rho, \phi_s^{\alpha\beta 0}, \phi_r^{\alpha\beta 0}) &= \mathcal{H}^{\alpha\beta 0}(\theta + \pi, \rho, -\phi_s^{\alpha\beta 0}, \phi_r^{\alpha\beta 0}). \tag{3.42}
 \end{aligned}$$

After the algebra required to transform this constraint to  $DQ0$  frame,

$$\begin{aligned}
 \mathcal{H}^{DQ0}(\theta, \rho, \phi_s^{DQ0}, \phi_r^{DQ0}) &= \mathcal{H}^{\alpha\beta 0}(\theta, \rho, P_{\alpha\beta 0 \rightarrow DQ0}^{-1}(\alpha + \theta) \phi_s^{DQ0}, P_{\alpha\beta 0 \rightarrow DQ0}^{-1}(\alpha) \phi_r^{DQ0}) \\
 &= \mathcal{H}^{\alpha\beta 0}(\theta + \pi, \rho, -P_{\alpha\beta 0 \rightarrow DQ0}^{-1}(\alpha + \theta) \phi_s^{DQ0}, P_{\alpha\beta 0 \rightarrow DQ0}^{-1}(\alpha) \phi_r^{DQ0}) \\
 &= \mathcal{H}^{DQ0}(\theta + \pi, \rho, -P_{\alpha\beta 0 \rightarrow DQ0}(\alpha + \theta + \pi) P_{\alpha\beta 0 \rightarrow DQ0}^{-1}(\alpha + \theta) \phi_s^{DQ0}, \\
 &\quad P_{\alpha\beta 0 \rightarrow DQ0}(\alpha) P_{\alpha\beta 0 \rightarrow DQ0}^{-1}(\alpha) \phi_r^{DQ0}),
 \end{aligned}$$

we obtain

$$\mathcal{H}^{DQ0}(\theta, \rho, \phi_s^D, \phi_s^Q, \phi_s^0, \phi_r^D, \phi_r^Q, \phi_r^0) = \mathcal{H}^{DQ0}(\theta + \pi, \rho, \phi_s^D, \phi_s^Q, -\phi_s^0, \phi_r^D, \phi_r^Q, \phi_r^0). \tag{3.43}$$

### 3.4.2 Symmetries due to rotor layout

Rotors of electric motors may present a saliency along orthogonal planes, called saliency planes. As was said in section 3.3.4.1 we take the rotor-linked  $a$ -axis and  $\alpha$ -axis in one of these planes. The possible cases are presented in fig. 3.5.

We are now considering the effect of all possible symmetries of the rotor. We will later make some assumptions on motor construction and use the conditions derived below to simplify the energy function.

#### 3.4.2.1 When the rotor is symmetric with respect to saliency plane

In this section we are going to assume that the rotor has a construction symmetry with respect to one of the saliency planes as in fig. 3.5b. Under this hypothesis, there is one invariance condition on top of those presented in section 3.4.1.

If the phases  $b$  and  $c$  are swapped in both the stator and the rotor and, if the direction of the rotation is reversed, then the energy does not change as a symmetry of the whole

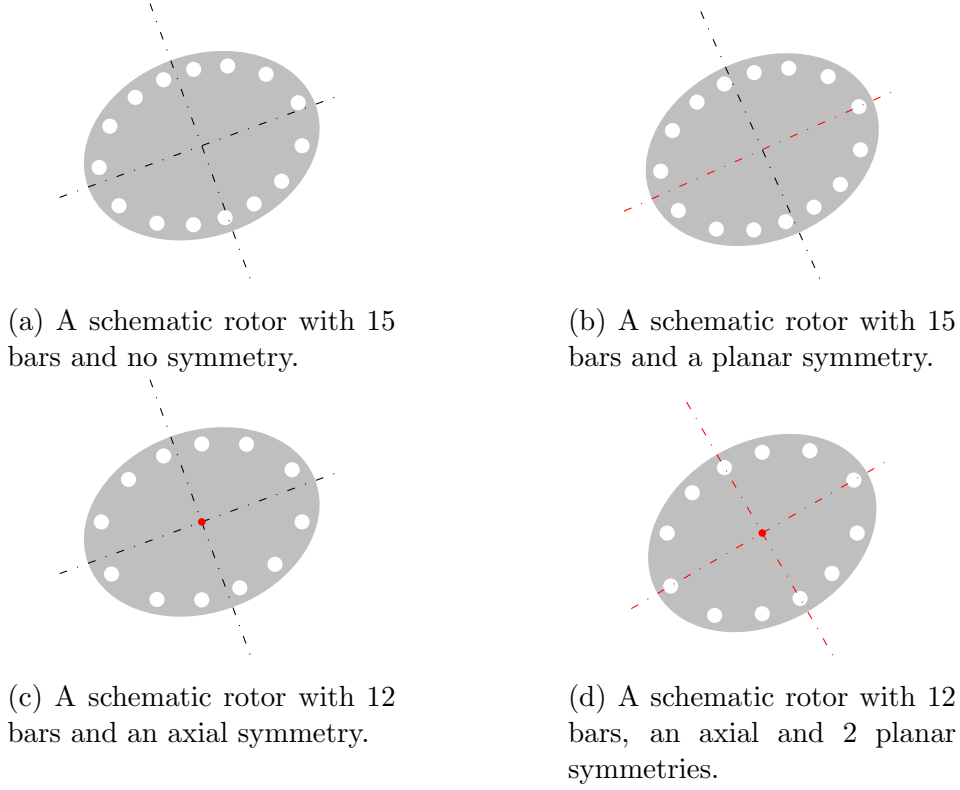


Figure 3.5 – The different configurations possible for the rotor.

motor with respect to the saliency plane puts the motor back in its initial state as shown in fig. 3.6. Thus, we have in the  $abc$  frame

$$\mathcal{H}^{abc}(\theta, \rho, \phi_s^{abc}, \phi_r^{abc}) = \mathcal{H}^{abc}(-\theta, -\rho, \mathcal{O}^{abc} \phi_s^{abc}, \mathcal{O}^{abc} \phi_r^{abc}) \quad (3.44)$$

with

$$\mathcal{O}^{abc} = \begin{pmatrix} 1 & 0 & 0 \\ 0 & 0 & 1 \\ 0 & 1 & 0 \end{pmatrix} \quad (3.45)$$

Expressed in the  $\alpha\beta 0$  frame this condition reads

$$\begin{aligned} \mathcal{H}^{\alpha\beta 0}(\theta, \rho, \phi_s^{\alpha\beta 0}, \phi_r^{\alpha\beta 0}) &= \mathcal{H}^{abc}(\theta, \rho, P_{abc \rightarrow \alpha\beta 0}^{-1} \phi_s^{\alpha\beta 0}, P_{abc \rightarrow \alpha\beta 0}^{-1} \phi_r^{\alpha\beta 0}) \\ &= \mathcal{H}^{abc}(-\theta, -\rho, \mathcal{O}^{abc} P_{abc \rightarrow \alpha\beta 0}^{-1} \phi_s^{\alpha\beta 0}, \mathcal{O}^{abc} P_{abc \rightarrow \alpha\beta 0}^{-1} \phi_r^{\alpha\beta 0}) \\ &= \mathcal{H}^{\alpha\beta 0}(-\theta, -\rho, P_{abc \rightarrow \alpha\beta 0} \mathcal{O}^{abc} P_{abc \rightarrow \alpha\beta 0}^{-1} \phi_s^{\alpha\beta 0}, \\ &\quad P_{abc \rightarrow \alpha\beta 0} \mathcal{O}^{abc} P_{abc \rightarrow \alpha\beta 0}^{-1} \phi_r^{\alpha\beta 0}) \\ \mathcal{H}^{\alpha\beta 0}(\theta, \rho, \phi_s^{\alpha\beta 0}, \phi_r^{\alpha\beta 0}) &= \mathcal{H}^{\alpha\beta 0}(-\theta, -\rho, \mathcal{O}^{\alpha\beta 0} \phi_s^{\alpha\beta 0}, \mathcal{O}^{\alpha\beta 0} \phi_r^{\alpha\beta 0}) \end{aligned} \quad (3.46)$$

where we used

$$\mathcal{O}^{\alpha\beta 0} := P_{abc \rightarrow \alpha\beta 0} \mathcal{O}^{abc} P_{abc \rightarrow \alpha\beta 0}^{-1} = \begin{pmatrix} 1 & 0 & 0 \\ 0 & -1 & 0 \\ 0 & 0 & 1 \end{pmatrix}.$$

This constraint is now transformed to  $DQ0$  frame as follows

$$\begin{aligned} \mathcal{H}^{DQ0}(\theta, \rho, \phi_s^{DQ0}, \phi_r^{DQ0}) &= \mathcal{H}^{\alpha\beta 0}(\theta, \rho, P_{\alpha\beta 0 \rightarrow DQ0}^{-1}(\alpha + \theta) \phi_s^{DQ0}, P_{\alpha\beta 0 \rightarrow DQ0}^{-1}(\alpha) \phi_r^{DQ0}) \\ &= \mathcal{H}^{\alpha\beta 0}(-\theta, -\rho, \mathcal{O}^{\alpha\beta 0} P_{\alpha\beta 0 \rightarrow DQ0}^{-1}(\alpha + \theta) \phi_s^{DQ0}, \\ &\quad \mathcal{O}^{\alpha\beta 0} P_{\alpha\beta 0 \rightarrow DQ0}^{-1}(\alpha) \phi_r^{DQ0}) \end{aligned}$$

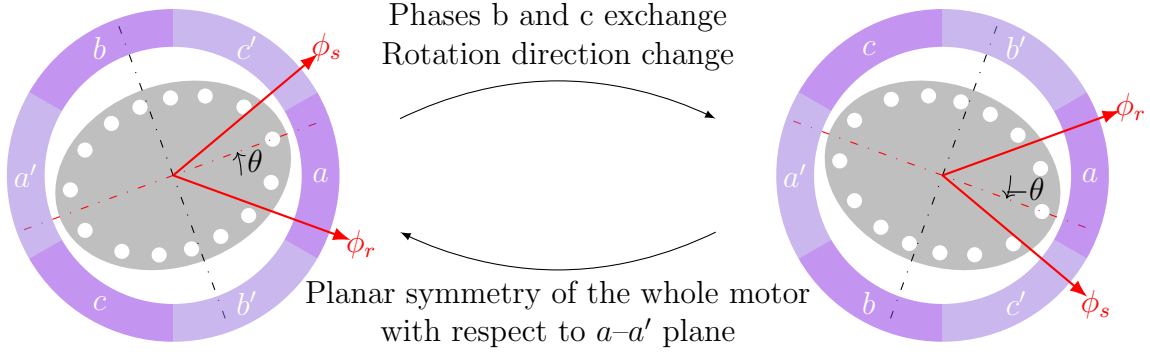


Figure 3.6 – Illustration of the stator and rotor phase exchange invariance when the rotor is symmetric with respect to a plane.

$$\begin{aligned} & \mathcal{O}^{\alpha\beta 0} P_{\alpha\beta 0 \rightarrow DQ0}^{-1}(\alpha) \phi_r^{DQ0} \\ &= \mathcal{H}^{DQ0}(-\theta, -\rho, P_{\alpha\beta 0 \rightarrow DQ0}(-\alpha - \theta) \mathcal{O}^{\alpha\beta 0} P_{\alpha\beta 0 \rightarrow DQ0}^{-1}(\alpha + \theta) \phi_s^{DQ0}, \\ & \quad P_{\alpha\beta 0 \rightarrow DQ0}(-\alpha) \mathcal{O}^{\alpha\beta 0} P_{\alpha\beta 0 \rightarrow DQ0}^{-1}(\alpha) \phi_r^{DQ0}) \end{aligned}$$

In the first and last equality  $\theta$  and  $\alpha$  are not the same as they both changed value in between. Rewritten component-wise this gives

$$\mathcal{H}^{DQ0}(\theta, \rho, \phi_s^D, \phi_s^Q, \phi_s^0, \phi_r^D, \phi_r^Q, \phi_r^0) = \mathcal{H}^{DQ0}(-\theta, -\rho, \phi_s^D, -\phi_s^Q, \phi_s^0, \phi_r^D, -\phi_r^Q, \phi_r^0). \quad (3.47)$$

### 3.4.2.2 When the rotor is symmetric with respect to rotation axis

In this section we will suppose that the rotor has a central symmetry with respect to its rotation axis as shown in fig. 3.5c. This hypothesis gives also a new invariance condition. Indeed, if the rotor currents are reversed and the rotor is rotated by  $\pi$ , the energy does not change as a rotation of the whole space by  $-\pi$  around the rotor axis allows us to go back to initial state as shown in fig. 3.7. Thus we have in the  $abc$  frame

$$\mathcal{H}^{abc}(\theta, \rho, \phi_s^{abc}, \phi_r^{abc}) = \mathcal{H}^{abc}(\theta + \pi, \rho, \phi_s^{abc}, -\phi_r^{abc}) \quad (3.48)$$

which gives in the  $\alpha\beta 0$  frame

$$\begin{aligned} \mathcal{H}^{\alpha\beta 0}(\theta, \rho, \phi_s^{\alpha\beta 0}, \phi_r^{\alpha\beta 0}) &= \mathcal{H}^{abc}(\theta, \rho, P_{abc \rightarrow \alpha\beta 0}^{-1} \phi_s^{\alpha\beta 0}, P_{abc \rightarrow \alpha\beta 0}^{-1} \phi_r^{\alpha\beta 0}) \\ &= \mathcal{H}^{abc}(\theta + \pi, \rho, P_{abc \rightarrow \alpha\beta 0}^{-1} \phi_s^{\alpha\beta 0}, -P_{abc \rightarrow \alpha\beta 0}^{-1} \phi_r^{\alpha\beta 0}) \\ &= \mathcal{H}^{\alpha\beta 0}(\theta + \pi, \rho, P_{abc \rightarrow \alpha\beta 0} P_{abc \rightarrow \alpha\beta 0}^{-1} \phi_s^{\alpha\beta 0}, -P_{abc \rightarrow \alpha\beta 0} P_{abc \rightarrow \alpha\beta 0}^{-1} \phi_r^{\alpha\beta 0}) \\ \mathcal{H}^{\alpha\beta 0}(\theta, \rho, \phi_s^{\alpha\beta 0}, \phi_r^{\alpha\beta 0}) &= \mathcal{H}^{\alpha\beta 0}(\theta + \pi, \rho, \phi_s^{\alpha\beta 0}, -\phi_r^{\alpha\beta 0}). \end{aligned} \quad (3.49)$$

In  $DQ0$  frame, for a non-salient motor ( $\alpha$  is the argument of  $\phi_r^{\alpha\beta}$ ), this gives

$$\begin{aligned} \mathcal{H}^{DQ0}(\theta, \rho, \phi_s^{DQ0}, \phi_r^{DQ0}) &= \mathcal{H}^{\alpha\beta 0}(\theta, \rho, P_{\alpha\beta 0 \rightarrow DQ0}^{-1}(\alpha + \theta) \phi_s^{DQ0}, P_{\alpha\beta 0 \rightarrow DQ0}^{-1}(\alpha) \phi_r^{DQ0}) \\ &= \mathcal{H}^{\alpha\beta 0}(\theta + \pi, \rho, P_{\alpha\beta 0 \rightarrow DQ0}^{-1}(\alpha + \theta) \phi_s^{DQ0}, -P_{\alpha\beta 0 \rightarrow DQ0}^{-1}(\alpha) \phi_r^{DQ0}) \\ &= \mathcal{H}^{DQ0}(\theta + \pi, \rho, P_{\alpha\beta 0 \rightarrow DQ0}(\alpha + \pi + \theta + \pi) P_{\alpha\beta 0 \rightarrow DQ0}^{-1}(\alpha + \theta) \phi_s^{DQ0}, \\ & \quad -P_{\alpha\beta 0 \rightarrow DQ0}(\alpha + \pi) P_{\alpha\beta 0 \rightarrow DQ0}^{-1}(\alpha) \phi_r^{DQ0}) \end{aligned}$$

and we find

$$\mathcal{H}^{DQ0}(\theta, \rho, \phi_s^D, \phi_s^Q, \phi_s^0, \phi_r^D, \phi_r^Q, \phi_r^0) = \mathcal{H}^{DQ0}(\theta + \pi, \rho, \phi_s^D, \phi_s^Q, \phi_s^0, \phi_r^D, \phi_r^Q, -\phi_r^0). \quad (3.50)$$

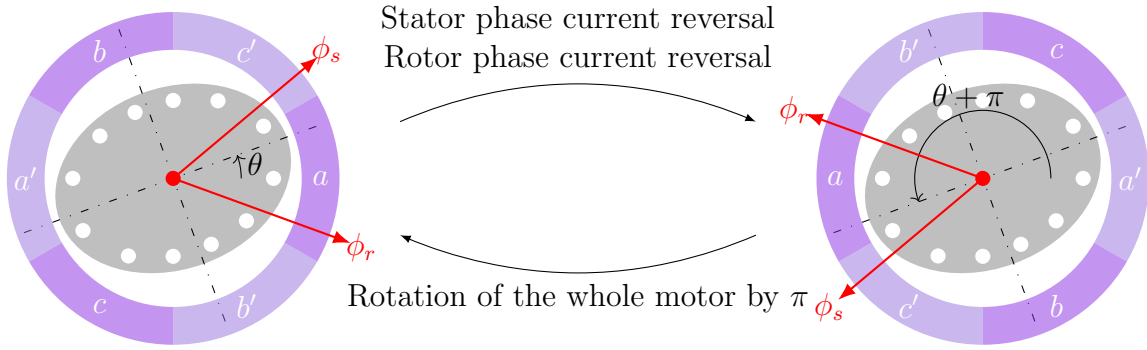


Figure 3.7 – Illustration of the stator and rotor phase current reversal invariance when the rotor is symmetric with respect to its rotation axis.

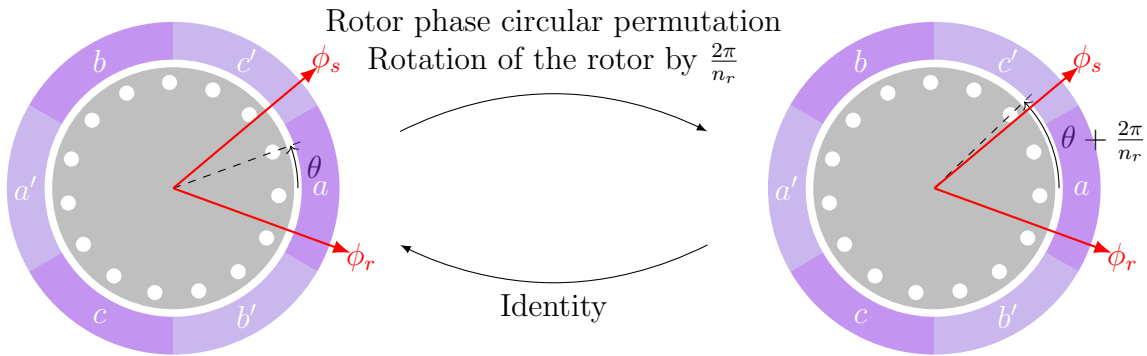


Figure 3.8 – Illustration of the rotor phase permutation invariance when the rotor is not salient.

In  $DQ0$  frame, for a salient motor ( $\alpha = 0$ ), this gives

$$\begin{aligned} \mathcal{H}^{DQ0}(\theta, \rho, \phi_s^{DQ0}, \phi_r^{DQ0}) &= \mathcal{H}^{\alpha\beta0}(\theta, \rho, P_{\alpha\beta0 \rightarrow DQ0}^{-1}(\theta) \phi_s^{DQ0}, \phi_r^{DQ0}) \\ &= \mathcal{H}^{\alpha\beta0}(\theta + \pi, \rho, P_{\alpha\beta0 \rightarrow DQ0}^{-1}(\theta) \phi_s^{DQ0}, -\phi_r^{DQ0}) \\ &= \mathcal{H}^{DQ0}(\theta + \pi, \rho, P_{\alpha\beta0 \rightarrow DQ0}(\theta + \pi) P_{\alpha\beta0 \rightarrow DQ0}^{-1}(\theta) \phi_s^{DQ0}, -\phi_r^{DQ0}) \end{aligned}$$

and after simplification, we obtain

$$\mathcal{H}^{DQ0}(\theta, \rho, \phi_s^D, \phi_s^Q, \phi_s^0, \phi_r^D, \phi_r^Q, \phi_r^0) = \mathcal{H}^{DQ0}(\theta + \pi, \rho, -\phi_s^D, -\phi_s^Q, \phi_s^0, -\phi_r^D, -\phi_r^Q, -\phi_r^0). \quad (3.51)$$

### 3.4.2.3 Non-salient rotor

In this section we are going to assume that the rotor is not salient with respect to any axis and has  $n_r$  bars. This means that if we rotate the rotor flux vector by  $-\frac{2\pi}{n_r}$  around the 0-axis and rotate the rotor by  $\frac{2\pi}{n_r}$  the energy will not be changed as the state of the motor is not changed as shown in fig. 3.8.

As there is an invariance by rotation around the rotor axis (which is the 0-axis) and as the  $abc$  frame is the only frame where physical reasonings can be done, we need to find the expression of a rotation around the 0-axis for vectors of the  $abc$  frame. We know that for vectors of the  $\alpha\beta0$  frame such a rotation is

$$\mathcal{R}^{\alpha\beta0}(\eta) := \begin{pmatrix} \cos \eta & -\sin \eta & 0 \\ \sin \eta & \cos \eta & 0 \\ 0 & 0 & 1 \end{pmatrix}, \quad (3.52)$$

so, the rotation for vectors of the  $abc$  frame will be

$$\begin{aligned} \mathcal{R}^{abc}(\eta) &:= P_{abc \rightarrow \alpha\beta 0}^{-1} \mathcal{R}^{\alpha\beta 0} P_{abc \rightarrow \alpha\beta 0} \\ &= \frac{2}{3} \begin{pmatrix} \frac{1}{2} + \cos(\eta) & \frac{1}{2} + \cos\left(\eta - \frac{4\pi}{3}\right) & \frac{1}{2} + \cos\left(\eta - \frac{2\pi}{3}\right) \\ \frac{1}{2} + \cos\left(\eta - \frac{2\pi}{3}\right) & \frac{1}{2} + \cos(\eta) & \frac{1}{2} + \cos\left(\eta - \frac{4\pi}{3}\right) \\ \frac{1}{2} + \cos\left(\eta - \frac{4\pi}{3}\right) & \frac{1}{2} + \cos\left(\eta - \frac{2\pi}{3}\right) & \frac{1}{2} + \cos(\eta) \end{pmatrix}. \end{aligned} \quad (3.53)$$

Thus in the  $abc$  frame, we have

$$\mathcal{H}^{abc}(\theta, \rho, \phi_s^{abc}, \phi_r^{abc}) = \mathcal{H}^{abc}\left(\theta + \frac{2\pi}{n_r}, \rho, \phi_s^{abc}, \mathcal{R}^{abc}\left(-\frac{2\pi}{n_r}\right)\phi_r^{abc}\right) \quad (3.54)$$

which gives in the  $\alpha\beta 0$  frame

$$\begin{aligned} \mathcal{H}^{\alpha\beta 0}(\theta, \rho, \phi_s^{\alpha\beta 0}, \phi_r^{\alpha\beta 0}) &= \mathcal{H}^{abc}(\theta, \rho, P_{abc \rightarrow \alpha\beta 0}^{-1}\phi_s^{\alpha\beta 0}, P_{abc \rightarrow \alpha\beta 0}^{-1}\phi_r^{\alpha\beta 0}) \\ &= \mathcal{H}^{abc}\left(\theta + \frac{2\pi}{n_r}, \rho, P_{abc \rightarrow \alpha\beta 0}^{-1}\phi_s^{\alpha\beta 0}, \mathcal{R}^{abc}\left(-\frac{2\pi}{n_r}\right)P_{abc \rightarrow \alpha\beta 0}^{-1}\phi_r^{\alpha\beta 0}\right) \\ &= \mathcal{H}^{\alpha\beta 0}\left(\theta + \frac{2\pi}{n_r}, \rho, P_{abc \rightarrow \alpha\beta 0}^{-1}\phi_s^{\alpha\beta 0}, \right. \\ &\quad \left. P_{abc \rightarrow \alpha\beta 0} \mathcal{R}^{abc}\left(-\frac{2\pi}{n_r}\right)P_{abc \rightarrow \alpha\beta 0}^{-1}\phi_r^{\alpha\beta 0}\right) \\ \mathcal{H}^{\alpha\beta 0}(\theta, \rho, \phi_s^{\alpha\beta 0}, \phi_r^{\alpha\beta 0}) &= \mathcal{H}^{\alpha\beta 0}\left(\theta + \frac{2\pi}{n_r}, \rho, \phi_s^{\alpha\beta 0}, \mathcal{R}^{\alpha\beta 0}\left(-\frac{2\pi}{n_r}\right)\phi_r^{\alpha\beta 0}\right). \end{aligned} \quad (3.55)$$

In the  $DQ0$  frame, this invariance gives

$$\begin{aligned} \mathcal{H}^{DQ0}(\theta, \rho, \phi_s^{DQ0}, \phi_r^{DQ0}) &= \mathcal{H}^{\alpha\beta 0}(\theta, \rho, P_{\alpha\beta 0 \rightarrow DQ0}^{-1}(\alpha + \theta)\phi_s^{DQ0}, P_{\alpha\beta 0 \rightarrow DQ0}^{-1}(\alpha)\phi_r^{DQ0}) \\ &= \mathcal{H}^{\alpha\beta 0}\left(\theta + \frac{2\pi}{n_r}, \rho, P_{\alpha\beta 0 \rightarrow DQ0}^{-1}(\alpha + \theta)\phi_s^{DQ0}, \right. \\ &\quad \left. \mathcal{R}^{\alpha\beta 0}\left(-\frac{2\pi}{n_r}\right)P_{\alpha\beta 0 \rightarrow DQ0}^{-1}(\alpha)\phi_r^{DQ0}\right) \\ &= \mathcal{H}^{DQ0}\left(\theta + \frac{2\pi}{n_r}, \rho, \right. \\ &\quad \left. P_{\alpha\beta 0 \rightarrow DQ0}(\alpha - \frac{2\pi}{n_r} + \theta + \frac{2\pi}{n_r})P_{\alpha\beta 0 \rightarrow DQ0}^{-1}(\alpha + \theta)\phi_s^{DQ0}, \right. \\ &\quad \left. P_{\alpha\beta 0 \rightarrow DQ0}(\alpha - \frac{2\pi}{n_r})\mathcal{R}^{\alpha\beta 0}\left(-\frac{2\pi}{n_r}\right)P_{\alpha\beta 0 \rightarrow DQ0}^{-1}(\alpha)\phi_r^{DQ0}\right) \end{aligned}$$

and after simplification, we find the simple  $\frac{2\pi}{n_r}$ -periodicity condition with respect to  $\theta$

$$\mathcal{H}^{DQ0}(\theta, \rho, \phi_s^D, \phi_s^Q, \phi_s^0, \phi_r^D, \phi_r^Q, \phi_r^0) = \mathcal{H}^{DQ0}\left(\theta + \frac{2\pi}{n_r}, \rho, \phi_s^D, \phi_s^Q, \phi_s^0, \phi_r^D, \phi_r^Q, \phi_r^0\right). \quad (3.56)$$

### 3.5 Connection to the grid

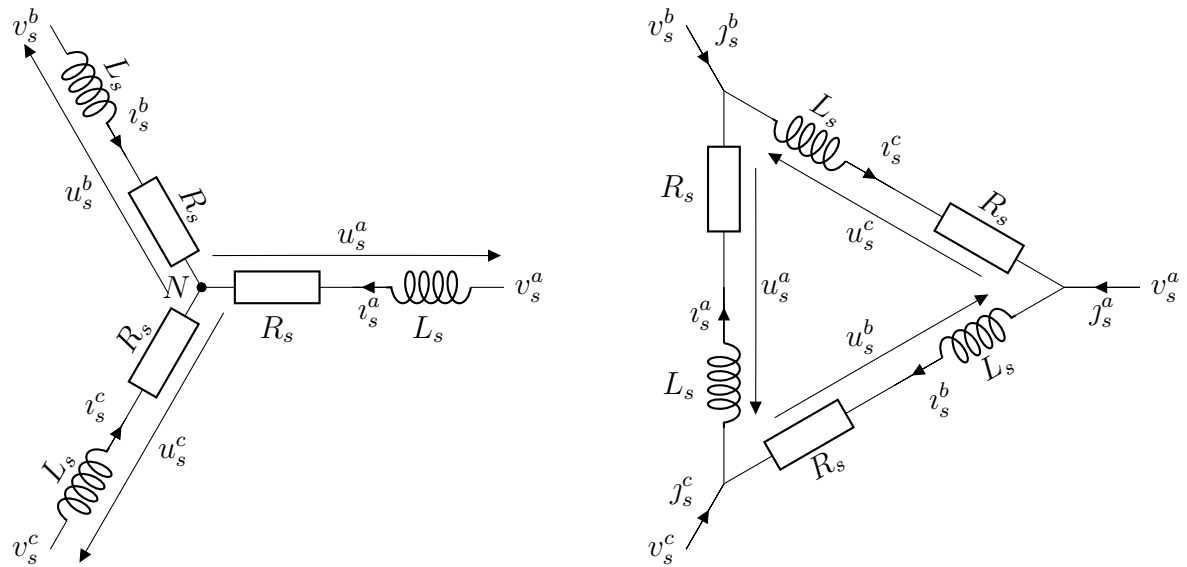
We now want to take into account how the windings are connected to the power source. There exist 2 main connection schemes for stator windings described in fig. 3.9. There are 2 possibilities for rotor windings:

- They are short circuited (see section 3.5.1);
- There are not any rotor windings but instead permanent magnets, which can be represented by fictitious windings, where a constant current circulates. (section 3.5.2).

The simplifications allowed by considering the implied constraints they impose on state variables are studied below. The reasoning can be done in many frames, so we introduce the  $xyz$  frame notation for any frame we have introduced so far and the  $xy0$  frame notation for any frame with the 0-axis (i.e.,  $\alpha\beta 0$ ,  $dq0$  or  $DQ0$ ).

	Symmetry	$\mathcal{H}^{DQ0}(\theta, \rho, \phi_s^D, \phi_s^Q, \phi_s^0, \phi_r^D, \phi_r^Q, \phi_r^0) =$	Condition
Stator	Phase permutation	$\mathcal{H}^{DQ0}(\theta + \frac{2\pi}{3}, \rho, \phi_s^D, \phi_s^Q, \phi_s^0, \phi_r^D, \phi_r^Q, \phi_r^0)$	Identical windings
	Current reversal	$\mathcal{H}^{DQ0}(\theta + \pi, \rho, \phi_s^D, \phi_s^Q, -\phi_s^0, \phi_r^D, \phi_r^Q, \phi_r^0)$	Axial symmetry
Salient Rotor	Phase exchange	$\mathcal{H}^{DQ0}(-\theta, -\rho, \phi_s^D, -\phi_s^Q, \phi_s^0, \phi_r^D, -\phi_r^Q, \phi_r^0)$	Planar symmetry
	Current reversal	$\mathcal{H}^{DQ0}(\theta + \pi, \rho, -\phi_s^D, -\phi_s^Q, \phi_s^0, -\phi_r^D, -\phi_r^Q, -\phi_r^0)$	Axial symmetry
Non-salient Rotor	Phase exchange	$\mathcal{H}^{DQ0}(-\theta, -\rho, \phi_s^D, -\phi_s^Q, \phi_s^0, \phi_r^D, -\phi_r^Q, \phi_r^0)$	Planar symmetry
	Current reversal	$\mathcal{H}^{DQ0}(\theta + \pi, \rho, \phi_s^D, \phi_s^Q, \phi_s^0, \phi_r^D, \phi_r^Q, -\phi_r^0)$	Axial symmetry
	Phase permutation	$\mathcal{H}^{DQ0}(\theta + \frac{2\pi}{n_r}, \rho, \phi_s^D, \phi_s^Q, \phi_s^0, \phi_r^D, \phi_r^Q, \phi_r^0)$	Identical windings

Table 3.2 – Constraints implied on the energy function by the symmetries of the electric motors.



(a) Star connection scheme (see section 3.5.3). (b) Delta connection scheme (see section 3.5.4).

Figure 3.9 – The 2 major connection scheme for electric motors.

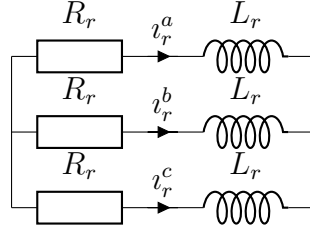


Figure 3.10 – The connection scheme for rotor windings: rotor windings are short-circuited.

### 3.5.1 Connection scheme for the rotor windings

The rotor windings of most current electric motors are short-circuited, which is the only case we will study. As can be seen on the equivalent circuit of fig. 3.10, the sum of the currents in the three phases will be constrained to 0, i.e.

$$i_r^a + i_r^b + i_r^c = 0 \quad (3.57)$$

This condition is very easily taken into account in any frame  $xy0$  having the 0-axis since it boils down to

$$i_r^0(\theta, \rho, \phi_s^{xy0}, \phi_r^{xy}, \phi_r^0) = \frac{\partial \mathcal{H}^{xy0}}{\partial \phi_r^0}(\theta, \rho, \phi_s^{xy0}, \phi_r^{xy}, \phi_r^0) = 0.$$

If the energy function is not degenerate, i.e.  $\frac{\partial^2 \mathcal{H}^{xy0}}{\partial \phi_r^0{}^2} \neq 0$ , then using the implicit function theorem,  $\phi_r^0$  can be expressed as function of  $\theta$ ,  $\rho$ ,  $\phi_s^{xy0}$  and  $\phi_r^{xy}$ . We can thus define the Hamiltonian function for a motor with short-circuited rotor windings by

$$\mathcal{H}_c^{xy0}(\theta, \rho, \phi_s^{xy0}, \phi_r^{xy}) := \mathcal{H}^{xy0}(\theta, \rho, \phi_s^{xy0}, \phi_r^{xy}, \phi_r^0(\theta, \rho, \phi_s^{xy0}, \phi_r^{xy})). \quad (3.58)$$

The partial derivative of this energy function with respect to the state will not be affected, since  $\forall x \in \{\theta, \rho, \phi_s, \phi_r\}$  we have

$$\frac{\partial \mathcal{H}_c^{xy0}}{\partial x} = \frac{\partial}{\partial x} \mathcal{H}^{xy0}(\theta, \rho, \phi_s^{xy0}, \phi_r^{xy}, \phi_r^0(\theta, \rho, \phi_s^{xy0}, \phi_r^{xy})) = \frac{\partial \mathcal{H}^{xy0}}{\partial x} + \frac{\partial \phi_r^0}{\partial x} \frac{\partial \mathcal{H}^{xy0}}{\partial \phi_r^0} = \frac{\partial \mathcal{H}^{xy0}}{\partial x},$$

where we used the fact that  $\frac{\partial \mathcal{H}^{xy0}}{\partial \phi_r^0}$  is constrained to 0 by the coupling. Thus the electromagnetic couplings are not changed

$$i_s^{xy0}(\theta, \rho, \phi_s^{xy0}, \phi_r^{xy}) = \frac{\partial \mathcal{H}_c^{xy0}}{\partial \phi_s^{xy0}}(\theta, \rho, \phi_s^{xy0}, \phi_r^{xy}) \quad (3.59a)$$

$$i_r^{xy}(\theta, \rho, \phi_s^{xy0}, \phi_r^{xy}) = \frac{\partial \mathcal{H}_c^{xy0}}{\partial \phi_r^{xy}}(\theta, \rho, \phi_s^{xy0}, \phi_r^{xy}) \quad (3.59b)$$

and the electromagnetic torque is given by an equation similar to eqs. (3.21c), (3.25d), (3.30d) and (3.36) depending on the chosen frame. The 0-axis rotor flux can then be decoupled in the state equations, which shows that the 0-axis rotor flux is constant. The state equations are otherwise similar to the previously obtained ones (see eqs. (3.20), (3.24), (3.29) and (3.33)).

### 3.5.2 Rotor without windings

PMSMs do not have rotor windings but instead their rotor is built using permanent magnets creating a constant magnetic field. To model the permanent magnets, we can define a fictitious constant current  $i_M$  looping inside the magnet [45, sec. 3.3] which creates a constant magnetic flux,  $\phi_M$ , equal to the flux of the permanent magnet. This constraint is most easily handled by the Lagrangian: In any rotor-linked frame  $xyz$ , we can define the Lagrangian under the constraint  $i_r^{xyz} = i_M$  constant as

$$\mathcal{L}_0^{xyz}(\theta, \omega, i_s^{xyz}) := \mathcal{L}^{xyz}(\theta, \omega, i_s^{xyz}, i_M) \quad (3.60)$$

associated with the Euler-Lagrange equations

$$\frac{d}{dt} \frac{\partial \mathcal{L}_0^{xyz}}{\partial i_s^{xyz}} = u_s^{xyz} - R_s i_s^{xyz} - \mathcal{J}_2 \omega \frac{\partial \mathcal{L}_0^{xyz}}{\partial i_s^{xyz}}(\theta, \omega, i_s^{xyz}) \quad (3.61a)$$

$$n \frac{d}{dt} \frac{\partial \mathcal{L}_0^{xyz}}{\partial \omega} = T_e(\theta, \omega, i_s^{xyz}) - T_L \quad (3.61b)$$

where we used

$$T_e(\theta, \omega, i_s^{xyz}) := n \frac{\partial \mathcal{L}_0^{xyz}}{\partial \theta}(\theta, \omega, i_s^{xyz}) + n i_s^T \mathcal{J}_3 \phi_s^{xyz}(\theta, \omega, i_s^{xyz}).$$

The generalized momenta associated with  $i_s^{xyz}$  and  $\omega$  are respectively

$$\begin{aligned} \phi_s^{xyz}(\theta, \omega, i_s^{xyz}) &:= \frac{\partial \mathcal{L}_0^{xyz}}{\partial i_s^{xyz}}(\theta, \omega, i_s^{xyz}) \\ \rho(\theta, \omega, i_s^{xyz}) &:= n^2 \frac{\partial \mathcal{L}_0^{xyz}}{\partial \omega}(\theta, \omega, i_s^{xyz}) \end{aligned}$$

as in the unconstrained case.

The associated Hamiltonian formulation is obtained as described in section 3.2.2 using a Legendre transformation

$$\mathcal{H}_0^{xyz} := i_s^{xyzT} \phi_s^{xyz} + \frac{\rho \omega}{n^2} - \mathcal{L} \quad (3.62)$$

which is a function of  $\theta$ ,  $\rho$  and  $\phi_s^{xyz}$ . The associated Hamilton's equations are

$$\frac{d\phi_s^{xyz}}{dt} = u_s^{xyz} - R_s i_s^{xyz} - \mathcal{J}_2 \omega \phi_s^{xyz} \quad (3.63a)$$

$$\frac{1}{n} \frac{d\rho}{dt} = T_e - T_L \quad (3.63b)$$

$$\frac{d\theta}{dt} = \omega(\theta, \rho, \phi_s^{xyz}) \quad (3.63c)$$

with

$$i_s^{xyz}(\theta, \rho, \phi_s^{xyz}) = \frac{\partial \mathcal{H}_0^{xyz}}{\partial \phi_s^{xyz}}(\theta, \rho, \phi_s^{xyz}) \quad (3.64a)$$

$$T_e(\theta, \rho, \phi_s^{xyz}) = -n \frac{\partial \mathcal{H}_0^{xyz}}{\partial \theta}(\theta, \omega, i_s^{xyz}) - n \phi_s^{xyzT} \mathcal{J}_3 i_s^{xyz}(\theta, \omega, i_s^{xyz}) \quad (3.64b)$$

$$\omega(\theta, \rho, \phi_s^{xyz}) = n^2 \frac{\partial \mathcal{H}_0^{xyz}}{\partial \rho}(\theta, \rho, \phi_s^{xyz}). \quad (3.64c)$$

Interestingly, the same result could have been obtained by considering that the fictitious currents do not dissipate energy, which is equivalent to setting  $R_r = 0$ . Consequently, the state equation for the rotor flux shows that in any rotor-linked frame, the rotor flux is equal to a constant  $\phi_M$  and  $\mathcal{H}_0^{xyz}(\theta, \rho, \phi_s^{xyz}) := \mathcal{H}^{xyz}(\theta, \rho, \phi_s^{xyz}, \phi_M)$  can be defined associated to the state equations eq. (3.63).

The case of the SynRM, which does not have windings nor permanent magnets on the rotor, can be handled similarly by considering that the permanent magnetic flux  $\phi_M$  and the current  $i_M$  are zero.

### 3.5.3 Star-connected electric machines

The star connection scheme described in fig. 3.9a constrains the sum of the three stator phase currents to be 0, i.e.

$$i_s^a + i_s^b + i_s^c = 0. \quad (3.65)$$

This constraint is very similar to the one we encountered in section 3.5.1. As previously this constraint is best handled in a frame  $xy0$  containing the 0-axis. In such a frame, it boils down to

$$i_s^0(\theta, \rho, \phi_s^{xy}, \phi_s^0, \phi_r^{xy0}) = \frac{\partial \mathcal{H}^{xy0}}{\partial \phi_s^0}(\theta, \rho, \phi_s^{xy}, \phi_s^0, \phi_r^{xy0}) = 0$$

which means by the implicit function theorem that  $\phi_s^0$  can be expressed as a function of  $\theta$ ,  $\rho$ ,  $\phi_s^{xy}$  and  $\phi_r^{xy0}$ , if the energy function is not degenerate ( $\frac{\partial^2 \mathcal{H}^{xy0}}{\partial \phi_s^0^2} \neq 0$ ). We can thus define the Hamiltonian of a star connected electric machine by

$$\mathcal{H}_*^{xy0}(\theta, \rho, \phi_s^{xy}, \phi_r^{xy0}) := \mathcal{H}^{xy0}(\theta, \rho, \phi_s^{xy}, \phi_s^0(\theta, \rho, \phi_s^{xy}, \phi_r^{xy0}), \phi_r^{xy0}). \quad (3.66)$$

Similar calculations as in section 3.5.1 show that the partial derivatives of the energy function with respect to the state variables are not affected and the 0-axis can be decoupled in the stator current-flux relations

$$i_s^{xy}(\theta, \rho, \phi_s^{xy}, \phi_r^{xy0}) = \frac{\partial \mathcal{H}_*^{xy0}}{\partial \phi_s^{xy}}(\theta, \rho, \phi_s^{xy}, \phi_r^{xy0}) \quad (3.67a)$$

$$i_r^{xy0}(\theta, \rho, \phi_s^{xy}, \phi_r^{xy0}) = \frac{\partial \mathcal{H}_*^{xy0}}{\partial \phi_r^{xy0}}(\theta, \rho, \phi_s^{xy}, \phi_r^{xy0}). \quad (3.67b)$$

The electromagnetic torque is given by an equation similar to eqs. (3.21c), (3.25d), (3.30d) and (3.36) depending on the chosen frame. The 0-axis stator flux can then be decoupled in the state equations, which shows that the 0-axis stator flux follows the dynamic

$$\frac{d\phi_s^0}{dt} = u_s^0. \quad (3.68)$$

The state equations are otherwise similar to the previously obtained ones (see eqs. (3.20), (3.24), (3.29) and (3.33)).

In this connection scheme, the drive imposes the potentials  $v_s^a$ ,  $v_s^b$ ,  $v_s^c$  and not the voltages  $u_s^a$ ,  $u_s^b$ ,  $u_s^c$  we used as input in our saturation model. The relation between voltages and potentials reads

$$\begin{aligned} u_s^a &= v_s^a - v_N \\ u_s^b &= v_s^b - v_N \\ u_s^c &= v_s^c - v_N \end{aligned}$$

Thus in  $xy0$  frame we have  $u_s^0 = v_s^0 - \sqrt{3}v_N = -\sqrt{3}v_N$  and  $u_s^{xy} = v_s^{xy}$ , consequently eq. (3.68) becomes

$$\frac{d\phi_s^0}{dt} = -\sqrt{3}v_N.$$

### 3.5.4 Delta-connected electric machines

The delta connection scheme described in fig. 3.9b implies that

$$u_s^a + u_s^b + u_s^c = 0. \quad (3.69)$$

This constraint is again best handled in a frame  $xy0$  containing the 0-axis where it boils down to

$$u_s^0 = 0.$$

Thus, in a delta connected electric machine the inputs are constrained, but the state is not. Thus, we cannot decouple the 0-axis in the general case of a saturated energy function as was done in section 3.5.3.

As in the case of the star connection scheme (see section 3.5.3) the drive does not impose the voltages  $u_s^a$ ,  $u_s^b$  and  $u_s^c$ , but the potentials  $v_s^a$ ,  $v_s^b$  and  $v_s^c$ . They are linked by the formulae

$$\begin{aligned} u_s^a &= v_s^c - v_s^b \\ u_s^b &= v_s^a - v_s^c \\ u_s^c &= v_s^b - v_s^a. \end{aligned}$$

However these equations do not determine uniquely the potentials when the voltages are fixed. Indeed we can choose freely

$$v_s^0 = \frac{1}{\sqrt{3}}(v_s^a + v_s^b + v_s^c)$$

and then the potentials are given as a function of the voltages by

$$\begin{aligned} v_s^a &= u_s^b - u_s^c + v_s^0 \\ v_s^b &= u_s^c - u_s^a + v_s^0 \\ v_s^c &= u_s^a - u_s^b + v_s^0. \end{aligned}$$

Furthermore, when the stator of an electric machine is delta connected, the currents in the stator windings are not measured. Indeed, we measure

$$\begin{aligned} j_s^a &= i_s^b - i_s^c \\ j_s^b &= i_s^c - i_s^a \\ j_s^c &= i_s^a - i_s^b. \end{aligned}$$

As for the voltages, these equations do not enable us to know the currents in the stator windings when the currents are measured: we can choose arbitrarily

$$i_s^0 = \frac{1}{\sqrt{3}}(i_s^a + i_s^b + i_s^c).$$

With that set, we can compute the currents in the windings by

$$\begin{aligned} i_s^a &= j_s^c - j_s^b + i_s^0 \\ i_s^b &= j_s^a - j_s^c + i_s^0 \\ i_s^c &= j_s^b - j_s^a + i_s^0. \end{aligned}$$

### 3.6 Unsaturated sinusoidal case

In this section we consider the simplest energy function possible: a quadratic form. Thus the currents will be linear functions of the fluxes and the model will be said to be unsaturated. Moreover we are going to suppose that the stator is sinusoidally wound, which means that we can make an arbitrary rotation of the stator variables around the rotation axis without changing the energy if the rotor is rotated by the same angle. Thus, the invariance condition eq. (3.37) is generalized into

$$\mathcal{H}^{abc}(\theta, \rho, \phi_s^{abc}, \phi_r^{abc}) = \mathcal{H}^{abc}(\theta + \eta, \rho, \mathcal{R}^{abc}(\eta)\phi_s^{abc}, \phi_r^{abc})$$

in the  $abc$  frame, which gives in the  $DQ0$  frame

$$\mathcal{H}^{DQ0}(\theta, \rho, \phi_s^D, \phi_s^Q, \phi_s^0, \phi_r^D, \phi_r^Q, \phi_r^0) = \mathcal{H}^{DQ0}(\theta + \eta, \rho, \phi_s^D, \phi_s^Q, \phi_s^0, \phi_r^D, \phi_r^Q, \phi_r^0) \quad (3.70)$$

in place of eq. (3.40). This means that the energy in the  $DQ0$  frame does not depend on  $\theta$ .

We will also assume that there is no product terms involving the speed  $\omega$  and the fluxes. Such a term would mean that the saturation changes depending on the speed of the motor, which has never been observed.

Under the aforementioned assumptions, the most general quadratic energy function of an electric motor can be written

$$\begin{aligned} \mathcal{H}^{DQ0}(\theta, \rho, \phi_s^{DQ0}, \phi_r^{DQ0}) &:= \frac{1}{2J_L n^2} \rho^2 + a + b^T \phi_s^{DQ0} + c^T \phi_r^{DQ0} \\ &\quad + \phi_s^{DQ0T} D \phi_s^{DQ0} + \phi_r^{DQ0T} E \phi_s^{DQ0} + \phi_r^{DQ0T} F \phi_r^{DQ0} \end{aligned} \quad (3.71)$$

where  $a \in \mathbb{R}$ ,  $(b, c) \in (\mathbb{R}^3)^2$  and  $(D, E, F) \in \mathcal{M}_3(\mathbb{R})^3$ . Without any loss of generality we can consider that  $D$  and  $F$  are symmetric matrices. However  $E$  might be non-symmetric. As energies are defined up to a constant, our energy function is parametrized by 27 parameters. But the conditions we obtained in section 3.4 constrain a lot of these parameters to be zero.

#### 3.6.1 For the universal electric motor

Let's consider the most general electric machine possible: it has a rotor with a saliency and windings. The rotor thus could have no symmetry as was underlined in section 3.4.2, but we will suppose we have some additional sensible symmetries. The stator will still have the symmetry presented in section 3.4.1.2.

To enforce the invariance condition eq. (3.43) the coefficients in front of odd powers of  $\phi_s^0$  must be 0, which cancels 6 of the parameters. On top of the stator symmetry, we

suppose that the rotor is symmetric with respect to its rotation axis. So eq. (3.51) must be enforced which implies that the coefficient of the linear terms are 0. With these 2 symmetry conditions, we have  $b = c = 0_{3,1}$  and the matrices of eq. (3.71) now look like

$$D = \begin{pmatrix} d_{1,1} & d_{1,2} & 0 \\ d_{2,1} & d_{2,2} & 0 \\ 0 & 0 & d_{3,3} \end{pmatrix} \quad E = \begin{pmatrix} e_{1,1} & e_{1,2} & 0 \\ e_{2,1} & e_{2,2} & 0 \\ e_{3,1} & e_{3,2} & 0 \end{pmatrix} \quad F = \begin{pmatrix} f_{1,1} & f_{1,2} & f_{1,3} \\ f_{2,1} & f_{2,2} & f_{2,3} \\ f_{3,1} & f_{3,2} & f_{3,3} \end{pmatrix}$$

Moreover, if the rotor is symmetric with respect to 2 orthogonal saliency planes, as defined in section 3.4.2.1, then the condition eq. (3.47) implies that terms with odd powers of  $\phi_s^D, \phi_s^Q, \phi_r^D, \phi_r^Q$  except  $\phi_s^D \phi_r^D$  and  $\phi_s^Q \phi_r^Q$  will be zero. This cancels 10 additional terms and the matrices  $D, E$  and  $F$  are diagonal.

With these two symmetries we can rewrite the energy function defined by eq. (3.71) as

$$\begin{aligned} \mathcal{H}^{DQ0}(\theta, \rho, \phi_s^{DQ0}, \phi_r^{DQ0}) &= \frac{1}{2J_L n^2} \rho^2 + \frac{1}{2} \phi_s^{DQ0T} \Gamma_{ls}^{DQ} \phi_s^{DQ0} + \frac{1}{2} \phi_r^{DQ0T} \Gamma_{lr}^{DQ} \phi_r^{DQ0} \\ &+ \frac{1}{2} (\phi_s^{DQ0} + \phi_r^{DQ0})^T \Gamma_m^{DQ} (\phi_s^{DQ0} + \phi_r^{DQ0}) \\ &+ \frac{1}{2} \Gamma_{ls}^0 \phi_s^{02} + \frac{1}{2} \Gamma_{lr}^0 \phi_r^{02} \end{aligned} \quad (3.72)$$

where

$$\begin{aligned} \Gamma_m^{DQ} &:= \begin{pmatrix} e_{1,1} & 0 \\ 0 & e_{2,2} \end{pmatrix} & \Gamma_{ls}^0 &:= 2d_{3,3} & \Gamma_{lr}^0 &:= 2f_{3,3}. \\ \Gamma_{ls}^{DQ} &:= \begin{pmatrix} 2d_{1,1} - e_{1,1} & 0 \\ 0 & 2d_{2,2} - e_{2,2} \end{pmatrix} & \Gamma_{lr}^{DQ} &:= \begin{pmatrix} 2f_{1,1} - e_{1,1} & 0 \\ 0 & 2f_{2,2} - e_{2,2} \end{pmatrix} \end{aligned}$$

This energy function is very similar to the one we will obtain in section 3.6.2 in the case of IMs. It can be seen as a ‘‘salient induction motor’’.

The state equations for such a machine are given by eq. (3.29) and the eqs. (3.30a) and (3.30b) give the current-flux relations in such motors

$$i_s^{DQ}(\theta, \rho, \phi_s^{DQ0}, \phi_r^{DQ0}) = \Gamma_m^{DQ} (\phi_s^{DQ0} + \phi_r^{DQ0}) + \Gamma_{ls}^{DQ} \phi_s^{DQ0} \quad (3.73a)$$

$$i_s^0(\theta, \rho, \phi_s^{DQ0}, \phi_r^{DQ0}) = \Gamma_{ls}^0 \quad (3.73b)$$

$$i_r^{DQ}(\theta, \rho, \phi_s^{DQ0}, \phi_r^{DQ0}) = \Gamma_m^{DQ} (\phi_s^{DQ0} + \phi_r^{DQ0}) + \Gamma_{lr}^{DQ} \phi_r^{DQ0} \quad (3.73c)$$

$$i_r^0(\theta, \rho, \phi_s^{DQ0}, \phi_r^{DQ0}) = \Gamma_{lr}^0. \quad (3.73d)$$

As this energy does not depend on  $\theta$ , the electromagnetic torque is given by

$$T_e(\theta, \rho, \phi_s^{DQ0}, \phi_r^{DQ0}) = (\Gamma_m^D + \Gamma_{ls}^D - \Gamma_m^Q - \Gamma_{ls}^Q) \phi_s^D \phi_s^Q + \Gamma_m^D \phi_r^D \phi_s^Q - \Gamma_m^Q \phi_r^Q \phi_s^D \quad (3.74)$$

To study the equilibrium when the input is a three-phase balanced sinusoidal source, we must go to a synchronous frame  $dq0$ , where the state equations are given by eq. (3.24) and the energy function form is conserved. However, for  $x \in \{m, ls, lr\}$ , the matrices  $\Gamma_x^{dq}$  depend on  $\theta - \theta_s$  and are given by

$$\begin{aligned} \Gamma_x^{dq} &:= \frac{\Gamma_x^D + \Gamma_x^Q}{2} I_2 + \frac{\Gamma_x^D - \Gamma_x^Q}{2} \begin{pmatrix} \cos 2(\theta - \theta_s) & -\sin 2(\theta - \theta_s) \\ -\sin 2(\theta - \theta_s) & -\cos 2(\theta - \theta_s) \end{pmatrix} \\ &= \frac{\Gamma_x^D + \Gamma_x^Q}{2} I_2 + \frac{\Gamma_x^D - \Gamma_x^Q}{2} Z - \frac{\Gamma_x^D - \Gamma_x^Q}{2} Y \end{aligned}$$

where we used the notations defined at the beginning of this document (page xv). Thus, if  $\exists x \in \{m, ls, lr\}$   $\Gamma_x^D - \Gamma_x^Q \neq 0$  the torque expression will involve terms depending on  $\theta - \theta_s$ . For them to be constant at the equilibrium, we must have  $\theta - \theta_s$  constant, i.e.  $\omega = \omega_s$ . Even though the current-flux relations look like those of the induction motor which is an asynchronous motor, this general motor is thus a synchronous motor. Moreover, at the equilibrium, there is no current in the rotor windings. This conclusion holds as long as the saliency is large enough to create the required electromagnetic  $T_e$  torque. When it is too small but still exists, there is no point of equilibrium, but a limit cycle where the electromagnetic torque  $T_e$  is around the load torque  $T_L$  and the electrical speed  $\omega$  oscillates between  $\omega_s$  and  $\omega_s - \omega_g$  where  $\omega_g = \frac{R_r T_L}{n \|\phi_r^{DQ}\|^2}$  is the well-known slip speed. Finally when there is no saliency at all ( $\forall x \in \{m, ls, lr\}$   $\Gamma_x^D = \Gamma_x^Q$ ) we find the case of the induction motor described in section 3.6.2 for which the equilibrium is at the electrical speed is  $\omega_s - \omega_g$ . There is thus a smooth transformation from this salient machine rotating at  $\omega_s$  into a non salient machine rotating at  $\omega_s - \omega_g$ .

### 3.6.2 For the IM

We are now considering the case of the induction machine. As was mentioned above, it has a non salient-rotor with a symmetry with respect to its axis.

However, there exist motors, the so-called skewed-rotor motors, whose rotor slots are not parallel with the rotor axis: They follow an helix with a large tread (see [34, sec. 4.12] and [38]). This is done to reduce torque harmonics due to rotor slotting. Skewed rotors cannot be symmetric with respect to any plane, because a planar symmetry changes the orientation of helices, i.e., of the rotor slots.

#### 3.6.2.1 Skewed-rotor induction motors

The symmetry of the stator and the rotor with respect to the rotation axis imply that all the coefficients of terms with a odd power of  $\phi_s^0$  or  $\phi_r^0$  are zero. This cancels 11 parameters among the 27 we have.

As the rotor and stator are supposed non-salient and sinusoidal, in any synchronous  $dq0$  frame, the energy is identical to the one in the particular  $DQ0$  frame. So  $b = c = 0$  and  $D, E$  and  $F$  commute with any rotation around the 0-axis, i.e.  $(D, E, F)$  are themselves rotations around the 0-axis.

Combining these hypotheses, the energy function can be rewritten

$$\begin{aligned} \mathcal{H}^{DQ0}(\theta, \rho, \phi_s^{DQ0}, \phi_r^{DQ0}) &= \frac{\rho^2}{2J_L n^2} + \frac{1}{2}(\phi_s^{DQ} + \phi_r^{DQ})^T \Gamma_m^{DQ} (\phi_s^{DQ} + \phi_r^{DQ}) + \Gamma_m^x \phi_r^{DQ T} \mathcal{J}_2 \phi_s^{DQ} \\ &+ \frac{1}{2} \phi_s^{DQ T} \Gamma_{ls}^{DQ} \phi_s^{DQ} + \frac{1}{2} \phi_r^{DQ T} \Gamma_{lr}^{DQ} \phi_r^{DQ} \\ &+ \frac{1}{2} \Gamma_{ls}^0 \phi_s^{0^2} + \frac{1}{2} \Gamma_{lr}^0 \phi_r^{0^2} \end{aligned} \quad (3.75)$$

where

$$\begin{aligned} \Gamma_m^{DQ} &:= \begin{pmatrix} \Gamma_m & 0 \\ 0 & \Gamma_m \end{pmatrix} = \begin{pmatrix} e_{1,1} & 0 \\ 0 & e_{2,2} \end{pmatrix} \\ \Gamma_{ls}^{DQ} &:= \begin{pmatrix} \Gamma_{ls} & 0 \\ 0 & \Gamma_{ls} \end{pmatrix} = \begin{pmatrix} 2d_{1,1} - e_{1,1} & 0 \\ 0 & 2d_{2,2} - e_{2,2} \end{pmatrix} \end{aligned}$$

$$\begin{aligned}\Gamma_{lr}^{DQ} &:= \begin{pmatrix} \Gamma_{lr} & 0 \\ 0 & \Gamma_{lr} \end{pmatrix} = \begin{pmatrix} 2f_{1,1} - e_{1,1} & 0 \\ 0 & 2d_{2,2} - f_{2,2} \end{pmatrix} \\ \Gamma_m^x &:= e_{2,1} = -e_{1,2} \\ \Gamma_{ls}^0 &:= 2d_{3,3} \\ \Gamma_{lr}^0 &:= 2f_{3,3}.\end{aligned}$$

It should be noted that this expression is valid for any synchronous  $dq0$  frame, as the matrices  $D$ ,  $E$  and  $F$  commute with rotations. The state equations and the electromagnetic torque are given by eqs. (3.24) and (3.25d) or eqs. (3.33) and (3.36) depending on the synchronous frame which is chosen. In any  $dq0$  frame, the current-flux relations will be given by

$$i_s^{dq} = \Gamma_m^{dq}(\phi_s^{dq} + \phi_r^{dq}) + \Gamma_{ls}^{dq}\phi_s^{dq} - \Gamma_m^x \mathcal{J}_2 \phi_r^{dq} \quad (3.76a)$$

$$i_s^0 = \Gamma_{ls}^0 \phi_s^0 \quad (3.76b)$$

$$i_r^{dq} = \Gamma_m^{dq}(\phi_s^{dq} + \phi_r^{dq}) + \Gamma_{lr}^{dq}\phi_r^{dq} + \Gamma_m^x \mathcal{J}_2 \phi_s^{dq} \quad (3.76c)$$

$$i_r^0 = \Gamma_{lr}^0 \phi_r^0. \quad (3.76d)$$

These are not the equations known as the unsaturated sinusoidal model of the induction motor. This is due to the fact that non-skewed rotor are usually assumed so there is another symmetry.

### 3.6.2.2 Non-skewed-rotor induction motors

On top of the symmetries of section 3.6.2.1, the rotor now presents a planar symmetry which further constrains the form we got for skewed-rotor induction machines. To enforce the condition eq. (3.47) we must have  $\Gamma_m^x = 0$ .

The energy function still has the form of eq. (3.75) but the matrices now read

$$\Gamma_m^{DQ} := \Gamma_m I_2 \quad \Gamma_{ls}^{DQ} := \Gamma_{ls} I_2 \quad \Gamma_{lr}^{DQ} := \Gamma_{lr} I_2$$

where  $I_2$  is the identity of  $\mathcal{M}_2(\mathbb{R})$  and thus the current-flux relations in any  $dq0$  frame simplify to

$$i_s^{dq} = \Gamma_m(\phi_s^{dq} + \phi_r^{dq}) + \Gamma_{ls}\phi_s^{dq} \quad (3.77a)$$

$$i_s^0 = \Gamma_{ls}^0 \phi_s^0 \quad (3.77b)$$

$$i_r^{dq} = \Gamma_m(\phi_s^{dq} + \phi_r^{dq}) + \Gamma_{lr}\phi_r^{dq} \quad (3.77c)$$

$$i_r^0 = \Gamma_{lr}^0 \phi_r^0. \quad (3.77d)$$

With the state form eq. (3.24) and the associated electromagnetic torque expression eq. (3.25d) these equations form the well-known unsaturated sinusoidal model of the induction motor.

### 3.6.3 For the PMSM

A PMSM is one kind of electric motor which has no windings in the rotor. In section 3.5.2, it is explained that in this case the equations concerning  $\phi_r$  can be decoupled in the state equations, and that it is then necessarily constant. In this section we are going to assume

that the rotor is salient in the sense of section 3.3.4.1. Hence, the general energy function eq. (3.71) boils down to

$$\mathcal{H}^{DQ0}(\theta, \rho, \phi_s^{DQ0}) := \frac{1}{2J_L n^2} \rho^2 + a' + b^T \phi_s^{DQ0} + \phi_s^{DQ0T} D \phi_s^{DQ0} \quad (3.78)$$

where

$$\begin{aligned} a' &= c^T \phi_r^{DQ0} + \phi_r^{DQ0T} F \phi_r^{DQ0} \\ b' &= b + E^T \phi_r^{DQ0} \end{aligned}$$

are constant because rotor flux is constant.

### 3.6.3.1 General case for a salient PMSM

The stator of a PMSM is symmetric with respect to the rotation axis, so, its energy function respects the condition of eq. (3.43). Hence, terms involving odd powers of  $\phi_s^0$  are forbidden. Choosing appropriately  $a'$ , the energy function  $\mathcal{H}^{DQ0}$  can be written under the form

$$\mathcal{H}^{DQ0}(\theta, \rho, \phi_s^{DQ0}) = \frac{1}{2J_L n^2} \rho^2 + \frac{1}{2} (\phi_s^{DQ} - \phi_M^{DQ})^T \Gamma_s^{DQ} (\phi_s^{DQ} - \phi_M^{DQ}) + \frac{1}{2} \Gamma_s^0 \phi_s^{02} \quad (3.79)$$

where  $\phi_M^{DQ}$ ,  $\Gamma_s^{DQ}$  and  $\Gamma_s^0$  are defined by

$$\Gamma_s^{DQ} := \begin{pmatrix} \Gamma_s^D & \Gamma_s^x \\ \Gamma_s^x & \Gamma_s^Q \end{pmatrix} = 2 \begin{pmatrix} d_{1,1} & d_{1,2} \\ d_{2,1} & d_{2,2} \end{pmatrix} \quad \Gamma_s^0 := 2d_{3,3}$$

$$\phi_M^{DQ} := - \left( \frac{\Gamma_s^{DQ} + \Gamma_s^{DQT}}{2} \right)^{-1} b' = -\Gamma_s^{DQ-1} b'.$$

The current-flux relations read

$$i_s^{DQ} = \Gamma_s^{DQ} (\phi_s^{DQ} - \phi_M^{DQ}) \quad (3.80a)$$

$$i_s^0 = \Gamma_s^0 \phi_s^0. \quad (3.80b)$$

### 3.6.3.2 Usual case for a salient PMSM

In most PMSMs the rotor flux is aligned with one of the saliency axes considered to be the  $D$ -axis. Thus the rotor is symmetric with a saliency plane and the condition eq. (3.47) must be enforced and the terms with odd powers of  $\phi_s^Q$  are zero. As we made the same assumptions as in Jebai [37], we recover the energy function proposed there

$$\mathcal{H}^{DQ0}(\theta, \rho, \phi_s^{DQ0}) = \frac{1}{2J_L n^2} \rho^2 + \frac{1}{2} \Gamma_s^D (\phi_s^D - \phi_M)^2 + \frac{1}{2} \Gamma_s^Q \phi_s^{Q2} + \frac{1}{2} \Gamma_s^0 \phi_s^{02} \quad (3.81)$$

with the associated current-flux relations

$$i_s^D = \Gamma_s^D (\phi_s^D - \phi_M) \quad (3.82a)$$

$$i_s^Q = \Gamma_s^Q \phi_s^Q \quad (3.82b)$$

$$i_s^0 = \Gamma_s^0 \phi_s^0 \quad (3.82c)$$

### 3.6.3.3 Non-salient PMSM

The non-salient case is obtained with  $\Gamma_s^D = \Gamma_s^Q = \Gamma_s$ . The  $DQ0$  frame is defined in this case by the permanent magnet flux. The energy then reads

$$\mathcal{H}^{DQ0}(\theta, \rho, \phi_s^{DQ0}) = \frac{1}{2J_L n^2} \rho^2 + \frac{1}{2} \Gamma_s (\phi_s^D - \phi_M)^2 + \frac{1}{2} \Gamma_s \phi_s^Q{}^2 + \frac{1}{2} \Gamma_s^0 \phi_s^0{}^2 \quad (3.83)$$

and the current-flux relations are then

$$i_s^D = \Gamma_s (\phi_s^D - \phi_M) \quad (3.84a)$$

$$i_s^Q = \Gamma_s \phi_s^Q \quad (3.84b)$$

$$i_s^0 = \Gamma_s^0 \phi_s^0. \quad (3.84c)$$

### 3.6.4 For the SynRM

SynRMs, like PMSMs, do not have windings in the rotor, but the constant rotor flux is zero. To produce a torque, we must have a salient rotor which will be symmetric with respect to its axis and two orthogonal planes.

When the symmetries are not taken into account, the energy function has the form given by eq. (3.78). As in the case of the PMSM, taking into account the symmetry with respect to the rotation axis cancels all the terms involving odd powers of  $\phi_s^0$ . Taking into account the symmetry of the rotor with respect to the two orthogonal saliency planes, we find that all the coefficients of terms with odd powers of  $\phi_s^D$  or  $\phi_s^Q$  will also be zero. Thus, the energy function for a SynRM reads

$$\mathcal{H}^{DQ0}(\theta, \rho, \phi_s^{DQ0}) = \frac{1}{2J_L n^2} \rho^2 + \frac{1}{2} \Gamma_s^D \phi_s^D{}^2 + \frac{1}{2} \Gamma_s^Q \phi_s^Q{}^2 + \frac{1}{2} \Gamma_s^0 \phi_s^0{}^2 \quad (3.85)$$

where

$$\Gamma_s^D = d_{1,1} \quad \Gamma_s^Q = d_{2,2} \quad \Gamma_s^0 = d_{3,3}.$$

The current-flux relations in the  $DQ0$  frame are then

$$i_s^D = \Gamma_s^D \phi_s^D \quad (3.86a)$$

$$i_s^Q = \Gamma_s^Q \phi_s^Q \quad (3.86b)$$

$$i_s^0 = \Gamma_s^0 \phi_s^0. \quad (3.86c)$$

## 3.7 Non-sinusoidal motor model

We are now considering the general case where the energy depends on  $\theta$  and is not necessarily quadratic. As in the unsaturated sinusoidal case developed in section 3.6, the symmetries obtained in section 3.4 will allow us to constrain the admissible functions.

Besides, as we are not interested in mechanical modeling, we will use in this section the simplest form for the kinetic energy which is  $\rho^2/(2J_L n^2)$ .

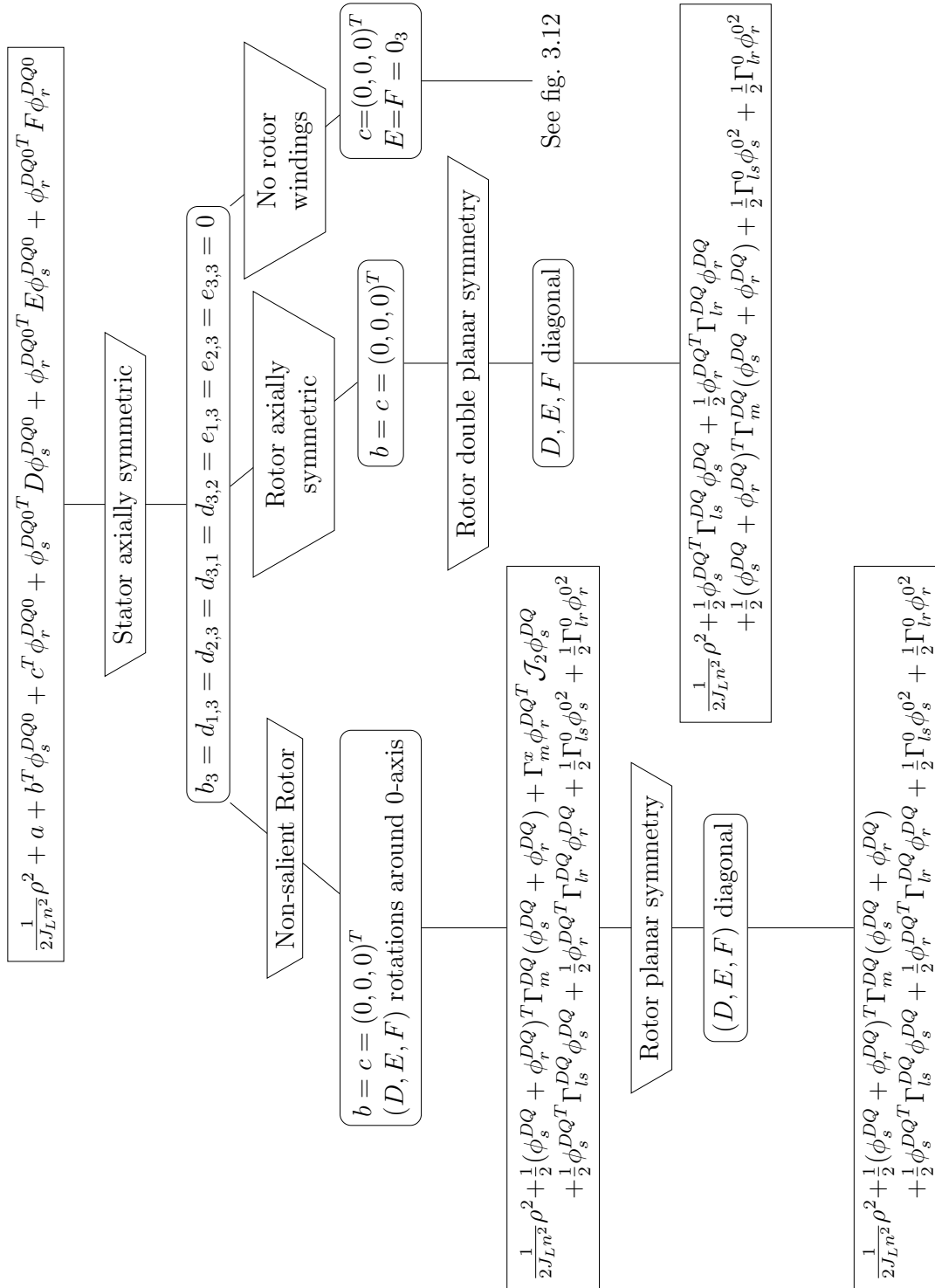


Figure 3.11 – Descending from general quadratic form to the energy functions of each electric motor using the symmetries presented on section 3.4. The symmetry hypotheses are given in trapezium, their consequences inside rounded rectangles. The energy-based models of the electric motors are given in rectangular nodes. Here the tree is pruned at the point where motors with no rotor windings are considered (see fig. 3.12 for this case).

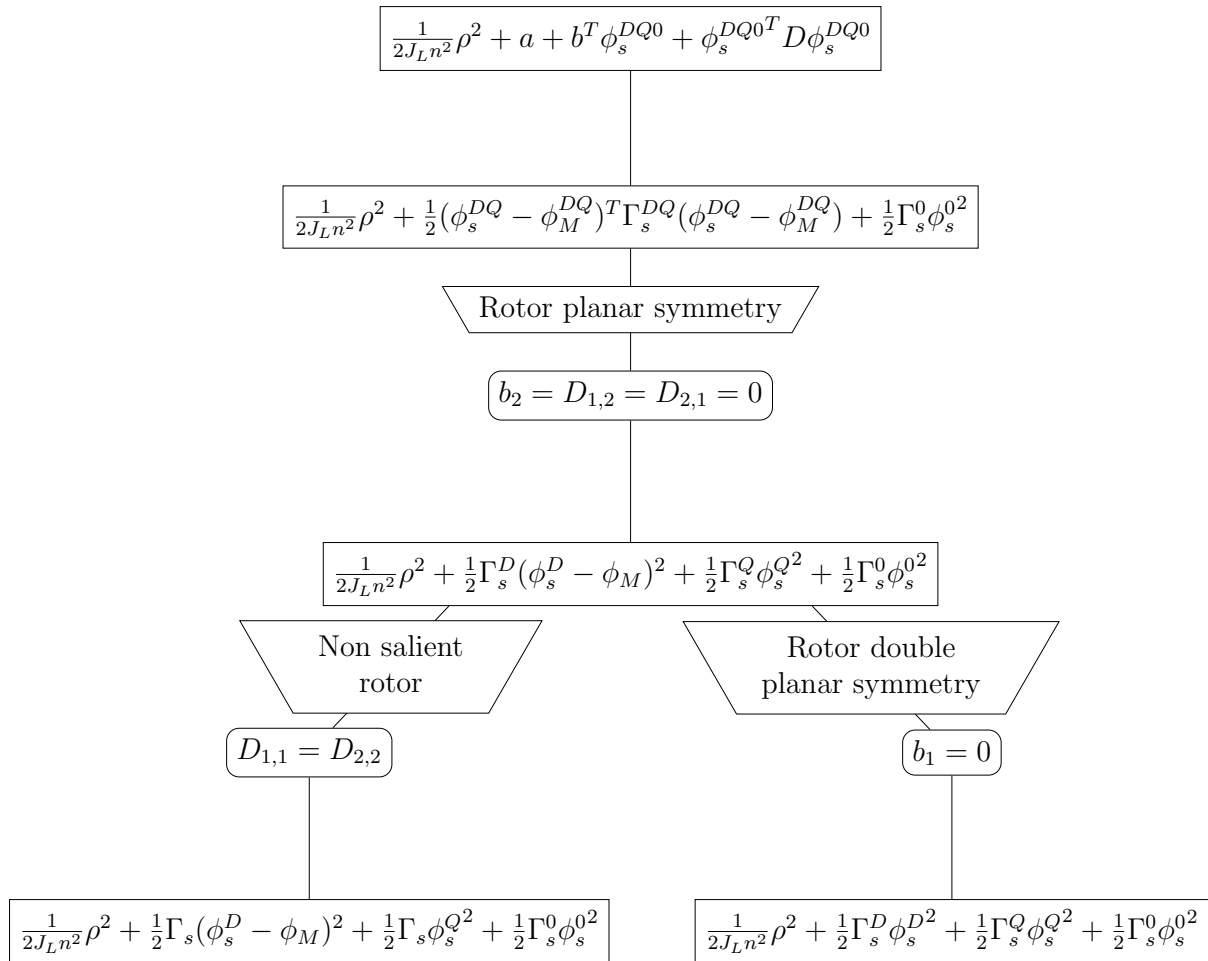


Figure 3.12 – Descending from quadratic form to the energy functions of each electric motor without rotor windings using the symmetries presented in section 3.4. The symmetry hypotheses are given in trapezia, their consequences inside rounded rectangles. The energy-based models of the electric motors are given in rectangular nodes.

### 3.7.1 In the general case

First of all, we suppose that the rotor windings are short-circuited, so the rotor 0-axis can be decoupled and we can define the constrained Hamiltonian  $\mathcal{H}_c^{DQ0}(\theta, \rho, \phi_s^{DQ0}, \phi_r^{DQ})$  (see section 3.5.1). Eq. (3.40) shows that  $\mathcal{H}_c^{DQ0}$  is  $\frac{2\pi}{3}$ -periodic with respect to  $\theta$ , hence it can be expanded as a Fourier series with respect to  $\theta$

$$\begin{aligned} \mathcal{H}_c^{DQ0}(\theta, \rho, \phi_s^{DQ0}, \phi_r^{DQ}) &= \frac{1}{2J_L n^2} \rho^2 + \overline{\mathcal{H}}^{DQ0}(\phi_s^{DQ0}, \phi_r^{DQ}) \\ &+ \sum_{k=1}^{\infty} a_{3k}(\phi_s^{DQ0}, \phi_r^{DQ}) \cos 3k\theta + b_{3k}(\phi_s^{DQ0}, \phi_r^{DQ}) \sin 3k\theta. \end{aligned} \quad (3.87)$$

On top of that, the stator of an electric motor is symmetric with respect to the 0-axis (see section 3.4.1.2), so  $\mathcal{H}^{DQ0}$  must respect the condition eq. (3.43), which implies

$$\begin{aligned} \overline{\mathcal{H}}^{DQ0}(\phi_s^D, \phi_s^Q, \phi_s^0, \phi_r^D, \phi_r^Q) &= \overline{\mathcal{H}}^{DQ0}(\phi_s^D, \phi_s^Q, -\phi_s^0, \phi_r^D, \phi_r^Q) \\ a_{3k}(\phi_s^D, \phi_s^Q, \phi_s^0, \phi_r^D, \phi_r^Q) &= (-1)^k a_{3k}(\phi_s^D, \phi_s^Q, -\phi_s^0, \phi_r^D, \phi_r^Q) \\ b_{3k}(\phi_s^D, \phi_s^Q, \phi_s^0, \phi_r^D, \phi_r^Q) &= (-1)^k b_{3k}(\phi_s^D, \phi_s^Q, -\phi_s^0, \phi_r^D, \phi_r^Q). \end{aligned}$$

Thus  $\overline{\mathcal{H}}^{DQ0}$ ,  $\{a_{6k}\}$  and  $\{b_{6k}\}$  are even with respect to  $\phi_s^0$  whereas  $\{a_{6k+3}\}$  and  $\{b_{6k+3}\}$  are odd with respect to  $\phi_s^0$ .

If we make the assumption that the rotor is symmetric with respect to the two orthogonal saliency planes as in section 3.6.1, then, due to eq. (3.47), we must have the parity conditions

$$\begin{aligned} \overline{\mathcal{H}}^{DQ0}(\phi_s^D, \phi_s^Q, \phi_s^0, \phi_r^D, \phi_r^Q) &= \overline{\mathcal{H}}^{DQ0}(\phi_s^D, -\phi_s^Q, \phi_s^0, \phi_r^D, -\phi_r^Q) = \overline{\mathcal{H}}^{DQ0}(-\phi_s^D, \phi_s^Q, \phi_s^0, -\phi_r^D, \phi_r^Q) \\ a_{3k}(\phi_s^D, \phi_s^Q, \phi_s^0, \phi_r^D, \phi_r^Q) &= a_{6k}(\phi_s^D, -\phi_s^Q, \phi_s^0, \phi_r^D, -\phi_r^Q) = a_{3k}(-\phi_s^D, \phi_s^Q, \phi_s^0, -\phi_r^D, \phi_r^Q) \\ b_{3k}(\phi_s^D, \phi_s^Q, \phi_s^0, \phi_r^D, \phi_r^Q) &= -b_{6k}(\phi_s^D, -\phi_s^Q, \phi_s^0, \phi_r^D, -\phi_r^Q) = -b_{3k}(-\phi_s^D, \phi_s^Q, \phi_s^0, -\phi_r^D, \phi_r^Q). \end{aligned}$$

With eqs. (3.30a) and (3.30b) we find the current-flux relations and with eq. (3.30d) the electromagnetic torque

$$\begin{aligned} i_s^{DQ0}(\theta, \rho, \phi_s^{DQ0}, \phi_r^{DQ}) &= \frac{\partial \overline{\mathcal{H}}^{DQ0}}{\partial \phi_s^{DQ0}}(\phi_s^{DQ0}, \phi_r^{DQ}) \\ &+ \sum_{k=1}^{\infty} \frac{\partial a_{3k}}{\partial \phi_s^{DQ0}}(\phi_s^{DQ0}, \phi_r^{DQ}) \cos 3k\theta \\ &+ \sum_{k=1}^{\infty} \frac{\partial b_{3k}}{\partial \phi_s^{DQ0}}(\phi_s^{DQ0}, \phi_r^{DQ}) \sin 3k\theta \end{aligned} \quad (3.88a)$$

$$\begin{aligned} i_r^{DQ}(\theta, \rho, \phi_s^{DQ0}, \phi_r^{DQ}) &= \frac{\partial \overline{\mathcal{H}}^{DQ0}}{\partial \phi_r^{DQ}}(\phi_s^{DQ0}, \phi_r^{DQ}) \\ &+ \sum_{k=1}^{\infty} \frac{\partial a_{3k}}{\partial \phi_r^{DQ}}(\phi_s^{DQ0}, \phi_r^{DQ}) \cos 3k\theta \\ &+ \sum_{k=1}^{\infty} \frac{\partial b_{3k}}{\partial \phi_r^{DQ}}(\phi_s^{DQ0}, \phi_r^{DQ}) \sin 3k\theta \end{aligned} \quad (3.88b)$$

$$\begin{aligned} T_e(\theta, \rho, \phi_s^{DQ0}, \phi_r^{DQ}) &= n i_s^{DQ0T} \mathcal{J}_3 \phi_s^{DQ0} \\ &+ n \sum_{k=1}^{\infty} 3k a_{3k}(\phi_s^{DQ0}, \phi_r^{DQ}) \sin 3k\theta \\ &- n \sum_{k=1}^{\infty} 3k b_{3k}(\phi_s^{DQ0}, \phi_r^{DQ}) \cos 3k\theta. \end{aligned} \quad (3.88c)$$

This shows that the currents and the torque are also  $\frac{2\pi}{3}$ -periodic with respect to  $\theta$ .

If the star connection scheme (see section 3.5.3) is used, then the stator 0-axis can be decoupled and we can define the associated energy function  $\mathcal{H}_*^{DQ}$  which does not depend on  $\phi_s^0$ . Thus the odd parity condition on  $\{a_{6k+3}\}$  and  $\{b_{6k+3}\}$  constrain them to be zero. Thus  $\mathcal{H}_*^{DQ}$  can be written

$$\begin{aligned} \mathcal{H}_*^{DQ}(\theta, \rho, \phi_s^{DQ}, \phi_r^{DQ}) &= \frac{1}{2J_L n^2} \rho^2 + \overline{\mathcal{H}}^{DQ}(\phi_s^{DQ}, \phi_r^{DQ}) \\ &+ \sum_{k=1}^{\infty} a_{6k}(\phi_s^{DQ}, \phi_r^{DQ}) \cos 6k\theta + b_{6k}(\phi_s^{DQ}, \phi_r^{DQ}) \sin 6k\theta \end{aligned} \quad (3.89)$$

and applying eqs. (3.30a) and (3.30b) we find that the currents and the electromagnetic torque are  $\frac{\pi}{3}$ -periodic with respect to  $\theta$

$$\begin{aligned} i_s^{DQ}(\theta, \rho, \phi_s^{DQ}, \phi_r^{DQ}) &= \frac{\partial \overline{\mathcal{H}}^{DQ}}{\partial \phi_s^{DQ}}(\phi_s^{DQ}, \phi_r^{DQ}) \\ &+ \sum_{k=1}^{\infty} \frac{\partial a_{6k}}{\partial \phi_s^{DQ}}(\phi_s^{DQ}, \phi_r^{DQ}) \cos 6k\theta \\ &+ \sum_{k=1}^{\infty} \frac{\partial b_{6k}}{\partial \phi_s^{DQ}}(\phi_s^{DQ}, \phi_r^{DQ}) \sin 6k\theta \end{aligned} \quad (3.90a)$$

$$\begin{aligned} i_r^{DQ}(\theta, \rho, \phi_s^{DQ}, \phi_r^{DQ}) &= \frac{\partial \overline{\mathcal{H}}^{DQ}}{\partial \phi_r^{DQ}}(\phi_s^{DQ}, \phi_r^{DQ}) \\ &+ \sum_{k=1}^{\infty} \frac{\partial a_{6k}}{\partial \phi_r^{DQ}}(\phi_s^{DQ}, \phi_r^{DQ}) \cos 6k\theta \\ &+ \sum_{k=1}^{\infty} \frac{\partial b_{6k}}{\partial \phi_r^{DQ}}(\phi_s^{DQ}, \phi_r^{DQ}) \sin 6k\theta \end{aligned} \quad (3.90b)$$

$$\begin{aligned} T_e(\theta, \rho, \phi_s^{DQ}, \phi_r^{DQ}) &= n_s^{DQT} \mathcal{J}_3 \phi_s^{DQ} \\ &+ n \sum_{k=1}^{\infty} 6k a_{6k}(\phi_s^{DQ}, \phi_r^{DQ}) \sin 6k\theta \\ &- n \sum_{k=1}^{\infty} 6k b_{6k}(\phi_s^{DQ}, \phi_r^{DQ}) \cos 6k\theta. \end{aligned} \quad (3.90c)$$

### 3.7.2 For the IM

IMs have non-salient rotors, so the condition eq. (3.56) holds. Moreover, as in the case of section 3.7.1, the rotor windings are short-circuited and the rotor is assumed to be symmetric with respect to its axis. Thus the energy function must respect both a  $\frac{\pi}{3}$ -periodicity condition and a  $\frac{2\pi}{n_r}$ -periodicity condition. Hence its period with respect to  $\theta$  is  $\frac{2\pi}{\text{lcm } 6, n_r} = \frac{2\pi}{n_{rs}}$  and decomposing in Fourier series we get

$$\begin{aligned} \mathcal{H}_c^{DQ0}(\theta, \rho, \phi_s^{DQ0}, \phi_r^{DQ}) &= \frac{1}{2J_L n^2} \rho^2 + \overline{\mathcal{H}}^{DQ0}(\phi_s^{DQ0}, \phi_r^{DQ}) \\ &+ \sum_{k=1}^{\infty} a_{n_{rs}k}(\phi_s^{DQ0}, \phi_r^{DQ}) \cos n_{rs}k\theta \\ &+ \sum_{k=1}^{\infty} b_{n_{rs}k}(\phi_s^{DQ0}, \phi_r^{DQ}) \sin n_{rs}k\theta. \end{aligned} \quad (3.91)$$

On top of that, the stator of an electric motor is symmetric with respect to the 0-axis (see section 3.4.1.2), so  $\mathcal{H}^{DQ0}$  must respect the condition eq. (3.43), which implies as previously  $\overline{\mathcal{H}}^{DQ0}$ ,  $\{a_{n_{rs}k}\}$  and  $\{b_{n_{rs}k}\}$  are even with respect to  $\phi_s^0$ .

Skewed-rotors IMs do not have any other symmetry. On the opposite as in section 3.6.2.2 non-skewed rotors are symmetric with respect to 2 orthogonal planes and eq. (3.47) leads to

$$\begin{aligned}\overline{\mathcal{H}}^{DQ0}(\phi_s^D, \phi_s^Q, \phi_s^0, \phi_r^D, \phi_r^Q) &= \overline{\mathcal{H}}^{DQ0}(\phi_s^D, -\phi_s^Q, \phi_s^0, \phi_r^D, -\phi_r^Q) = \overline{\mathcal{H}}^{DQ0}(-\phi_s^D, \phi_s^Q, \phi_s^0, -\phi_r^D, \phi_r^Q) \\ a_{6k}(\phi_s^D, \phi_s^Q, \phi_s^0, \phi_r^D, \phi_r^Q) &= a_{6k}(\phi_s^D, -\phi_s^Q, \phi_s^0, \phi_r^D, -\phi_r^Q) = a_{6k}(-\phi_s^D, \phi_s^Q, \phi_s^0, -\phi_r^D, \phi_r^Q) \\ b_{6k}(\phi_s^D, \phi_s^Q, \phi_s^0, \phi_r^D, \phi_r^Q) &= -b_{6k}(\phi_s^D, -\phi_s^Q, \phi_s^0, \phi_r^D, -\phi_r^Q) = -b_{6k}(-\phi_s^D, \phi_s^Q, \phi_s^0, -\phi_r^D, \phi_r^Q).\end{aligned}$$

Similarly as in section 3.7.1 the currents and the torque are  $\frac{2\pi}{n_{rs}}$ -periodic with respect to  $\theta$ .

### 3.7.3 For the PMSM

As PMSMs do not have rotor windings,  $\phi_r$  can be decoupled. Besides its stator still respects the phase permutation symmetry described in section 3.4.1.1, so the condition eq. (3.40) should be respected and the energy function is  $\frac{2\pi}{3}$ -periodic with respect to  $\theta$ . Consequently its Fourier series read

$$\mathcal{H}^{DQ0}(\theta, \rho, \phi_s^{DQ0}) = \frac{1}{2J_L n^2} \rho^2 + \overline{\mathcal{H}}^{DQ0}(\phi_s^{DQ0}) + \sum_{k=1}^{\infty} a_{3k}(\phi_s^{DQ0}) \cos 3k\theta + b_{3k}(\phi_s^{DQ0}) \sin 3k\theta. \quad (3.92)$$

The stator of a PMSM is also symmetric with respect to its axis so the condition eq. (3.43) gives

$$\begin{aligned}\overline{\mathcal{H}}^{DQ0}(\phi_s^D, \phi_s^Q, \phi_s^0) &= \overline{\mathcal{H}}^{DQ0}(\phi_s^D, \phi_s^Q, -\phi_s^0) \\ a_{3k}(\phi_s^D, \phi_s^Q, \phi_s^0) &= (-1)^k a_{3k}(\phi_s^D, \phi_s^Q, -\phi_s^0) \\ b_{3k}(\phi_s^D, \phi_s^Q, \phi_s^0) &= (-1)^k b_{3k}(\phi_s^D, \phi_s^Q, -\phi_s^0)\end{aligned}$$

which means  $\overline{\mathcal{H}}^{DQ0}$ ,  $\{a_{6k}\}$  and  $\{b_{6k}\}$  are even with respect to  $\phi_s^0$  whereas  $\{a_{6k+3}\}$  and  $\{b_{6k+3}\}$  are odd with respect to  $\phi_s^0$ .

In most cases the rotor is also symmetric with respect to one plane which defines the  $D$ -axis. In such a case the condition eq. (3.47) reads

$$\begin{aligned}\overline{\mathcal{H}}^{DQ0}(\phi_s^D, \phi_s^Q, \phi_s^0) &= \overline{\mathcal{H}}^{DQ0}(\phi_s^D, -\phi_s^Q, \phi_s^0) \\ a_{3k}(\phi_s^D, \phi_s^Q, \phi_s^0) &= a_{3k}(\phi_s^D, -\phi_s^Q, \phi_s^0) \\ b_{3k}(\phi_s^D, \phi_s^Q, \phi_s^0) &= -b_{3k}(\phi_s^D, -\phi_s^Q, \phi_s^0)\end{aligned}$$

which means  $\overline{\mathcal{H}}^{DQ0}$  and  $\{a_{3k}\}$  are even with respect to  $\phi_s^Q$ , whereas  $\{b_{3k}\}$  are odd with respect to  $\phi_s^Q$ .

Applying eqs. (3.30a) and (3.30d), one gets the current-flux relations and the electromagnetic torque expression

$$\begin{aligned}i_s^{DQ0}(\theta, \rho, \phi_s^{DQ0}) &= \frac{\partial \overline{\mathcal{H}}^{DQ0}}{\partial \phi_s^{DQ0}}(\phi_s^{DQ0}) \\ &+ \sum_{k=1}^{\infty} \frac{\partial a_{3k}}{\partial \phi_s^{DQ0}}(\phi_s^{DQ0}) \cos 3k\theta + \frac{\partial b_{3k}}{\partial \phi_s^{DQ0}}(\phi_s^{DQ0}) \sin 3k\theta\end{aligned} \quad (3.93a)$$

$$T_e(\theta, \rho, \phi_s^{DQ0}) = n i_s^{DQ0T} \mathcal{J}_3 \phi_s^{DQ0} - n \sum_{k=1}^{\infty} 3k a_{3k}(\phi_s^{DQ0}) \sin 3k\theta + 3k b_{3k}(\phi_s^{DQ0}) \cos 3k\theta \quad (3.93b)$$

which shows that the current and the torque are  $\frac{2\pi}{3}$ -periodic with respect to  $\theta$ .

When the star connection scheme is used, the stator 0-axis can be decoupled (as shown in section 3.5.3) and we can define the associated energy function which does not depend on  $\phi_s^0$ . Thus the odd parity condition on  $\{a_{6k+3}\}$  and  $\{b_{6k+3}\}$  boils down to all of them being zero.  $\mathcal{H}_*^{DQ}$  can thus be written

$$\mathcal{H}_*^{DQ}(\theta, \rho, \phi_s^{DQ}) = \frac{1}{2J_L n^2} \rho^2 + \overline{\mathcal{H}}^{DQ}(\phi_s^{DQ}) + \sum_{k=1}^{\infty} a_{6k}(\phi_s^{DQ}) \cos 6k\theta + b_{6k}(\phi_s^{DQ}) \sin 6k\theta. \quad (3.94)$$

Using the eq. (3.67a) for the stator currents and the eq. (3.30d) for the electromagnetic torque we find

$$i_s^{DQ}(\theta, \rho, \phi_s^{DQ}) = \frac{\partial \overline{\mathcal{H}}^{DQ}}{\partial \phi_s^{DQ}}(\phi_s^{DQ}) + \sum_{k=1}^{\infty} \frac{\partial a_{6k}}{\partial \phi_s^{DQ}}(\phi_s^{DQ}) \cos 6k\theta + \frac{\partial b_{6k}}{\partial \phi_s^{DQ}}(\phi_s^{DQ}) \sin 6k\theta \quad (3.95a)$$

$$T_e(\theta, \rho, \phi_s^{DQ}) = n i_s^{DQT} \mathcal{J}_3 \phi_s^{DQ} - n \sum_{k=1}^{\infty} -6k a_{6k}(\phi_s^{DQ}) \sin 6k\theta + 6k b_{6k}(\phi_s^{DQ}) \cos 6k\theta \quad (3.95b)$$

which shows that, when the star connection scheme is used, they should be  $\frac{\pi}{3}$ -periodic with respect to  $\theta$ . This can be illustrated by the curves in Jebai [37, fig. 4.4] where  $\frac{\pi}{3}$ -periodic oscillations can be seen in the measured currents and electromagnetic torque.

### 3.7.4 For the SynRM

As SynRM stators respect the phase permutation symmetry presented in section 3.4.1.1, the energy function of an SynRM in the  $DQ0$  frame is  $\frac{2\pi}{3}$  periodic with respect to  $\theta$ , hence it can be expanded as a Fourier series with respect to  $\theta$

$$\mathcal{H}^{DQ0}(\theta, \rho, \phi_s^{DQ0}) = \frac{1}{2J_L n^2} \rho^2 + \overline{\mathcal{H}}^{DQ0}(\phi_s^{DQ0}) + \sum_{k=1}^{\infty} a_{3k}(\phi_s^{DQ0}) \cos 3k\theta + b_{3k}(\phi_s^{DQ0}) \sin 3k\theta. \quad (3.96)$$

As the stator is symmetric with respect to the 0-axis, the condition eq. (3.43) must be respected. As in section 3.7.3  $\overline{\mathcal{H}}^{DQ0}$ ,  $\{a_{6k}\}$  and  $\{b_{6k}\}$  are even with respect to  $\phi_s^0$  whereas  $\{a_{6k+3}\}$  and  $\{b_{6k+3}\}$  are odd with respect to  $\phi_s^0$ .

Moreover the rotor is symmetric with respect to the two saliency planes, so using eq. (3.47),

$$\begin{aligned} \overline{\mathcal{H}}^{DQ0}(\phi_s^D, \phi_s^Q, \phi_s^0) &= \overline{\mathcal{H}}^{DQ0}(\phi_s^D, -\phi_s^Q, \phi_s^0) = \overline{\mathcal{H}}^{DQ0}(-\phi_s^D, \phi_s^Q, \phi_s^0) \\ a_{3k}(\phi_s^D, \phi_s^Q, \phi_s^0) &= a_{3k}(\phi_s^D, -\phi_s^Q, \phi_s^0) = a_{3k}(-\phi_s^D, \phi_s^Q, \phi_s^0) \\ b_{3k}(\phi_s^D, \phi_s^Q, \phi_s^0) &= -b_{3k}(\phi_s^D, -\phi_s^Q, \phi_s^0) = -b_{3k}(-\phi_s^D, \phi_s^Q, \phi_s^0) \end{aligned}$$

which means  $\overline{\mathcal{H}}^{DQ0}$  and  $\{a_{3k}\}$  are even with respect to  $\phi_s^D$  and  $\phi_s^Q$ , whereas  $\{b_{6k}\}$  are odd with respect to  $\phi_s^D$  and  $\phi_s^Q$ .

Applying eqs. (3.30a) and (3.30d), one gets the current-flux relations and the electromagnetic torque expression

$$\begin{aligned} i_s^{DQ0}(\theta, \rho, \phi_s^{DQ0}) &= \frac{\partial \bar{\mathcal{H}}^{DQ0}}{\partial \phi_s^{DQ0}}(\phi_s^{DQ0}) \\ &+ \sum_{k=1}^{\infty} \frac{\partial a_{3k}}{\partial \phi_s^{DQ0}}(\phi_s^{DQ0}) \cos 3k\theta + \frac{\partial b_{3k}}{\partial \phi_s^{DQ0}}(\phi_s^{DQ0}) \sin 3k\theta \end{aligned} \quad (3.97a)$$

$$\begin{aligned} T_e(\theta, \rho, \phi_s^{DQ0}) &= n i_s^{DQ0T} \mathcal{J}_3 \phi_s^{DQ0} \\ &- n \sum_{k=1}^{\infty} -3k a_{3k}(\phi_s^{DQ0}) \sin 3k\theta + 3k b_{3k}(\phi_s^{DQ0}) \cos 3k\theta \end{aligned} \quad (3.97b)$$

which shows that the current and the torque are  $\frac{2\pi}{3}$ -periodic with respect to  $\theta$ .

As in the PMSM case (see section 3.7.3), when the star connection scheme is used, the 0-axis can be decoupled in the energy function, so the  $\{a_{6k+3}\}$  and  $\{b_{6k+3}\}$  are zero and thus the current and the electromagnetic torque are  $\frac{\pi}{3}$ -periodic with respect to  $\theta$ .

### 3.7.5 Experimental results

The torque ripple due to non-sinusoidal windings is a well-known phenomenon and has been highlighted on many kinds of motors (see [39–41] for the IM and [24–26] for the PMSMs). The main harmonics are always at  $3k$  or  $6k$  and it has also been shown that the harmonics power decreases rapidly with  $k$ .

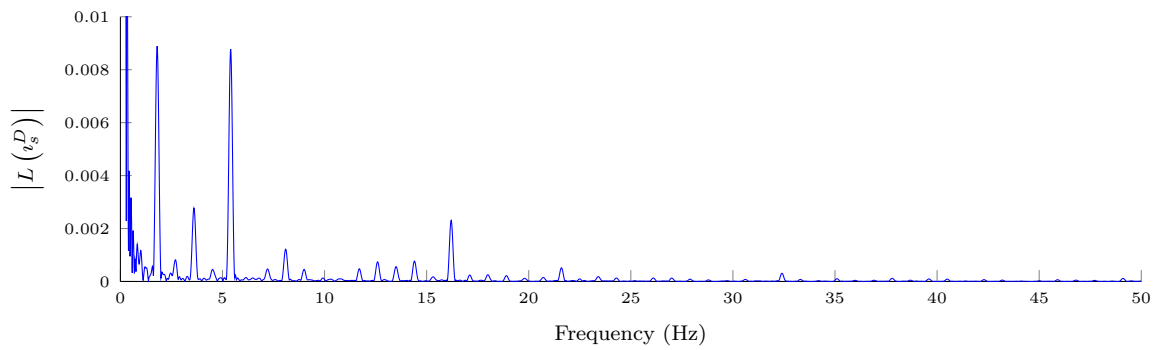
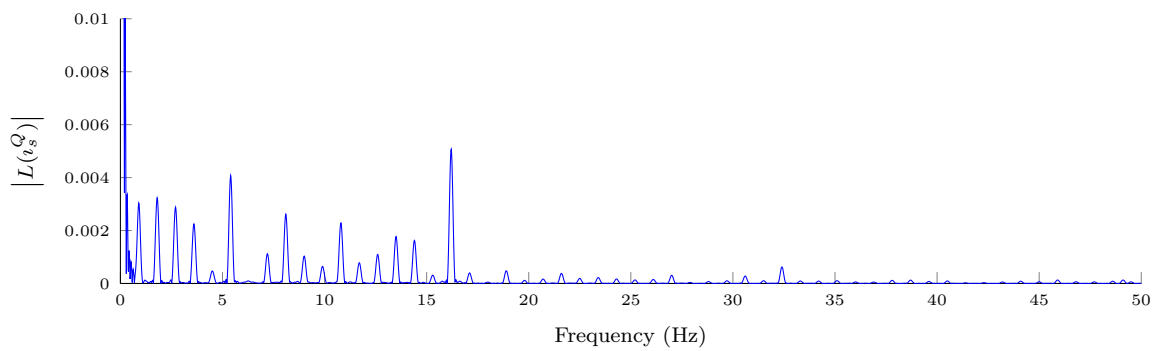
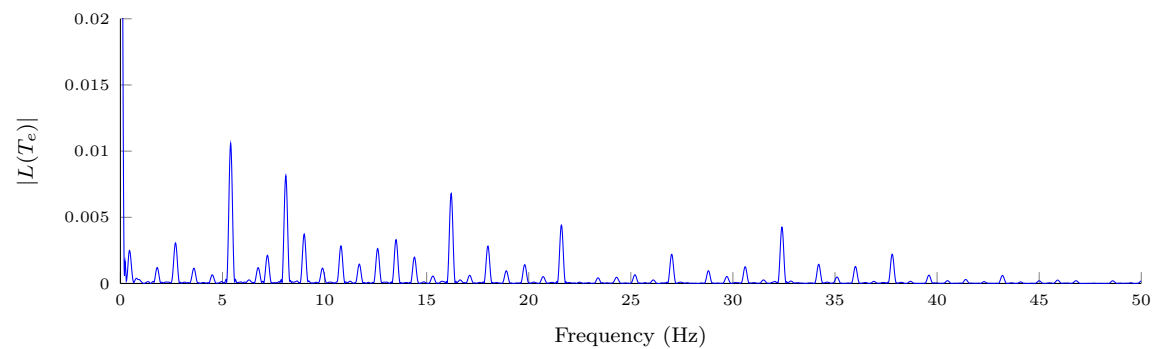
On the dSpace<sup>®</sup> test bench, we recorded the stator currents  $i_s^{abc}$ , the mechanical speed  $\omega_m$  and the electromagnetic torque  $T_e$  while the motor (SynRM table 2.1 or IM table 2.2) was excited with a  $0.9Hz$  sinusoidal voltage, the load machine being disconnected. Similar tests have been made on the PMSM, see Jebai [37]. Open-loop control was chosen since closed-loop control would mix the harmonics. However, there are still additional harmonics coming from the voltage drops, described in section 2.3.1, and the load machine harmonics, presented in section 2.3.3. As the amplitude of harmonics are quite small, we give the spectra of the recorded signals which were obtained off-line by FFT. Fig. 3.13 for the SynRM and fig. 3.14 show the spectra of the recorded signals. The main harmonics are listed in table 3.3 for the SynRM and table 3.4 for the IM, where it can be seen that the harmonics with the largest amplitude are indeed obtained at  $6k\omega_s$  ( $k \in \mathbb{N}^*$ ).

The tables show that these phenomena are very small with respect to rated values. To simplify the models, we are going to neglect these effects in the modeling phase and consider it as a noise in the control design phase. The only terms we will consider later will be  $\bar{\mathcal{H}}^{DQ0}$ , the nonlinear fundamental of the energy function and the kinetic energy.

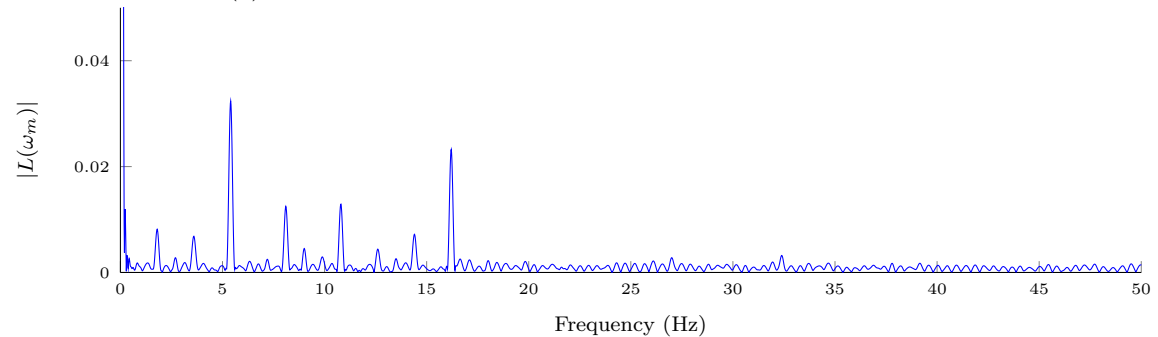
## 3.8 Saturated sinusoidal motor model

As shown in section 3.7.5, harmonics in the measurements are quite small with respect to the fundamental, which means that  $\bar{\mathcal{H}}^{DQ0}$  is a very good approximation of  $\mathcal{H}^{DQ0}$  for the all electric motors studied in this document. Thus, the invariance conditions for a saturated sinusoidal motor will be exactly those of the fundamentals in section 3.7 recalled in table 3.5.

As this approximation will be used in the rest of the document, we find it judicious to show what the sinusoidal assumption means in term of saliency (see section 3.8.1) and

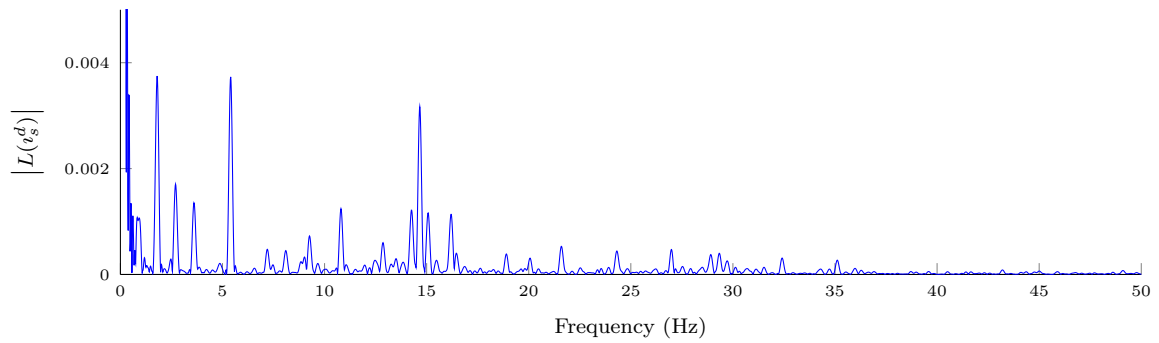
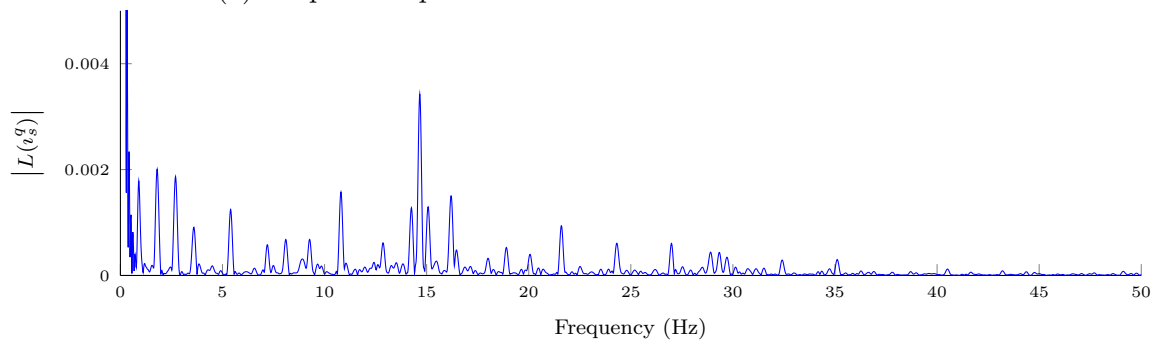
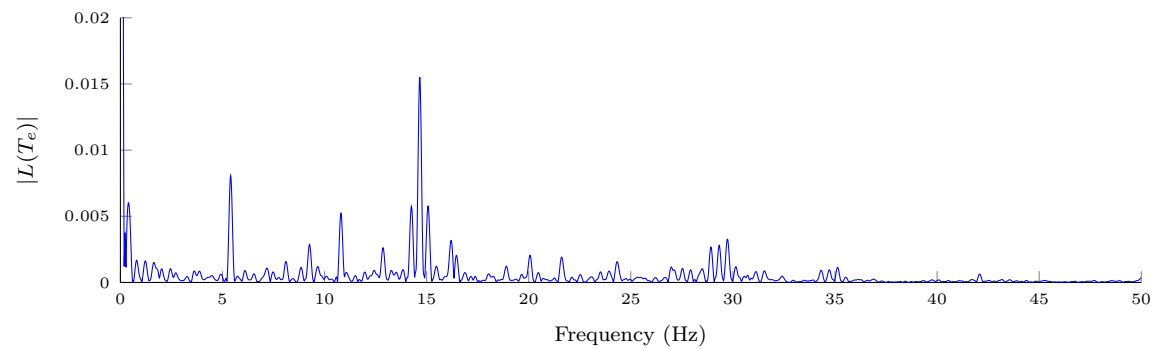
(a) Amplitude spectrum of the stator current on  $D$ -axis.(b) Amplitude spectrum of the stator current on  $Q$ -axis.

(c) Amplitude spectrum of the electromagnetic torque.

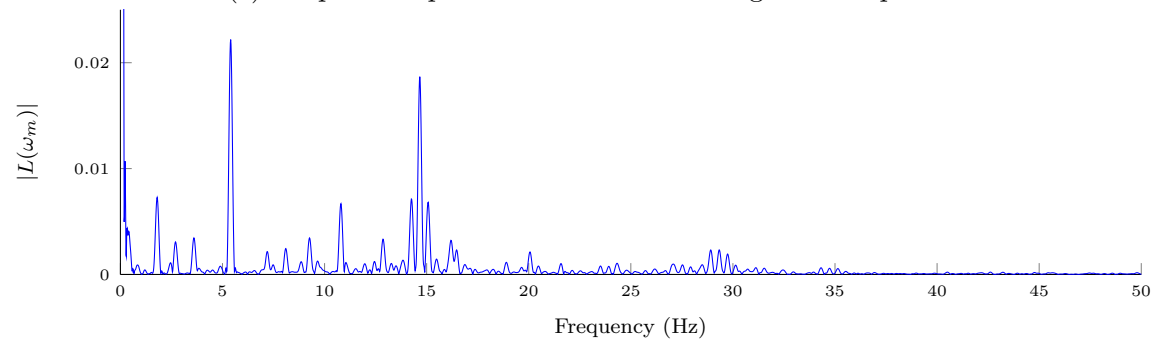


(d) Amplitude spectrum of the mechanical speed.

Figure 3.13 – Spectra of the signals recorded on the SynRM described by table 2.1.

(a) Amplitude spectrum of the stator current on  $D$ -axis.(b) Amplitude spectrum of the stator current on  $Q$ -axis.

(c) Amplitude spectrum of the electromagnetic torque.



(d) Amplitude spectrum of the mechanical speed.

Figure 3.14 – Spectra of the signals recorded on the IM described by table 2.2.

Frequency	$ L(i_s^D) $	$ L(i_s^Q) $	$ L(T_e) $	$ L(\omega_m) $	Signification
0.9Hz	–	0.003A	–	–	$\omega_s$
1.8Hz	0.008A	0.003A	–	0.008Hz	$2\omega_s$
2.7Hz	–	0.003A	0.003N.m	–	$3\omega_s$
3.6Hz	0.003A	0.002A	–	0.007Hz	$4\omega_s$
5.4Hz	0.008A	0.004A	0.011N.m	0.032Hz	$6\omega_s$
7.2Hz	–	0.001A	0.002N.m	–	$8\omega_s$
8.1Hz	0.001A	0.001A	0.008N.m	0.012Hz	$9\omega_s$
9.0Hz	–	0.001A	0.003N.m	–	$10\omega_s$
10.8Hz	–	0.002A	0.003N.m	0.013Hz	$12\omega_s$
11.7Hz	–	0.001A	–	–	$13\omega_s$
12.6Hz	–	0.001A	0.003N.m	–	$14\omega_s$
13.5Hz	–	0.002A	0.003N.m	–	$15\omega_s$
14.4Hz	–	0.002A	–	0.007Hz	$16\omega_s$
16.2Hz	0.002A	0.005A	0.007N.m	0.023Hz	$18\omega_s$
18.0Hz	–	–	0.003N.m	–	$20\omega_s$
21.6Hz	–	–	0.004N.m	–	$24\omega_s$
27.0Hz	–	–	0.002N.m	–	$30\omega_s$
32.4Hz	–	–	0.004N.m	–	$36\omega_s$
37.8Hz	–	–	0.002N.m	–	$42\omega_s$

Table 3.3 – Main harmonics in the response of the SynRM described by table 2.1.

how the saturated case differs from the unsaturated case presented in section 3.6 (see section 3.8.2). Moreover, since a star-connected motor is always used in the rest of the document, the 0-axis can be decoupled and we will consider that the model of the electric motor is given by one of the energy functions  $\mathcal{H}^{\alpha\beta}$ ,  $\mathcal{H}^{dq}$  or  $\mathcal{H}^{DQ}$ , depending on the chosen frame, omitting the star subscript for the sake of clearness.

### 3.8.1 About saliency

In the literature on signal injection two concepts of saliency are introduced: the mechanical saliency and the magnetic saliency (see Ha, Sul, *et al.* [42], Jansen and Lorenz [78]). The mechanical saliency is due to the design of the electric motor whereas the magnetic saliency is caused by the saturation of magnetic paths. However these concepts are generally not properly explained in the literature and we try here to rectify this. Our conclusions are summarized in table 3.6.

#### 3.8.1.1 Mechanical saliency

In the traditional literature (Krause, Wasynczuk, *et al.* [56] for instance) the salient motors refers to electric motors whose rotor has a particular axis defined by its geometry. However, the permanent magnet flux is traditionally not taken into account. In this document however we prefer to take it into account as the permanent magnet flux really defines a specific direction. Thus non-salient PMSMs will be considered as mechanically salient motors.

Frequency	$ L(\imath_s^d) $	$ L(\imath_s^q) $	$ L(T_e) $	$ L(\omega_m) $	Signification
0.4Hz	–	–	0.006N.m	–	$\omega_m$
0.9Hz	–	0.002A	–	–	$\omega_s$
1.8Hz	0.004A	0.002A	–	0.004Hz	$2\omega_s$
2.7Hz	0.002A	0.002A	–	0.002Hz	$3\omega_s$
3.6Hz	0.001A	0.001A	–	0.002Hz	$4\omega_s$
5.4Hz	0.004A	0.001A	0.008N.m	0.011Hz	$6\omega_s$
7.2Hz	–	–	–	0.001Hz	$8\omega_s$
8.1Hz	–	–	0.002N.m	0.001Hz	$9\omega_s$
9.3Hz	–	–	0.003N.m	0.002Hz	$36\omega_m - 6\omega_s$
10.8Hz	0.001A	0.002A	0.005N.m	0.003Hz	$12\omega_s$
12.9Hz	–	–	0.003N.m	0.002Hz	$36\omega_m - 2\omega_s$
14.3Hz	0.001A	0.001A	0.006N.m	0.004Hz	$35\omega_m$
14.7Hz	0.003A	0.003A	0.015N.m	0.009Hz	$36\omega_m$
15.1Hz	0.001A	0.001A	0.004N.m	0.004Hz	$37\omega_m$
16.2Hz	0.001A	0.002A	0.003N.m	0.002Hz	$18\omega_s$
16.5Hz	–	–	0.002N.m	0.001Hz	$36\omega_m + 2\omega_s$
20.1Hz	–	–	0.002N.m	0.001Hz	$36\omega_m + 6\omega_s$
21.6Hz	–	0.001A	0.002N.m	–	$24\omega_s$
28.9Hz	–	–	0.003N.m	0.001Hz	$71\omega_m$
29.3Hz	–	–	0.003N.m	0.001Hz	$72\omega_m$
29.7Hz	–	–	0.003N.m	0.001Hz	$73\omega_m$

Table 3.4 – Main harmonics in the response of the IM described by table 2.2.

For non-salient electric motors there is no particular direction for the rotor, thence the energy remains unchanged whatever the position of the rotor, i.e.  $\forall \eta \in ] - \pi, \pi ]$

$$\mathcal{H}^{abc}(\theta, \rho, \phi_s^{abc}, \phi_r^{abc}) = \mathcal{H}^{abc}(\theta + \eta, \rho, \phi_s^{abc}, \mathcal{R}^{abc}(-\eta)\phi_r^{abc}) \quad (3.98a)$$

$$\mathcal{H}^{abc}(\theta, \rho, \phi_s^{abc}, \phi_r^{abc}) = \mathcal{H}^{abc}(\theta + \eta, \rho, \mathcal{R}^{abc}(\eta)\phi_s^{abc}, \phi_r^{abc}). \quad (3.98b)$$

When rewritten in the  $dq$  frame for a star-connected machine, they gives

$$\mathcal{H}^{dq}(\theta, \rho, \phi_s^{dq}, \phi_r^{dq}) = \mathcal{H}^{dq}(\theta + \eta, \rho, \phi_s^{dq}, \phi_r^{dq}) \quad (3.99a)$$

$$\mathcal{H}^{dq}(\theta, \rho, \phi_s^{dq}, \phi_r^{dq}) = \mathcal{H}^{dq}(\theta + \eta, \rho, \mathcal{R}^{dq}(\eta)\phi_s^{dq}, \mathcal{R}^{dq}(\eta)\phi_r^{dq}). \quad (3.99b)$$

Eq. (3.99a) means that the energy function of a non-salient sinusoidal motor in  $dq$  frame does not depend on theta either. By eq. (3.99b), the energy function of a non-salient machine is independent on  $\theta$  in any frame identical to the  $dq$  frame up to a rotation around the 0-axis which includes the  $\alpha\beta$  and  $DQ$  frames as in the unsaturated case. In contrast salient electric motor will not satisfy neither eq. (3.98) nor eq. (3.99). Consequently, their energy function will depend on  $\theta$  through  $\theta_s - \theta$

$$\mathcal{H}^{dq}(\theta, \rho, \phi_s^{dq}, \phi_r^{dq}) = \mathcal{H}^{DQ}(\rho, P_{dq \rightarrow DQ}(\theta_s - \theta)\phi_s^{dq}, P_{dq \rightarrow DQ}(\theta_s - \theta)\phi_r^{dq}) \quad (3.100)$$

where we used again that the energy function in the  $DQ$  frame does not depend on  $\theta$  for sinusoidal machines.

	Symmetry	$\mathcal{H}^{DQ0}(\rho, \phi_s^D, \phi_s^Q, \phi_s^0, \phi_r^D, \phi_r^Q, \phi_r^0)$	Condition
Stator	Current reversal	$\mathcal{H}^{DQ0}(\rho, \phi_s^D, \phi_s^Q, -\phi_s^0, \phi_r^D, \phi_r^Q, \phi_r^0)$	Axial symmetry
Salient Rotor	Phase exchange	$\mathcal{H}^{DQ0}(-\rho, \phi_s^D, -\phi_s^Q, \phi_s^0, \phi_r^D, -\phi_r^Q, \phi_r^0)$	Planar symmetry
	Current reversal	$\mathcal{H}^{DQ0}(\rho, -\phi_s^D, -\phi_s^Q, \phi_s^0, -\phi_r^D, -\phi_r^Q, -\phi_r^0)$	Axial symmetry
Non-salient Rotor	Phase exchange	$\mathcal{H}^{DQ0}(-\rho, \phi_s^D, -\phi_s^Q, \phi_s^0, \phi_r^D, -\phi_r^Q, \phi_r^0)$	Planar symmetry
	Current reversal	$\mathcal{H}^{DQ0}(\rho, \phi_s^D, \phi_s^Q, \phi_s^0, \phi_r^D, \phi_r^Q, -\phi_r^0)$	Axial symmetry

Table 3.5 – Symmetry constraints on the form of the Hamiltonian for sinusoidal nonlinear models.

As the energy function in  $dq$  frames depends on  $\theta_s - \theta$ , all salient electric motors rotate at the electrical speed  $\omega_s$  when the equilibrium is reached, otherwise the energy of the electric motor would not be constant in  $dq$  frames. In contrast the non-salient motors, such as the IM, can rotate at any speed at equilibrium.

### 3.8.1.2 Magnetic saliency

In the literature [42, 78, 85] it has been shown that the response of electric machines to signal injection depends on the direction of the injection and a lot of experimental data given in this document will confirm this. For SynRMs and salient PMSMs, this is very well explained by the fact that the saliency influences the HF response. However for non-salient PMSM and IM it is much more difficult to explain.

Indeed in section 4.2.3 we prove that the HF current response of a star-connected IM to voltage injection in  $dq$  frames can be computed as

$$\tilde{i}_s^{dq} = \frac{\partial^2 \mathcal{H}^{dq}}{\partial \phi_s^{dq2}}(\phi_s^{dq}, \phi_r^{dq}) \tilde{u}_s^{dq}$$

where  $\tilde{u}_s^{dq}$  is the amplitude of the injected voltage in the chosen  $dq$  frame. Similar proofs can be applied to the PMSM (see [37, 43]) and the SynRM and we obtain

$$\tilde{i}_s^{DQ} = \frac{\partial^2 \mathcal{H}^{DQ}}{\partial \phi_s^{DQ2}}(\phi_s^{DQ}, \phi_r^{DQ}) \tilde{u}_s^{DQ}.$$

When the response and the injection are expressed in the orthogonal frame of the injection  $vw$  where  $v$  is along the instantaneous injection axis we obtain

$$\tilde{i}_s^{vw} = P_{vw \rightarrow DQ}^{-1}(\theta_i) \frac{\partial^2 \mathcal{H}^{DQ}}{\partial \phi_s^{DQ2}}(\phi_s^{DQ}, \phi_r^{DQ}) P_{vw \rightarrow DQ}(\theta_i) \begin{pmatrix} \tilde{u}_s \\ 0 \end{pmatrix}$$

Electric motor	Model type	Mechanically salient	Magnetically non salient
SynRM	unsaturated	Yes	Yes
	saturated	Yes	Yes
Salient PMSM	unsaturated	Yes	Yes
	saturated	Yes	Yes
Non-salient PMSM	unsaturated	Yes	No
	saturated	Yes	Yes
IM	unsaturated	No	No
	saturated	No	Yes

Table 3.6 – Summary of section 3.8.1

where  $P_{vw \rightarrow DQ}$  is the rotation of  $\mathbb{R}^2$  of angle  $-\theta_i$

$$P_{vw \rightarrow DQ}(\theta_i) = \begin{pmatrix} \cos \theta_i & \sin \theta_i \\ -\sin \theta_i & \cos \theta_i \end{pmatrix},$$

$\theta_i$  being the angle between  $DQ$  and  $vw$  frames.

For the unsaturated SynRM and the unsaturated salient PMSM we easily obtain from eqs. (3.79) and (3.85) that

$$\frac{\partial^2 \mathcal{H}^{dq}}{\partial \phi_s^{DQ^2}}(\phi_s^{DQ}, \phi_r^{DQ}) = \begin{pmatrix} \Gamma_s^D & 0 \\ 0 & \Gamma_s^Q \end{pmatrix}$$

does not commute with rotations and thus the HF current response to HF signal injection depends on the injection axis. However for the unsaturated non-salient PMSM and the IM we have (see eqs. (3.75) and (3.83))

$$\frac{\partial^2 \mathcal{H}^{dq}}{\partial \phi_s^{DQ^2}}(\phi_s^{DQ}, \phi_r^{DQ}) = \begin{pmatrix} \Gamma_s & 0 \\ 0 & \Gamma_s \end{pmatrix}$$

which commutes with rotations. Thus, the unsaturated model does not explain why the HF current response of the motor to HF signal injection depends on the injection axis. It should be noted that the unsaturated non-salient PMSM is in this the second category, whereas it is mechanically salient. Consequently we deal with a different kind of saliency which is usually qualified as “magnetic” as magnetic saturation can cause it as we show below.

We now consider saturated electric motors. In this case  $\frac{\partial^2 \mathcal{H}^{DQ}}{\partial \phi_s^{DQ^2}}(\phi_s^{DQ}, \phi_r^{DQ})$  is a symmetric matrix, however its diagonal terms may not be equal and the anti-diagonal terms may not be zero. Consequently, this matrix does not commute with rotations and the HF current response to HF signal injection depends on the injection axis. For the non-salient PMSM and the IM this dependency cannot be explained with the unsaturated motor model and we have to take into account magnetic saturation.

### 3.8.2 Chord and tangent inductances

In the unsaturated SynRM case we have for the current-flux relations

$$i_s^D = \Gamma_s^D \phi_s^D \quad (3.101a)$$

$$i_s^Q = \Gamma_s^Q \phi_s^Q \quad (3.101b)$$

which defines the inverse inductances as being

$$\Gamma_s^D = \frac{i_s^D}{\phi_s^D} = \frac{\partial i_s^D}{\partial \phi_s^D} = \frac{\partial^2 \mathcal{H}^{DQ}}{\partial \phi_s^{D2}} \quad (3.102a)$$

$$\Gamma_s^Q = \frac{i_s^Q}{\phi_s^Q} = \frac{\partial i_s^Q}{\partial \phi_s^Q} = \frac{\partial^2 \mathcal{H}^{DQ}}{\partial \phi_s^{Q2}}. \quad (3.102b)$$

However for the saturated SynRM case, the quotient of the currents by the fluxes is not equal to the partial derivatives of the currents by the fluxes. Thus we have two kinds of inverse inductances. In the literature they are usually defined and studied in the one dimensional case [44, 46], which is not suitable for us. Yet, we will stick to the denominations of tangent inductances (also called dynamic inductances) for the partial derivatives and chord inductances (also called static inductances) for the quotient.

We define the tangent inductances, denoted  $L^t$ , as the partial derivatives of the fluxes with respect to the currents, which depend on the currents. Conversely we can define the tangent inverse inductances,  $\Gamma_t$ , as the partial derivatives of the currents with respect to the fluxes which are much more handy when using Hamiltonian models. For the SynRM we have

$$\Gamma_{t_s}^{DQ}(\phi_s^{DQ}) := \frac{\partial i_s^{DQ}}{\partial \phi_s^{DQ}}(\phi_s^{DQ}) = \frac{\partial^2 \mathcal{H}^{DQ}}{\partial \phi_s^{DQ2}}(\phi_s^{DQ}). \quad (3.103)$$

Defining the chord inductances, denoted  $L^c$ , in the two-dimensional case is a bit more difficult. Admittedly we can define the chord inverse inductances,  $\Gamma_c$ , as

$$\Gamma_{c_s}^{DQ}(\phi_s^{DQ}) := \begin{pmatrix} \frac{i_s^D(\phi_s^{DQ})}{\phi_s^D} & 0 \\ 0 & \frac{i_s^Q(\phi_s^{DQ})}{\phi_s^Q} \end{pmatrix}$$

but this is not the most judicious definition as the chord inverse inductance on one axis depends on the fluxes of both axis. The problem can be restated as follows: finding a matrix  $\Gamma_{c_s}^{DQ}$  such that  $i_s^{DQ} = \Gamma_{c_s}^{DQ} \phi_s^{DQ}$ . However this equation does not define properly  $\Gamma_{c_s}^{DQ}$  and we can add the additional constraint that we would like the diagonal terms to depend only on the flux of the corresponding axis. The most sensible definition is thus

$$\Gamma_{c_s}^{DQ}(\phi_s^{DQ}) := \begin{pmatrix} \frac{i_s^D(\phi_s^D, 0)}{\phi_s^D} & \frac{i_s^D(\phi_s^D, \phi_s^Q) - i_s^D(\phi_s^D, 0)}{\phi_s^Q} \\ \frac{i_s^Q(\phi_s^D, \phi_s^Q) - i_s^Q(0, \phi_s^Q)}{\phi_s^D} & \frac{i_s^Q(0, \phi_s^Q)}{\phi_s^Q} \end{pmatrix}. \quad (3.104)$$

The definition of the chord and tangent inverse inductances is illustrated in fig. 3.15 for the saturated SynRM case, where it can be seen that, as in the one-dimensional case, tangent inverse inductances are related to the tangent space of the current-flux surface and chord inductances are related to paths from the origin to the working point.

For the PMSM similar definitions can be used. The tangent inverse inductances are defined as

$$\Gamma_{t_s}^{DQ}(\phi_s^{DQ}) := \frac{\partial i_s^{DQ}}{\partial \phi_s^{DQ}}(\phi_s^{DQ}) = \frac{\partial^2 \mathcal{H}^{DQ}}{\partial \phi_s^{DQ2}}(\phi_s^{DQ}). \quad (3.105)$$

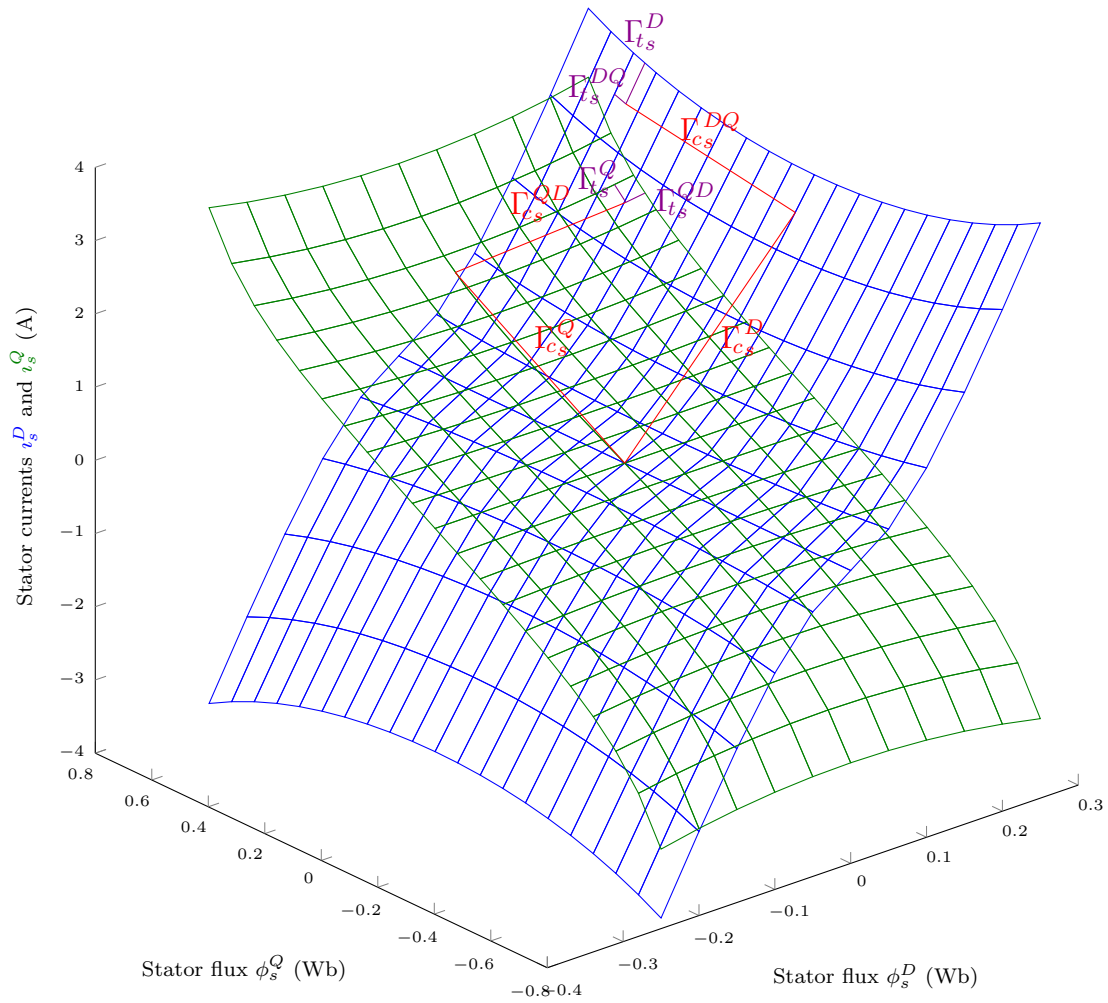


Figure 3.15 – The currents as functions of the fluxes from the model obtained in section 5.2. The slopes of the red lines are chord inverse inductances and the slopes of the violet lines are tangent inverse inductances.

and the chord inverse inductances as

$$\Gamma_{c_s}^{DQ}(\phi_s^{DQ}) := \begin{pmatrix} \frac{\iota_s^D(\phi_s^D, 0)}{\phi_s^D - \phi_M^D} & \frac{\iota_s^D(\phi_s^D, \phi_s^Q) - \iota_s^D(\phi_s^D, 0)}{\phi_s^Q - \phi_M^Q} \\ \frac{\iota_s^Q(\phi_s^D, \phi_s^Q) - \iota_s^Q(0, \phi_s^Q)}{\phi_s^D - \phi_M^D} & \frac{\iota_s^Q(0, \phi_s^Q)}{\phi_s^Q - \phi_M^Q} \end{pmatrix}. \quad (3.106)$$

and thus  $\iota_s^{DQ} = \Gamma_{c_s}^{DQ}(\phi_s^{DQ} - \phi_M^{DQ})$ .

Generalizing the definition of the tangent inductances for the IM, we find

$$\Gamma_{t_s}^{dq}(\phi_s^{dq}, \phi_r^{dq}) := \frac{\partial \iota_s^{dq}}{\partial \phi_s^{dq}} = \frac{\partial^2 \mathcal{H}^{dq}}{\partial \phi_s^{dq^2}} \quad (3.107a)$$

$$\Gamma_{t_m}^{dq}(\phi_s^{dq}, \phi_r^{dq}) := \frac{\partial \iota_s^{dq}}{\partial \phi_r^{dq}} = \frac{\partial^2 \mathcal{H}^{dq}}{\partial \phi_s^{dq} \partial \phi_r^{dq}} = \frac{\partial^2 \mathcal{H}^{dq}}{\partial \phi_r^{dq} \partial \phi_s^{dq}} = \frac{\partial \iota_r^{dq}}{\partial \phi_s^{dq}} \quad (3.107b)$$

$$\Gamma_{t_r}^{dq}(\phi_s^{dq}, \phi_r^{dq}) := \frac{\partial \iota_r^{dq}}{\partial \phi_r^{dq}} = \frac{\partial^2 \mathcal{H}^{dq}}{\partial \phi_r^{dq^2}}. \quad (3.107c)$$

However generalizing the definition of chord inverse inductances for the IM is quite difficult and we did not find any suitable definition. We can still say that the chord inverse inductances exist and verify the relations

$$\iota_s^{dq} = \Gamma_{c_m}^{dq}(\phi_s^{dq}, \phi_r^{dq})(\phi_s^{dq} + \phi_r^{dq}) + \Gamma_{cl_s}^{dq}(\phi_s^{dq}, \phi_r^{dq})\phi_s^{dq} \quad (3.108a)$$

$$\iota_r^{dq} = \Gamma_{c_m}^{dq}(\phi_s^{dq}, \phi_r^{dq})(\phi_s^{dq} + \phi_r^{dq}) + \Gamma_{cl_r}^{dq}(\phi_s^{dq}, \phi_r^{dq})\phi_r^{dq} \quad (3.108b)$$

which are inspired from eqs. (3.77a) and (3.77c).

### 3.9 Partial conclusion

In this chapter results of analytical mechanics are adapted to electric motors, which simplify their modeling. This approach justifies the modeling of magnetic saturation in the fictitious  $dq$  frame, whereas it happens in the physical  $abc$  frame. It also proves that the expression of electromagnetic torque is not affected by magnetic saturation. Besides the saturated models for electric motors, constructed following this approach, automatically verify the reciprocity conditions, which are constraints that current-flux relations must satisfy to be physically acceptable.

This approach also handles very easily constraints due to the symmetries in the layout of electric motors and constraints due to the connection schemes of stator and rotor windings. The variables held constant by the connection scheme are decoupled from the model and the symmetries are reflected on the form of the energy function in  $DQ$  frame.

Using this approach we can retrieve more easily the unsaturated sinusoidal models for electric motors and similarities between the diverse electric motors are highlighted. We also predicted the forms of ripples due to non-sinusoidality and showed we can neglect them in experiments as they are quite small with respect to nominal values. The expected forms of saturated sinusoidal models are described but no explicit model is given. This is addressed in chapter 5.



# Chapter 4

## Low-speed observability issues

### Chapitre 4 — Problèmes d’observabilité à basse vitesse

*Ce chapitre est consacré à une étude théorique de l’injection de signal pour le contrôle « sans capteur » des machines électriques. Il commence par une étude de l’observabilité des machines électriques, qui s’avèrent être non observables sur les trajectoires où la pulsation stator est nulle. Une étude plus poussée autour de ces trajectoires montre que ce problème peut être théoriquement contourné et que l’injection de signal est une mise en pratique du critère théorique. Alternativement, elle peut être vue comme une méthode permettant d’obtenir des mesures supplémentaires sans ajouter de capteur. C’est cette dernière approche qui permet de construire facilement des observateurs pour les flux ou la vitesse de rotation qui convergent à basse vitesse et même à vitesse nulle.*

The “sensorless” observability of electric motors, that is to say the possibility to retrieve the state of electric motors from the knowledge of inputs and current measurements, is studied in section 4.1.4. We show that “sensorless” control for electric motors at low stator frequency,  $\omega_s$ , is inherently difficult as the state of the motor cannot be retrieved accurately. Then, by studying the observability of the induction machine around such trajectories, we find that “sensorless” observability can be recovered if a permanent excitation is added (see section 4.1.5). Following Jansen and Lorenz [78] we chose to inject a HF signal. The effects of HF signal injection are described and explained in section 4.2, using second order averaging (see Sanders, Verhulst, *et al.* [47, sec. 2.9]). Finally in section 4.4, using HF signal injection, we design “sensorless” flux and speed observers for IMs.

### 4.1 Low speed observability issues

We study here the “sensorless” observability of electric motors. As we want to regulate their speed, the observability will be studied on permanent trajectories where the motor rotates at constant speed,  $\omega_{s,e}$ . As shown in section 4.1.2, in any  $dq$  frame, these trajectories are equilibria, hence any  $dq$  frame is most suitable to carry out the observability study. It is shown in section 4.1.4 that observability on the desired trajectories is not possible when  $\omega_{s,e} = 0$ . By studying observability around such trajectories in section 4.1.5, we find that observability can be recovered thanks to a permanent excitation.

### 4.1.1 Bibliography

Observability criteria were applied to “sensorless” control of electric motors in Malrait [17, secs. 4.2.5, 4.3] for IMs and in Vaclavek and Blaha [48] for PMSMs. This is summarized in Glumineau and de Leon Morales [67, ch. 2]. To our knowledge, observability of SynRMs has never been studied.

In the aforementioned literature, the observability study is carried out in the  $\alpha\beta$  frame, as the measurements and controls can easily be expressed in this frame. However, in the  $\alpha\beta$  frame, the permanent trajectories of interest are not equilibria and nonlinear observability criteria must be used.

The conclusions of these studies are that PMSMs are not observable on trajectories where  $\omega_{s,e} = \omega_e = 0$  and IMs are not observable when  $\omega_e = \omega_{s,e} - \omega_{g,e} = -\omega_{g,e}$ . All this can be summarized by saying that PMSMs and IMs are not observable when  $\omega_{s,e} = 0$ .

### 4.1.2 Steady-state trajectory

We are considering that the electric motor is star-connected and fed with a balanced three-phase voltage  $u_{s,e}^{abc}$  of frequency  $\omega_{s,e}$ . In its domain of operation, under these conditions, it yields a constant torque  $T_{L,e}$  and rotates at a constant speed  $\omega_e$ . In the  $abc$  frame, this is obviously not an equilibrium as the input depends on time.

To get an equilibrium we change to a synchronous  $dq0$  frame rotating at  $\omega_{s,e}$ . In this frame the input voltage  $u_{s,e}^{dq}$  is constant and so are the fluxes  $\phi_{s,e}^{dq}$  and  $\phi_{r,e}^{dq}$  and the currents  $i_{s,e}^{dq}$  and  $i_{r,e}^{dq}$ . We have thus

$$0 = u_{s,e}^{dq} - R_s i_{s,e}^{dq} - \mathcal{J}_2 \omega_{s,e} \phi_{s,e}^{dq} \quad (4.1a)$$

$$0 = -R_r i_{r,e}^{dq} - \mathcal{J}_2 (\omega_{s,e} - \omega_e) \phi_{r,e}^{dq} \quad (4.1b)$$

$$0 = T_{e,e} - T_{L,e} \quad (4.1c)$$

where

$$\mathcal{J}_2 = \begin{pmatrix} 0 & -1 \\ 1 & 0 \end{pmatrix} \quad (4.2)$$

### 4.1.3 Model

A framework for electric machine modeling was developed in chapter 3. It can handle all electric motor types and can convey all conservative phenomena. However, as said in section 3.8, the sinusoidal motor is a very good representation of most three-phase electric motors. We will thus consider only sinusoidal models in this section.

The  $DQ$  frame is not adapted to the observability study because it is unknown and not properly defined when there is no rotor flux. As we are considering trajectories close to the trajectory of section 4.1.2, it is better to be in the synchronous  $dq$  frame rotating at  $\omega_{s,e}$ . The effect of this transformation depends on whether the motor is mechanically salient (see section 3.8.1.1) or not.

#### 4.1.3.1 Non salient case

For mechanically non-salient motors (see section 3.8.1.1), we simply have

$$\mathcal{H}^{dq}(\rho, \phi_s^{dq}, \phi_r^{dq}) = \mathcal{H}^{DQ}(\rho, \phi_s^{dq}, \phi_r^{dq}) \quad (4.3)$$

as the energy in any  $dq$  frame should be equal to the energy in the particular  $DQ$  frame (see section 3.8). The current-flux relations will thus be

$$i_s^{dq}(\phi_s^{dq}, \phi_r^{dq}) = \frac{\partial \mathcal{H}^{dq}}{\partial \phi_s^{dq}}(\phi_s^{dq}, \phi_r^{dq}) = \frac{\partial \mathcal{H}^{DQ}}{\partial \phi_s^{DQ}}(\phi_s^{dq}, \phi_r^{dq}) \quad (4.4a)$$

$$i_r^{dq}(\phi_s^{dq}, \phi_r^{dq}) = \frac{\partial \mathcal{H}^{dq}}{\partial \phi_r^{dq}}(\phi_s^{dq}, \phi_r^{dq}) = \frac{\partial \mathcal{H}^{DQ}}{\partial \phi_r^{DQ}}(\phi_s^{dq}, \phi_r^{dq}). \quad (4.4b)$$

Using eq. (3.25d) and eq. (3.36) and the fact that rotation matrices commute with  $\mathcal{J}_2$ , the electromagnetic torque can be obtained with any of the formulae

$$\begin{aligned} T_e(\phi_s^{dq}, \phi_r^{dq}) &= n\phi_r^{dqT} \mathcal{J}_2 i_r^{dq}(\phi_s^{dq}, \phi_r^{dq}) \\ &= -n\phi_s^{dqT} \mathcal{J}_2 i_s^{dq}(\phi_s^{dq}, \phi_r^{dq}). \end{aligned} \quad (4.5)$$

#### 4.1.3.2 Salient case

Since we consider sinusoidally wound electric motor,  $\mathcal{H}^{DQ}$  do not depend on  $\theta$ . Hence, for a mechanically salient electric motor (see section 3.8.1.1), the energy in any  $dq$  frame will depend on  $\theta$  through  $\theta_s - \theta$  and can be written

$$\mathcal{H}^{dq}(\theta_s - \theta, \rho, \phi_s^{dq}, \phi_r^{dq}) = \mathcal{H}^{DQ}(\rho, P_{dq0 \rightarrow DQ0}(\theta - \theta_s)\phi_s^{dq}, P_{dq0 \rightarrow DQ0}(\theta - \theta_s)\phi_r^{dq}).$$

To compact notations, we define  $\eta = \theta_s - \theta$  and  $\mathcal{R}(\eta)$  as the rotation around the 0-axis by the angle  $\eta$  and get

$$\mathcal{H}^{dq}(\eta, \rho, \phi_s^{dq}, \phi_r^{dq}) = \mathcal{H}^{DQ}(\rho, \mathcal{R}(\eta)\phi_s^{dq}, \mathcal{R}(\eta)\phi_r^{dq}). \quad (4.6)$$

The current-flux relations read

$$i_s^{dq}(\eta, \phi_s^{dq}, \phi_r^{dq}) = \frac{\partial \mathcal{H}^{dq}}{\partial \phi_s^{dq}}(\eta, \phi_s^{dq}, \phi_r^{dq}) = \mathcal{R}^T(\eta) \frac{\partial \mathcal{H}^{DQ}}{\partial \phi_s^{DQ}}(\mathcal{R}(\eta)\phi_s^{dq}, \mathcal{R}(\eta)\phi_r^{dq}) \quad (4.7a)$$

$$i_r^{dq}(\eta, \phi_s^{dq}, \phi_r^{dq}) = \frac{\partial \mathcal{H}^{dq}}{\partial \phi_r^{dq}}(\eta, \phi_s^{dq}, \phi_r^{dq}) = \mathcal{R}^T(\eta) \frac{\partial \mathcal{H}^{DQ}}{\partial \phi_r^{DQ}}(\mathcal{R}(\eta)\phi_s^{dq}, \mathcal{R}(\eta)\phi_r^{dq}) \quad (4.7b)$$

and the electromagnetic torque can be calculated as

$$\begin{aligned} T_e(\eta, \phi_s^{dq}, \phi_r^{dq}) &= -n \frac{\partial \mathcal{H}^{dq}}{\partial \theta}(\eta, \phi_s^{dq}, \phi_r^{dq}) + n\phi_r^{dqT} \mathcal{J}_2 i_r^{dq}(\eta, \phi_s^{dq}, \phi_r^{dq}) \\ &= n\phi_s^{dqT} \mathcal{R}^T(\eta) \mathcal{J}_2^T \frac{\partial \mathcal{H}^{DQ}}{\partial \phi_s^{DQ}}(\mathcal{R}(\eta)\phi_s^{dq}, \mathcal{R}(\eta)\phi_r^{dq}) \\ &\quad + n\phi_r^{dqT} \mathcal{R}^T(\eta) \mathcal{J}_2^T \frac{\partial \mathcal{H}^{DQ}}{\partial \phi_r^{DQ}}(\mathcal{R}(\eta)\phi_s^{dq}, \mathcal{R}(\eta)\phi_r^{dq}) \\ &\quad + n\phi_r^{dqT} \mathcal{J}_2 \mathcal{R}^T(\eta) \frac{\partial \mathcal{H}^{DQ}}{\partial \phi_r^{DQ}}(\mathcal{R}(\eta)\phi_s^{dq}, \mathcal{R}(\eta)\phi_r^{dq}) \\ &= -n\phi_s^{dqT} \mathcal{J}_2 \mathcal{R}^T(\eta) \frac{\partial \mathcal{H}^{DQ}}{\partial \phi_s^{DQ}}(\mathcal{R}(\eta)\phi_s^{dq}, \mathcal{R}(\eta)\phi_r^{dq}) \\ &= -n\phi_s^{dqT} \mathcal{J}_2 i_s^{dq}(\eta, \phi_s^{dq}, \phi_r^{dq}) \end{aligned} \quad (4.8)$$

since  $\mathcal{J}_2$  commutes with rotations.

### 4.1.3.3 State form

We want to get the load torque as well as the state variables. We will thus add it to the state and suppose it is constant. Thus, in the general case, the state equations for the observability study are

$$\frac{d\phi_s^{dq}}{dt} = u_s^{dq} - R_s \iota_s^{dq} - \mathcal{J}_2 \omega_{s,e} \phi_s^{dq} \quad (4.9a)$$

$$\frac{d\phi_r^{dq}}{dt} = -R_r \iota_r^{dq} - \mathcal{J}_2 (\omega_{s,e} - \omega) \phi_r^{dq} \quad (4.9b)$$

$$\frac{d\omega}{dt} = \frac{n}{J_L} (T_e - T_L) \quad (4.9c)$$

$$\frac{d\eta}{dt} = \omega_{s,e} - \omega \quad (4.9d)$$

$$\frac{dT_L}{dt} = 0. \quad (4.9e)$$

For non-salient motors,  $\eta$  is defined up to a constant as an anti-derivative of  $\omega_{s,e} - \omega$ . Since it does not appear in the right-hand side of the equations this will not be a problem as it can be removed from the state in this case. In fact we will see that in the case of non-salient electric motors  $\eta$  or equivalently  $\theta$ , is not observable.

The physical input is  $u_s^{abc}$ . Nevertheless, as we know the transformation matrices from the  $abc$  frame to the chosen  $dq0$  frame (via the  $\alpha\beta0$  frame), we can consider that  $u_s^{dq}$  is our input. Similarly we can consider  $\iota_s^{dq}$  as the measurement even though the physical measurement is  $\iota_s^{abc}$ . As  $\omega_s$  is constant on the studied trajectories,  $\omega_{s,e}$  in eq. (4.9) can be considered as a parameter.

As was said in section 3.5.2 some electric machines do not have rotor windings. For such machines the rotor flux is constant in the  $DQ$  frame and thus could be removed from the state equations. The current-flux relations are still valid but the partial derivatives of the energy function with respect to the rotor flux will be zero.

## 4.1.4 Linear observability

In section 4.1.3 we obtained saturated models of electric motors we want to study on the steady-state trajectory introduced in section 4.1.2. We will prove that all the electric motors are first-order observable when  $\omega_{s,e} \neq 0$  whereas they are first-order unobservable when  $\omega_{s,e} = 0$ . In the latter case only the acceleration  $\frac{d\omega}{dt}$  can be recovered from the measurement  $\iota_s^{dq}$ . Depending on the saliency, the unobservability condition  $\omega_{s,e} = 0$  defines straight lines in the  $(\omega_m, T_L)$ -plane, which are shown on fig. 4.1.

### 4.1.4.1 Linearization of the model

The linearized model state equations are given by

$$\frac{d\delta\phi_s^{dq}}{dt} = \delta u_s^{dq} - R_s \delta \iota_s^{dq} - \mathcal{J}_2 \omega_{s,e} \delta \phi_s^{dq} \quad (4.10a)$$

$$\frac{d\delta\phi_r^{dq}}{dt} = -R_r \delta \iota_r^{dq} - \mathcal{J}_2 \omega_{g,e} \delta \phi_r^{dq} + \mathcal{J}_2 \phi_{r,e}^{dq} \delta \omega \quad (4.10b)$$

$$\frac{d\delta\omega}{dt} = \frac{n}{J_L} (\delta T_e - \delta T_L) \quad (4.10c)$$

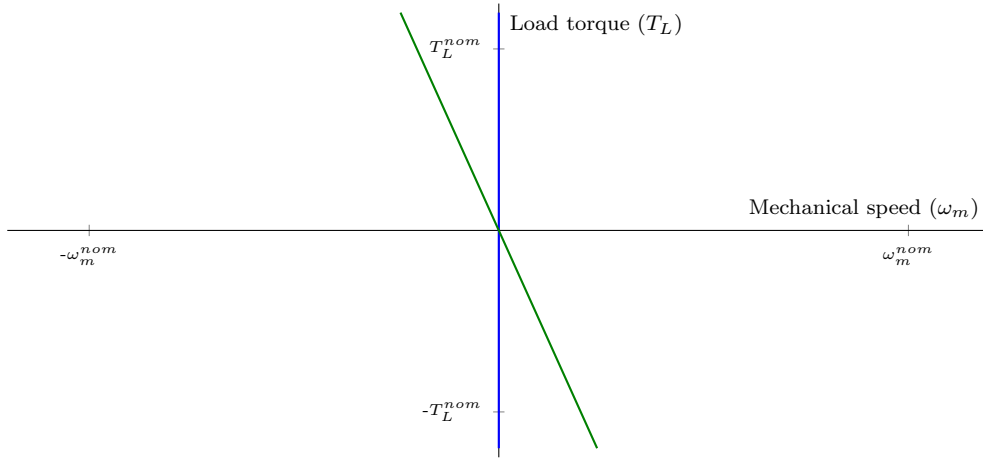


Figure 4.1 – Loci of unobservable working points for electric motors (in red for SynRMs and PMSMs and in magenta for IMs).

$$\frac{d\delta\eta}{dt} = -\delta\omega \quad (4.10d)$$

$$\frac{d\delta T_L}{dt} = 0 \quad (4.10e)$$

where we introduced the slip speed  $\omega_{g,e} = \omega_{s,e} - \omega_e$ , which is zero for salient motors. Linearizing either eq. (4.5) or eq. (4.8), we obtain the linearized electromagnetic torque

$$\delta T_e = -n\phi_{s,e}^{dqT} \mathcal{J}_2 \delta i_s^{dq} + n i_{s,e}^{dqT} \mathcal{J}_2 \delta \phi_s^{dq}. \quad (4.11)$$

**Non-salient case** When linearized, the current-flux relations eq. (4.4) give

$$\delta i_s^{dq} = \frac{\partial^2 \mathcal{H}^{dq}}{\partial \phi_s^{dq2}} (\phi_{s,e}^{dq}, \phi_{r,e}^{dq}) \delta \phi_s^{dq} + \frac{\partial^2 \mathcal{H}^{dq}}{\partial \phi_s^{dq} \partial \phi_r^{dq}} (\phi_{s,e}^{dq}, \phi_{r,e}^{dq}) \delta \phi_r^{dq} \quad (4.12a)$$

$$\delta i_r^{dq} = \frac{\partial^2 \mathcal{H}^{dq}}{\partial \phi_r^{dq} \partial \phi_s^{dq}} (\phi_{s,e}^{dq}, \phi_{r,e}^{dq}) \delta \phi_s^{dq} + \frac{\partial^2 \mathcal{H}^{dq}}{\partial \phi_r^{dq2}} (\phi_{s,e}^{dq}, \phi_{r,e}^{dq}) \delta \phi_r^{dq}. \quad (4.12b)$$

**Salient case** The currents now depend on  $\eta$  as well. Linearizing eq. (4.7) we get for the linearized current-flux relations

$$\begin{aligned} \delta i_s^{dq} &= \mathcal{R}^T(\eta_e) \mathcal{J}_2^T \frac{\partial \mathcal{H}^{DQ}}{\partial \phi_s^{DQ}} \delta \eta \\ &+ \mathcal{R}^T(\eta_e) \frac{\partial^2 \mathcal{H}^{DQ}}{\partial \phi_s^{DQ2}} \mathcal{J}_2 \mathcal{R}(\eta_e) \phi_{s,e}^{dq} \delta \eta + \mathcal{R}^T(\eta_e) \frac{\partial^2 \mathcal{H}^{DQ}}{\partial \phi_s^{DQ} \partial \phi_r^{DQ}} \mathcal{J}_2 \mathcal{R}(\eta_e) \phi_{r,e}^{dq} \delta \eta \\ &+ \mathcal{R}^T(\eta_e) \frac{\partial^2 \mathcal{H}^{DQ}}{\partial \phi_s^{DQ2}} \mathcal{R}(\eta_e) \delta \phi_s^{dq} + \mathcal{R}^T(\eta_e) \frac{\partial^2 \mathcal{H}^{DQ}}{\partial \phi_s^{DQ} \partial \phi_r^{DQ}} \mathcal{R}(\eta_e) \delta \phi_r^{dq} \end{aligned} \quad (4.13a)$$

$$\begin{aligned} \delta i_r^{dq} &= \mathcal{R}^T(\eta_e) \mathcal{J}_2^T \frac{\partial \mathcal{H}^{DQ}}{\partial \phi_r^{DQ}} \delta \eta \\ &+ \mathcal{R}^T(\eta_e) \frac{\partial^2 \mathcal{H}^{DQ}}{\partial \phi_r^{DQ} \partial \phi_s^{DQ}} \mathcal{J}_2 \mathcal{R}(\eta_e) \phi_{s,e}^{dq} \delta \eta + \mathcal{R}^T(\eta_e) \frac{\partial^2 \mathcal{H}^{DQ}}{\partial \phi_r^{DQ2}} \mathcal{J}_2 \mathcal{R}(\eta_e) \phi_{r,e}^{dq} \delta \eta \\ &+ \mathcal{R}^T(\eta_e) \frac{\partial^2 \mathcal{H}^{DQ}}{\partial \phi_r^{DQ} \partial \phi_s^{DQ}} \mathcal{R}(\eta_e) \delta \phi_s^{dq} + \mathcal{R}^T(\eta_e) \frac{\partial^2 \mathcal{H}^{DQ}}{\partial \phi_r^{DQ2}} \mathcal{R}(\eta_e) \delta \phi_r^{dq} \end{aligned} \quad (4.13b)$$

Non-salient case	Salient case
	$\Delta l_s^{dq} := -\mathcal{R}^T(\eta_e) \mathcal{J}_2 \frac{\partial^2 \mathcal{H}^{DQ}}{\partial \phi_s^{DQ}} (\mathcal{R}(\eta_e) \phi_{s,e}^{dq}, \mathcal{R}(\eta_e) \phi_{r,e}^{dq})$
	$+ \mathcal{R}^T(\eta_e) \frac{\partial^2 \mathcal{H}^{DQ}}{\partial \phi_s^{DQ^2}} (\mathcal{R}(\eta_e) \phi_{s,e}^{dq}, \mathcal{R}(\eta_e) \phi_{r,e}^{dq}) \mathcal{J}_2 \mathcal{R}(\eta_e) \phi_{s,e}^{dq}$
$\Delta l_s^{dq} := 0$	$+ \mathcal{R}^T(\eta_e) \frac{\partial^2 \mathcal{H}^{DQ}}{\partial \phi_s^{DQ} \partial \phi_r^{DQ}} (\mathcal{R}(\eta_e) \phi_{s,e}^{dq}, \mathcal{R}(\eta_e) \phi_{r,e}^{dq}) \mathcal{J}_2 \mathcal{R}(\eta_e) \phi_{r,e}^{dq}$
$\Delta l_r^{dq} := 0$	$\Delta l_r^{dq} := -\mathcal{R}^T(\eta_e) \mathcal{J}_2 \frac{\partial^2 \mathcal{H}^{DQ}}{\partial \phi_r^{DQ}} (\mathcal{R}(\eta_e) \phi_{s,e}^{dq}, \mathcal{R}(\eta_e) \phi_{r,e}^{dq})$
	$+ \mathcal{R}^T(\eta_e) \frac{\partial^2 \mathcal{H}^{DQ}}{\partial \phi_r^{DQ} \partial \phi_s^{DQ}} (\mathcal{R}(\eta_e) \phi_{s,e}^{dq}, \mathcal{R}(\eta_e) \phi_{r,e}^{dq}) \mathcal{J}_2 \mathcal{R}(\eta_e) \phi_{s,e}^{dq}$
	$+ \mathcal{R}^T(\eta_e) \frac{\partial^2 \mathcal{H}^{DQ}}{\partial \phi_r^{DQ^2}} (\mathcal{R}(\eta_e) \phi_{s,e}^{dq}, \mathcal{R}(\eta_e) \phi_{r,e}^{dq}) \mathcal{J}_2 \mathcal{R}(\eta_e) \phi_{r,e}^{dq}$
$\frac{\partial^2 \mathcal{H}^{dq}}{\partial \phi_s^{dq^2}} = \frac{\partial^2 \mathcal{H}^{DQ}}{\partial \phi_s^{DQ^2}} (\phi_{s,e}^{dq}, \phi_{r,e}^{dq})$	$\frac{\partial^2 \mathcal{H}^{dq}}{\partial \phi_s^{dq^2}} = \mathcal{R}^T(\eta_e) \frac{\partial^2 \mathcal{H}^{DQ}}{\partial \phi_s^{DQ^2}} (\mathcal{R}(\eta_e) \phi_{s,e}^{dq}, \mathcal{R}(\eta_e) \phi_{r,e}^{dq}) \mathcal{R}(\eta_e)$
$\frac{\partial^2 \mathcal{H}^{dq}}{\partial \phi_r^{dq} \partial \phi_s^{dq}} = \frac{\partial^2 \mathcal{H}^{DQ}}{\partial \phi_r^{DQ} \partial \phi_s^{DQ}} (\phi_{s,e}^{dq}, \phi_{r,e}^{dq})$	$\frac{\partial^2 \mathcal{H}^{dq}}{\partial \phi_r^{dq} \partial \phi_s^{dq}} = \mathcal{R}^T(\eta_e) \frac{\partial^2 \mathcal{H}^{DQ}}{\partial \phi_r^{DQ} \partial \phi_s^{DQ}} (\mathcal{R}(\eta_e) \phi_{s,e}^{dq}, \mathcal{R}(\eta_e) \phi_{r,e}^{dq}) \mathcal{R}(\eta_e)$
$\frac{\partial^2 \mathcal{H}^{dq}}{\partial \phi_s^{dq} \partial \phi_r^{dq}} = \frac{\partial^2 \mathcal{H}^{DQ}}{\partial \phi_s^{DQ} \partial \phi_r^{DQ}} (\phi_{s,e}^{dq}, \phi_{r,e}^{dq})$	$\frac{\partial^2 \mathcal{H}^{dq}}{\partial \phi_s^{dq} \partial \phi_r^{dq}} = \mathcal{R}^T(\eta_e) \frac{\partial^2 \mathcal{H}^{DQ}}{\partial \phi_s^{DQ} \partial \phi_r^{DQ}} (\mathcal{R}(\eta_e) \phi_{s,e}^{dq}, \mathcal{R}(\eta_e) \phi_{r,e}^{dq}) \mathcal{R}(\eta_e)$
$\frac{\partial^2 \mathcal{H}^{dq}}{\partial \phi_r^{dq^2}} = \frac{\partial^2 \mathcal{H}^{DQ}}{\partial \phi_r^{DQ^2}} (\phi_{s,e}^{dq}, \phi_{r,e}^{dq})$	$\frac{\partial^2 \mathcal{H}^{dq}}{\partial \phi_r^{dq^2}} = \mathcal{R}^T(\eta_e) \frac{\partial^2 \mathcal{H}^{DQ}}{\partial \phi_r^{DQ^2}} (\mathcal{R}(\eta_e) \phi_{s,e}^{dq}, \mathcal{R}(\eta_e) \phi_{r,e}^{dq}) \mathcal{R}(\eta_e)$

Table 4.1 – Matrix parameters aggregates defined to unify the salient and non-salient cases.

where the dependencies of the matrix partial derivatives of the energy function on the fluxes  $\mathcal{R}(\eta_e) \phi_{s,e}^{dq}$  and  $\mathcal{R}(\eta_e) \phi_{r,e}^{dq}$  are hidden as they are constants since  $\frac{d\eta_e}{dt} = \omega_{s,e} - \omega_e = 0$  for salient electric motors (see section 3.8.1.1).

**Unification** Both eqs. (4.12) and (4.13) can be conveyed under the following form

$$\delta l_s^{dq} = \Delta l_s^{dq} \delta \eta + \frac{\partial^2 \mathcal{H}^{dq}}{\partial \phi_s^{dq^2}} \delta \phi_s^{dq} + \frac{\partial^2 \mathcal{H}^{dq}}{\partial \phi_s^{dq} \partial \phi_r^{dq}} \delta \phi_r^{dq} \quad (4.14a)$$

$$\delta l_r^{dq} = \Delta l_r^{dq} \delta \eta + \frac{\partial^2 \mathcal{H}^{dq}}{\partial \phi_r^{dq} \partial \phi_s^{dq}} \delta \phi_s^{dq} + \frac{\partial^2 \mathcal{H}^{dq}}{\partial \phi_r^{dq^2}} \delta \phi_r^{dq} \quad (4.14b)$$

where the variables aggregates are defined appropriately, see table 4.1.

The linearized system can be written in the standard form for linear systems as

$$\frac{d\delta X}{dt} = A\delta X + B\delta U \quad (4.15a)$$

$$\delta Y = C\delta X \quad (4.15b)$$

with  $\delta X = (\delta \phi_s^{dq}, \delta \phi_r^{dq}, \delta \omega, \delta \eta, \delta T_L)^T$ ,  $\delta U = \delta u_s^{dq}$ ,  $\delta Y = \delta l_s^{dq}$  and

$$A := \begin{pmatrix} -R_s \frac{\partial^2 \mathcal{H}^{dq}}{\partial \phi_s^{dq^2}} - \mathcal{J}_2 \omega_{s,e} & -R_s \frac{\partial^2 \mathcal{H}^{dq}}{\partial \phi_s^{dq} \partial \phi_r^{dq}} & 0_{2,1} & -R_s \Delta l_s^{dq} & 0_{2,1} \\ -R_r \frac{\partial^2 \mathcal{H}^{dq}}{\partial \phi_r^{dq} \partial \phi_s^{dq}} & -R_r \frac{\partial^2 \mathcal{H}^{dq}}{\partial \phi_r^{dq^2}} - \mathcal{J}_2 \omega_{g,e} & \mathcal{J}_2 \phi_{r,e}^{dq} & -R_r \Delta l_r^{dq} & 0_{2,1} \\ \frac{n^2}{J_L} \phi_{s,e}^{dq} \mathcal{J}_2 - \frac{n^2}{J_L} \phi_{s,e}^{dq} \mathcal{J}_2 \frac{\partial^2 \mathcal{H}^{dq}}{\partial \phi_s^{dq^2}} & -\frac{n^2}{J_L} \phi_{s,e}^{dq} \mathcal{J}_2 \frac{\partial^2 \mathcal{H}^{dq}}{\partial \phi_s^{dq} \partial \phi_r^{dq}} & 0 & \frac{n^2}{J_L} \phi_{s,e}^{dq} \mathcal{J}_2 \Delta l_s^{dq} & -\frac{n}{J_L} \\ 0_{1,2} & 0_{1,2} & -1 & 0 & 0 \\ 0_{1,2} & 0_{1,2} & 0 & 0 & 0 \end{pmatrix}$$

$$B := \begin{pmatrix} I_2 & 0_{2,2} & 0_{2,1} & 0_{2,1} & 0_{2,1} \end{pmatrix}^T \quad C := \begin{pmatrix} \frac{\partial^2 \mathcal{H}^{dq}}{\partial \phi_s^{dq^2}} & \frac{\partial^2 \mathcal{H}^{dq}}{\partial \phi_s^{dq} \partial \phi_r^{dq}} & 0_{2,1} & \Delta \iota_s^{dq} & 0_{2,1} \end{pmatrix}.$$

#### 4.1.4.2 Linear observability study

The Kalman criterion could be used but it leads to very tedious computations in this general case. Indeed, it implies computing the rank of an 7x7 matrix. We will thus chose an alternative approach relying on the definition of first-order observability: A system is observable on a permanent trajectory when all the linearized state variables can be expressed as linear combinations of the linearized inputs, the linearized outputs and their derivatives. We are thus going to compute the derivatives of the linearized measurement  $\delta \iota_s^{dq}$  and we will then show that the linearized state variables can be expressed as a linear combination of these variables. This method is strictly equivalent to Kalman criterion, so we will have the rank of a 7x7 matrix to compute, however simplifications are more easily handled. To simplify even further the notations we will use the notation  $LC(\dots)$  for any linear combination of its arguments.

First of all we have

$$\delta \iota_s^{dq} = \Delta \iota_s^{dq} \delta \eta + \frac{\partial^2 \mathcal{H}^{dq}}{\partial \phi_s^{dq^2}} \delta \phi_s^{dq} + \frac{\partial^2 \mathcal{H}^{dq}}{\partial \phi_s^{dq} \partial \phi_r^{dq}} \delta \phi_r^{dq}. \quad (4.16)$$

The first time-derivative of the linearized measurement  $\delta \iota_s^{dq}$  reads

$$\begin{aligned} \frac{d\delta \iota_s^{dq}}{dt} &= \Delta \iota_s^{dq} \frac{d\eta}{dt} + \frac{\partial^2 \mathcal{H}^{dq}}{\partial \phi_s^{dq^2}} \frac{d\delta \phi_s^{dq}}{dt} + \frac{\partial^2 \mathcal{H}^{dq}}{\partial \phi_s^{dq} \partial \phi_r^{dq}} \frac{d\delta \phi_r^{dq}}{dt} \\ &= - \left( R_r \frac{\partial^2 \mathcal{H}^{dq}}{\partial \phi_s^{dq} \partial \phi_r^{dq}} \frac{\partial^2 \mathcal{H}^{dq}}{\partial \phi_r^{dq} \partial \phi_s^{dq}} + \frac{\partial^2 \mathcal{H}^{dq}}{\partial \phi_s^{dq^2}} \mathcal{J}_2 \omega_{s,e} \right) \delta \phi_s^{dq} \\ &\quad - \frac{\partial^2 \mathcal{H}^{dq}}{\partial \phi_s^{dq} \partial \phi_r^{dq}} \left( R_r \frac{\partial^2 \mathcal{H}^{dq}}{\partial \phi_r^{dq^2}} + \mathcal{J}_2 \omega_{g,e} \right) \delta \phi_r^{dq} \\ &\quad - R_r \frac{\partial^2 \mathcal{H}^{dq}}{\partial \phi_s^{dq} \partial \phi_r^{dq}} \Delta \iota_r^{dq} \delta \eta + \left( \frac{\partial^2 \mathcal{H}^{dq}}{\partial \phi_s^{dq} \partial \phi_r^{dq}} \mathcal{J}_2 \phi_{r,e}^{dq} - \Delta \iota_s^{dq} \right) \delta \omega + LC(\delta u_s^{dq}, \delta \iota_s^{dq}). \end{aligned} \quad (4.17)$$

When there are rotor windings, we define the matrices

$$\Omega_r = R_r \frac{\partial^2 \mathcal{H}^{dq}}{\partial \phi_r^{dq} \partial \phi_s^{dq}} - R_r \frac{\partial^2 \mathcal{H}^{dq}}{\partial \phi_r^{dq^2}} \left( \frac{\partial^2 \mathcal{H}^{dq}}{\partial \phi_s^{dq} \partial \phi_r^{dq}} \right)^{-1} \frac{\partial^2 \mathcal{H}^{dq}}{\partial \phi_s^{dq^2}} \quad (4.18a)$$

$$X_r = \frac{\partial^2 \mathcal{H}^{dq}}{\partial \phi_s^{dq} \partial \phi_r^{dq}} \mathcal{J}_2 \left( \frac{\partial^2 \mathcal{H}^{dq}}{\partial \phi_s^{dq} \partial \phi_r^{dq}} \right)^{-1} \quad (4.18b)$$

which are not properly defined when there are no rotor windings. However when there are no rotor windings, the energy and thus the measurements do not depend on  $\delta \phi_r^{dq}$ . We can thus take them to be zero in this case. Using these notations we find

$$\begin{aligned} \frac{d\delta \iota_s^{dq}}{dt} &= \frac{\partial^2 \mathcal{H}^{dq}}{\partial \phi_s^{dq} \partial \phi_r^{dq}} \left( \Omega_r - R_r \frac{\partial^2 \mathcal{H}^{dq}}{\partial \phi_r^{dq} \partial \phi_s^{dq}} \right) \left( \frac{\partial^2 \mathcal{H}^{dq}}{\partial \phi_s^{dq^2}} \right)^{-1} \delta \iota_s^{dq} + X_r \omega_{g,e} \delta \iota_s^{dq} \\ &= -M_1 \delta \phi_s^{dq} - v_2 \delta \eta + v_3 \delta \omega + LC(\delta u_s^{dq}, \delta \iota_s^{dq}). \end{aligned} \quad (4.19)$$

where the following matrices were used

$$\begin{aligned}
M_1 &:= \frac{\partial^2 \mathcal{H}^{dq}}{\partial \phi_s^{dq} \partial \phi_r^{dq}} \Omega_r + \frac{\partial^2 \mathcal{H}^{dq}}{\partial \phi_s^{dq2}} \mathcal{J}_2 \omega_{s,e} - X_r \frac{\partial^2 \mathcal{H}^{dq}}{\partial \phi_s^{dq2}} \omega_{g,e} \\
v_2 &:= \frac{\partial^2 \mathcal{H}^{dq}}{\partial \phi_s^{dq} \partial \phi_r^{dq}} \left( \Omega_r - R_r \frac{\partial^2 \mathcal{H}^{dq}}{\partial \phi_r^{dq} \partial \phi_s^{dq}} \right) \left( \frac{\partial^2 \mathcal{H}^{dq}}{\partial \phi_s^{dq2}} \right)^{-1} \Delta \iota_s^{dq} - X_r \omega_{g,e} \Delta \iota_s^{dq} + R_r \frac{\partial^2 \mathcal{H}^{dq}}{\partial \phi_s^{dq} \partial \phi_r^{dq}} \Delta \iota_r^{dq} \\
v_3 &:= \frac{\partial^2 \mathcal{H}^{dq}}{\partial \phi_s^{dq} \partial \phi_r^{dq}} \mathcal{J}_2 \phi_{r,e}^{dq} - \Delta \iota_s^{dq}.
\end{aligned}$$

Differentiating the previous expression with respect to time we find

$$\begin{aligned}
&\frac{d^2 \delta \iota_s^{dq}}{dt^2} - \frac{\partial^2 \mathcal{H}^{dq}}{\partial \phi_s^{dq} \partial \phi_r^{dq}} \left( \Omega_r - R_r \frac{\partial^2 \mathcal{H}^{dq}}{\partial \phi_r^{dq} \partial \phi_s^{dq}} \right) \left( \frac{\partial^2 \mathcal{H}^{dq}}{\partial \phi_s^{dq2}} \right)^{-1} \frac{d \delta \iota_s^{dq}}{dt} + X_r \omega_{g,e} \frac{d \delta \iota_s^{dq}}{dt} \\
&= M_1 \mathcal{J}_2 \omega_{s,e} \delta \phi_s^{dq} + v_2 \delta \omega + v_3 \frac{d \delta \omega}{dt} + LC(\delta u_s^{dq}, \delta \iota_s^{dq}, \delta \dot{u}_s^{dq}, \delta \dot{\iota}_s^{dq}). \tag{4.20}
\end{aligned}$$

$$\begin{aligned}
&\frac{d^3 \delta \iota_s^{dq}}{dt^3} - \frac{\partial^2 \mathcal{H}^{dq}}{\partial \phi_s^{dq} \partial \phi_r^{dq}} \left( \Omega_r - R_r \frac{\partial^2 \mathcal{H}^{dq}}{\partial \phi_r^{dq} \partial \phi_s^{dq}} \right) \left( \frac{\partial^2 \mathcal{H}^{dq}}{\partial \phi_s^{dq2}} \right)^{-1} \frac{d^2 \delta \iota_s^{dq}}{dt^2} + X_r \omega_{g,e} \frac{d^2 \delta \iota_s^{dq}}{dt^2} \\
&= M_1 (\omega_{s,e})^2 \delta \phi_s^{dq} + v_2 \frac{d \delta \omega}{dt} + v_3 \frac{d^2 \delta \omega}{dt^2} + LC(\delta u_s^{dq}, \delta \iota_s^{dq}, \delta \dot{u}_s^{dq}, \delta \dot{\iota}_s^{dq}). \tag{4.21}
\end{aligned}$$

From eq. (4.10c) and eq. (4.11) we have

$$\frac{d \delta \omega}{dt} = \frac{n^2}{J_L} \iota_{s,e}^{dq T} \mathcal{J}_2 \delta \phi_s^{dq} - \frac{n}{J_L} \delta T_L - LC(\delta \iota_s^{dq}) \tag{4.22}$$

and consequently  $\forall i \geq 2$

$$\frac{d^i \delta \omega}{dt^i} = \frac{n^2}{J_L} \omega_{s,e}^{i-1} \iota_{s,e}^{dq T} \mathcal{J}_2^i \delta \phi_s^{dq} - LC(\delta u_s^{dq}, \delta \iota_s^{dq}, \dots, \delta u_s^{dq(i-2)}, \delta \iota_s^{dq(i-2)}, \delta \iota_s^{dq(i-1)}) \tag{4.23}$$

which is a linear combination of the inputs, the outputs and their derivatives when  $\omega_{s,e} = 0$ .

Before concluding we should discuss the invertibility of the matrix  $M_1$ . When there are no rotor windings, this is trivial as it boils down to the Hessian of the energy function multiplied by  $\mathcal{J}_2$ . However when there are rotor windings, this is more complicated and we must suppose that we are not far from the unsaturated case where this matrix has the form  $aI_2 + b\mathcal{J}_2$  which is always invertible as a matrix of rotation. Thus  $M_1$  will be supposed invertible as it is close to a rotation matrix. Moreover  $\forall x \in \mathbb{R}^2 \quad \det(M_1 \mathcal{J}_2 M_1^{-1} x, x) \neq 0$  as  $M_1 \mathcal{J}_2 M_1^{-1}$  is close to the rotation of angle  $\frac{\pi}{2}$  ( $\mathcal{J}_2$ ).

**Rotor windings and saliency** When there are rotor windings and a saliency, the state of the motor is of dimension 7. Yet when  $\omega_{s,e} = 0$ , it can be seen from eqs. (4.16) and (4.19) to (4.23) that the observability matrix has the same rank as

$$\begin{pmatrix}
\frac{\partial^2 \mathcal{H}^{dq}}{\partial \phi_s^{dq2}} & \frac{\partial^2 \mathcal{H}^{dq}}{\partial \phi_s^{dq} \partial \phi_r^{dq}} & 0_{2,1} & \Delta \iota_s^{dq} & 0_{2,1} \\
-M_1 & 0_{2,2} & v_3 & -v_2 & 0_{2,1} \\
\frac{n^2}{J_L} v_3 \iota_{s,e}^{dq T} \mathcal{J}_2 & 0_{2,2} & v_2 & 0_{2,1} & -\frac{n}{J_L} v_3 \\
\frac{n^2}{J_L} v_2 \iota_{s,e}^{dq T} \mathcal{J}_2 & 0_{2,2} & 0_{2,1} & 0_{2,1} & -\frac{n}{J_L} v_2
\end{pmatrix}.$$

The first four lines of this matrix are admittedly of rank 4 as  $\frac{\partial^2 \mathcal{H}^{dq}}{\partial \phi_s^{dq^2}}$  and  $M_1$  are invertible, but the last four lines have only 2 independent columns and thus is of rank 2. The total rank of the observability matrix can thus not exceed 6. Moreover further derivations do not give more information. Hence the state of the electric motor is not observable. We can only recover  $\frac{d\delta\omega}{dt}$  from  $\frac{d^3\delta i_s^{dq}}{dt^3}$ . When  $\omega_{s,e} \neq 0$ , we can show from from eqs. (4.16) and (4.19) to (4.23) that the observability matrix has the same rank as

$$\begin{pmatrix} \frac{\partial^2 \mathcal{H}^{dq}}{\partial \phi_s^{dq^2}} & \frac{\partial^2 \mathcal{H}^{dq}}{\partial \phi_s^{dq} \partial \phi_r^{dq}} & 0_{2,1} & \Delta i_s^{dq} & 0_{2,1} \\ -M_1 & 0_{2,2} & v_3 & -v_2 & 0_{2,1} \\ \frac{n^2}{J_L} v_3 i_{s,e}^{dq T} \mathcal{J}_2 & 0_{2,2} & v_2 + M_1 \mathcal{J}_2 M_1^{-1} v_3 \omega_{s,e} & -M_1 \mathcal{J}_2 M_1^{-1} v_2 \omega_{s,e} & -\frac{n}{J_L} v_3 \\ \frac{n^2}{J_L} v_2 i_{s,e}^{dq T} \mathcal{J}_2 & 0_{2,2} & v_3 & -v_2 & -\frac{n}{J_L} v_2 \end{pmatrix}$$

thus, if  $v_2$  and  $v_3$  are independent vectors, the system is observable as the observability matrix is of rank 7.

**Rotor windings without saliency** When there is no rotor saliency the state of the motor can be reduced to dimension 6 by removing  $\eta$ . However  $v_2$  is zero and it can be seen from eqs. (4.16), (4.19), (4.20), (4.22) and (4.23) that the observability matrix has the same rank as

$$\begin{pmatrix} \frac{\partial^2 \mathcal{H}^{dq}}{\partial \phi_s^{dq^2}} & \frac{\partial^2 \mathcal{H}^{dq}}{\partial \phi_s^{dq} \partial \phi_r^{dq}} & 0_{2,1} & 0_{2,1} & 0_{2,1} \\ -M_1 & 0_{2,2} & v_3 & 0_{2,1} & 0_{2,1} \\ \frac{n^2}{J_L} v_3 i_{s,e}^{dq T} \mathcal{J}_2 & 0_{2,2} & 0_{2,1} & 0_{2,1} & -\frac{n}{J_L} v_3 \end{pmatrix}.$$

whose last 2 lines are collinear. Further derivations do not give more information. The rank of the observability matrix is thus bounded by 5. Hence the system is not observable. Again we can only recover  $\frac{d\delta\omega}{dt}$  from  $\frac{d^2\delta i_s^{dq}}{dt^2}$ . When  $\omega_{s,e} \neq 0$ , the observability matrix has the same rank as

$$\begin{pmatrix} \frac{\partial^2 \mathcal{H}^{dq}}{\partial \phi_s^{dq^2}} & \frac{\partial^2 \mathcal{H}^{dq}}{\partial \phi_s^{dq} \partial \phi_r^{dq}} & 0_{2,1} & 0_{2,1} \\ -M_1 & 0_{2,2} & v_3 & 0_{2,1} \\ \frac{n^2}{J_L} v_3 i_{s,e}^{dq T} \mathcal{J}_2 & 0_{2,2} & M_1 \mathcal{J}_2 M_1^{-1} v_3 \omega_{s,e} & -\frac{n}{J_L} v_3 \end{pmatrix}$$

where  $M_1 \mathcal{J}_2 M_1^{-1} v_3$  and  $v_3$  are independent. Thus the rank of the observability matrix is 6 and the system is observable.

**Saliency without rotor windings** When there are no rotor windings the state of the motor can be reduced to dimension 5 by removing  $\phi_r^{dq}$ . However  $v_2$  is zero and we find from eqs. (4.16), (4.19), (4.20) and (4.22) that the rank of the observability matrix is

$$\begin{pmatrix} \frac{\partial^2 \mathcal{H}^{dq}}{\partial \phi_s^{dq^2}} & 0_{2,1} & \Delta i_s^{dq} & 0_{2,1} \\ 0_{2,2} & v_3 & 0_{2,1} & 0_{2,1} \\ \frac{n^2}{J_L} v_3 i_{s,e}^{dq T} \mathcal{J}_2 & 0_{2,1} & 0_{2,1} & -\frac{n}{J_L} v_3 \end{pmatrix}$$

whose last four lines have only two independent columns. The total rank of this matrix cannot exceed 4 and further derivations do not give more information. Hence the system is not observable. We can only recover  $\frac{d\delta\omega}{dt}$  from  $\frac{d^2\delta i_s^{dq}}{dt^2}$ . When  $\omega_{s,e} \neq 0$ , the observability

matrix has the same rank as

$$\begin{pmatrix} \frac{\partial^2 \mathcal{H}^{dq}}{\partial \phi_s^{dq^2}} & 0_{2,1} & \Delta \iota_s^{dq} & 0_{2,1} \\ -\frac{\partial^2 \mathcal{H}^{dq}}{\partial \phi_s^{dq^2}} \mathcal{J}_2 \omega_{s,e} & -\Delta \iota_s^{dq} & 0_{2,1} & 0_{2,1} \\ -\frac{n^2}{J_L} \Delta \iota_s^{dq} \iota_{s,e}^{dq T} \mathcal{J}_2 & -\frac{\partial^2 \mathcal{H}^{dq}}{\partial \phi_s^{dq^2}} \mathcal{J}_2 \omega_{s,e} \left( \frac{\partial^2 \mathcal{H}^{dq}}{\partial \phi_s^{dq^2}} \right)^{-1} \Delta \iota_s^{dq} & 0_{2,1} & \frac{n}{J_L} \Delta \iota_s^{dq} \end{pmatrix}.$$

As the last two lines are independent with any other lines and as  $\frac{\partial^2 \mathcal{H}^{dq}}{\partial \phi_s^{dq^2}} \mathcal{J}_2 \left( \frac{\partial^2 \mathcal{H}^{dq}}{\partial \phi_s^{dq^2}} \right)^{-1} \Delta \iota_s^{dq}$  and  $\Delta \iota_s^{dq}$  are not collinear, this matrix is of rank 5. Hence the state of the system is observable.

#### 4.1.4.3 Conclusion on linear observability

With this generic approach we showed that

- All sinusoidal electric motors are unobservable on permanent trajectories where  $\omega_{s,e} = 0$ . In all the cases, only the acceleration can be recovered from the measurements;
- On permanent trajectories where  $\omega_{s,e} \neq 0$ , the electric motors are observable.

Furthermore, the position cannot be retrieved when the rotor is non-salient (IM), since it can be decoupled from the state.

#### 4.1.5 Nonlinear observability

In section 4.1.4 we showed that all electric motors are unobservable on permanent trajectories where  $\omega_{s,e} = 0$  which means that “sensorless” control of electric motors around these trajectories is inherently difficult. Still we would like to design a “sensorless” observer which works near such trajectories, because it is interesting from an industrial point of view, as explained in section 1.2.5. We are thus going to consider trajectories which are close to the permanent trajectory but on which the IM is observable thanks to the stator currents measurement (see fig. 4.2 for an example of such a trajectory). To investigate the observability of the electric motors, we must use nonlinear observability. This approach was deployed for the saturated sinusoidal PMSM in Jebai [37] and we are going to apply it here to the IM. The study will be done in the synchronous  $dq$  frame rotating at  $\omega_{s,e}$ .

As in the generic case of section 4.1.4 the state of the IM is  $X := (\phi_s^{dq T}, \phi_r^{dq T}, \omega, T_L)^T$ , the input is  $U := (u_s^{dq T}, 0_{1,2}, T_L, 0)^T$  and the measurement  $Y := \iota_s^{dq}$ . The system can be written as

$$\frac{dX}{dt} = A(X) + U \quad (4.24a)$$

$$Y = C(X) \quad (4.24b)$$

where the vector fields  $A$  and  $C$  are defined by

$$A : X \in \mathbb{R}^6 \mapsto \begin{pmatrix} -R_s \iota_s^{dq}(\phi_s^{dq}, \phi_r^{dq}) - \mathcal{J}_2 \omega_{s,e} \phi_s^{dq} \\ -R_r \iota_r^{dq}(\phi_s^{dq}, \phi_r^{dq}) - \mathcal{J}_2 (\omega_{s,e} - \omega) \phi_r^{dq} \\ \frac{n}{J_L} (T_e(\phi_s^{dq}, \phi_r^{dq}) - T_L) \\ 0 \end{pmatrix} \in \mathbb{R}^6 \quad (4.25a)$$

$$C : X \in \mathbb{R}^6 \mapsto \iota_s^{dq}(\phi_s^{dq}, \phi_r^{dq}) \in \mathbb{R}^2. \quad (4.25b)$$

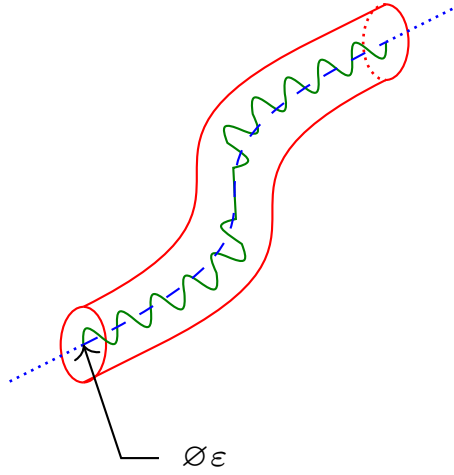


Figure 4.2 – The **desired permanent trajectory** where the IM is unobservable and an example of a **close trajectory** on which the motor may be observable.

For nonlinear observability, there exists a criterion similar to Kalman criterion: The matrix constituted by the 0th, 1st, ... Lie derivatives of the measurement along the flow of the system must be full rank. We now compute these Lie derivatives.

The zeroth Lie derivative of  $C$  along the flow of  $A$  is

$$\mathcal{L}_A^0 C = \begin{pmatrix} \frac{\partial^2 \mathcal{H}^{dq}}{\partial \phi_s^{dq^2}} & \frac{\partial^2 \mathcal{H}^{dq}}{\partial \phi_s^{dq} \partial \phi_r^{dq}} & 0_{2,2} \end{pmatrix}. \quad (4.26)$$

Then we have

$$\begin{aligned} \frac{d\iota_s^{dq}}{dt} &= \frac{\partial^2 \mathcal{H}^{dq}}{\partial \phi_s^{dq^2}} \frac{d\phi_s^{dq}}{dt} + \frac{\partial^2 \mathcal{H}^{dq}}{\partial \phi_s^{dq} \partial \phi_r^{dq}} \frac{d\phi_r^{dq}}{dt} \\ &= \frac{\partial^2 \mathcal{H}^{dq}}{\partial \phi_s^{dq^2}} (u_s^{dq} - R_s \iota_s^{dq} - \mathcal{J}_2 \omega_{s,e} \phi_s^{dq}) + \frac{\partial^2 \mathcal{H}^{dq}}{\partial \phi_s^{dq} \partial \phi_r^{dq}} (-R_r \iota_r - \mathcal{J}_2 (\omega_{s,e} - \omega) \phi_r^{dq}) \end{aligned}$$

and the first Lie derivative of  $C$  along the flow of  $A$  is

$$\mathcal{L}_A^1 C = \begin{pmatrix} \frac{\partial}{\partial \phi_s^{dq}} \frac{d\iota_s^{dq}}{dt} & \frac{\partial}{\partial \phi_r^{dq}} \frac{d\iota_s^{dq}}{dt} & \frac{\partial}{\partial \omega} \frac{d\iota_s^{dq}}{dt} & 0_{2,1} \end{pmatrix} \quad (4.27)$$

with

$$\begin{aligned} \frac{\partial}{\partial \phi_s^{dq}} \frac{d\iota_s^{dq}}{dt} &\sim -\frac{\partial^2 \mathcal{H}^{dq}}{\partial \phi_s^{dq^2}} \mathcal{J}_2 \omega_{s,e} - R_r \frac{\partial^2 \mathcal{H}^{dq}}{\partial \phi_s^{dq} \partial \phi_r^{dq}} \frac{\partial^2 \mathcal{H}^{dq}}{\partial \phi_r^{dq} \partial \phi_s^{dq}} \\ &\quad + \frac{\partial}{\partial \phi_s^{dq}} \left( \frac{\partial^2 \mathcal{H}^{dq}}{\partial \phi_s^{dq^2}} \frac{d\phi_s^{dq}}{dt} + \frac{\partial^2 \mathcal{H}^{dq}}{\partial \phi_s^{dq} \partial \phi_r^{dq}} \frac{d\phi_r^{dq}}{dt} \right) \\ \frac{\partial}{\partial \phi_r^{dq}} \frac{d\iota_s^{dq}}{dt} &\sim \frac{\partial^2 \mathcal{H}^{dq}}{\partial \phi_s^{dq} \partial \phi_r^{dq}} \left( -R_r \frac{\partial^2 \mathcal{H}^{dq}}{\partial \phi_r^{dq^2}} - \mathcal{J}_2 (\omega_{s,e} - \omega) \right) \\ &\quad + \frac{\partial}{\partial \phi_r^{dq}} \left( \frac{\partial^2 \mathcal{H}^{dq}}{\partial \phi_s^{dq^2}} \frac{d\phi_s^{dq}}{dt} + \frac{\partial^2 \mathcal{H}^{dq}}{\partial \phi_s^{dq} \partial \phi_r^{dq}} \frac{d\phi_r^{dq}}{dt} \right) \\ \frac{\partial}{\partial \omega} \frac{d\iota_s^{dq}}{dt} &= \frac{\partial^2 \mathcal{H}^{dq}}{\partial \phi_s^{dq} \partial \phi_r^{dq}} \mathcal{J}_2 \phi_r^{dq}. \end{aligned}$$

where  $\sim$  means equality up to a matrix combination of the previous lines of the Lie derivative matrix and where we used notations similar to  $\frac{\partial}{\partial \phi_s} \left( \frac{\partial^2 \mathcal{H}^{dq}}{\partial \phi_s^{dq^2}} \frac{d\phi_s^{dq}}{dt} \right)$  to mean partial derivatives are taken only from the matrix  $\frac{\partial^2 \mathcal{H}^{dq}}{\partial \phi_s^{dq^2}}$  and not from the vector  $\frac{d\phi_s^{dq}}{dt}$ .

The second time-derivative of the measurements is given by

$$\begin{aligned}
\frac{d^2 \iota_s^{dq}}{dt^2} &= \frac{\partial^2 \mathcal{H}^{dq}}{\partial \phi_s^{dq^2}} \frac{d u_s^{dq}}{dt} - R_s \frac{\partial^2 \mathcal{H}^{dq}}{\partial \phi_s^{dq^2}} \frac{d \iota_s^{dq}}{dt} - \frac{\partial^2 \mathcal{H}^{dq}}{\partial \phi_s^{dq^2}} \mathcal{J}_2 \omega_{s,e} \frac{d \phi_s^{dq}}{dt} - R_r \frac{\partial^2 \mathcal{H}^{dq}}{\partial \phi_s^{dq} \partial \phi_r^{dq}} \frac{\partial^2 \mathcal{H}^{dq}}{\partial \phi_r^{dq} \partial \phi_s^{dq}} \frac{d \phi_s^{dq}}{dt} \\
&+ \frac{\partial^2 \mathcal{H}^{dq}}{\partial \phi_s^{dq} \partial \phi_r^{dq}} \left( -R_r \frac{\partial^2 \mathcal{H}^{dq}}{\partial \phi_r^{dq^2}} - \mathcal{J}_2(\omega_{s,e} - \omega) \right) \frac{d \phi_r^{dq}}{dt} + \frac{\partial^2 \mathcal{H}^{dq}}{\partial \phi_s^{dq} \partial \phi_r^{dq}} \mathcal{J}_2 \phi_r^{dq} \frac{d \omega}{dt} \\
&+ \frac{\partial}{\partial \phi_s^{dq}} \left( \frac{\partial^2 \mathcal{H}^{dq}}{\partial \phi_s^{dq^2}} \frac{d \phi_s^{dq}}{dt} + \frac{\partial^2 \mathcal{H}^{dq}}{\partial \phi_s^{dq} \partial \phi_r^{dq}} \frac{d \phi_r^{dq}}{dt} \right) \frac{d \phi_s^{dq}}{dt} \\
&+ \frac{\partial}{\partial \phi_r^{dq}} \left( \frac{\partial^2 \mathcal{H}^{dq}}{\partial \phi_s^{dq^2}} \frac{d \phi_s^{dq}}{dt} + \frac{\partial^2 \mathcal{H}^{dq}}{\partial \phi_s^{dq} \partial \phi_r^{dq}} \frac{d \phi_r^{dq}}{dt} \right) \frac{d \phi_r^{dq}}{dt} \\
&= \frac{\partial^2 \mathcal{H}^{dq}}{\partial \phi_s^{dq^2}} \frac{d u_s^{dq}}{dt} - R_s \frac{\partial^2 \mathcal{H}^{dq}}{\partial \phi_s^{dq^2}} \frac{d \iota_s^{dq}}{dt} \\
&- \left( \frac{\partial^2 \mathcal{H}^{dq}}{\partial \phi_s^{dq^2}} \mathcal{J}_2 \omega_{s,e} + R_r \frac{\partial^2 \mathcal{H}^{dq}}{\partial \phi_s^{dq} \partial \phi_r^{dq}} \frac{\partial^2 \mathcal{H}^{dq}}{\partial \phi_r^{dq} \partial \phi_s^{dq}} \right) (u_s^{dq} - R_s \iota_s^{dq} - \mathcal{J}_2 \omega_{s,e} \phi_s^{dq}) \\
&+ \frac{\partial^2 \mathcal{H}^{dq}}{\partial \phi_s^{dq} \partial \phi_r^{dq}} \left( -R_r \frac{\partial^2 \mathcal{H}^{dq}}{\partial \phi_r^{dq^2}} - \mathcal{J}_2(\omega_{s,e} - \omega) \right) (-R_r \iota_r^{dq} - \mathcal{J}_2(\omega_{s,e} - \omega) \phi_r^{dq}) \\
&+ \frac{n^2}{J_L} \frac{\partial^2 \mathcal{H}^{dq}}{\partial \phi_s^{dq} \partial \phi_r^{dq}} \mathcal{J}_2 \phi_r^{dq} \iota_s^{dq T} \mathcal{J}_2 \phi_s^{dq} - \frac{n}{J_L} \frac{\partial^2 \mathcal{H}^{dq}}{\partial \phi_s^{dq} \partial \phi_r^{dq}} \mathcal{J}_2 \phi_r^{dq} T_L \\
&+ \frac{\partial}{\partial \phi_s^{dq}} \left( \frac{\partial^2 \mathcal{H}^{dq}}{\partial \phi_s^{dq^2}} \frac{d \phi_s^{dq}}{dt} + \frac{\partial^2 \mathcal{H}^{dq}}{\partial \phi_s^{dq} \partial \phi_r^{dq}} \frac{d \phi_r^{dq}}{dt} \right) (u_s^{dq} - R_s \iota_s^{dq} - \mathcal{J}_2 \omega_{s,e} \phi_s^{dq}) \\
&+ \frac{\partial}{\partial \phi_r^{dq}} \left( \frac{\partial^2 \mathcal{H}^{dq}}{\partial \phi_s^{dq^2}} \frac{d \phi_s^{dq}}{dt} + \frac{\partial^2 \mathcal{H}^{dq}}{\partial \phi_s^{dq} \partial \phi_r^{dq}} \frac{d \phi_r^{dq}}{dt} \right) (-R_r \iota_r^{dq} - \mathcal{J}_2(\omega_{s,e} - \omega) \phi_r^{dq})
\end{aligned}$$

and consequently the second Lie derivative of  $C$  along the flow of  $A$  is

$$\mathcal{L}_A^2 C = \begin{pmatrix} \frac{\partial}{\partial \phi_s^{dq}} \frac{d^2 \iota_s^{dq}}{dt^2} & \frac{\partial}{\partial \phi_r^{dq}} \frac{d^2 \iota_s^{dq}}{dt^2} & \frac{\partial}{\partial \omega} \frac{d^2 \iota_s^{dq}}{dt^2} & \frac{\partial}{\partial T_L} \frac{d^2 \iota_s^{dq}}{dt^2} \end{pmatrix}. \quad (4.28)$$

with

$$\begin{aligned}
\frac{\partial}{\partial \phi_s^{dq}} \frac{d^2 \iota_s^{dq}}{dt^2} &\sim -\frac{\partial^2 \mathcal{H}^{dq}}{\partial \phi_s^{dq^2}} \omega_{s,e}^2 + R_r \frac{\partial^2 \mathcal{H}^{dq}}{\partial \phi_s^{dq} \partial \phi_r^{dq}} \frac{\partial^2 \mathcal{H}^{dq}}{\partial \phi_r^{dq} \partial \phi_s^{dq}} \mathcal{J}_2 \omega_{s,e} \\
&- R_r \frac{\partial^2 \mathcal{H}^{dq}}{\partial \phi_s^{dq} \partial \phi_r^{dq}} \left( -R_r \frac{\partial^2 \mathcal{H}^{dq}}{\partial \phi_r^{dq^2}} - \mathcal{J}_2(\omega_{s,e} - \omega) \right) \frac{\partial^2 \mathcal{H}^{dq}}{\partial \phi_r^{dq} \partial \phi_s^{dq}} \\
&+ \frac{n^2}{J_L} \frac{\partial^2 \mathcal{H}^{dq}}{\partial \phi_s^{dq} \partial \phi_r^{dq}} \mathcal{J}_2 \phi_r^{dq} \iota_s^{dq T} \mathcal{J}_2 \\
&+ \text{Terms in } \frac{d \phi_s^{dq}}{dt} \text{ and } \frac{d \phi_r^{dq}}{dt} \text{ we do not need to compute} \\
\frac{\partial}{\partial \phi_r^{dq}} \frac{d^2 \iota_s^{dq}}{dt^2} &\sim \frac{\partial^2 \mathcal{H}^{dq}}{\partial \phi_s^{dq} \partial \phi_r^{dq}} \left( -R_r \frac{\partial^2 \mathcal{H}^{dq}}{\partial \phi_r^{dq^2}} - \mathcal{J}_2(\omega_{s,e} - \omega) \right)^2 + \frac{\partial^2 \mathcal{H}^{dq}}{\partial \phi_s^{dq} \partial \phi_r^{dq}} \mathcal{J}_2 \frac{d \omega}{dt}
\end{aligned}$$

$$\begin{aligned}
& + \text{Terms in } \frac{d\phi_s^{dq}}{dt} \text{ and } \frac{d\phi_r^{dq}}{dt} \text{ we do not need to compute} \\
\frac{\partial}{\partial \omega} \frac{d^2 \iota_s^{dq}}{dt^2} & \sim \frac{\partial^2 \mathcal{H}^{dq}}{\partial \phi_s^{dq} \partial \phi_r^{dq}} \mathcal{J}_2 \frac{d\phi_r^{dq}}{dt} + \frac{\partial^2 \mathcal{H}^{dq}}{\partial \phi_s^{dq} \partial \phi_r^{dq}} \left( -R_r \frac{\partial^2 \mathcal{H}^{dq}}{\partial \phi_r^{dq^2}} - \mathcal{J}_2(\omega_{s,e} - \omega) \right) \mathcal{J}_2 \phi_r^{dq} \\
& + \frac{\partial}{\partial \phi_r^{dq}} \left( \frac{\partial^2 \mathcal{H}^{dq}}{\partial \phi_s^{dq^2}} \frac{d\phi_s^{dq}}{dt} + \frac{\partial^2 \mathcal{H}^{dq}}{\partial \phi_s^{dq} \partial \phi_r^{dq}} \frac{d\phi_r^{dq}}{dt} \right) \mathcal{J}_2 \phi_r^{dq} \\
\frac{\partial}{\partial T_L} \frac{d^2 \iota_s^{dq}}{dt^2} & = -\frac{n}{J_L} \frac{\partial^2 \mathcal{H}^{dq}}{\partial \phi_s^{dq} \partial \phi_r^{dq}} \mathcal{J}_2 \phi_r^{dq}
\end{aligned}$$

where  $\sim$  means equality up to a matrix linear combination of the first four lines of the Lie derivative matrix.

Subtracting  $\frac{\partial^2 \mathcal{H}^{dq}}{\partial \phi_s^{dq} \partial \phi_r^{dq}} \left( -R_r \frac{\partial^2 \mathcal{H}^{dq}}{\partial \phi_r^{dq^2}} - \mathcal{J}_2(\omega_{s,e} - \omega) \right) \left( \frac{\partial^2 \mathcal{H}^{dq}}{\partial \phi_s^{dq} \partial \phi_r^{dq}} \right)^{-1}$  multiplied by the first two lines from the third and fourth lines, we show that

$$\begin{aligned}
\frac{\partial}{\partial \phi_s^{dq}} \frac{d\iota_s^{dq}}{dt} & \sim -\frac{\partial^2 \mathcal{H}^{dq}}{\partial \phi_s^{dq^2}} \mathcal{J}_2 \omega_{s,e} - \frac{\partial^2 \mathcal{H}^{dq}}{\partial \phi_s^{dq} \partial \phi_r^{dq}} \Omega_r + X_r(\omega_{s,e} - \omega) \frac{\partial^2 \mathcal{H}^{dq}}{\partial \phi_s^{dq^2}} \\
& + \frac{\partial}{\partial \phi_s^{dq}} \left( \frac{\partial^2 \mathcal{H}^{dq}}{\partial \phi_s^{dq^2}} \frac{d\phi_s^{dq}}{dt} + \frac{\partial^2 \mathcal{H}^{dq}}{\partial \phi_s^{dq} \partial \phi_r^{dq}} \frac{d\phi_r^{dq}}{dt} \right) \\
\frac{\partial}{\partial \phi_r^{dq}} \frac{d\iota_s^{dq}}{dt} & \sim \frac{\partial}{\partial \phi_r^{dq}} \left( \frac{\partial^2 \mathcal{H}^{dq}}{\partial \phi_s^{dq^2}} \frac{d\phi_s^{dq}}{dt} + \frac{\partial^2 \mathcal{H}^{dq}}{\partial \phi_s^{dq} \partial \phi_r^{dq}} \frac{d\phi_r^{dq}}{dt} \right) \\
\frac{\partial}{\partial \omega} \frac{d\iota_s^{dq}}{dt} & = \frac{\partial^2 \mathcal{H}^{dq}}{\partial \phi_s^{dq} \partial \phi_r^{dq}} \mathcal{J}_2 \phi_r^{dq}.
\end{aligned}$$

where  $\Omega_r$  and  $X_r$  have been defined in the previous section by eqs. (4.18a) and (4.18b).

Subtracting  $\frac{\partial^2 \mathcal{H}^{dq}}{\partial \phi_s^{dq} \partial \phi_r^{dq}} \left( -R_r \frac{\partial^2 \mathcal{H}^{dq}}{\partial \phi_r^{dq^2}} - \mathcal{J}_2(\omega_{s,e} - \omega) \right)^2 \left( \frac{\partial^2 \mathcal{H}^{dq}}{\partial \phi_s^{dq} \partial \phi_r^{dq}} \right)^{-1}$  multiplied by the first two lines from the last two lines, we show that

$$\begin{aligned}
\frac{\partial}{\partial \phi_s^{dq}} \frac{d^2 \iota_s^{dq}}{dt^2} & \sim -\frac{\partial^2 \mathcal{H}^{dq}}{\partial \phi_s^{dq^2}} \omega_{s,e}^2 + R_r \frac{\partial^2 \mathcal{H}^{dq}}{\partial \phi_s^{dq} \partial \phi_r^{dq}} \frac{\partial^2 \mathcal{H}^{dq}}{\partial \phi_r^{dq} \partial \phi_s^{dq}} \mathcal{J}_2 \omega_{s,e} \\
& - \frac{\partial^2 \mathcal{H}^{dq}}{\partial \phi_s^{dq} \partial \phi_r^{dq}} \left( -R_r \frac{\partial^2 \mathcal{H}^{dq}}{\partial \phi_r^{dq^2}} - \mathcal{J}_2(\omega_{s,e} - \omega) \right) \Omega_r \\
& + \frac{\partial^2 \mathcal{H}^{dq}}{\partial \phi_s^{dq} \partial \phi_r^{dq}} \left( -R_r \frac{\partial^2 \mathcal{H}^{dq}}{\partial \phi_r^{dq^2}} - \mathcal{J}_2(\omega_{s,e} - \omega) \right) \left( \frac{\partial^2 \mathcal{H}^{dq}}{\partial \phi_s^{dq} \partial \phi_r^{dq}} \right)^{-1} X_r(\omega_{s,e} - \omega) \frac{\partial^2 \mathcal{H}^{dq}}{\partial \phi_s^{dq^2}} \\
& + \frac{n^2}{J_L} \frac{\partial^2 \mathcal{H}^{dq}}{\partial \phi_s^{dq} \partial \phi_r^{dq}} \mathcal{J}_2 \phi_r^{dq} \iota_s^{dq^T} \mathcal{J}_2 \\
& + \text{Terms in } \frac{d\phi_s^{dq}}{dt} \text{ and } \frac{d\phi_r^{dq}}{dt} \text{ we do not need to compute} \\
\frac{\partial}{\partial \phi_r^{dq}} \frac{d^2 \iota_s^{dq}}{dt^2} & \sim \frac{\partial^2 \mathcal{H}^{dq}}{\partial \phi_s^{dq} \partial \phi_r^{dq}} \mathcal{J}_2 \frac{d\omega}{dt} \\
& + \text{Terms in } \frac{d\phi_s^{dq}}{dt} \text{ and } \frac{d\phi_r^{dq}}{dt} \text{ we do not need to compute} \\
\frac{\partial}{\partial \omega} \frac{d^2 \iota_s^{dq}}{dt^2} & \sim \frac{\partial^2 \mathcal{H}^{dq}}{\partial \phi_s^{dq} \partial \phi_r^{dq}} \mathcal{J}_2 \frac{d\phi_r^{dq}}{dt} + \frac{\partial^2 \mathcal{H}^{dq}}{\partial \phi_s^{dq} \partial \phi_r^{dq}} \left( -R_r \frac{\partial^2 \mathcal{H}^{dq}}{\partial \phi_r^{dq^2}} - \mathcal{J}_2(\omega_{s,e} - \omega) \right) \mathcal{J}_2 \phi_r^{dq} \\
& + \frac{\partial}{\partial \phi_r^{dq}} \left( \frac{\partial^2 \mathcal{H}^{dq}}{\partial \phi_s^{dq^2}} \frac{d\phi_s^{dq}}{dt} + \frac{\partial^2 \mathcal{H}^{dq}}{\partial \phi_s^{dq} \partial \phi_r^{dq}} \frac{d\phi_r^{dq}}{dt} \right) \mathcal{J}_2 \phi_r^{dq}
\end{aligned}$$

$$\frac{\partial}{\partial T_L} \frac{d^2 \iota_s^{dq}}{dt^2} = -\frac{n}{J_L} \frac{\partial^2 \mathcal{H}^{dq}}{\partial \phi_s^{dq} \partial \phi_r^{dq}} \mathcal{J}_2 \phi_r^{dq}$$

Subtracting  $\frac{\partial^2 \mathcal{H}^{dq}}{\partial \phi_s^{dq} \partial \phi_r^{dq}} \left( -R_r \frac{\partial^2 \mathcal{H}^{dq}}{\partial \phi_r^{dq^2}} - \mathcal{J}_2(\omega_{s,e} - \omega) \right) \left( \frac{\partial^2 \mathcal{H}^{dq}}{\partial \phi_s^{dq} \partial \phi_r^{dq}} \right)^{-1}$  multiplied by the third and fourth lines from the last two lines we show

$$\begin{aligned} \frac{\partial}{\partial \phi_s^{dq}} \frac{d^2 \iota_s^{dq}}{dt^2} &\sim -\frac{\partial^2 \mathcal{H}^{dq}}{\partial \phi_s^{dq^2}} \omega_{s,e}^2 + \frac{\partial^2 \mathcal{H}^{dq}}{\partial \phi_s^{dq} \partial \phi_r^{dq}} \Omega_r \mathcal{J}_2 \omega_{s,e} - X_r \frac{\partial^2 \mathcal{H}^{dq}}{\partial \phi_s^{dq^2}} \mathcal{J}_2 \omega_{s,e} \\ &\quad + \frac{n^2}{J_L} \frac{\partial^2 \mathcal{H}^{dq}}{\partial \phi_s^{dq} \partial \phi_r^{dq}} \mathcal{J}_2 \phi_r^{dq} \iota_s^{dqT} \mathcal{J}_2 \\ &\quad + \text{Terms in } \frac{d\phi_s^{dq}}{dt} \text{ and } \frac{d\phi_r^{dq}}{dt} \text{ we do not need to compute} \\ \frac{\partial}{\partial \phi_r^{dq}} \frac{d^2 \iota_s^{dq}}{dt^2} &\sim \frac{\partial^2 \mathcal{H}^{dq}}{\partial \phi_s^{dq} \partial \phi_r^{dq}} \mathcal{J}_2 \frac{d\omega}{dt} \\ &\quad + \text{Terms in } \frac{d\phi_s^{dq}}{dt} \text{ and } \frac{d\phi_r^{dq}}{dt} \text{ we do not need to compute} \\ \frac{\partial}{\partial \omega} \frac{d^2 \iota_s^{dq}}{dt^2} &\sim \frac{\partial^2 \mathcal{H}^{dq}}{\partial \phi_s^{dq} \partial \phi_r^{dq}} \mathcal{J}_2 \frac{d\phi_r^{dq}}{dt} \\ &\quad + \frac{\partial}{\partial \phi_r^{dq}} \left( \frac{\partial^2 \mathcal{H}^{dq}}{\partial \phi_s^{dq^2}} \frac{d\phi_s^{dq}}{dt} + \frac{\partial^2 \mathcal{H}^{dq}}{\partial \phi_s^{dq} \partial \phi_r^{dq}} \frac{d\phi_r^{dq}}{dt} \right) \mathcal{J}_2 \phi_r^{dq} \\ \frac{\partial}{\partial T_L} \frac{d^2 \iota_s^{dq}}{dt^2} &= -\frac{n}{J_L} \frac{\partial^2 \mathcal{H}^{dq}}{\partial \phi_s^{dq} \partial \phi_r^{dq}} \mathcal{J}_2 \phi_r^{dq} \end{aligned}$$

**When  $\omega_{s,e} \neq 0$**  On the permanent trajectory introduced in section 4.1.2 when  $\omega_{s,e} \neq 0$  we recover of course the results obtained for linear observability in section 4.1.4, as nonlinear observability on a permanent trajectory is equivalent to linear observability. Namely, the IM is observable on permanent trajectories where  $\omega_{s,e} \neq 0$ , as the Lie derivatives matrix has the same rank as

$$\begin{pmatrix} \frac{\partial^2 \mathcal{H}^{dq}}{\partial \phi_s^{dq^2}} & \frac{\partial^2 \mathcal{H}^{dq}}{\partial \phi_s^{dq} \partial \phi_r^{dq}} & 0_{2,1} & 0_{2,1} \\ -M_1 & 0_{2,2} & \frac{\partial^2 \mathcal{H}^{dq}}{\partial \phi_s^{dq} \partial \phi_r^{dq}} \mathcal{J}_2 \phi_r^{dq} & 0_{2,1} \\ \frac{n^2}{J_L} \frac{\partial^2 \mathcal{H}^{dq}}{\partial \phi_s^{dq} \partial \phi_r^{dq}} \mathcal{J}_2 \phi_r^{dq} \iota_s^{dqT} \mathcal{J}_2 & 0_{2,2} & M_1 \mathcal{J}_2 \omega_{s,e} M_1^{-1} \frac{\partial^2 \mathcal{H}^{dq}}{\partial \phi_s^{dq} \partial \phi_r^{dq}} \mathcal{J}_2 \phi_r^{dq} & -\frac{n}{J_L} \frac{\partial^2 \mathcal{H}^{dq}}{\partial \phi_s^{dq} \partial \phi_r^{dq}} \mathcal{J}_2 \phi_r^{dq} \end{pmatrix}$$

where  $M_1 \mathcal{J}_2 M_1^{-1} \frac{\partial^2 \mathcal{H}^{dq}}{\partial \phi_s^{dq} \partial \phi_r^{dq}} \mathcal{J}_2 \phi_r^{dq}$  and  $\frac{\partial^2 \mathcal{H}^{dq}}{\partial \phi_s^{dq} \partial \phi_r^{dq}} \mathcal{J}_2 \phi_r^{dq}$  are not collinear vectors. Thus this matrix is of rank 6 and the IM is observable on permanent trajectories where  $\omega_{s,e} \neq 0$ .

**When  $\omega_{s,e} = 0$**  On the permanent trajectory we retrieve of course the results we got in section 4.1.4: The IM is unobservable on permanent trajectories when  $\omega_{s,e} = 0$ . This can be seen as

$$\begin{aligned} \mathcal{L}_A^2 C &\sim \left( \frac{n^2}{J_L} \frac{\partial^2 \mathcal{H}^{dq}}{\partial \phi_s^{dq} \partial \phi_r^{dq}} \mathcal{J}_2 \phi_r^{dq} \iota_s^{dqT} \mathcal{J}_2 \quad 0_{2,2} \quad 0_{2,1} \quad -\frac{n}{J_L} \frac{\partial^2 \mathcal{H}^{dq}}{\partial \phi_s^{dq} \partial \phi_r^{dq}} \mathcal{J}_2 \phi_r^{dq} \right) \\ &\sim \frac{\partial^2 \mathcal{H}^{dq}}{\partial \phi_s^{dq} \partial \phi_r^{dq}} \mathcal{J}_2 \phi_r^{dq} \left( \iota_s^{dqT} \mathcal{J}_2 \quad 0_{1,2} \quad 0_{1,1} \quad -\frac{n}{J_L} \right) \end{aligned}$$

up to a matrix linear combination of the first four lines of the Lie derivative matrix. The 0th, 1st and 2nd Lie derivative matrix is thus not full rank.

Moreover, removing the terms in  $u_s^{dq}$ ,  $i_s^{dq}$  and their derivatives and using  $\omega_{s,e} = 0$  we obtain for  $n \geq 2$

$$\begin{aligned} \frac{d^n i_s^{dq}}{dt^n} &= \frac{\partial^2 \mathcal{H}^{dq}}{\partial \phi_s^{dq} \partial \phi_r^{dq}} \left( -R_r \frac{\partial^2 \mathcal{H}^{dq}}{\partial \phi_r^{dq^2}} + \mathcal{J}_2 \omega \right)^{(n-1)} (-R_r i_r^{dq} + \mathcal{J}_2 \omega \phi_r^{dq}) \\ &+ \frac{n^2}{J_L} \frac{\partial^2 \mathcal{H}^{dq}}{\partial \phi_s^{dq} \partial \phi_r^{dq}} \left( -R_r \frac{\partial^2 \mathcal{H}^{dq}}{\partial \phi_r^{dq^2}} + \mathcal{J}_2 \omega \right)^{(n-2)} \mathcal{J}_2 \phi_r^{dq} i_s^{dq^T} \mathcal{J}_2 \phi_s^{dq} \\ &- \frac{n}{J_L} \frac{\partial^2 \mathcal{H}^{dq}}{\partial \phi_s^{dq} \partial \phi_r^{dq}} \left( -R_r \frac{\partial^2 \mathcal{H}^{dq}}{\partial \phi_r^{dq^2}} + \mathcal{J}_2 \omega \right)^{(n-2)} \mathcal{J}_2 \phi_r^{dq} T_L \end{aligned}$$

whose first term can be canceled by adding a (matrix) linear combination of  $\frac{di_s^{dq}}{dt}$ . Thus

$$\mathcal{L}_A^n C \sim \frac{\partial^2 \mathcal{H}^{dq}}{\partial \phi_s^{dq} \partial \phi_r^{dq}} \left( -R_r \frac{\partial^2 \mathcal{H}^{dq}}{\partial \phi_r^{dq^2}} + \mathcal{J}_2 \omega \right) \mathcal{J}_2 \phi_r^{dq} \begin{pmatrix} i_s^{dq^T} \mathcal{J}_2 & 0_{1,2} & 0_{1,1} & -\frac{n}{J_L} \end{pmatrix}$$

which which is collinear to  $\mathcal{L}_A^2 C$ . The Lie derivative matrix is thus of rank 5.

**Around a permanent trajectory at  $\omega_{s,e} = 0$**  As was said at the beginning of the section we are now considering a trajectory which is close to the target permanent trajectory. This means that the time derivatives of the fluxes and the speed are not zero any more. The Lie derivative matrix thus has the same rank as

$$\begin{pmatrix} \frac{\partial^2 \mathcal{H}^{dq}}{\partial \phi_s^{dq^2}} & \frac{\partial^2 \mathcal{H}^{dq}}{\partial \phi_s^{dq} \partial \phi_r^{dq}} & 0_{2,1} & 0_{2,1} \\ -M_1 + \frac{\partial M_2}{\partial \phi_s^{dq}} & \frac{\partial M_2}{\partial \phi_r^{dq}} & \frac{\partial^2 \mathcal{H}^{dq}}{\partial \phi_s^{dq} \partial \phi_r^{dq}} \mathcal{J}_2 \phi_r^{dq} & 0_{2,1} \\ \frac{n^2}{J_L} \frac{\partial^2 \mathcal{H}^{dq}}{\partial \phi_s^{dq} \partial \phi_r^{dq}} \mathcal{J}_2 \phi_r^{dq} i_s^{dq^T} \mathcal{J}_2 & \frac{\partial^2 \mathcal{H}^{dq}}{\partial \phi_s^{dq} \partial \phi_r^{dq}} \mathcal{J}_2 \frac{d\omega}{dt} & \frac{\partial M_2}{\partial \phi_r^{dq}} \mathcal{J}_2 \phi_r^{dq} & -\frac{n}{J_L} \frac{\partial^2 \mathcal{H}^{dq}}{\partial \phi_s^{dq} \partial \phi_r^{dq}} \mathcal{J}_2 \phi_r^{dq} \end{pmatrix}$$

where  $M_2 = \frac{\partial^2 \mathcal{H}^{dq}}{\partial \phi_s^{dq^2}} \frac{d\phi_s^{dq}}{dt} + \frac{\partial^2 \mathcal{H}^{dq}}{\partial \phi_s^{dq} \partial \phi_r^{dq}} \frac{d\phi_r^{dq}}{dt}$ . Assuming the rank of the first four lines is not modified by the addition of the time derivatives, the observability is recovered as soon as any of

$$\det \left( \frac{\partial^2 \mathcal{H}^{dq}}{\partial \phi_s^{dq} \partial \phi_r^{dq}} \mathcal{J}_2 \frac{d\omega}{dt}, \frac{\partial^2 \mathcal{H}^{dq}}{\partial \phi_s^{dq} \partial \phi_r^{dq}} \mathcal{J}_2 \phi_r^{dq} \right) \quad (4.29a)$$

$$\det \left( \frac{\partial}{\partial \phi_r^{dq}} \left( \frac{\partial^2 \mathcal{H}^{dq}}{\partial \phi_s^{dq^2}} \frac{d\phi_s^{dq}}{dt} + \frac{\partial^2 \mathcal{H}^{dq}}{\partial \phi_s^{dq} \partial \phi_r^{dq}} \frac{d\phi_r^{dq}}{dt} \right) \mathcal{J}_2 \phi_r^{dq}, \frac{\partial^2 \mathcal{H}^{dq}}{\partial \phi_s^{dq} \partial \phi_r^{dq}} \mathcal{J}_2 \phi_r^{dq} \right) \quad (4.29b)$$

is large enough. To satisfy eq. (4.29a) we must have a large  $\frac{d\omega}{dt}$ , which is not desirable, as we want to control  $\omega$  close to its constant reference. But eq. (4.29b) can be satisfied without perturbing much the behavior of the electric motor: In section 4.2 it will be shown that we can ensure  $\frac{d\phi_s^{dq}}{dt}$  large enough while keeping the other state variables close to the permanent trajectory.

## 4.2 High frequency injection effects

In section 4.1 we showed that observability can be recovered near permanent trajectories where  $\omega_{s,e} = 0$ , under the condition that  $\frac{d\phi_s^{dq}}{dt} \neq 0$ . We present in section 4.2.1 methods to ensure this condition is verified.

We focus on high frequency signal injection (HF injection) which was introduced by Jansen and Lorenz [78], Corley and Lorenz [85]. We prove in section 4.2.3 that the condition  $\frac{d\phi_s^{dq}}{dt} \neq 0$  can be ensured without disturbing too much the other state variables. In particular we will see that the speed of the motor is very close to the target speed.

### 4.2.1 Bibliography on signal injection

Multiple techniques are proposed in the literature to enforce one of the conditions eqs. (4.29a) and (4.29b). The most interesting are those based on signal injection, otherwise the effects are too small to be measurable on a real implementation.

The preferred type of signal injection uses the motor response to a high-frequency signal as proposed by Jansen and Lorenz [78] for IMs and Corley and Lorenz [85] for PMSMs. This technique was generalized to SynRMs, in Capecchi, Guglielmi, *et al.* [49] for instance. It is generally explained on the equivalent magnetic circuit of the motor. Indeed, it can be shown that the signal injection propagates in the leakage flux paths which are saturated by the magnetic flux (see [2, 28, 50–52]). The stator current response of the motor to signal injection thus depends on the orientation of the magnetic flux. The other state variables of the motor are mostly unaffected by the injection. Extensive reviews of HF signal injection techniques are given in Holtz [53] and Sul [23, sec. 6.4].

An alternative technique for signal injection is proposed in Hinkkanen, Leppänen, *et al.* [54], Li and Wu [55], where a low-frequency signal is used. It is superimposed on the control signals as well. Thanks to its effects on the currents, the speed of the motor can again be obtained. However, the motor is much more disturbed by low-frequency than by high-frequency signal injection. That is why this technique is less employed.

### 4.2.2 High-frequency injection

First of all, in the case of signal injection, a HF signal is a signal whose frequency is higher than the natural frequencies of the electric motor. Hereafter is a small review of existing types of HF injection (see Holtz [53] for more details).

In the literature two methods are proposed to inject HF signals

**HF voltage signal injection** A HF voltage signal is superimposed to the output of the controller and its effect on stator currents is extracted from the measurements. This method is the most widely used (see for instance [2, 4, 50, 52]) because it is the most simple to implement.

**HF current signal injection** A HF current signal is superimposed to the input of a broad bandwidth current controller. It results in the control voltage having HF harmonics which are extracted. This method is far less used because it is more difficult to implement. Indeed we must have a current controller which does not filter out the injected signal. This type of injection is discussed in Ha and Sul [57] and used in Rudolph, Laczynski, *et al.* [52].

In the literature we find also different polarizations for the injected signal

**Axial polarization** The injected signal oscillates along an axis slowly, with respect to the high frequency, moving in the  $\alpha\beta$  frame where it can be written using complex variables

$$\tilde{u}_s^{\alpha\beta}(t) = \tilde{u}e^{j\theta_i(t)}f(\Omega t). \quad (4.30)$$

This kind of signal is used by Yoon and Sul [4], Jebai [37].

**Circular polarization** The injected signal is a constant amplitude space vector rotating at high frequency with respect to the  $\alpha\beta$  frame where it can be written using complex variables

$$\tilde{u}_s^{\alpha\beta}(t) = \tilde{u}e^{j\Omega t}. \quad (4.31)$$

This kind of signal is used by Jansen and Lorenz [78].

**Elliptical polarization** Similarly to circular polarization, the injected signal rotates at high frequency with respect to the  $\alpha\beta$  frame, but now its amplitude varies periodically at the same frequency. In the  $\alpha\beta$  frame this can be written using complex variables

$$\tilde{u}_s^{\alpha\beta}(t) = \tilde{u}e^{j\Omega t}f(\Omega t). \quad (4.32)$$

This kind of injection is used in Bottiglieri, Consoli, *et al.* [58].

It should be noted that, due to the usage of sine and cosine, circular and elliptical polarizations are difficult to implement as the high frequency may be close to the PWM frequency.

Finally we should decide on the shape of the signal injected. Using a sinusoidal injection has the same drawbacks as circular polarization. Yoon and Sul [4], Jebai [37] proposed a square wave signal which is much simpler to implement, when injection and PWM frequencies are close to each other.

We chose to use HF voltage injection, thus avoiding to take the current controller into account to predict the effects of HF injection. For the frequency of the injected signal to be high enough with respect to the electrical time constants of the motors (see section 2.1), we selected it to be  $500Hz$ , which is five times the bandwidth of the current controller we use. The chosen sampling and PWM frequency being  $4kHz$ , we cannot generate proper sinusoids as we have only eight points per HF period. We thus used experimentally a square-wave signal polarized along an axis.

### 4.2.3 Second order averaging

We are now considering the case of HF voltage signal injection, which was elected as it is much simpler to implement. The input voltages are  $u_s^{\alpha\beta}(t) = \bar{u}_s^{\alpha\beta}(t) + \tilde{u}_s^{\alpha\beta}(t, \Omega t)$  where  $\tilde{u}_s^{\alpha\beta}$ , the injected HF signal, is periodic with respect to its second variable. Using second-order averaging (see [47, sec. 2.9]), we will show that the effects of HF voltage signal injection are of order 1 in  $\frac{1}{\Omega}$  on the stator flux and of order 2 in  $\frac{1}{\Omega}$  on the other state variables, which includes the speed. At first order, the behavior of electric motor is not modified by signal injection, except for  $\frac{d\phi_s^{\alpha\beta}}{dt}$  which is of order 1 similarly to  $\tilde{u}_s^{\alpha\beta}$ .

The equations of an electric motor eq. (3.20) in the  $\alpha\beta$  frame can be rewritten

$$\frac{dX}{dt} = A(X) + \bar{U}(t) + \tilde{U}(t, \Omega t) \quad (4.33)$$

with

$$X = \begin{pmatrix} \phi_s^{\alpha\beta} \\ \phi_r^{\alpha\beta} \\ \omega \\ \theta \end{pmatrix} \quad A(X) = \begin{pmatrix} -R_s i_s^{\alpha\beta}(\theta, \rho, \phi_s^{\alpha\beta}, \phi_r^{\alpha\beta}) \\ -R_r i_r^{\alpha\beta}(\theta, \rho, \phi_s^{\alpha\beta}, \phi_r^{\alpha\beta}) \\ \frac{n}{J_L} T_e(\theta, \rho, \phi_s^{\alpha\beta}, \phi_r^{\alpha\beta}) \\ \omega \end{pmatrix}$$

$$\bar{U}(t) = \begin{pmatrix} \bar{u}_s^{\alpha\beta}(t)^T & 0 & T_L(t) & 0 \end{pmatrix}^T \quad \tilde{U}(t, \Omega t) = \begin{pmatrix} \tilde{u}_s^{\alpha\beta}(t, \Omega t)^T & 0 & 0 & 0 \end{pmatrix}^T.$$

Following Sanders, Verhulst, *et al.* [47, sec. 3.3], to obtain the standard form of averaging, we change the time-scale of eq. (4.33) by defining the “fast time”  $\sigma = \Omega t$  and include the “slow” time  $t$  in the state

$$\frac{dX}{d\sigma} = \varepsilon \left( A(X) + \bar{U}(t) + \tilde{U}(t, \sigma) \right) \quad (4.34a)$$

$$\frac{dt}{d\sigma} = \varepsilon. \quad (4.34b)$$

where  $\varepsilon = \frac{1}{\Omega}$ . The corresponding averaged system is

$$\frac{d\bar{X}}{d\sigma} = \varepsilon \left( A(\bar{X}) + \bar{U}(t) \right) \quad (4.35a)$$

$$\frac{dt}{d\sigma} = \varepsilon \quad (4.35b)$$

which describes the behavior of an electric motor in the absence of HF signal injection.

Under the assumptions that  $A$  is Lipschitz and that the system eq. (4.35a) is asymptotically stable, the theorem of averaging [47, Th. 5.5.1] states that the difference between  $X$ , solution of eq. (4.34), and  $\bar{X}$ , solution of eq. (4.35) with the same initial condition, is dominated by  $\varepsilon$  for all  $t \geq 0$ . As eq. (4.35) are the dynamical equations of the electric motor without signal injection, this means that the HF injection does not disturb the electric motor at first order. This is an essential feature of HF injection which otherwise could not be used, as altering the behavior of the electric motor is not desirable.

To explain the response of electric motors to signal injection, we thus need to solve eq. (4.34) at a higher order in  $\varepsilon = \frac{1}{\Omega}$ . We introduce the concept of pseudo-identity transformation (see [47, sec. 2.9])

$$X = \Upsilon(\check{X}, \sigma, \varepsilon) = \check{X} + \sum_{k=1}^{\infty} \varepsilon^k \Upsilon_k(\check{X}, t, \sigma). \quad (4.36)$$

Substituting eq. (4.36), truncated at order 1 in  $\varepsilon$ , into eq. (4.34), we find

$$\frac{d\check{X}}{d\sigma} + \varepsilon \frac{\partial \Upsilon_1}{\partial \check{X}} \frac{d\check{X}}{d\sigma} + \varepsilon^2 \frac{\partial \Upsilon_1}{\partial t} + \varepsilon \frac{\partial \Upsilon_1}{\partial \sigma} = \varepsilon \left( A(\check{X}) + \bar{U}(t) + \varepsilon \frac{\partial A}{\partial \check{X}} \Upsilon_1 + \tilde{U}(t, \sigma) \right).$$

By truncating this expression at order 2 in  $\varepsilon$  and grouping the terms by order in  $\varepsilon$ , we obtain

$$\frac{d\bar{X}}{d\sigma} = \varepsilon \underbrace{\left( A(\bar{X}) + \bar{U}(t) + \tilde{U}(t, \sigma) - \frac{\partial \Upsilon_1}{\partial \sigma} \right)}_{\bar{A}_1(\bar{X}, t)} + \varepsilon^2 \left( \frac{\partial A}{\partial \check{X}} \Upsilon_1 - \frac{\partial \Upsilon_1}{\partial \check{X}} \bar{A}_1 - \frac{\partial \Upsilon_1}{\partial t} \right)$$

where we find the first homological equation

$$\frac{\partial \Upsilon_1}{\partial \sigma} = A(\bar{X}) + \bar{U}(t) + \tilde{U}(t, \sigma) - \bar{A}_1(\bar{X}, t). \quad (4.37)$$

As we want to ensure  $\bar{A}_1$  does not depend on  $\sigma$ , we choose  $\Upsilon_1(\check{X}, t, \sigma)$  to be the anti-derivative of  $\tilde{U}(t, \sigma)$  with zero mean in  $\sigma$  and  $\bar{A}_1(\bar{X}, t) = A(\bar{X}) + \bar{U}(t)$ . As  $\frac{\partial \Upsilon_1}{\partial t}$  also has

zero mean when averaged with respect to  $\sigma$ , the averaging of the term of order 2 in  $\varepsilon$  gives 0. Thus  $\bar{X}$  is again the solution of eq. (4.35), but the improved estimate of  $X$  reads  $\bar{X} + \varepsilon \Upsilon_1(t, \sigma) + O(\varepsilon^2)$  shows the effect of HF injection on the response of the electric machine.

Particularizing this result with the form of  $\tilde{U}$ , we find that the only state variable affected by HF voltage injection at order 1 in  $\varepsilon$  is the stator flux. All other state variables are affected only at order 2 or more in  $\varepsilon$ . The behavior of electric motors is thus not modified much by signal injection, which is an essential feature of HF injection.

**Axial polarization** Using complex variables, from eq. (4.30), we obtain  $\underline{\phi}_s^{\alpha\beta} = \bar{\phi}_s^{\alpha\beta} + \frac{\tilde{u}}{\Omega} e^{j\theta_i(t)} F(\Omega t)$  where  $F$  is the anti-derivative of  $f$  with zero mean. Thus

$$\begin{aligned} \underline{\iota}_s^{\alpha\beta} &= \frac{\partial \mathcal{H}^{\alpha\beta}}{\partial \underline{\phi}_s^{\alpha\beta*}} \left( \theta, \rho, \bar{\phi}_s^{\alpha\beta} + \frac{\tilde{u}}{\Omega} e^{j\theta_i(t)} F(\Omega t), \bar{\phi}_s^{\alpha\beta*} + \frac{\tilde{u}}{\Omega} e^{-j\theta_i(t)} F(\Omega t), \bar{\phi}_r^{\alpha\beta}, \bar{\phi}_r^{\alpha\beta*} \right) \\ &= \bar{\iota}_s^{\alpha\beta} + \frac{\partial^2 \mathcal{H}^{\alpha\beta}}{\partial \underline{\phi}_s^{\alpha\beta*} \partial \underline{\phi}_s^{\alpha\beta}} \frac{\tilde{u}}{\Omega} e^{j\theta_i(t)} F(\Omega t) + \frac{\partial^2 \mathcal{H}^{\alpha\beta}}{\partial \underline{\phi}_s^{\alpha\beta*2}} \frac{\tilde{u}}{\Omega} e^{-j\theta_i(t)} F(\Omega t) \end{aligned} \quad (4.38)$$

**Circular polarization** Using complex variables, from eq. (4.31), we obtain  $\underline{\phi}_s^{\alpha\beta} = \bar{\phi}_s^{\alpha\beta} - j \frac{\tilde{u}}{\Omega} e^{j\Omega t}$  and thus

$$\begin{aligned} \underline{\iota}_s^{\alpha\beta} &= \frac{\partial \mathcal{H}^{\alpha\beta}}{\partial \underline{\phi}_s^{\alpha\beta*}} \left( \theta, \rho, \bar{\phi}_s^{\alpha\beta} - j \frac{\tilde{u}}{\Omega} e^{j\Omega t}, \bar{\phi}_s^{\alpha\beta*} + j \frac{\tilde{u}}{\Omega} e^{-j\Omega t}, \bar{\phi}_r^{\alpha\beta}, \bar{\phi}_r^{\alpha\beta*} \right) \\ &= \bar{\iota}_s^{\alpha\beta} - \frac{\partial^2 \mathcal{H}^{\alpha\beta}}{\partial \underline{\phi}_s^{\alpha\beta*} \partial \underline{\phi}_s^{\alpha\beta}} j \frac{\tilde{u}}{\Omega} e^{j\Omega t} + \frac{\partial^2 \mathcal{H}^{\alpha\beta}}{\partial \underline{\phi}_s^{\alpha\beta*2}} j \frac{\tilde{u}}{\Omega} e^{-j\Omega t} \end{aligned} \quad (4.39)$$

The slowly varying current,  $\bar{\iota}_s^{\alpha\beta}$ , and the HF current ripple can be separately extracted from the current measurement by techniques presented in section 7.1.3.

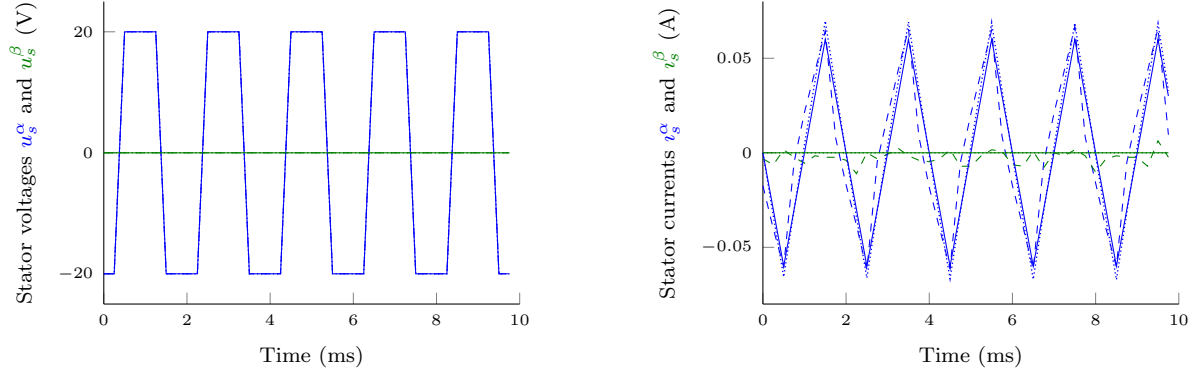
It can be checked that the obtained current ripple in experiments or simulation is close to the prediction of theory on an unsaturated IM (see fig. 4.3). The slight difference between experimental data and simulation or theory comes from the voltage drops on the test bench (see section 2.3.1). Moreover, we verified experimentally that the effect of HF injection on the speed is negligible and in simulation we also confirmed that the effect of HF injection is negligible on the rotor flux  $\phi_r^{\alpha\beta}$  as predicted by the theory.

#### 4.2.4 Using lower frequencies

For some industrial applications the frequency  $\Omega$  must be limited to lower frequencies, closer to the natural frequencies. In this case, the triangle wave is altered as can be seen in fig. 4.4. As the high frequency  $\Omega$  is reduced,  $\frac{1}{\Omega}$  cannot be considered small enough any more.

We go one order further in the averaging process to get an error in  $O\left(\frac{1}{\Omega^3}\right)$ . We substitute eq. (4.36), truncated at order 2 in  $\varepsilon$ , into eq. (4.34), find

$$\begin{aligned} &\frac{d\check{X}}{d\sigma} + \varepsilon \frac{\partial \Upsilon_1}{\partial \check{X}} \frac{d\check{X}}{d\sigma} + \varepsilon^2 \frac{\partial \Upsilon_1}{\partial t} + \varepsilon \frac{\partial \Upsilon_1}{\partial \sigma} + \varepsilon^2 \frac{\partial \Upsilon_2}{\partial \check{X}} \frac{d\check{X}}{d\sigma} + \varepsilon^3 \frac{\partial \Upsilon_2}{\partial t} + \varepsilon^2 \frac{\partial \Upsilon_2}{\partial \sigma} \\ &= \varepsilon \left( A(\check{X}) + \bar{U}(t) + \varepsilon \frac{\partial A}{\partial \check{X}} \Upsilon_1 + \varepsilon^2 \frac{\partial A}{\partial \check{X}} \Upsilon_2 + \tilde{U}(t, \sigma) \right). \end{aligned}$$



(a) Stator voltage with square wave HF signal injection along the  $\alpha$ -axis.

(b) Stator current with triangular wave ripple.

Figure 4.3 – Stator voltage with injected HF signal with the corresponding current responses traced from theory (solid lines), obtained by simulation (dotted lines) and experimentally measured on the IM described by table 2.2. To be in the range where the current-flux relations are unsaturated, there is no fundamental voltages and currents.

and, after grouping the terms of the same order in  $\varepsilon$  and truncating at order 3, we obtain

$$\begin{aligned}
 \frac{d\bar{X}}{d\sigma} &= \varepsilon \underbrace{\left( A(\bar{X}) + \bar{U}(t) + \tilde{U}(t, \sigma) - \frac{\partial \Upsilon_1}{\partial \sigma} \right)}_{\bar{A}_1(\bar{X}, t)} \\
 &+ \varepsilon^2 \underbrace{\left( \frac{\partial A}{\partial X} \Upsilon_1 - \frac{\partial \Upsilon_1}{\partial \check{X}} \bar{A}_1 - \frac{\partial \Upsilon_1}{\partial t} - \frac{\partial \Upsilon_2}{\partial \sigma} \right)}_{\bar{A}_2(\bar{X}, t)} \\
 &+ \varepsilon^3 \left( \frac{\partial A}{\partial X} \Upsilon_2 - \frac{\partial \Upsilon_1}{\partial \check{X}} \bar{A}_2 - \frac{\partial \Upsilon_2}{\partial \check{X}} \bar{A}_1 - \frac{\partial \Upsilon_2}{\partial t} \right).
 \end{aligned}$$

The first line of the above equation leads to the same first homological equation as in second order averaging (eq. (4.37)). It is solved similarly to obtain  $\bar{A}_1(\bar{X}, t) = A(\bar{X}) + \bar{U}(t)$  and  $\Upsilon_1(\check{X}, t, \sigma)$  is again the anti-derivative of  $\tilde{U}(t, \sigma)$  with respect to  $\sigma$  with zero mean. The second line gives the second homological equation

$$\frac{\partial \Upsilon_2}{\partial \sigma} = \frac{\partial A}{\partial X} \Upsilon_1 - \frac{\partial \Upsilon_1}{\partial t} - \bar{A}_2(\bar{X}, t). \quad (4.40)$$

where we used  $\frac{\partial \Upsilon_1}{\partial \check{X}} \equiv 0$ . To solve it we choose  $\Upsilon_2(\check{X}, t, \sigma)$  as the anti-derivative of  $\frac{\partial A}{\partial X} \Upsilon_1 - \frac{\partial \Upsilon_1}{\partial t}$  with respect to  $\sigma$  with zero mean and obtain  $\bar{A}_2(\bar{X}, t) = 0$ . Assuming partial derivatives of  $\Upsilon_1$  and  $\Upsilon_2$  also have zero mean, we find that  $\bar{X}$  is the solution of eq. (4.34). The improved estimate of  $X$  now reads  $\bar{X} + \varepsilon \Upsilon_1(t, \sigma) + \varepsilon^2 \Upsilon_2(\bar{X}, t, \sigma) + O(\varepsilon^3)$ . Third order averaging shows that all state variables are affected by HF injection at order 2 in  $\frac{1}{\Omega}$ .

As can be seen in fig. 4.4, using averaging at order 3 indeed improves the approximation of the current ripple. Continuing further would improve the results even more, but the calculations become really hard.

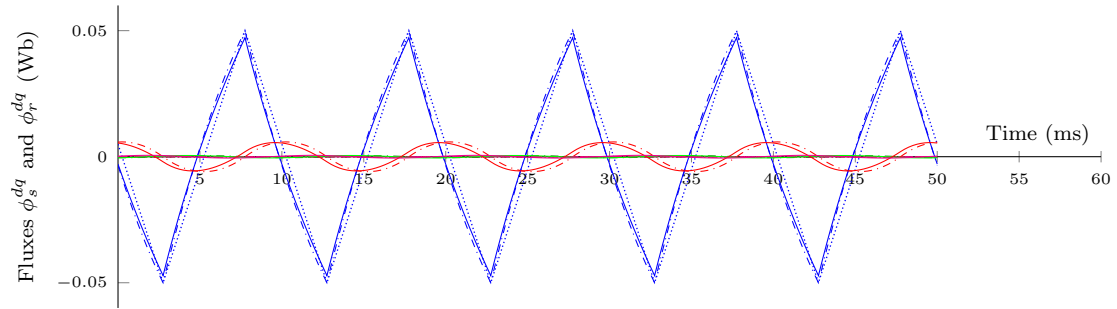
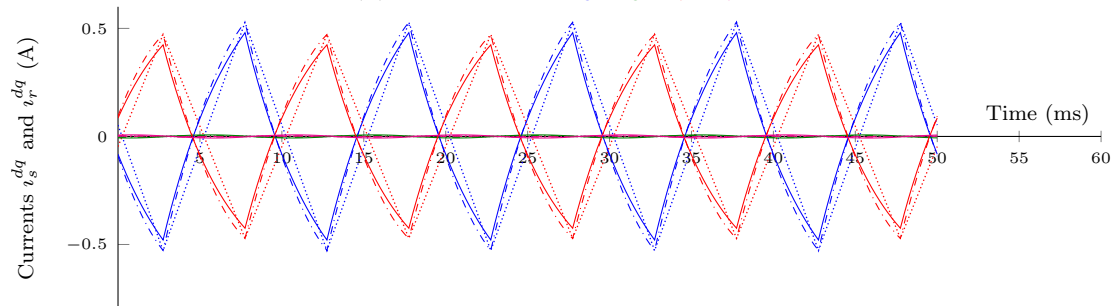
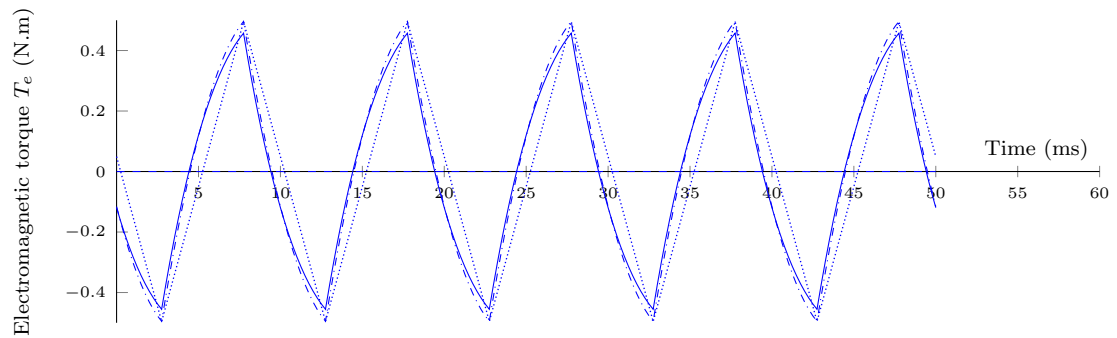
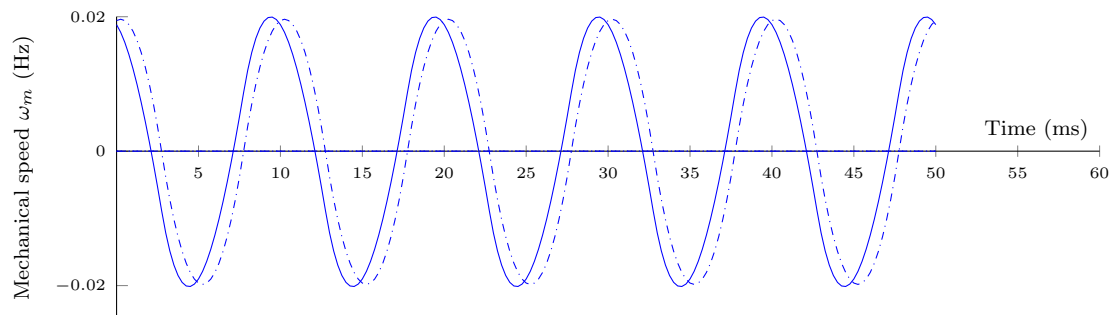
(a) HF ripple in  $\phi_s^d, \phi_s^q, \phi_r^d, \phi_r^q$ .(b) HF ripple in  $i_s^d, i_s^q, i_r^d, i_r^q$ .(c) HF ripple in  $T_e$ .(d) HF ripple in  $\omega_m$ .

Figure 4.4 – Reconstruction of HF ripples using averaging (1st order dashed, 2nd order dotted, 3rd order dash-dotted) compared to the real HF ripples obtained in simulation (solid line) on an unsaturated IM at  $\Omega = 100Hz$ .

### 4.3 Obtaining virtual measurements by HF injection

In this section HF injection is considered in the more general context of nonlinear systems, as proposed in Combes, Jebai, *et al.* [12]. Because electric motors are Multiple-Input Multiple-Output systems, we will generalize this study. More precisely, the model of the system we want to control can be written under state form as

$$\frac{dx}{dt} = f(x) + g(x)u \quad (4.41a)$$

$$y = h(x) \quad (4.41b)$$

where  $x \in \mathbb{R}^n$ ,  $u \in \mathbb{R}^m$  and  $y \in \mathbb{R}^l$ ;  $f$ ,  $g$  and  $h$  are smooth enough maps.

As shown in section 4.3.2, in the general case the supplementary information obtained by HF signal injection reads

$$y_v := \mathcal{L}_g h(x) = \frac{\partial h}{\partial g}(x)g(x). \quad (4.42)$$

As explained in section 4.3.3, these  $l = \dim(y)$  additional “virtual” measurements can be retrieved from the  $l = \dim(y)$  measurements  $y$  in the time-scale of the injection, when the system is excited by HF signal injection. We can thus assume we have them when designing the controller. However, to satisfactorily prove the main result in section 4.3.2, we need a technical lemma on second-order averaging for exponentially stable systems.

#### 4.3.1 Second-order averaging for exponentially stable systems

The approximations given by first- and second-order averaging are a priori valid only on the timescale  $\frac{1}{\varepsilon}$ , as stated by Sanders, Verhulst, *et al.* [47, theorems 2.8.1; 2.9.2]. However, with the additional assumption of exponential stability of the averaged system, they can be continued to infinity. This is a well-known result for first-order averaging, see e.g. [47, Theorem 5.5.1], recalled below.

**Lemma 1.** *Consider the two systems*

$$\frac{dx}{dt} = \varepsilon F_1(x, t) \quad (4.43a)$$

$$\frac{dz}{dt} = \varepsilon G_1(z), \quad (4.43b)$$

where  $F_1$  is periodic with respect to  $t$  and  $G_1$  is its average on one period. We suppose that the origin is an exponentially stable equilibrium for eq. (4.43b). Then, there exist a compact neighborhood  $\mathcal{V}$  of the origin, such that  $\forall z_0 \in \mathcal{V}$  the solution  $z(t)$  of eq. (4.43b) with initial condition  $z_0$  at  $t_0$  is valid on  $[t_0, +\infty[$ . Besides, there exists  $\varepsilon_0 > 0$  such that  $\forall \varepsilon \in [0, \varepsilon_0[$ , the solution  $x(t)$  of eq. (4.43a) with initial condition  $x_0 = z_0$  at  $t_0$  is valid on  $[t_0, +\infty[$  and  $\exists C \in \mathbb{R}^+$  such that

$$\sup_{t \in [t_0, +\infty[} \|x(t) - z(t)\| < C\varepsilon. \quad (4.44)$$

The following lemma, which does not seem to exist in the literature, extends this result to the case of second-order averaging.

**Lemma 2.** *Consider the two systems*

$$\frac{dx}{dt} = \varepsilon F_1(x, t) + \varepsilon^2 F_2(x, t) \quad (4.45a)$$

$$\frac{dz}{dt} = \varepsilon G_1(z) + \varepsilon^2 G_2(z) \quad (4.45b)$$

where  $F_1$  and  $F_2$  are periodic with respect to  $t$  and  $G_1$  and  $G_2$  are obtained as in section 4.3.2. We suppose that the origin is an exponentially stable equilibrium for eq. (4.43b). Then, there exists a compact neighborhood  $\mathcal{V}$  of the origin and  $\varepsilon_0 > 0$  such that  $\forall \varepsilon \in [0, \varepsilon_0[$  and  $\forall z_0 \in \mathcal{V}$ , the solution  $z(t)$  of eq. (4.45b) with initial condition  $z_0$  at  $t_0$  and the solution  $x(t)$  of eq. (4.45a) with initial condition  $x_0 = z_0 + \varepsilon \Upsilon_1(z_0, 0)$  at  $t_0$  are valid on  $[t_0, +\infty[$  and  $\exists C \in \mathbb{R}^+$  such that

$$\sup_{t \in [t_0, +\infty[} \|x(t) - z(t) - \varepsilon \Upsilon_1(z, t)\| < C\varepsilon^2,$$

where  $\Upsilon_1$  is defined as in section 4.3.2.

*Proof.*  $\mathcal{V}$  is chosen as a compact included in the domain of attraction of the origin and  $z_0 \in \mathcal{V}$ . Then by a perturbation theorem (e.g. Khalil [59, Theorem 8.1]),  $\exists \varepsilon_1 > 0$  such that  $\forall \varepsilon \in [0, \varepsilon_1[$  eq. (4.45b) admits a solution starting at  $z_0$  on  $[t_0, +\infty[$ . Besides, we know from [47, Lemma 2.9.1] that eq. (4.45a) can be transformed into

$$\frac{dy}{dt} = \varepsilon G_1(y) + \varepsilon^2 \tilde{G}_2(y, t)$$

by the change of variables  $x = y + \varepsilon \Upsilon_1(y, t)$ . By a perturbation theorem (e.g. Khalil [59, Th. 8.1]),  $\exists \varepsilon_2 > 0$  such that  $\forall \varepsilon \in [0, \varepsilon_2[$  eq. (4.45a) admits a solution on  $[t_0, +\infty[$  starting at  $x_0 = z_0 + \varepsilon \Upsilon_1(z_0, 0)$ .

We call  $\xi(t) = z(t) + \varepsilon \Upsilon_1(z, t)$ . We know from [47, Lemma 2.9.2] that

$$\exists L \in \mathbb{R}^+ \quad \forall t \in \left[ t_0, t_0 + \frac{L}{\varepsilon} \right[ \quad \|x(t) - \xi(t)\| < C\varepsilon^2.$$

We partition the time into segments of length  $\frac{L}{\varepsilon}$

$$\bigcup_{m \in \mathbb{N}} I_m = \bigcup_{m \in \mathbb{N}} \left[ t_0 + m \frac{L}{\varepsilon}, t_0 + (m+1) \frac{L}{\varepsilon} \right].$$

On each segment  $I_m$  we define  $z_m$  as the solution of the truncated averaged equation eq. (4.45b) with a initial condition verifying  $x_m(t_0 + m \frac{L}{\varepsilon}) = z_m(t_0 + m \frac{L}{\varepsilon}) + \varepsilon \Upsilon_1(z_m(t_0 + m \frac{L}{\varepsilon}), t_0)$  and also  $\xi_m := z_m + \varepsilon \Upsilon_1(z_m, t)$ . We note  $\|\cdot\|_{I_m} := \sup_{t \in I_m} \|\cdot\|$ .

$m \in \mathbb{N}$  is now fixed. From the theorem of second-order averaging [47, Theorem 2.9.2]  $\exists k$  such that

$$\|\xi_m - x\|_{I_m} \leq k\varepsilon^2$$

and from the definition of the truncated pseudo-identity transformation  $\Upsilon(z, t) = z + \varepsilon \Upsilon_1(z, t)$ ,  $\exists \lambda$  such that

$$\begin{aligned} \|\xi - \xi_m\|_{I_m} &= \|\Upsilon(z, t) - \Upsilon(z_m, t)\|_{I_m} \leq (1 + \varepsilon\lambda) \|z - z_m\|_{I_m} \\ \|z - z_m\|_{I_m} &= \|\Upsilon^{-1}(\xi, t) - \Upsilon^{-1}(\xi_m, t)\|_{I_m} \leq (1 + \varepsilon\lambda) \|\xi - \xi_m\|_{I_m}. \end{aligned}$$

Besides from (see [47, Lemma 5.2.7])

$$\|z - z_m\|_{I_m} \leq \kappa \left\| z \left( t_0 + m \frac{L}{\varepsilon} \right) - z_m \left( t_0 + m \frac{L}{\varepsilon} \right) \right\|$$

which can be rewritten by prolonging  $z_m$  on  $I_{m-1}$

$$\|z - z_m\|_{I_m} \leq \kappa \|z - z_m\|_{I_{m-1}},$$

where  $\kappa$  can be made as small as desired by taking  $\varepsilon$  small enough. By applying the triangle inequality, we find

$$\begin{aligned} \|\xi - x\|_{I_m} &\leq \|\xi - \xi_m\|_{I_m} + \|\xi_m - x\|_{I_m} \\ &\leq (1 + \varepsilon\lambda) \|z - z_m\|_{I_m} + k\varepsilon^2 \\ &\leq (1 + \varepsilon\lambda)\kappa \|z - z_m\|_{I_{m-1}} + k\varepsilon^2 \\ &\leq (1 + \varepsilon\lambda)\kappa(1 + \varepsilon\lambda) \|\xi - \xi_m\|_{I_{m-1}} + k\varepsilon^2 \\ &\leq \kappa' \|\xi - x\|_{I_{m-1}} + k(1 + \kappa')\varepsilon^2 \end{aligned}$$

where  $\kappa' = (1 + \varepsilon\lambda)\kappa(1 + \varepsilon\lambda) < 1$  is smaller than 1 for  $0 \leq \varepsilon < \varepsilon_3$ .

Then with a simple recursion we obtain

$$\begin{aligned} \|\xi - x\|_{I_m} &\leq \kappa'^m \|\xi - x\|_{I_0} + \left( \sum_{n=0}^{m-1} \kappa'^n \right) (1 + \kappa')k\varepsilon^2 \\ \|\xi - x\|_{I_m} &\leq \kappa'^{m+1} \|\xi(t_0) - x(t_0)\| + \left( \sum_{n=0}^m \kappa'^n \right) (1 + \kappa')k\varepsilon^2. \end{aligned}$$

Using the fact that  $\xi(t_0) = x(t_0)$  and that the sum is monotonically increasing, we obtain that

$$\|\xi - x\|_{I_m} \leq \frac{1 + \kappa'}{1 - \kappa'} k\varepsilon^2.$$

Finally, as the previous equation is valid for all  $m \in \mathbb{N}$ , we find that

$$\sup_{t \in [t_0, \infty[} \|\xi - x\| = \sup_{m \in \mathbb{N}} \|\xi - x\|_{I_m} \leq \frac{1 + \kappa'}{1 - \kappa'} k\varepsilon^2 =: C\varepsilon^2.$$

Taking  $\varepsilon_0 := \min(\{\varepsilon_1, \varepsilon_2, \varepsilon_3\})$ , completes the proof.  $\square$

Even though we do not prove it here, we suppose that this result is still valid for higher-order averaging approximations.

### 4.3.2 Signal injection for nonlinear systems

Consider the system eq. (4.41a) with the two outputs eqs. (4.41b) and (4.42). Assume we have designed a suitable control law

$$u = \alpha(\eta, y, y_v, t) \tag{4.46a}$$

$$\frac{d\eta}{dt} = a(\eta, y, y_v, t), \tag{4.46b}$$

with  $\eta \in \mathbb{R}^p$ . By “suitable”, we mean the closed-loop system

$$\frac{d\bar{x}}{dt} = f(\bar{x}) + g(\bar{x})\alpha(\bar{\eta}, h(\bar{x}), \mathcal{L}_g h(\bar{x}), t) \tag{4.47a}$$

$$\frac{d\bar{\eta}}{dt} = a(\bar{\eta}, h(\bar{x}), \mathcal{L}_g h(\bar{x}), t) \tag{4.47b}$$

has the desired exponentially stable equilibrium point (or family of equilibrium points); we have changed the notation of the state to  $(\bar{x}, \bar{\eta})$ , so as to distinguish between the solutions of eqs. (4.47) and (4.49).

A control law using HF signal injection can be written

$$u = \alpha(\eta, \bar{y}, \bar{y}_v, t) + f(\Omega t) \quad (4.48a)$$

$$\frac{d\eta}{dt} = a(\eta, \bar{y}, \bar{y}_v, t) \quad (4.48b)$$

$$\bar{y} = h(x) + \varepsilon \kappa(x, \Omega t) + O(\varepsilon^2) \quad (4.48c)$$

$$\bar{y}_v = \mathcal{L}_g h(x) + \varepsilon \kappa_v(x, \Omega t) + O(\varepsilon^2) \quad (4.48d)$$

where  $f$  is a periodic function with period 1 and zero mean, i.e.  $\int_0^1 f(\sigma) d\sigma = 0$ ;  $\kappa$  and  $\kappa_v$  are correction functions which are 1-periodic and have zero mean with respect to their second argument;  $\Omega := \frac{1}{\varepsilon}$  is a “large” parameter, so that the signal superimposed to the base control law is fast-varying. Corollary 1 explains how  $\kappa$  and  $\kappa_v$  are chosen so that  $\bar{y}$  and  $\bar{y}_v$  corresponds to actually available signals. The closed-loop system then reads

$$\frac{dx}{dt} = f(x) + g(x)\alpha(\eta, \bar{y}, \bar{y}_v, t) + g(x)f(\Omega t) \quad (4.49a)$$

$$\frac{d\eta}{dt} = a(\eta, \bar{y}, \bar{y}_v, t) \quad (4.49b)$$

$$\bar{y} = h(x) + \varepsilon \kappa(x, \Omega t) + O(\varepsilon^2) \quad (4.49c)$$

$$\bar{y}_v = \mathcal{L}_g h(x) + \varepsilon \kappa_v(x, \Omega t) + O(\varepsilon^2) \quad (4.49d)$$

The goal of injecting a fast-varying oscillation is to “create” the virtual output  $y_v$ , while not disturbing too much the system.

The following theorem characterizes the effect of signal injection by comparing the solutions of eqs. (4.47) and (4.49).

**Theorem 1.** *Let  $(\bar{x}(t), \bar{\eta}(t))$  and  $(x(t), \eta(t))$  be the solution of the closed-loop systems eqs. (4.47) and (4.49) respectively, starting from the same initial condition. Then for all  $t \geq 0$ ,*

$$x(t) = \bar{x}(t) + \varepsilon g(\bar{x}(t))F(\Omega t) + O(\varepsilon^2) \quad (4.50a)$$

$$\eta(t) = \bar{\eta}(t) + O(\varepsilon^2) \quad (4.50b)$$

$$y(t) = h(\bar{x}(t)) + \varepsilon \mathcal{L}_g h(\bar{x}(t))F(\Omega t) + O(\varepsilon^2), \quad (4.50c)$$

where  $F$  is the (of course also 1-periodic) anti-derivative of  $f$  with zero mean, i.e.

$$F(\sigma) := \int_0^\sigma f(\tau) d\tau - \int_0^1 \int_0^s f(\tau) d\tau ds.$$

In other words, signal injection

- has a small effect (of order  $\varepsilon$ ) on the state variables directly affected by the input;
- has a very small effect (of order  $\varepsilon^2$ ) on the state variables not directly affected by the input. In many systems of interest, and in particular in electric motors where only the fluxes and the currents are directly affected and we want to control the speed (or the position) of the rotor, the input affects directly only some state variables whereas the control objective is a combination of other stable variables; the control objective is thus hardly affected by the high-frequency excitation;

- creates a small ripple (of order  $\varepsilon$ ) in the measured output. The amplitude of this ripple is precisely the virtual output. A procedure to extract  $h(\bar{x}(t))$  and  $\mathcal{L}_g h(\bar{x}(t))$  from  $y(t)$  is presented in section 4.3.3; using these signals in the control law of eq. (4.48) amounts to a particular choice of  $\kappa$  and  $\kappa_v$ , see corollary 1.

*Proof.* The proof is a direct application of second-order averaging for differential equations [47, section 2.9], with slow time dependence [47, section 3.3]. We first recall the main result of this theory, and then apply it to our case.

Consider the perturbed system

$$\frac{dX}{d\sigma} = \varepsilon F_1(X, \sigma) + \varepsilon^2 F_2(X, \sigma)$$

with initial condition  $X(0) := \bar{X}_0 + \varepsilon \Upsilon_1(\bar{X}_0, 0)$ , where  $F_1$  is  $T$ -periodic with respect to their third arguments, and the averaged system

$$\frac{d\bar{X}}{d\sigma} = \varepsilon G_1(\bar{X}) + \varepsilon^2 G_2(\bar{X}) \quad (4.51)$$

with initial condition  $\bar{X}(0) := \bar{X}_0$ ; finally,  $G_1$ ,  $\Upsilon_1$  and  $G_2$  are defined by

$$\begin{aligned} G_1(\bar{X}) &:= \frac{1}{T} \int_0^T F_1(\bar{X}, s) ds \\ \gamma_1(\bar{X}, \sigma) &:= \int_0^\sigma [F_1(\bar{X}, s) - G_1(\bar{X})] ds \\ \Upsilon_1(\bar{X}, \sigma) &:= \zeta_1(\bar{X}, \sigma) - \frac{1}{T} \int_0^T \gamma_1(\bar{X}, s) ds \\ K_2(\bar{X}, \sigma) &:= F_2(\bar{X}, \sigma) + \frac{\partial F_1}{\partial X}(\bar{X}, \sigma) \Upsilon_1(\bar{X}, \sigma) - \frac{\partial \Upsilon_1}{\partial X}(\bar{X}, \sigma) G_1(\bar{X}, \sigma) \\ G_2(\bar{X}) &:= \frac{1}{T} \int_0^T K_2(\bar{X}, s) ds. \end{aligned}$$

The theory of second-order averaging then asserts that the solution  $X(\sigma)$  of the perturbed system and the solution  $\bar{X}(\sigma)$  of the perturbed system are related by

$$X(\sigma) = \bar{X}(\sigma) + \varepsilon \Upsilon_1(\bar{X}, \sigma) + O(\varepsilon^2)$$

on the timescale  $\frac{1}{\varepsilon}$ . If moreover the averaged system has an exponentially stable equilibrium point with region of attraction  $\mathcal{D}$ , and if the initial condition  $\bar{X}_0$  belongs to a compact subset of  $\mathcal{D}$ , then this approximation can be continued to infinity by lemma 1.

To apply this result to our case, we define  $X := (x, \eta, t)$  and  $\varepsilon := \frac{1}{\Omega}$ . Then we rewrite eq. (4.49) in the fast time  $\sigma := \Omega t = \frac{t}{\varepsilon}$ . This yields

$$\frac{dX}{d\sigma} = \varepsilon (\bar{F}_1(X) + \tilde{F}_1(X) f(\sigma)) + \varepsilon^2 F_2(X, \sigma) + O(\varepsilon^3),$$

where

$$\begin{aligned} \bar{F}_1(X, \sigma) &:= \begin{pmatrix} f(x) + g(x)\alpha(\eta, h(x), \mathcal{L}_g h(x), t) \\ a(\eta, h(x), \mathcal{L}_g h(x), t) \\ 1 \end{pmatrix} \\ \tilde{F}_1(X) &:= \begin{pmatrix} g(x) \\ 0_{p,1} \\ 0 \end{pmatrix} \\ F_2(X, \sigma) &:= \begin{pmatrix} g(x) (\partial_2 \alpha(\eta, h(x), \mathcal{L}_g h(x), t) \kappa(x, \sigma) + \partial_3 \alpha(\eta, h(x), \mathcal{L}_g h(x), t) \kappa_v(x, \sigma)) \\ \partial_2 a(\eta, h(x), \mathcal{L}_g h(x), t) \kappa(x, \sigma) + \partial_3 a(\eta, h(x), \mathcal{L}_g h(x), t) \kappa_v(x, \sigma) \\ 0 \end{pmatrix}. \end{aligned}$$

We then find

$$\begin{aligned}
G_1(\bar{X}) &= \bar{F}_1(\bar{X}) \\
\gamma_1(\bar{X}, \sigma) &= \tilde{F}_1(\bar{X}) \int_0^\sigma f(s) ds \\
\Upsilon_1(\bar{X}, \sigma) &= \tilde{F}_1(\bar{X}) F(\sigma) \\
K_2(\bar{X}, \sigma) &= F_2(\bar{X}, \sigma) - \tilde{F}'_1(\bar{X}) \bar{F}_1(\bar{X}) F(\sigma) \\
&\quad + \bar{F}'_1(\bar{X}) \tilde{F}_1(\bar{X}) F(\sigma) + \tilde{F}'_1(\bar{X}) \tilde{F}_1(\bar{X}) F(\sigma) f(\sigma) \\
G_2(\bar{X}) &= 0,
\end{aligned}$$

remembering that  $\kappa$ ,  $\kappa_v$ ,  $f$ ,  $F$  and thus  $Ff$  have zero mean. We then rewrite the averaged system eq. (4.51) in the slow time  $t$  to find exactly the closed-loop system eq. (4.47). Moreover,  $X$  and  $\bar{X}$  are related by

$$X(t) = \bar{X}(t) + \varepsilon \tilde{F}_1(\bar{X}(t)) F(\Omega t) + O(\varepsilon^2),$$

which is eqs. (4.50a) and (4.50b). Finally, we get eq. (4.50c) by injecting eq. (4.50a) in the expression of the output,

$$\begin{aligned}
y(t) &= h(x(t)) \\
&= h(\bar{x}(t) + \varepsilon g(\bar{x}(t)) F(\Omega t) + O(\varepsilon^2)) \\
&= h(\bar{x}(t)) + \varepsilon \mathcal{L}_g h(\bar{x}(t)) F(\Omega t) + O(\varepsilon^2).
\end{aligned}$$

We have assumed without loss of generality that  $F(0) = 0$ , which implies  $X(0) = \bar{X}(0)$ , as this is always possible by suitably shifting in time the signal  $f$ .  $\square$

**Corollary 1.** *Assume the signals  $h(\bar{x}(t))$  and  $\mathcal{L}_g h(\bar{x}(t))$  in eq. (4.50c) are available. Then the control law eq. (4.48) is actually implementable by choosing*

$$\begin{aligned}
\kappa(x, \Omega t) &:= -\varepsilon \mathcal{L}_g h(x) F(\Omega t) \\
\kappa_v(x, \Omega t) &:= -\varepsilon \mathcal{L}_g^2 h(x) F(\Omega t).
\end{aligned}$$

*Proof.* Using eq. (4.50a) we obviously have

$$\begin{aligned}
h(x) - \varepsilon \mathcal{L}_g h(x) F(\Omega t) &= h(\bar{x} + \varepsilon g(\bar{x}) F(\Omega t) + O(\varepsilon^2)) \\
&\quad - \varepsilon \mathcal{L}_g h(\bar{x} + \varepsilon g(\bar{x}) F(\Omega t) + O(\varepsilon^2)) F(\Omega t) \\
&= h(\bar{x}) + O(\varepsilon^2) \\
\mathcal{L}_g h(x) - \varepsilon \mathcal{L}_g^2 h(x) F(\Omega t) &= \mathcal{L}_g h(\bar{x}) + O(\varepsilon^2),
\end{aligned}$$

i.e.  $\bar{y} = h(\bar{x})$  in eq. (4.48c) and  $\bar{y}_v = \mathcal{L}_g h(\bar{x})$  in eq. (4.48d).  $\square$

### 4.3.3 Extracting the measurements

We now turn to extracting the information contained in eq. (4.50c), so that the  $h(\bar{x}(t))$  and  $\mathcal{L}_g h(\bar{x}(t))$  are available as proposed in corollary 1 and the control law proposed in eq. (4.46) can be implemented. In other words, given a signal of the form

$$y(t) = \bar{y}(t) + \varepsilon \tilde{y}(t) F(\Omega t) + \nu(t), \quad (4.52)$$

corrupted by the measurement noise  $\nu$ , we would like to recover its components  $\bar{y}(t)$  and  $\tilde{y}(t)$ . We will show this can be achieved by the estimators

$$\widehat{\bar{y}}(t) := \frac{1}{T} \int_{t-T}^t y(\tau) d\tau \quad (4.53a)$$

$$\widehat{\tilde{y}}(t) := \frac{\frac{1}{T} \int_{t-T}^t \left( y\left(\tau - \frac{T}{2}\right) - \widehat{\bar{y}}(\tau) \right) F\left(\Omega\left(\tau - \frac{T}{2}\right)\right) d\tau}{\frac{1}{T} \int_{t-T}^t F^2(\Omega\tau) d\tau}, \quad (4.53b)$$

where  $T := n\varepsilon = \frac{n}{\Omega}$  is a multiple of the HF signal period. We study the accuracy of these estimators without noise in section 4.3.3.1, and their sensitivity to noise in section 4.3.3.2. Indeed, since the noise is additive and enters the estimators linearly, the two issues can be studied independently.

### 4.3.3.1 Accuracy of the estimators

**Proposition 1.** *The accuracy of the estimators eq. (4.53a) and eq. (4.53b) is as follows*

$$\widehat{\bar{y}}(t) = \bar{y}\left(t - \frac{T}{2}\right) + O(T^2) = \bar{y}(t) + O(T) \quad (4.54a)$$

$$\widehat{\tilde{y}}(t) = \tilde{y}(t) + O\left(\frac{T^2}{\varepsilon}\right) \quad (4.54b)$$

*Proof.* The signals  $\bar{y}$  and  $\tilde{y}$  are considered to be continuously derivable. Such signals can be written as Taylor series with integral remainder

$$\begin{aligned} \bar{y}(t - \delta t) &= \bar{y}(t) - \delta t \dot{\bar{y}}(t) + \delta t^2 \bar{R}(t, \delta t) \\ \tilde{y}(t - \delta t) &= \tilde{y}(t) - \delta t \dot{\tilde{y}}(t) + \delta t^2 \tilde{R}(t, \delta t), \end{aligned}$$

with for all  $t \in \mathbb{R}$ ,  $\bar{R}(t, \delta t)$  and  $\tilde{R}(t, \delta t)$  bounded for  $\delta t \in [0, T]$ . Using these expressions, we find

$$\begin{aligned} \widehat{\bar{y}}(t) &= \frac{1}{T} \int_{t-T}^t \bar{y}(\tau) d\tau + \varepsilon \frac{1}{T} \int_{t-T}^t \tilde{y}(\tau) F(\Omega\tau) d\tau \\ &= \frac{1}{T} \int_0^T \bar{y}(t - \delta t) d\delta t + \varepsilon \frac{1}{T} \int_0^T \tilde{y}(t - \delta t) F(\Omega(t - \delta t)) d\delta t \\ &= \bar{y}(t) \frac{1}{T} \int_0^T d\delta t - \dot{\bar{y}}(t) \frac{1}{T} \int_0^T \delta t d\delta t + \frac{1}{T} \int_0^T \delta t^2 \bar{R}(t, \delta t) d\delta t \\ &\quad + \varepsilon \tilde{y}(t) \frac{1}{T} \int_0^T F(\Omega(t - \sigma)) d\delta t - \varepsilon \dot{\tilde{y}}(t) \frac{1}{T} \int_0^T \delta t F(\Omega(t - \sigma)) d\delta t \\ &\quad + \varepsilon \frac{1}{T} \int_0^T \delta t^2 \tilde{R}(t, \delta t) F(\Omega(t - \sigma)) d\delta t \\ &= \bar{y}(t) - \frac{T}{2} \dot{\bar{y}}(t) + \frac{T^2}{3} O(1) \\ &\quad + \varepsilon^2 \mathcal{F}(\Omega t) - \frac{\varepsilon T^2}{3} \sup_{\delta t \in [0, T]} (|F(\Omega(t - \delta t))|) O(1) \\ &= \bar{y}\left(t - \frac{T}{2}\right) + O(T^2) \end{aligned}$$

where  $\mathcal{F}$  is the anti-derivative of  $F$  with zero mean. Consequently, we have

$$\frac{y\left(t - \frac{T}{2}\right) - \widehat{\bar{y}}(t)}{\varepsilon} = \tilde{y}\left(t - \frac{T}{2}\right) F\left(\Omega\left(t - \frac{T}{2}\right)\right) + O\left(\frac{T^2}{\varepsilon}\right)$$

which leads to

$$\begin{aligned}
\overline{F\hat{y}}(t) &= \frac{1}{T} \int_{t-T}^t \tilde{y}\left(\tau - \frac{T}{2}\right) F\left(\Omega\left(\tau - \frac{T}{2}\right)\right)^2 + O\left(\frac{T^2}{\varepsilon}\right) \\
&= \frac{1}{T} \int_0^T \tilde{y}\left(t - \delta t - \frac{T}{2}\right) F\left(\Omega\left(t - \delta t - \frac{T}{2}\right)\right)^2 d\delta t + O\left(\frac{T^2}{\varepsilon}\right) \\
&= \tilde{y}\left(t - \frac{T}{2}\right) \frac{1}{T} \int_0^T F\left(\Omega\left(t - \delta t - \frac{T}{2}\right)\right)^2 d\delta t \\
&\quad - \dot{\tilde{y}}\left(t - \frac{T}{2}\right) \frac{1}{T} \int_0^T \delta t F\left(\Omega\left(t - \delta t - \frac{T}{2}\right)\right)^2 d\delta t \\
&\quad + \frac{1}{T} \int_0^T \delta t^2 \tilde{R}\left(t - \frac{T}{2}, \delta t\right) F\left(\Omega\left(t - \delta t - \frac{T}{2}\right)\right)^2 d\delta t + O\left(\frac{T^2}{\varepsilon}\right) \\
&= \overline{F^2\tilde{y}}\left(t - \frac{T}{2}\right) - \varepsilon \dot{\tilde{y}}\left(t - \frac{T}{2}\right) \mathcal{F}_2\left(\Omega\left(t - \frac{T}{2}\right)\right) \\
&\quad + \frac{T^2}{3} \sup_{\delta t \in [0, T]} \left| F^2\left(t - \delta t - \frac{T}{2}\right) \right| O(1) + O\left(\frac{T^2}{\varepsilon}\right) \\
&= \overline{F^2\tilde{y}}(t) + O\left(\frac{T^2}{\varepsilon}\right)
\end{aligned}$$

where  $\mathcal{F}_2$  is the anti-derivative of  $F^2$  with zero mean. □

It should be noted that the simpler formula

$$\hat{\tilde{y}}(t) = \frac{\frac{1}{T} \int_{t-T}^t y(\tau) F\left(\frac{\tau}{\varepsilon}\right) d\tau}{\varepsilon \frac{1}{T} \int_{t-T}^t F\left(\frac{\tau}{\varepsilon}\right)^2 d\tau} \quad (4.55)$$

proposed in Jebai, Malrait, *et al.* [43] by considering  $\bar{y}$  and  $\tilde{y}$  are constant on one period  $\varepsilon$  of the high-frequency signal is less accurate than eq. (4.53b), since valid only if  $\bar{y}$  and  $\tilde{y}$  vary very slowly.

### 4.3.3.2 Sensitivity to noise

As the virtual measurement estimate is scaled by a factor  $\varepsilon$ , it may be more sensitive to noise than the original measurement. To study this issue, we assume the measurement noise  $\nu$  is white with Power Spectral Density PSD  $[\nu]$  (independent on the frequency). For simplicity, we moreover consider eq. (4.55) instead of eq. (4.53b). The additive noise  $\nu$  obviously creates additive noises on the estimates  $\hat{\tilde{y}}$  and  $\hat{\bar{y}}$ , denoted respectively  $\tilde{\nu}$  and  $\bar{\nu}$ . Their PSDs are given by

$$\begin{aligned}
\text{PSD}[\bar{\nu}](\omega) &= \text{PSD}[\nu](\omega) |H(j\omega)|^2 \\
\text{PSD}[\tilde{\nu}](\omega) &= \frac{1}{\varepsilon^2 F^2} \text{PSD}[F\nu](\omega) |H(j\omega)|^2,
\end{aligned}$$

where  $H(j\omega) := \frac{1-e^{-jT\omega}}{jT\omega} = \exp\left(-j\frac{T}{2}\omega\right) \text{sinc}\left(\frac{T}{2}\omega\right)$  is the transfer function of the sliding average. It remains to compute PSD  $[F\nu]$ , i.e. the Fourier transform of the autocorrelation

of  $F(\Omega t)\nu(t)$  which is non-stationary. The autocorrelation is

$$\begin{aligned} R(\tau) &= \lim_{\Delta T \rightarrow \infty} \frac{1}{2\Delta T} \int_{-\Delta T}^{\Delta T} F(\Omega t)F(\Omega(t+\tau))\nu(t)\nu(t+\tau)dt \\ &= \lim_{\Delta T \rightarrow \infty} \frac{1}{2\Delta T} \int_{-\Delta T}^{\Delta T} F(\Omega t)F(\Omega(t+\tau))dt \lim_{\Delta T \rightarrow \infty} \frac{1}{2\Delta T} \int_{-\Delta T}^{\Delta T} \nu(t)\nu(t+\tau)dt \\ &= \left( \Omega \int_0^{\frac{1}{\Omega}} F(\Omega t)F(\Omega(t+\tau))dt \right) \text{PSD}[\nu] \delta(\tau) \\ &= \overline{F^2} \text{PSD}[\nu] \delta(\tau), \end{aligned}$$

since  $F$  and  $\nu$  are independent. The signal  $\nu(t)F(\Omega t)$  thus behaves in average as a white noise with a reduced PSD.

As the cardinal sine function is bounded by the inverse function after one period, the gain of the sliding average over a time range  $n\varepsilon$  is bounded by the gain of a low-pass filter with bandwidth  $2\frac{2\pi}{T}$ . The estimators  $\hat{y}$  and  $\tilde{y}$  thus have a built-in filtering effect. To decrease the influence of measurement noise, we can therefore

- increase the amplitude of the high-frequency oscillation  $f$ , without exceeding  $O(1)$
- average on a longer time by using a larger  $n$ , at the cost of a larger delay.

## 4.4 State estimator using high frequency injection

As explained in sections 4.2 and 4.3, HF frequency injection in IMs gives two new virtual measurements

$$\tilde{i}_s^{dq} = \frac{\partial^2 \mathcal{H}^{dq} \tilde{u}_s^{dq}}{\partial \phi_s^{dq2} \Omega} \quad (4.56)$$

on top of the still available current  $i_s^{dq}$  measurements. In the SynRM and PMSM cases (see Capecchi, Guglielmi, *et al.* [49] and Jebai, Malrait, *et al.* [43] respectively), the virtual measurements directly depend on the position of the rotor. Hence the rotor position can easily be retrieved thanks to signal injection.

However, in the IM case, neither the rotor position nor its speed can be retrieved directly from the virtual measurements. Nevertheless, the rotor and stator fluxes can be retrieved from the currents and the virtual measurements, provided an accurate saturated model of the IM is known, as is explained in section 4.4.1. But we will also show that in some kind of IMs whose magnetic saliency is too small, this estimation is greatly disturbed by measurement errors and thus unusable. This issue is addressed in section 4.4.2, where an observer for the rotor speed and the stator and rotor fluxes is proposed.

### 4.4.1 Flux estimator

As explained above, thanks to HF voltage injection, we obtain two virtual measurements

$$\tilde{i}_s^{dq} = \frac{\partial \mathcal{H}^{dq}}{\partial \phi_s^{dq}}(\overline{\phi}_s^{dq}, \overline{\phi}_r^{dq}) \quad (4.57a)$$

$$\tilde{i}_s^{dq} = \frac{\partial^2 \mathcal{H}^{dq}}{\partial \phi_s^{dq2}}(\overline{\phi}_s^{dq}, \overline{\phi}_r^{dq}) \tilde{\phi}_s^{dq}. \quad (4.57b)$$

Function	Expression	Parameter	Value
$f_m(x)$	$\Gamma_m^{dq} \left(1 + \frac{x^2}{\phi_m^2}\right)$	$\Gamma_m^{dq}$	$0.52H^{-1}$
$f_L(x)$	$\Gamma_L^{dq} \left(1 + \frac{x^2}{\phi_L^2}\right)$	$\Gamma_L^{dq}$	$4.25H^{-1}$
		$\phi_m$	$3.16Wb$
		$\phi_L$	$1Wb$

Table 4.2 – Magnetic parameters for the model eq. (4.59)

Eq. (4.57) is a non linear system with 4 equations and 4 unknowns. The implicit function theorem states that it can be inverted if

$$\det \begin{pmatrix} \frac{\partial^2 \mathcal{H}^{dq}}{\partial \phi_s^{dq^2}} & \frac{\partial^2 \mathcal{H}^{dq}}{\partial \phi_s^{dq} \partial \phi_r^{dq}} \\ \frac{\partial}{\partial \phi_s^{dq}} \left( \frac{\partial^2 \mathcal{H}^{dq}}{\partial \phi_s^{dq^2}} \tilde{\phi}_s^{dq} \right) & \frac{\partial}{\partial \phi_r^{dq}} \left( \frac{\partial^2 \mathcal{H}^{dq}}{\partial \phi_s^{dq^2}} \tilde{\phi}_s^{dq} \right) \end{pmatrix} \neq 0 \quad (4.58)$$

where the matrix is computed at the flux working point  $(\bar{\phi}_s^{dq}, \bar{\phi}_r^{dq})$ . Under this condition, we manage to estimate the fluxes around the permanent trajectory  $\omega_{s,e} = 0$ , which is not possible without HF injection, as was shown in section 4.1.4.

However, the condition eq. (4.58) is not always verified, depending on the motor model, the working point and on the direction of the injection. Indeed, the determinant will be an offset sinusoidal function with respect to the HF injection direction, which crosses the horizontal axis at some point depending on the working point.

We still tried this approach in simulation on an IM driven by a closed loop control law with speed measurement at low speed. The IM is modeled by the energy function

$$\begin{aligned} \underline{\mathcal{H}}^{dq}(\rho, \underline{\phi}_s^{dq}, \underline{\phi}_r^{dq}) &= \frac{1}{2J_L n^2} \rho^2 + \frac{1}{2} f_m \left( \left| \underline{\phi}_s^{dq} + \underline{\phi}_r^{dq} \right| \right) \left| \underline{\phi}_s^{dq} + \underline{\phi}_r^{dq} \right|^2 \\ &\quad + \frac{1}{2} f_L \left( \left| \underline{\phi}_s^{dq} - \underline{\phi}_r^{dq} \right| \right) \left| \underline{\phi}_s^{dq} - \underline{\phi}_r^{dq} \right|^2. \end{aligned} \quad (4.59)$$

with parameters listed in table 4.2. This model is proposed in section 5.3.3 to explain the behavior of an unloaded IM. For this model we numerically found out that the condition eq. (4.58) is always true for directions congruent with  $\frac{\pi}{18}$  modulo  $\frac{\pi}{2}$ . We applied the method proposed in section 7.1.3 to obtain the averaged stator current  $\bar{i}_s^{dq}$  and the amplitude of stator current ripple the  $\tilde{i}_s^{dq}$ . The results of the simulation are given in fig. 4.5. Even though the norm of the flux is well estimated, the estimation of its angle is not good enough. As with the theoretical stator current amplitude, the fluxes are exactly estimated, we can conclude that the estimation errors stems from the measurement error on  $\tilde{i}_s^{dq}$ .

Indeed the error on the measurement of the stator current ripple amplitude  $\tilde{i}_s^{dq}$  impacts greatly the flux estimation. This is due to the fact that eq. (4.59) can be seen as a perturbation of the unsaturated model which does not verify the condition eq. (4.58) at any point. Using the scalar product of  $\mathcal{S}_2(\mathbb{R})$  introduced in the notation section (page xv), the projection of  $\frac{\partial^2 \mathcal{H}^{dq}}{\partial \phi_s^{dq^2}}$  on  $\text{span}(\{I_2\})^\perp$  is very small with respect to its projection on  $I_2$ . We can thus note

$$\frac{\partial^2 \mathcal{H}^{dq}}{\partial \phi_s^{dq^2}} = \alpha(\phi_s^{dq}, \phi_r^{dq}) I_2 + \varepsilon M(\phi_s^{dq}, \phi_r^{dq})$$

where  $M \in \text{span}(\{Z, Y\})$  and then the last 2 lines of the matrix of eq. (4.58) can be

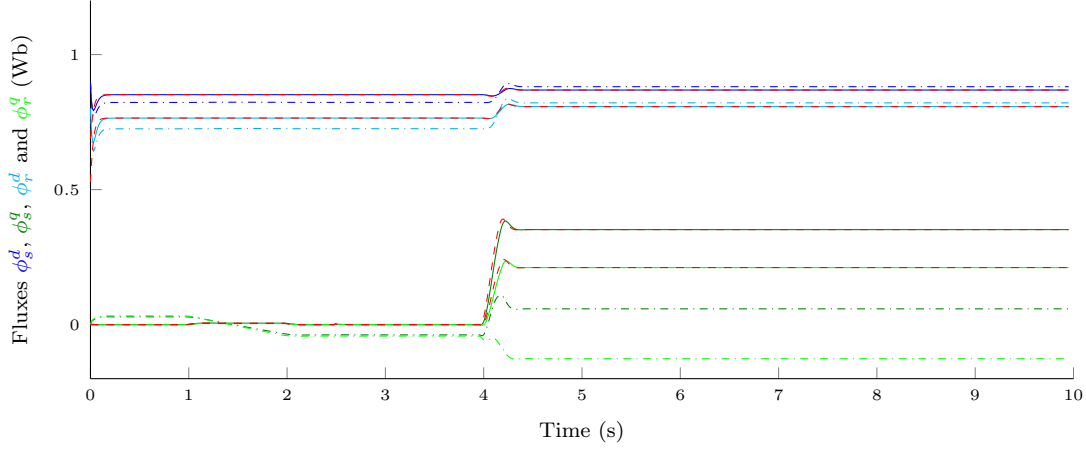


Figure 4.5 – Simulated flux (red dashed lines) and fluxes estimated using the measured current ripple (dash-dotted lines) and using the theoretical current ripple (solid lines).

written as

$$\begin{pmatrix} \tilde{\phi}_s^d \\ \tilde{\phi}_s^q \end{pmatrix} \begin{pmatrix} \frac{\partial \alpha}{\partial \phi_s^d} & \frac{\partial \alpha}{\partial \phi_s^q} & \frac{\partial \alpha}{\partial \phi_r^d} & \frac{\partial \alpha}{\partial \phi_r^q} \end{pmatrix} + \varepsilon \left( \frac{\partial}{\partial \phi_s^{dq}} \left( M(\phi_s^{dq}, \phi_r^{dq}) \tilde{\phi}_s^{dq} \right) \frac{\partial}{\partial \phi_r^{dq}} \left( M(\phi_s^{dq}, \phi_r^{dq}) \tilde{\phi}_s^{dq} \right) \right) \quad (4.60)$$

which means that the determinant of eq. (4.58) is of order  $\varepsilon$ . Consequently, the accuracy of the estimator will be low, which is what is observed in fig. 4.5.

From this computation, we can conclude that to retrieve observability of the fluxes at low-speed, the projection of  $\frac{\partial^2 \mathcal{H}^{dq}}{\partial \phi_s^{dq2}}$  on  $\text{span}(\{I_2\})^\perp$  must be large enough which is equivalent to having a large  $\frac{\partial^2 \mathcal{H}^{dq}}{\partial \phi_s^{dq*2}}$ .

#### 4.4.2 Full state estimator

The conclusion of section 4.4.1 is very pessimistic. Indeed, it states that on some IMs the fluxes cannot be retrieved from the virtual measurements  $\tilde{v}_s^{dq}$  and  $\tilde{v}_s^{dq}$ .

Nevertheless, signal injection still provides additional information: the projection of  $\frac{\partial^2 \mathcal{H}^{dq}}{\partial \phi_s^{dq2}}$  on  $\text{span}(\{I_2\})$ , which can be expressed as  $\frac{1}{2} \left( \frac{\partial^2 \mathcal{H}^{dq}}{\partial \phi_s^{dq2}} + \frac{\partial^2 \mathcal{H}^{dq}}{\partial \phi_s^{q2}} \right)$  or, using complex variables,  $\frac{\partial^2 \mathcal{H}^{dq}}{\partial \phi_s^{dq} \partial \phi_s^{dq*}}$ . This signal will be noted  $\tilde{y}$  here. Besides, the condition eq. (4.58) does not coincide with the condition found by the nonlinear observability study (eq. (4.29a)). All this let us hope that low speed “sensorless” observability may still be recovered thanks to HF injection.

We thus study the linear observability of the IM at low speed with only one virtual measurement. In addition to observe the fluxes we now want also the mechanical speed. The linearized matrices are

$$A := \begin{pmatrix} -R_s \frac{\partial^2 \mathcal{H}^{dq}}{\partial \phi_s^{dq2}} - \mathcal{J}_2 \omega_s & -R_s \frac{\partial^2 \mathcal{H}^{dq}}{\partial \phi_s^{dq} \partial \phi_r^{dq}} & 0_{2,1} \\ -R_r \frac{\partial^2 \mathcal{H}^{dq}}{\partial \phi_r^{dq} \partial \phi_s^{dq}} & -R_r \frac{\partial^2 \mathcal{H}^{dq}}{\partial \phi_r^{dq2}} - \mathcal{J}_2 (\omega_s - n \omega_m) & \mathcal{J}_2 \phi_r^{dq} \\ 0_{1,2} & 0_{1,2} & 0 \end{pmatrix}$$

$$C := \begin{pmatrix} \frac{\partial^2 \mathcal{H}^{dq}}{\partial \phi_s^{dq} \partial \phi_r^{dq}} & \frac{\partial^2 \mathcal{H}^{dq}}{\partial \phi_s^{dq} \partial \phi_r^{dq}} & 0_{2,1} \\ \frac{\partial}{\partial \phi_s^{dq}} \left( \frac{\partial^2 \mathcal{H}^{dq}}{\partial \phi_s^{dq2}} + \frac{\partial^2 \mathcal{H}^{dq}}{\partial \phi_s^{q2}} \right) & \frac{\partial}{\partial \phi_r^{dq}} \left( \frac{\partial^2 \mathcal{H}^{dq}}{\partial \phi_s^{dq2}} + \frac{\partial^2 \mathcal{H}^{dq}}{\partial \phi_s^{q2}} \right) & 0 \end{pmatrix}$$

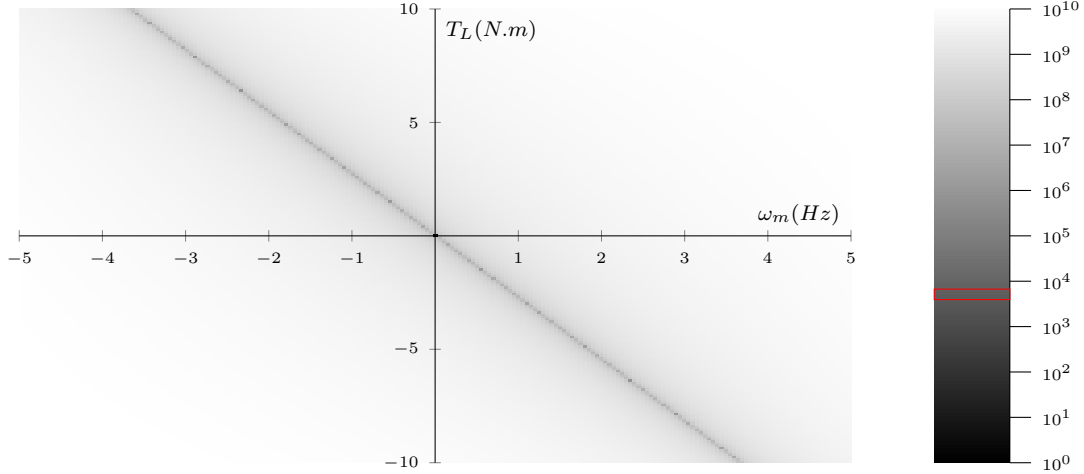


Figure 4.6 – Absolute value of the observability criterion in logarithmic scale. For comparison, the red rectangle is the determinant which is obtained in for the criterion of section 4.4.1.

where the third equation was not used so that we do not need to include  $T_L$  which would complicate the study.

We numerically computed the determinant of the observability matrix

$$\mathcal{O} := \begin{pmatrix} C \\ CA \end{pmatrix}$$

where only the 2 first lines of  $A$  are used. The result as a function of the mechanical speed and electromagnetic torque is shown in fig. 4.6. It is compared to the value of the determinant of eq. (4.58) and we thus found out that the observability is far better.

These results are very encouraging. We designed an observer for the flux and the speed in the following way. Classically we used the error on the currents to adjust the estimates of the fluxes by

$$\frac{d\hat{\phi}_s^{dq}}{dt} = u_s^{dq} - R_s \hat{i}_s^{dq} - \mathcal{J}_2 \omega_s \hat{\phi}_s^{dq} + L(\iota_s^{dq,m} - \hat{i}_s^{dq}) \quad (4.61a)$$

$$\frac{d\hat{\phi}_r^{dq}}{dt} = -R_r \hat{i}_r^{dq} - \mathcal{J}_2(\omega_s - n\hat{\omega}_m) \hat{\phi}_r^{dq} \quad (4.61b)$$

where we used the compact notations

$$\hat{i}_s^{dq} := \frac{\partial \mathcal{H}^{dq}}{\partial \phi_s^{dq}}(\hat{\phi}_s^{dq}, \hat{\phi}_r^{dq})$$

$$\hat{i}_r^{dq} := \frac{\partial \mathcal{H}^{dq}}{\partial \phi_r^{dq}}(\hat{\phi}_s^{dq}, \hat{\phi}_r^{dq}).$$

At this point, the virtual measurement was not used yet, but estimate of the speed was not designed yet either. The error dynamics read

$$\frac{d\Delta\phi_s^{dq}}{dt} = -(R_s + L)(\iota_s^{dq} - \hat{i}_s^{dq}) - \mathcal{J}_2 \omega_s \Delta\phi_s^{dq} \quad (4.62a)$$

$$\frac{d\Delta\phi_r^{dq}}{dt} = -R_r(\iota_r^{dq} - \hat{i}_r^{dq}) - \mathcal{J}_2(\omega_s - n\omega_m) \Delta\phi_r^{dq} + \mathcal{J}_2 n \Delta\omega_m \hat{\phi}_r^{dq}. \quad (4.62b)$$

Following Lohmiller and Slotine [60], the associated virtual displacement can be obtained by linearizing these equations around 0. Let our metric on virtual displacements be

$$E := \frac{\|\delta\Delta\phi_s^{dq}\|^2}{2(R_s + L)} + \frac{\|\delta\Delta\phi_r^{dq}\|^2}{2R_r}$$

where we noted  $\delta\Delta\phi_s^{dq}$  and  $\delta\Delta\phi_r^{dq}$  the virtual displacements associated with  $\Delta\phi_s^{dq}$  and  $\Delta\phi_r^{dq}$  respectively. Its time derivative is calculated as follows

$$\begin{aligned} \frac{dE}{dt} &= -\delta\Delta\phi_s^{dqT} \left( \frac{\partial^2 \mathcal{H}^{dq}}{\partial \phi_s^{dq2}} \delta\Delta\phi_s^{dq} - \frac{\partial^2 \mathcal{H}^{dq}}{\partial \phi_s^{dq} \partial \phi_r^{dq}} \delta\Delta\phi_r^{dq} + \mathcal{J}_2 \frac{\omega_s}{R_s + L} \delta\Delta\phi_s^{dq} \right) \\ &\quad - \delta\Delta\phi_r^{dqT} \left( \frac{\partial^2 \mathcal{H}^{dq}}{\partial \phi_r^{dq} \partial \phi_s^{dq}} \delta\Delta\phi_s^{dq} - \frac{\partial^2 \mathcal{H}^{dq}}{\partial \phi_r^{dq2}} \delta\Delta\phi_r^{dq} + \mathcal{J}_2 \frac{\omega_s - n\omega_m}{R_r} \delta\Delta\phi_s^{dq} \right) \\ &\quad + \delta\Delta\phi_r^{dqT} \mathcal{J}_2 \Delta\omega_m \hat{\phi}_r^{dq} \\ &= \begin{pmatrix} -\delta\Delta\phi_s^{dqT} & \delta\Delta\phi_r^{dqT} \end{pmatrix} \begin{pmatrix} \frac{\partial^2 \mathcal{H}^{dq}}{\partial \phi_s^{dq2}} + \mathcal{J}_2 \frac{\omega_s}{R_s + L} & \frac{\partial^2 \mathcal{H}^{dq}}{\partial \phi_s^{dq} \partial \phi_r^{dq}} \\ \frac{\partial^2 \mathcal{H}^{dq}}{\partial \phi_r^{dq} \partial \phi_s^{dq}} & \frac{\partial^2 \mathcal{H}^{dq}}{\partial \phi_r^{dq2}} + \mathcal{J}_2 \frac{\omega_s - n\omega_m}{R_r} \end{pmatrix} \begin{pmatrix} -\delta\Delta\phi_s^{dq} \\ \delta\Delta\phi_r^{dq} \end{pmatrix} \\ &\quad + \delta\Delta\phi_r^{dqT} \mathcal{J}_2 \Delta\omega_m \hat{\phi}_r^{dq} \end{aligned} \quad (4.63)$$

which shows by contraction (see [60]) that the observer would be a good estimator of the fluxes if there were no error on the speed estimate (for instance in the case a control law with a mechanical speed sensor), as the Hessian of the energy is definite positive.

Eq. (4.62) also shows that a positive  $\Delta\omega_m$  induces a overestimated rotor flux which in turn leads with the proposed model to an over estimated current ripple. The following scheme is proposed to get an estimate of  $\omega_m$

$$\frac{d\omega^i}{dt} = \tilde{K}_i \left( \frac{1}{2} \left( \frac{\partial^2 \mathcal{H}^{dq}}{\partial \phi_s^{dq2}} (\hat{\phi}_s^{dq}, \hat{\phi}_r^{dq}) + \frac{\partial^2 \mathcal{H}^{dq}}{\partial \phi_s^{dq2}} (\hat{\phi}_s^{dq}, \hat{\phi}_r^{dq}) \right) - \tilde{y} \right) \quad (4.64a)$$

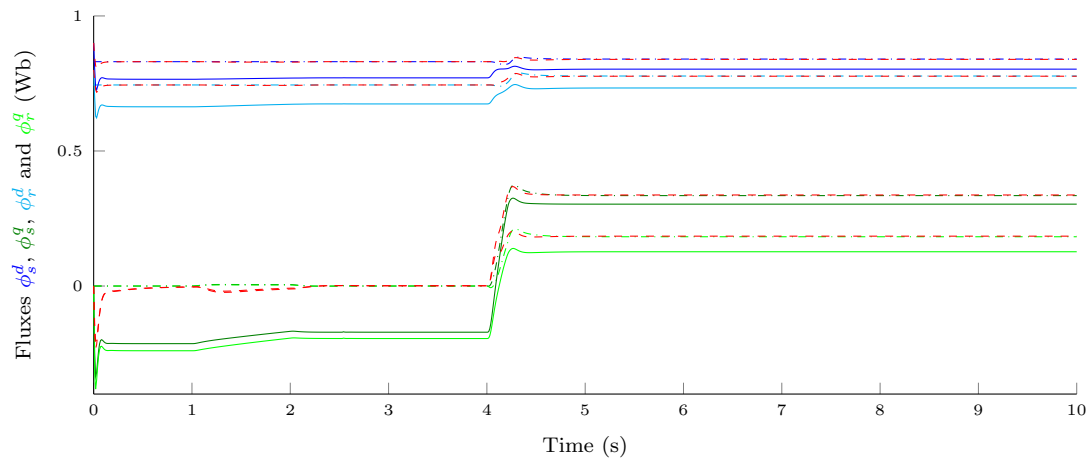
$$\hat{\omega}_m = \omega^i + \tilde{K}_p \left( \frac{1}{2} \left( \frac{\partial^2 \mathcal{H}^{dq}}{\partial \phi_s^{dq2}} (\hat{\phi}_s^{dq}, \hat{\phi}_r^{dq}) + \frac{\partial^2 \mathcal{H}^{dq}}{\partial \phi_s^{dq2}} (\hat{\phi}_s^{dq}, \hat{\phi}_r^{dq}) \right) - \tilde{y} \right). \quad (4.64b)$$

The proposed observer was tested in the same model as in section 4.4.1 (see eq. (4.59) and table 4.2). To test the observed we simulated a “sensored” control law under MATLAB Simulink<sup>®</sup>. Signal injection was used and the virtual measurement  $\tilde{y}$  was retrieved using the procedure described in section 7.1.3. The bandwidth of the speed estimation in the state observer was set to  $10Hz$ . Simulation results are given in fig. 4.7 which shows a far better flux estimation than obtained in section 4.4.1. Besides, the speed estimate could be used in a “sensorless” control law.

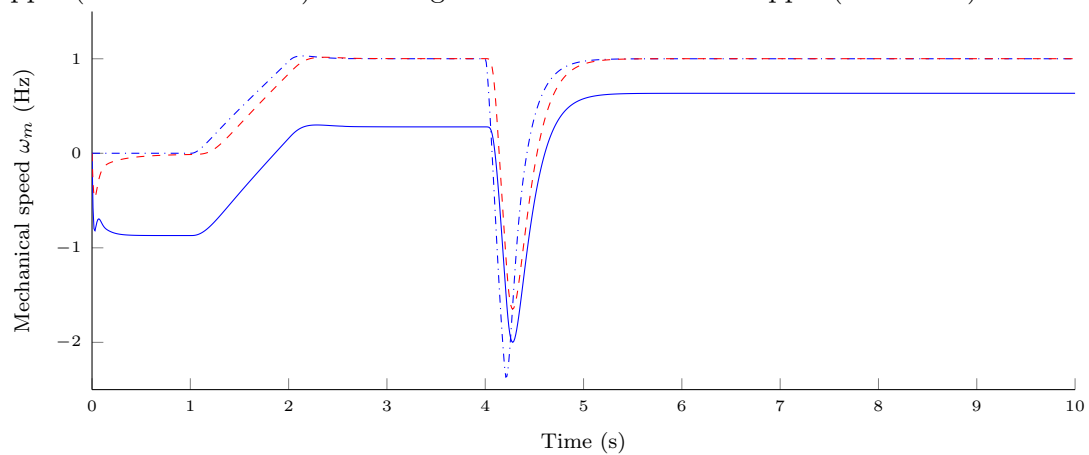
This show how signal injection can be used to retrieve the speed of an IM with a small magnetic saliency. The procedure is far more involved than for PMSMs (see Jebai, Malrait, *et al.* [43]) or SynRMs (see Capecchi, Guglielmi, *et al.* [49]). We think that the proposed method could also be used to improve existing “sensorless” control laws using signal injection.

## 4.5 Partial conclusion

This chapter studies the observability of electric motors. Thanks to the similarities found by the modeling approach presented in chapter 3, a generic first-order observability result



(a) Simulated flux (red dashed lines) and fluxes estimated using the measured current ripple (dash-dotted lines) and using the theoretical current ripple (solid lines).



(b) Simulated speed (red dashed lines) and speeds estimated using the measured current ripple (dash-dotted lines) and using the theoretical current ripple (solid lines).

Figure 4.7 – Estimating the flux and speed thanks to the observer proposed in section 4.4.2 on the simulated IM with the model given by eq. (4.59) and table 4.2.

can be given: all electric motors are unobservable at first order with the sole stator current measurements when the stator excitation frequency  $\omega_{s,e}$  and its derivatives are zero. A nonlinear observability study adds no further information as long as we stay at the desired equilibrium, but it also shows that observability may be recovered on some close trajectories.

HF voltage signal injection is one of the solutions to implement such trajectories. A thorough analysis of this technique, which can be generalized to nonlinear systems, shows that additional information is retrieved. In the case of IMs, this information can be used to solve the low-speed observability problem. Observers which can retrieve the fluxes and the rotor angular speed are presented. However these results are still partial and can be improved.

# Chapter 5

## Identification of the magnetic models

### Chapitre 5 — Identification des modèles magnétiques

*Ce chapitre détaille les tentatives faites pour trouver des modèles magnétiques permettant d'expliquer les effets observés par injection de signal sur deux types de moteurs électriques. Le moteur synchrone à reluctance s'est avéré assez facile à modéliser et deux techniques pour le modéliser sont proposées dans ce chapitre. À cause d'effets liés à l'hystérésis magnétique, les deux techniques donnent des résultats sensiblement différents, mais tout de même compatibles. Au contraire, la modélisation du moteur à induction est bien plus ardue, à cause des deux variables d'état supplémentaires qui ne sont pas mesurées. Des résultats expérimentaux, ainsi que des tentatives de modélisation, sont donnés, mais aucun modèle complet n'a pu être trouvé pour modéliser les effets de l'injection de signal.*

Using the framework proposed in chapter 3 we now want to obtain models for real electric motors, namely the two described in section 2.1. As we always use star connected electric machines, thanks to the energy based approach this only involves finding the right function  $\mathcal{H}^{DQ}$ .

To calibrate the models we will use information retrieved using signal injection, the technique proposed in section 4.2 to retrieve low speed “sensorless” observability of electric motors. As explained there, thanks to HF signal injection we get additional measurements which are particularly useful to tune the model.

### 5.1 Preliminaries: Existing models for electric motors

Here is a review of traditional saturated models for SynRMs in section 5.1.1 and for IMs in section 5.1.2. We then recall the proposed saturated energy-based models.

#### 5.1.1 Saturation models for SynRMs

As in SynRMs electromagnetic torque is created by the difference between the  $d$ -axis and  $q$ -axis inductances, magnetic saturation is emphasized in most SynRM control literature.

Kilthau and Pacas [61], Stumberger, Stumberger, *et al.* [62] give interesting experimental data highlighting the saturation of inductances by the flux on both axes. Kilthau and Pacas [61] even propose a polynomial model for the saturation of the inductances as a function of the current, however it seems that the reciprocity conditions (see [29, 30])

are not enforced by their approach, which may thus lead to an invalid model from the point of view of the power balance.

Vagati, Pastorelli, *et al.* [63] propose a more rigorous modeling method, which relies on co-energy and thus enforces the reciprocity conditions. They also give experimental data, but no detailed model.

Finally Qu, Tuovinen, *et al.* [64] also give a model, which respects the reciprocity conditions, where the current are polynomial functions of the fluxes. Rewritten with our notations, the relations current-flux they propose read

$$\begin{aligned} \iota_s^D(\phi_s^{DQ}) &= \frac{\phi_s^D}{L_s^{0D}} \left( 1 + |\alpha\phi_s^D|^a + \frac{\gamma L_s^{0D}}{d+2} |\phi_s^D|^c |\phi_s^Q|^{d+2} \right) \\ \iota_s^Q(\phi_s^{DQ}) &= \frac{\phi_s^Q}{L_s^{0Q}} \left( 1 + |\beta\phi_s^Q|^b + \frac{\gamma L_s^{0Q}}{c+2} |\phi_s^D|^{c+2} |\phi_s^Q|^d \right) \end{aligned}$$

and stem from the energy function

$$\begin{aligned} \mathcal{H}^{DQ}(\phi_s^{DQ}) &= \frac{\rho^2}{2J_L n^2} \\ &+ \frac{1}{2L_s^{0D}} \left( 1 + \frac{|\alpha\phi_s^D|^a}{a+2} \right) \phi_s^{D2} + \frac{1}{2L_s^{0Q}} \left( 1 + \frac{|\beta\phi_s^Q|^b}{b+2} \right) \phi_s^{Q2} + \frac{\gamma |\phi_s^D|^{c+2} |\phi_s^Q|^{d+2}}{(c+2)(d+2)}. \end{aligned}$$

They calibrated the model (all positive real numbers) by measuring the back-EMF while the motor is run at 30% of the nominal speed.

## 5.1.2 Saturation models for IMs

IMs have been around for much longer than SynRMs. Hence there is a very detailed literature on the saturation of an IM, even though it is not as large as for SynRMs. In IMs, there are many magnetic paths which saturate differently:

- The main magnetic path where the magnetizing flux  $\phi_m^{dq} = \frac{\phi_s^{dq} + \phi_r^{dq}}{2}$  circulates, and
- The leakage magnetic paths where the leakage fluxes circulate.

### 5.1.2.1 Main magnetic path saturation

The main magnetic path saturation has been studied a lot because it limits the torque the IM can yield. The usual model for main flux saturation can be written  $\phi_m^{dq} = L_m^{dq} (\|\iota_m^{dq}\|^2) \iota_m^{dq}$  or equivalently  $\iota_m^{dq} = \Gamma_m^{dq} (\|\phi_m^{dq}\|^2) \phi_m^{dq}$  where  $\iota_m^{dq} = \frac{\iota_s^{dq} + \iota_r^{dq}}{2}$  (see for instance [17, 21]). This model is compatible with our energy-based approach. Indeed the associated energy function in  $dq$  reads

$$\mathcal{H}^{dq}(\phi_s^{dq}) = \frac{1}{2J_L n^2} \rho^2 + \frac{1}{2} F_m^{dq} (\phi_m^{dqT} \phi_m^{dq}) + \frac{1}{2} \Gamma_l^{dq} \phi_s^{dqT} \phi_s^{dq} + \frac{1}{2} \Gamma_r^{dq} \phi_r^{dqT} \phi_r^{dq} \quad (5.1)$$

where  $F_m^{dq}$  is the anti-derivative of  $\Gamma_m^{dq} - \Gamma_l^{dq}$ .

The problem is to find a suitable function  $L_m^{dq}$  or  $\Gamma_m^{dq}$ . Some of the possible functions  $L_m^{dq}$  or  $\Gamma_m^{dq}$  are given in [17, 21, 65, 66, 68]. These saturation functions for the main flux path explain well the torque limitation. However, as can be shown in simulation, it does not explain the effects of signal injection at all. This can be explained intuitively, because the HF signal injection does not follow the main flux paths but only the leakage flux paths, whose impedance at high frequencies is lower (see Jansen and Lorenz [78]).

### 5.1.2.2 Leakage magnetic path saturation

In fact, as emphasized by Boldea and Nassar [34], there are many leakage flux paths. Ojo, Consoli, *et al.* [20], Lipo and Consoli [69] model the saturation of each of these individual paths. This lead to a quite complicated model which is hardly rewritable in terms of energy or usable for control.

However Hinkkanen, Repo, *et al.* [46], Tuovinen, Hinkkanen, *et al.* [70] propose to start from the unsaturated model where all these magnetic paths are aggregated into one or two paths. This approach is closer to energy based modeling as it does not detail the internal layout of the motor. However [46] does not provide an explicit model. In [70] an explicit model is proposed which respects the reciprocity conditions. They start from the so-called “T-model” of the induction machine which however does not lead to the same Hamilton’s equations as those presented here for saturated electric motors. They propose to express the rotor current as a polynomial function of the magnetizing flux and the leakage flux. Calibration methods for this model are proposed in Ranta [68] and references therein.

In Sudhoff, Aliprantis, *et al.* [71] a more complex model is proposed for the relation between rotor flux  $\phi_r^{dq}$  and rotor current  $i_r^{dq}$  in IMs, which is written as a transfer function. This means that the proposed model has more state variables than traditional models. The proposed model cannot be easily expressed in our framework. In [72] a method is proposed to calibrate such models on real IMs.

### 5.1.3 Saturated energy-based models for electric motors

The premises of the proposed framework are found in Basic, Malrait, *et al.* [35], Basic, Jebai, *et al.* [36] where Lagrangian and Hamiltonian models are proposed for IMs and PMSMs. Magnetic saturation is also taken into account. Even though it is not clearly stated, the symmetry constraints found in section 3.4 are respected by the proposed models. However no experimental data is provided in these articles.

The first application of the proposed framework can be found in Jebai [37] where a saturated model is designed for PMSMs. The proposed model is a polynomial perturbation of the unsaturated model which respects the symmetry constrains (see section 3.4). The proposed energy function reads

$$\begin{aligned} \mathcal{H}^{DQ}(\rho, \phi_s^{DQ}) &= \frac{1}{2J_L n^2} \rho^2 \\ &+ \frac{1}{2L_s^D} (\phi_s^D - \phi_M)^2 + \frac{1}{2L_s^Q} (\phi_s^Q)^2 + \sum_{m=3}^4 \sum_{n=0}^{\lfloor \frac{m}{2} \rfloor} \alpha_{m-2n, 2n} (\phi_s^D - \phi_M)^{m-2n} (\phi_s^Q)^{2n} \end{aligned}$$

and leads to the current-flux relations

$$\begin{aligned} i_s^D(\phi_s^D) &= \frac{\partial \mathcal{H}^{DQ}}{\partial \phi_s^D} = \frac{\phi_s^D - \phi_M}{L_s^D} + \sum_{m=2}^3 \sum_{n=0}^{\lfloor \frac{m}{2} \rfloor} (m-2n+1) \alpha_{m-2n+1, 2n} (\phi_s^D - \phi_M)^{m-2n} (\phi_s^Q)^{2n} \\ i_s^Q(\phi_s^Q) &= \frac{\partial \mathcal{H}^{DQ}}{\partial \phi_s^Q} = \frac{\phi_s^Q}{L_s^Q} + \sum_{m=2}^3 \sum_{n=1}^{\lfloor \frac{m}{2} \rfloor} 2n \alpha_{m-(2n-1), 2n} (\phi_s^D - \phi_M)^{m-(2n-1)} (\phi_s^Q)^{2n-1}. \end{aligned}$$

This can be seen as a Taylor series expansion around the nominal flux working point of the PMSM, which does not change much as the flux remains close to the rotor flux. A calibration procedure using HF signal injection was then proposed in [37].

## 5.2 A saturated SynRM model

In this section we will derive the simplest saturated sinusoidal model describing experimental observations for the SynRM described in section 2.1.1. As was explained at the beginning of section 3.8, the model should be expressed in the  $DQ0$  frame so that the energy function does not depend on  $\theta$ . Moreover the motor being star-connected, the 0 axis can be decoupled when doing magnetic modeling (see section 3.5.3). Hence, it can be expressed as  $\mathcal{H}^{DQ}(\rho, \phi_s^{DQ})$  with the energy function being even with respect to  $\phi_s^D$  and  $\phi_s^Q$  as recalled in table 3.5.

### 5.2.1 Using HF injection

From section 4.2.3 we know that HF injection gives us insight on the partial derivatives of the energy function, also called tangent inductances (see section 3.8.2). In this section we are going to use this information to design a saturation model for SynRMs.

#### 5.2.1.1 Experimental procedure

To study cross-saturation we need to have non-zero constant flux on both  $D$  and  $Q$  axes, which creates torque. To prevent the motor from rotating under this torque we lock the rotor.

We then need to identify the orientation of the  $DQ$  frame with respect to the  $\alpha\beta$  frame. By convention, we take  $D$  axis to be the smallest inductance axis and  $Q$  axis to have the largest inductance. Two methods can be used:

- Use HF injection under zero flux which will enable us to retrieve easily the  $D$  and  $Q$  axes by maximizing and minimizing the size of the HF current ripple on the injection axis or
- Inject nominal DC current along the supposed  $Q$  axis and correct until the torque-meter gives the lowest value.

I used the second method, which turned out to be more accurate when done manually.

A constant voltage  $u_s^{DQ}$  is then set which produces a measured constant current  $i_s^{DQ}$ . The currents are the only piece of information we can obtain on the magnetic state of the motor as the fluxes  $\phi_s^{DQ}$  cannot be measured.

To gather all the information which can be found using HF injection, we inject the HF voltage along an axis rotating slowly (at  $\dot{\theta}_i = \omega_i = 1Hz$ ) in the  $DQ$  frame. This defines a new  $vw$  frame with  $P_{DQ \rightarrow vw}(\theta_i) = \mathcal{R}(-\theta_i)$ , the rotation of  $\mathbb{R}^2$  by the angle  $-\theta_i$ . Using complex notations it reads  $\tilde{u}_s^{DQ} = \tilde{u}e^{j\omega_i t} f(\Omega t)$ . This HF injection creates current ripple on both the injection and quadrature axes.

#### 5.2.1.2 Theoretical analysis

According to section 4.2.3, the injection  $\tilde{u}_s^{DQ}$  produces the current ripple in the  $DQ$  frame

$$\tilde{i}_s^{DQ} = 2 \frac{\partial^2 \mathcal{H}^{DQ}}{\partial \phi_s^{DQ} \partial \phi_s^{DQ*}} \frac{\tilde{u}}{\Omega} e^{j\omega_i t} F(\Omega t) + 2 \frac{\partial^2 \mathcal{H}^{DQ}}{\partial \phi_s^{DQ*2}} \frac{\tilde{u}}{\Omega} e^{-j\omega_i t} F(\Omega t) \quad (5.2)$$

and transforming back to  $vw$  frame

$$\tilde{i}_s^{vw} = \tilde{i}_s^{DQ} e^{-j\omega_i t} = 2 \frac{\partial^2 \mathcal{H}^{DQ}}{\partial \underline{\phi}_s^{DQ} \partial \underline{\phi}_s^{DQ*}} \frac{\tilde{u}}{\Omega} F(\Omega t) + 2 \frac{\partial^2 \mathcal{H}^{DQ}}{\partial \underline{\phi}_s^{DQ*2}} \frac{\tilde{u}}{\Omega} e^{-j2\omega_i t} F(\Omega t). \quad (5.3)$$

Projecting on the axes of the  $vw$  frame, we find the expression of the recorded ripples

$$\begin{aligned} \tilde{i}_s^v = \Re \tilde{i}_s^{vw} &= 2 \frac{\partial^2 \mathcal{H}^{DQ}}{\partial \underline{\phi}_s^{DQ} \partial \underline{\phi}_s^{DQ*}} \frac{\tilde{u}}{\Omega} F(\Omega t) \\ &+ 2 \left| \frac{\partial^2 \mathcal{H}^{DQ}}{\partial \underline{\phi}_s^{DQ*2}} \right| \frac{\tilde{u}}{\Omega} \cos \left( 2\omega_i t - \text{Arg} \frac{\partial^2 \mathcal{H}^{DQ}}{\partial \underline{\phi}_s^{DQ*2}} \right) F(\Omega t) \end{aligned} \quad (5.4a)$$

$$\tilde{i}_s^w = \Im \tilde{i}_s^{vw} = -2 \left| \frac{\partial^2 \mathcal{H}^{DQ}}{\partial \underline{\phi}_s^{DQ*2}} \right| \frac{\tilde{u}}{\Omega} \sin \left( 2\omega_i t - \text{Arg} \frac{\partial^2 \mathcal{H}^{DQ}}{\partial \underline{\phi}_s^{DQ*2}} \right) F(\Omega t) \quad (5.4b)$$

as  $\frac{\partial^2 \mathcal{H}^{DQ}}{\partial \underline{\phi}_s^{DQ} \partial \underline{\phi}_s^{DQ*}}$  is real. Thus, the amplitude of the current ripple on the injection axis should

be modulated by a sinusoid of amplitude  $2 \left| \frac{\partial^2 \mathcal{H}^{DQ}}{\partial \underline{\phi}_s^{DQ*2}} \right|$  with an offset  $2 \frac{\partial^2 \mathcal{H}^{DQ}}{\partial \underline{\phi}_s^{DQ} \partial \underline{\phi}_s^{DQ*}}$  whereas on the quadrature axis the modulating signal is a  $\frac{\pi}{2}$  phase-shifted sinusoid with the same amplitude and no offset. This is really observed experimentally and we can easily extract the partial derivatives of the complex energy function by heterodyning (see section 7.1.3).

However due to the saliency it is more handy to use the real energy function. Its partial derivatives can easily be computed from the partial derivatives of the complex energy function eq. (5.4) using the chain rule

$$\begin{aligned} \Gamma_{t_s}^D &= \frac{1}{L_s^D} = \frac{\partial^2 \mathcal{H}^{DQ}}{\partial \phi_s^{D2}} = \frac{\partial^2 \mathcal{H}^{DQ}}{\partial \underline{\phi}_s^{DQ2}} + 2 \frac{\partial^2 \mathcal{H}^{DQ}}{\partial \underline{\phi}_s^{DQ} \partial \underline{\phi}_s^{DQ*}} + \frac{\partial^2 \mathcal{H}^{DQ}}{\partial \underline{\phi}_s^{DQ*2}} \\ &= 2 \frac{\partial^2 \mathcal{H}^{DQ}}{\partial \underline{\phi}_s^{DQ} \partial \underline{\phi}_s^{DQ*}} + 2 \left| \frac{\partial^2 \mathcal{H}^{DQ}}{\partial \underline{\phi}_s^{DQ*2}} \right| \cos \left( \text{Arg} \frac{\partial^2 \mathcal{H}^{DQ}}{\partial \underline{\phi}_s^{DQ*2}} \right) \end{aligned} \quad (5.5a)$$

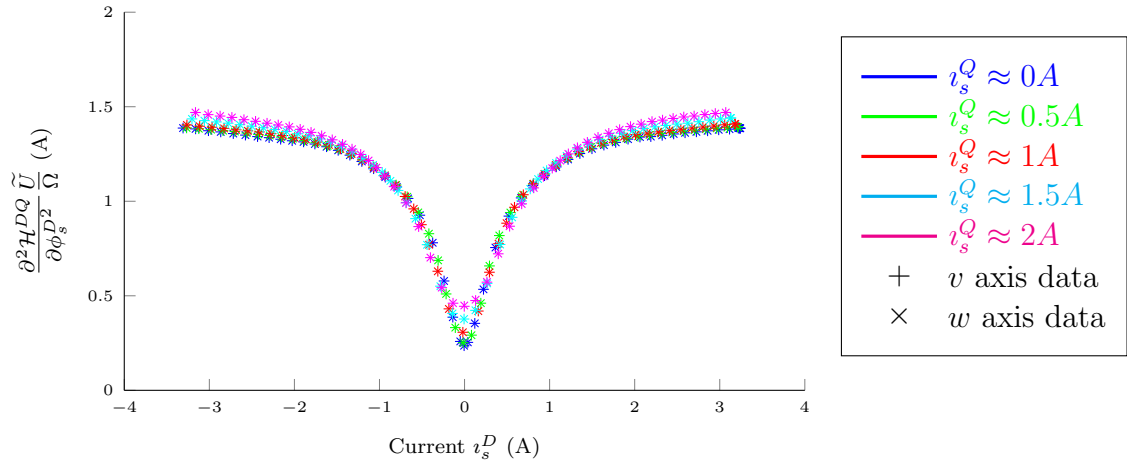
$$\begin{aligned} \Gamma_{t_s}^Q &= \frac{1}{L_s^Q} = \frac{\partial^2 \mathcal{H}^{DQ}}{\partial \phi_s^{Q2}} = -\frac{\partial^2 \mathcal{H}^{DQ}}{\partial \underline{\phi}_s^{DQ2}} + 2 \frac{\partial^2 \mathcal{H}^{DQ}}{\partial \underline{\phi}_s^{DQ} \partial \underline{\phi}_s^{DQ*}} - \frac{\partial^2 \mathcal{H}^{DQ}}{\partial \underline{\phi}_s^{DQ*2}} \\ &= 2 \frac{\partial^2 \mathcal{H}^{DQ}}{\partial \underline{\phi}_s^{DQ} \partial \underline{\phi}_s^{DQ*}} - 2 \left| \frac{\partial^2 \mathcal{H}^{DQ}}{\partial \underline{\phi}_s^{DQ*2}} \right| \cos \left( \text{Arg} \frac{\partial^2 \mathcal{H}^{DQ}}{\partial \underline{\phi}_s^{DQ*2}} \right) \end{aligned} \quad (5.5b)$$

$$\begin{aligned} \frac{\partial^2 \mathcal{H}^{DQ}}{\partial \phi_s^D \partial \phi_s^Q} &= j \frac{\partial^2 \mathcal{H}^{DQ}}{\partial \underline{\phi}_s^{DQ2}} - j \frac{\partial^2 \mathcal{H}^{DQ}}{\partial \underline{\phi}_s^{DQ*2}} \\ &= 2 \left| \frac{\partial^2 \mathcal{H}^{DQ}}{\partial \underline{\phi}_s^{DQ*2}} \right| \sin \left( \text{Arg} \frac{\partial^2 \mathcal{H}^{DQ}}{\partial \underline{\phi}_s^{DQ*2}} \right) \end{aligned} \quad (5.5c)$$

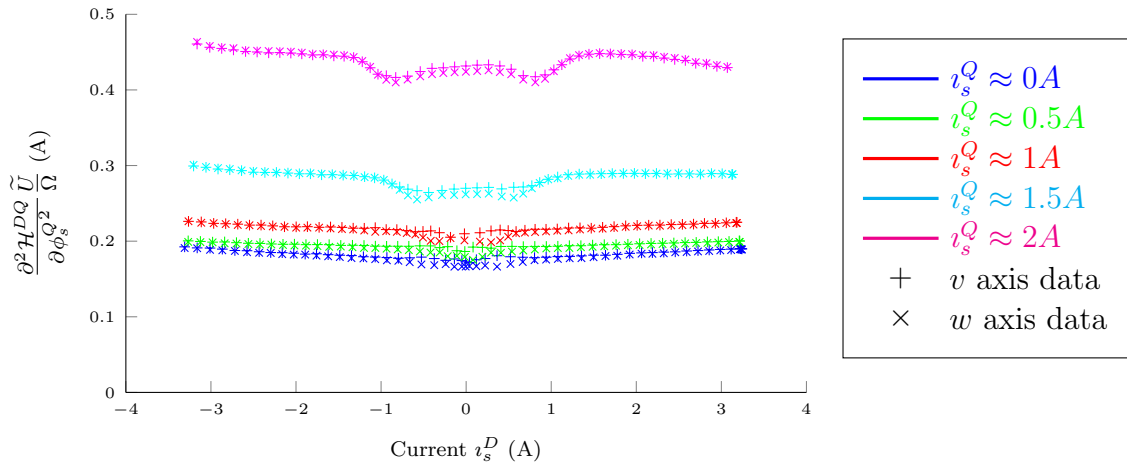
where we used the fact that  $\frac{\partial^2 \mathcal{H}^{DQ}}{\partial \underline{\phi}_s^{DQ*2}}$  is the complex conjugate of  $\frac{\partial^2 \mathcal{H}^{DQ}}{\partial \underline{\phi}_s^{DQ2}}$ .

### 5.2.1.3 Experimental results

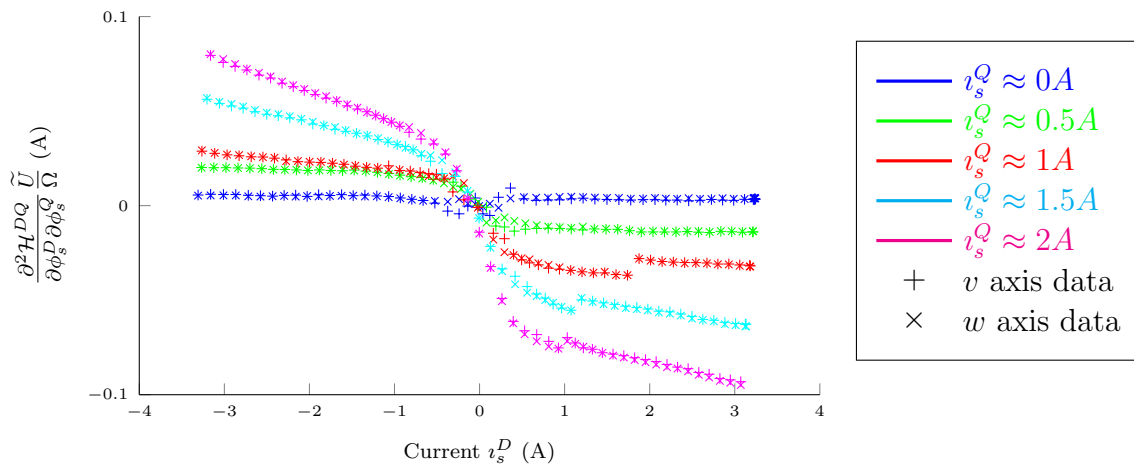
We used this method on the 0.75kW SynRM motor described in section 2.1.1. Fig. 5.1 shows the results of the experiments, extracted using the aforementioned method. The tests were made for some fixed levels on  $i_s^Q$  and steps of approximately 0.2A on  $i_s^D$ .



(a)  $\frac{\partial^2 \mathcal{H}^{DQ}}{\partial \phi_s^{D^2}} \tilde{u} \tilde{\Omega}$  as a function of the stator currents  $i_s^D$  and  $i_s^Q$ .



(b)  $\frac{\partial^2 \mathcal{H}^{DQ}}{\partial \phi_s^{Q^2}} \tilde{u} \tilde{\Omega}$  as a function of the stator currents  $i_s^D$  and  $i_s^Q$ .



(c)  $\frac{\partial^2 \mathcal{H}^{DQ}}{\partial \phi_s^D \partial \phi_s^Q} \tilde{u} \tilde{\Omega}$  as a function of the stator currents  $i_s^D$  and  $i_s^Q$ .

Figure 5.1 – Information retrieved using HF injection on a 0.75kW SynRM (see table 2.1).

Due to the parity of the energy function with respect to  $\phi_s^D$  and  $\phi_s^Q$  (see section 3.4.2.1), its partial derivatives have the parities described in table 5.1. The current-flux relations should be invertible and we find that  $\phi_s^D$  is odd with respect to  $i_s^D$  and even with respect to  $i_s^Q$  and  $\phi_s^Q$  is odd with respect to  $i_s^Q$  and even with respect to  $i_s^D$ . Thus the curves of figs. 5.1a and 5.1b should be even whereas those of fig. 5.1c should be odd, which is indeed what is observed.

	$\phi_s^D$	$\phi_s^Q$
$i_s^D = \frac{\partial \mathcal{H}^{DQ}}{\partial \phi_s^D}$	odd	even
$i_s^Q = \frac{\partial \mathcal{H}^{DQ}}{\partial \phi_s^Q}$	even	odd
$\Gamma_{t_s}^D = \frac{\partial^2 \mathcal{H}^{DQ}}{\partial \phi_s^{D2}}$	even	even
$\Gamma_{t_s}^Q = \frac{\partial^2 \mathcal{H}^{DQ}}{\partial \phi_s^{Q2}}$	even	even
$\frac{\partial^2 \mathcal{H}^{DQ}}{\partial \phi_s^D \partial \phi_s^Q}$	odd	odd

Table 5.1 – Parities of the partial derivatives of the energy function  $\mathcal{H}^{DQ}$  with respect to  $\phi_s^D$  and  $\phi_s^Q$ .

We notice in fig. 5.1 that we obtain the same values using  $v$  or  $w$  axis data, as stated by theory. Fig. 5.1a shows that there is obviously an important saturation of  $L_s^D$  by  $i_s^D$ , but there is also some cross-saturation of  $L_s^D$  by  $i_s^Q$ . On the contrary,  $L_s^Q$  is not saturated by  $i_s^D$  even though it still saturates due to  $i_s^Q$  as shown by fig. 5.1b. Fig. 5.1c shows that there is a small cross-saturation effect.

#### 5.2.1.4 A saturated model for the SynRM

Having made these observations we propose the following form for the energy function of SynRMs

$$\mathcal{H}^{DQ}(\rho, \phi_s^{DQ}) = \frac{1}{2J_L n^2} \rho^2 + \frac{1}{2} f^D(\phi_s^{D2}) + \frac{1}{2} f^Q(\phi_s^{Q2}) + \frac{1}{2} f^x(\phi_s^{Q2}) \phi_s^{D2}. \quad (5.6)$$

with  $f^x(0) = 0$  which is a generalization of the polynomial model proposed in Qu, Tuovinen, *et al.* [64]. We find for the tangent inverse inductances

$$\begin{aligned} \Gamma_{t_s}^D(\phi_s^D, \phi_s^Q) &= f^{D'}(\phi_s^{D2}) + 2f^{D''}(\phi_s^{D2}) \phi_s^{D2} + f^x(\phi_s^{Q2}) \\ \Gamma_{t_s}^Q(\phi_s^D, \phi_s^Q) &= f^{Q'}(\phi_s^{Q2}) + 2f^{Q''}(\phi_s^{Q2}) \phi_s^{Q2} + (f^{x'}(\phi_s^{Q2}) + 2f^{x''}(\phi_s^{Q2}) \phi_s^{Q2}) \phi_s^{D2} \end{aligned}$$

which synthesizes the main saturation effects as well as cross-saturation. Considering these expressions when one of the fluxes is 0

$$\begin{aligned} \Gamma_{t_s}^D(\phi_s^D, 0) &= f^{D'}(\phi_s^{D2}) + 2f^{D''}(\phi_s^{D2}) \phi_s^{D2} \\ \Gamma_{t_s}^D(0, \phi_s^Q) &= f^{D'}(0) + f^x(\phi_s^{Q2}) \\ \Gamma_{t_s}^Q(0, \phi_s^Q) &= f^{Q'}(\phi_s^{Q2}) + 2f^{Q''}(\phi_s^{Q2}) \phi_s^{Q2} \\ \Gamma_{t_s}^Q(\phi_s^D, 0) &= f^{Q'}(0), \end{aligned}$$

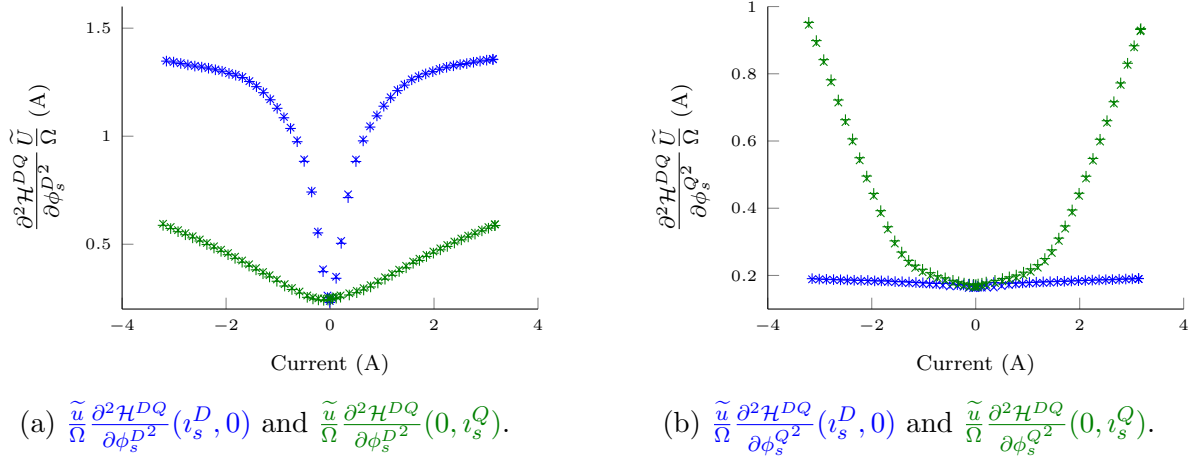


Figure 5.2 – Partial derivatives of the energy function when one of the fluxes is 0. + mark injection  $v$  axis data and  $\times$  quadrature  $w$  axis data.

we find a simple way to determine the saturation functions. Due to the structure of the chosen model the cross-saturation is decoupled when tests are made on one of the saliency axes.

However, as we cannot measure the fluxes, the experimental measurements are functions of the currents which are given by

$$\begin{aligned} \iota_s^D(\phi_s^D, 0) &= f^{D'}(\phi_s^{D^2}) \phi_s^D \\ \iota_s^Q(0, \phi_s^Q) &= f^{Q'}(\phi_s^{Q^2}) \phi_s^Q. \end{aligned}$$

On both the  $D$  and  $Q$  axes we have  $\iota_s = f(\phi_s^2) \phi_s$  and  $\Gamma_{t_s} = \frac{\partial \iota_s}{\partial \phi_s} = f(\phi_s^2) + 2f'(\phi_s^2) \phi_s^2$ . We define  $\mathbf{f}(\iota_s) = f(\phi_s(\iota_s)^2)$  and using the dot to denote the total derivative with respect to  $\iota_s$  we get

$$\begin{aligned} \iota_s &= \mathbf{f} \phi_s \\ 1 &= \dot{\mathbf{f}} \phi_s + \mathbf{f} \dot{\phi}_s \\ \Gamma_{t_s} &= \mathbf{f} + \mathbf{f} \frac{\dot{\phi}_s}{\phi_s} \end{aligned}$$

where the second relation was obtained by taking the total derivative with respect to  $\iota_s$  of the first one. Combining the 2 last relations we find

$$\Gamma_{t_s} = \mathbf{f} + \frac{1 - \mathbf{f} \dot{\phi}_s}{\dot{\phi}_s} = \frac{1}{\dot{\phi}_s}. \quad (5.7)$$

Thus  $\phi_s$  can be retrieved from the experimental data collected using HF signal injection. For the method to work properly we need to have enough working points. This is not the case in the experiment presented in fig. 5.1 as we only have 5 points for  $\iota_s^Q$ . We did two similar experiments with one flux being zero in each experiment and obtained the results in fig. 5.2 where we have one data point each 0.1A approximately on  $\iota_s^D$  or  $\iota_s^Q$ . We applied to these measurements the method proposed above to compute the flux and got the current-flux relation shown in fig. 5.3.

Because the derivative of an arbitrarily close fit to a curve can be arbitrarily far from the derivative of the curve, we should not fit the current-flux curves in fig. 5.3 but instead use this relation to find  $\Gamma_{t_s}^D(\phi_s^D, 0)$  and  $\Gamma_{t_s}^Q(0, \phi_s^Q)$  which are represented in fig. 5.4.

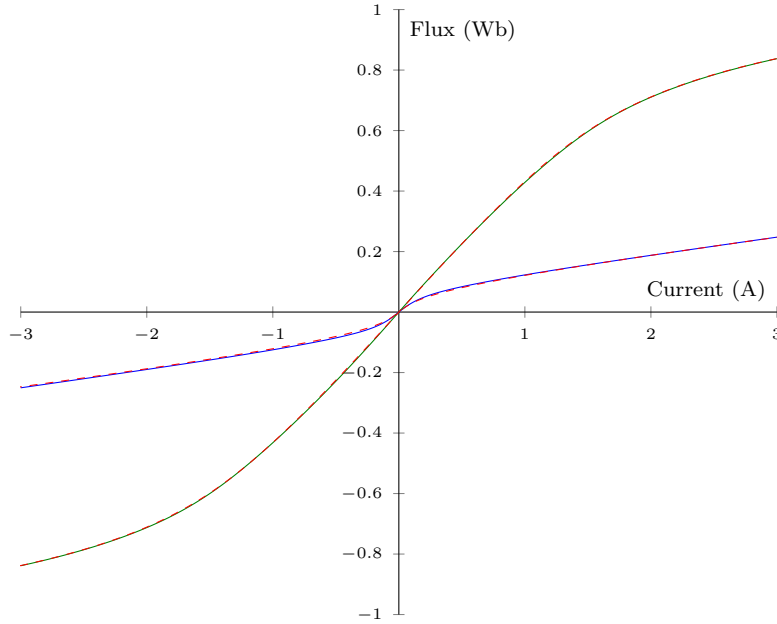


Figure 5.3 – The main current-flux relations  $\phi_s^D(i_s^D, 0)$  and  $\phi_s^Q(0, i_s^Q)$  obtained using the HF signal injection data.

The variation of  $\Gamma_{t_s}^Q$  with respect to  $\phi_s^D$  (blue curve in fig. 5.4b) is so small it can be taken constant. The shape of the curve  $\Gamma_{t_s}^Q(0, \phi_s^Q)$  (in green in fig. 5.4b) can be represented by a third or fourth order polynomial in  $\phi_s^{Q2}$  and similarly  $\Gamma_{t_s}^D(0, \phi_s^Q)$  (in green in fig. 5.4a) can be modeled by a first or second order polynomial in  $\phi_s^{Q2}$ , which agrees with the polynomial model proposed in Qu, Tuovinen, *et al.* [64]. However the curve  $\Gamma_{t_s}^D(\phi_s^D, 0)$  (in blue in fig. 5.4a) looks like a Lorentzian or a Gaussian function. As Lorentzian functions can be integrated more easily than Gaussian, we will choose this type of function. Depending on the type of the curve we used nonlinear least squares or polynomial fitting and obtained the parameters given in table 5.2 together with the inverse inductances expression. After integration of these expressions we find the analytical current-flux relations

$$i_s^D(\phi_s^D, \phi_s^Q) = \Gamma_{0_s}^D \left( 1 + \frac{\phi_2^{D2}}{\phi_1^{D2}} f_1 \left( \frac{\phi_s^{D2}}{\phi_2^{D2}} \right) + \frac{\phi_s^{Q4}}{\phi_2^{Q4}} + \frac{\phi_s^{Q2}}{\phi_1^{Q2}} \right) \phi_s^D \quad (5.8a)$$

$$i_s^Q(\phi_s^D, \phi_s^Q) = \Gamma_{0_s}^Q \left( 1 + \frac{\phi_s^{Q2}}{3\phi_1^{Q2}} - \frac{\phi_s^{Q4}}{5\phi_2^{Q4}} + \frac{\phi_s^{Q6}}{7\phi_3^{Q6}} + 2\frac{\phi_s^{D2}\phi_s^{Q2}}{\phi_2^{Q4}} + \frac{\phi_s^{D2}}{\phi_1^{Q2}} \right) \phi_s^Q \quad (5.8b)$$

where we used the  $C^\infty$  function

$$x \in \mathbb{R} \mapsto f_1(x) = \begin{cases} 1 - \frac{\arctan \sqrt{|x|}}{\sqrt{|x|}} & \text{si } x > 0 \\ \frac{\arctan \sqrt{|x|}}{\sqrt{|x|}} - 1 & \text{si } x < 0 \\ 0 & \text{si } x = 0. \end{cases}$$

Integrating again we find the model functions

$$f^D(\phi_s^{D2}) = \Gamma_{0_s}^D \left( \phi_s^{D2} + \frac{\phi_2^{D4}}{\phi_1^{D2}} F_1 \left( \frac{\phi_s^{D2}}{\phi_2^{D2}} \right) \right)$$

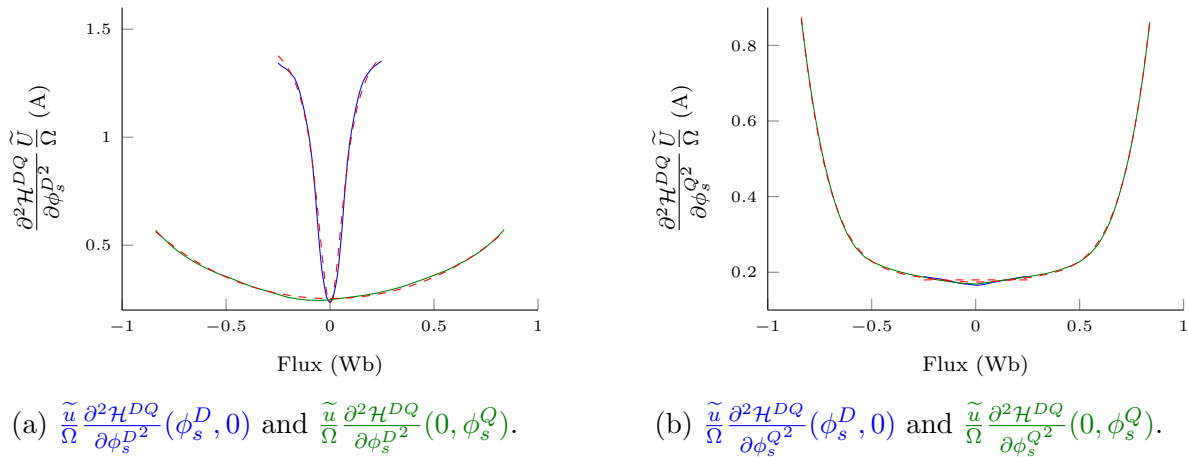


Figure 5.4 – Partial derivatives of the energy function when one of the fluxes is 0 represented as functions of the fluxes and the models (dashed red curves).

$$f^Q(\phi_s^{Q^2}) = \Gamma_{0_s}^Q \left( \frac{\phi_s^{Q^8}}{28\phi_3^{Q^6}} - \frac{\phi_s^{Q^6}}{15\phi_2^{Q^4}} + \frac{\phi_s^{Q^4}}{6\phi_1^{Q^2}} + \phi_s^{Q^2} \right)$$

$$f^x(\phi_s^{Q^2}) = \Gamma_{0_s}^D \left( \frac{\phi_s^{Q^4}}{\phi_2^{x^4}} + \frac{\phi_s^{Q^2}}{\phi_1^{x^2}} \right)$$

where  $F_1$  is the anti-derivative of  $f_1$  which vanishes at 0, is given by

$$x \in \mathbb{R} \mapsto F_1(x) = |x| - 2\sqrt{|x|} \arctan \sqrt{|x|} + \ln(1 + |x|).$$

Finally replacing these expressions in eq. (5.6), we find the energy function

$$\begin{aligned} \mathcal{H}^{DQ}(\rho, \phi_s^{DQ}) = & \frac{1}{2J_L n^2} \rho^2 + \frac{1}{2} \Gamma_{0_s}^D \left( 1 + \frac{\phi_2^{D^2}}{\phi_1^{D^2}} f_2 \left( \frac{\phi_s^{D^2}}{\phi_2^{D^2}} \right) + \frac{\phi_s^{Q^4}}{\phi_2^{x^4}} + \frac{\phi_s^{Q^2}}{\phi_1^{x^2}} \right) \phi_s^{D^2} \\ & + \frac{1}{2} \Gamma_{0_s}^Q \left( 1 + \frac{\phi_s^{Q^2}}{6\phi_1^{Q^2}} - \frac{\phi_s^{Q^4}}{15\phi_2^{Q^4}} + \frac{\phi_s^{Q^6}}{28\phi_3^{Q^6}} \right) \phi_s^{Q^2} \end{aligned} \quad (5.9)$$

where we used the  $C^\infty$  function  $f_2$  defined by

$$x \in \mathbb{R} \mapsto f_2(x) = \begin{cases} 2f_1(x) - \operatorname{sgn} x + \frac{\ln(1+|x|)}{x} & \text{si } x \neq 0 \\ 0 & \text{si } x = 0. \end{cases}$$

### 5.2.1.5 Checking the model

To check that this model conveys accurately the effects of signal injection we simulated it using Simulink<sup>®</sup> software. We measured the currents and the associated ripples for some experimental working points and computed the relative error between the experimental data and the simulation results. We obtained the results shown in table 5.3 which are very satisfactory, even though you may think that the phase is poorly represented. This is due to the fact that at some working points the amplitude of the sinusoid we want to fit is very small and so the algorithm cannot find the phase accurately.

Inverse inductance	Expression	Parameters
$\Gamma_{t_s}^D(\phi_s^D, 0) = \frac{1}{L_s^D} \left( 1 + \frac{1}{\phi_1^{D^2}} \frac{\phi_s^{D^2}}{1 + \frac{\phi_s^{D^2}}{\phi_2^{D^2}}} \right)$		$L_s^D$ 0.339H $\phi_1^D$ 0.036Wb $\phi_2^D$ 0.083Wb
$\Gamma_{t_s}^D(0, \phi_s^Q) = \frac{1}{L_s^D} \left( \frac{\phi_s^{Q^4}}{\phi_2^{x^4}} + \frac{\phi_s^{Q^2}}{\phi_1^{x^2}} + 1 \right)$		$L_s^D$ 0.316H $\phi_1^x$ 0.824Wb $\phi_2^x$ 1.275Wb
$\Gamma_{t_s}^Q(0, \phi_s^Q) = \frac{1}{L_s^Q} \left( \frac{\phi_s^{Q^6}}{\phi_3^{Q^6}} - \frac{\phi_s^{Q^4}}{\phi_2^{Q^4}} + \frac{\phi_s^{Q^2}}{\phi_1^{Q^2}} + 1 \right)$		$L_s^Q$ 0.459H $\phi_1^Q$ 0.924Wb $\phi_2^Q$ 0.759Wb $\phi_3^Q$ 0.648Wb
$\Gamma_{t_s}^Q(\phi_s^D, 0) = \frac{1}{L_s^Q}$		$L_s^Q$ 0.445H

Table 5.2 – Expression of the model for inverse inductances as functions of the fluxes. Parameters were fitted on data obtained using HF signal injection on the 0.75kW SynRM described in table 2.1.

Variable	Axis	Maximum relative error	Average relative error
$2 \frac{\partial^2 \underline{\mathcal{H}}^{DQ}}{\partial \phi_s^* \partial \phi_s} \frac{\tilde{u}}{\Omega}$	$v$	3.9%	1.1%
	$w$	0.4%	0.1%
$2 \left  \frac{\partial^2 \underline{\mathcal{H}}^{DQ}}{\partial \phi_s^{*2}} \right  \frac{\tilde{u}}{\Omega}$	$v$	5.3%	1.5%
	$w$	5.6%	1.7%
$\text{Arg} \frac{\partial^2 \underline{\mathcal{H}}^{DQ}}{\partial \phi_s^{*2}}$	$v$	5.9°	0.3°
	$w$	5.8°	0.3°

Table 5.3 – Relative error between experimental data and model simulation results.

	$v_s^a$	$v_s^b$	$v_s^c$	$u_s^a$	$u_s^b$	$u_s^c$	$u_s^D$	$u_s^Q$
Axe $a$	$\pm \frac{V_{bus}}{2}$	$\mp \frac{V_{bus}}{2}$	$\mp \frac{V_{bus}}{2}$	$\pm \frac{2}{3}V_{bus}$	$\mp \frac{1}{3}V_{bus}$	$\mp \frac{1}{3}V_{bus}$	$\pm \frac{2}{3}V_{bus}$	0
Axe $b$	$\mp \frac{V_{bus}}{2}$	$\pm \frac{V_{bus}}{2}$	$\mp \frac{V_{bus}}{2}$	$\mp \frac{1}{3}V_{bus}$	$\pm \frac{2}{3}V_{bus}$	$\mp \frac{1}{3}V_{bus}$	$\mp \frac{1}{3}V_{bus}$	$\pm \frac{\sqrt{3}}{3}V_{bus}$
Axe $c$	$\mp \frac{V_{bus}}{2}$	$\mp \frac{V_{bus}}{2}$	$\pm \frac{V_{bus}}{2}$	$\mp \frac{1}{3}V_{bus}$	$\mp \frac{1}{3}V_{bus}$	$\pm \frac{2}{3}V_{bus}$	$\mp \frac{1}{3}V_{bus}$	$\pm \frac{\sqrt{3}}{3}V_{bus}$

Table 5.4 – Values of the potentials and voltage drops set on the  $abc$  frame axes during Inform method and corresponding voltage drops in the  $DQ$  frame.

## 5.2.2 Using the Inform method

Industrial drives made by Schneider Electric use the so-called Inform method at standstill to estimate magnetic parameters at some working points. This method can also be used to estimate the saturated current-flux relations.

### 5.2.2.1 Experimental procedure

First of all we use a DC injection on  $\alpha$  axis to align it with the  $Q$  axis (which is taken to have the largest inductance). Once the rotor is aligned, the Inform sequence is started. It consists of series of short potential pulses on the three axes of the  $abc$  frame. The length of the pulses is extended until the desired current is reached. Each pulse can be subdivided in 3 steps

1. The potentials are set at  $+\frac{V_{bus}}{2}$  for the chosen axis and  $-\frac{V_{bus}}{2}$  on the other axes during a fourth of the pulse length
2. The potentials are reversed to the opposite of their initial values during half of the pulse length
3. The potentials are set back to their initial values during the last fourth of the pulse length.

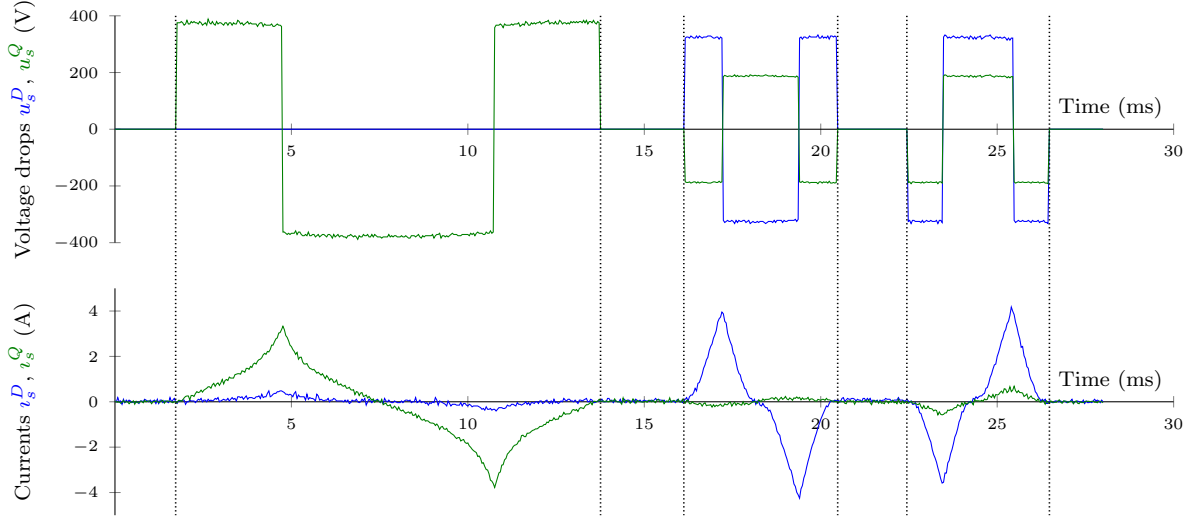
### 5.2.2.2 Theoretical analysis

Supposing the coils are symmetric we find the voltage drops at the bounds of the (star-connected) coils during Inform pulses (see table 5.4). We then apply  $abc \rightarrow DQ$  transformation to the currents and voltages since the model is most easily written in the  $DQ$  frame.

As can be seen from table 5.4, the Inform method do not allow to study cross-saturation as the voltage on the  $D$  is proportional to the voltage on the  $Q$  axis. Thus we will consider a Hamiltonian without cross-saturation ( $f_x \equiv 0$  in eq. (5.6)). As we are at standstill ( $\omega = 0$ ), the model of the SynRM is given by

$$\frac{d\phi_s^D}{dt} = u_s^D - R_s f^{D'}(\phi_s^{D2}) \phi_s^D \quad (5.10a)$$

$$\frac{d\phi_s^Q}{dt} = u_s^Q - R_s f^{Q'}(\phi_s^{Q2}) \phi_s^Q. \quad (5.10b)$$

Figure 5.5 – Voltage drops and currents in the  $DQ$  frame

It was empirically noticed that

$$\begin{aligned}\Gamma_{0_s}^D &\leq f^{D'}(\phi_s^{D^2}) \leq \Gamma_{\infty_s}^D \\ \Gamma_{0_s}^Q &\leq f^{Q'}(\phi_s^{Q^2}) \leq \Gamma_{\infty_s}^Q\end{aligned}$$

so, using the fact that  $u_s^{DQ}$  is piecewise constant, on all the intervals  $[t_b, t_e]$  where it is constant

$$\phi_s^D(t_b) + \frac{1}{\Gamma_{0_s}^D R_s} u_s^D (1 - e^{-R_s \Gamma_{0_s}^D t'}) \leq \phi_s^D(t) \leq \phi_s^D(t_b) + \frac{1}{\Gamma_{\infty_s}^D R_s} u_s^D (1 - e^{-R_s \Gamma_{\infty_s}^D t'}) \quad (5.11a)$$

$$\phi_s^Q(t_b) + \frac{1}{\Gamma_{0_s}^Q R_s} u_s^Q (1 - e^{-R_s \Gamma_{0_s}^Q t'}) \leq \phi_s^Q(t) \leq \phi_s^Q(t_b) + \frac{1}{\Gamma_{\infty_s}^Q R_s} u_s^Q (1 - e^{-R_s \Gamma_{\infty_s}^Q t'}). \quad (5.11b)$$

where  $t' = t - t_b$ . Starting from 0, to reach the desired current level  $I$ , the length of the first part of an Inform pulse is not more than  $\frac{1}{\Gamma_{0_s}^D R_s} \ln\left(1 - \frac{\Gamma_{0_s}^D R_s I}{\Gamma_{\infty_s}^D u_s^D}\right) \approx \frac{I}{\Gamma_{\infty_s}^D u_s^D}$  for  $D$  axis or  $\frac{1}{\Gamma_{0_s}^Q R_s} \ln\left(1 - \frac{\Gamma_{0_s}^Q R_s I}{\Gamma_{\infty_s}^Q u_s^Q}\right) \approx \frac{I}{\Gamma_{\infty_s}^Q u_s^Q}$  for  $Q$  axis, which are small with respect to the time constants  $\frac{1}{R_s \Gamma_{0_s}^D}$  and  $\frac{1}{R_s \Gamma_{0_s}^Q}$ . Thus the fluxes can be approximated as the integral of the voltage drops over time.

### 5.2.2.3 Experimental results

We measured using a numeric oscilloscope the 3 currents  $i_s^{abc}$  and the bus voltage  $V_{bus}$  during the auto-tuning of an industrial VSD. After transforming the voltages and the currents to the  $DQ$  frame we obtain the curves of fig. 5.5.

Finally integrating the voltage drops over time as described in the previous paragraph we get the current-flux relation plotted in fig. 5.6.

## 5.2.3 A saturated model for the SRM

The shapes of the curves are identical to those which were retrieved using HF injection data. Thus we are going to use the same model functions. The parameters in table 5.5 were obtained using the same method as previously. However the current-flux relations were

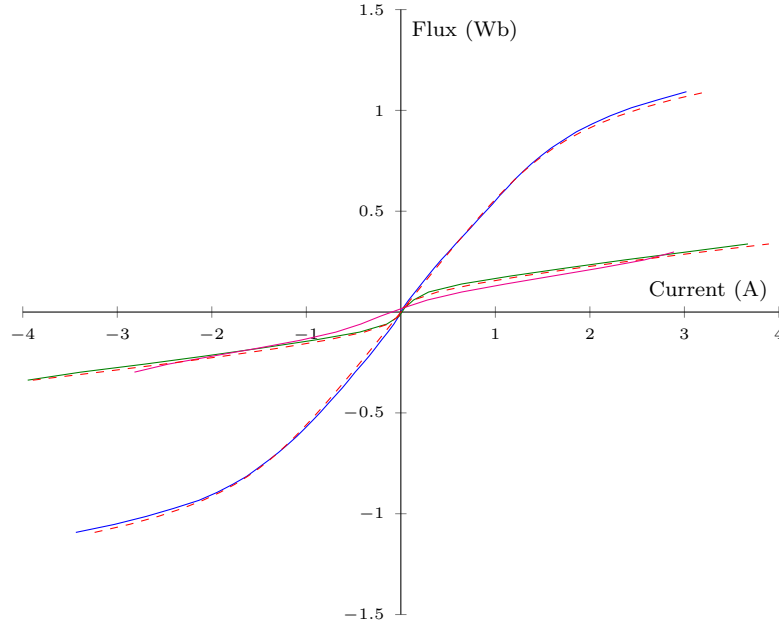


Figure 5.6 – Main current-flux relations obtained from Inform data when applied along  $a$ ,  $b$  and  $c$  axes and the models for  $\iota_s^D(\phi_s^D, 0)$  and  $\iota_s^Q(0, \phi_s^Q)$

Current	Expression	Parameters
$\iota_s^D(\phi_s^D, 0)$	$= \frac{1}{L_s^D} \left( 1 + \frac{\phi_2^{D2}}{\phi_1^{D2}} f_1 \left( \frac{\phi_s^{D2}}{\phi_2^{D2}} \right) \right) \phi_s^D$	$L_s^{0D}$ 0.584H $\phi_1^D$ 0.033Wb $\phi_2^D$ 0.148Wb
$\iota_s^Q(0, \phi_s^Q)$	$= \frac{1}{L_s^Q} \left( \frac{\phi_s^{Q6}}{7\phi_3^{Q6}} - \frac{\phi_s^{Q4}}{5\phi_2^{Q4}} + \frac{\phi_s^{Q2}}{3\phi_1^{Q2}} + 1 \right) \phi_s^Q$	$L_s^{0Q}$ 0.590H $\phi_1^Q$ 1.278Wb $\phi_2^Q$ 0.947Wb $\phi_3^Q$ 0.810Wb

Table 5.5 – Expression of the model for inverse inductances as functions of the fluxes. Parameters were fitted for the current-flux relation obtained thanks to Inform method.

fitted directly because information on the derivatives of the current-flux relation is not available, so this model will not represent very accurately HF injection results. Besides, using the Inform method, cross-saturation cannot be modeled. The energy model is given by

$$\begin{aligned} \mathcal{H}^{DQ}(\rho, \phi_s^{DQ}) = & \frac{1}{2J_L n^2} \rho^2 + \frac{1}{2} \Gamma_{0s}^D \left( 1 + \frac{\phi_2^{D2}}{\phi_1^{D2}} f_2 \left( \frac{\phi_s^{D2}}{\phi_2^{D2}} \right) \right) \phi_s^{D2} \\ & + \frac{1}{2} \Gamma_{0s}^Q \left( 1 + \frac{\phi_s^{Q2}}{6\phi_1^{Q2}} + \frac{\phi_s^{Q4}}{15\phi_2^{Q4}} + \frac{\phi_s^{Q6}}{28\phi_3^{Q6}} \right) \phi_s^{Q2} \end{aligned} \quad (5.12)$$

where  $f_2$  is the special function introduced previously and the parameters are given in table 5.5.

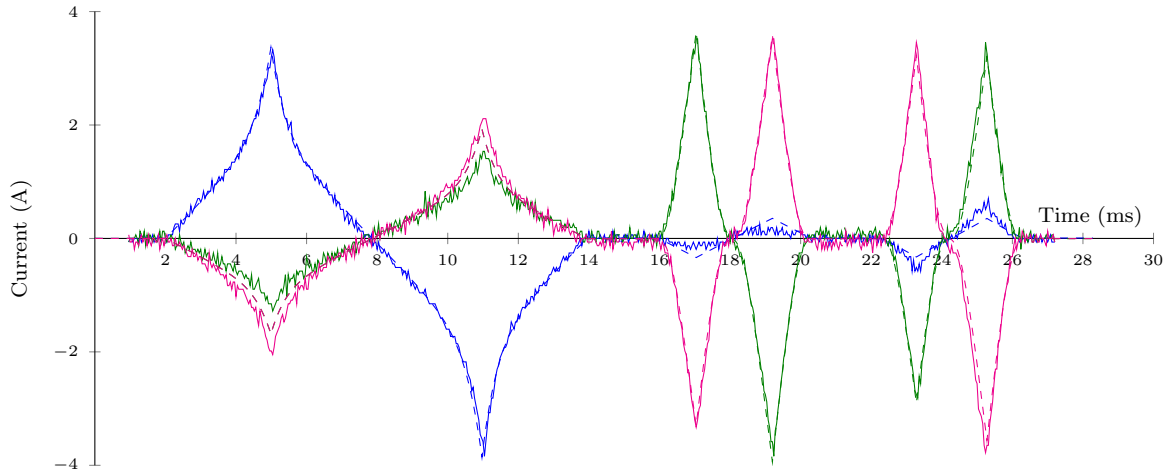


Figure 5.7 – Measured (solid lines) and simulated (dashed lines) currents on  $a$ ,  $b$  and  $c$  axes during an Inform sequence at nominal current on the SynRM described by table 2.1.

### 5.2.3.1 Validating the model

To check that this model reproduces what was experimentally observed we simulated an Inform sequence using Simulink<sup>®</sup> software. The result is plotted with dashed lines in fig. 5.7 which shows that the simulated currents are very close to the measured ones. Moreover the only differences are a priori due to alignment errors, as there should be symmetries between  $b$  and  $c$  axis currents. Thus, the effects of Inform sequence are satisfactorily reproduced by the model. However, this model may not reproduce accurately the effects of signal injection as we did not fit tangent inductances.

## 5.2.4 Conclusion

In fig. 5.8 we plotted the current-flux relations obtained by HF signal injection and by the Inform method. The  $D$  axis curves are quite close and the difference can be explained by experimental errors. However the  $Q$  axis curves differs by approximately 20% which cannot be explained by experimental errors. Indeed in the Inform test, the inverter voltage drops (see section 2.3.1) and the dead times (see section 2.3.2) bias the voltages by less than 3V (i.e. a relative error of 0.5%) while the currents and the bus voltage are measured accurately by calibrated current clamp and differential probes on a digital oscilloscope. In the signal injection test, the errors due to inverter non-linearities can be relatively larger, up to 10% as the voltages involved are lower, but the accuracy of the current measurement with dSpace<sup>®</sup> is 1% in the worst case. This is really strange as the simulations of both models give results really close to experiments.

A potential explanation is given in Cordier, Landsmann, *et al.* [73] which states that, as the HF injection follows Raleigh loops (an effect due to magnetic hysteresis detailed in section 5.3.2), the HF ripple is amplified. This means that the current-flux relations will be shrunk, which is what is observed in fig. 5.8. The Inform test could also be affected by magnetic hysteresis, but the main hysteresis cycle (see fig. 5.12) will be followed in this case. The method we used in section 5.2.2 to obtain the current-flux relations with Inform data is not sensitive to hysteresis. To see if there really was hysteresis in our SynRM, we plotted the real fluxes and currents which are obtained using Inform method at 120% of the nominal current. To obtain more readable curves, the data were filtered using a

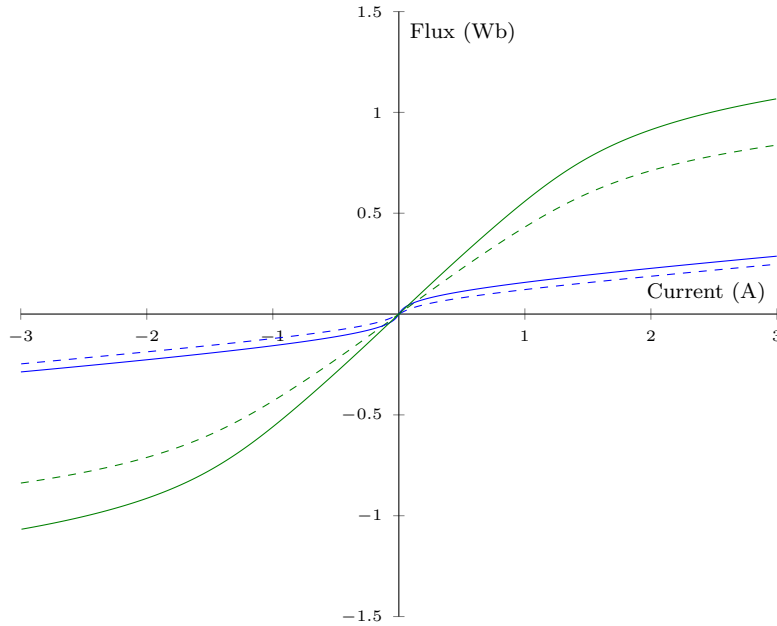


Figure 5.8 – Current-flux relations  $\phi_s^D(i_s^D, 0)$  and  $\phi_s^Q(0, i_s^Q)$  obtained by signal injection (dashed line) and Inform method (solid line).

sliding average filter on 4 points, but no further processing was done to cancel hysteresis. The results are plotted in fig. 5.9 where a small hysteresis cycle can be noticed.

Furthermore, after computing the reachable torque under nominal current we found that the model obtained with the Inform method is closer to motor manufacturer data at the nominal working point because nominal torque is not reached under nominal current for the model designed using HF signal injection. We are thus going to keep the model obtained with the Inform method for the main saturation in the next chapters. However, cross-saturation will be modeled using the data collected using signal injection, as the Inform method do not provide any information on cross-saturation.

### 5.3 A saturated IM model

We are going to devise the most-simple saturated model for the IM. On the contrary to the SynRM, the IM has a non-salient rotor so we can work in any synchronous  $dq0$  frame. The stator is star-connected and the rotor is short-circuited, so the 0 axis can be decoupled for both the stator and rotor fluxes as demonstrated in sections 3.5.1 and 3.5.3. We again neglect non-sinusoidal effects (see section 3.7) and design a saturated sinusoidal model for IMs. According to section 3.8 the energy function in the chosen  $dq$  frame can be written as  $\mathcal{H}^{dq}(\rho, \phi_s^{dq}, \phi_r^{dq})$  and has the invariance constraints listed in table 3.5.

This being said, the IM is still much more difficult to model than the SynRM due to the fact that there are 2 new state variables which are not measured. To simplify the modeling, we will make assumptions on the model and then design the most simple tests.

Unfortunately we did not manage to obtain a model representing the HF response of the IM. However we developed interesting ideas which could be enhanced and reused in the future. That is why I present here our approach which relies on energy. It should be noted that all models enforcing the reciprocity conditions (see Sauer [30]) can be modeled using this approach which is quite generic.

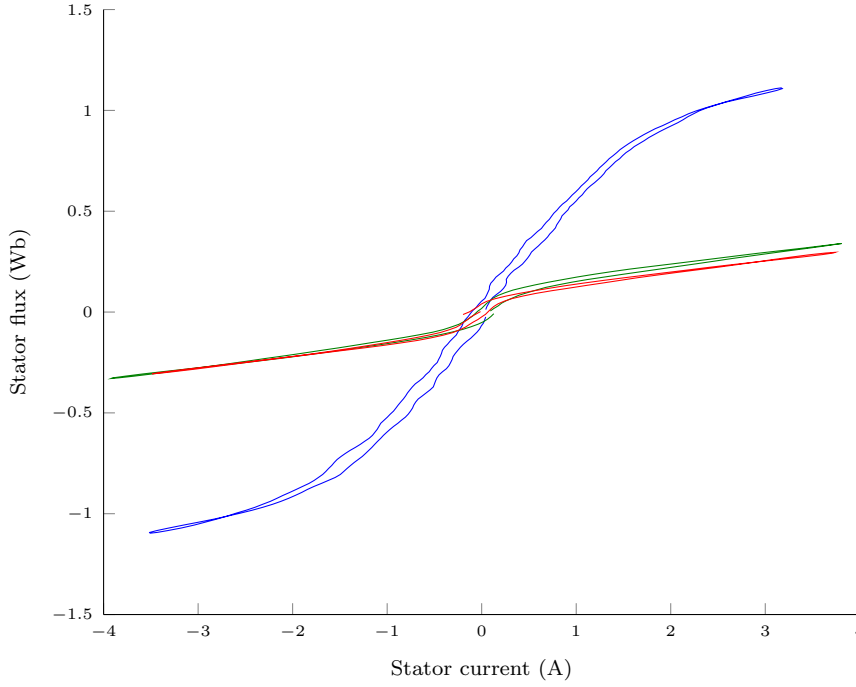


Figure 5.9 – Current-flux relations obtained without deleting hysteresis:  $\phi_s^D(i_s^D, 0)$  obtained by a step on  $a$ -axis and  $\phi_s^Q(0, i_s^Q)$  obtained by a step on  $b$ -axis or  $c$ -axis. For the  $a$ -axis and  $b$ -axis test the flux is first increased to its maximum value, then decreased to its minimum value and finally reset to 0 and the for  $c$ -axis it is done in the opposite order. We can notice that there is indeed a slight hysteresis effect.

### 5.3.1 Zero load tests

At first, we followed the approach proposed in the literature, that is to say start from an unsaturated model and replace the inductances by nonlinear functions (see [17, 70]). However, we applied this idea to the energy function instead of the current-flux relations. This has the notable advantage of ensuring the reciprocity conditions (see [30]). In section 3.6.2 we found the energy function associated to the saturated sinusoidal model of a non-skewed-rotor IM recalled here using complex notations

$$\mathcal{H}^{dq}(\rho, \underline{\phi}_s^{dq}, \underline{\phi}_r^{dq}) = \frac{1}{2J_L n^2} \rho^2 + \frac{1}{2} \Gamma_m^{dq} |\underline{\phi}_s^{dq} + \underline{\phi}_r^{dq}|^2 + \frac{1}{2} \Gamma_{ls}^{dq} |\underline{\phi}_s^{dq}|^2 + \frac{1}{2} \Gamma_{lr}^{dq} |\underline{\phi}_r^{dq}|^2. \quad (5.13)$$

As we don't have any clue regarding the values of the leakage inductances, we suppose that they are equal  $\Gamma_{ls}^{DQ} = \Gamma_{lr}^{DQ} = \Gamma_l^{DQ}$  in a first time. The energy function eq. (5.13) can thus be rewritten

$$\mathcal{H}^{dq}(\rho, \underline{\phi}_s^{dq}, \underline{\phi}_r^{dq}) = \frac{1}{2J_L n^2} \rho^2 + \frac{1}{2} \Gamma_M^{dq} |\underline{\phi}_s^{dq} + \underline{\phi}_r^{dq}|^2 + \frac{1}{2} \Gamma_L^{dq} |\underline{\phi}_s^{dq} - \underline{\phi}_r^{dq}|^2. \quad (5.14)$$

with  $\Gamma_M^{dq} := \Gamma_m^{dq} + \frac{\Gamma_l^{dq}}{2}$  and  $\Gamma_L^{dq} := \frac{\Gamma_l^{dq}}{2}$ . The terms of this expressions are related to well described phenomena, the second being the energy stored in the mutual inductance whereas the third is associated with leakage energy. The first idea which arises is thus to saturate each energy with the associated flux

$$\mathcal{H}^{dq}(\rho, \underline{\phi}_s^{dq}, \underline{\phi}_r^{dq}) = \frac{1}{2J_L n^2} \rho^2 + \frac{1}{2} f_M \left( |\underline{\phi}_s^{dq} + \underline{\phi}_r^{dq}|^2 \right) + \frac{1}{2} f_L \left( |\underline{\phi}_s^{dq} - \underline{\phi}_r^{dq}|^2 \right). \quad (5.15)$$

Due to the special structure of the model, tests at zero load should be sufficient to characterize the model. That is why we chose to do no-load tests in a first place.

### 5.3.1.1 Experimental procedure

IMs produce a torque only when there is a difference of speed between the fluxes and the rotor. Thus, to make zero load tests at standstill we just set a constant voltage along some axis (any axis can be taken as the motor is non salient) which will be the  $d$  axis (this will be the axis of the flux). This voltage creates a current along the same axis only. We injected an HF signal along this axis or the quadrature axis, which is sufficient to parametrize the model eq. (5.15). Similarly to the SynRM case addressed in section 5.2.1.2, this will enable us to retrieve

$$\begin{aligned}\tilde{\gamma}_s^d &= \frac{\partial^2 \mathcal{H}^{dq}}{\partial \phi_s^{d^2}} \frac{\tilde{u}}{\Omega} F(\Omega t) = \frac{\partial^2 \underline{\mathcal{H}}^{dq}}{\partial \underline{\phi}_s^* \partial \underline{\phi}_s} \frac{\tilde{u}}{\Omega} F(\Omega t) + \frac{\partial^2 \underline{\mathcal{H}}^{dq}}{\partial \underline{\phi}_s^{*2}} \frac{\tilde{u}}{\Omega} F(\Omega t) \\ \tilde{\gamma}_s^q &= \frac{\partial^2 \mathcal{H}^{dq}}{\partial \phi_s^{q^2}} \frac{\tilde{u}}{\Omega} F(\Omega t) = \frac{\partial^2 \underline{\mathcal{H}}^{dq}}{\partial \underline{\phi}_s^* \partial \underline{\phi}_s} \frac{\tilde{u}}{\Omega} F(\Omega t) - \frac{\partial^2 \underline{\mathcal{H}}^{dq}}{\partial \underline{\phi}_s^{*2}} \frac{\tilde{u}}{\Omega} F(\Omega t)\end{aligned}$$

We recorded one point every 0.1A. This test is the simplest possible and has the additional advantage of avoiding non-sinusoidal effects.

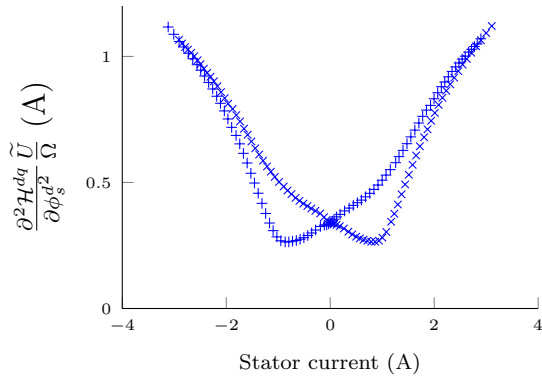
To confirm the validity of this test, we made other zero load tests using the load machine to drive the motor at synchronous speed  $\omega_s = n\omega_m = 1.6Hz$ . As in the previous tests, we set a constant voltage along some axis of the chosen  $dq$  frame and injected a HF signal along this axis or the quadrature axis. We repeated this experiment for one value of the stator current every 0.1A.

### 5.3.1.2 Experimental results

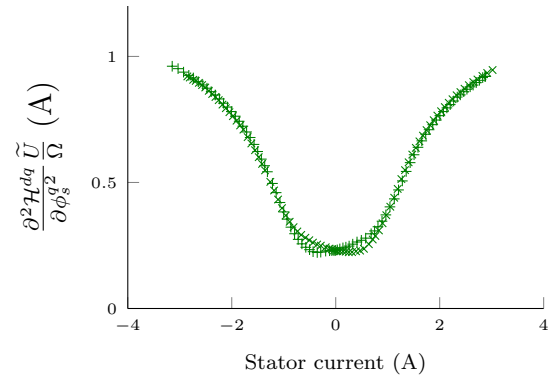
Surprisingly, if we make the tests described in the previous paragraph, we get non symmetrical curves which is in contradiction with theory which forecasts even curves (see section 3.4). This is explained by the hysteresis phenomenon in magnetic materials which is described in section 5.3.2. This phenomenon cannot be taken into account by our energy-based approach as it is non-conservative. Moreover, as we want the simplest model for control, modeling hysteresis is not desirable. To avoid it which is not paramount in control, we will do 2 tests:

- The constant voltage is increased from negative values to positive values and
- The constant voltage is decreased from positive values to negative values.

The results of the test at standstill are given in fig. 5.10 where we can see that the test with increasing current gives curves which are the exact symmetric of those obtained with decreasing currents. We also notice that the magnetic saturation has an important effect on all the inductances. However the  $d$  and  $q$  axes inductances are saturated similarly which was not the case in the SynRM where saturation curves differed greatly. Similar results with a reduced effect of hysteresis are found running tests at synchronous speed (see fig. 5.11).

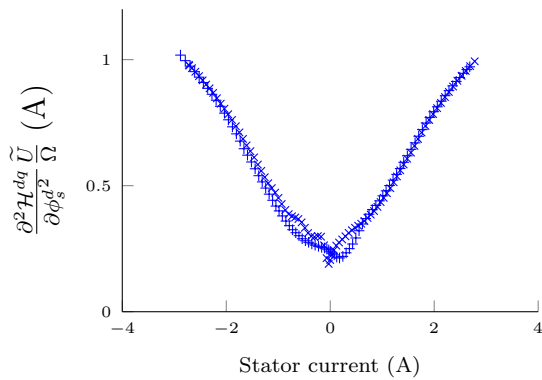


(a) Stator current ripple on the flux axis  
 $\frac{\partial^2 \mathcal{H}^{dq}}{\partial \phi_s^{d^2}}(\phi_s^{dq}, \phi_r^{dq}) \tilde{u} \tilde{\Omega}$ .

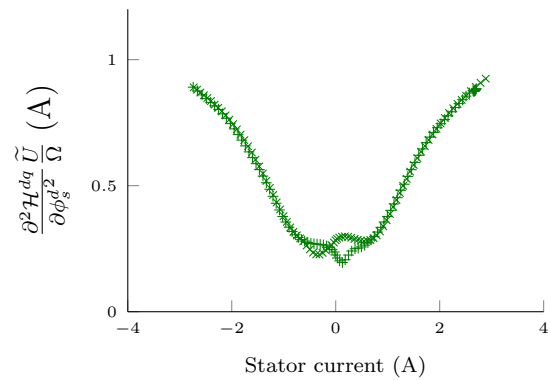


(b) Stator current ripple on the orthogonal axis  
 $\frac{\partial^2 \mathcal{H}^{dq}}{\partial \phi_s^{q^2}}(\phi_s^{dq}, \phi_r^{dq}) \tilde{u} \tilde{\Omega}$ .

Figure 5.10 – Stator current ripple amplitudes on the flux and quadrature axes during tests at standstill for the IM described by table 2.2 with increasing current (+) and decreasing current (×).



(a) Stator current ripple on the flux axis  
 $\frac{\partial^2 \mathcal{H}^{dq}}{\partial \phi_s^{d^2}}(\phi_s^{dq}, \phi_r^{dq}) \tilde{u} \tilde{\Omega}$ .



(b) Stator current ripple on the orthogonal axis  
 $\frac{\partial^2 \mathcal{H}^{dq}}{\partial \phi_s^{q^2}}(\phi_s^{dq}, \phi_r^{dq}) \tilde{u} \tilde{\Omega}$ .

Figure 5.11 – Stator current ripple amplitudes on the flux and quadrature axes during tests at synchronous speed for the IM described by table 2.2 with increasing current (+) and decreasing current (×).

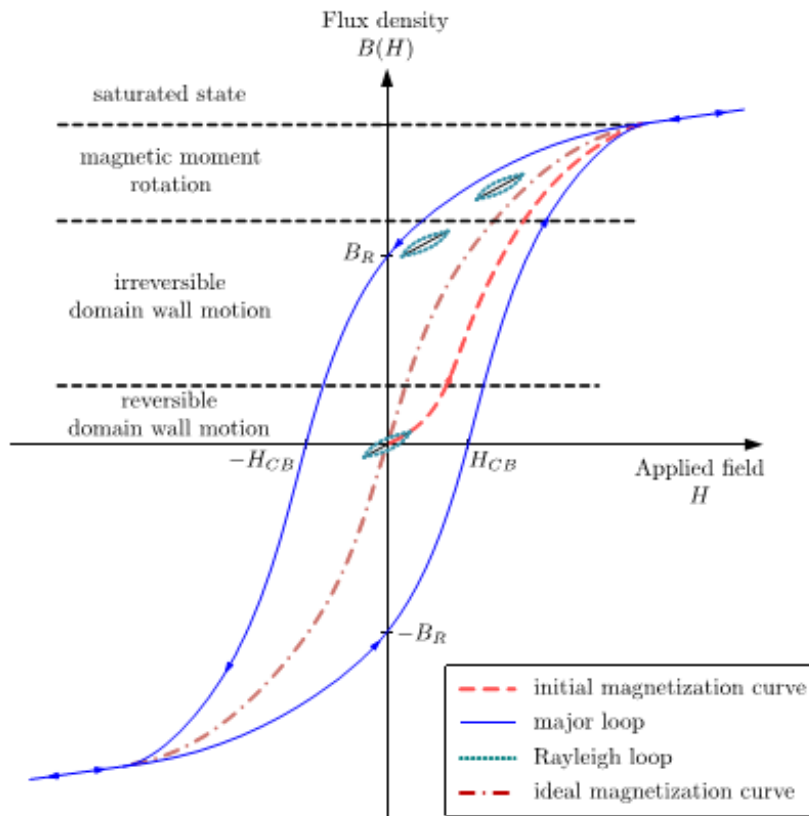


Figure 5.12 – Effects of magnetic hysteresis on magnetic materials (taken from Cordier, Landsmann, *et al.* [73]).

## 5.3.2 Hysteresis

### 5.3.2.1 Presentation of the phenomenon

When written in matter, Maxwell equations define 2 new fields, the magnetic induction field  $\mathbf{H}$  and the electric displacement field, associated respectively with the magnetic field  $\mathbf{B}$  and the electric field (see Mukerji, Khan, *et al.* [18, ch. 1]). The relation between  $\mathbf{H}$  and  $\mathbf{B}$  is given by

$$\mathbf{B} = \mu_0(\mathbf{H} + \mathbf{M}) \quad (5.16)$$

where  $\mu_0$  is the vacuum permeability and  $\mathbf{M}$  is called the magnetization and is the cause of magnetic hysteresis in ferromagnetic materials. In such materials  $\mathbf{M}$  is a function of the previous state of the material and the variation of  $\mathbf{H}$ . This creates what is called the hysteresis cycle shown in blue in fig. 5.12.

As we are doing HF signal injection, there is one other effect we should mention: When the magnetic material is submitted to HF, the main hysteresis cycle is not followed. Instead small cycles which are called Rayleigh loops are followed (in green in fig. 5.12).

Magnetic hysteresis modeling is still an open subject. There exist a lot of magnetic hysteresis models (see listings in [74–77]), each one representing some experimental effects but none taking all phenomena of fig. 5.12 into account. Furthermore much effort has been done to model magnetic hysteresis along one axis whereas to model the IM a 2D model of hysteresis is needed as the fluxes are rotating around the motor axis.

### 5.3.2.2 Magnetic hysteresis at fundamental frequency

During our tests, we magnetized the motor in the negative or positive and then increased or decreased the current. The fundamental flux follow thus the hysteresis cycle. This phenomenon can easily explain the experimental results. Indeed, for a given current, the flux will not be the same if the current is increasing or decreasing. Knowing that the curves should be even with respect to  $\phi_s^d$  in the absence of hysteresis, we can easily explain the symmetry observed between the curves.

As we are not interested in modeling magnetic hysteresis in electric motors we would like to get the ripple as if the relation current-flux was the dash-dotted curve in fig. 5.12. The best approximation of this ideal curve (which is never followed) we can obtain from our experimental results is the average of the increasing and the decreasing tests for every current level. The approximation is obviously incorrect in the middle part of the curve but it is quite good for higher flux and in particular around nominal flux.

### 5.3.2.3 Finding the cause of hysteresis

It would be interesting (for the next section) to know whether the magnetic hysteresis is caused by the stator iron, the rotor iron or both. We carried out the following two experiments on the IM described in section 2.1.2:

**First experiment** The motor is magnetized using a constant current along an axis before beginning of the recording. We then inject a HF signal with no fundamental along an axis while rotating the rotor. We computed the stator current ripple amplitude along the axis and the quadrature axis and got the curves shown in fig. 5.13.

**Second experiment** The motor is again magnetized using a constant current along an axis before beginning of the recording. We then inject a HF signal along an axis slowly rotating synchronously with the rotor. We computed the stator current ripple amplitude along the injection and quadrature axes and obtained the curves shown in fig. 5.14.

In fig. 5.13 we notice that the amplitude of the ripple changes only when the rotor is rotating whereas it only changes when the injection and the rotor electrical position are desynchronized as can be seen in fig. 5.14. This means that hysteresis in the IM is caused by the rotor iron. The curves of fig. 5.14 are much more noisy as the stator of the IM is not sinusoidally wound.

### 5.3.2.4 Magnetic hysteresis and HF injection

According to what was said in section 5.3.2.1 and Cordier, Landsmann, *et al.* [73] the HF response of the motor to an injected signal should follow the Rayleigh loops and the HF response should consequently be affected by hysteresis. However as shown in section 4.2.3 HF voltage injection does not affect the rotor flux (at first order). So the response on the stator current should not be affected by hysteresis caused by the rotor iron. This is verified in experiments as the HF stator current ripple is triangular which would not be the case otherwise.

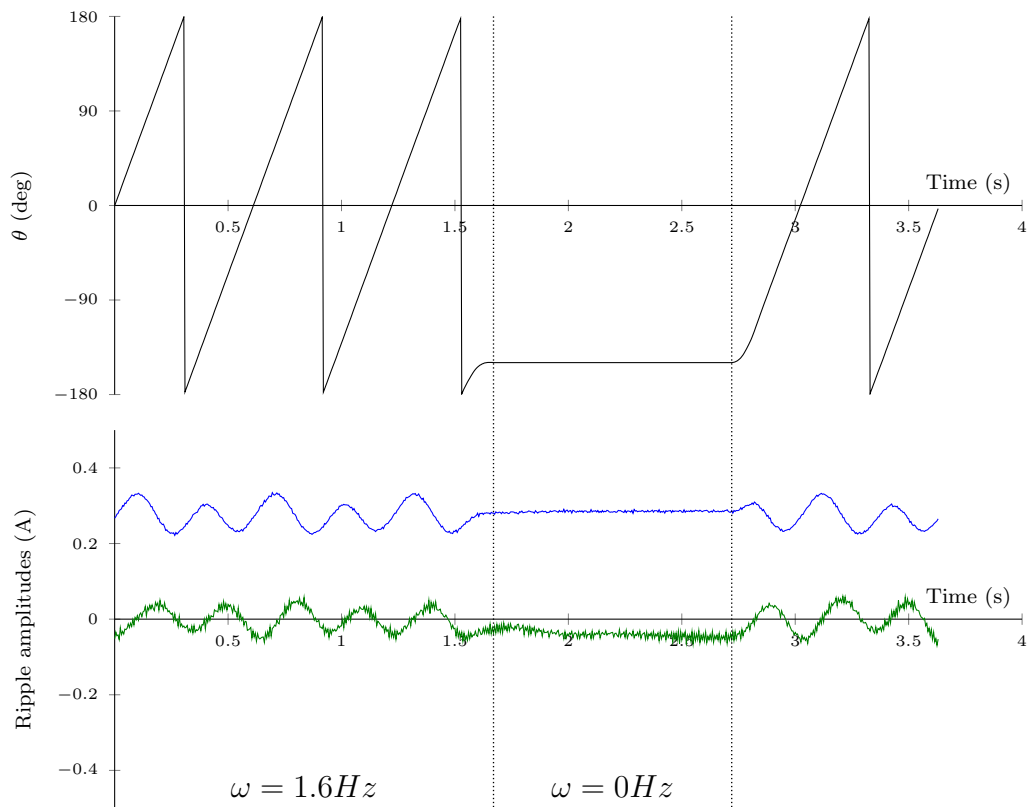


Figure 5.13 – The electrical angle  $\theta$  (solid black line) and the stator current ripple amplitude along the **injection** and the **quadrature** axes recorded during the first experiment on the IM described in table 2.2.

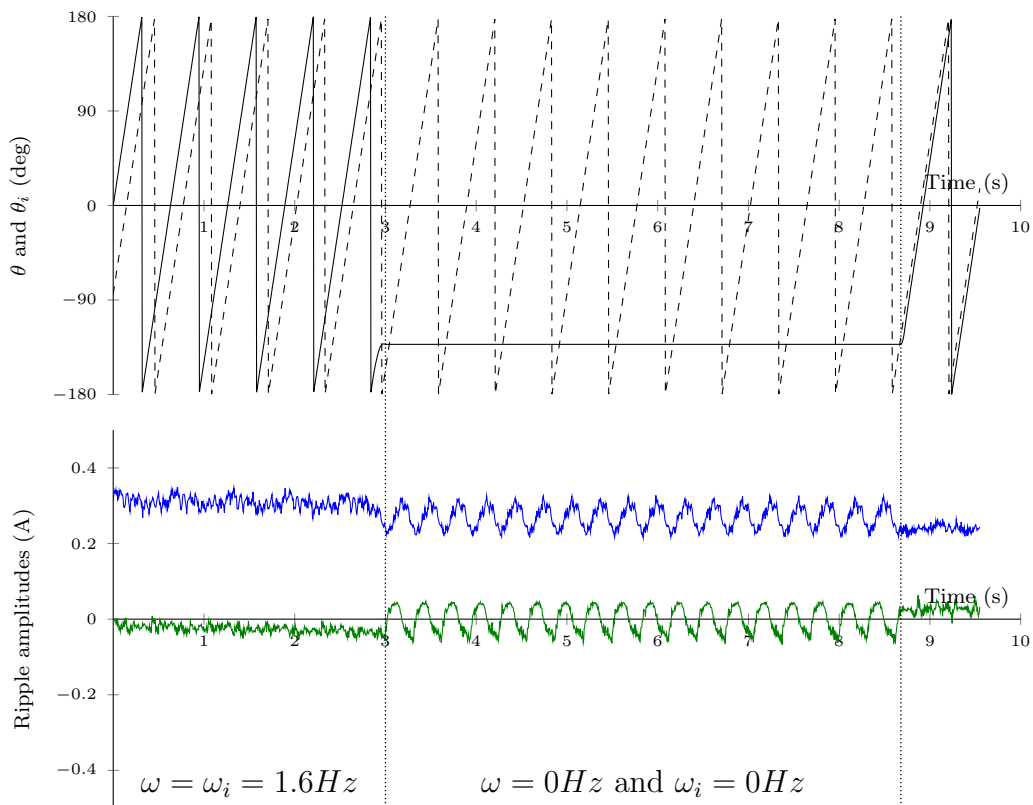


Figure 5.14 – The electrical angle  $\theta$  (solid black line), the injection axis angle  $\theta_i$  (dashed black line) and the stator current ripple amplitude along the **injection** and the **quadrature** axes recorded during the second experiment on on the IM described in table 2.2.

### 5.3.3 A model for zero load test results

The energy function of eq. (5.15) leads to the current-flux relations

$$\underline{i}_s^{dq} + \underline{i}_r^{dq} = f'_M \left( \left| \underline{\phi}_s^{dq} + \underline{\phi}_r^{dq} \right|^2 \right) \left( \underline{\phi}_s^{dq} + \underline{\phi}_r^{dq} \right) \quad (5.17a)$$

$$\underline{i}_s^{dq} - \underline{i}_r^{dq} = f'_L \left( \left| \underline{\phi}_s^{dq} - \underline{\phi}_r^{dq} \right|^2 \right) \left( \underline{\phi}_s^{dq} - \underline{\phi}_r^{dq} \right). \quad (5.17b)$$

The saturation of the magnetizing current-flux relation (here eq. (5.17a)) is well-known and has been well studied because it has great influence on control laws as said in section 5.1.2.1. We will use the model proposed by Malrait [17] which is with our notations

$$\underline{\phi}_s^{dq} + \underline{\phi}_r^{dq} = L_l^{dq} (\underline{i}_s^{dq} + \underline{i}_r^{dq}) + 2f \left( L_m^{dq} \left| \underline{i}_s^{dq} + \underline{i}_r^{dq} \right| \right) \frac{(\underline{i}_s^{dq} + \underline{i}_r^{dq})}{\left| \underline{i}_s^{dq} + \underline{i}_r^{dq} \right|} = F \left( \left| \underline{i}_s^{dq} + \underline{i}_r^{dq} \right| \right) (\underline{i}_s^{dq} + \underline{i}_r^{dq}).$$

To invert this relation we need to get the module of the magnetizing flux as a function of the currents which is obtained by multiplying this relation by its complex conjugate and take the square root

$$\left| \underline{\phi}_s^{dq} + \underline{\phi}_r^{dq} \right| = \left( L_l^{dq} + \frac{2f \left( L_m^{dq} \left| \underline{i}_s^{dq} + \underline{i}_r^{dq} \right| \right)}{\left| \underline{i}_s^{dq} + \underline{i}_r^{dq} \right|} \right) \left| \underline{i}_s^{dq} + \underline{i}_r^{dq} \right| = F \left( \left| \underline{i}_s^{dq} + \underline{i}_r^{dq} \right| \right) \left| \underline{i}_s^{dq} + \underline{i}_r^{dq} \right|.$$

With  $G$  denoting the inverse of  $x \mapsto F(x)x$  the magnetizing flux-current relation is given by

$$\underline{i}_s^{dq} + \underline{i}_r^{dq} = \frac{1}{F \left( G \left( \left| \underline{\phi}_s^{dq} + \underline{\phi}_r^{dq} \right| \right) \right)} \left( \underline{\phi}_s^{dq} + \underline{\phi}_r^{dq} \right). \quad (5.18)$$

However this function cannot explain the HF response of the IM. Indeed in the interval where the current-flux relation is linear, the ripple amplitude would be constant. Yet the ripple varies by a factor 3 or 4 as can be seen on fig. 5.10.

This can be explained thanks to the saturation of the leakage flux. In section 5.3.1 we made the hypothesis that the leakage flux is saturated by itself. However on second thoughts we realized that it is quite difficult to get the shape of the curve on fig. 5.10. Moreover Tuovinen, Hinkkanen, *et al.* [70] propose a saturation of the leakage flux by the magnetizing flux. This can easily explain the shape of the experimental curves figs. 5.10 and 5.11. We thus replace the energy function of eq. (5.15) by

$$\mathcal{H}^{dq}(\rho, \underline{\phi}_s^{dq}, \underline{\phi}_r^{dq}) = \frac{1}{2J_L n^2} \rho^2 + \frac{1}{2} f_M \left( \left| \underline{\phi}_s^{dq} + \underline{\phi}_r^{dq} \right|^2 \right) + \frac{1}{2} \Gamma_L^{dq} f_L \left( \left| \underline{\phi}_s^{dq} + \underline{\phi}_r^{dq} \right|^2 \right) \left| \underline{\phi}_s^{dq} - \underline{\phi}_r^{dq} \right|^2. \quad (5.19)$$

With the saturation functions given by

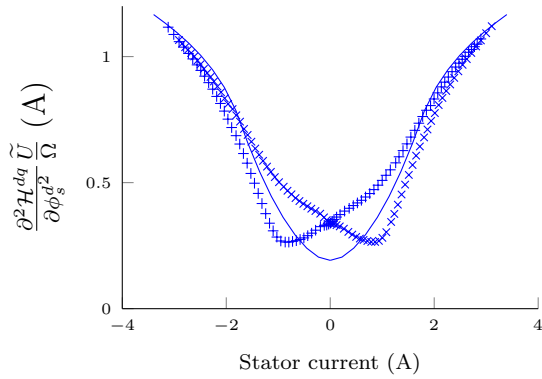
$$f'_M(\phi_m^2) = \frac{1}{F(G(\phi_m))} \quad (5.20a)$$

$$f_L(\phi_m^2) = 1 + \frac{\phi_m^2}{\phi_0^2} \quad (5.20b)$$

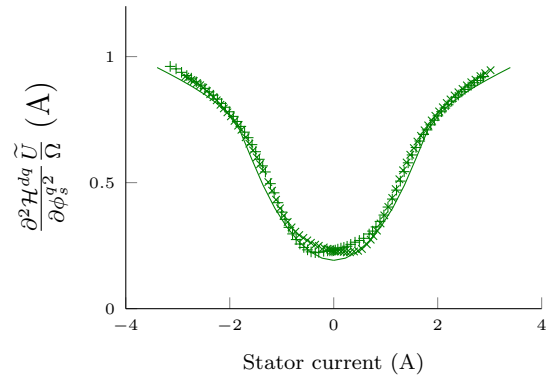
and the parameters given in table 5.6 we obtained the solid lines drawn in fig. 5.15. This is quite a good result and we can hope that this model can also represent the HF response of a motor under load.

Magnetic parameter	Numeric value
$L_m^{dq}$	$0.420H$
$L_l^{dq} = L_{ls}^{dq} = L_{lr}^{dq}$	$0.117H$
$\phi_1$	$0.7Wb$
$\phi_2$	$0.85Wb$
$\phi_0$	$0.952Wb$

Table 5.6 – The magnetic parameters of the model given by eqs. (5.19) and (5.20) ( $\phi_1$  and  $\phi_2$  are defined in [17]).



(a) Stator current ripple amplitude on the flux axis  $\frac{\partial^2 \mathcal{H}^{dq}}{\partial \phi_s^{dq2}}(\phi_s^{dq}, \phi_r^{dq}) \frac{\tilde{u}}{\tilde{\Omega}}$ .



(b) Stator current ripple amplitude on the orthogonal axis  $\frac{\partial^2 \mathcal{H}^{dq}}{\partial \phi_s^{dq2}}(\phi_s^{dq}, \phi_r^{dq}) \frac{\tilde{u}}{\tilde{\Omega}}$ .

Figure 5.15 – Experimental HF response (+ and  $\times$ ) obtained on the IM described in table 2.2 and simulated HF response (solid lines) using the model described by eqs. (5.19) and (5.20) with the parameters from table 5.6.

### 5.3.4 Tests with load

IMs yield a torque under the condition that  $\omega_s \neq \omega$ . We thus have 2 basic solutions: Either rotating the IM with the load machine at  $\omega_s = 0$  or locking the rotor and taking  $\omega_s \neq 0$ . As we are interested by the low speed domain and as the load machine cannot rotate regularly at low speed under torque, we must choose the second solution. The drawback is that we will have to filter out the noise caused by the non-sinusoidality of the stator wirings.

#### 5.3.4.1 Experimental protocol

The IM is locked using the brake of the test bench. We inject some constant current along the  $d$  axis of a  $dq$  frame which rotates at the chosen frequency  $\omega_s$  with respect to the  $\alpha\beta$  frame.

We also inject a  $\pm 20V$  HF square signal of frequency  $500Hz$  along an axis rotating slowly (at  $\omega_i = \dot{\theta}_i = 1Hz$ ) with respect to the chosen  $dq$  frame. The HF response is measured along the injection axis  $u$  and the orthogonal axis  $v$ . As in section 5.2.1.2 this allows us to get  $\frac{\partial^2 \mathcal{H}^{dq}}{\partial \phi_s^* \partial \phi_s}$  and the modulus and phase of  $\frac{\partial^2 \mathcal{H}^{dq}}{\partial \phi_s^{*2}}$ .

#### 5.3.4.2 Experimental results

The aforementioned test was repeated for some values of  $\omega_s$  and for each  $0.1A$  for the constant current. After adequate processing to extract the ripple and remove the noise caused by non-sinusoidality of the motor, we obtained the curves shown in fig. 5.16.

By contrast with the curves of figs. 5.10 and 5.11 increasing or decreasing current has the same effect which means that hysteresis does not affect the results anymore.

Considering the symmetries of the energy function (see section 3.4) we can prove that its partial derivatives have the parities listed in table 5.7. Moreover when the stator current is reverted all fluxes components are reverted whereas when the stator speed is reverted only  $\phi_s^q$  and  $\phi_r^q$  are reverted. Thus the curves of figs. 5.16a and 5.16b should be even with respect to the stator current and the stator speed whereas the curves of fig. 5.16c should be even with respect to the stator current and odd with respect to the stator speed. The data plotted in fig. 5.16 obviously agree with what was foretold using the symmetries of the IM.

We also notice that the amplitude of the magnetic saliency is very small: It hardly goes above  $0.1A$ . For modeling this is not a problem but when trying to control the IM using signal injection we will have to use a larger HF injection.

Finally the model eqs. (5.19) and (5.20) do not convey what is observed under load. Neither the shape of the curves of fig. 5.16a nor the large phase variation in fig. 5.16c can be explained by the proposed model. It seems that the load and thus the appearance of rotor currents has an important effect on the HF response.

Compared to the case of the PMSM (see [37]) a much wider flux range is covered as in the SynRM case. This will prevent us from using a Taylor series as in the case of the SynRM. However the whole flux range is not used in normal operation of the IM as the flux remains usually close to its nominal value. We thus carried out another test with a more constant flux.

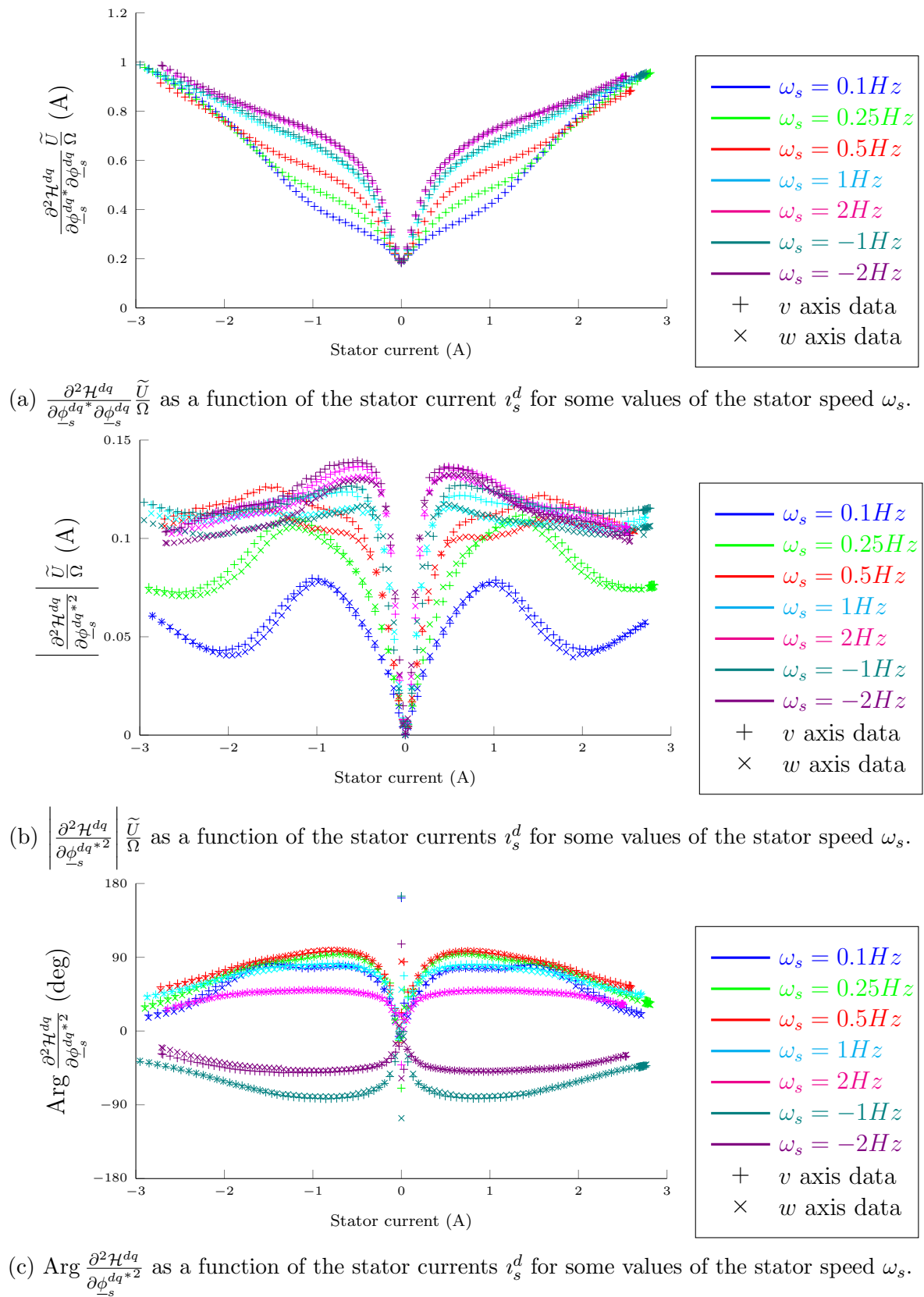


Figure 5.16 – Information extracted using HF injection applied to the 0.75kW IM described in table 2.2.

	$\phi_s^d$	$\phi_s^q$	$\phi_r^d$	$\phi_r^q$
$i_s^d = \frac{\partial \mathcal{H}^{dq}}{\partial \phi_s^d}$	odd	even	even	even
$i_s^q = \frac{\partial \mathcal{H}^{dq}}{\partial \phi_s^q}$	even	odd	even	even
$\Gamma_{t_s}^d = \frac{\partial^2 \mathcal{H}^{dq}}{\partial \phi_s^{d2}}$	even	even	even	even
$\Gamma_{t_s}^q = \frac{\partial^2 \mathcal{H}^{dq}}{\partial \phi_s^{q2}}$	even	even	even	even
$\frac{\partial^2 \mathcal{H}^{dq}}{\partial \phi_s^d \partial \phi_s^q}$	odd	odd	even	even

Table 5.7 – Parities of the paratial derivatives of the energy function.

### 5.3.4.3 Experimental protocol

The IM is still locked but instead of choosing the constant current we inject, we compute the voltage needed to achieve a constant flux target. We thus ensure that the flux is aligned along the  $d$  axis and has the desired norm. As before we inject a  $\pm 20V$  HF square signal along an axis rotating slowly (at  $\omega_i = \dot{\theta}_i = 1Hz$ ) with respect to the chosen  $dq$  frame. The HF response is measured along the injection axis  $u$  and the orthogonal axis  $v$ .

### 5.3.4.4 Experimental results

The aforementioned test was repeated for some values of the flux norm and for each  $0.1Hz$  for  $\omega_s$ . We thus obtained the experimental points represented in fig. 5.17.

Again hysteresis does not affect the results. We also find the same symmetries as before: The curves in figs. 5.17a and 5.17b are even with respect to the stator speed whereas the curves in fig. 5.17c are odd with respect to the stator speed. They should also be even with respect to the flux, but this is not visible as we only used positive fluxes.

As noted previously the amplitude of the magnetic saliency is quite small as in the previous tests. Moreover, contrarily to intuition, it decreases when the flux increases. The only solution we have is thus to increase the amplitude of the HF signal.

The phase again varies greatly around zero load. We can observe that it is almost in quadrature with the estimated direction of the rotor flux  $\phi_r^{dq}$ , i.e. the estimated direction of the rotor current  $i_r^{dq}$ . Our model obviously do not convey this phenomenon.

### 5.3.5 Modeling tentatives

From the result of the section section 5.3.4 it becomes obvious that the model, eqs. (5.19) and (5.20), is not sufficient to describe the induction machine. Moreover the model is valid only in the domain where the IM does not yield any power.

To control the IM a more accurate model is needed. We would like it to be valid at least in the range  $[0.5\phi_r^n, 1.5\phi_r^n]$  which is the range where the motor will be most probably used. We thus avoid the range where hysteresis has a notable effect. For its design we are going to use again the energy-based framework which was fruitful until now. Our interesting attempts to model the magnetic saturation of the IM under load are presented in this section, even though we failed to obtain a model conveying all the observed effects.

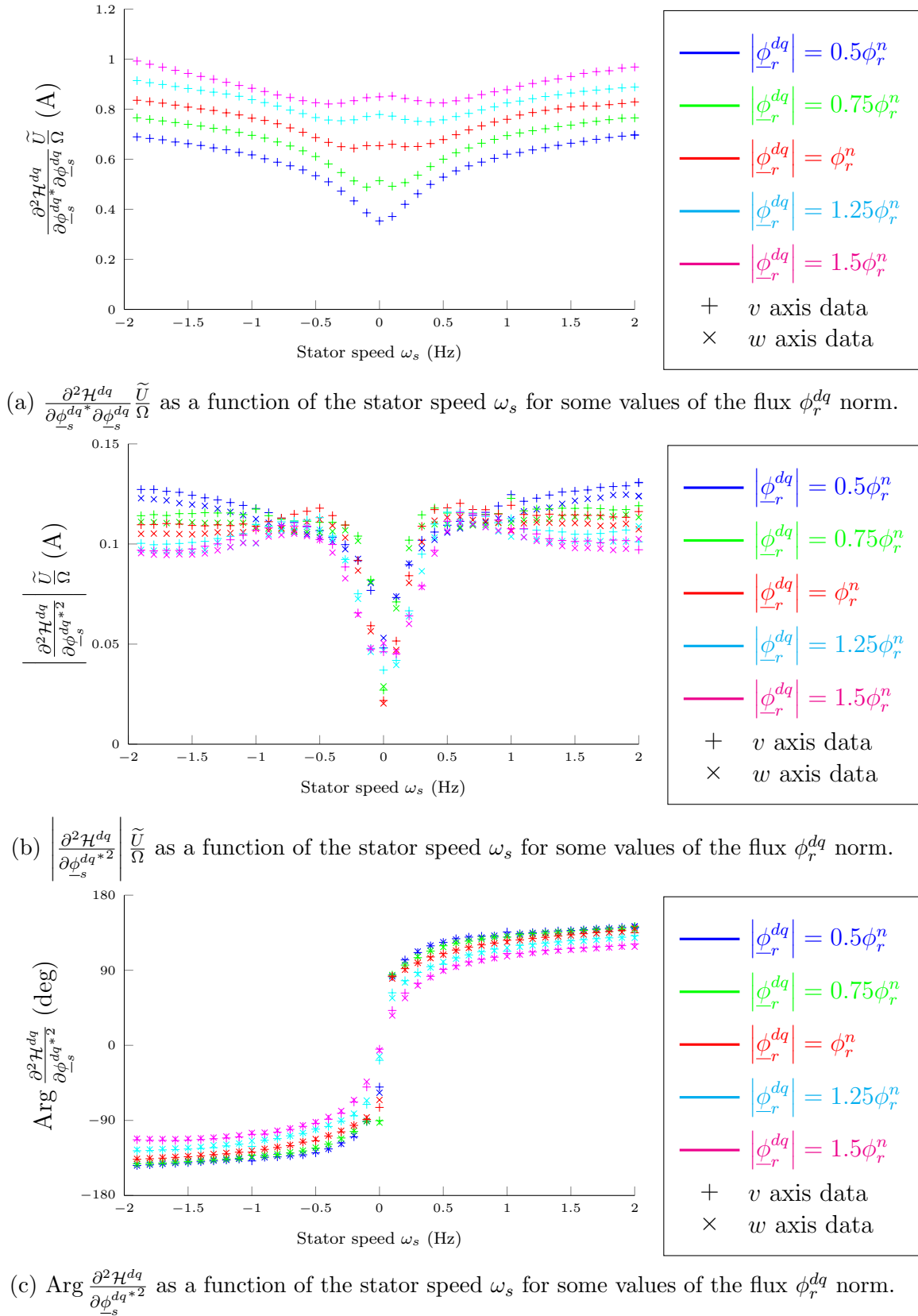


Figure 5.17 – Information extracted at almost constant flux using HF injection applied to the 0.75kW IM described in table 2.2.

### 5.3.5.1 Rotation of the eigen-spaces of the current-flux relation

The energy function which gave good results at zero load (see eq. (5.19)) can be written with complex variables (see section 3.2.3 for how they can be used with energy-based modeling)

$$\mathcal{H}^{dq}(\theta, \rho, \underline{\phi}_s^{dq}, \underline{\phi}_s^{dq*}, \underline{\phi}_r^{dq*}, \underline{\phi}_r^{dq}) = \left( \begin{array}{c} \underline{\phi}_r^{dq} \\ \underline{\phi}_s^{dq} \end{array} \right)^\dagger \underline{\mathcal{R}}^\dagger(0, \frac{\pi}{4}, 0) \Gamma \left( |\underline{\phi}_m^{dq}|^2 \right) \underline{\mathcal{R}}(0, \frac{\pi}{4}, 0) \left( \begin{array}{c} \underline{\phi}_r^{dq} \\ \underline{\phi}_s^{dq} \end{array} \right) \quad (5.21)$$

where  $\underline{\mathcal{R}}(0, \frac{\pi}{4}, 0) \in SO(2) \subset \mathcal{M}_2(\mathbb{R})$  is the rotation of angle  $\frac{\pi}{4}$ . As it seems that the phase of the eigenvectors is modified, our idea is to change the orientation of the eigenvectors by changing this rotation. As we are working with complex numbers, we will be working with the unit group  $SU(2) \subset \mathcal{M}_2(\mathbb{C})$  which can be parametrized as follows

$$\underline{\mathcal{R}}(\eta_x, \eta_y, \eta_z) := \left( \begin{array}{cc} e^{j\eta_z} \cos(\eta_y) & e^{j\eta_x} \sin(\eta_y) \\ -e^{-j\eta_x} \sin(\eta_y) & e^{-j\eta_z} \cos(\eta_y) \end{array} \right).$$

To obtain the curves of figs. 5.16 and 5.17  $\eta_x$ ,  $\eta_y$  and  $\eta_z$  must depend on the fluxes and be equal to 0,  $\frac{\pi}{4}$  and 0 respectively when there is no load. This can lead to quite complex computations in the general case. Thus we will suppose that the disturbance is small enough and use the first order approximation of  $\underline{\mathcal{R}}$

$$\underline{\mathcal{R}}(\eta_x, \eta_y, \eta_z) = \left( \begin{array}{cc} 1 + j\eta_z + o(\eta_x, \eta_y, \eta_z) & \eta_y(1 + j\eta_x) + o(\eta_x, \eta_x\eta_z) \\ -\eta_y(1 - j\eta_x) + o(\eta_x, \eta_x\eta_z) & 1 - j\eta_z + o(\eta_x, \eta_y, \eta_z) \end{array} \right) \quad (5.22a)$$

$$\approx \left( \begin{array}{cc} 1 & 0 \\ 0 & 1 \end{array} \right) + \left( \begin{array}{cc} 0 & j \\ j & 0 \end{array} \right) \eta_y \eta_x + \left( \begin{array}{cc} 0 & 1 \\ -1 & 0 \end{array} \right) \eta_y + \left( \begin{array}{cc} j & 0 \\ 0 & -j \end{array} \right) \eta_z \quad (5.22b)$$

$$\approx I_2 + j\sigma_x \eta_y \eta_x + j\sigma_y \eta_y + j\sigma_z \eta_z \quad (5.22c)$$

where  $\sigma_x$ ,  $\sigma_y$  and  $\sigma_z$  are Pauli matrices.

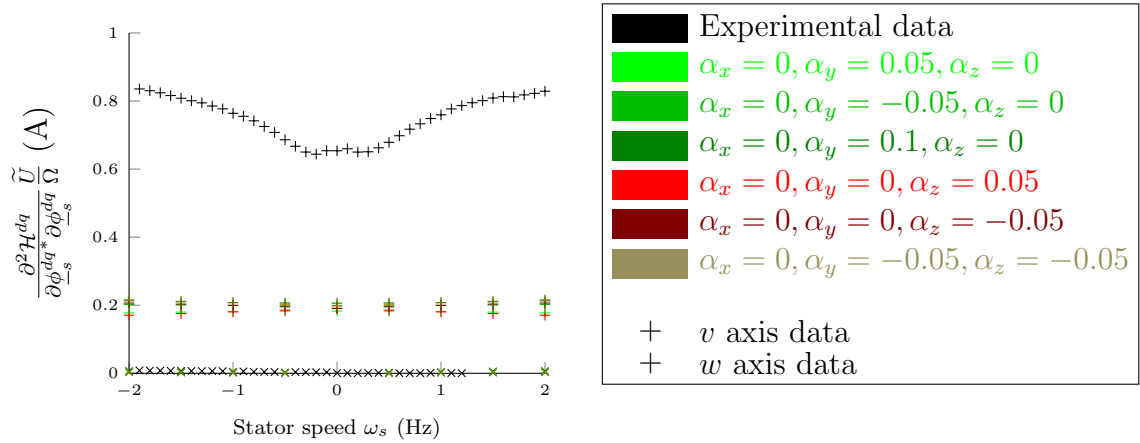
As the computations are quite tedious due to the dependencies of the angle on the fluxes even with the first order approximation of matrices of  $SU(2)$ , I tested only the most simple case in simulation: The angles  $\eta_x$ ,  $\eta_y$  and  $\eta_z$  are linear functions of  $\Im(\underline{\phi}_s^{dq} \underline{\phi}_r^{dq*})^2$  with coefficients  $\alpha_x$ ,  $\alpha_y$  and  $\alpha_z$ . For the inverse inductance matrix  $\Gamma$ , we used both the unsaturated model (see fig. 5.18), to see the effects of each term, and the saturated model developed in section 5.3.3 (see fig. 5.19) which worked at zero torque.

As simulations did not gave good results, this approach was abandoned because it seemed sterile and rapidly lead to very complex computations.

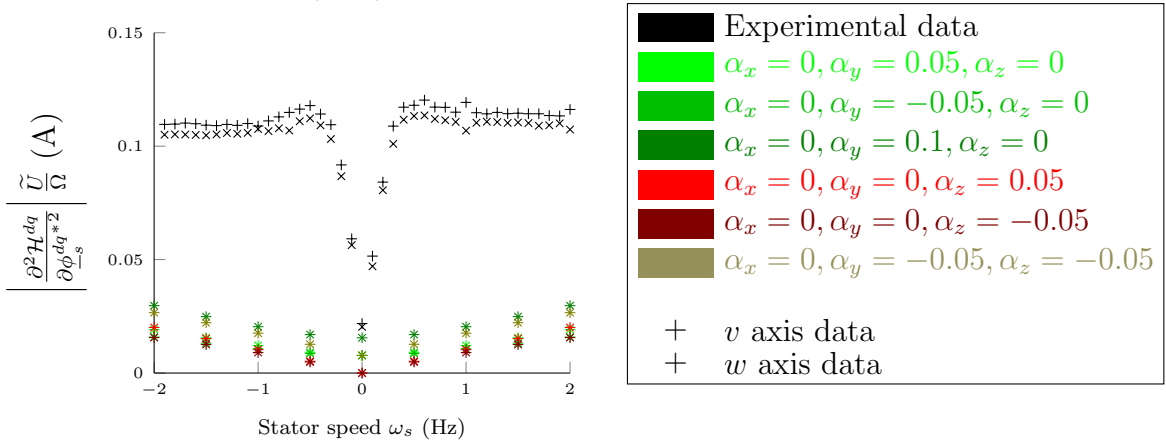
### 5.3.5.2 Different leakage inductances

As the presence of rotor current seems to impact greatly the measured ripple we studied more carefully the layout of the rotor and discovered by comparing to the literature [78] that the motor has most probably closed slots on the rotor (whereas stator slots are open). Thus taking equal leakage inductances is not possible and we must consider that they are not equal. Besides the current response to HF signal injection is mainly caused by the saturation of the leakage flux paths (see section 5.1.2). We still would like to have a formula similar to eq. (5.14) and we find

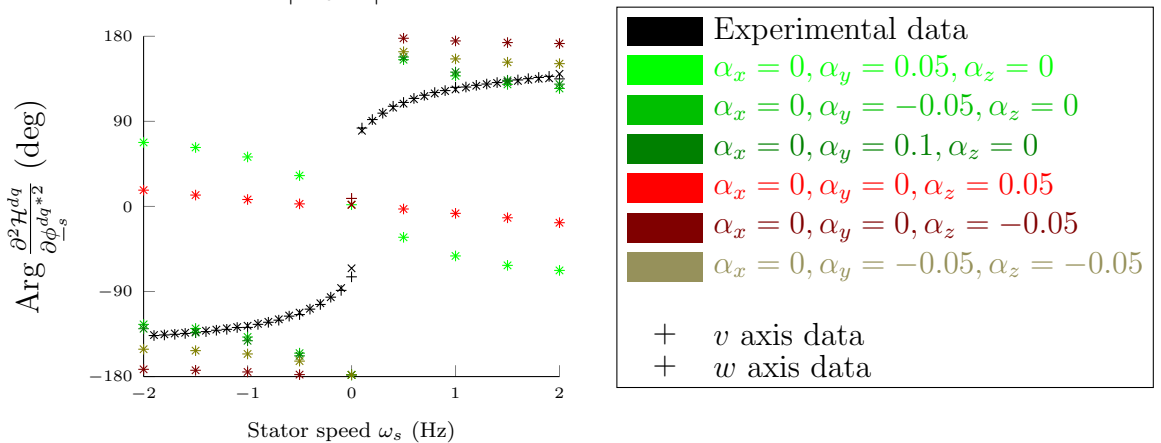
$$\begin{aligned} \underline{\mathcal{H}}^{dq}(\rho, \underline{\phi}_s^{dq}, \underline{\phi}_r^{dq}) &= \frac{1}{2J_L n^2} \rho^2 + \frac{1}{2} \Gamma_M^{dq} |\underline{\phi}_s^{dq} + \underline{\phi}_r^{dq}|^2 + \frac{1}{2} \Gamma_L^{dq} |\underline{\phi}_s^{dq} - \underline{\phi}_r^{dq}|^2 \\ &\quad + \Gamma_X^{dq} \Re\left( (\underline{\phi}_s^{dq} + \underline{\phi}_r^{dq})(\underline{\phi}_s^{dq} - \underline{\phi}_r^{dq})^* \right) \end{aligned} \quad (5.23)$$



(a)  $\frac{\partial^2 \mathcal{H}^{dq}}{\partial \phi_{-s}^{dq*} \partial \phi_{-s}^{dq}} \tilde{\Omega}$  as a function of the stator speed  $\omega_s$ .



(b)  $\left| \frac{\partial^2 \mathcal{H}^{dq}}{\partial \phi_{-s}^{dq*2}} \tilde{\Omega} \right|$  as a function of the stator speed  $\omega_s$ .



(c)  $\text{Arg} \frac{\partial^2 \mathcal{H}^{dq}}{\partial \phi_{-s}^{dq*2}} \tilde{\Omega}$  as a function of the stator speed  $\omega_s$ .

Figure 5.18 – Testing the modeling approach of section 5.3.5.1 in simulation on an unsaturated IM model under nominal flux with the parameters  $\eta_x$ ,  $\eta_y$  and  $\eta_z$  linearly depending on  $\Im(\phi_s^{dq} \phi_r^{dq*})^2$  to understand the effects of the parameter of the rotation  $\mathcal{R}$ .

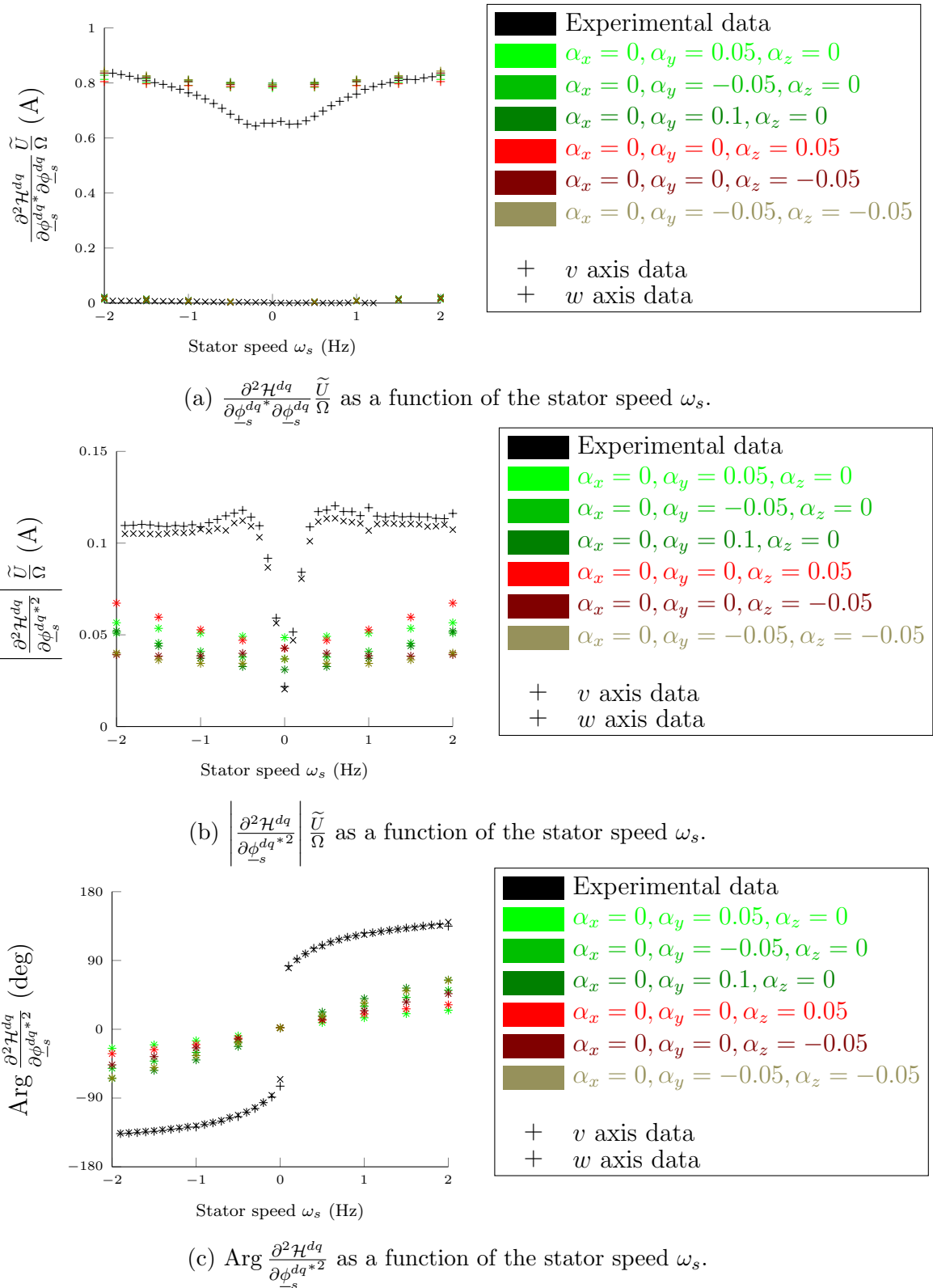


Figure 5.19 – Testing the modeling approach proposed in section 5.3.5.1 in simulation on a saturated IM model under nominal flux with the parameters  $\eta_x$ ,  $\eta_y$  and  $\eta_z$  linearly depending on  $\Im(\phi_{-s}^{dq} \phi_{-r}^{dq*})^2$ .

with  $\Gamma_M^{dq} := \Gamma_m^{dq} + \frac{\Gamma_{ls}^{dq} + \Gamma_{lr}^{dq}}{4}$ ,  $\Gamma_L^{dq} := \frac{\Gamma_{ls}^{dq} + \Gamma_{lr}^{dq}}{4}$  and  $\Gamma_X^{dq} := \frac{\Gamma_{ls}^{dq} - \Gamma_{lr}^{dq}}{4}$ . This is a generalization of eq. (5.14) the eigenvectors are not aligned with  $(1, 1)^T$  and  $(1, -1)^T$  any more.

Of course we need to saturate the inductances. For the magnetizing inductance  $\Gamma_M^{dq}$  we stick to the function proposed in section 5.3.3. But for the leakage inductance there is no model in the literature. Moreover we cannot even get the shape of these functions. We tried sensible functions based on sensible shapes. However the results were not good enough.

### 5.3.5.3 Polynomial term creating no ripple at zero load

The major problem with Hamiltonian modeling stems from the fact that the 2 state variables (i.e.  $\underline{\phi}_s^{dq}$  and  $\underline{\phi}_r^{dq}$ ) are almost collinear. Indeed, these are fluxes going through the stator and rotor surfaces respectively and these surfaces are by construction as close as possible. Thus, there will not be an important difference between the two fluxes. Therefore in most Hamiltonian models, the phase of the stator current ripple amplitude is almost aligned with the main flux (see [57, 78]), but this is not what is observed in the experiments.

Indeed during experiments it was found to be almost in quadrature with respect to the estimated value of  $\underline{\phi}_r^{dq}$ . To a lesser extent this is signaled in Yoon and Sul [4] where the maximum of the ripple amplitude shifts by  $20^\circ$  from the flux axis. It would thus be interesting to find terms creating a ripple orthogonal to  $\underline{\phi}_r^{dq}$  or  $\underline{\phi}_r^{dq^2}$ . We try it on the simplest energy function possible, the polynomial

$$P(\underline{\phi}_s^{dq}, \underline{\phi}_s^{dq*}, \underline{\phi}_r^{dq}, \underline{\phi}_r^{dq*}) = \sum_{(a_1, a_2, a_3, a_4) \in \mathbb{N}^4} \alpha_{a_1 a_2 a_3 a_4} \underline{\phi}_s^{dq^{a_1}} \underline{\phi}_s^{dq^{*a_2}} \underline{\phi}_r^{dq^{a_3}} \underline{\phi}_r^{dq^{*a_4}}. \quad (5.24)$$

Creating a ripple orthogonal to  $\underline{\phi}_r^{dq}$  is not possible, when the symmetry conditions are respected. However creating a ripple orthogonal to  $\underline{\phi}_r^{dq^2}$  is possible under the following conditions.

**Real Hamiltonian** The energy function should be real that is to say it should be equal to its complex conjugate which reads

$$P(\underline{\phi}_s^{dq}, \underline{\phi}_s^{dq*}, \underline{\phi}_r^{dq}, \underline{\phi}_r^{dq*}) = P(\underline{\phi}_s^{dq*}, \underline{\phi}_s^{dq}, \underline{\phi}_r^{dq*}, \underline{\phi}_r^{dq}) \quad (5.25)$$

**Invariance** The energy function should be invariant by rotation and the symmetry described in section 3.4.2.1, that is to say, including the previous condition

$$P(\underline{\phi}_s^{dq}, \underline{\phi}_s^{dq*}, \underline{\phi}_r^{dq}, \underline{\phi}_r^{dq*}) = P\left(\left|\underline{\phi}_s^{dq}\right|^2, 2\Re(\underline{\phi}_s^{dq} \underline{\phi}_r^{dq*}), \left|\underline{\phi}_r^{dq}\right|^2\right) \quad (5.26)$$

**Orthogonality** The double derivative of the energy function with respect to  $\underline{\phi}_s^{dq*}$  should be orthogonal to  $\underline{\phi}_r^{dq^2}$  which means that the dot product between them should be zero, i.e.

$$\begin{aligned} & - \sum_{(a_1, a_2, a_3, a_4) \in \mathbb{N}^4} a_2(a_2 - 1) \alpha_{a_1 a_2 a_3 a_4} \underline{\phi}_s^{dq^{a_1}} \underline{\phi}_s^{dq^{*a_2-2}} \underline{\phi}_r^{dq^{a_3}} \underline{\phi}_r^{dq^{*a_4+2}} \\ & = \sum_{(a'_1, a'_2, a'_3, a'_4) \in \mathbb{N}^4} a'_2(a'_2 - 1) \alpha_{a'_1 a'_2 a'_3 a'_4} \underline{\phi}_s^{dq^{a'_2-2}} \underline{\phi}_s^{dq^{*a'_1}} \underline{\phi}_r^{dq^{a'_4+2}} \underline{\phi}_r^{*a'_3} \end{aligned} \quad (5.27)$$

These relations give constraints on the coefficients  $\alpha_{a_1 a_2 a_3 a_4}$  of the polynomial:

- Eq. (5.25) is equivalent to  $\forall(a_1, a_2, a_3, a_4) \in \mathbb{N}^4$

$$\alpha_{a_1 a_2 a_3 a_4} = \alpha_{a_2 a_1 a_4 a_3} \quad (5.28)$$

- Eq. (5.26) implies to  $\forall(a_1, a_2, a_3, a_4) \in \mathbb{N}^4$

$$(a_1 + a_3) \neq (a_2 + a_4) \Rightarrow \alpha_{a_1 a_2 a_3 a_4} = 0 \quad (5.29)$$

- Eq. (5.27) is equivalent to  $\forall(a_1, a_2, a_3, a_4) \in \mathbb{N}^4$

$$(a_2 + 2)(a_2 + 1)\alpha_{a_1(a_2+2)(a_3+2)a_4} = -(a_1 + 2)(a_1 + 1)\alpha_{a_2(a_1+2)(a_4+2)a_3} \quad (5.30)$$

It was found algorithmically that the constraints eqs. (5.28) to (5.30) can be verified simultaneously, the lower degree polynomials being

$$\begin{aligned} & \frac{\phi_{\underline{s}}^{dq} \phi_{\underline{s}}^{dq*2}}{\phi_{\underline{r}}^{dq^2} \phi_{\underline{r}}^{dq*}} + \frac{\phi_{\underline{s}}^{dq^2} \phi_{\underline{s}}^{dq*}}{\phi_{\underline{r}}^{dq} \phi_{\underline{r}}^{dq*2}} - \frac{1}{3} \frac{\phi_{\underline{s}}^{dq^3} \phi_{\underline{r}}^{dq^3}}{\phi_{\underline{s}}^{dq^3} \phi_{\underline{r}}^{dq*3}} - \frac{1}{3} \frac{\phi_{\underline{s}}^{dq^3} \phi_{\underline{r}}^{dq*3}}{\phi_{\underline{s}}^{dq^3} \phi_{\underline{r}}^{dq*3}} \\ & \frac{\phi_{\underline{s}}^{dq^2} \phi_{\underline{s}}^{dq*2}}{\phi_{\underline{r}}^{dq^2} \phi_{\underline{r}}^{dq*2}} - \frac{1}{6} \frac{\phi_{\underline{s}}^{dq^4} \phi_{\underline{r}}^{dq^4}}{\phi_{\underline{s}}^{dq^4} \phi_{\underline{r}}^{dq*4}} - \frac{1}{6} \frac{\phi_{\underline{s}}^{dq^4} \phi_{\underline{r}}^{dq*4}}{\phi_{\underline{s}}^{dq^4} \phi_{\underline{r}}^{dq*4}} \\ & \frac{\phi_{\underline{s}}^{dq} \phi_{\underline{s}}^{dq*2}}{\phi_{\underline{r}}^{dq^3} \phi_{\underline{r}}^{dq*2}} + \frac{\phi_{\underline{s}}^{dq^2} \phi_{\underline{s}}^{dq*}}{\phi_{\underline{r}}^{dq^2} \phi_{\underline{r}}^{dq*3}} - \frac{1}{3} \frac{\phi_{\underline{s}}^{dq^3} \phi_{\underline{r}}^{dq^4} \phi_{\underline{r}}^{dq*}}{\phi_{\underline{s}}^{dq^3} \phi_{\underline{r}}^{dq} \phi_{\underline{r}}^{dq*4}} - \frac{1}{3} \frac{\phi_{\underline{s}}^{dq^3} \phi_{\underline{r}}^{dq} \phi_{\underline{r}}^{dq*4}}{\phi_{\underline{s}}^{dq^3} \phi_{\underline{r}}^{dq} \phi_{\underline{r}}^{dq*4}} \end{aligned}$$

As can be seen in fig. 5.20 in blue when one of these polynomial terms is added to an unsaturated energy function the phase matches the experimental phase. On the other hand the mean value and the amplitude of the ripple are badly modeled of course. However when saturation is added (in green in fig. 5.20) to the leakage inductance, the quality of the phase model decreases and the modeling of the mean value and amplitude of ripple are not increased much.

#### 5.3.5.4 Lagrangian-based modeling in dq frame

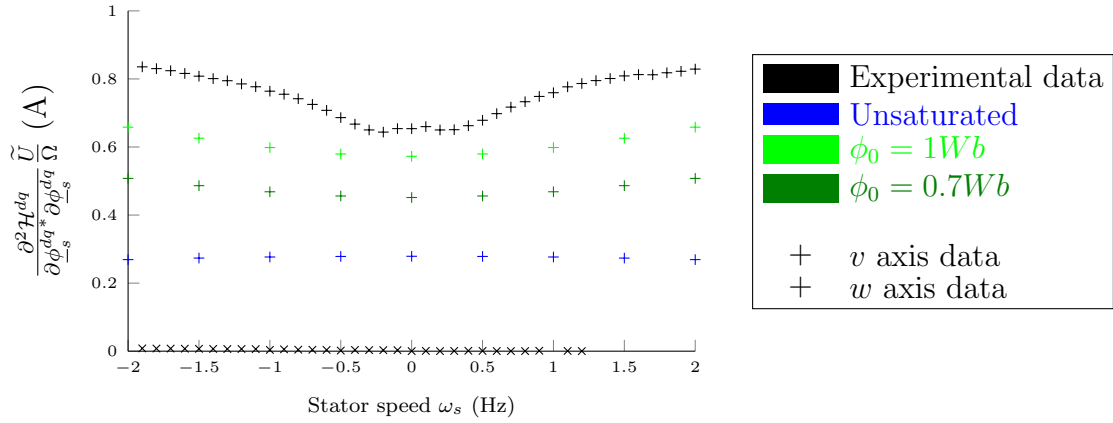
The rotor current seems to have a great influence on the stator current ripple amplitude as was demonstrated in section 5.3.4. Besides the phase of the ripple was experimentally shown to be in the direction of the rotor current. It seems that the rotor slots bridges (see [34, ch. 4-6]) are saturated by the leakage flux created by the rotor current. It could be thus interesting to have the rotor current  $i_r^{dq}$  as one of our state variables. To do this we just have to use Lagrangian based modeling. The only problem is that we will not have such simple equations as the Lagrangian does not yield state equations directly.

A Lagrangian model of a generic electric motor is given in the  $abc$  frame in section 3.2.4. Applying the same method as in sections 3.3.2 and 3.3.3 this model can be transformed to  $dq0$  frame. After decoupling the 0 axis as in section 3.5, Euler-Lagrange equations in  $dq$  frame in the case of a sinusoidal motor are given by

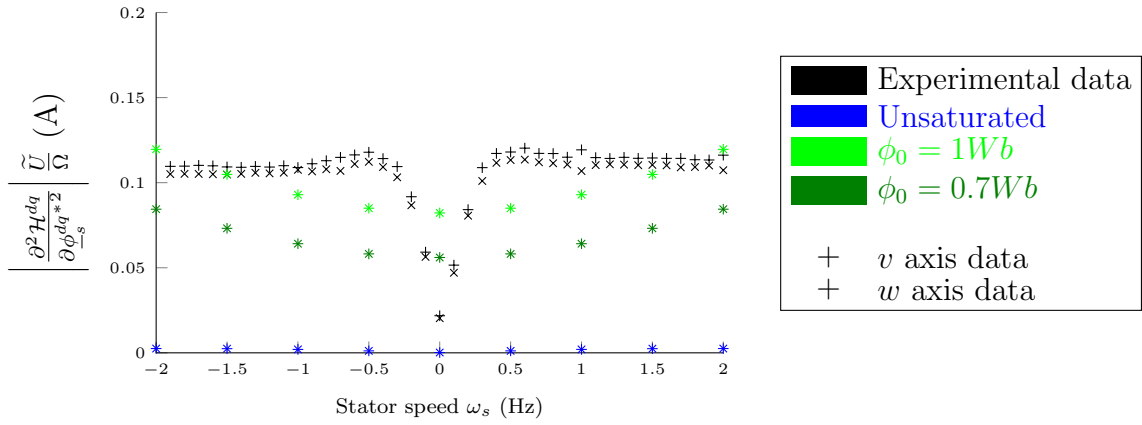
$$\frac{d}{dt} \frac{\partial \mathcal{L}^{dq}}{\partial i_s^{dq}} = u_s^{dq} - R_s i_s^{dq} - j\omega_s \frac{\partial \mathcal{L}^{dq}}{\partial i_s^{dq}} \quad (5.31a)$$

$$\frac{d}{dt} \frac{\partial \mathcal{L}^{dq}}{\partial i_r^{dq}} = -R_r i_r^{dq} - j(\omega_s - \omega) \frac{\partial \mathcal{L}^{dq}}{\partial i_r^{dq}} \quad (5.31b)$$

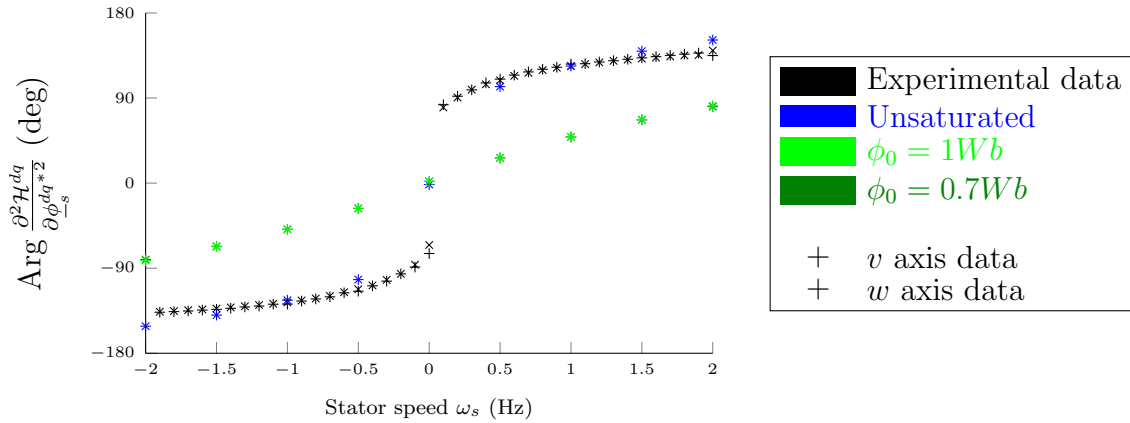
$$\frac{d}{dt} \frac{\partial \mathcal{L}^{dq}}{\partial \omega} = \frac{\partial \mathcal{L}^{dq}}{\partial i_r^{dq}} \mathcal{J}_2 i_r^{dq} - \frac{T_L}{n} \quad (5.31c)$$



(a)  $\frac{\partial^2 \mathcal{H}^{dq}}{\partial \phi_s^{dq*} \partial \phi_s^{dq}} \tilde{U}$  as a function of the stator speed  $\omega_s$ .



(b)  $\left| \frac{\partial^2 \mathcal{H}^{dq}}{\partial \phi_s^{dq*2}} \right| \tilde{U}$  as a function of the stator speed  $\omega_s$ .



(c)  $\text{Arg} \frac{\partial^2 \mathcal{H}^{dq}}{\partial \phi_s^{dq*2}}$  as a function of the stator speed  $\omega_s$ .

Figure 5.20 – Testing the modeling approach proposed in section 5.3.5.3 in simulation on a saturated IM model under nominal flux with 100 times the polynomial of order 6 added to the energy function.

which are not a state form as expected. Using the chain rule and supposing that the flux-current relations do not depend on  $\omega$  we find

$$\begin{pmatrix} \frac{d}{dt} \frac{\partial \mathcal{L}^{dq}}{\partial i_s^{dq}} \\ \frac{d}{dt} \frac{\partial \mathcal{L}^{dq}}{\partial i_r^{dq}} \end{pmatrix} = \frac{d}{dt} \begin{pmatrix} \frac{\partial \mathcal{L}^{dq}}{\partial i_s^{dq}} \\ \frac{\partial \mathcal{L}^{dq}}{\partial i_r^{dq}} \end{pmatrix} = \begin{pmatrix} \frac{\partial^2 \mathcal{L}^{dq}}{\partial i_s^{dq} \partial i_s^{dq}} & \frac{\partial^2 \mathcal{L}^{dq}}{\partial i_s^{dq} \partial i_r^{dq}} \\ \frac{\partial^2 \mathcal{L}^{dq}}{\partial i_r^{dq} \partial i_s^{dq}} & \frac{\partial^2 \mathcal{L}^{dq}}{\partial i_r^{dq} \partial i_r^{dq}} \end{pmatrix} \begin{pmatrix} \frac{di_s^{dq}}{dt} \\ \frac{di_r^{dq}}{dt} \end{pmatrix} = \frac{\partial^2 \mathcal{L}^{dq}}{\partial (i_s^{dq}, i_r^{dq})^2} \begin{pmatrix} \frac{di_s^{dq}}{dt} \\ \frac{di_r^{dq}}{dt} \end{pmatrix}$$

where  $\frac{\partial^2 \mathcal{L}^{dq}}{\partial (i_s^{dq}, i_r^{dq})^2}$  is the Hessian matrix of the magnetic part of the Lagrangian function. Using the currents and the speed as state variables and supposing the mechanical energy is  $\frac{1}{2} J_L \left(\frac{\omega}{n}\right)^2$ , we find as state form

$$\begin{pmatrix} \frac{d}{dt} i_s^{dq} \\ \frac{d}{dt} i_r^{dq} \\ \frac{d}{dt} \omega \end{pmatrix} = \begin{pmatrix} \left( \frac{\partial^2 \mathcal{L}^{dq}}{\partial (i_s^{dq}, i_r^{dq})^2} \right)^{-1} & 0_{4,1} \\ 0_{1,4} & \frac{n}{J_L} \end{pmatrix} \begin{pmatrix} u_s^{dq} - R_s i_s^{dq} - j \omega_s \frac{\partial \mathcal{L}^{dq}}{\partial i_s^{dq}} \\ -R_r i_r^{dq} - j(\omega_s - \omega) \frac{\partial \mathcal{L}^{dq}}{\partial i_r^{dq}} \\ n \frac{\partial \mathcal{L}^{dq}}{\partial i_r^{dq}} \mathcal{J}_2 i_r^{dq} - T_L \end{pmatrix}. \quad (5.32)$$

We know from section 4.2.3 that the stator voltage ripple  $\tilde{u}_s^{dq} = \tilde{u} f(\Omega t)$  creates a stator flux ripple  $\tilde{\phi}_s^{dq} = \frac{\tilde{u}}{\Omega} F(\Omega t)$ . At first order the current ripple can be expressed

$$\begin{pmatrix} \tilde{i}_s^{dq} \\ \tilde{i}_r^{dq} \end{pmatrix} = \begin{pmatrix} \frac{\partial^2 \mathcal{L}^{dq}}{\partial (i_s^{dq}, i_r^{dq})^2} \end{pmatrix}^{-1} \begin{pmatrix} \frac{\tilde{u}}{\Omega} F(\Omega t) \\ 0_{2,1} \end{pmatrix} \quad (5.33)$$

using the chain rule as above. Alternatively, using the Jacobian matrices of the flux-current relations, the stator current ripple can be expressed as

$$\tilde{i}_s^{dq} = \left( \frac{\partial \phi_s^{dq}}{\partial i_s^{dq}} - \frac{\partial \phi_s^{dq}}{\partial i_r^{dq}} \left( \frac{\partial \phi_r^{dq}}{\partial i_r^{dq}} \right)^{-1} \frac{\partial \phi_r^{dq}}{\partial i_s^{dq}} \right)^{-1} \frac{\tilde{u}}{\Omega} F(\Omega t). \quad (5.34)$$

We showed how to make a Lagrangian-based model of an IM and computed the expected stator current ripple using the partial derivatives of the energy function. The currents are now state variables which is advantageous. However it has a major drawback: The algebraic calculation of the ripple are almost impossible. Despite this problem I wrote some Lagrangian models of IM based on

$$\begin{aligned} \mathcal{L}^{dq}(\omega, i_s^{dq}, i_r^{dq}) &= \frac{1}{2} \frac{J_L}{n^2} \omega^2 + \frac{1}{2} f_m \left( |i_s^{dq} + i_r^{dq}|^2 \right) + \frac{1}{2} L_{ls} f_l \left( |i_s^{dq} + i_r^{dq}|^2 \right) |i_s^{dq}|^2 \\ &\quad + \frac{1}{2} L_{lr} f_l \left( |i_s^{dq} + i_r^{dq}|^2 \right) f_r \left( |i_r^{dq}|^2 \right) |i_r^{dq}|^2 \end{aligned} \quad (5.35)$$

with the parameters given in table 5.8. This expression includes the main flux path saturation (see [17, 21]) through  $f_m$  but also leakage flux path saturation as in section 5.3.3 through  $f_l$  and saturation of the rotor leakage flux path through  $f_r$ . It gave quite good results as can be seen in fig. 5.21 but I could not tune correctly the coefficients and was not able fit the experimental curves.

### 5.3.5.5 Other choices of state variables in dq frame

The preceding sections shows that we have to trade off between the complexity of the calculations and the choice of state variables. It is very advantageous to have the rotor current as a state variable as it seems to have a great effect on the saturation of the motor.

Model	Function Expression	Parameters
1	$f_m \left( \left  \underline{z}_s^{dq} + \underline{z}_r^{dq} \right ^2 \right) = L_m$ $f_l \left( \left  \underline{z}_s^{dq} + \underline{z}_r^{dq} \right ^2 \right) = 1$ $f_r \left( \left  \underline{z}_r^{dq} \right ^2 \right) = x_r^\infty + \frac{1-x_r^\infty}{1+\frac{\left  \underline{z}_r^{dq} \right ^2}{i_0^2}}$	$L_m = 0.42H$ $L_{ls} = 0.09H$ $L_{lr} = 0.15H$ $x_r^\infty = 0.2$ $i_0 = 0.32A$
2	$f_m \left( \left  \underline{z}_s^{dq} + \underline{z}_r^{dq} \right ^2 \right) = L_m$ $f_l \left( \left  \underline{z}_s^{dq} + \underline{z}_r^{dq} \right ^2 \right) = 1$ $f_r \left( \left  \underline{z}_r^{dq} \right ^2 \right) = x_r^\infty + \frac{1-x_r^\infty}{1+\frac{\left  \underline{z}_r^{dq} \right ^2}{i_0}}$	$L_m = 0.42H$ $L_{ls} = 0.12H$ $L_{lr} = 0.12H$ $x_r^\infty = 0.5$ $i_0 = 0.1A$
3	$f_m \left( \left  \underline{z}_s^{dq} + \underline{z}_r^{dq} \right ^2 \right)$ see Malrait [17] $f_l \left( \left  \underline{z}_s^{dq} + \underline{z}_r^{dq} \right ^2 \right) = x_l^\infty + \frac{1-x_l^\infty}{1+\frac{\left  \underline{z}_s^{dq} + \underline{z}_r^{dq} \right ^2}{i_1}}$ $f_r \left( \left  \underline{z}_r^{dq} \right ^2 \right) = x_r^\infty + \frac{1-x_r^\infty}{1+\frac{\left  \underline{z}_r^{dq} \right ^2}{i_0}}$	$L_m = 0.42H$ $L_{ls} = 0.07H$ $L_{lr} = 0.14H$ $\phi_1 = 0.7Wb$ $\phi_2 = 1.2Wb$ $x_l^\infty = 0.25$ $i_1 = 2A$ $x_r^\infty = 0.25$ $i_0 = 0.32A$

Table 5.8 – Saturation functions and parameters tested in simulation with the Lagrangian model eq. (5.35).

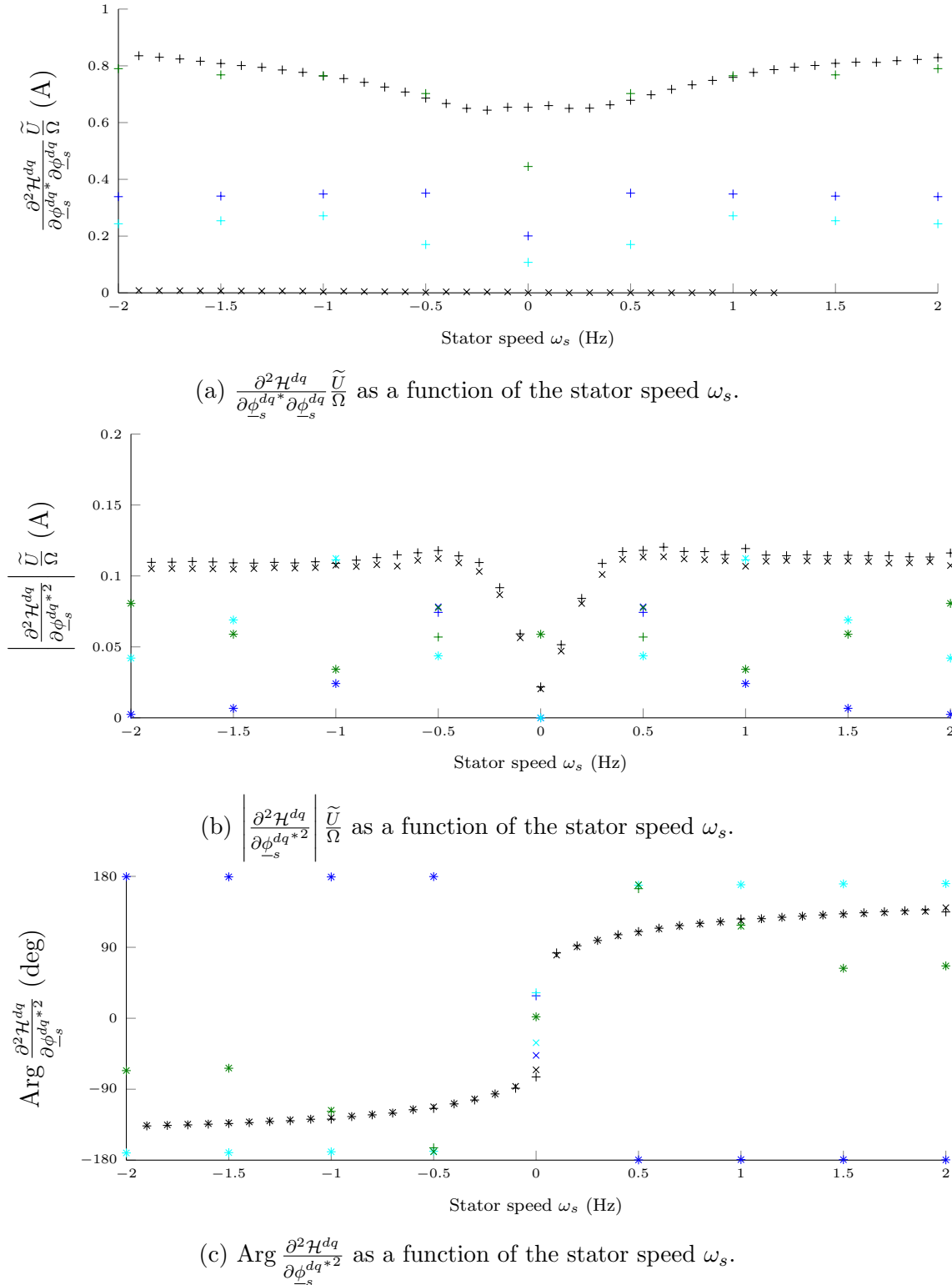


Figure 5.21 – Testing the modeling approach proposed in section 5.3.5.4 in simulation on a saturated IM model under nominal flux with the saturation functions and parameters listed in table 5.8.

But if the stator current is also used the calculations are too difficult. Thus we will choose the stator flux as the other state variable. It should be noted that we thus get similar state variables as Tuovinen, Hinkkanen, *et al.* [70].

To obtain such a model, we should make a partial Legendre transformation

$$\mathcal{E}^{dq} = \phi_s^{dqT} \iota_s^{dq} + \frac{\rho\omega}{n^2} - \mathcal{L}^{dq} \quad (5.36)$$

which gives, when its differential is written in the sinusoidal case,

$$\begin{aligned} d\mathcal{E}^{dq} &= \phi_s^{dqT} d\iota_s^{dq} + \iota_s^{dqT} d\phi_s^{dq} + \frac{\rho}{n^2} d\omega + \frac{\omega}{n^2} d\rho - \frac{\partial\mathcal{L}^{dq}}{\partial\omega} d\omega - \frac{\partial\mathcal{L}^{dqT}}{\partial\iota_s^{dq}} d\iota_s^{dq} - \frac{\partial\mathcal{L}^{dqT}}{\partial\iota_r^{dq}} d\iota_r^{dq} \\ &= \iota_s^{dqT} d\phi_s^{dq} + \omega d\rho - \frac{\partial\mathcal{L}^{dqT}}{\partial\iota_r^{dq}} d\iota_r^{dq}. \end{aligned}$$

Thus  $\mathcal{E}^{dq}$  can be seen as a function of  $\omega$ ,  $\phi_s^{dq}$  and  $\iota_r^{dq}$  which is exactly what we wanted. Identifying the above equation with the usual differential expression, we find

$$n^2 \frac{\partial\mathcal{E}^{dq}}{\partial\rho} = \omega \quad (5.37a)$$

$$\frac{\partial\mathcal{E}^{dq}}{\partial\phi_s^{dq}} = \iota_s^{dq} \quad (5.37b)$$

$$\frac{\partial\mathcal{E}^{dq}}{\partial\iota_r^{dq}} = -\frac{\partial\mathcal{L}^{dqT}}{\partial\iota_r^{dq}} = -\phi_r^{dq}. \quad (5.37c)$$

Euler-Lagrange equations are then transformed into

$$\frac{d\phi_s^{dq}}{dt} = u_s^{dq} - R_s \iota_s^{dq} - \mathcal{J}\omega_s \phi_s^{dq} \quad (5.38a)$$

$$\frac{d}{dt} \frac{\partial\mathcal{E}^{dq}}{\partial\iota_r^{dq}} = R_r \iota_r^{dq} - \mathcal{J}(\omega_s - \omega) \frac{\partial\mathcal{E}^{dq}}{\partial\iota_r^{dq}} \quad (5.38b)$$

$$\frac{1}{n} \frac{d\rho}{dt} = -n \frac{\partial\mathcal{E}^{dq}}{\partial\iota_r^{dq}} \mathcal{J}_2 \iota_r^{dq} - T_L \quad (5.38c)$$

which is not a state form. As in the Lagrangian case a state-form can be obtained using the chain rule in the following way

$$\frac{d}{dt} \frac{\partial\mathcal{E}^{dq}}{\partial\iota_r^{dq}} = \frac{\partial^2\mathcal{E}^{dq}}{\partial\iota_r^{dq} \partial\phi_s^{dq}} \frac{d\phi_s^{dq}}{dt} + \frac{\partial^2\mathcal{E}^{dq}}{\partial\iota_r^{dq^2}} \frac{d\iota_r^{dq}}{dt}$$

where we supposed as always that the magnetic part of this energy function does not depend on  $\rho$ . The state-form thus reads

$$\begin{pmatrix} \frac{d}{dt} \phi_s^{dq} \\ \frac{d}{dt} \iota_r^{dq} \\ \frac{d}{dt} \omega \end{pmatrix} \begin{pmatrix} I_2 & & \\ -\left(\frac{\partial^2\mathcal{E}^{dq}}{\partial\iota_r^{dq^2}}\right)^{-1} \frac{\partial^2\mathcal{E}^{dq}}{\partial\iota_r^{dq} \partial\phi_s^{dq}} & \left(\frac{\partial^2\mathcal{E}^{dq}}{\partial\iota_r^{dq^2}}\right)^{-1} & \\ 0_{1,2} & 0_{1,2} & 1 \end{pmatrix} \begin{pmatrix} u_s^{dq} - R_s \iota_s^{dq} - \mathcal{J}\omega_s \phi_s^{dq} \\ -R_r \iota_r^{dq} - \mathcal{J}(\omega_s - \omega) \phi_r^{dq} \\ \frac{n^2}{\mathcal{J}_L} \phi_r^{dq} \mathcal{J}_2 \iota_r^{dq} - \frac{n}{\mathcal{J}_L} T_L \end{pmatrix}. \quad (5.39)$$

where the current-flux relations are given by eq. (5.37). The current-flux relations are now less complex than they are in the Lagrangian case above. We have only to invert a 2x2 matrix in the real case.

The ripple can be computed similarly as in the Lagrangian case. The differential of the current-flux relations reads

$$d \begin{pmatrix} i_s^{dq} \\ \phi_r^{dq} \end{pmatrix} = \begin{pmatrix} \frac{\partial^2 \mathcal{E}^{dq}}{\partial \phi_s^{dq2}} & \frac{\partial^2 \mathcal{E}^{dq}}{\partial \phi_s^{dq} \partial i_r^{dq}} \\ \frac{\partial^2 \mathcal{E}^{dq}}{\partial i_r^{dq} \partial \phi_s^{dq}} & \frac{\partial^2 \mathcal{E}^{dq}}{\partial i_r^{dq2}} \end{pmatrix} d \begin{pmatrix} \phi_s^{dq} \\ i_r^{dq} \end{pmatrix}$$

As we know from section 4.2.3 that the voltage injection  $\tilde{u}_s^{dq} = \tilde{u}f(\Omega t)$  creates a stator flux ripple  $\tilde{\phi}_s^{dq} = \frac{\tilde{u}}{\Omega}F(\Omega t)$  and no rotor flux ripple, the ripple on the stator current will be given by

$$\tilde{i}_s^{dq} = \left( \frac{\partial^2 \mathcal{E}^{dq}}{\partial \phi_s^{dq2}} - \frac{\partial^2 \mathcal{E}^{dq}}{\partial \phi_s^{dq} \partial i_r^{dq}} \left( \frac{\partial^2 \mathcal{E}^{dq}}{\partial i_r^{dq2}} \right)^{-1} \frac{\partial^2 \mathcal{E}^{dq}}{\partial i_r^{dq} \partial \phi_s^{dq}} \right) \frac{\tilde{u}}{\Omega} F(\Omega t) \quad (5.40)$$

As the state form, this expression is simpler than the one we obtained for the Lagrangian as there is only a 2x2 matrix to invert. This energy function is thus a trade-off between the complexity of the calculations and the fact that we don't want to have collinear state variables.

We designed some models based on the energy function

$$\begin{aligned} \mathcal{E}^{dq}(\rho, \phi_s^{dq}, \phi_r^{dq}) &= \frac{1}{2} f_m (|\phi_s^{dq}|^2) - \frac{1}{2} f_x (|\phi_s^{dq}|^2) \Re(\phi_s^{dq} i_r^{dq*}) - \frac{1}{2} L_{lr} f_r \left( \left| i_r^{dq} - \frac{\phi_s^{dq}}{L_{lr}} \right|^2 \right) |i_r^{dq}|^2 \\ &+ \frac{1}{2} \frac{1}{J_L n^2} \rho^2 \end{aligned} \quad (5.41)$$

with the parameters listed in table 5.9 and got quite good results as can be seen in fig. 5.22 since we could make some calculations. However we were not able to make a model explaining all the curves of fig. 5.17.

### 5.3.5.6 Hamiltonian-based modeling in DQ frame

In the two previous sections we showed that the only computationally possible choice of state variables is the stator and rotor fluxes. However those are quite close from one another. In section 3.3.4.2 we designed a model for non-salient motors in the  $DQ$  frame which is recalled below for convenience. As the motor is star-connected the 0-axis can be decoupled and we study the sinusoidal case. Moreover due to the definition of the  $DQ$  frame in the non-salient case  $\phi_r^Q \equiv 0$ . We will thus denote  $\phi_r^D$  by  $\phi_r$ . With all these simplifications the state-form reads

$$\frac{d\phi_s^{DQ}}{dt} = u_s^{DQ} - R_s i_s^{DQ} - \mathcal{J}_2 \left( \omega + R_r \frac{i_r^Q}{\phi_r} \right) \phi_s^{DQ} \quad (5.42a)$$

$$\frac{d\phi_r}{dt} = -R_r i_r^D \quad (5.42b)$$

$$\frac{1}{n} \frac{d\rho}{dt} = T_e - T_L \quad (5.42c)$$

with the associated current-flux relations

$$i_s^{DQ} = \frac{\partial \mathcal{H}^{DQ}}{\partial \phi_s^{DQ}} \quad (5.43a)$$

$$i_r^D = \frac{\partial \mathcal{H}^{DQ}}{\partial \phi_r} \quad (5.43b)$$

Model	Function	Expression	Parameters
1	$f_m$	$\left( \left  \frac{\phi_s^{dq}}{L_s} \right ^2 \right) = \frac{1}{L_m + L_{ls}} \left  \phi_s^{dq} \right ^2$	$L_m = 0.42H$
	$f_x$	$\left( \left  \frac{\phi_s^{dq}}{L_s} \right ^2 \right) = \frac{L_m}{L_m + L_{ls}}$	$L_{ls} = 0.12H$
	$f_r$	$\left( \left  \frac{\phi_r^{dq}}{L_r} \right ^2 \right) = x_r^\infty + \frac{1 - x_r^\infty}{1 + \frac{\left  \phi_r^{dq} \right ^2}{i_0^2}}$	$L_{lr} = 0.25H$ $x_r^\infty = 0.2$ $i_0 = 0.32A$
2	$f_m$	$\left( \left  \frac{\phi_s^{dq}}{L_s} \right ^2 \right) = \frac{\left  \phi_s \right ^2}{L_m + L_{ls}} \left( 1 + \frac{\left  \phi_s \right ^{2p}}{\phi_0^{2p}} \right)$	$L_m = 0.6H$
	$f_x$	$\left( \left  \frac{\phi_s^{dq}}{L_s} \right ^2 \right) = \frac{L_m}{L_m + L_{ls}}$	$L_{ls} = 0.12H$
	$f_r$	$\left( \left  \frac{\phi_r^{dq}}{L_r} \right ^2 \right) = x_r^\infty + \frac{1 - x_r^\infty}{1 + \frac{\left  \phi_r^{dq} \right ^2}{i_0}}$	$L_{lr} = 0.25H$ $p = 3$ $\phi_0 = 1.5Wb$ $x_r^\infty = 0.1$ $i_0 = 1.41A$
3	$f_m$	$\left( \left  \frac{\phi_s^{dq}}{L_s} + \frac{\phi_r^{dq}}{L_r} \right ^2 \right) = \frac{\left  \phi_s \right ^2}{L_m + L_{ls}} \left( 1 + \frac{\left  \phi_s \right ^{2p}}{\phi_0^{2p}} \right)$	$L_m = 0.42H$
	$f_x$	$\left( \left  \frac{\phi_s^{dq}}{L_s} \right ^2 \right) = 1 + \frac{\left  \phi_s^{dq} \right ^2}{\phi_1^2}$	$L_{ls} = 0.12H$
	$f_r$	$\left( \left  \frac{\phi_r^{dq}}{L_r} \right ^2 \right) = x_r^\infty + \frac{1 - x_r^\infty}{1 + \frac{\left  \phi_r^{dq} \right ^2}{i_0}}$	$L_{lr} = 0.25H$ $p = 5$ $\phi_0 = 1.3Wb$ $\phi_1 = 1Wb$ $x_r^\infty = 0.5$ $i_0 = 1A$

Table 5.9 – Saturation functions and parameters tested in simulation with the energy model eq. (5.41).

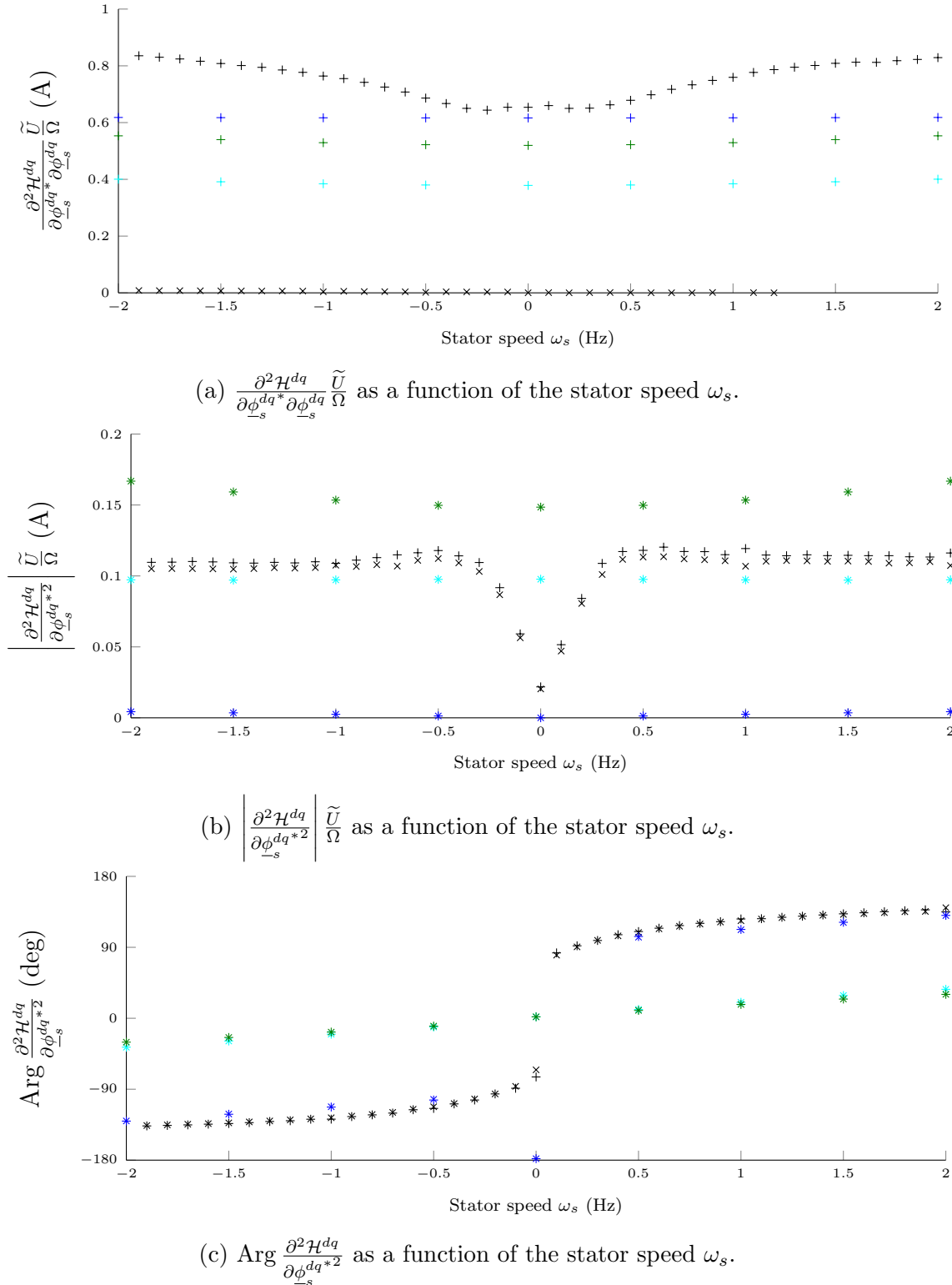


Figure 5.22 – Testing the modeling approach proposed in section 5.3.5.5 in simulation on a saturated IM model under nominal flux with the saturation functions and parameters listed in table 5.9.

$$i_r^Q = \frac{1}{\phi_r} \left( \phi_s^{DQ^T} \mathcal{J}_2 i_s^{DQ} \right) \quad (5.43c)$$

$$\omega = n^2 \frac{\partial \mathcal{H}^{DQ}}{\partial \rho} \quad (5.43d)$$

$$T_e = -n \phi_s^{DQ^T} \mathcal{J}_2 i_s^{DQ}. \quad (5.43e)$$

Thanks to this special change of frame we were able to remove another state variable. In this frame the IM has only three state variables which is very interesting. This change of variables is obviously not valid at zero flux but this is not a problem as the IM does not yield any torque at zero flux.

As we are interested in working points close to constant rotor flux  $\phi_r$  will be considered almost constant. We are thus close to the PMSM case developed in Jebai [37] and recalled in section 5.1.3. However the saturation is too important to be modeled by third or fourth order polynomial as were used there. We thus tried different functions but did not find any model to represent the experimental results.

This formulation seems strangely to be totally different than what was obtained in a  $dq$  frame. However, the  $DQ$  state variables can be expressed using  $dq$  variables

$$\phi_s^D = \frac{\phi_s^{dq^T} \phi_r^{dq}}{\|\phi_r^{dq}\|} = \frac{\Re(\underline{\phi}_r^{dq*} \underline{\phi}_s^{dq})}{|\underline{\phi}_r^{dq}|} \quad (5.44a)$$

$$\phi_s^Q = \frac{\phi_s^{dq^T} \mathcal{J}_2 \phi_r^{dq}}{\|\phi_r^{dq}\|} = \frac{\Im(\underline{\phi}_r^{dq*} \underline{\phi}_s^{dq})}{|\underline{\phi}_r^{dq}|} \quad (5.44b)$$

as they are the projection of the stator and rotor fluxes on the rotor flux. Changing the frame is thus equivalent to working with special combinations of state variables.

### 5.3.6 Conclusion

In this section we tried to devise a saturated IM model which conveys the effects of HF voltage signal injection. IM modeling is much more complex than SynRM or PMSM modelling due to the presence of unmeasured rotor variables.

In a first time we considered a simple extension of the unsaturated sinusoidal IM model. Doing so we faced unexpected phenomena linked with magnetic hysteresis occurring in the rotor core. We could fit a model for no load experimental data. However the experimental results drastically change as soon as the IM is under load. We could unfortunately not find a suitable model which conveys the effects observed experimentally due to lack of time. This might also be due to two-dimensional magnetic hysteresis effects for which no complete model exist.



# Chapter 6

## “Sensorless” motor control at medium and high speed

### Chapitre 6 — Contrôle « sans capteur » à moyenne et haute vitesse

*Ce chapitre propose une loi de contrôle « sans capteur » conçue initialement pour le moteur synchrone à reluctance. Sa stabilité est prouvée pour le modèle saturé en s'appuyant sur la séparation des échelles de temps. L'influence des limitations de courant stator et de tension stator (imposées par le variateur de vitesse) est étudiée et détaillée dans le cas non saturé. Le point de fonctionnement choisi est optimisé afin de minimiser les pertes par effet Joule dans les enroulements du stator. Grâce aux similarités entre moteurs synchrones à reluctance et à aimant permanent, cette loi est très facilement étendue à ces derniers.*

In chapter 3 we described a general framework to build consistent models for electric machines. Thanks to this original approach, we are able to convey the behavior of electric machines using one scalar function. We now want to design a “sensorless” control law which is based on such models. Furthermore, this modeling approach shows that electric motors are very similar from one another: by choosing the parameters of a fictitious generic electric motor one can transform it into an IM, a PMSM or a SynRM. This let us think that a generic control law for all kind of electric motors can be designed. However, we were not able to generalize it to IMs yet. Currently it can only handle SynRMs and PMSMs.

We showed in section 4.1.4 that all electric motors are not linearly observable on permanent trajectories where  $\omega_{s,e} = 0$  when they are not instrumented using mechanical sensors. Due to parametric errors, this unobservability zone extends to the low speed domain. The control of electric motors is thus inherently difficult at low speed where we need to resort to HF injection (see Capecci, Guglielmi, *et al.* [49], Jansen and Lorenz [78], Corley and Lorenz [85] and chapter 7). This is the reason why the control laws described in this section can only be used to control electric motors at rated or high speeds.

### 6.1 A control law for the SynRM

Speaking in terms of energy-based models, the SynRM was shown in section 3.6 to be the most simple electric motor. It is thus logical to consider it in the first place. The control law will then be extended to the PMSM (see section 6.2).

We first express the model under a form which is suitable for the control in section 6.1.2. Secondly, the proposed control law is described and its stability is proven (see sections 6.1.3 and 6.1.4). Thirdly, we consider how the torque is limited by the current and voltage limitations and how to get maximum efficiency from the SynRM in all cases (see sections 6.1.5 and 6.1.6). It will lead us to reconsider the so-called “field-weakening” approach (see section 6.1.1 for details). Finally, in section 6.1.7 we give simulation results which highlight the performance of the control law, even when pushed to its limits.

### 6.1.1 Preliminary: Existing control laws

Capecchi, Guglielmi, *et al.* [49], Lagerquist, Boldea, *et al.* [79] propose control laws which can be separated in the following parts:

**Flux and speed observers** Allows to get an estimate of the speed and fluxes, from the current measurements. Sometimes, they are separated, but not always.

**Speed controller** It regulates the speed based on the estimate provided by the speed observer. It outputs a torque reference.

**Flux or current controller** It controls the currents, or equivalently the fluxes, so that the SynRM yields the desired torque.

Even though it is not stated clearly, the stability of those control laws relies on time scale separation between these parts.

The computation of the flux reference from of the torque reference is critical to design efficient control laws. The locus of the most efficient working points is often found experimentally (see Lagerquist, Boldea, *et al.* [79]), because it depends of the model nonlinearities. Malekian, Sharif, *et al.* [80] gives the solution in the unsaturated SynRM case, which will be detailed in section 6.1.6, to show how it can be adapted to the saturated model.

At higher speeds the flux must be limited, otherwise the needed voltage might be too high. This is traditionally called “field weakening”. Lagerquist, Boldea, *et al.* [79] and Malekian, Sharif, *et al.* [80] propose two approaches, the second one being the best, as it allows to reach some working points which are not reachable using the first one.

### 6.1.2 SynRM model

We consider here a star-connected saturated sinusoidal SynRM. Under these assumptions it is shown in sections 3.5.3 and 3.8 that the behavior of the SynRM can be conveyed by the energy function  $\mathcal{H}^{DQ}(\rho, \phi_s^{DQ})$  associated with the state equations eq. (3.29). Moreover, the energy can be separated in two parts: the kinetic energy, depending only on  $\rho$ , the kinetic momentum, which will be taken as  $\rho^2/(2J_L n^2)$ , since we are not interested in mechanical modeling; and the magnetic energy, depending only on  $\phi_s^{DQ}$  in the sinusoidal case. That said, the state eq. (3.29) rewrites

$$\frac{d\phi_s^{DQ}}{dt} = u_s^{DQ} - R_s i_s^{DQ}(\phi_s^{DQ}) - \mathcal{J}_2 \omega \phi_s^{DQ} \quad (6.1a)$$

$$\frac{J_L}{n} \frac{d\omega}{dt} = T_e(\phi_s^{DQ}) - T_L \quad (6.1b)$$

$$\frac{d\theta}{dt} = \omega \quad (6.1c)$$

where

$$i_s^{DQ}(\phi_s^{DQ}) = \frac{\partial \mathcal{H}^{DQ}}{\partial \phi_s^{DQ}}(\phi_s^{DQ}) \quad (6.2a)$$

$$T_e(\phi_s^{DQ}) = n i_s^{DQT} \mathcal{J}_2 \phi_s^{DQ}. \quad (6.2b)$$

However, the position of the  $DQ$  frame is not known in “sensorless” control laws. The measurements are the currents in the chosen  $dq$  frame,  $i_s^{dq}$ , and the controls, the voltages in the chosen  $dq$  frame,  $u_s^{dq}$ .  $\theta_s$  being the angle between the  $\alpha\beta$  and the chosen  $dq$  frames, the relations between  $dq$  and  $DQ$  variables are

$$u_s^{DQ} = \mathcal{R}(-\eta) u_s^{dq} \quad (6.3a)$$

$$i_s^{dq} = \mathcal{R}(\eta) i_s^{DQ} \quad (6.3b)$$

where the angle of the rotation is  $\eta := \theta - \theta_s$ . Fig. 6.1 gives the respective positions of the different frames. Looking back to the system eqs. (6.1), (6.3a) and (6.3b) we see that  $\theta$  enters the equations only as  $\eta$ . The state equations can thus be rewritten

$$\frac{d\phi_s^{DQ}}{dt} = \mathcal{R}(-\eta) u_s^{dq} - R_s i_s^{DQ}(\phi_s^{DQ}) - \mathcal{J}_2 \omega \phi_s^{DQ} \quad (6.4a)$$

$$\frac{J_L}{n} \frac{d\omega}{dt} = T_e(\phi_s^{DQ}) - T_L \quad (6.4b)$$

$$\frac{d\eta}{dt} = \omega - \omega_s \quad (6.4c)$$

where  $\omega_s := \frac{d\theta_s}{dt}$  and the stator currents and the electromagnetic torque are given by eqs. (6.2a) and (6.2b) respectively. Eq. (6.4) with the 2 current measurements eq. (6.3b) represents the state form of the SynRM. The controls at our disposal are the 2 voltages  $u_s^{dq}$  and the stator speed  $\omega_s$ .

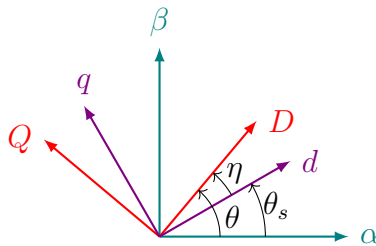


Figure 6.1 – Respective position of the different frames.

### 6.1.3 Control law description

The control law proposed hereafter relies on time-scale separation (see Khalil [59, ch. 9.2]). In section 6.1.3.1 we describe how to drive the stator flux to its reference, but this requires that the chosen  $dq$  frame is a good estimate of the  $DQ$  frame. This is ensured thanks to the controller, described in section 6.1.3.2, which will also yield an estimate of the speed. Using this speed estimate, we control the motor to the desired speed reference using the controller described in section 6.1.3.3. From the output of this controller which is the electromagnetic torque we compute the flux reference, following the procedure described in section 6.1.6. The design of the proposed control law is summarized in fig. 6.2.

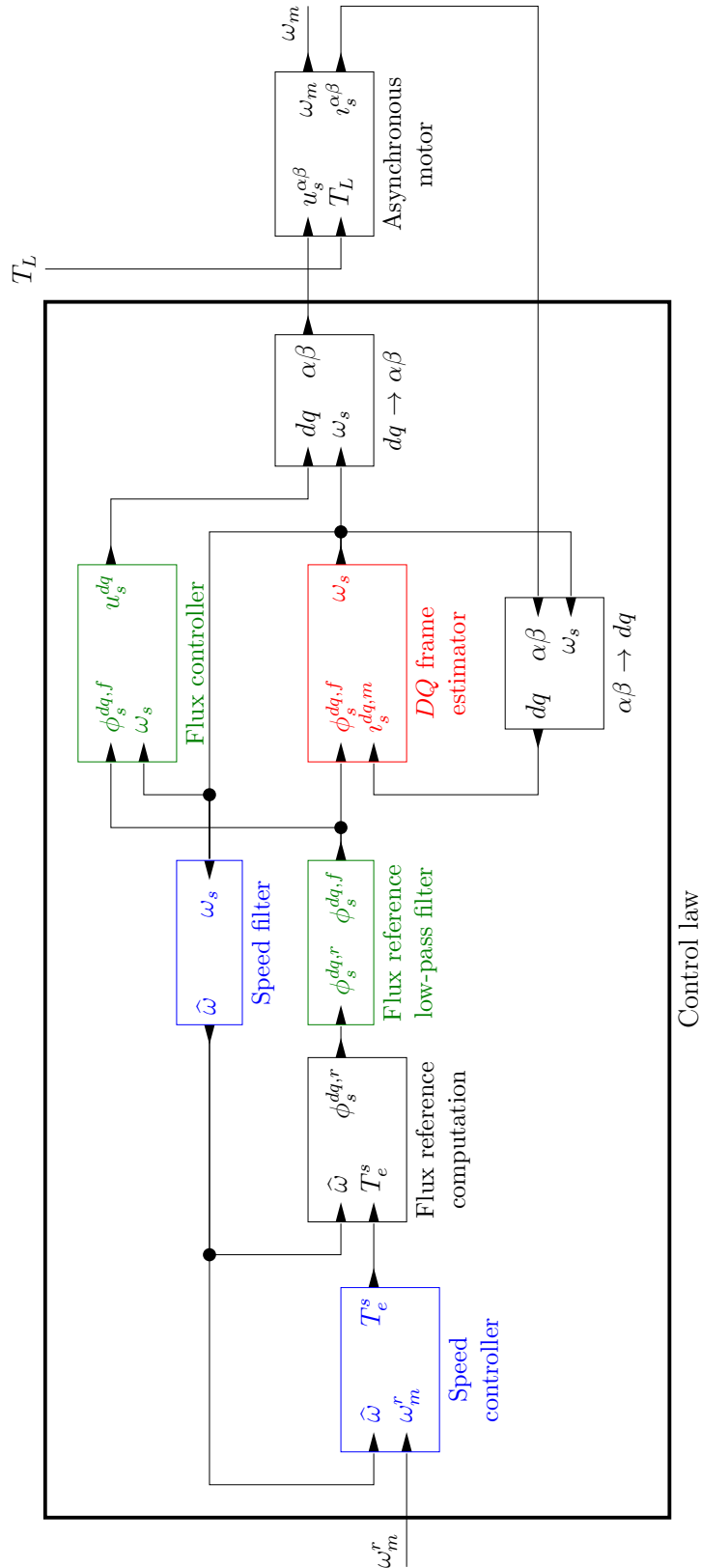


Figure 6.2 – A schematic representation of the proposed control law. The controllers time-scales, identified in section 6.1.4, are represented by the colors: **Red for the fastest**, **blue for the slowest** and **green for the intermediate time-scale**. Black blocks represent algebraic computations.

### 6.1.3.1 Flux controller

The aim of this controller is to stabilize the stator flux to the flux reference  $\phi_s^{dq,r}$  using the voltages controls. To ensure time scale separation, the flux reference  $\phi_s^{dq,r}$  is first low-pass filtered at frequency  $\varpi_0^\phi$

$$\frac{d\phi_s^{dq,f}}{dt} = \varpi_0^\phi (\phi_s^{dq,r} - \phi_s^{dq,f}). \quad (6.5)$$

The filtered stator flux reference is then used as reference by a feed-forward controller for the flux eq. (6.4a)

$$u_s^{dq} = \frac{d\phi_s^{dq,f}}{dt} + R_s \frac{\partial \mathcal{H}^{DQ}}{\partial \phi_s^{DQ}} (\phi_s^{dq,f}) + \mathcal{J}_2 \omega_s \phi_s^{dq,f} + v_s^{dq}, \quad (6.6)$$

where  $v_s^{dq}$  is the new input which can be used after the feed-forward has been applied to stabilize the control law.

Injecting eq. (6.6) into the model eq. (6.4a) we obtain

$$\begin{aligned} \frac{d\phi_s^{DQ}}{dt} = & \mathcal{R}(-\eta)v_s^{dq} - R_s \left( \frac{\partial \mathcal{H}^{DQ}}{\partial \phi_s^{DQ}} (\phi_s^{DQ}) - \frac{\partial \mathcal{H}^{DQ}}{\partial \phi_s^{DQ}} (\phi_s^{dq,f}) \right) - \mathcal{J}_2 \omega (\phi_s^{DQ} - \mathcal{R}(-\eta)\phi_s^{dq,f}) \\ & - \mathcal{J}_2 (\omega - \omega_s) \mathcal{R}(-\eta)\phi_s^{dq,f} + \mathcal{R}(-\eta) \frac{d\phi_s^{dq,f}}{dt} + R_s (\mathcal{R}(-\eta) - I_2) \frac{\partial \mathcal{H}^{DQ}}{\partial \phi_s^{DQ}} (\phi_s^{dq,f}). \end{aligned}$$

Noting that  $-\mathcal{J}_2 (\omega - \omega_s) \mathcal{R}(-\eta)\phi_s^{dq,f} + \mathcal{R}(-\eta) \frac{d\phi_s^{dq,f}}{dt} = \frac{d\mathcal{R}(-\eta)\phi_s^{dq,f}}{dt} = \frac{d\phi_s^{DQ,f}}{dt}$ , we obtain

$$\begin{aligned} \frac{d}{dt} (\phi_s^{DQ} - \phi_s^{DQ,f}) = & -R_s \left( \frac{\partial \mathcal{H}^{DQ}}{\partial \phi_s^{DQ}} (\phi_s^{DQ}) - \frac{\partial \mathcal{H}^{DQ}}{\partial \phi_s^{DQ}} (\mathcal{R}(\eta)\phi_s^{DQ,f}) \right) - \mathcal{J}_2 \omega (\phi_s^{DQ} - \phi_s^{DQ,f}) \\ & + R_s (\mathcal{R}(-\eta) - I_2) \frac{\partial \mathcal{H}^{DQ}}{\partial \phi_s^{DQ}} (\mathcal{R}(\eta)\phi_s^{DQ,f}) + \mathcal{R}(-\eta)v_s^{dq}. \end{aligned} \quad (6.7)$$

This means that the variable which is susceptible to converge to zero is  $\phi_s^{DQ} - \phi_s^{DQ,f}$  and not  $\phi_s^{DQ} - \phi_s^{dq,f}$ , as could be expected. Of course, we will try to ensure that both frames are identical using the controller described hereafter, but to ensure time scale separation, we should use  $\phi_s^{DQ,f}$ .

### 6.1.3.2 Saliency frame estimation

Estimating the position of the  $DQ$  frame is equivalent to ensuring  $\eta$  converges to 0. However  $\eta$  is not measured. Thus we first need to estimate  $\eta$  using the currents measurements. Then, given the simplicity of eq. (6.4c), a PI controller on this estimate ensures the convergence of  $\eta$  to 0 up to the estimation error.

On the one hand, the current measurements rewritten in terms of the chosen state variables read

$$i_s^{dq} = \mathcal{R}(\eta)i_s^{DQ} = \mathcal{R}(\eta) \frac{\partial \mathcal{H}^{DQ}}{\partial \phi_s^{DQ}} (\phi_s^{DQ}). \quad (6.8)$$

On the other hand, the measurement estimate  $\hat{i}_s^{dq}$  from the flux reference  $\phi_s^{dq,f}$  is

$$\hat{i}_s^{dq} = \frac{\partial \mathcal{H}^{DQ}}{\partial \phi_s^{DQ}} (\phi_s^{dq,f}) = \frac{\partial \mathcal{H}^{DQ}}{\partial \phi_s^{DQ}} (\mathcal{R}(\eta)\phi_s^{DQ,f}). \quad (6.9)$$

Assuming now that  $\eta$  is sufficiently small we obtain at first order

$$i_s^{dq} - \hat{i}_s^{dq} = \left( \frac{\partial \mathcal{H}^{DQ}}{\partial \phi_s^{DQ}}(\phi_s^{DQ}) - \frac{\partial \mathcal{H}^{DQ}}{\partial \phi_s^{DQ}}(\phi_s^{DQ,f}) \right) + \eta \left( \mathcal{J}_2 \frac{\partial \mathcal{H}^{DQ}}{\partial \phi_s^{DQ}}(\phi_s^{DQ}) - \frac{\partial^2 \mathcal{H}^{DQ}}{\partial \phi_s^{DQ^2}} \mathcal{J}_2 \phi_s^{DQ,f} \right) \quad (6.10)$$

whose first term will not be large, if the flux controller of section 6.1.3.1 is initialized correctly and converges, and whose second term is  $\eta$  up to a vector factor. We thus get two estimates of  $\eta$ . The problem is now to combine them in such a way that the factor is not too small.

With the notations introduced in section 3.8.2 for sinusoidal nonlinear electric machine models, the vector factor of the last term of eq. (6.10) rewrites  $\mathcal{J}_2 \frac{\partial \mathcal{H}^{DQ}}{\partial \phi_s^{DQ}}(\phi_s^{DQ}) - \frac{\partial^2 \mathcal{H}^{DQ}}{\partial \phi_s^{DQ^2}} \mathcal{J}_2 \phi_s^{DQ,f} = (\mathcal{J}_2 \Gamma_{c_s}^{DQ} - \Gamma_{t_s}^{DQ} \mathcal{J}_2) \phi_s^{DQ,f}$  when the equilibrium  $\phi_{s,e}^{DQ} = \phi_s^{DQ,f}$  is reached. It is thus the stator flux left-multiplied by a matrix conveying the saliency. To combine the two estimates of  $\eta$  we got, it is thus logic to take the scalar or vector product with the stator flux. All in all, we propose as estimate of  $\eta$

$$\begin{aligned} \hat{\eta} &= \frac{\phi_s^{dq,fT} \kappa (i_s^{dq} - \hat{i}_s^{dq})}{\phi_s^{dq,fT} \kappa \left( \mathcal{J}_2 \frac{\partial \mathcal{H}^{DQ}}{\partial \phi_s^{DQ}}(\phi_s^{dq,f}) - \frac{\partial^2 \mathcal{H}^{DQ}}{\partial \phi_s^{DQ^2}} \mathcal{J}_2 \phi_s^{dq,f} \right)} \\ &= \eta \frac{\phi_s^{dq,fT} \kappa \left( \mathcal{J}_2 \frac{\partial \mathcal{H}^{DQ}}{\partial \phi_s^{DQ}}(\phi_s^{DQ}) - \frac{\partial^2 \mathcal{H}^{DQ}}{\partial \phi_s^{DQ^2}} \mathcal{J}_2 \phi_s^{DQ,f} \right)}{\phi_s^{dq,fT} \kappa \left( \mathcal{J}_2 \frac{\partial \mathcal{H}^{DQ}}{\partial \phi_s^{DQ}}(\phi_s^{dq,f}) - \frac{\partial^2 \mathcal{H}^{DQ}}{\partial \phi_s^{DQ^2}} \mathcal{J}_2 \phi_s^{dq,f} \right)} \\ &\quad + \frac{\phi_s^{dq,fT} \kappa \left( \frac{\partial \mathcal{H}^{DQ}}{\partial \phi_s^{DQ}}(\phi_s^{DQ}) - \frac{\partial \mathcal{H}^{DQ}}{\partial \phi_s^{DQ}}(\phi_s^{DQ,f}) \right)}{\phi_s^{dq,fT} \kappa \left( \mathcal{J}_2 \frac{\partial \mathcal{H}^{DQ}}{\partial \phi_s^{DQ}}(\phi_s^{dq,f}) - \frac{\partial^2 \mathcal{H}^{DQ}}{\partial \phi_s^{DQ^2}} \mathcal{J}_2 \phi_s^{dq,f} \right)} \\ &= a_\eta \eta + b_\eta \end{aligned} \quad (6.11)$$

where  $\kappa \in \mathcal{M}_2(\mathbb{R})$  will be chosen later to ensure stability and we have  $a_\eta \approx 1$ ,  $b_\eta \approx 0$ . This choice for the estimate of  $\eta$  obviously implies that the stator flux must not be zero. We will see in section 6.1.6 how this condition is ensured.

As was said at the beginning of this section, the estimate  $\hat{\eta}$  is then used by a fast PI controller to regulate  $\eta$  to 0 thanks to the input  $\omega_s$

$$\omega_s = K_p^\eta \hat{\eta} + \eta^i \quad (6.12a)$$

$$\frac{d\eta^i}{dt} = K_i^\eta \hat{\eta}. \quad (6.12b)$$

When the equations of this controller are injected in eq. (6.4c), we obtain

$$\frac{d\eta}{dt} = \omega - \omega_s = \omega - K_p^\eta (a_\eta \eta + b_\eta) - \eta^i \quad (6.13a)$$

$$\frac{d\eta^i}{dt} = K_i^\eta (a_\eta \eta + b_\eta). \quad (6.13b)$$

At the equilibrium we will have  $\omega_{s,e} = \omega_e$  which means that  $\omega_s$  will be an estimate of  $\omega$  we can use in the mechanical loop hereafter.

### 6.1.3.3 Speed controller

First of all, to ensure time-scale separation, the speed estimate should be low-pass filtered with bandwidth  $\varpi_0^\omega$

$$\frac{d\hat{\omega}}{dt} = \varpi_0^\omega(\omega_s - \hat{\omega}). \quad (6.14)$$

The speed  $\omega$  which is driven by the electromagnetic torque  $T_e$ , as can be seen in eq. (6.4b), is controlled to its reference  $\omega^r$  by a PI controller on the error  $\omega^r - \hat{\omega}$ . However current and voltage limitations impose some constraints on the value of the torque  $T_e$ . It is shown in section 6.1.5 that the electromagnetic torque cannot exceed the value  $T_e^l(\omega)$ . An anti-windup term is thus added to the PI controller which reads

$$T_e^r = \frac{J_L}{n} K_p^\omega(\omega^r - \hat{\omega}) + \omega^i \quad (6.15a)$$

$$T_e^s = \min(\max(T_e^r, -T_e^l(\hat{\omega})), T_e^l(\hat{\omega})) \quad (6.15b)$$

$$\frac{d\omega^i}{dt} = \frac{J_L}{n} K_i^\omega(\omega^r - \hat{\omega}) + 2\frac{K_i^\omega}{K_p^\omega}(T_e^s - T_e^r) \quad (6.15c)$$

Consequently, outside of the torque limitation domain, the speed of the motor will follow

$$\frac{d\omega}{dt} = \frac{n}{J_L}(T_e(\phi_s^{DQ}) - T_e(\phi_s^{dq,r})) + K_p^\omega(\omega^r - \hat{\omega}) + \frac{n}{J_L}\omega^i - \frac{n}{J_L}T_L \quad (6.16a)$$

$$\frac{d\omega^i}{dt} = \frac{J_L}{n} K_i^\omega(\omega^r - \hat{\omega}). \quad (6.16b)$$

The flux reference computation from  $T_e^s$  is described in section 6.1.6. It is shown there that due to voltage limitation the flux reference  $\phi_s^{dq,r}$  will depend not only on  $T_e$  but also on  $\hat{\omega}$ .

## 6.1.4 Stability of the control law

In this section we will prove that the control law is stable using the singular perturbation theorem. Both unsaturated and saturated SynRMs will be considered. However, for the sake of simplicity, parametric errors and limitations will not be considered.

### 6.1.4.1 Equations of the controlled SynRM

To show the time-scale separations we regroup here all the SynRM and controller equations (eqs. (6.5), (6.7), (6.13), (6.14) and (6.16))

$$\frac{d\eta^i}{dt} = K_i^\eta(a_\eta\eta + b_\eta) \quad (6.17a)$$

$$\frac{d\eta}{dt} = \omega - K_p^\eta(a_\eta\eta + b_\eta) - \eta^i \quad (6.17b)$$

$$\begin{aligned} \frac{d}{dt}(\phi_s^{DQ} - \phi_s^{DQ,f}) &= -R_s \left( \frac{\partial \mathcal{H}^{DQ}}{\partial \phi_s^{DQ}}(\phi_s^{DQ}) - \frac{\partial \mathcal{H}^{DQ}}{\partial \phi_s^{DQ}}(\mathcal{R}(\eta)\phi_s^{DQ,f}) \right) - \mathcal{J}_2\omega(\phi_s^{DQ} - \phi_s^{DQ,f}) \\ &\quad + R_s(\mathcal{R}(-\eta) - I_2) \frac{\partial \mathcal{H}^{DQ}}{\partial \phi_s^{DQ}}(\phi_s^{dq,f}) + \mathcal{R}(-\eta)v_s^{dq} \end{aligned} \quad (6.17c)$$

$$\frac{d\phi_s^{dq,f}}{dt} = \varpi_0^\phi(\phi_s^{dq,r}(T_e, \hat{\omega}) - \phi_s^{dq,f}) \quad (6.17d)$$

Time-scale	Bandwidth	Gains	Parameters
$DQ$ frame estimation	$\Omega_0^\eta = 100Hz$	$K_i^\eta = \Omega_0^{\eta^2}$ $K_p^\eta = 2\xi_\eta\Omega_0^\eta$	$\xi_\eta = 0.7$
Stator flux	$\Omega_0^\phi = 25Hz$	$\varpi_0^\phi = k_\phi\Omega_0^\phi$	$k_\phi = 1$
Speed	$\Omega_0^\omega = 5Hz$	$\varpi_0^\omega = k_\omega\Omega_0^\omega$ $K_i^\omega = \Omega_0^{\omega^2}$ $K_p^\omega = 2\xi_\omega\Omega_0^\omega$	$k_\omega = 3.8$ $\xi_\omega = 1$

Table 6.1 – Gains used in the SynRM control law.

$$\frac{d\hat{\omega}}{dt} = \varpi_0^\omega (K_p^\eta (a_\eta \eta + b_\eta) + \eta^i - \hat{\omega}) \quad (6.17e)$$

$$\frac{d\omega^i}{dt} = \frac{J_L}{n} K_i^\omega (\omega^r - \hat{\omega}) \quad (6.17f)$$

$$\frac{d}{dt}(\omega - \omega^r) = \frac{n}{J_L} (T_e(\phi_s^{DQ}) - T_e(\phi_s^{dq,r})) + K_p^\omega (\omega^r - \hat{\omega}) + \frac{n}{J_L} \omega^i - \frac{n}{J_L} T_L. \quad (6.17g)$$

The chosen bandwidths for the controllers and the filters are listed in table 6.1. We apply a standard normalisation process on the equations to make the time scales appear

$$\frac{1}{\Omega_0^\eta} \frac{d\eta^{i'}}{dt} = (a_\eta \eta + b_\eta) \quad (6.18a)$$

$$\frac{1}{\Omega_0^\eta} \frac{d\eta}{dt} = \frac{\omega}{\Omega_0^\eta} - 2\xi_\eta (a_\eta \eta + b_\eta) - \eta^{i'} \quad (6.18b)$$

$$\begin{aligned} \frac{1}{\Omega_0^\phi} \frac{d}{dt} (\phi_s^{DQ} - \phi_s^{DQ,f}) &= \frac{1}{\Omega_0^\phi} \mathcal{R}(-\eta) v_s^{dq} - \frac{R_s}{\Omega_0^\phi} \left( \frac{\partial \mathcal{H}^{DQ}}{\partial \phi_s^{DQ}} (\phi_s^{DQ}) - \frac{\partial \mathcal{H}^{DQ}}{\partial \phi_s^{DQ}} (\mathcal{R}(\eta) \phi_s^{DQ,f}) \right) \\ &\quad - \mathcal{J}_2 \frac{\omega}{\Omega_0^\phi} (\phi_s^{DQ} - \phi_s^{DQ,f}) + \frac{R_s}{\Omega_0^\phi} (\mathcal{R}(-\eta) - I_2) \frac{\partial \mathcal{H}^{DQ}}{\partial \phi_s^{DQ}} (\phi_s^{dq,f}) \end{aligned} \quad (6.18c)$$

$$\frac{1}{\Omega_0^\phi} \frac{d\phi_s^{dq,f}}{dt} = k_\phi (\phi_s^{dq,r} (T_e, \hat{\omega}) - \phi_s^{dq,f}) \quad (6.18d)$$

$$\frac{1}{\Omega_0^\omega} \frac{d\hat{\omega}}{dt} = k_\omega (2\xi_\eta \Omega_0^\eta (a_\eta \eta + b_\eta) + \Omega_0^\eta \eta^{i'} - \hat{\omega}) \quad (6.18e)$$

$$\frac{1}{\Omega_0^\omega} \frac{d\omega^{i'}}{dt} = (\omega^r - \hat{\omega}) \quad (6.18f)$$

$$\begin{aligned} \frac{1}{\Omega_0^\omega} \frac{d}{dt} (\omega - \omega^r) &= \frac{n}{J_L} \frac{1}{\Omega_0^\omega} (T_e(\phi_s^{DQ}) - T_e(\phi_s^{dq,r})) + 2\xi_\omega (\omega^r - \hat{\omega}) + \omega^{i'} \\ &\quad - \frac{n}{J_L} \frac{T_L}{\Omega_0^\omega}. \end{aligned} \quad (6.18g)$$

where  $\eta^{i'} = \frac{\eta^i}{\Omega_0^\eta}$  and  $\omega^{i'} = \frac{n}{J_L} \frac{\omega^i}{\Omega_0^\omega}$  are the normalized values of the integral states  $\eta^i$  and  $\omega^i$  respectively. Noting  $\Omega_0^\phi$  is of the order of magnitude of  $\frac{R_s}{L_s^d}$  and  $\frac{R_s}{L_s^q}$ , it is clear that eqs. (6.18a) and (6.18b) on the one side and eqs. (6.18c) and (6.18d) on the other side form a system in standard Tikhonov form, on which the singular perturbation theorem (see Khalil [59, Th. 9.3]) can be applied. However  $\omega_s = 2\xi_\eta \Omega_0^\eta (a_\eta \eta + b_\eta) + \Omega_0^\eta \eta^{i'}$  should not be in eq. (6.18e) for the whole system to be in a suitable form. To circumvent this

problem we compute  $\omega_s$  using eq. (6.18b) and inject it in eq. (6.18e) thus obtaining

$$\frac{1}{\Omega_0^\omega} \frac{d}{dt} (\hat{\omega} + \varpi_0^\omega \eta) = k_\omega (\omega - \hat{\omega}).$$

We see that the right-hand side of this equation does not depend on  $\omega_s$  any more. The variable  $\hat{\omega}' = \hat{\omega} + \varpi_0^\omega \eta$  is thence a good candidate for a slow variable. We rewrite eqs. (6.18e) to (6.18g) using this variable as a replacement of  $\hat{\omega}$

$$\frac{1}{\Omega_0^\omega} \frac{d\hat{\omega}'}{dt} = k_\omega (\omega - \hat{\omega}') + k_\omega^2 \Omega_0^\omega \eta \quad (6.19a)$$

$$\frac{1}{\Omega_0^\omega} \frac{d\omega^{i'}}{dt} = (\omega^r - \hat{\omega}') + k_\omega \Omega_0^\omega \eta \quad (6.19b)$$

$$\begin{aligned} \frac{1}{\Omega_0^\omega} \frac{d}{dt} (\omega - \omega^r) &= \frac{n}{J_L} \frac{1}{\Omega_0^\omega} (T_e(\phi_s^{DQ}) - T_e(\phi_s^{dq,r})) + 2\xi_\omega (\omega^r - \hat{\omega}') + \omega^{i'} \\ &\quad - \frac{n}{J_L} \frac{1}{\Omega_0^\omega} T_L + 2k_\omega \xi_\omega \Omega_0^\omega \eta. \end{aligned} \quad (6.19c)$$

Eqs. (6.18a) to (6.18d) on the one side and eqs. (6.19a) to (6.19c) on the other now form a system under standard Tikhonov form.

We have thus separated three time-scales

- The fastest time-scale with bandwidth  $\Omega_0^\eta$ . The state variables  $\eta^{i'}$  and  $\eta$  evolve in this time scale.
- The intermediate time scale which is around  $\Omega_0^\phi$  with the state variables  $\phi_s^{DQ} - \phi_s^{DQ,f}$  and  $\phi_s^{dq,f}$ .
- The slowest time-scale, where mechanical variables  $\hat{\omega}'$ ,  $\omega^{i'}$  and  $\omega - \omega^r$  evolve, with bandwidth  $\Omega_0^\omega$ .

#### 6.1.4.2 Saliency frame estimation time scale

We consider here the eqs. (6.18a) and (6.18b), recalled hereafter for convenience, which evolve in the fastest time-scale

$$\frac{1}{\Omega_0^\eta} \frac{d\eta^{i'}}{dt} = (a_\eta \eta + b_\eta) \quad (6.20a)$$

$$\frac{1}{\Omega_0^\eta} \frac{d\eta}{dt} = \frac{\omega}{\Omega_0^\eta} - 2\xi_\eta (a_\eta \eta + b_\eta) - \eta^{i'}. \quad (6.20b)$$

As  $a_\eta$  and  $b_\eta$  are functions of slower variables, this is a two-dimensional linear system whose characteristic polynomial is

$$\left( \frac{X}{\Omega_0^\eta} \right)^2 + 2\xi_\eta a_\eta \frac{X}{\Omega_0^\eta} + a_\eta.$$

As  $a_\eta \approx 1$  is ensured by slower time scale controllers this system is exponentially stable uniformly in the slower time scale variables. Consequently, the singular perturbation theorem can be applied and, in slower time scales, we can consider that the equilibrium

$$\eta_e = -\frac{b_\eta}{a_\eta} = -\frac{\phi_s^{dq,fT} \kappa \left( \frac{\partial \mathcal{H}^{DQ}}{\partial \phi_s^{DQ}} (\phi_s^{DQ}) - \frac{\partial \mathcal{H}^{DQ}}{\partial \phi_s^{DQ}} (\phi_s^{DQ,f}) \right)}{\phi_s^{dq,fT} \kappa \left( \mathcal{J}_2 \frac{\partial \mathcal{H}^{DQ}}{\partial \phi_s^{DQ}} (\phi_s^{DQ}) - \frac{\partial^2 \mathcal{H}^{DQ}}{\partial \phi_s^{DQ^2}} \mathcal{J}_2 \phi_s^{DQ,f} \right)} \quad (6.21)$$

has been reached.

### 6.1.4.3 Flux time-scale

The system of eqs. (6.18c) and (6.18d) is triangular by blocs as eq. (6.18d) do not depend on  $\Delta\phi_s^{DQ} = \phi_s^{DQ} - \phi_s^{DQ,f}$ . Moreover the flux reference filter eq. (6.18d) is obviously exponentially stable uniformly on the flux reference. We thus have only to prove that eq. (6.18c) is exponentially stable uniformly on the speed and the flux reference.

The aim of our control law is to ensure that the fluxes converges to their target. We will thus consider that  $\Delta\phi_s^{DQ}$  is small. Besides we know that in this time-scale eq. (6.21) is reached. Thus, as

$$\eta = -\frac{\phi_s^{dq,fT} \kappa \frac{\partial^2 \mathcal{H}^{DQ}}{\partial \phi_s^{DQ^2}} \Delta\phi_s^{DQ}}{\phi_s^{dq,fT} \kappa \left( \mathcal{J}_2 \frac{\partial \mathcal{H}^{DQ}}{\partial \phi_s^{DQ}} (\phi_s^{DQ}) - \frac{\partial^2 \mathcal{H}^{DQ}}{\partial \phi_s^{DQ^2}} \mathcal{J}_2 \phi_s^{DQ,f} \right)},$$

it can be considered small as well in eq. (6.18c), which rewrites with this observation

$$\begin{aligned} \frac{1}{\Omega_0^\phi} \frac{d\Delta\phi_s^{DQ}}{dt} &= -\frac{R_s}{\Omega_0^\phi} \frac{\partial^2 \mathcal{H}^{DQ}}{\partial \phi_s^{DQ^2}} \Delta\phi_s^{DQ} - \mathcal{J}_2 \frac{\omega}{\Omega_0^\phi} \Delta\phi_s^{DQ} \\ &\quad + \frac{R_s}{\Omega_0^\phi} \left( \frac{\partial^2 \mathcal{H}^{DQ}}{\partial \phi_s^{DQ^2}} \mathcal{J}_2 \phi_s^{dq,f} - \mathcal{J}_2 \frac{\partial \mathcal{H}^{DQ}}{\partial \phi_s^{DQ}} (\phi_s^{dq,f}) \right) \eta + \mathcal{R}(-\eta) v_s^{dq}. \end{aligned}$$

Linearizing around the equilibrium  $\phi_{s,e}^{DQ} = \phi_s^{DQ,f}$ , we find

$$\begin{aligned} \frac{1}{\Omega_0^\phi} \frac{d\Delta\phi_s^{DQ}}{dt} &= -\frac{R_s}{\Omega_0^\phi} \frac{\left( \phi_s^{dq,fT} \kappa \left( \mathcal{J}_2 \frac{\partial \mathcal{H}^{DQ}}{\partial \phi_s^{DQ}} (\phi_s^{dq,f}) - \frac{\partial^2 \mathcal{H}^{DQ}}{\partial \phi_s^{DQ^2}} \mathcal{J}_2 \phi_s^{dq,f} \right) \right) \frac{\partial^2 \mathcal{H}^{DQ}}{\partial \phi_s^{DQ^2}} \Delta\phi_s^{DQ}}{\phi_s^{dq,fT} \kappa \left( \mathcal{J}_2 \frac{\partial \mathcal{H}^{DQ}}{\partial \phi_s^{DQ}} (\phi_s^{dq,f}) - \frac{\partial^2 \mathcal{H}^{DQ}}{\partial \phi_s^{DQ^2}} \mathcal{J}_2 \phi_s^{dq,f} \right)} \\ &\quad + \frac{R_s}{\Omega_0^\phi} \frac{\left( \frac{\partial^2 \mathcal{H}^{DQ}}{\partial \phi_s^{DQ^2}} \mathcal{J}_2 \phi_s^{dq,f} - \mathcal{J}_2 \frac{\partial \mathcal{H}^{DQ}}{\partial \phi_s^{DQ}} (\phi_s^{dq,f}) \right) \left( \phi_s^{dq,fT} \kappa \frac{\partial^2 \mathcal{H}^{DQ}}{\partial \phi_s^{DQ^2}} \Delta\phi_s^{DQ} \right)}{\phi_s^{dq,fT} \kappa \left( \mathcal{J}_2 \frac{\partial \mathcal{H}^{DQ}}{\partial \phi_s^{DQ}} (\phi_s^{dq,f}) - \frac{\partial^2 \mathcal{H}^{DQ}}{\partial \phi_s^{DQ^2}} \mathcal{J}_2 \phi_s^{dq,f} \right)} \\ &\quad - \frac{\omega}{\Omega_0^\phi} \mathcal{J}_2 \Delta\phi_s^{DQ} + \mathcal{R}(-\eta) v_s^{dq} \\ &= -\frac{R_s}{\Omega_0^\phi} \frac{-\mathcal{J}_2 \kappa^T \phi_s^{dq,f} \left( \mathcal{J}_2 \frac{\partial \mathcal{H}^{DQ}}{\partial \phi_s^{DQ}} (\phi_s^{dq,f}) - \frac{\partial^2 \mathcal{H}^{DQ}}{\partial \phi_s^{DQ^2}} \mathcal{J}_2 \phi_s^{dq,f} \right)^T \mathcal{J}_2 \frac{\partial^2 \mathcal{H}^{DQ}}{\partial \phi_s^{DQ^2}} \Delta\phi_s^{DQ}}{\phi_s^{dq,fT} \kappa \left( \mathcal{J}_2 \frac{\partial \mathcal{H}^{DQ}}{\partial \phi_s^{DQ}} (\phi_s^{dq,f}) - \frac{\partial^2 \mathcal{H}^{DQ}}{\partial \phi_s^{DQ^2}} \mathcal{J}_2 \phi_s^{dq,f} \right)} \\ &\quad - \frac{\omega}{\Omega_0^\phi} \mathcal{J}_2 \Delta\phi_s^{DQ} + \mathcal{R}(-\eta) v_s^{dq} \\ &= A \Delta\phi_s^{DQ} + \mathcal{R}(-\eta) v_s^{dq} \end{aligned}$$

where we used  $\forall (x, y, z) \in (\mathbb{R}^2)^3 \quad (x^T y) z - y(x^T z) = -\mathcal{J}_2 x(y^T \mathcal{J}_2 z) = (-\mathcal{J}_2 x y^T \mathcal{J}_2) z$  to combine the first two terms. we thus have a simple two dimensional linear system. Using the fact that  $\forall (x, y) \in (\mathbb{R}^2)^2$  we have on the one hand  $\text{tr}(-\mathcal{J}_2 x y^T \mathcal{J}_2 + \mathcal{J}_2) = \text{tr}(-\mathcal{J}_2 x y^T \mathcal{J}_2) = x^T y$  and on the other hand  $\det(-\mathcal{J}_2 x y^T \mathcal{J}_2 - \mathcal{J}_2) = 1 - x^T \mathcal{J}_2 y$ , we find for the linear system

$$\text{tr } A = -\frac{R_s}{\Omega_0^\phi} \frac{\phi_s^{dq,fT} \kappa \left( \mathcal{J}_2 \frac{\partial \mathcal{H}^{DQ}}{\partial \phi_s^{DQ}} (\phi_s^{dq,f}) - \frac{\partial^2 \mathcal{H}^{DQ}}{\partial \phi_s^{DQ^2}} \mathcal{J}_2 \phi_s^{dq,f} \right)}{\phi_s^{dq,fT} \kappa \left( \mathcal{J}_2 \frac{\partial \mathcal{H}^{DQ}}{\partial \phi_s^{DQ}} (\phi_s^{dq,f}) - \frac{\partial^2 \mathcal{H}^{DQ}}{\partial \phi_s^{DQ^2}} \mathcal{J}_2 \phi_s^{dq,f} \right)} = -\frac{R_s}{\Omega_0^\phi} \quad (6.22a)$$

$$\det A = \left( \frac{\omega}{\Omega_0^\phi} \right)^2 + \frac{\omega R_s \phi_s^{dq,fT} \kappa \mathcal{J}_2 \left( \mathcal{J}_2 \frac{\partial \mathcal{H}^{DQ}}{\partial \phi_s^{DQ}} (\phi_s^{dq,f}) - \frac{\partial^2 \mathcal{H}^{DQ}}{\partial \phi_s^{DQ^2}} \mathcal{J}_2 \phi_s^{dq,f} \right)}{\Omega_0^\phi \Omega_0^\phi \phi_s^{dq,fT} \kappa \left( \mathcal{J}_2 \frac{\partial \mathcal{H}^{DQ}}{\partial \phi_s^{DQ}} (\phi_s^{dq,f}) - \frac{\partial^2 \mathcal{H}^{DQ}}{\partial \phi_s^{DQ^2}} \mathcal{J}_2 \phi_s^{dq,f} \right)}. \quad (6.22b)$$

As said before, due to the choice we made for the error signal  $\hat{\eta}$ , we must ensure that the stator flux norm is larger than some minimal value. Moreover, it will obviously be impossible to ensure the needed exponential stability uniformly in  $\omega$  if  $\omega$  is allowed to go to zero. This is due to unobservability of the SynRM at  $\omega = \omega_s = 0$  (see section 4.1). That is why this control law is designed only for rated and high speed. We can thus suppose that  $\exists \varepsilon > 0 \quad \omega > \Omega_0^\phi \sqrt{\varepsilon \frac{R_s}{\Omega_0^\phi}}$ . Under these conditions we must ensure  $\text{tr } A < 0$   $\det > \varepsilon |\text{tr } A|$ . By setting

$$\kappa = -\mathcal{J}_2 \left( \mathcal{J}_2 \Gamma_{c_s}^{DQ} - \Gamma_{t_s}^{DQ} \mathcal{J}_2 \right)^{-1} \mathcal{J}_2 \quad (6.23)$$

the second term of the determinant will be cancelled and thus  $\det A > \varepsilon |\text{tr } A|$  which ensures exponential stability uniformly in  $\omega$  and  $\phi_s^{dq,f}$  of this system. The whole system eqs. (6.18c) and (6.18d) is thus exponentially stable uniformly in  $\omega$  and  $\phi_s^{dq,r}$ . It should be noted that the input  $v_s^{dq}$  of the flux feed-forward was not used to stabilize the controller. However it can be helpful to deal with parametric errors or limitations in a real implementation.

#### 6.1.4.4 Speed time-scale

In this time-scale, we can assume that the flux converged to its reference, which implies that  $T_e(\phi_s^{DQ}) = T_e(\phi_s^{dq,r})$ , on the one hand and that  $\eta = 0$ , on the other hand. Thus eq. (6.19) rewrites

$$\frac{1}{\Omega_0^\omega} \frac{d\hat{\omega}'}{dt} = k_\omega (\omega - \hat{\omega}') \quad (6.24a)$$

$$\frac{1}{\Omega_0^\omega} \frac{d\omega^{i'}}{dt} = -(\omega - \omega^r) + (\omega - \hat{\omega}') \quad (6.24b)$$

$$\frac{1}{\Omega_0^\omega} \frac{d}{dt} (\omega - \omega^r) = -2\xi_\omega (\omega - \omega^r) + 2\xi_\omega (\omega - \hat{\omega}') + \omega^{i'} - \frac{n}{J_L} \frac{1}{\Omega_0^\omega} T_L. \quad (6.24c)$$

This is a linear system associated with the Hurwitz matrix

$$\begin{pmatrix} -k_\omega - 2\xi_\omega & -1 & 2\xi_\omega \\ 1 & 0 & -1 \\ 2\xi_\omega & 1 & -2\xi_\omega \end{pmatrix}.$$

#### 6.1.4.5 Conclusion

We proved here the stability of the proposed control law for the SynRM at rated or high speed. The proof was made in the saturated case and relies on the fact that the saliency matrix  $(\mathcal{J}_2 \Gamma_{c_s}^{DQ} - \Gamma_{t_s}^{DQ} \mathcal{J}_2)$  can be inverted. This is the case for unsaturated SynRM as it is equal to  $(\Gamma_s^D - \Gamma_s^Q)Y$ . For saturated SynRMs without cross-saturation it becomes

$$\begin{pmatrix} 0 & \Gamma_{t_s}^D - \Gamma_{c_s}^Q \\ \Gamma_{c_s}^D - \Gamma_{t_s}^Q & 0 \end{pmatrix}$$

which will also be invertible as long as none of the terms vanish. Finally for saturated SynRM with cross-saturation, the property will hold as long as the saliency is not too important as we will be close to the unsaturated case.

However limitations on the voltage and the currents were not handled. These cases should be handled before a real implementation is considered. We also did not consider parametric errors which will occur in a real implementation. The feed-forward input  $v_s^{DQ}$  may be helpful in this case even though it was not needed in the basic case presented hereinabove.

### 6.1.5 Torque limitation

The maximal reachable torque  $T_e^l$  under voltage and current limitations is determined here. It can be restated as the optimization problem

$$T_e^l = \max \left( \left\{ T_e(\phi_s^{DQ}) \quad \|\iota_s^{DQ}\| < I^l \text{ and } \|u_s^{DQ}\| < U^l \right\} \right). \quad (6.25)$$

The obtained torque limitation will be used for the speed controller anti-windup (see section 6.1.3.3).

First of all we have

$$\frac{\partial T_e}{\partial \phi_s^{DQ}} = -n \mathcal{J}_2 \iota_s^{DQ} + n \left( \frac{\partial \iota_s^{DQ}}{\partial \phi_s^{DQ}} \right)^T \mathcal{J}_2 \phi_s^{DQ} = -n (\mathcal{J}_2 \Gamma_{c_s}^{DQ} - \Gamma_{t_s}^{DQ} \mathcal{J}_2) \phi_s^{DQ}$$

which is zero only at the origin of the flux plane. Thus the solutions of the problem described by eq. (6.25) will be on the boundaries.

Secondly, the constraints are not expressed in terms of stator fluxes but in terms of stator currents and voltages. The current constraint is easily converted to a flux constraint as the currents are functions of the fluxes. However the voltages are not functions of the fluxes only. Indeed from eq. (6.4a) we obtain

$$u_s^{DQ} = \frac{d\phi_s^{DQ}}{dt} + R_s \iota_s^{DQ} + \mathcal{J}_2 \omega \phi_s^{DQ}.$$

As the variation of the flux and the Ohmic losses are very small with respect to the voltage limitation, the constraint can be simplified into  $\|\phi_s^{DQ}\| < \frac{U^l}{\omega}$  when it is active. Moreover the constraints can equivalently be expressed as

$$\|\iota_s^{DQ}\|^2 = \iota_s^{DQT} \iota_s^{DQ} < I^l{}^2 \quad (6.26a)$$

$$\|\phi_s^{DQ}\|^2 = \phi_s^{DQT} \phi_s^{DQ} < \frac{U^l{}^2}{\omega^2} \quad (6.26b)$$

whose gradients are

$$\begin{aligned} \frac{\partial \iota_s^{DQT} \iota_s^{DQ}}{\partial \phi_s^{DQ}} &= 2 \frac{\partial \iota_s^{DQ}}{\partial \phi_s^{DQ}} \iota_s^{DQ} = 2 \Gamma_{t_s}^{DQ} \Gamma_{c_s}^{DQ} \phi_s^{DQ} \\ \frac{\partial \phi_s^{DQT} \phi_s^{DQ}}{\partial \phi_s^{DQ}} &= 2 \phi_s^{DQ}. \end{aligned}$$

From the expression of the constraints, we see that, at low speed, only the current constraint will be active whereas, at high speed, only the voltage constraint will be active. By continuity, there will be a speed range  $[\omega_l, \omega_h]$  in which both constraints will be active. This is illustrated by fig. 6.3.

We now solve the optimization problem described by eq. (6.25) in the case of the unsaturated SynRM.

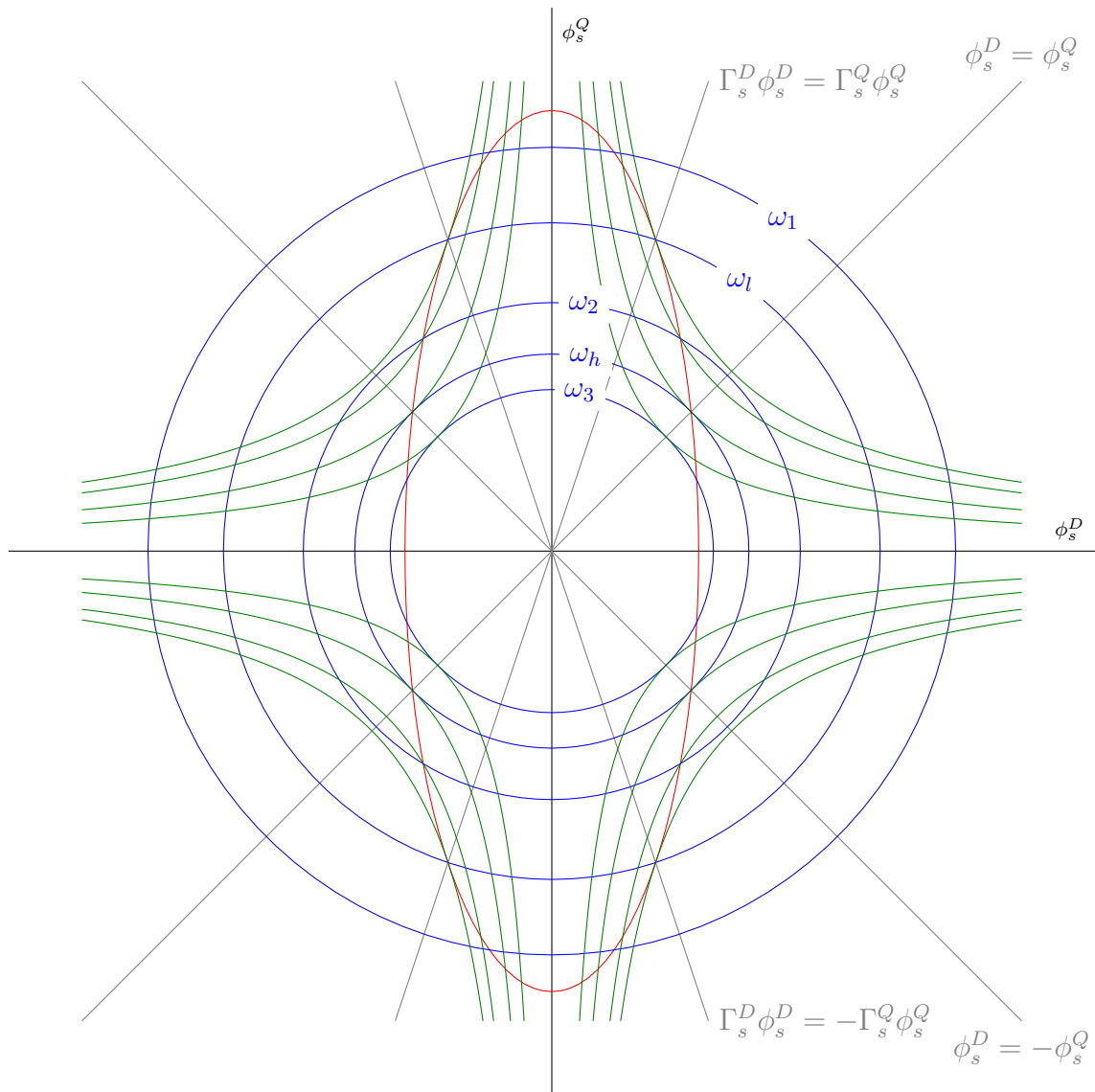


Figure 6.3 – The **red ellipsis** is the current limitation constraint, **blue circles** are voltage limitations at speeds  $\omega_1 < \omega_l < \omega_2 < \omega_h < \omega_3$  and the **green hyperlolaes** are maximum reachable torque isolines. When the speed increases, the radius of the voltage constraint circle decreases and the maximum reachable torque isoline move towards the origin which means the maximum reachable torque decreases.

**In the speed range**  $|\omega| \in [0, \omega_l]$  Only the current constraint is active. The maximum torque is reached at the points where the gradient of  $T_e$  is collinear to the gradient of the current constraint, which are at the intersections between the boundary and the line where  $\Gamma_s^D \phi_s^D = \Gamma_s^Q \phi_s^Q$ . At these points the torque is

$$T_e^l = \frac{n}{2} \left( \frac{1}{\Gamma_s^Q} - \frac{1}{\Gamma_s^D} \right) I^l{}^2.$$

Moreover the speed  $\omega_l$  is such that both the voltage and the current boundaries crosses the line  $\Gamma_s^D \phi_s^D = \Gamma_s^Q \phi_s^Q$  at the same point, i.e

$$\omega_l = \sqrt{\frac{2\Gamma_s^{D2}\Gamma_s^{Q2}}{\Gamma_s^{D2} + \Gamma_s^{Q2}} \frac{U^l}{I^l}}$$

**In the speed range**  $|\omega| \in [\omega_h, +\infty[$  Only the voltage constraint is active. The maximum torque is reached at the points where the gradient of  $T_e$  is collinear to the gradient of the voltage constraint, which are at the intersections between the boundary and the line where  $\phi_s^D = \phi_s^Q$ . At these points the torque is

$$T_e^l = \frac{n}{2} (\Gamma_s^D - \Gamma_s^Q) \left( \frac{U^l}{\omega} \right)^2.$$

Moreover the speed  $\omega_h$  is such that both the voltage and the current boundaries crosses the line  $\phi_s^D = \phi_s^Q$  at the same point, i.e

$$\omega_h = \sqrt{\frac{\Gamma_s^{D2} + \Gamma_s^{Q2}}{2} \frac{U^l}{I^l}}$$

**In the speed range**  $|\omega| \in [\omega_l, \omega_h]$  Both constraints are active. The maximum torque is thus reached at points where the boundaries intersect. These points have coordinates which verify

$$\phi_s^{D2} = \frac{I^l{}^2 - \Gamma_s^{Q2} \left( \frac{U^l}{\omega} \right)^2}{\Gamma_s^{D2} - \Gamma_s^{Q2}}$$

$$\phi_s^{Q2} = \frac{I^l{}^2 - \Gamma_s^{D2} \left( \frac{U^l}{\omega} \right)^2}{\Gamma_s^{Q2} - \Gamma_s^{D2}}$$

and thus the maximum reachable torque is

$$T_e^l = n \frac{\left| I^l{}^2 - \Gamma_s^{Q2} \left( \frac{U^l}{\omega} \right)^2 \right|^{1/2} \left| I^l{}^2 - \Gamma_s^{D2} \left( \frac{U^l}{\omega} \right)^2 \right|^{1/2}}{\Gamma_s^D + \Gamma_s^Q}$$

In fig. 6.4 we plotted the maximum reachable torque under current and voltage limitation for a unsaturated SynRM. We note that as expected the maximum torque is constant at low speed, then it begins to decrease and finally for very high speeds the torque decreases as  $1/\omega^2$ .

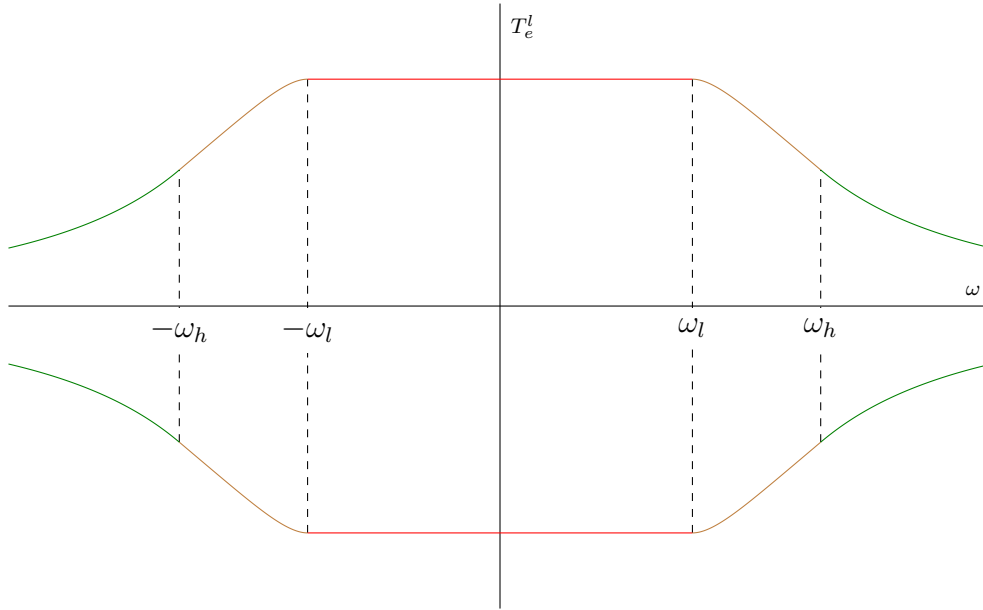


Figure 6.4 – The maximum reachable torque  $T_e^l$  as a function of  $\omega$ . The domains of speed where the constraints are active are highlighted by color. **The curve is red** when only the current constraint is active, **green** when only the voltage constraint is active and **brown** when both constraints are active.

### 6.1.6 Optimal flux working point

We present now how the flux reference  $\phi_s^{DQ,r}$  is computed from the electromagnetic torque  $T_e^s$  coming from the speed controller.

On the one hand, we must ensure that the unstable flux points of the control law are avoided. For the saturated SynRM, we have to compute the places where the saliency matrix defined in section 6.1.4.5 is invertible. This must be done numerically. In the unsaturated case the problem is much simpler, as it boils to avoiding the origin of the flux plane. When the torque is high enough this condition is automatically ensured, however when we are at low torque we can choose between setting the flux on the higher or the lower inductance axis. As the SynRM is stable in open-loop at low torque when the flux is set on the largest inductance axis, this method is favored.

On the other hand, we want to minimize the energy consumed to produce the torque  $T_e^s$  computed by the speed controller. Looking at the power balance in the SynRM we easily find that this is equivalent to minimizing the current and thus the optimization problem we want to solve is

$$\phi_s^{DQ,r} = \operatorname{argmin} \left( \left\{ \|\iota_s^{DQ}(\phi_s^{DQ})\| \quad T_e(\phi_s^{DQ}) = T_e^s \text{ and } \|u_s^{DQ}\| < U^l \right\} \right). \quad (6.27)$$

The problem described by eq. (6.27) surely has a solution, as the torque is limited by the maximum reachable torque computed in the previous section 6.1.5. In the unsaturated SynRM case, when the voltage limitation is not active, the optimal point is reached at the intersections between the torque constraint and the lines  $\Gamma_s^D \phi_s^D = \pm \Gamma_s^Q \phi_s^Q$  which is

$$\phi_s^D = \pm \sqrt{\frac{T_e^s}{n\Gamma_s^{D2} \left( \frac{1}{\Gamma_s^Q} - \frac{1}{\Gamma_s^D} \right)}} \quad (6.28a)$$

$$\phi_s^Q = \pm \sqrt{\frac{T_e^s}{n\Gamma_s^{Q^2} \left( \frac{1}{\Gamma_s^Q} - \frac{1}{\Gamma_s^D} \right)}}. \quad (6.28b)$$

Due to voltage limitation this point may not be reachable. The optimal points will be at intersections between the torque constraint and the voltage boundary which are given by

$$(\phi_s^{D^2}, \phi_s^{Q^2}) = \begin{cases} \left( \frac{1}{2} \left( \frac{U^l}{\omega} \right)^2 + \frac{1}{2} \sqrt{\left( \frac{U^l}{\omega} \right)^2 - \left( \frac{2Te^s}{n(\Gamma_s^D - \Gamma_s^Q)} \right)^2}, \frac{1}{2} \left( \frac{U^l}{\omega} \right)^2 - \frac{1}{2} \sqrt{\left( \frac{U^l}{\omega} \right)^2 - \left( \frac{2Te^s}{n(\Gamma_s^D - \Gamma_s^Q)} \right)^2} \right) \\ \left( \frac{1}{2} \left( \frac{U^l}{\omega} \right)^2 - \frac{1}{2} \sqrt{\left( \frac{U^l}{\omega} \right)^2 - \left( \frac{2Te^s}{n(\Gamma_s^D - \Gamma_s^Q)} \right)^2}, \frac{1}{2} \left( \frac{U^l}{\omega} \right)^2 + \frac{1}{2} \sqrt{\left( \frac{U^l}{\omega} \right)^2 - \left( \frac{2Te^s}{n(\Gamma_s^D - \Gamma_s^Q)} \right)^2} \right) \end{cases}$$

Of the four solutions only the two closer to the lines  $\Gamma_s^D \phi_s^D = \pm \Gamma_s^Q \phi_s^Q$  are optimal. If  $L_s^D$  is the smaller inductance, then we should select the value for which  $\phi_s^{D^2} < \phi_s^{Q^2}$ , i.e.

$$\phi_s^D = \pm \sqrt{\frac{1}{2} \left( \frac{U^l}{\omega} \right)^2 - \frac{1}{2} \sqrt{\left( \frac{U^l}{\omega} \right)^2 - \left( \frac{2Te^s}{n(\Gamma_s^D - \Gamma_s^Q)} \right)^2}} \quad (6.29a)$$

$$\phi_s^Q = \pm \sqrt{\frac{1}{2} \left( \frac{U^l}{\omega} \right)^2 + \frac{1}{2} \sqrt{\left( \frac{U^l}{\omega} \right)^2 - \left( \frac{2Te^s}{n(\Gamma_s^D - \Gamma_s^Q)} \right)^2}} \quad (6.29b)$$

Fig. 6.5 illustrates the shift of the optimal flux reference from the line  $\Gamma_s^D \phi_s^D = \Gamma_s^Q \phi_s^Q$  where the optimal points are when the voltage constraint is not active to the line  $\phi_s^D = \phi_s^Q$  where the optimal point is when the voltage constraint is active.

### 6.1.7 Simulation results

To check that the time-scale separation is valid, the control law was implemented on an unsaturated SynRM model. We used as parameters those of table 2.1 with the current limitation  $I^l = 5A$  and  $U^l = 550V$ . The simulation was run using Simulink<sup>®</sup> with a continuous time control law.

We give here some interesting test results:

- Mechanical speed 1s ramp from 0Hz to nominal value 25Hz under zero load in fig. 6.6;
- Load torque step from 0N.m to nominal value 5N.m at nominal mechanical speed 25Hz in fig. 6.7;
- Load torque 10s triangle from 0N.m to 8N.m at  $\omega_m = 100Hz$ . This test was run to show that the proposed control law handles well the voltage and current limitation. Indeed it can be seen in fig. 6.8 that the maximum theoretical torque is reached for all speeds.

As can be seen in figs. 6.6 and 6.7, the control law responds well to changes in the reference  $\omega_m^r$  and rejects well the disturbance  $T_L$  in the absence of parametric errors. Fig. 6.8 shows that limitations are enforced and that maximum efficiency is always reached. The control law was simulated in continuous time which will not be the case for a real

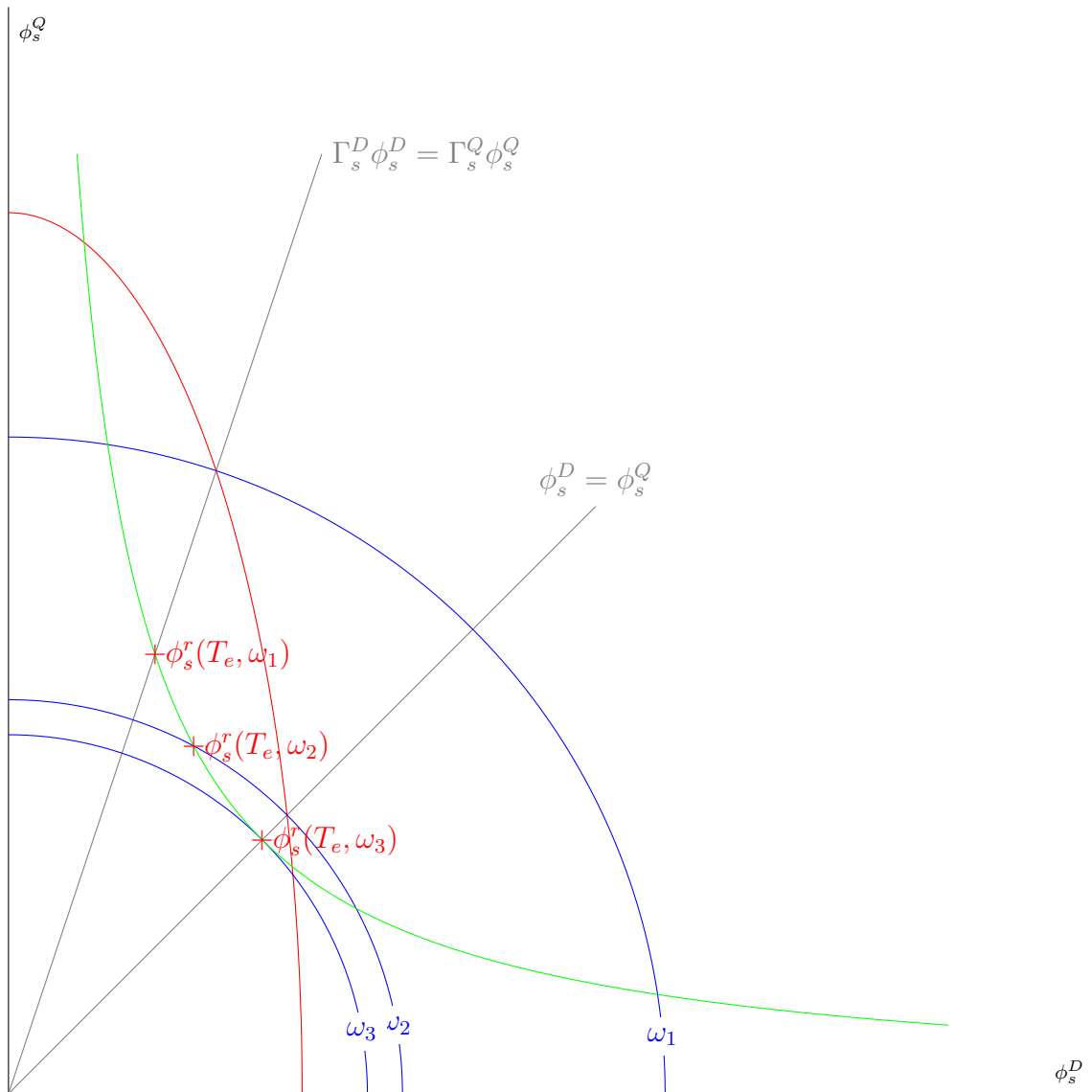


Figure 6.5 – The red ellipsis is the current limitation constraint, blue circles are voltage limitations at speeds  $\omega_1 < \omega_2 < \omega_3$  and the green hyperbolae are torque target isoline. When the the speed increases, the optimal flux reference shifts from the optimal position under current limitation to the optimal position under voltage limitation.

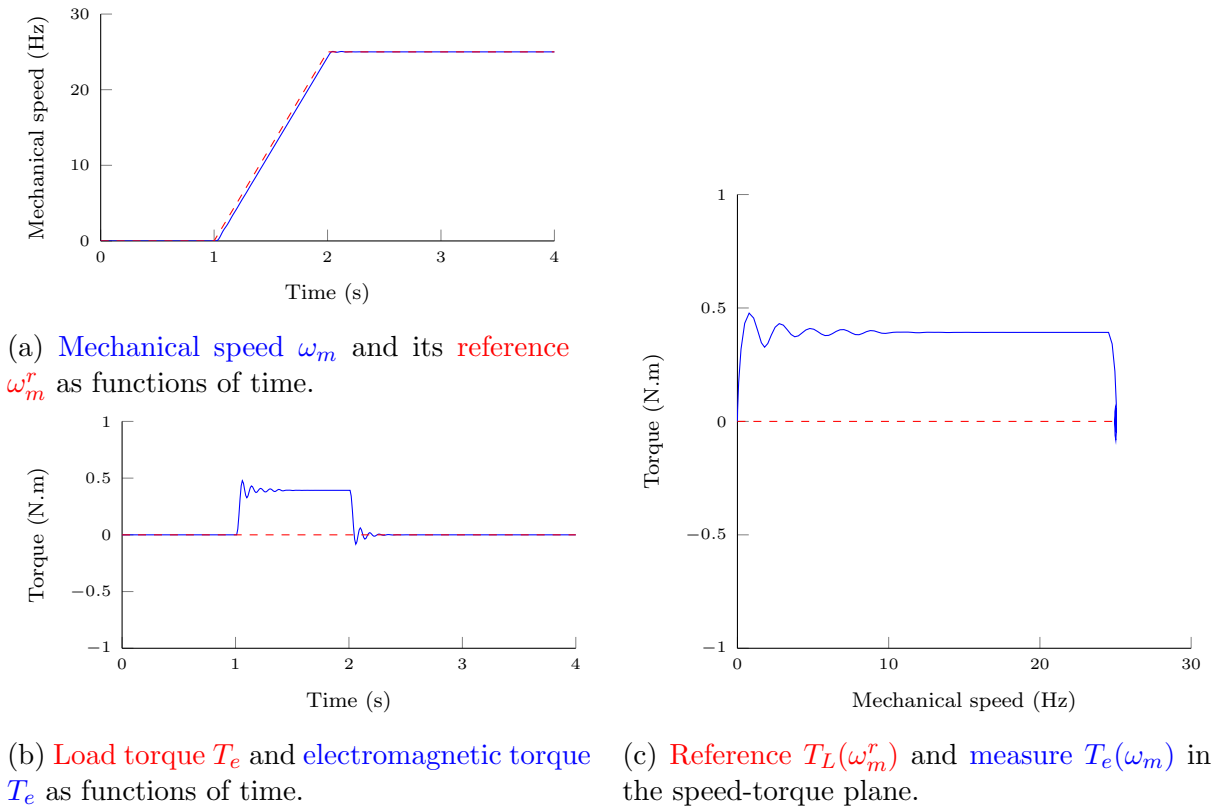


Figure 6.6 – Results of the test where the speed was ramped from  $0Hz$  to nominal value  $25Hz$  under zero load for the SynRM described by table 2.1.

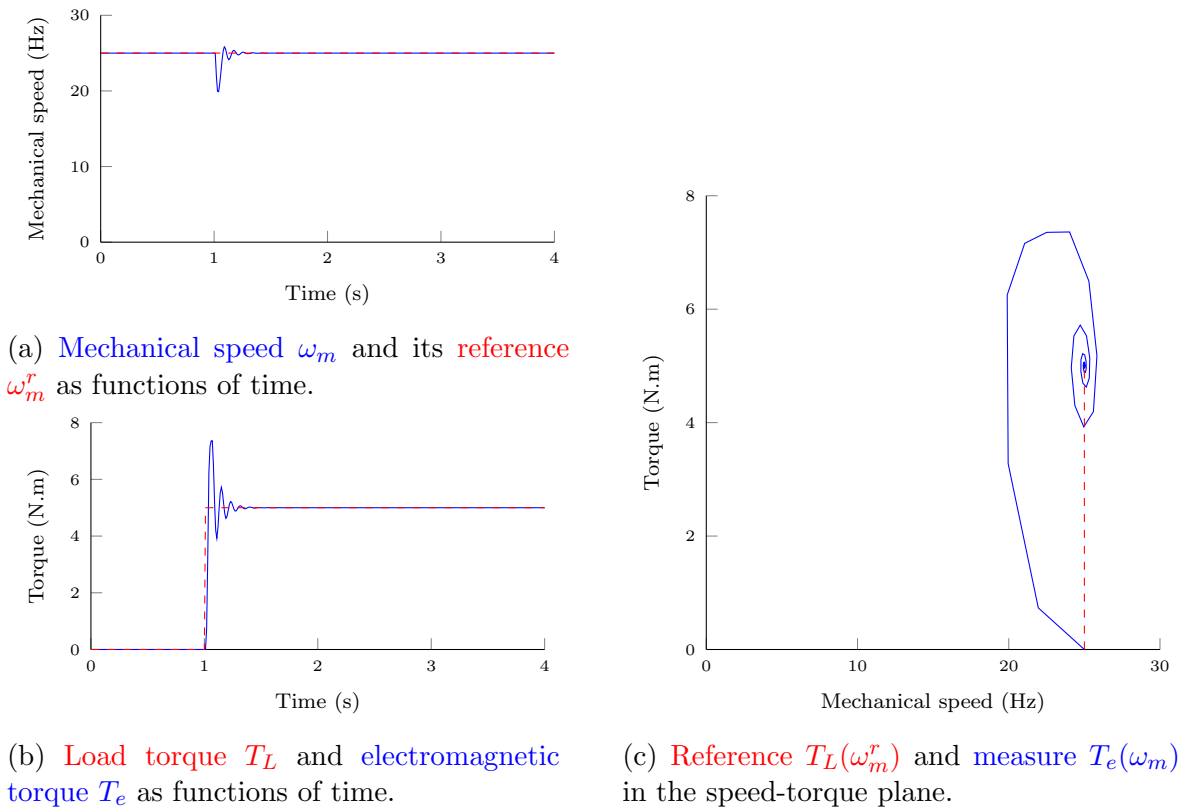


Figure 6.7 – Results of the test where the torque was stepped from  $0N.m$  to nominal value  $5N.m$  at nominal mechanical speed  $25Hz$  for the SynRM described by table 2.1.

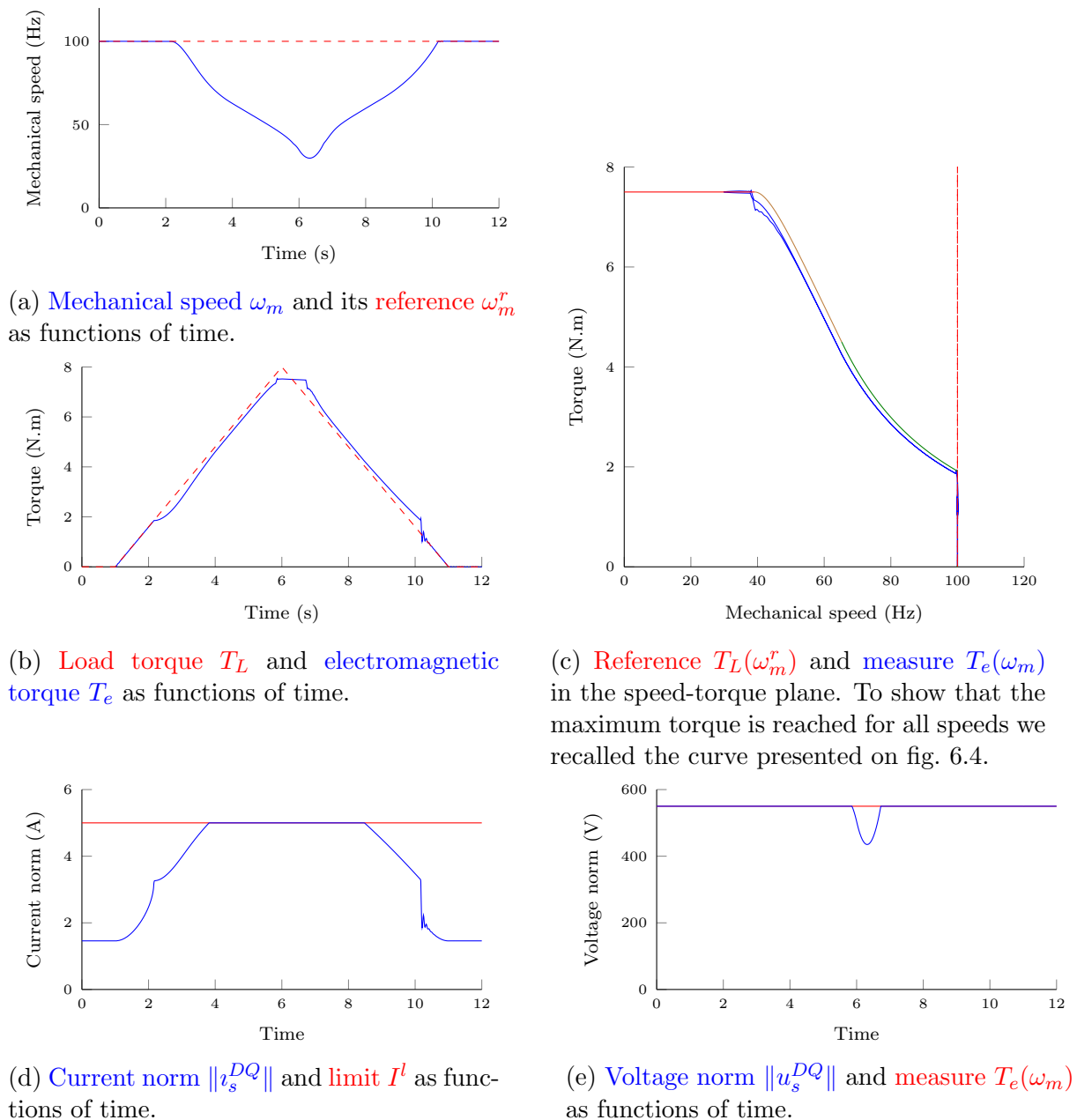


Figure 6.8 – Results of the test where we ensured that the current and voltage limitations are well handled. The test was run on the SynRM described by table 2.1.

implementation. Using Euler explicit discretization scheme, when the sample time is high enough this is not a problem, but at high speeds with a reasonable sample time some undesirable ripple appears. This is caused by the fact that the eigenvalues of the flux controller (eq. (6.18c)) have large imaginary parts at high speeds. This problem can be solved by handling the discretization process with care and using the feed-forward input  $v_s^{dq}$  to change the positions of the eigenvalues in the complex plane.

## 6.2 Generalisation to the PMSM

Under the same assumptions made for the SynRM in section 6.1.2, the same Hamilton’s equations as eq. (6.1) are obtained. Only the expressions of the currents and the electromagnetic torque differ. As the control law described in section 6.1.3 does mostly not depend on these expressions, it should work for PMSMs as well. The only places where the current expressions were used in the description or the proof of stability of the control law is the design of the estimate of the error angle  $\eta$  and the coupling matrix. The computations of the maximum torque under current and voltage limitations and the optimal flux working point must also be adapted. Having made these remarks, we will not detail the control law proposed for the PMSM but only give the modifications.

“Sensorless” control of salient and non-salient PMSMs has been studied extensively and description of “Sensorless” control laws for PMSMs can be found in textbooks (Sul [23, secs. 6.2, 6.3] and Glumineau and de Leon Morales [67, chs. 4, 6] for instance). The proposed control laws rely on the observer-controller scheme, as those proposed for SynRMs listed in section 6.1.1. The calculation of the optimal flux working point for a given torque reference can be found in Chiasson [45, sec. 9.2] for the non-salient PMSMs and Meyer and Bocker [81] for salient PMSMs. This is reviewed in sections 6.2.2 and 6.2.3 of this document.

As it is a generalization, the control law proposed here still works for SynRMs. In between the classical PMSMs (low saliency and high flux) and SynRMs (high saliency and no flux) are the Permanent Magnet Assisted SynRMs (see Guglielmi, Pastorelli, *et al.* [82]), which present a high saliency, like SynRMs, but also have a small flux, like PMSMs. The control law proposed here can be applied to such motors which can be seen as highly salient PMSMs.

### 6.2.1 Estimation of the saliency frame

The computations which lead to eq. (6.10) are still valid as the currents are still given as partial derivatives of the energy function with respect to the fluxes. However the expression for the vector factor of its second term we obtain by using the notations of section 3.8.2 is altered. It now reads  $\mathcal{J}_2 \Gamma_{c_s}^{DQ} \phi_s^{DQ,f} - \Gamma_{t_s}^{DQ} \mathcal{J}_2 \phi_s^{DQ,f} - \mathcal{J}_2 \Gamma_{c_s}^{DQ} \phi_M^{DQ}$ , where  $\phi_s^{DQ,f}$  is not easily factorized any more. Nevertheless, looking at the chosen coupling matrix (see eq. (6.23)), we note that it in fact ensures  $\kappa^T \phi_s^{dq,f}$  is proportional to  $\left( \mathcal{J}_2 \frac{\partial \mathcal{H}^{DQ}}{\partial \phi_s^{DQ}} (\phi_s^{dq,f}) - \frac{\partial^2 \mathcal{H}^{DQ}}{\partial \phi_s^{DQ^2}} \mathcal{J}_2 \phi_s^{dq,f} \right)$ . We thus propose as error signal

$$\hat{\eta} = \frac{\left( \mathcal{J}_2 \frac{\partial \mathcal{H}^{DQ}}{\partial \phi_s^{DQ}} (\phi_s^{dq,f}) - \frac{\partial^2 \mathcal{H}^{DQ}}{\partial \phi_s^{DQ^2}} \mathcal{J}_2 \phi_s^{dq,f} \right)^T \kappa (i_s^{dq} - \hat{i}_s^{dq})}{\left( \mathcal{J}_2 \frac{\partial \mathcal{H}^{DQ}}{\partial \phi_s^{DQ}} (\phi_s^{dq,f}) - \frac{\partial^2 \mathcal{H}^{DQ}}{\partial \phi_s^{DQ^2}} \mathcal{J}_2 \phi_s^{dq,f} \right)^T \kappa \left( \mathcal{J}_2 \frac{\partial \mathcal{H}^{DQ}}{\partial \phi_s^{DQ}} (\phi_s^{dq,f}) - \frac{\partial^2 \mathcal{H}^{DQ}}{\partial \phi_s^{DQ^2}} \mathcal{J}_2 \phi_s^{dq,f} \right)}$$

$$\begin{aligned}
&= \eta \frac{\left( \mathcal{J}_2 \frac{\partial \mathcal{H}^{DQ}}{\partial \phi_s^{DQ}} (\phi_s^{dq,f}) - \frac{\partial^2 \mathcal{H}^{DQ}}{\partial \phi_s^{DQ^2}} \mathcal{J}_2 \phi_s^{dq,f} \right)^T \kappa \left( \mathcal{J}_2 \frac{\partial \mathcal{H}^{DQ}}{\partial \phi_s^{DQ}} (\phi_s^{DQ}) - \frac{\partial^2 \mathcal{H}^{DQ}}{\partial \phi_s^{DQ^2}} \mathcal{J}_2 \phi_s^{DQ,f} \right)}{\left( \mathcal{J}_2 \frac{\partial \mathcal{H}^{DQ}}{\partial \phi_s^{DQ}} (\phi_s^{dq,f}) - \frac{\partial^2 \mathcal{H}^{DQ}}{\partial \phi_s^{DQ^2}} \mathcal{J}_2 \phi_s^{dq,f} \right)^T \kappa \left( \mathcal{J}_2 \frac{\partial \mathcal{H}^{DQ}}{\partial \phi_s^{DQ}} (\phi_s^{dq,f}) - \frac{\partial^2 \mathcal{H}^{DQ}}{\partial \phi_s^{DQ^2}} \mathcal{J}_2 \phi_s^{dq,f} \right)} \\
&+ \frac{\left( \mathcal{J}_2 \frac{\partial \mathcal{H}^{DQ}}{\partial \phi_s^{DQ}} (\phi_s^{dq,f}) - \frac{\partial^2 \mathcal{H}^{DQ}}{\partial \phi_s^{DQ^2}} \mathcal{J}_2 \phi_s^{dq,f} \right)^T \kappa \left( \frac{\partial \mathcal{H}^{DQ}}{\partial \phi_s^{DQ}} (\phi_s^{DQ}) - \frac{\partial \mathcal{H}^{DQ}}{\partial \phi_s^{DQ}} (\phi_s^{DQ,f}) \right)}{\left( \mathcal{J}_2 \frac{\partial \mathcal{H}^{DQ}}{\partial \phi_s^{DQ}} (\phi_s^{dq,f}) - \frac{\partial^2 \mathcal{H}^{DQ}}{\partial \phi_s^{DQ^2}} \mathcal{J}_2 \phi_s^{dq,f} \right)^T \kappa \left( \mathcal{J}_2 \frac{\partial \mathcal{H}^{DQ}}{\partial \phi_s^{DQ}} (\phi_s^{dq,f}) - \frac{\partial^2 \mathcal{H}^{DQ}}{\partial \phi_s^{DQ^2}} \mathcal{J}_2 \phi_s^{dq,f} \right)} \\
&= a_\eta \eta + b_\eta \tag{6.30}
\end{aligned}$$

where  $a_\eta \approx 1$  and  $b_\eta \approx 0$ . The coupling matrix  $\kappa \in \mathcal{M}_2(\mathbb{R})$  is chosen hereafter for stability of the control law as in the SynRM case. If the PMSM is very salient and has a low permanent magnet flux, i.e. if we consider the so-called Permanent Magnet Assisted SynRM (see [82]), the denominator could vanish. However, we will ensure in the flux reference computation that it does never occur.

All the rest of the control law is identical. Tikhonov theorem can again be applied and the three time-scales can again be separated as in section 6.1.4. As the form of the estimate of  $\eta$ ,  $\hat{\eta} = a_\eta \eta + b_\eta$ , is unchanged in the fast time-scale, the fast time-scale is still exponentially stable uniformly in the slower variables. The expression (see eq. (6.21)) of  $\eta$  at the equilibrium is of course altered and becomes

$$\eta_e = -\frac{b_\eta}{a_\eta} = -\frac{\left( \mathcal{J}_2 \frac{\partial \mathcal{H}^{DQ}}{\partial \phi_s^{DQ}} (\phi_s^{dq,f}) - \frac{\partial^2 \mathcal{H}^{DQ}}{\partial \phi_s^{DQ^2}} \mathcal{J}_2 \phi_s^{dq,f} \right)^T \kappa \left( \frac{\partial \mathcal{H}^{DQ}}{\partial \phi_s^{DQ}} (\phi_s^{DQ}) - \frac{\partial \mathcal{H}^{DQ}}{\partial \phi_s^{DQ}} (\phi_s^{DQ,f}) \right)}{\left( \mathcal{J}_2 \frac{\partial \mathcal{H}^{DQ}}{\partial \phi_s^{DQ}} (\phi_s^{dq,f}) - \frac{\partial^2 \mathcal{H}^{DQ}}{\partial \phi_s^{DQ^2}} \mathcal{J}_2 \phi_s^{dq,f} \right)^T \kappa \left( \mathcal{J}_2 \frac{\partial \mathcal{H}^{DQ}}{\partial \phi_s^{DQ}} (\phi_s^{DQ}) - \frac{\partial^2 \mathcal{H}^{DQ}}{\partial \phi_s^{DQ^2}} \mathcal{J}_2 \phi_s^{DQ,f} \right)}.$$

Similar computations as those made in section 6.1.4.3 lead to the trace and determinant of the linearized flux error system

$$\text{tr } A = -\frac{R_s}{\Omega_0^\phi} \frac{\Delta \iota_s^{ctT} \kappa \Delta \iota_s^{ct}}{\Delta \iota_s^{ctT} \kappa \Delta \iota_s^{ct}} = -\frac{R_s}{\Omega_0^\phi} \tag{6.31a}$$

$$\det A = \left( \frac{\omega}{\Omega_0^\phi} \right)^2 + \frac{\omega}{\Omega_0^\phi} \frac{R_s}{\Omega_0^\phi} \frac{\Delta \iota_s^{ctT} \kappa \mathcal{J}_2 \Delta \iota_s^{ct}}{\Delta \iota_s^{ctT} \kappa \Delta \iota_s^{ct}}. \tag{6.31b}$$

where we used  $\Delta \iota_s^{ct} = \left( \mathcal{J}_2 \frac{\partial \mathcal{H}^{DQ}}{\partial \phi_s^{DQ}} (\phi_s^{dq,f}) - \frac{\partial^2 \mathcal{H}^{DQ}}{\partial \phi_s^{DQ^2}} \mathcal{J}_2 \phi_s^{dq,f} \right)$  for the sake of compactness. By simply taking  $\kappa = I_2$ , the second term of the determinant is canceled out. Thus assuming we are not at low speed ( $\exists \varepsilon > 0 \quad \omega > \Omega_0^\phi \sqrt{\varepsilon \frac{R_s}{\Omega_0^\phi}}$ ), we have  $\text{tr } A < 0$  and  $\det A > \varepsilon |\text{tr } A|$ , which means that the linearized flux-error system is exponentially stable uniformly in  $\omega$  and  $\phi_s^{dq,f}$ .

The rest of the proof is identical to what is done in section 6.1.4 and is thus not repeated here. The proposed control law ensures stability of the speed of a PMSM under torque disturbance as soon as the speed is high enough.

## 6.2.2 Torque limitation

As the expressions of the electromagnetic torque and the currents as functions of the fluxes is not the same for PMSMs and SynRMs, the maximum torque a PMSM can reach under current and voltage limitation will not be the same. However the reasoning is the same and the results are similar as what is obtained in section 6.1.5.

The optimization problem we want to solve is still

$$T_e^l = \max \left( \left\{ T_e(\phi_s^{DQ}) \quad \|\iota_s^{DQ}\| < I^l \text{ and } \|u_s^{DQ}\| < U^l \right\} \right). \quad (6.32)$$

The gradient of the electromagnetic torque is now given by

$$\frac{\partial T_e}{\partial \phi_s^{DQ}} = -n \mathcal{J}_2 \iota_s^{DQ} + n \left( \frac{\partial \iota_s^{DQ}}{\partial \phi_s^{DQ}} \right)^T \mathcal{J}_2 \phi_s^{DQ} = -n (\mathcal{J}_2 \Gamma_{c_s}^{DQ} - \Gamma_{t_s}^{DQ} \mathcal{J}_2) \phi_s^{DQ} + n \mathcal{J}_2 \Gamma_{c_s}^{DQ} \phi_M^{DQ}$$

which may vanish. But this will never occur as the flux reference computation ensures that this term (which is also in the denominator of the estimate of  $\eta$ ) does not vanish. Thus the optimal torque is reached on the boundaries.

With the same reasoning as before the constraints can be expressed as

$$\|\iota_s^{DQ}\|^2 = \iota_s^{DQT} \iota_s^{DQ} < I^l{}^2 \quad (6.33a)$$

$$\|\phi_s^{DQ}\|^2 = \phi_s^{DQT} \phi_s^{DQ} < \frac{U^l{}^2}{\omega^2} \quad (6.33b)$$

whose gradients are

$$\begin{aligned} \frac{\partial \iota_s^{DQT} \iota_s^{DQ}}{\partial \phi_s^{DQ}} &= 2 \frac{\partial \iota_s^{DQ}}{\partial \phi_s^{DQ}} \iota_s^{DQ} = 2 \Gamma_{t_s}^{DQ} \Gamma_{c_s}^{DQ} (\phi_s^{DQ} - \phi_M^{DQ}) \\ \frac{\partial \phi_s^{DQT} \phi_s^{DQ}}{\partial \phi_s^{DQ}} &= 2 \phi_s^{DQ}. \end{aligned}$$

Similarly to the SynRM, at low speed, the voltage constraint is inactive. However, if the current constraint is too small there will be a point where the two authorized sets are disjoint and thus there will be a speed the motor cannot overpass without violating one of the constraints. When the current limitation is large enough, there is no such problem and we will have 3 speed domains as in the SynRM case.

In the general unsaturated case, the optimization problem described by eq. (6.32) can be solved analytically as for the SynRM, however the calculations are messier and of little interest (see [81]). We will only give here the analytic solution for the non-salient case where  $\Gamma_s^D = \Gamma_s^Q = \Gamma_s$ , which is also given in Chiasson [45, sec. 9.2]. In this case the  $D$ -axis is defined by the direction of the permanent magnet flux  $\phi_M$ . The other cases will only be illustrated in fig. 6.9 which was created using PMSMs with parameters given on table 6.2.

First of all, we search when the constraint domains can be disjoint: it can occur at high speeds, when the origin is not included in the current constraint domain, i.e. when  $I^l < \Gamma_s^D \phi_M$ . In this case the motor cannot rotate faster than

$$\omega^l = \frac{U^l}{\Gamma_s \phi_M - I^l} \quad (6.34)$$

without violating the voltage limitation. The reference is thus saturated by this value  $\omega^l$ .

**When only the current constraint is active** In the non-salient case, torque is proportional to  $\phi_s^Q$  and maximum torque is reached when all the current is along  $Q$  axis, i.e.

$$\begin{aligned} \phi_s^D &= \phi_M \\ \phi_s^Q &= \frac{I^l}{\Gamma_s} \end{aligned}$$

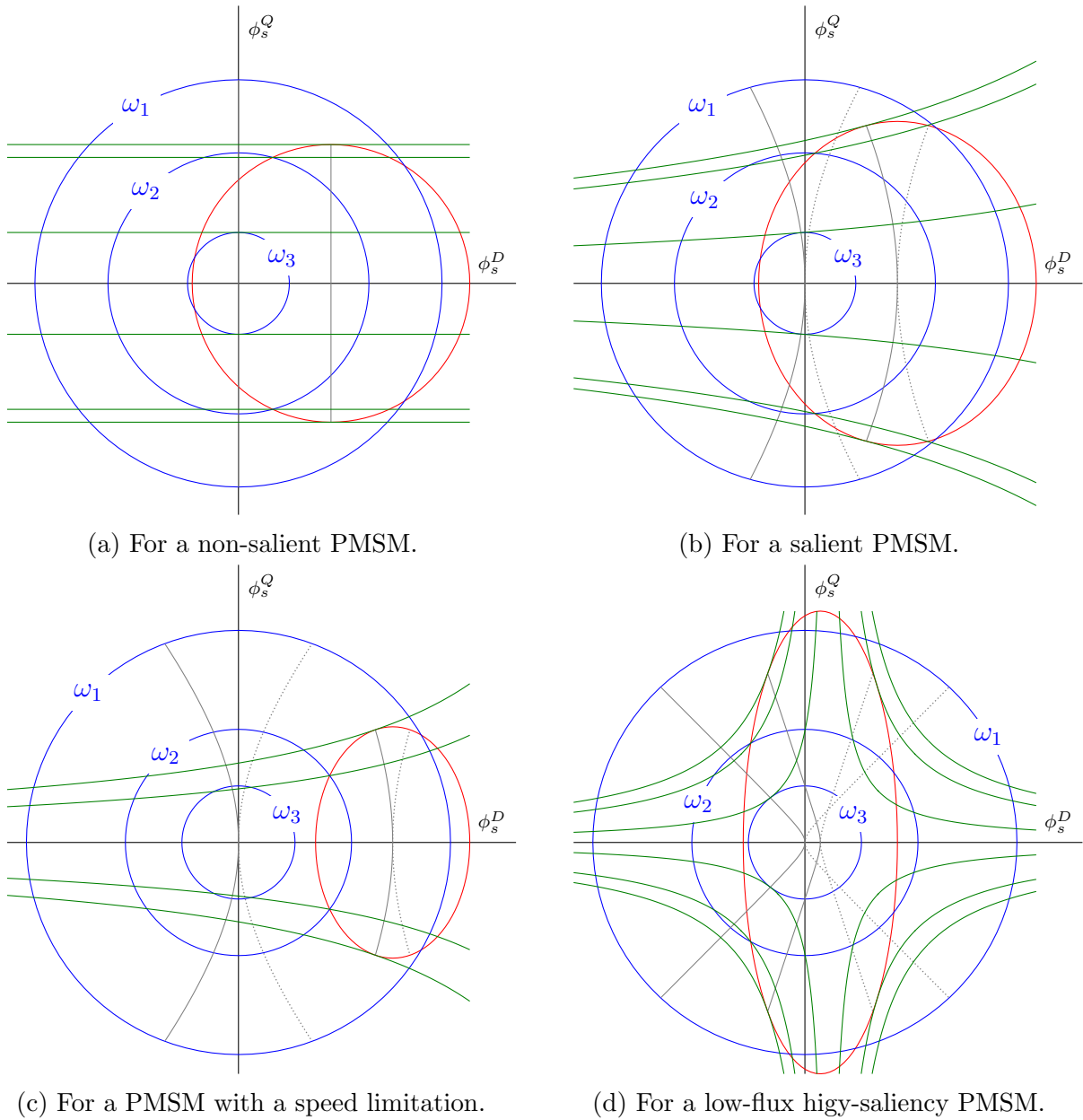


Figure 6.9 – Maximum torque under current (red ellipses) and voltage (blue circles) limitations for different speeds  $\omega_1 < \omega_2 < \omega_3$ . The gray lines are the loci of critical points for the current or the voltage at given torque (This problem will be solved in section 6.2.3), the solid lines being the loci of the global extrema and the dashed line being only local extrema. The green hyperbolae are the maximum reachable torque isolines at the different speeds. Again when the speeds increases, the radius of the voltage constraint decreases and the torque isoline goes closer to the horizontal axis, which means that the maximum reachable torque decreases.

and consequently

$$T_e^l = n\phi_M I^l. \quad (6.35)$$

The speed above which the voltage constraint becomes active, is the speed at which this point is on the voltage constraint boundary,

$$\omega_l = \sqrt{\frac{\Gamma_s^2 U^l{}^2}{I^l{}^2 + \Gamma_s^2 \phi_M^2}}. \quad (6.36)$$

**When only the voltage constraint is active** The torque being proportional to  $\phi_s^Q$ , the maximum torque is reached when all the flux is on  $Q$  axis, i.e.

$$\begin{aligned} \phi_s^D &= 0 \\ \phi_s^Q &= \frac{U^l}{\omega} \end{aligned}$$

and thence

$$T_e^l = n\Gamma_s \phi_M \frac{U^l}{\omega}. \quad (6.37)$$

The speed below which the current constraint becomes active is the speed at which this point is on the current constraint boundary,

$$\omega_h = \sqrt{\frac{\Gamma_s^2 U^l{}^2}{I^l{}^2 - \Gamma_s^2 \phi_M^2}}, \quad (6.38)$$

assuming the domains are not disjoint.

**When both constraints are active** The maximum torque is reached at the intersection of the voltage and current constraint boundaries which is at the coordinates

$$\begin{aligned} \phi_s^d &= \frac{1}{2}\phi_M + \frac{1}{2\phi_M} \left(\frac{U^l}{\omega}\right)^2 - \frac{1}{2\phi_M} \left(\frac{I^l}{\Gamma_s}\right)^2 \\ \phi_s^q &= \pm \frac{1}{2\phi_M} \sqrt{\left(\left(\phi_M + \frac{U^l}{\omega}\right)^2 - \left(\frac{I^l}{\Gamma_s}\right)^2\right) \left(\left(\phi_M - \frac{U^l}{\omega}\right)^2 - \left(\frac{I^l}{\Gamma_s}\right)^2\right)}. \end{aligned}$$

Consequently the maximum reachable torque is

$$T_e^l = \frac{n}{2}\Gamma_s \sqrt{\left(\left(\phi_M + \frac{U^l}{\omega}\right)^2 - \left(\frac{I^l}{\Gamma_s}\right)^2\right) \left(\left(\phi_M - \frac{U^l}{\omega}\right)^2 - \left(\frac{I^l}{\Gamma_s}\right)^2\right)}. \quad (6.39)$$

### 6.2.3 Optimal flux working point

We extend here the results obtained for SynRMs in section 6.1.6 to PMSMs.

On the one side, we want to avoid the domains where the control law is unstable, that is to say where the vector  $\left(\mathcal{J}_2 \frac{\partial \mathcal{H}^{DQ}}{\partial \phi_s^{DQ}}(\phi_s^{dq,f}) - \frac{\partial^2 \mathcal{H}^{DQ}}{\partial \phi_s^{DQ}{}^2} \mathcal{J}_2 \phi_s^{dq,f}\right)$  vanishes. For saturated PMSMs, these domains can have a quite complex shape which must be computed numerically.

Number	Characteristic	$\phi_M$	$L_s^D$	$L_s^Q$
1	Non-salient PMSM	$1Wb$	$0.3H$	$0.3H$
2	PMSM with small saliency	$1Wb$	$0.3H$	$0.35H$
3	PMSM with speed limit	$1Wb$	$0.1H$	$0.15H$
4	PMSM with large saliency and low flux	$0.1Wb$	$0.1H$	$0.3H$

Table 6.2 – Characteristics of the simulated PMSMs.

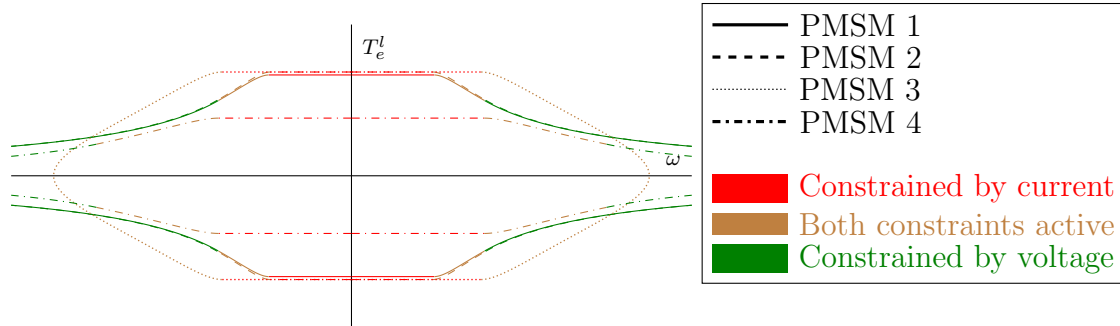


Figure 6.10 – The maximum reachable torque  $T_e^l$  as a function of  $\omega$  for the motors listed in table 6.2. The domains of speed where the constraints are active are highlighted by color.

When unsaturated PMSMs are considered, it boils down to avoiding the point  $(\phi_s^D, \phi_s^Q) = \left( \frac{\Gamma_s^D}{\Gamma_s^D - \Gamma_s^Q} \phi_M, 0 \right)$ .

On the other side, we want to minimize the losses. In PMSMs the losses are given by  $R_s \|\iota_s^{DQ}\|^2$  as for SynRMs. We thus want to solve the optimization problem

$$\phi_s^{DQ,r} = \operatorname{argmin}(\{ \|\iota_s^{DQ}(\phi_s^{DQ})\|^2 \quad T_e(\phi_s^{DQ}) = T_e^s \text{ and } \|u_s^{DQ}\| < U^l \}). \quad (6.40)$$

As  $|T_e^s| < T_e^l$  and  $|\omega^r| < \omega^l$  this problem has certainly a solution. It is now solved in the case of the non-salient unsaturated PMSM (see also [45, sec. 9.2]).

When the voltage constraint is not active the optimal point is

$$\phi_s^D = 0 \quad (6.41a)$$

$$\phi_s^Q = \frac{T_e}{n\Gamma_s\phi_M} \quad (6.41b)$$

which means that all the current is on  $Q$  axis. When this point is not achievable, the optimal point will be at the intersection between the torque constraint and the voltage boundary which is in the half-plane  $\phi_s^D \geq 0$ , given by

$$\phi_s^D = \sqrt{\left( \frac{U^l}{\omega} \right)^2 - \left( \frac{T_e}{n\Gamma_s\phi_M} \right)^2} \quad (6.42a)$$

$$\phi_s^Q = \frac{T_e}{n\Gamma_s\phi_M}. \quad (6.42b)$$

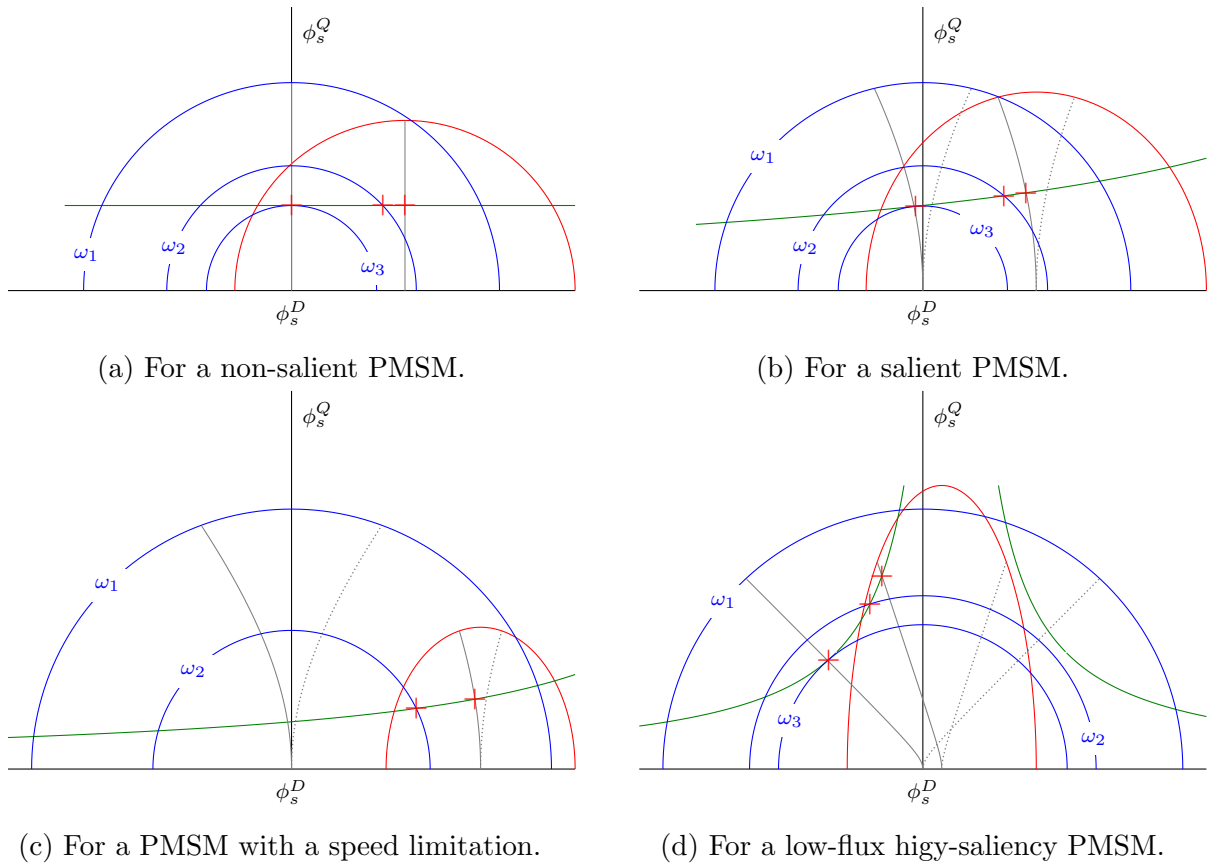


Figure 6.11 – The **red ellipsis** is the current limitation constraint, **blue circles** are voltage limitations at speeds  $\omega_1 < \omega_2 < \omega_3$  and the **green hyperbolae** are torque target isoline. For a given torque and a given speed, the optimal flux reference is materialized as a **red cross**. When the the speed increases, the optimal flux reference shifts from the optimal position under current limitation to the optimal position under voltage limitation.

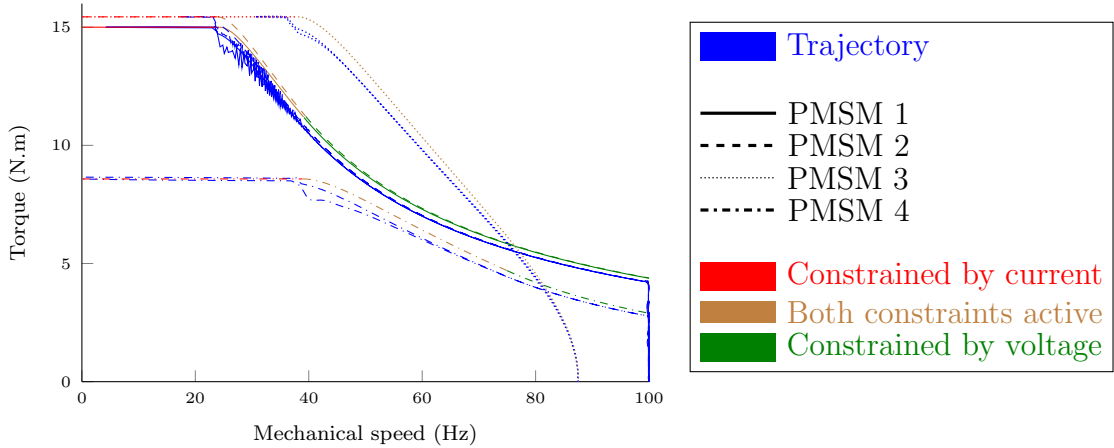


Figure 6.12 – Trajectory in the speed-torque plane during a load-torque from  $0N.m$  to  $16N.m$  triangle at  $\omega_m = 100Hz$  for the PMSMs with magnetic parameters given in table 6.2.

### 6.2.4 Simulation results

The proposed control law has been simulated on unsaturated PMSMs with parameters given in table 6.2. We used only the following scenario: a  $10s$  load torque triangle from  $0N.m$  to  $16N.m$  at  $\omega_m = 100Hz$ . This scenario was chosen because it is the most difficult and it highlights the fact that the control law behaves correctly at high speed and high torque. The simulation was done under Simulink<sup>®</sup> using a continuous time control law. The resulting trajectory in the speed-torque plane is given in fig. 6.12.

## 6.3 Partial conclusion

In this chapter is presented a “sensorless” control law for SynRM at medium to high speed. The proof of stability of the control law is detailed. On the unsaturated SynRM model, we also study the constraints implied by the stator voltage and current limitations and the computation of the optimal flux reference to reach a given torque. Simulation results are also given.

Due to the similarities between SynRM and PMSM models, this control law can easily be extended to control salient and non salient PMSMs. Only a few changes are required. We again give the constraints imposed by current and voltage limitations and the computation of the optimal flux reference to reach a given torque on any unsaturated PMSM. Simulations results are given for a few unsaturated PMSM models.

Admittedly parametric sensitivity of the proposed control law should be analyzed, but we disregarded it due to lack of time. Besides we think that the proposed control law can be extended to IMs, even though we did not have enough time to write a thorough proof.



# Chapter 7

## “Sensorless” low speed motor control

### Chapitre 7 — Contrôle « sans capteur » à basse vitesse

*Ce chapitre est consacré à la mise en œuvre de l’injection de signal pour le contrôle « sans capteur » à basse vitesse du moteur à induction. Les moyens expérimentaux contraignent fortement le choix de la fréquence de l’injection qui ne doit pas être trop basse, pour ne pas interférer avec le contrôleur, ni trop haute, à cause de la fréquence PWM. Les retards de la boucle d’acquisition posent aussi un problème qui est résolu par l’utilisation d’un observateur d’oscillation du flux stator. Ce chapitre se termine avec la description d’une loi de contrôle « sans capteur » pour le moteur à induction à basse vitesse en suivant l’approche traditionnelle et le mise en évidence du mauvais conditionnement de ces méthodes pour certains moteurs.*

We are now interested in low speed “sensorless” control for electric motors. As is explained in section 4.1, electric motors are poorly observable at low speed, and even unobservable at zero speed. In section 4.2 a method to recover observability even at zero speed is proposed: HF signal injection. We will have to resort to this technique in order to achieve low speed “sensorless” control of electric motors.

That is why, we devote section 7.1 to the interaction between HF signal injection and the control law. It turns out to be more involved than in the theoretical approach of section 4.3 due to implementation constraints. We then try in section 7.2 to apply signal injection to control the IM described in section 2.1.2. Doing this, we faced again the problem signaled in section 4.4.1, i.e. the ill-conditioning of the virtual measurements obtained by signal injection on IMs with a small magnetic saliency. However, the promising approach proposed in section 4.4.2 is not applied due to time shortage.

## 7.1 Using high frequency injection for control

We showed in section 4.2 that HF injection is a solution to retrieve observability on the trajectories which are close to the permanent trajectory at  $\omega_{s,e} = 0$  where motors have been proven to be unobservable in section 4.1. In section 4.3, we explained in a theoretical way how signal injection can be integrated with a control law. We see in this section how the experimental constraints hinder this theoretical approach. Namely, the injection frequency must be squeezed in between the bandwidth of the controller ( $\approx 100Hz$ ) and the PWM frequency ( $4kHz$ ).

### 7.1.1 High frequency injection in closed loop

Our aim is to design a “sensorless” control law, but the study in section 4.2 was done in open loop and section 4.3 is very theoretical. We show here how it applies to electric motors, where the controller bandwidth below and the PWM frequency above constrain the signal injection.

#### 7.1.1.1 Ideal control law

The system to be controlled can be expressed by eq. (4.33), recalled here

$$\frac{dX}{dt} = A(X) + U(t) \quad (7.1)$$

where  $U(t)$  is the sum of the HF signal injection  $\tilde{U}(t, \Omega t)$  and the low frequency input of the system  $\bar{U}(t)$ . The control of the system  $\bar{u}_s^{\alpha\beta}(t)$  is now given by the output of the controller which is described by

$$\bar{u}_s^{\alpha\beta}(t) = \Sigma(\eta, \iota_s^{\alpha\beta, m}, \omega_m^r, \phi_r^r) \quad (7.2a)$$

$$\frac{d\eta}{dt} = I(\eta, \iota_s^{\alpha\beta, m}, \omega_m^r, \phi_r^r) \quad (7.2b)$$

where  $\eta$  is the state of the controller. On the contrary to what is done in section 4.3, the demodulation procedure is embedded in the controller.

Setting

$$\begin{aligned} \mathcal{X} &= \begin{pmatrix} X \\ \eta \end{pmatrix} \\ \tilde{U}(t, \Omega t) &= \begin{pmatrix} \tilde{U}(t, \Omega t) \\ 0_{\dim(\eta), 1} \end{pmatrix} \\ \mathcal{A}(\mathcal{X}, \omega_m^r, \phi_r^r) &= \begin{pmatrix} A(X) \\ 0_{\dim(\eta), 1} \end{pmatrix} + \begin{pmatrix} \Sigma(\eta, \iota_s^{\alpha\beta, m}(X), \omega_m^r, \phi_r^r) \\ 0_{2, 1} \\ T_L(t) \\ 0 \\ I(\eta, \iota_s^{\alpha\beta, m}(X), \omega_m^r, \phi_r^r) \end{pmatrix}, \end{aligned}$$

the system can be rewritten as

$$\frac{d\mathcal{X}}{dt} = \mathcal{A}(\mathcal{X}, \omega_m^r, \phi_r^r) + \tilde{U}(t, \Omega t), \quad (7.3)$$

which is very similar to eq. (7.1) up to the vector field expressions. The controller is designed to have a 100Hz bandwidth which is five times lower than the frequency  $\Omega$ . Under these conditions, second order averaging (see section 4.2.3 and [47, sec. 2.9]) is still a good enough approximation and we can show that HF injection has an effect of amplitude  $\frac{1}{\Omega}$  on the stator flux and even lower on the other state variables. Thus HF injection does not disturb much the behavior of the control law. The flux ripple will be almost identical to what was observed in the open loop case.

We verified this conclusion with a simulation using the saturated IM model given by eq. (4.59) with the saturation functions given by table 4.2 controlled at low speed using the speed sensor. We ran two simulations

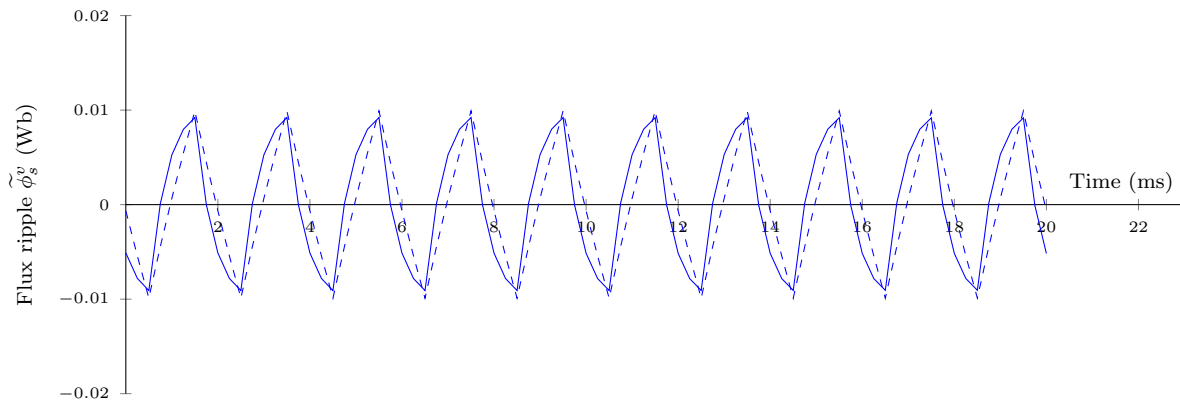


Figure 7.1 – Comparison between closed loop ripple (solid line) and open loop ripple (dashed line) on the stator flux along the injection axis  $u$ .

- The current controller was fed with the unfiltered measured current;
- The current controller was fed with the measured current from which the effects of the injection have been filtered out (see section 7.1.3 to see how this can be done).

During both simulations, the stator flux was recorded and we found that the 2 records only differ by the shape of the flux ripple, as shown by fig. 7.1. This is due to the fact that the second order averaging is less valid, as the bandwidth of the current controller is too close to the injection frequency. It could be taken into account as was done in section 4.2.4.

### 7.1.1.2 Implementation on the test bench

When the same test was done on the test bench, we discovered that the current ripple was not at all what is expected of the results of section 7.1.1.1. Surprisingly, the current ripple was far larger than we expected.

After investigation, we found out that it was caused by the delays in the control application ( $1T_{PWM} = 2.5 \cdot 10^{-4}s$ ) and in the current measurement ( $1T_{PWM} = 2.5 \cdot 10^{-4}s$ ). Indeed as said in section 2.2.1, the voltage is imposed at the bounds of the electric motor one period after having been computed by the control law and the current measurement is seen by the controller one period after having been computed. From the controller point of view, this can be modeled by a two-period delay on the current measurement.

This was verified with simulations where we used two models (with and without delay) and recorded the simulated stator flux in both simulations. As can be seen in fig. 7.2 the stator flux ripple is totally modified by this two-period delay on the current measurement. The results of averaging found in section 7.1.1.1 stating that the stator flux ripple is not affected much are not valid any more.

## 7.1.2 A flux ripple observer

To solve the problem mentioned in section 7.1.1.2, we can obviously filter out the HF injection from the measured current before feeding it to the control law. Indeed, the averaged current can be extracted by low-pass filtering or using a sliding average on one period of the HF signal as described in section 4.3.3. However, this is not really satisfactory, as we have to take into account the delay the estimator introduces (see

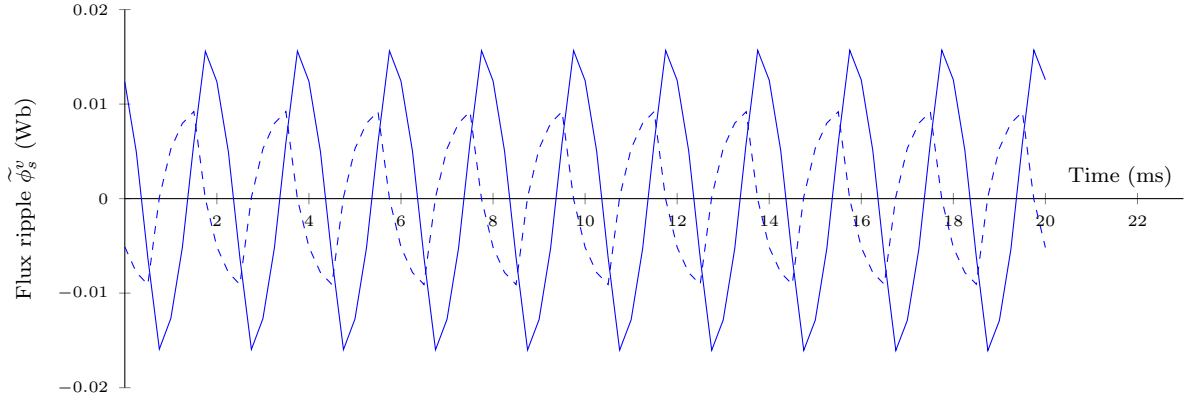


Figure 7.2 – Comparison between closed loop stator flux ripple with (solid line) and without (dashed line) delay along the injection axis  $u$ .

proposition 1) in the current controller design. We preferred an alternative approach which enables us to obtain the flux ripple thanks to a flux ripple observer.

### 7.1.2.1 Description of the observer

The stator flux in  $\alpha\beta$  frame evolves according to

$$\frac{d\phi_s^{\alpha\beta}}{dt} = u_s^{\alpha\beta} - R_s i_s^{\alpha\beta} \quad (7.4)$$

where the variable can be separated according to their time scales

$$\begin{aligned} u_s^{\alpha\beta} &= \bar{u}_s^{\alpha\beta} + \tilde{u}_s^{\alpha\beta} \\ i_s^{\alpha\beta} &= \bar{i}_s^{\alpha\beta} + \tilde{i}_s^{\alpha\beta} \\ \phi_s^{\alpha\beta} &= \bar{\phi}_s^{\alpha\beta} + \tilde{\phi}_s^{\alpha\beta}. \end{aligned}$$

As was shown in section 4.2.3,  $\bar{\phi}_s^{\alpha\beta}$  obeys to the averaged equation

$$\frac{d\bar{\phi}_s^{\alpha\beta}}{dt} = \bar{u}_s^{\alpha\beta} - R_s \bar{i}_s^{\alpha\beta} \quad (7.5)$$

and consequently

$$\frac{d\tilde{\phi}_s^{\alpha\beta}}{dt} = \tilde{u}_s^{\alpha\beta} - R_s \tilde{i}_s^{\alpha\beta}. \quad (7.6)$$

To estimate the stator flux ripple  $\tilde{\phi}_s^{\alpha\beta}$ , we consider the following observer

$$\frac{d\hat{\tilde{\phi}}_s^{\alpha\beta}}{dt} = u_s^{\alpha\beta} - \hat{R}_s i_s^{\alpha\beta} - \Omega \tilde{K} \int_{t-\frac{1}{\Omega}}^t \hat{\tilde{\phi}}_s^{\alpha\beta}(s) ds \quad (7.7)$$

where  $u_s^{\alpha\beta}$  is the (known) control,  $i_s^{\alpha\beta}$  is measured and  $\tilde{K}$  is the observer gain. Subtracting eq. (7.6) from eq. (7.7), we obtain the dynamic of the error  $\Delta\tilde{\phi}_s^{\alpha\beta}$  between the estimated

flux ripple  $\widehat{\phi}_s^{\alpha\beta}$  and the real one  $\widetilde{\phi}_s^{\alpha\beta}$

$$\begin{aligned}\frac{d\Delta\widetilde{\phi}_s^{\alpha\beta}}{dt} &= \bar{u}_s^{\alpha\beta} - R_s\bar{v}_s^{\alpha\beta} - \Delta R_s\bar{v}_s^{\alpha\beta} - \Omega\widetilde{K} \int_{t-\frac{1}{\Omega}}^t \widehat{\phi}_s^{\alpha\beta}(s)ds \\ &= \bar{u}_s^{\alpha\beta} - R_s\bar{v}_s^{\alpha\beta} - \Delta R_s\bar{v}_s^{\alpha\beta} - \Omega\widetilde{K} \int_{t-\frac{1}{\Omega}}^t \Delta\widetilde{\phi}_s^{\alpha\beta}(s)ds\end{aligned}$$

where we used the notation  $\Delta R_s = \widehat{R}_s - R_s$  and the fact that  $\widehat{\phi}_s^{\alpha\beta}$  has zero mean on intervals of length  $\frac{1}{\Omega}$  as was shown in section 4.2.3. The averaged variables follow the usual equation of the electric machine. Besides, we are on a permanent trajectory where  $\omega_{s,e} \approx 0$ . Consequently, we have  $\bar{u}_s^{\alpha\beta} - R_s\bar{v}_s^{\alpha\beta} \approx 0$ . Moreover, we are going to consider that the stator resistance is well known and thus  $\Delta R_s \approx 0$ . Taking into account these approximations, we obtain as dynamics of the error

$$\frac{d\Delta\widetilde{\phi}_s^{\alpha\beta}}{dt} = -\Omega\widetilde{K} \int_{t-\frac{1}{\Omega}}^t \Delta\widetilde{\phi}_s^{\alpha\beta}(s)ds \quad (7.8)$$

which has only one equilibrium point  $\Delta\widetilde{\phi}_s^{\alpha\beta} = 0$ .

### 7.1.2.2 Stability of the observer

We are going to study the stability of the observer to determine the values of  $\widetilde{K}$  for which the observer is stable. In the most general case,  $\widetilde{K}$  could be chosen as a matrix but due to the form of the eq. (7.8), it will be better to take a scalar gain (or a diagonal matrix). The two axes  $\alpha$  and  $\beta$  can be decoupled and we obtain after applying Laplace transform two scalar systems of the form

$$sX(s) - x_0 = U(s) - \Omega\widetilde{K} \frac{1 - \exp\left(-\frac{s}{\Omega}\right)}{s} X(s)$$

where  $x_0$  is the initial value of the error. This can be rewritten

$$X(s) = \frac{\frac{1}{\widetilde{K}}}{1 + \frac{\Omega}{s} \left(1 - \frac{s}{\Omega} + \frac{s^2}{\Omega\widetilde{K}} - \exp\left(-\frac{s}{\Omega}\right)\right)} (U(s) + x_0).$$

The equation of the associated Nyquist locus is

$$N(\varpi) = \frac{\Omega}{j\varpi} \left(1 - \frac{j\varpi}{\Omega} - \frac{\varpi^2}{\Omega\widetilde{K}} - \exp\left(-j\frac{\varpi}{\Omega}\right)\right) \quad \varpi \in ]-\infty, +\infty[. \quad (7.9)$$

Around  $\varpi = 0$ , the Nyquist locus is approximated by

$$N(\varpi) = j\varpi \left(\frac{1}{\widetilde{K}} - \frac{1}{2\Omega}\right) - \frac{\varpi^2}{6\Omega^2} + o(\varpi^3)$$

and near  $\pm\infty$

$$N(\varpi) \sim j\frac{\varpi}{\widetilde{K}} - 1.$$

We thus find the limits of the Nyquist locus given in table 7.1. Even though the calculation of the limits of Nyquist locus is informative, it is not sufficient: it only proves that for

Condition	$\lim_{\varpi \rightarrow -\infty}$	$\lim_{\varpi \rightarrow 0^-}$	$\lim_{\varpi \rightarrow 0^+}$	$\lim_{\varpi \rightarrow +\infty}$
$\widetilde{K} < 2\Omega$	$-j\infty$	$j0^-$	$j0^+$	$+j\infty$
$\widetilde{K} = 2\Omega$	$-j\infty$	$0^-$	$0^-$	$+j\infty$
$\widetilde{K} > 2\Omega$	$-j\infty$	$j0^+$	$j0^-$	$+j\infty$

Table 7.1 – Limits of Nyquist locus depending on the value of  $\widetilde{K}$ .

$\widetilde{K} > 2\Omega = 1000Hz$  the Nyquist locus crosses the horizontal axis in another place than the origin, but we cannot say whether it loops around the point of affix  $z = -1$ .

The Nyquist locus crosses the horizontal axis at the pulsations  $\varpi_0$  given by

$$\Im(N(\varpi_0)) = 0 \Leftrightarrow 1 - \frac{\varpi_0^2}{\Omega\widetilde{K}} = \cos \frac{\varpi_0}{\Omega} \quad (7.10)$$

It can easily be proven that

- For  $\widetilde{K} \leq 2\Omega$ , there is only one solution:  $\varpi_0 = 0Hz$ ;
- For  $\widetilde{K} > 2\Omega$ , there are 3 solutions among which is obviously  $\varpi_0 = 0Hz$ .

If  $\widetilde{K} \leq 2\Omega$  we are sure that the observer is stable, because the Nyquist locus crosses the horizontal axis only at the origin, but it is only a sufficient condition as there are higher values of  $\widetilde{K}$  for which the Nyquist locus does not loop around the point of affix  $z = -1$ . For  $\widetilde{K} > 2\Omega$  we consider the abscissae of these points which are given by

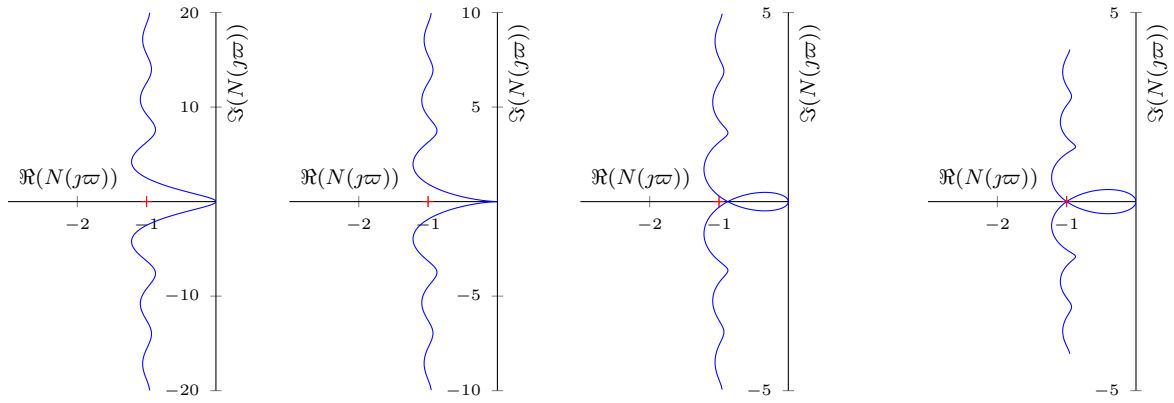
$$\begin{aligned} \Re(N(j\varpi_0)) &= -1 - \frac{\Omega}{\varpi_0} \sin \frac{\varpi_0}{\Omega} \\ &= -1 \pm \frac{\Omega}{\varpi_0} \sqrt{1 - \left(1 - \frac{\varpi_0^2}{\Omega\widetilde{K}}\right)^2} \\ &= -1 \pm \sqrt{\frac{2\Omega}{\widetilde{K}} - \frac{\varpi_0^2}{\widetilde{K}^2}} \end{aligned} \quad (7.11)$$

We have thus  $\Re(N(j\varpi_0)) = -1 \Leftrightarrow \widetilde{K} = \frac{\varpi_0^2}{2\Omega}$  and  $\sin \frac{\varpi_0}{\Omega} = -1 \Leftrightarrow \varpi_0 \equiv 0[\pi\Omega]$ . Consequently, the highest value of  $\widetilde{K}$  for which the observer is stable is  $\widetilde{K}_0 = \frac{\pi^2}{2}\Omega \approx 2467.4Hz$ .

To illustrate this proof, I plotted the Nyquist loci for some interesting values of  $\widetilde{K}$  in fig. 7.3. In simulations and experiments I chose the value  $\widetilde{K} = 2000Hz$  which ensures a fast convergence still ensuring a stability margin. This can be verified in fig. 7.4 which shows the observed stator flux ripple compared to the real one obtained in simulation.

### 7.1.3 Extracting the information from the current ripple

As in section 4.3.3, we want to separate the fundamental current, used for controlling the motor, and the HF current which is the response of the motor to HF voltage injection.



(a) For  $\tilde{K} = 500Hz$ . (b) For  $\tilde{K} = 1000Hz$ . (c) For  $\tilde{K} = 2000Hz$ . (d) For  $\tilde{K} = \tilde{K}_0 = 2467Hz$ .

Figure 7.3 – Nyquist loci for some values of  $\tilde{K}$ .

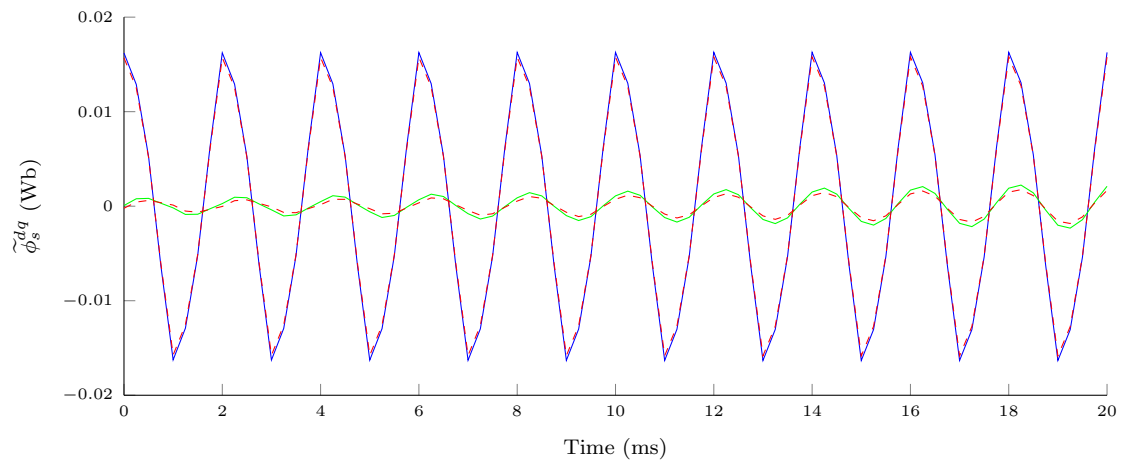


Figure 7.4 – Observed stator flux ripple (solid lines) on  $d$  and  $q$  axes compared to simulated stator flux ripple (dashed red lines).

### 7.1.3.1 Obtaining the fundamental current and the current ripple

The traditional method uses a low-pass filter to get the fundamental current and a band-pass or a high-pass filter to obtain the current ripple (see [2, 4]). As the response of the motor to HF injection has zero mean, we preferred using a sliding average on a HF period, to extract the fundamental current, as is proposed in section 4.3.3. As stated by proposition 1, this allows us to retrieve the ripple with an error of order  $\frac{1}{\Omega^2}$  with a delay of  $\frac{1}{2\Omega}$ . The ripple  $\tilde{i}_s^{\alpha\beta}$  can be obtained by subtracting the fundamental current from the measured current delayed by  $\frac{1}{2\Omega}$  as in eq. (4.53b).

We showed in section 7.1.1 that filtering the fundamental current was not really needed for the control law to work. We thus only need to extract the current ripple and the information it contains.

Once the fundamental current and the current ripple  $\tilde{i}_s^{\alpha\beta}$  are separated, the information it contains on the state of the motor, which is contained in its amplitude, needs to be extracted.

### 7.1.3.2 Obtaining the amplitude of the current ripple

In the literature ([78] for instance), the most widely used approach to extract the amplitude of the current ripple is to heterodyne it

**Axial polarization** From eq. (4.38) with a sinusoidal injection ( $F(\sigma) = \sin(2\pi\sigma + \varphi)$ ), we get by heterodyning

$$\begin{aligned} \underline{i}_s^{\alpha\beta} F(\Omega t) &= \tilde{i}_s^{\alpha\beta} F(\Omega t) + \frac{\tilde{u}}{\Omega} \frac{\partial^2 \mathcal{H}^{\alpha\beta}}{\partial \underline{\phi}_s^{\alpha\beta} \partial \underline{\phi}_s^{\alpha\beta*}} e^{j\theta_i(t)} F^2(\Omega t) + \frac{\tilde{u}}{\Omega} \frac{\partial^2 \mathcal{H}^{\alpha\beta}}{\partial \underline{\phi}_s^{\alpha\beta*2}} e^{-j\theta_i(t)} F^2(\Omega t) \\ &= \tilde{i}_s^{\alpha\beta} \sin(2\pi\Omega t + \varphi) + \frac{\tilde{u}}{2\Omega} \left( \frac{\partial^2 \mathcal{H}^{\alpha\beta}}{\partial \underline{\phi}_s^{\alpha\beta} \partial \underline{\phi}_s^{\alpha\beta*}} e^{j\theta_i(t)} + \frac{\partial^2 \mathcal{H}^{\alpha\beta}}{\partial \underline{\phi}_s^{\alpha\beta*2}} e^{-j\theta_i(t)} \right) \\ &\quad + \frac{\tilde{u}}{2\Omega} \left( \frac{\partial^2 \mathcal{H}^{\alpha\beta}}{\partial \underline{\phi}_s^{\alpha\beta} \partial \underline{\phi}_s^{\alpha\beta*}} e^{j\theta_i(t)} + \frac{\partial^2 \mathcal{H}^{\alpha\beta}}{\partial \underline{\phi}_s^{\alpha\beta*2}} e^{-j\theta_i(t)} \right) \sin(2 \cdot 2\pi\Omega t + 2\varphi) \end{aligned} \quad (7.12)$$

from which the slowly varying term  $\frac{\tilde{u}}{2\Omega} \left( \frac{\partial^2 \mathcal{H}^{\alpha\beta}}{\partial \underline{\phi}_s^{\alpha\beta} \partial \underline{\phi}_s^{\alpha\beta*}} + \frac{\partial^2 \mathcal{H}^{\alpha\beta}}{\partial \underline{\phi}_s^{\alpha\beta*2}} e^{-2j\theta_i(t)} \right)$  can be extracted by low-pass filtering.

**Circular polarization** From eq. (4.39) we obtain by heterodyning

$$-je^{-j\Omega t} \underline{i}_s^{\alpha\beta} = -je^{-j\Omega t} \tilde{i}_s^{\alpha\beta} + \frac{\tilde{u}}{\Omega} \frac{\partial^2 \mathcal{H}^{\alpha\beta}}{\partial \underline{\phi}_s^{\alpha\beta} \partial \underline{\phi}_s^{\alpha\beta*}} - \frac{\tilde{u}}{\Omega} \frac{\partial^2 \mathcal{H}^{\alpha\beta}}{\partial \underline{\phi}_s^{\alpha\beta*2}} e^{-2j\Omega t} \quad (7.13a)$$

$$je^{j\Omega t} \underline{i}_s^{\alpha\beta} = je^{j\Omega t} \tilde{i}_s^{\alpha\beta} - \frac{\tilde{u}}{\Omega} \frac{\partial^2 \mathcal{H}^{\alpha\beta}}{\partial \underline{\phi}_s^{\alpha\beta} \partial \underline{\phi}_s^{\alpha\beta*}} e^{2j\Omega t} + \frac{\tilde{u}}{\Omega} \frac{\partial^2 \mathcal{H}^{\alpha\beta}}{\partial \underline{\phi}_s^{\alpha\beta*2}} \quad (7.13b)$$

from which the slowly varying terms  $\frac{\tilde{u}}{\Omega} \frac{\partial^2 \mathcal{H}^{\alpha\beta}}{\partial \underline{\phi}_s^{\alpha\beta} \partial \underline{\phi}_s^{\alpha\beta*}}$  and  $\frac{\tilde{u}}{\Omega} \frac{\partial^2 \mathcal{H}^{\alpha\beta}}{\partial \underline{\phi}_s^{\alpha\beta*2}}$  can be extracted by low-pass filtering.

As explained in Jebai [37] and section 4.3.3, the method of eq. (7.12) can be extended to non-sinusoidal zero mean functions. Indeed the same information can be obtained by

taking the sliding average of  $\underline{\hat{i}}_s^{\alpha\beta} F(\Omega t)$  on a HF period and dividing by the sliding average of  $F^2(\Omega t)$ .

However, we saw in section 7.1.1.2 that HF injection is affected by delays due to implementation. To circumvent this problem, we used the flux ripple observer to estimate the flux ripple. We can get the same information as previously by computing

$$\frac{\int_{t-\frac{1}{\Omega}}^t \underline{\hat{i}}_s^{\alpha\beta} \left(\underline{\hat{\phi}}_s^{\alpha\beta}\right)^*}{\int_{t-\frac{1}{\Omega}}^t \left|\underline{\hat{\phi}}_s^{\alpha\beta}\right|^2} \approx \frac{\partial^2 \underline{\mathcal{H}}^{\alpha\beta}}{\partial \underline{\phi}_s^{\alpha\beta} \partial \underline{\phi}_s^{\alpha\beta*}} + \frac{\partial^2 \underline{\mathcal{H}}^{\alpha\beta}}{\partial \underline{\phi}_s^{\alpha\beta*2}} e^{-2j \text{Arg} \underline{\hat{\phi}}_s^{\alpha\beta}} \quad (7.14)$$

where  $\text{Arg} \underline{\hat{\phi}}_s^{\alpha\beta}$  can be approximated using

$$\frac{\int_{t-\frac{1}{\Omega}}^t \left(\underline{\hat{\phi}}_s^{\alpha\beta}\right)^2}{\int_{t-\frac{1}{\Omega}}^t \left|\underline{\hat{\phi}}_s^{\alpha\beta}\right|^2} \approx e^{2j \text{Arg} \underline{\hat{\phi}}_s^{\alpha\beta}}. \quad (7.15)$$

## 7.2 IM low speed “sensorless” control

A brief study of the literature in section 7.2.1 about “sensorless” control of the IM show that the virtual measurement which is traditionally used to retrieve low speed observability, is the orientation of the rotor flux. Consequently, we show in section 7.2.2 that it can indeed be retrieved thanks to the virtual measurement and construct in section 7.2.3 a robust control law using this supplementary measurement to achieve low speed “sensorless” control of an IM. This is done in simulation, so that the virtual measurement is available. Finally, we try in section 7.2.4 the proposed “sensorless” control law with the estimation procedure for the orientation of the rotor flux on a real IM (see section 2.1.2).

### 7.2.1 Bibliography

In the literature (see [2, 4, 52, 78]), “sensorless” control of IMs at low speed relies on the determination of a magnetic saliency using HF injection. This magnetic saliency is caused by the term  $\frac{\partial^2 \underline{\mathcal{H}}^{dq}}{\partial \underline{\phi}_s^{dq*2}}$ . Indeed, when the injection response is rewritten in the injection frame  $vw$  as done in section 5.2.1.2, we obtain for an axial injection

$$\underline{\hat{i}}_s^v = 2 \frac{\partial^2 \underline{\mathcal{H}}^{dq}}{\partial \underline{\phi}_s^{dq} \partial \underline{\phi}_s^{dq*}} \frac{\tilde{u}}{\Omega} F(\Omega t) + 2 \left| \frac{\partial^2 \underline{\mathcal{H}}^{dq}}{\partial \underline{\phi}_s^{dq*2}} \right| \frac{\tilde{u}}{\Omega} \cos \left( 2\omega_i t - \text{Arg} \frac{\partial^2 \underline{\mathcal{H}}^{dq}}{\partial \underline{\phi}_s^{dq*2}} \right) F(\Omega t) \quad (7.16a)$$

$$\underline{\hat{i}}_s^w = -2 \left| \frac{\partial^2 \underline{\mathcal{H}}^{dq}}{\partial \underline{\phi}_s^{dq*2}} \right| \frac{\tilde{u}}{\Omega} \sin \left( 2\omega_i t - \text{Arg} \frac{\partial^2 \underline{\mathcal{H}}^{dq}}{\partial \underline{\phi}_s^{dq*2}} \right) F(\Omega t), \quad (7.16b)$$

which shows that the amplitude of the response depends on the position of the injection. A similar result is obtained in the case of a circular injection. Thanks to this saliency, an information on  $\text{Arg} \frac{\partial^2 \underline{\mathcal{H}}^{dq}}{\partial \underline{\phi}_s^{dq*2}}$  is obtained, either by computing the arctangent of eq. (7.16b) over eq. (7.16a) whose first term has been filtered out (see [2, 4]), or using a PLL (see

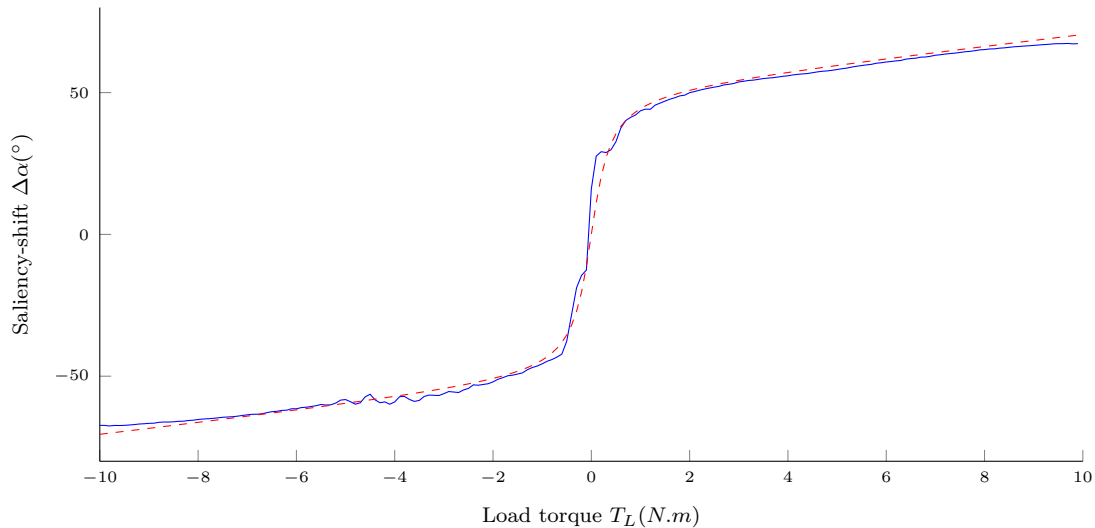


Figure 7.5 – Saliency orientation shift  $\Delta\alpha$  as a function of the load torque.

[53]). This information can be directly fed to the vector control algorithm as in [2] or used by an observer to retrieve estimates of the speed [4] or the fluxes [78].

It is generally assumed that the largest HF response is in the direction of the main flux (see [2, 52, 78] for instance), which can be physically explained: the main flux saturates the leakage inductances, which increase the size of the HF response. However, Yoon and Sul [4] notice a saliency orientation shift from the main flux axis by approximately  $20^\circ$ .

## 7.2.2 Observing the rotor flux angle

We will here follow the proposition of the literature (see section 7.2.1) and extract the saliency direction from the eq. (7.14). We propose to regulate the direction of the injection by a PI on the imaginary part of eq. (7.14). Then, at steady state, we have

$$\text{Arg} \frac{\partial^2 \mathcal{H}^{\alpha\beta}}{\partial \underline{\phi}_s^{\alpha\beta*2}} = 2 \text{Arg} \tilde{\underline{\phi}}_s^{\alpha\beta}$$

which can be obtained using eq. (7.15). However, according to Yoon and Sul [4], the saliency may not be in the direction of the rotor flux axis. The difference between the direction of the saliency and the position of the rotor flux

$$\Delta\alpha = \text{Arg} \frac{\partial^2 \mathcal{H}^{\alpha\beta}}{\partial \underline{\phi}_s^{\alpha\beta*2}} - \text{Arg} \underline{\phi}_r^{\alpha\beta} \quad (7.17)$$

is called the saliency shift. With the experimental results presented in figs. 5.16c and 5.17c, the test IM presents certainly a saliency orientation shift. To estimate it, we inject a HF signal and apply the aforementioned method to get the saliency orientation, while the motor is being driven at low speed by a control law using the encoder of the test bench. With this experiment we found out that saliency orientation does mostly not depend on the speed, but it has a strong dependency on the torque as shown by the solid blue line in fig. 7.5.

It can be modeled by

$$\Delta\alpha = \frac{2}{3} \arctan 3T_L + \frac{\pi}{90} T_L \quad (7.18)$$

as shown by the dashed red line in fig. 7.5. By removing it from the measured value of the saliency orientation, the rotor flux direction can be estimated

$$\hat{\alpha} = \text{Arg} \frac{\partial^2 \mathcal{H}^{\alpha\beta}}{\partial \underline{\phi}_s^{\alpha\beta*2}} - \Delta\alpha = \text{Arg} \frac{\partial^2 \mathcal{H}^{\alpha\beta}}{\partial \underline{\phi}_s^{\alpha\beta*2}} - \frac{2}{3} \arctan 3T_L - \frac{\pi}{90} T_L. \quad (7.19)$$

### 7.2.3 A control law using the rotor flux angle

Thanks to HF injection and the proposed signal processing (see sections 7.1.3 and 7.2.2), the rotor flux direction  $\alpha = \text{Arg} \phi_r^{\alpha\beta}$  can be used to design a controller for the IM. Basically we inserted a so-called flux controller between the current and the speed controller. This new controller is in charge of ensuring that the control  $dq$  is oriented along the estimated rotor flux. The proposed control law is represented as a bloc scheme in fig. 7.6.

The proposed control law is based on an existing “sensorless” control law for IMs described succinctly hereafter. This control law is based on the unsaturated model of the IM with state variables  $i_s^{dq}$  and  $\varphi_r^{dq}$  which reads

$$\sigma L_s \frac{di_s^{dq}}{dt} = u_s^{dq} - (R_s + R_r^{eq}) i_s^{dq} - \mathcal{J}_\sigma L_s \omega_s i_s^{dq} + \frac{1}{T_r} \varphi_r^{dq} - j\omega \varphi_r^{dq} \quad (7.20a)$$

$$\frac{d\varphi_r^{dq}}{dt} = R_r^{eq} i_s^{dq} - \frac{1}{T_r} \varphi_r^{dq} - j(\omega_s - \omega) \varphi_r^{dq} \quad (7.20b)$$

$$\frac{J_L}{n} \frac{d\omega}{dt} = T_e - T_L \quad (7.20c)$$

where  $T_e(i_s^{dq}, \varphi_r^{dq}) = n \frac{L_m}{L_r} i_s^{dqT} \mathcal{J}_2 \varphi_r^{dq}$ ,  $T_r := \frac{L_r}{R_r}$ ,  $R_r^{eq} := R_r \frac{L_m^2}{L_r^2}$  and  $\sigma := \frac{L_m^2}{L_s L_r}$ . The nonlinearity of the studied IM is used only to explain the results obtained by signal injection.

The current controller is based on the feed-forward

$$u_s^{dq} = \frac{di_s^{dq,f}}{dt} + (R_s + R_r^{eq}) i_s^{dq,f} + \mathcal{J}_\sigma L_s \omega_s i_s^{dq,f} - \frac{1}{T_r} \hat{\varphi}_r^{dq} + v_s^{dq} \quad (7.21)$$

where the input after feed-forward,  $v_s^{dq}$ , is used to  $q$ -axis current

$$v_s^d = 0 \quad (7.22a)$$

$$v_s^q = K_p^i (i_s^{q,f} - i_s^{q,m}) + i^i \quad (7.22b)$$

$$\frac{di^i}{dt} = K_i^i (i_s^{q,f} - i_s^{q,m}). \quad (7.22c)$$

The flux is observed thanks to the observer

$$\frac{d\hat{\varphi}_r^{dq}}{dt} = R_r^{eq} \hat{i}_s^{dq} - \frac{1}{T_r} \hat{\varphi}_r^{dq} - j\hat{\omega}_g \hat{\varphi}_r^{dq}. \quad (7.23)$$

At the equilibrium of this controller, thanks to the value of the integral state  $i^i$ , an estimate of the speed  $\hat{\omega}_m$  can be obtained. After filtering, this speed will be used in the mechanical loop as an estimate of the IM speed.

The current reference is computed from the required torque and rotor flux

$$i_s^{d,r} = \frac{L_r}{L_m^2} \varphi_r^r \quad (7.24a)$$

$$i_s^{q,r} = \frac{T_e^r}{n \varphi_r^r} \quad (7.24b)$$

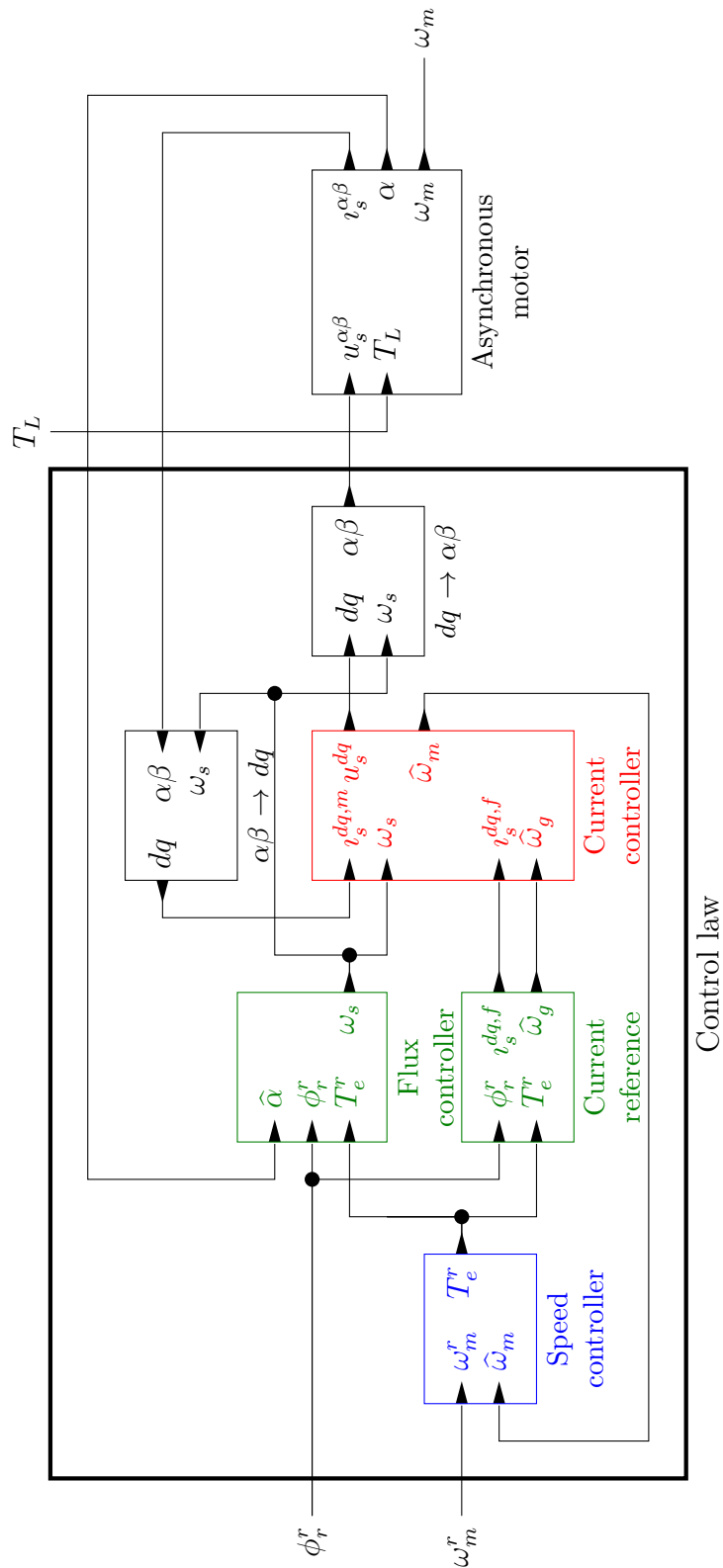


Figure 7.6 – Bloc scheme of the control law. The time-scales of the controllers have been highlighted with colors: red for the fastest, green for the intermediate and blue for the slowest time-scale.

which are low-pass filtered to obtain  $i_s^{dq,f}$ . The estimate of the slip speed  $\hat{\omega}_g$  is given by

$$\hat{\omega}_g = \frac{R_r^{eq} T_e^r}{n \varphi_r^2}. \quad (7.25)$$

However, instead of adding  $\hat{\omega}$  to  $\hat{\omega}_g$  to obtain  $\omega_s$ , we use now a PI controller on  $\alpha - \theta_s$  to ensure  $d$ -axis is collinear to the rotor flux

$$\frac{d\alpha^i}{dt} = K_p^\alpha (\alpha - \theta_s) \quad (7.26a)$$

$$\omega_s = K_i^\alpha (\alpha - \theta_s) + \alpha^i. \quad (7.26b)$$

The mechanical controller is similar to the one proposed in section 6.1.3.3, recalled here

$$T_e^r = \frac{J_L}{n} K_p^\omega (\omega^r - \hat{\omega}) + \omega^i \quad (7.27a)$$

$$T_e^s = \min(\max(T_e^r, -T_e^l(\hat{\omega})), T_e^l(\hat{\omega})) \quad (7.27b)$$

$$\frac{d\omega^i}{dt} = \frac{J_L}{n} K_i^\omega (\omega^r - \hat{\omega}) + 2 \frac{K_i^\omega}{K_p^\omega} (T_e^s - T_e). \quad (7.27c)$$

This control law was tested in simulation on a motor where the virtual measurement  $\alpha$  was added. It really allows “sensorless” operation of the IM at low speed and is robust to parametric errors.

## 7.2.4 Using HF injection for low speed “sensorless” control

Having seen the performances of the control law proposed in section 7.2.3, we can hope that, when the estimated value of  $\alpha$  given by eq. (7.19) is used instead of its real value, the behavior of the controlled IM will be similar.

In simulation we noticed that the performance did not meet our expectations, but is still worked well for saturated IMs with a small saliency orientation shift (e.g. model eq. (4.59) with parameters table 4.2). By carefully tuning the gains and the parameters of the unsaturated IM model used in the control law, we were able to control a saturated IM with a large saliency orientation shift as modeled by eq. (7.18).

However, we were never able to make this work on a real IM, because the control law proposed in section 7.2.3 is not robust enough to support the problems caused by a real implementation on the test bench. After analysis of the results, we found out that a huge ripple in  $6\omega_s$  disturbs  $\hat{\alpha}$  as shown in fig. 7.7. This ripple is caused by a non-sinusoidal stator as explained in section 3.7 and inverter voltage drops (see section 2.3.1). However it should not be so large, as non-sinusoidal effects seemed negligible in section 3.7.5.

The amplification of the  $6\omega_s$  ripple is due to the fact that amplitude of variation of the ripple size is very small on this motor. Indeed, it can be seen in figs. 5.16b and 5.17b, that it does not exceed  $0.15A$  with an injection of amplitude  $40V$  ( $\tilde{u} = 20V$ ) and frequency  $\Omega = 500Hz$  whereas the average size is around  $1A$  for the same injection. The estimation is thus badly conditioned. This problem is also noticed in section 4.4.1, when we try to build a flux observer thanks to information obtained with HF injection.

After looking at the articles [4, 78, 83, 84], we found out that the important ratio is

$$\frac{2(L_s^d - L_s^q)}{L_s^d + L_s^q} = \frac{2(\Gamma_{t_s}^d - \Gamma_{t_s}^q)}{\Gamma_{t_s}^d + \Gamma_{t_s}^q} = \frac{\left| \frac{\partial^2 \mathcal{H}^{dq}}{\partial \phi_s^{dq*2}} \right|}{\frac{\partial^2 \mathcal{H}^{dq}}{\partial \phi_s^{dq} \partial \phi_s^{dq*}}}. \quad (7.28)$$

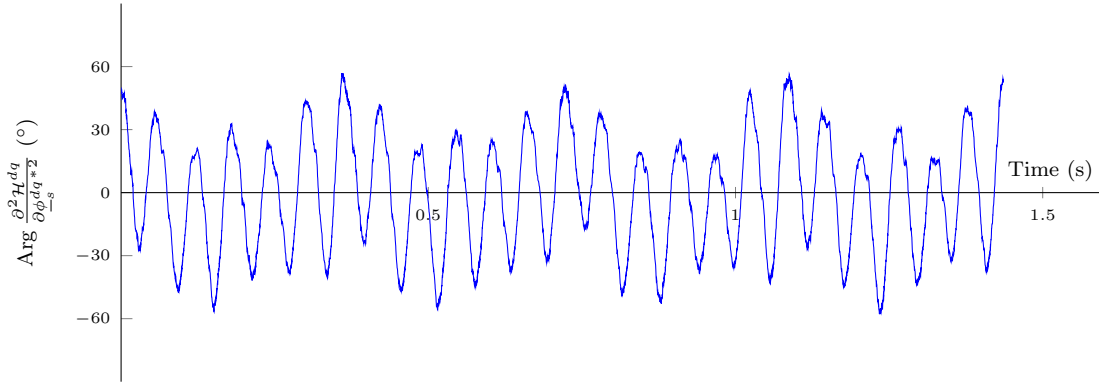


Figure 7.7 – The error signal obtained on the IM described by table 2.2 while  $\omega_s$  was around  $-17.5H_z$ . A large  $6\omega_s$  harmonic can be observed.

Source	Larger saliency ratio	Smaller saliency ratio
Simulated IM (eq. (4.59) and table 4.2)	0.08	0.019
Test IM (table 2.2)	0.12	0.02
Jansen and Lorenz [78, fig. 11]	0.2	0.15
Yoon and Sul [4, fig. 4]	0.08	0.03
Drevenšek, Žarko, <i>et al.</i> [83, fig. 11]	0.5	0.5
Zatocil [84, fig. 3]	0.18	0.03

Table 7.2 – Saliency ratios, as defined by eq. (7.28), computed for the test IM, described by table 2.2, and IM from the literature.

Table 7.2 compares the ratio obtained for the tested IM and the IM used in the literature. The saliency ratios found in the literature vary in a wide range. It seems that very careful signal processing is needed to achieve “sensorless” control of IMs using this technique. This may not be feasible in an industrial VSD.

### 7.3 Partial conclusion

In this chapter implementation problems of a “sensorless” control law for an IM at low speed on the test bench described in section 2.2 is considered. Due to the close bandwidth of the current controller and the injection frequency, we choose not to filter out the HF current response before feeding it in the current controller. In an ideal implementation this would not have any undesirable effect. However, we realized that the delays in the control loop greatly affected the results. This problem was circumvented by constructing a flux ripple observer, which is used to estimate the real value of the stator flux ripple.

A low-speed “sensorless” control law, relying on the estimation of the saliency due to magnetic saturation, was then proposed. However we realized that on the tested motor the saliency was too small for this method to be reliable because of non-sinusoidal effects. This is due to a low conditioning of the proposed method, which is greatly disturbed by these uncompensated disturbances.

# Conclusion

A new approach to electric motor modeling was proposed here. Thanks to it, electric motors can be modeled by a single scalar energy function without knowing all the details of their internal layout. This approach also justifies the modeling of magnetic saturation in a rotating orthogonal frame (such as  $dq$  or  $DQ$  frames) whereas it occurs in the physical  $abc$  frame. Besides this modeling approach highlights the similarities between electric motors. Using the new models, the observability of electric machines is considered, and all electric motors turn out to be “sensorlessly” unobservable at zero stator frequency. High frequency signal injection is presented as a good solution to the loss of observability at low speed. When considered in a the general context of nonlinear systems, it proves to be a mean of adding virtual measurements, whereby flux or speed observers can be designed. An energy based model for a Synchronous Reluctance Motor is proposed. The methods we used to obtain it are easily generalizable to any kind of Synchronous Reluctance Motor. However, modeling an Induction Machine turned out to be very difficult due to the lack of information and no satisfactory model was found. Indeed, the rotor variables cannot be accurately estimated. Thanks to the similarities between electric motors, underlined by energy-based modeling, a control law designed for Synchronous Reluctance Motors can easily be generalized to Permanent Magnet Synchronous Motors. Finally the low speed “sensorless” control of electric machines is considered. The effect of signal injection on the control law is quantified and methods to extract the information contained in the response of the motor are proposed. Besides, the control of our induction machine with a small magnetic saliency turned out to be impossible using the traditional approaches, which was expected from the results on observability using signal injection, but the improved speed observer could not be satisfactorily used in closed loop on a real system due to the lack of a proper model. Indeed for this observer to be implemented, a complete model of the current-flux relations and their differentials (the relations linking the flux to the Hessian of the energy function) is required.

The present work can be improved in many ways. First, the proposed modeling approach can be extended to take into account magnetic hysteresis, whose effects are noticeable when high frequency injection is used on Synchronous Reluctance Motors or Induction Machines. Besides a way to reliably estimate the rotor current or flux must be found so that sensible models for Induction Machines can be designed. Secondly, the performance of the control law using the flux and speed observer for lowly salient electric motors can be improved by designing a better nonlinear observer and integrating it in the control law.



# Bibliography

- [1] A. Jebai, P. Combes, F. Malrait, P. Martin, and P. Rouchon, “Energy-based modeling of electric motors”, *Decision and Control (CDC), IEEE 53rd Annual Conference on*, pp. 6009–6016 (2014).
- [2] P. Brandstetter, P. Bilek, J. Szotkowski, and P. Vaculik, “Sensorless control of asynchronous motor using voltage signal injection”, *Progress in Electromagnetics Research Symposium (PIERS)*, pp. 1421–1425 (2011).
- [3] T. Wolbank, H. Giuliani, and R. Woehrschimmel, “High dynamic sensorless control of induction machines at zero speed using transient excitation technique”, *IEEE Annual Power Electronics Specialists Conference (PESC), Records of*, pp. 2456–2461 (2005).
- [4] Y.-D. Yoon and S.-K. Sul, “Sensorless control for Induction Machines based on square-wave voltage injection”, *Power Electronics, IEEE Transactions on*, vol. 29, pp. 3637–3645 (2014).
- [5] KSB, Manual for “Synchronous Reluctance Motor KSB SuPremE A”
- [6] Leroy Somer, Catalog for “Moteurs asynchrones triphasés fermés, carter alliage d’aluminium, 0.045 à 200kW”
- [7] J. Lakemeier, A. Tenge, and F. Wishmeier for dSpace GmbH, User guide for “dSpace AC motor control solution”, v. 7.1.1 (2011)
- [8] Schneider Electric, Catalog for “Variable Speed Drives Altivar 71”
- [9] Vacuumschmelze, Datasheet for “T60404-N4644-X400” (2009)
- [10] N. Francey for Vibro-meter, Manual for “Torquemaster TM200 series”, v. 4 (1997)
- [11] Schneider Electric, Datasheet for “XCC1912PS11RN”
- [12] P. Combes, A. Jebai, F. Malrait, P. Martin, and P. Rouchon, “Adding virtual measurements by HF signal injection”, submitted to *American Control Conference (ACC)* (2016).
- [13] A. R. Weber and G. Steiner, “An accurate identification and compensation method for nonlinear inverter characteristics for AC motor drives”, *Instrumentation and Measurement Technology (I2MTC), IEEE International Conference on*, pp. 821–826 (2012).

- [14] F. Gabriel, F. De Belie, *et al.*, “Compensating the influence of the stator resistor and inverter nonlinearities in signal-injection based sensorless strategies”, *Vehicle Power and Propulsion, IEEE Conference on*, pp. 249–256 (2009).
- [15] J. M. Guerrero, M. Leetmaa, F. Briz, A. Zamarró, and L. R. D., “Inverter nonlinearity effects in high-frequency signal-injection-based sensorless control methods”, *Industry Applications, IEEE Transactions on*, vol. 41, pp. 618–626 (2005).
- [16] T. M. Wolbank and J. L. Machl, “Influence of inverter-nonlinearity and measurement setup on zero speed sensorless control of AC machines based on voltage pulse injection”, *Industrial Electronics Society (IECon), IEEE 31st Annual Conference of the*, pp. 1568–1573 (2005).
- [17] F. Malrait, *Problèmes d’identification et d’observabilité du moteur à induction pour la variation de vitesse industrielle “sans capteur”*. PhD thesis, MINES ParisTech, Schneider Toshiba Inverter Europe (2001).
- [18] S. K. Mukerji, A. S. Khan, and Y. P. Singh, *Electromagnetics for electrical machines* (CRC Press, 2015).
- [19] J. A. A. Melkebeek and D. Novotny, “The influence of saturation on induction machine drive dynamics”, *Industry Applications, IEEE Transactions on*, vol. IA-19, pp. 671–681 (1983).
- [20] J. Ojo, A. Consoli, and T. Lipo, “An improved model of saturated induction machines”, *Industry Applications, IEEE Transactions on*, vol. 26, pp. 212–221 (1990).
- [21] C. Sullivan and S. Sanders, “Models for induction machines with magnetic saturation of the main flux path”, *Industry Applications, IEEE Transactions on*, vol. 31, pp. 907–917 (1995).
- [22] F. Briz, M. Degner, A. Diez, and R. Lorenz, “Measuring, modeling, and decoupling of saturation-induced saliencies in carrier-signal injection-based sensorless AC drives”, *Industry Applications, IEEE Transactions on*, vol. 37, pp. 1356–1364 (2001).
- [23] S.-K. Sul, *Control of electric machine drive systems* (Wiley-IEEE Press, 2011).
- [24] N. Bianchi and S. Bolognani, “Design techniques for reducing the cogging torque in surface-mounted PM motors”, *Industry Applications, IEEE Transactions on*, vol. 38, pp. 1259–1265 (2002).
- [25] V. Petrovic, R. Ortega, A. Stankovic, and G. Tadmor, “Design and implementation of an adaptive controller for torque ripple minimization in PM synchronous motors”, *Power Electronics, IEEE Transactions on*, vol. 15, pp. 871–880 (2000).
- [26] Z. Zhu and D. Howe, “Analytical prediction of the cogging torque in radial-field permanent magnet brushless motors”, *Magnetics, IEEE Transactions on*, vol. 28, pp. 1371–1374 (1992).
- [27] M. Degner and R. Lorenz, “Position estimation in induction machines utilizing rotor bar slot harmonics and carrier-frequency signal injection”, *Industry Applications, IEEE Transactions on*, vol. 36, pp. 736–742 (2000).

- [28] N. Teske, G. Asher, M. Sumner, and K. Bradley, “Encoderless position estimation for symmetric cage induction machines under loaded conditions”, *Industry Applications, IEEE Transactions on*, vol. 37, pp. 1793–1800 (2001).
- [29] J. Melkebeek and J. Willems, “Reciprocity relations for the mutual inductances between orthogonal axis windings in saturated salient-pole machines”, *Industry Applications, IEEE Transactions on*, vol. 26, pp. 107–114 (1990).
- [30] P. Sauer, “Constraints on saturation modeling in AC machines”, *Energy Conversion, IEEE Transactions on*, vol. 7, pp. 161–167 (1992).
- [31] L. Landau and E. Lifshitz, *Mécanique* (Mir, Moscou, 1982).
- [32] J. M. Raimond, “Mécanique analytique”, Course handout of ENS.
- [33] D. C. White and H. H. Woodson, *Electromechanical energy conversion* (John Wiley & sons, inc., 1958).
- [34] I. Boldea and S. A. Nassar, *The induction machine handbook* (CRC Press, 2001).
- [35] D. Basic, F. Malrait, and P. Rouchon, “Euler-Lagrange models with complex currents of three-phase electrical machines and observability issues”, *Automatic Control, IEEE Transactions on*, vol. 55, pp. 212–217 (2010).
- [36] D. Basic, A. Jebai, F. Malrait, P. Martin, and P. Rouchon, “Using Hamiltonians to model saturation in space vector representations of AC electrical machines”, *Advances in the Theory of Control, Signals and Systems with Physical Modeling*, pp. 41–48 (2011).
- [37] A. Jebai, *Low speed sensorless synchronous motor control*. PhD thesis, Mines Paris-Tech, Schneider Toshiba Inverter Europe (2013).
- [38] C. Gerada, K. Bradley, M. Sumner, and P. Sewell, “Evaluation and modeling of cross saturation due to leakage flux in vector-controlled induction machines”, *Industry Applications, IEEE Transactions on*, vol. 43, pp. 694–702 (2007).
- [39] H. R. Fudeh and C. M. Ong, “Modeling and analysis of induction machines containing space harmonics. 1: Modeling and Transformation”, *Power Apparatus and Systems, IEEE Transactions on*, vol. 102, pp. 2608–2615 (1983).
- [40] J. F. Gieras, “Analysis of multilayer rotor induction-motor with higher space harmonics taken into account”, *Electric Power Applications, IEEE Proceedings on*, vol. 138, pp. 59–67 (1991).
- [41] P. Vas, “Extension of the unified theory of electrical machines — Effects of space harmonics in the transformed equations of 3-phase and 2-phase induction machines”, *Archiv Fur Elektrotechnik*, vol. 66, pp. 125–133 (1983).
- [42] J.-I. Ha, S.-K. Sul, K. Ide, I. Murokita, and K. Sawamura, “Physical understanding of high frequency injection method to sensorless drives of an induction machine”, *35th IAS Annual Meeting and World Conference on Industrial Applications of Electrical Energy*, pp. 1802–1808 (2000).

- [43] A. Jebai, F. Malrait, P. Martin, and P. Rouchon, "Signal injection and averaging for position estimation of Permanent-Magnet Synchronous Motors", *Decision and Control (CDC), IEEE 51st Annual Conference on*, pp. 7608–7613 (2012).
- [44] F. M. L. L. De Belie, J. A. A. Melkebeek, *et al.*, "A nonlinear model for synchronous machines to describe high-frequency signal based position estimators", *Electric Machines and Drives, IEEE International Conference on*, pp. 696–703 (2005).
- [45] J. Chiasson, *Modeling and high performance control of electric machines* (Wiley-IEEE Press, 2005).
- [46] M. Hinkkanen, A. -K. Repo, M. Ranta, and J. Luomi, "Small-signal modeling of mutual saturation in induction machines", *Industry Applications, IEEE Transactions on*, vol. 46, pp. 965–973 (2010).
- [47] J. Sanders, F. Verhulst, and J. Murdock, *Averaging methods in nonlinear dynamical systems* (Springer, 2005).
- [48] P. Vaclavek and P. Blaha, "Synchronous Machine drive observability analysis for sensorless control design", *Control Applications, IEEE International Conference on*, pp. 1113–1117 (2007).
- [49] E. Capecchi, P. Guglielmi, M. Pastorelli, and A. Vagati, "Position-sensorless control of the transverse-laminated synchronous reluctance motor", *Industry Applications, IEEE Transactions on*, vol. 37, pp. 1768–1776 (2001).
- [50] G. Bottiglieri, G. Scelba, G. Scarcella, A. Testa, and A. Consoli, "Sensorless speed estimation in induction motor drives", *Electric Machines and Drives, IEEE International Conference on*, pp. 624–630 (2003).
- [51] A. Consoli, G. Bottiglieri, G. Scarcella, and G. Scelba, "Flux and voltage calculations of induction motors supplied by low- and-high-frequency currents", *Industry Applications, IEEE Transactions on*, vol. 45, pp. 737–746 (2009).
- [52] C. Rudolph, T. Laczynski, and B. Orlik, "Sensorless field oriented control of induction motors considering main flux saturation effects on test signal injection", *IEEE Annual Power Electronics Specialists Conference (PESC), Records of*, pp. 2306–2312 (2004).
- [53] J. Holtz, "Sensorless control of induction machines - With or without signal injection?", *Industrial Electronics, IEEE Transactions on*, vol. 53, pp. 7–30 (2006).
- [54] M. Hinkkanen, V.-M. Leppänen, and J. Luomi, "Flux observer enhanced with low-frequency signal injection allowing sensorless zero-frequency operation of induction motors", *Industry Applications, IEEE Transactions on*, vol. 41, pp. 52–59 (2005).
- [55] Y. Li and S. Wu, "A new method of speed-sensorless control of induction motor at very low speed", *Advanced Electromechanical Motion Systems and Electric Drives Joint Symposium (ELECTROMOTION), 8th International Symposium on* (2009).
- [56] P. Krause, O. Wasynczuk, and S. Sudhoff, *Analysis of electrical machinery and drive systems* (Wiley-IEEE Press, 2002).

- [57] J.-I. Ha and S.-K. Sul, "Sensorless field-orientation control of an induction machine by high-frequency signal injection", *Industry Applications, IEEE Transactions on*, vol. 35, pp. 45–51 (1999).
- [58] G. Bottiglieri, A. Consoli, G. Scarcella, and G. Scelba, "Zero-sequence flux and voltage of induction motors supplied with low-and-high-frequency currents", *Electric Machines and Drives, IEEE International Conference on*, pp. 1201–1207 (2007).
- [59] H. K. Khalil, *Nonlinear systems* (Prentice-Hall, Inc., 2002).
- [60] W. Lohmiller and J.-J. E. Slotine, "On contraction analysis for nonlinear systems", *Automatica*, vol. 34, pp. 683–696 (1998).
- [61] A. Kilthau and J. Pacas, "Appropriate models for the control of the synchronous reluctance machine", *Industry Applications Conference, Conference Record of the*, pp. 2289–2295 (2002).
- [62] G. Stumberger, B. Stumberger, D. Dolinar, and A. Hamler, "Cross magnetization effect on inductances of linear synchronous reluctance motor under load conditions", *Magnetics, IEEE Transactions on*, vol. 37, pp. 3658–3662 (2001).
- [63] A. Vagati, M. Pastorelli, F. Scapino, and G. Franceschini, "Impact of cross saturation in synchronous reluctance motors of the transverse-laminated type", *Industry Applications, IEEE Transactions on*, vol. 36, pp. 1039–1046 (2000).
- [64] Z. Qu, T. Tuovinen, and M. Hinkkanen, "Inclusion of magnetic saturation in dynamic models of synchronous reluctance motors", *Electrical Machines (ICEM), International Conference on*, pp. 994–1000 (2012).
- [65] A. Ganji, P. Guillaume, R. Pintelon, and P. Lataire, "Induction motor dynamic and static inductance identification using a broadband excitation technique", *Energy Conversion, IEEE Transactions on*, vol. 13, pp. 15–20 (1998).
- [66] T. Vyncke, F. M L L. De Belie, *et al.*, "A Simulink state-space model of induction machines including magnetizing-flux saturation", *Power Electronics, Electrical Drives, Automation and Motion (SPEEDAM), International Symposium on*, pp. 1453–1458 (2006).
- [67] A. Glumineau and J. de Leon Morales, *Sensorless AC electric motor control* (Springer International Publishing, 2015).
- [68] M. Ranta, *Dynamic induction machine models including magnetic saturation and iron losses*. PhD thesis, Aalto University, Department of Electrical Engineering (2013).
- [69] T. Lipo and A. Consoli, "Modeling and Simulation of Induction Motors with Saturable Leakage Reactances", *Industry Applications, IEEE Transactions on*, vol. IA-20, pp. 180–189 (1984).
- [70] T. Tuovinen, M. Hinkkanen, and J. Luomi, "Modeling of saturation due to main and leakage flux interaction in induction machines", *Industry Applications, IEEE Transactions on*, vol. 46, pp. 937–945 (2010).

- [71] S. D. Sudhoff, D. C. Aliprantis, B. T. Kuhn, and P. L. Chapman, “An induction machine model for predicting inverter-machine interaction”, *Energy Conversion, IEEE Transactions on*, vol. 17, pp. 203–210 (2002).
- [72] S. D. Sudhoff, B. T. Kuhn, P. L. Chapman, and D. C. Aliprantis, “Experimental characterization procedure for use with an advanced induction machine model”, *Energy Conversion, IEEE Transactions on*, vol. 18, pp. 48–56 (2003).
- [73] J. Cordier, P. Landsmann, and R. Kennel, “The influence of magnetic hysteresis on HF injection based inductance calculation”, *IEEE Energy Conversion Congress and Exposition (ECCE)*, pp. 638–645 (2011).
- [74] Y. O. Amor, *Contribution à la modélisation de l’hystérésis magnétique en vue de l’analyse par éléments finis des systèmes de chauffage par induction*. PhD thesis, Université de Nantes, École polytechnique (2000).
- [75] F. Grayal, *Interfaces sigma-delta avancées pour capteur de champ magnétique*. PhD thesis, École centrale de Lyon (2007).
- [76] P. Kis, *Jiles-Atherton model implementation to edge finite element method*. PhD thesis, Budapest University of Technology and Economics (2006).
- [77] Y. Troxler, *A Simple Model for Magnetic Hysteresis and Saturation in a PMSM*. Master thesis, Swiss Federal institute of Zürich (2011).
- [78] P. Jansen and R. Lorenz, “Transducerless field orientation concepts employing saturation-induced saliencies in induction machines”, *Industry Applications, IEEE Transactions on*, vol. 32, pp. 1380–1393 (1996).
- [79] R. Lagerquist, I. Boldea, and T. J. Miller, “Sensorless control of the synchronous reluctance motor”, *Industry Applications, IEEE Transactions on*, vol. 30, pp. 673–682 (1994).
- [80] K. Malekian, M. Sharif, and J. Milimonfared, “An optimal current vector control for synchronous reluctance motors incorporating field weakening”, *Advances in Motion Control (AMC), International Workshop on*, pp. 393–398 (2008).
- [81] M. Meyer and J. Bocker, “Optimum control for Interior Permanent Magnet Synchronous Motors (IPMSM) in constant torque and flux weakening range”, *Power Electronics and Motion Control, 12th International Conference on*, pp. 282–286 (2006).
- [82] P. Guglielmi, M. Pastorelli, G. Pellegrino, and A. Vagati, “Position-sensorless control of Permanent-Magnet-Assisted Synchronous Reluctance Motor”, *Industry Applications, IEEE Transactions on*, vol. 40, pp. 615–622 (2004).
- [83] D. Drevenšek, D. Žarko, and T. Lipo, “A study of sensorless control of induction motor at zero speed utilizing high frequency voltage injection”, *European Power Electronics (EPE) Journal*, vol. 13, pp. 7–11 (2003).
- [84] H. Zatocil, “Sensorless control of AC machines using high-frequency excitation”, *Power Electronics and Motion Control, 13th Conference on*, pp. 1024–1032 (2008).

- [85] M. Corley and R. Lorenz, “Rotor position and velocity estimation for a permanent magnet synchronous machine at standstill and high speeds”, *31th IAS Annual Meeting and World Conference on Industry Applications*, pp. 36–41 (1996).





## Injection de signal et contrôle « sans capteurs » des moteurs électriques

**Résumé :** Cette thèse propose une étude approfondie de certains aspects des algorithmes de contrôle « sans capteur ». Grâce aux progrès faits en électronique, ces algorithmes sont devenus ces dernières années un standard que les clients attendent de tous les variateurs de vitesse pour tous les moteurs électriques. Cependant, le contrôle « sans capteur » des moteurs électriques à basse vitesse est particulièrement difficile à cause d'une limitation théorique expliquée ici par une étude d'observabilité. L'injection de signal est une technique prometteuse pour contourner ce problème, mais ses effets demeurent mal compris. En particulier le traditionnel modèle sinusoïdal non-saturé ne permet pas d'expliquer les résultats expérimentaux. Par conséquent, on propose ici une nouvelle méthode pour modéliser les moteurs électriques. Elle est nettement plus simple que les approches traditionnelles et permet de justifier rigoureusement la modélisation de la saturation dans le repère  $dq$  fictif. Les effets de l'injection de signal sont ensuite expliqués grâce à une séparation des échelles de temps. Replacée dans le contexte plus général des systèmes non-linéaires, elle s'avère être une technique permettant d'obtenir des informations supplémentaires sans ajouter de capteur. Les informations ainsi obtenues permettent théoriquement le contrôle des moteurs électriques « sans capteur » à basse vitesse, mais la mise en œuvre de cette solution pour certains types de moteurs peut demeurer compliquée à cause de contraintes industrielles. On montre aussi comment les modèles proposés peuvent être calibrés expérimentalement pour le cas du Moteur Synchronique à Reluctance et du Moteur à Induction sans charge. À cause du manque de mesures et d'effets liés à l'hystérésis dans les matériaux ferromagnétiques, on n'a malheureusement pas réussi à obtenir un modèle expliquant le comportement du Moteur à Induction en charge. Par ailleurs, grâce à la similarité entre les moteurs électriques mise en évidence par l'approche de modélisation proposée ici, on a pu concevoir une loi permettant de contrôler aussi bien un Moteur Synchronique à Reluctance que n'importe quel Moteur Synchronique à Aimants Permanents.

**Mots clés :** Contrôle non-linéaire, Moteurs électriques, Modélisation, Contrôle sans capteurs, Injection de signal

### Signal injection and “sensorless” control of electric motors

**Abstract:** This thesis proposes an in-depth study of some aspects of “sensorless” control algorithms for electric machines. Over the past few years, thanks to the progress made in electronics, “sensorless” control laws became a standard expected from any variable speed drive for any electric motor. However low-speed “sensorless” operation of electric motors is inherently difficult, due to a theoretical limitation explained here by an observability study. Signal injection is a promising solution to circumvent this limitation, but its effects are not yet fully understood. In particular, experimental results are not explained by traditional unsaturated sinusoidal models for electric motors. Hence a new modeling approach for electric motors is proposed here. It is much simpler than the usual ones and explains thoroughly why saturation can be modeled in the nonphysical  $dq$  frame. Signal injection effects are then explained using a multiple time-scale approach and, when put into the general context of nonlinear systems, it turns out to be a technique which allows to obtain more information without adding sensors. Thanks to this additional information, “sensorless” control of electric motors becomes theoretically possible, even though the implementation remains challenging due to industrial constraints. Models for the Synchronous Reluctance Motor and the Induction Motor at no load are designed using the proposed approach and calibrated on experimental data but the procedure failed for the Induction Motor under load due to a lack of measurements combined to hysteresis effects. Besides, thanks to the similarities between electric motors, underlined by the proposed modeling approach, we are able to generalize the proof of a “sensorless” control law designed for Synchronous Reluctance Motors to any kind of Permanent Magnet Synchronous Motor.

**Keywords:** Nonlinear control, electric motors, modeling, Sensorless control, Signal injection